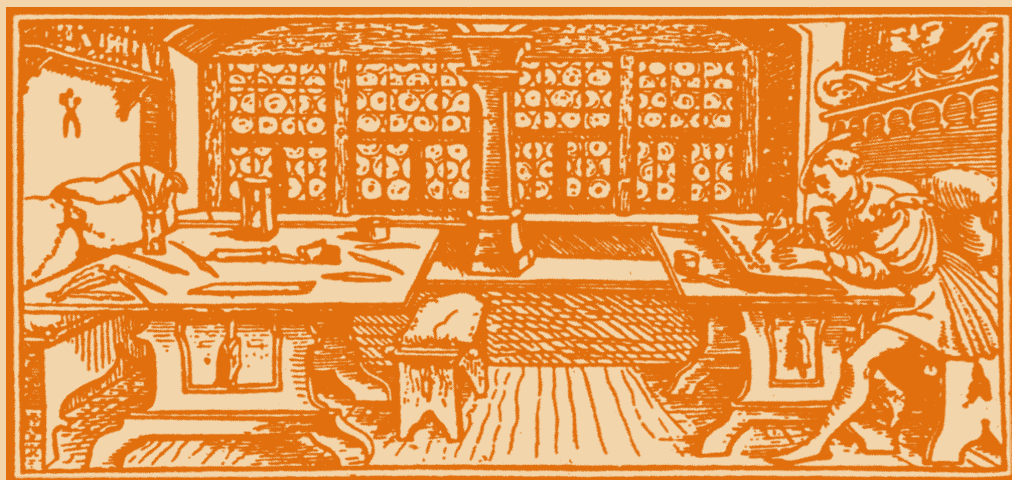


STUDIA

UNIVERSITATIS
BABEȘ-BOLYAI

C h e m i a

C L U J - N A P O C A 2 0 0 5



STUDIA UNIVERSITATIS BABEȘ-BOLYAI CHEMIA

1

EDITORIAL OFFICE: Republicii no. 24, 400015 Cluj-Napoca ♦ Phone 0264-40.53.52

SUMAR - CONTENTS - SOMMAIRE - INHALT

| | |
|--|-----|
| C. G. ILEA, S. DORNEANU, A. IMRE, P. ILEA, Reticulated vitreous carbon (RVC) electrode reactor for copper ions removal from dilute solutions | 3 |
| R. SILAGHI-DUMITRESCU, I. SILAGHI-DUMITRESCU, Discontinuum between ferrous-superoxo and ferric-peroxo in heme $[\text{FeO}_2]^9$ complexes? | 11 |
| R. SILAGHI-DUMITRESCU, "High-valent" ferryl-oxo complexes: how "high" are they really? | 17 |
| M. TOMOAIA-COTISEL, V.-D. POP, G. TOMOAIA, A. MOCANU, C. RACZ, C.-R. ISPAS, O. PASCU, O. C. BOROSTEAN, Atomic force microscopy studies of Langmuir-Blodgett films. 4. The influence of aluminium substrate on dipalmitoyl phosphatidylcholine nanolayers | 23 |
| M. TOMOAIA-COTISEL, C. RACZ, G. TOMOAIA, C. FLOARE, R. TÖTOS, L. BOBOS, O. PASCU, A. DUMITRU, Molecular structure and monolayer properties of some carotenoids | 39 |
| G. TOMOAIA, M. TOMOAIA-COTISEL, C. RACZ, C.-R. ISPAS, C. FLOARE, Langmuir kinetics and adsorption mechanism at the oil/water interface | 47 |
| A. MOCANU, G. TOMOAIA, C. FLOARE, R. TÖTOS, O.-C. BOROSTEAN, M. TOMOAIA-COTISEL, Thermodynamic approach on specific interactions in lipid and carotenoid nanofilms | 59 |
| S. A. SPINEAN, G. L. TURDEAN, I. C. POPESCU, Biosensor for amperometric detection of catechol based on mushroom tissue and a methylene green-nafion modified electrode | 67 |
| S. DRAGAN, M. DRAGAN, Theoretische beschreibung der kristallisation aus überkritischen gasen in poröser matrix | 75 |
| S. DRAGAN, M. DRAGAN, Experimental study of dry desulphurization process with calcium oxide. Characterization of calcium oxide structure | 89 |
| A. GHIRISAN, A. POP, M. MOCEANU, V. MICLAUS, Sedimentation. Koagulation. Flocculation. II. Anwendung polymerer flockungsmittel | 97 |
| A. POP, A. GHIRISAN, S. DRAGAN, Beschreibung des hydrodynamischen models des druckverlustes durch eine katalysatorschicht | 105 |
| A. GHIRISAN, M. AZAD, Sedimentation und flockung der hefesuspension | 113 |

| | |
|---|-----|
| V. MICLAUS, I. BROS, Z. MOLDOVAN, C. CIMPOIU, E. SURDUCAN, N. PALIBRODA, The identification by MS and GC/MS of photodegradation products of Indomethacin ointment..... | 121 |
| M. STAN, M. LANG, A. SAVALL, K.-G. SERANO, E. WEISS, M. JITARU, Voltammetric investigation of some food and textile dyes..... | 129 |
| M. JITARU, L. R. MANDOC, C. MIHAI, O. TUDORAN, Electrochemical behavior of phenols in aqueous solution – fundamentals for their electrochemical degradation in waste waters | 137 |
| M. SOCOL, I. BALDEA, An alternative application of flow graph theory in chemistry, pharmacokinetics and chemical engineering processes..... | 143 |
| G.-C. BUCSE, I. BALDEA, Kinetics and mechanism of p-xylene oxidation by Ce(IV) in aqueous acid medium. LFER as an argument to the oxidation mechanism..... | 157 |
| L. VLASE, I. BALDEA, S. LEUCUTA, L. RUS, L. COPOLOVICI, Kinetic study on Omeprazole acid reaction at different pH values by using HPLC..... | 169 |
| L. M. MURESAN, C. ISVORANU, Composite carbon electrode with enhanced stability based on polyaniline incorporating prussian blue for amperometric detection of H ₂ O ₂ | 175 |
| T. FRENTIU, M. PONTA, E. DARVASI, M. URSU, M. SENIL, E. CORDOS, Comparative study of digestion procedures of soils and water sediments using different HCl/HNO ₃ ratios for multielemental determination..... | 183 |
| M. PONTA, T. FRENTIU, E. DARVASI, A. BONDA, E. CORDOS, Environmental and occupational exposure to Cr, Cu, Pb and Zn of population in Baia-Mare using as index the absorption of contaminants in hair..... | 193 |
| C. BERGHIAN, N. PLE, A. TURCK, M. DARABANTU, First report on 3,7-dioxar-1-azabicyclo[3.3.0]oct-c-5-ylmethoxy system substituting s-triazine..... | 201 |
| M. PINTEA, M. DARABANTU, M. FAZEKAS, P. LAMEIRAS, C. BERGHIAN, I. DELHOM, C. BELE, N. PLE, First synthesis, rotamerism and herbicidal evaluation of substituted s-triazines with serinolic fragments (I): open-chain structures | 209 |
| M. FAZEKAS, M. DARABANTU, M. PINTEA, P. LAMEIRAS, C. BELE, C. BERGHIAN, N. PLE, First synthesis, rotamerism and herbicidal evaluation of substituted s-triazines with serinolic fragments (II): amino-1,3-dioxanes of (1S, 2S)-p-nitrophenylserinols..... | 219 |
| J. BODIS, L. BODIS, J. A. LERCHER, Mass transfer rate during three phase catalytic reductive amination over supported noble metals | 229 |
| R. GROPEANU, T. PANEA, I. PANEA, Synthesis and structure assignment of some new alkyl-(10H-phenothiazin-3-yl)-carbonates | 237 |
| R. GROPEANU, A. WOJCZECOWSKI-POP, M. TINTAS, R. TURDEAN, I. GROSU, Synthesis and stereochemistry of a new series of 2,2'-disubstituted-5,5-bis(bromomethyl)-1,3-dioxanes..... | 247 |
| B. R. H. MISCA, Is it possible to apply unitary mathematical treatment to fluid flow? | 253 |
| E. M. RUS, G. TARALUNGA, D. M. CONSTANTIN, Electrochemical behaviour of OLT-35 low carbon steel in alkaline (1M KOH) aqueous solution | 261 |
| G. TARALUNGA, CS. BOLLA, E. M. RUS, D. M. CONSTANTIN, Electrochemical power sources with RbAg ₄ I ₅ | 271 |
| C. CORMOS, A.-M. CORMOS, S. AGACHI, Modeling and simulation of the carbonation process of ammoniacal brine using CHEMCAD | 277 |
| A.-M. CORMOS, C. CORMOS, A. FRIEDL, S. AGACHI, Modeling and simulation of the scrubbing unit waste incineration plant | 289 |
| S. RADA, I. SILAGHI-DUMITRESCU, Structural, energetic and electronic properties of pure/doped BN nanotubes | 297 |

RETICULATED VITREOUS CARBON (RVC) ELECTRODE REACTOR FOR COPPER IONS REMOVAL FROM DILUTE SOLUTIONS

C. G. ILEA^{*}, S. DORNEANU^{**}, A. IMRE^{*}, P. ILEA^{**}

*"Babes-Bolyai" University, Faculty of Chemistry and Chemical Engineering
Department of Chemical Engineering, ^{*} Department of Physical Chemistry
11 Arany Janos Str. 400028 Cluj-Napoca, Romania. E-mail:pilea@chem.ubbcluj.ro*

ABSTRACT. The present work shows the results of a Cu^{2+} electroextraction test from a diluted solution (500 ppm) using an electrochemical reactor with a reticulated vitreous carbon cathode. This technique allows the recovery of approximately 90% of the copper ions from the solution. A mathematical model for the design of an electrochemical reactor for Cu^{2+} electroextraction was built. Using the geometric dimensions of the designed electrochemical reactor, a simulation of the electroextraction process was done in order to compare the calculated data with the experimental ones. A good agreement is observed and small differences were recorded only at the end of the experiment.

INTRODUCTION

Nowadays, metal ion removal from wastewaters is one of the main environmental issues and also one of the most important applications of cathodic treatment of aqueous effluents [1-2]. In this context, this research was focused on the electrochemical removal of copper from dilute wastewater. Copper is one of the main pollutants and it also has a great economical importance. Its recovery in a pure state is greatly desired and it can only be achieved using an electrochemical method. Due to the possibility of a high dilution of the wastewater, the electrochemical recovery method must use a mass transfer enhancement technique. Using a volumic cathode such as a reticulated vitreous carbon (RVC) cathode [3] is one of the widely used options. Therefore, the main objective of the following work is to study the perspective of copper ion removal from diluted wastewaters with the aid of a RVC electrode. This was done via an experimental research using a laboratory scale electrochemical reactor (ER) equipped with a RVC cathode. The main experimental parameters of the process were identified and evaluated. Also, in order to design a continuous ER for wastewater processing, a mathematical model of the process was elaborated.

EXPERIMENTAL RESULTS

The experimental set-up includes a home-made cylindrical ER equipped with a cylindrical working electrode (RVC, 20 ppi, $\Phi_{\text{out}} = 24$ mm, $\Phi_{\text{in}} = 14$ mm, $h = 12$ mm) and a concentric cylindrical sieve acting as a counter electrode (lead with 1% Ag, $\Phi_{\text{out}} = 10$ mm, $\Phi_{\text{in}} = 8$ mm, $h = 12$ mm). The counter electrode is placed inside the working electrode as it can be observed in Figure 1.

Potentiostatic measurements at room temperature were performed using an analogical potentiostat controlled by a HP Kayak PC via a National Instruments PCI 6024E data acquisition board. LabView5.1® software (National Instruments)

was used for the experiment control and data acquisition. The synthetic electrolyte solution (500 ppm Cu^{2+} , 25°C) was recycled using a centrifugal pump.

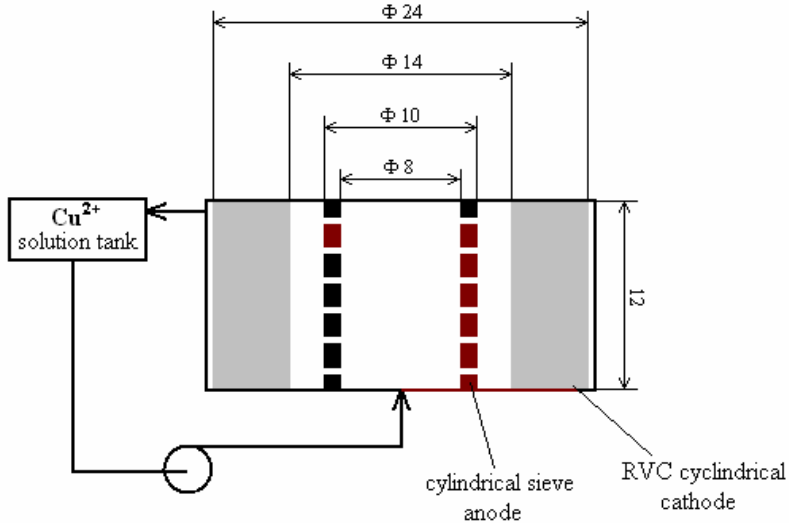


Figure 1. Scheme of the laboratory scale ER for the Cu^{2+} ions recovery

In order to estimate the concentration of copper ions, reduction limiting current measurements were performed using a Cu rotating disk electrode (RDE). Figure 2 presents the calibration plot for the limiting current vs. Cu^{2+} electrolyte concentration recorded at different rotation velocities of the RDE.

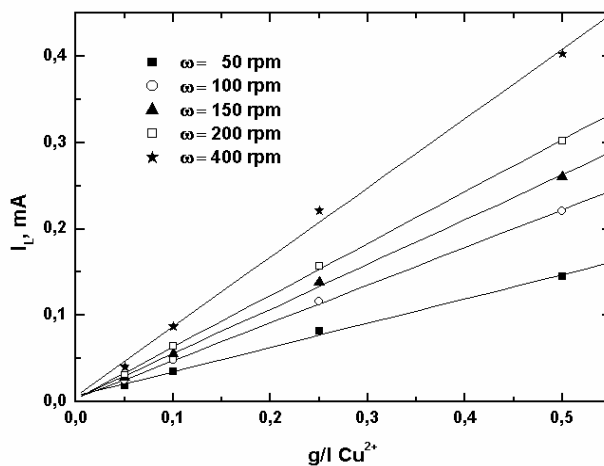


Figure 2. Limiting current vs. Cu^{2+} concentration calibration plot at different RDE rotation velocities, ω .

A Cu^{2+} electroextraction test was done with the experimental ER setup. Data for a series of successive cathodic extractions, performed in potentiostatic conditions ($E = -0.400 \text{ V/SCE}$), are presented in the Table.1.

The results presented in Table 1 show that it is possible to decrease the Cu^{2+} concentration with one order of magnitude, simultaneously with a 15% decrease of the initial cell voltage.

Table.1.

Experimental results for successive cathodic extractions,
performed in potentiostatic conditions ($E = -0.400 \text{ V/SCE}$);
volume of solution = 75mL, initial concentration of $\text{Cu}^{2+} = 500 \text{ ppm}$.

| Time (min) | Q (A s) | $\text{C}_{\text{Cu}^{2+}}^*$ (ppm) | Cell voltage (V) | Current efficiency (%) |
|------------|---------|-------------------------------------|------------------|------------------------|
| 15 | 30,36 | 388 | 4,0 | 84 |
| 30 | 37,31 | 271 | 3,9 | 71 |
| 45 | 42,82 | 141 | 3,7 | 69 |
| 60 | 33,27 | 51 | 3,4 | 62 |

*final concentration of Cu^{2+} ions

This test also shows that approximately 90% of the initial copper can be recovered during 60 minutes of electroextraction.

REACTOR DESIGN MODEL

A mathematical model was elaborated in order to obtain the geometric characteristics of a continuous ER for the recovery of Cu^{2+} ions from dilute wastewaters. The main purpose of this model is to design a proper cylindrical RVC cathode in order to achieve the desired conversion of the Cu^{2+} ions. The unknown variables of the model were: the mass transfer coefficient – k_m ; the thickness of the cylindrical cathode (CC) – δ ; the length of the CC – L ; the inner diameter of the CC – d_1 . In order to uniquely determine their values, four equations must be used. Thus, the equations of the model are [4, 5, 7]:

1) The Plug Flow Reactor design equation:

$$X = 1 - e^{-\frac{k_m \cdot A_e \cdot L}{\bar{v}}}, \quad (1)$$

where X represents the desired conversion; A_e – the specific area of the RVC (20 ppi, $1038 \text{ m}^2/\text{m}^3$ [6]);

$$\bar{v} = \frac{V_f}{\frac{\pi}{4} [(d_1 + 2 \cdot \delta)^2 - d_1^2]} \quad (2)$$

is the average velocity of the liquid flow inside the reactor and V_f is wastewater feed flow rate.

2) The mass transfer equation:

$$\text{Sh} = a \cdot \text{Re}^b \cdot \text{Sc}^c, \quad (3)$$

where
$$Sh = \frac{k_m \cdot 2 \cdot \delta}{D_{Cu^{2+}}} \quad (4)$$

is the Sherwood number;

$$Re = \frac{\bar{v} \cdot 2 \cdot \delta}{\nu} \quad (5)$$

is the Reynolds number;

$$Sc = \frac{\nu}{D_{Cu^{2+}}} \quad (6)$$

is the Schmidt number; according to [4] the exponent values are: $a = 1.44$, $b = 0.58$, $c = 1/3$; the Cu^{2+} ion diffusion coefficient is $D_{Cu^{2+}} = 7.6 \cdot 10^{-10} \text{ (m}^2/\text{s)}$;

$\nu = 1.22 \cdot 10^{-6} \text{ (m}^2/\text{s)}$ is the cinematic viscosity.

3) The limiting current equation:

$$\frac{I_L}{A_e \cdot V} = z \cdot F \cdot k_m \cdot c_{in} \quad (7)$$

where I_L is the limiting current; V is the volume of the **CC**; $z = 2$ is the number of transferred electrons for the cathodic reaction; $F = 96487 \text{ As/Eg}$, is the Faraday number; $c_{in} = 500 \text{ ppm}$ is the Cu^{2+} inlet concentration. The left term of the equation, representing the limiting current density, was experimentally determined and a value of $6,4 \text{ A/m}^2$ was used in order to solve the model.

4) A dimensional restriction:

In order to have a proper geometric shape of the reactor, the following restriction should be fulfilled:

$$d_i/\delta = 3.5. \quad (8)$$

The model was solved using the MATLAB® software for different values of conversions and wastewater feed flow rates. For all simulations, the determined value for the mass transfer coefficient was $k_m = 4.2 \cdot 10^{-6} \text{ m/s}$. The dependence of the reactor (cathode) length with respect to different desired conversion values, at different feed flow rates is presented in Figure 3. Figures 4 and 5 present the dependence of the cathode thickness and inner diameter, respectively, versus wastewater feed flow rate values at different desired conversions.

The data presented in figures 3-5 allow the design of an ER with an RVC cathode taking into consideration the initial concentration, the required conversion value and the mass transport parameters. Given the fact that each, the galvanostatic or the potetiostatic operation, has its own advantages and disadvantages, it is possible to determine the most advantageous alternative, based on the proposed model taking into account criteria like the duration of wastewater processing and/or the required energy consumption.

Using the geometric dimensions of the ER given by the design model, an electroextraction process simulation was done in order to compare the data with the experimental results. Figure 6 presents a comparison between the model based extraction simulation and the experimental data. A good agreement between them can be observed.

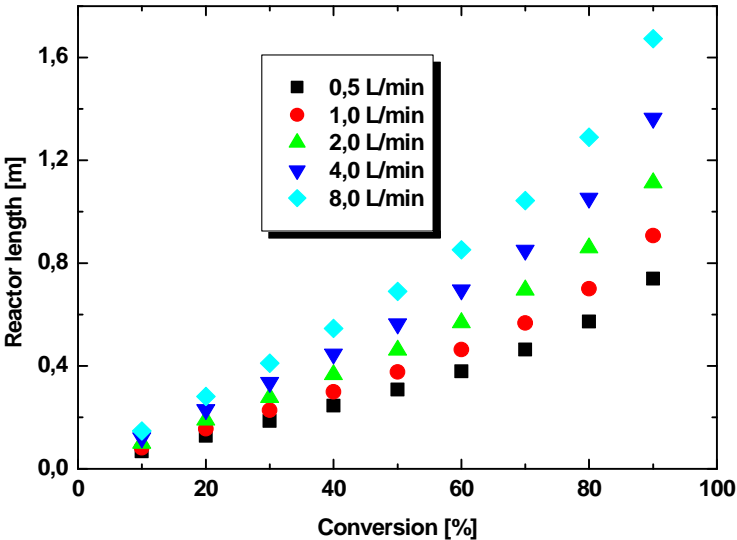


Figure 3. The influence of desired conversion on the reactor length at different feed flow rate values

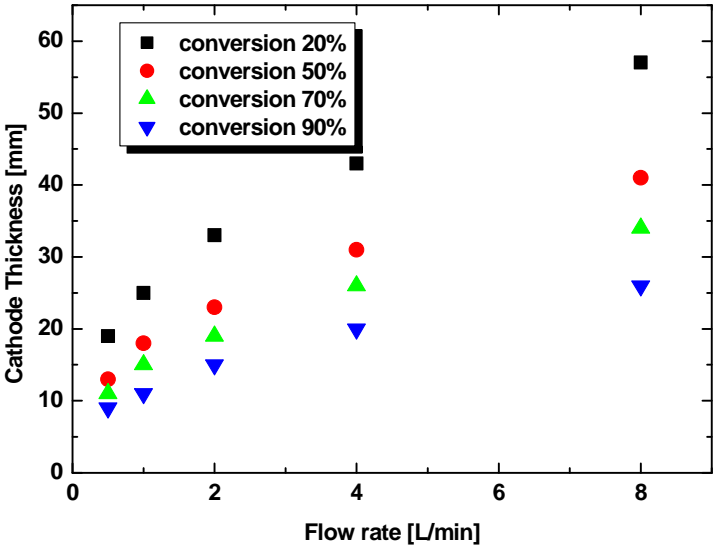


Figure 4. The influence of the feed flow rate on the RVC cathode thickness at different conversion values

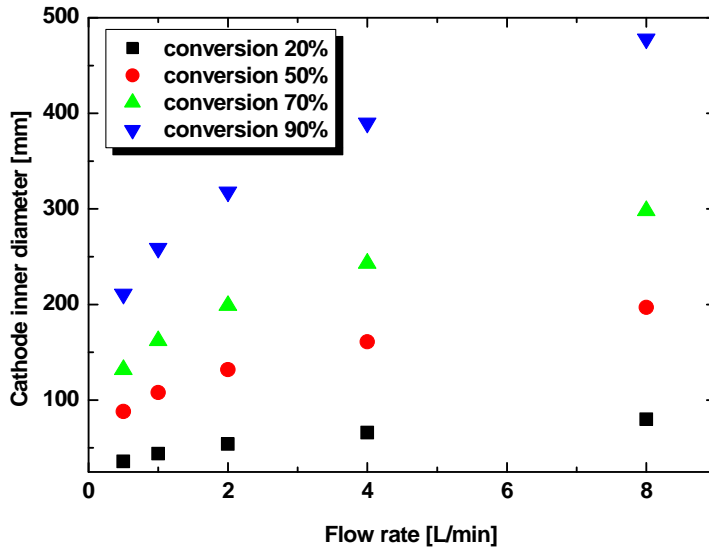


Figure 5. The influence of feed flow rate on the RVC cathode inner diameter for different conversion values

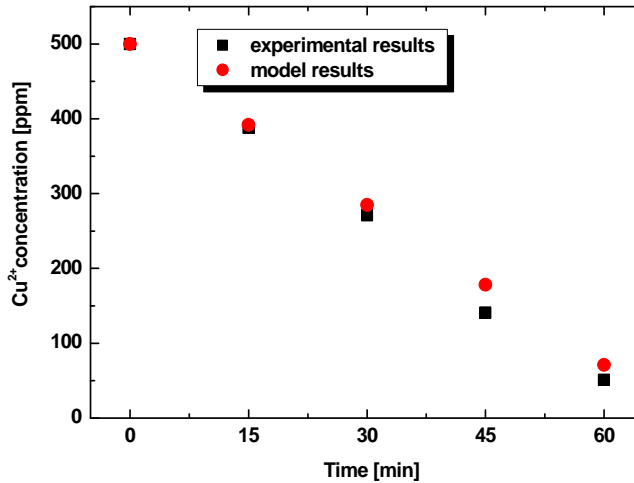


Figure 6. Comparison between experimental and mathematical model results

CONCLUSIONS

The model based design shows that reasonable dimensions for the ER can be obtained for the explored range of flow-rates at a desired conversion.

The reactor length increases with the desired conversion and the flow area, dependent on the inner diameter and the thickness of the RVC cathode. It also increases with the desired feed flow rate value.

Comparing the theoretical model with the experimental results, a good agreement is observed, only small differences being observed at the end of the experiment.

REFERENCES

- [1] K. Jüttner, U. Galla, H. Schmieder, *Electrochim. Acta*, **2000**, 45, 2575.
- [2] F.C. Walsh, *Pure Appl. Chem.*, **2001**, 73, 1819.
- [3] J.C. Bazan, J.M. Bisang, *J. Appl. Electrochem.*, **2004**, 34, 501
- [4] F. Coeuret, A. Storck, "Génie Electrochimique" (Technique et Documentation, Paris), 1984.
- [5] K. Scott, "Electrochemical Processes for Clean Technology" (The Royal Society of Chemistry, Cambridge, UK), 1995.
- [6] Energy Research and Generation Inc., „Reticulated Vitreous Carbon (An exciting new material)", 1976, prospect.
- [7] C.G. Ilea, "Modelling and optimization of the Cu²⁺ ions recovery from waste waters by electrochemical extraction", Diploma Thesis, "Babes-Bolyai" University, Cluj-Napoca, 2002.

DISCONTINUUM BETWEEN FERROUS-SUPEROXO AND FERRIC-PEROXO IN HEME $[\text{FeO}_2]^9$ COMPLEXES?

RADU SILAGHI-DUMITRESCU^{a,b*} and IOAN SILAGHI-DUMITRESCU^b

^aDepartment of Chemistry and Center for Metalloenzyme Studies, University of Georgia, Athens, Georgia 30602, U.S.A., and ^bDepartment of Chemistry, "Babeș-Bolyai" University, Cluj-Napoca RO-3400, Romania.

ABSTRACT. Low-spin $[\text{FeO}_2]^9$ complexes (where the superscript denotes the sum of iron d electrons and dioxygen π^* electrons), generally described as ferric-peroxo or ferrous-superoxo, have been implicated in the catalytic cycles of heme and non-heme proteins. Experimental observation of these complexes, mainly by ENDOR spectroscopy, has led to two distinct descriptions of heme $[\text{FeO}_2]^9$, depending on whether or not hydrogen bonding to the oxygen ligand is available. Hydrogen-bonded $[\text{FeO}_2]^9$ were described as ferric-peroxo, while non hydrogen-bonded $[\text{FeO}_2]^9$ were described as ferrous-superoxo. Reported here is a DFT investigation of the effects of hydrogen bonding on the structure of heme $[\text{FeO}_2]^9$ complexes. Calculated bond lengths, spin densities and hyperfine couplings all argue against a ferrous-superoxo/ferric-peroxo discontinuum. Possible implications of this finding are discussed.

INTRODUCTION

$S=1/2$ $[\text{FeO}_2]^9$ complexes,[1] generally described as ferric-peroxo or ferrous-superoxo,[2-13] have been implicated in the catalytic cycles of heme and non-heme proteins. Experimental observation of such hemoprotein complexes, mainly by cryoradiolytic ENDOR spectroscopy,[3, 5-9, 14, 15] has led to two distinct descriptions of heme $[\text{FeO}_2]^9$, depending on whether or not hydrogen bonding to the oxygen ligand is available. Hydrogen-bonded $[\text{FeO}_2]^9$, as observed in cytochrome P450,[6-9] nitric oxide synthase,[5] horseradish peroxidase,[14, 15] hemoglobin and myoglobin,[4, 16] were described as ferric-peroxo. Non hydrogen-bonded $[\text{FeO}_2]^9$, as observed in a hemoglobin variant and in model compounds,[3] were described as ferrous-superoxo. Intrigued by this apparent discontinuum, we report a DFT investigation of the effects of hydrogen bonding on the structure of heme $[\text{FeO}_2]^9$ complexes. Calculated bond lengths, spin densities and hyperfine couplings all argue against a ferrous-superoxo/ferric-peroxo discontinuum.

RESULTS AND DISCUSSION

Figure 1 shows models examined in the present study,[17-19] mimicking the active sites of thiolate- and histidine-ligated $[\text{FeO}_2]^9$ previously characterized via cryoradiolytic spectroscopies.[3, 5-7, 14, 16] Calculated bond lengths, spin densities and charges for these models (cf. Table 1) suggest a strong superoxo character for the dioxygenic ligand, consistent with previous theoretical findings.[10, 13] An increased peroxo character, manifested in longer O-O bond lengths, higher oxygen charges, and lower oxygen spin densities, is seen upon addition of hydrogen bond donors and upon inclusion of solvation effects. There is no evidence, however, for a superoxo-peroxo *discontinuum*.

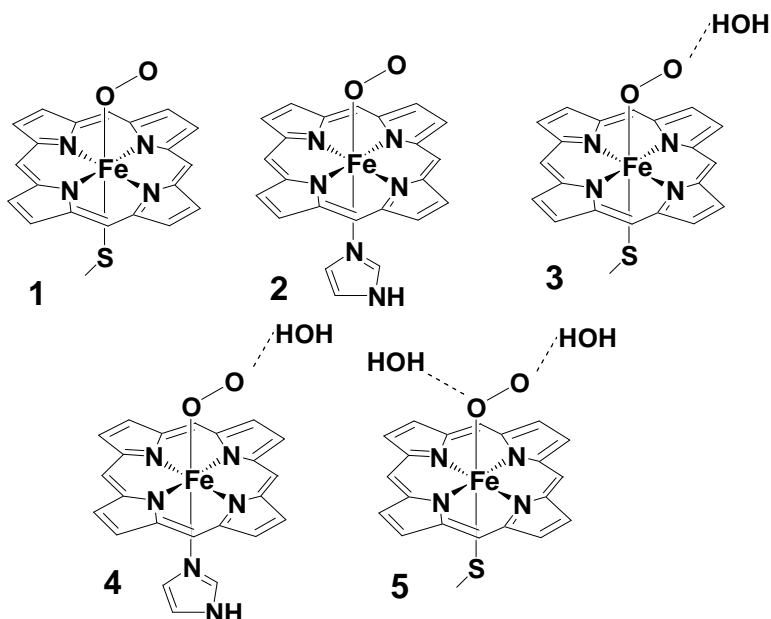


Figure 1. $[\text{FeO}_2]^9$ models employed in the present study.[20]

Table 1.

Calculated bond lengths (Å) and Mulliken partial atomic charges and spin densities (the latter shown in parentheses), for Figure 1 models.

| model | Fe-O | O-O | Fe-X | Fe | O1 ^a | O2 ^b |
|----------------------|------|------|------|-------------|-----------------|-----------------|
| 1 | 1.93 | 1.32 | 2.43 | 1.12 (0.80) | -0.25 (0.41) | -0.23 (0.59) |
| 2 | 1.90 | 1.31 | 2.14 | 1.27 (0.03) | -0.26 (0.38) | -0.23 (0.40) |
| 3 | 1.92 | 1.34 | 2.42 | 1.09 (0.39) | -0.28 (0.38) | -0.31 (0.38) |
| 4 | 1.88 | 1.33 | 2.13 | 1.26 (0.17) | -0.26 (0.40) | -0.26 (0.43) |
| 5^c | 1.94 | 1.35 | 2.39 | 1.05 (0.57) | -0.34 (0.33) | -0.39 (0.34) |

^airon-bound oxygen atom. ^bnon iron-bound oxygen atom ^csolvated model ($\epsilon=4.333$)

Table 2 shows DFT-calculated hyperfine couplings for oxygen and protons in the Figure 1 models.[21] For reference, we include in Table 1 calculated parameters for free superoxide as well as for a number of related heme adducts[8, 13, 22, 23]: ferric-hydroxo (model of hemoprotein resting states), ferric-hydroperoxo (resulted from protonation of $[\text{FeO}_2]^9$), perferryl[24]-oxo (resulted from heterolytic cleavage of the O-O bond in the ferric-hydroperoxo complexes), and perferryl-hydroxo (resulted from protonation of the perferryl-oxo).

Proton couplings shown in Table 1 agree well with experimental observations.[3-7, 16, 25] Thus, protons hydrogen bonded to the “superoxo” ligand in $[\text{FeO}_2]^9$ feature couplings of the same order of magnitude as the hydroperoxo protons, all of which are significantly more larger than porphyrin protons.

Table 2.

Calculated isotropic Fermi contact couplings (italics) and anisotropic spin dipole couplings (^{17}O values given in Gauss, ^1H values in MHz). Oxygen atoms labeled as in Table 1.

| model | O1 | O2 | H ^a |
|--------------------------|---------------------------|---------------------------|---|
| OO ⁻ | -8.5 24.3/22.0/-46.3 | -8.5 24.3/22.0/-46.3 | - |
| Fe(III)-OH ^b | -3.50 8.0/7.2/-15.2 | - | -6.58 -8.9/-7.9/16.8 |
| Fe(V)-OH ^b | -6.92 10.7/4.6/-15.3 | - | 4.40 -15.0/-14.1/29.1 |
| Fe(V)=O ^b | -10.07 30.8/-1.7/-29.0 | - | - |
| Fe(III)-OOH ^b | -5.37 13.0/12.0/-25.0 | -1.39 4.2/3.5/-7.7 | -2.01 -6.5/1.3/5.2 |
| 1 | -10.96 24.8/23.2/-47.9 | -11.81 30.6/30.4/-61.0 | - |
| 2 | -8.97 22.9/18.4/-41.3 | -9.72 26.1/21.8/-48.0 | - |
| 3 | -10.90 22.4/20.1/-42.5 | -8.76 20.2/19.0/-39.2 | -1.15 -8.5/-8.3/16.9 |
| 4 | -10.14 23.4/19.8/-43.2 | -9.61 23.0/20.2/-43.1 | -2.02 -9.34/-8.9/18.2 |
| 5 ^b | -10.35 19.7/18.5/-38.1 | -7.57 17.7/17.4/-35.1 | 0.10 -4.8/ -4.3/ 9.1 -0.39 -5.0/-4.9/9.9 |

^ahydroperoxo or hydroxo protons, or water protons hydrogen-bonded to the superoxo ligand.

^bheme-thiolate models. ^csolvated model ($\epsilon=4.333$)

Consistent with expectations based on spin densities (Table 1, Refs.[10, 13]), the magnitude of the calculated ^{17}O coupling increases in the order Fe(III)-OH-Fe(III)-OOH ~perferryl-hydroxo < perferryl-oxo-[FeO₂]⁹-superoxide. For [FeO₂]⁹, *no evidence is seen for a discontinuum*, where addition of one or more hydrogen bonds, and/or inclusion of dielectric effects, would induce a shift from a purely ferric-peroxo to purely ferrous-superoxo description of [FeO₂]⁹.

Models **2** and **1** feature ^{17}O couplings essentially identical to free superoxide, consistent with experimental data on non-hydrogen bonded [FeO₂]⁹. [3] The calculated A_{zz} parameters for free superoxide and for **2** are 20-25 G lower than experimental values [3] but are still >20 G higher than calculated for ferric-hydro(per)oxo complexes - thus reproducing the experimental trend. [3, 5-7, 9, 16]

[FeO₂]⁹ hemoprotein species, trapped by cryoradiolysis of [FeO₂]⁸ complexes in various hemoproteins, were clearly described as ferric-peroxo, on the basis of a typical ferric EPR signal and of very reduced ^{17}O hyperfine coupling (only one of the two oxygen atoms in fact exhibited readily detectable coupling, of ~7 G). [3, 5-7, 9, 16] By contrast, with a hemoglobin lacking hydrogen bonding interactions to the dioxygenic ligand, the cryoradiolytically trapped [FeO₂]⁹ species exhibited a superoxide-like EPR signal, and ^{17}O hyperfine couplings from *both* oxygen atoms, with values essentially

identical to those reported for free superoxide. Responsible for this apparent ferric-peroxo/ferrous-superoxo discontinuum was assumed to be hydrogen bonding to the peroxo ligand.[3] Our results now suggest this assumption to be unwarranted, and intriguingly implicate that with most hemoproteins the *first species* detected upon $[\text{FeO}_2]^8$ cryoradiolysis is in fact *already protonated*. A *second species*, formed from the proposed “non-protonated” $[\text{FeO}_2]^9$, was also detected with cryoradiolytic spectroscopies, and was assigned as *protonated* $[\text{FeO}_2]^9$ (ferric-hydroperoxo).[3, 5-7, 14, 16, 25] A *third species* detected in cryoradiolysis experiments with P450, subsequent to “ferric-hydroperoxo”, was a “product-bound” state.[6, 25] Our results now imply either that the second species is an isomer of the first (ferric-hydroperoxo) species, or that the second species in fact represents a state placed *between* “ferric-hydroperoxo” and “product-bound” in the P450 catalytic cycle. For instance, the second species may be a previously unrecognized protonated Compound I – which, as seen in Tables and as pointed out by us elsewhere,[23, 26] would well masquerade as a ferric-hydroperoxo or ferric-hydroxo.

Previous computations on **1** and **2** placed ~one spin unit on the oxygen atoms and negligible spin on the iron. We challenged the obvious ferrous-superoxo assignment[3] with the speculation that **1** and **2** were in fact best described as ferric-superoxo.[13] Results shown here support the latter. The possible meaning of the different degrees of antiferromagnetic coupling/covalence between the ferric center and the porphyrin in **1** and **2** (suggested by Table 1) is currently investigated with more suitable approaches.

EXPERIMENTAL

Geometries were optimized with the BP86 functional, which uses the gradient-corrected exchange functional proposed by Becke (1988),[18] the correlation functional by Perdew (1986),[19] and the DN** numerical basis set (comparable in size to 6-31G**), as implemented in Spartan.[17] For the SCF calculations, a fine grid was used, and the convergence criteria were set to 10^{-6} (for the root-mean square of electron density) and 10^{-8} (energy), respectively. For geometry optimization, convergence criteria were set to 0.001 au (maximum gradient criterion) and 0.0003 (maximum displacement criterion). Charges and spin densities were derived from Mulliken population analyses after DFT geometry optimization. Hyperfine couplings were obtained from UBP86/6-31G**/Gaussian98[21] energy calculations at geometries shown in Table 1.

ACKNOWLEDGMENT. Drs. V. W. Huang and E. D. Coulter (UGA) are thanked for helpful discussions.

REFERENCES

- [1] We use the $[\text{FeO}_2]^9$ notation, as originally proposed by Jackson et al; note, however, that the alternative $[\text{FeO}_2]^6$ notation is used by Hoffman and co-workers.
- [2] R. Silaghi-Dumitrescu, I. Silaghi-Dumitrescu, E. D. Coulter, D. M. Kurtz, Jr., Inorg. Chem. 2003, **42**, 446-456.
- [3] R. Davydov, J. D. Satterlee, H. Fujii, A. Sauer-Masarwa, D. H. Busch, B. M. Hoffman, J. Am. Chem. Soc. 2003, **125**, 16340-16346.

- [4] R. Kappl, M. Hoehn-Berlage, J. Huettermann, N. Bartlett, M. C. Symons, *Biochim. Biophys. Acta* 1985, **827**, 327-343.
- [5] R. Davydov, A. Ledbetter-Rogers, P. Martasek, M. Larukhin, M. Sono, J. H. Dawson, B. S. Siler Masters, B. M. Hoffman, *Biochemistry* 2002, **41**.
- [6] R. Davydov, T. M. Makris, V. Kofman, D. E. Werst, S. L. Sligar, B. M. Hoffman, *J. Am. Chem. Soc.* 2001, **123**, 1403-1415.
- [7] R. Davydov, I. M. MacDonald, T. M. Makris, S. G. Sligar, B. M. Hoffman, *J. Am. Chem. Soc.* 1999, **121**, 10654-10655.
- [8] I. Schlichting, J. Berendzen, K. Chu, R. M. Sweet, D. Ringe, G. A. Petsko, S. G. Sligar, *Science* 2000, **287**, 1615-1622.
- [9] D. E. Benson, K. S. Suslick, S. G. Sligar, *Biochemistry* 1997, **36**, 5104-5107.
- [10] D. Harris, G. Loew, L. Waskell, *J. Am. Chem. Soc.* 1998, **120**, 4308-4318.
- [11] T. A. Jackson, E. Yikilmaz, A. F. Miller, T. C. Brunold, *J. Am. Chem. Soc.* 2003, **125**, 10833-10845.
- [12] R. Carrasco, I. Morgenstern-Badarau, J. Cano, *Chem. Commun.* 2003, 436-437.
- [13] R. Silaghi-Dumitrescu, I. Silaghi-Dumitrescu, *Rev. Roum. Chim.* 2004, **3-4**, 257-268.
- [14] I. G. Denisov, T. M. Makris, S. G. Sligar, *J. Biol. Chem.* 2002, **277**, 42706-42710.
- [15] G. I. Berglund, G. H. Carlsson, A. T. Smith, H. Szoke, A. Henriksen, J. Hajdu, *Nature* 2002, **417**, 463-468.
- [16] R. M. Davydov, T. Yoshida, M. Ikeda-Saito, B. M. Hoffman, *J. Am. Chem. Soc.* 1999, **121**, 10656-10657.
- [17] Spartan 5.0, Wavefunction, Inc., 18401 Von Karman Avenue Suite 18370, Irvine, CA 92612 U.S.A.
- [18] A. D. Becke, *Phys. Rev.* 1988, 3098-3100.
- [19] J. P. Perdew, *Phys. Rev.* 1986, **B33**, 8822-8824.
- [20] Results consistent with those shown in Table 1 were obtained with other models, which included hydrogen bonding to the thiolate ligand and a P450 substrate mimic in the form of methane placed within hydrogen bonding distance from the iron-bound oxygen atom.
- [21] Gaussian 98 (Revision A.1), M. J. Frisch, G. W. Trucks, H. B. Schlegel, G. E. Scuseria, M. A. Robb, J. R. Cheeseman, V. G. Zakrzewski, J. A. Montgomery, R. E. Stratmann, J. C. Burant, S. Dapprich, J. M. Millam, A. D. Daniels, K. N. Kudin, M. C. Strain, O. Farkas, J. Tomasi, V. Barone, M. Cossi, R. Cammi, B. Mennucci, C. Pomelli, C. Adamo, S. Clifford, J. Ochterski, G. A. Petersson, P. Y. Ayala, Q. Cui, K. Morokuma, D. K. Malick, A. D. Rabuck, K. Raghavachari, J. B. Foresman, J. Cioslowski, J. V. Ortiz, B. B. Stefanov, G. Liu, A. Liashenko, P. Piskorz, I. Komaromi, R. Gomperts, R. L. Martin, D. J. Fox, T. Keith, M. A. Al-Laham, C. Y. Peng, A. Nanayakkara, C. Gonzalez, M. Challacombe, P. M. W. Gill, B. G. Johnson, W. Chen, M. W. Wong, J. L. Andres, M. Head-Gordon, E. S. Replogle and J. A. Pople, Gaussian, Inc., Pittsburgh PA, 1998.
- [22] M. Sono, M. P. Roach, E. D. Coulter, J. H. Dawson, *Chem. Rev.* 1996, **96**, 2841-2887.
- [23] R. Silaghi-Dumitrescu, D. M. Kurtz Jr., *CHEMTRACTS-Inorg. Chem.* 2003, **16**, 722-728.
- [24] We use the notation "perferryl" for brevity; these species are in fact unanimously described as S=1 Fe(IV) + porphyrin cation radical.
- [25] R. Davydov, V. Kofman, H. Fuji, T. Yoshida, M. Ikeda-saito, B. M. Hoffman, *J. Am. Chem. Soc.* 2002, **124**, 1798-1808.
- [26] R. Silaghi-Dumitrescu, *J. Biol. Inorg. Chem.* 2004, **9**, 471-476.

“HIGH-VALENT” FERRYL-OXO COMPLEXES: HOW “HIGH” ARE THEY REALLY?

RADU SILAGHI-DUMITRESCU

Department of Chemistry and Center for Metalloenzyme Studies, University of Georgia, Athens, Georgia 30602, U.S.A., and Department of Chemistry, “Babes-Bolyai” University, Cluj-Napoca RO-400028, Romania

ABSTRACT. $S=1$ $[\text{FeO}]^{2+}$ complexes are implicated in key biological oxidations with heme and non-heme enzymatic systems. These complexes are unanimously described as $S=1$ Fe(IV) covalently bound to O^{2-} . Reported here are UMP2/6-311+G** results for $S=1$ $[\text{FeO}]^{2+}$ in an octahedral ligand field, intriguingly suggesting that (1) the degree of iron-oxygen covalence may have previously been overestimated, and (2) the limiting description as $\{S=1/2 \text{ Fe(III)} + S=1/2 \text{ O}^{\cdot-}\}$ is more suitable than $\{\text{Fe(IV)} + \text{O}^{2-}\}$.

INTRODUCTION

$S=1$ $[\text{FeO}]^{2+}$ complexes have been implicated in key biological oxidations with heme and non-heme enzymatic systems.[1-3] These complexes are unanimously described as $S=1$ Fe(IV) covalently bound to O^{2-} (cf Scheme 1).[1, 3-11] As reviewed in Ref¹⁰, such description is consistent with extensive experimental data, including magnetic susceptibility, Mössbauer, EPR, NMR, resonance Raman, EXAFS, and X-ray crystallography. Further, semiempirical,[12-14] X- α ,[15] DFT,[6, 8, 9] UHF,[16] RHF and CASSCF[11] calculations yielded pictures consistent with a strongly covalent Fe(IV)-oxo unit.

The main two lines of evidence supporting the Fe(IV)-oxo description come from Mössbauer spectroscopy and computational chemistry. Mössbauer parameters for biologically relevant $S=1$ $[\text{FeO}]^{2+}$ complexes were found to be more consistent with an Fe(IV) description than with Fe(II) or Fe(III).[17-23] While Mössbauer spectroscopy is generally assumed to be an infallible tool for pinpointing iron oxidation states, examples are known to the contrary. For instance, a recent exemplary synergy of spectroscopic, structural, and computational data on $S=1/2$ $[\text{FeNO}]^7$ complexes has shown that in a series of ferrous complexes, changes in the identity of one ligand altered Mössbauer parameters to extents similar to those observed upon a change in formal iron oxidation state.[24]

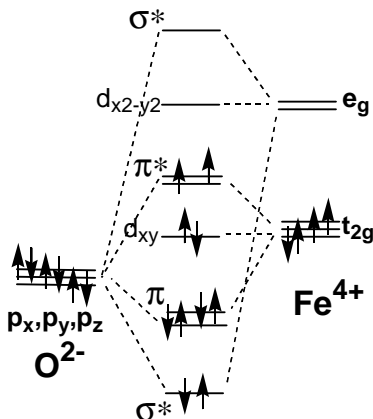
Kohn-Sham (DFT)[6, 8, 9] as well as RHF-CASSCF[11] orbitals computed by various groups have yielded a picture of the Fe-O interaction in $S=1$ $[\text{FeO}]^{2+}$ complexes, consistent with strong Fe(IV)-oxo covalence. The two unpaired electrons were found to be evenly delocalized onto the iron and oxygen atoms, within π^*_{xz} and π^*_{yz} orbitals. The convergence of CASSCF and DFT results on this issue provides a strong theoretical foundation for interpreting the available experimental data.

Previous attempts to provide a detailed molecular orbital description of $S=1$ $[\text{FeO}]^{2+}$ either relied on DFT, or on restricted Hartree-Fock based approaches. Seeking to further our understanding of bonding in these important biological

complexes, we report here on the molecular orbital picture in an octahedral $S=1$ $[\text{FeO}]^{2+}$, obtained with an unrestricted MP2 approach. Intriguingly, we find that (1) the degree of iron-oxygen covalence may have previously been overestimated, and (2) the limiting description as $\{S=1/2 \text{ Fe}^{3+} + S=1/2 \text{ O}^{\cdot-}\}$ is more suitable than $\{\text{Fe(IV)} + \text{O}^{2-}\}$.

RESULTS AND DISCUSSION

Scheme 2 shows the UMP2/6-311+G** molecular orbital diagram for a $S=1$ $[\text{FeO}]^{2+}$ complex in an octahedral environment (for reference, the equivalent diagram obtained with a standard density functional, UBP86, is shown as Supporting Information; the latter agrees entirely with previous RHF/CASSCF and DFT results).[25, 26] First, we note that, as expected (cf. Scheme 1), the iron d_{xy} orbital (38α , 37β) is doubly-occupied, while the d_{z^2} and $d_{x^2-y^2}$ (essentially, 43α , 44α , 44β , 42β) are empty. In the iron-oxygen σ molecular orbital (40α , 39β), the oxygen contribution appears stronger than the iron contribution. This is consistent with a picture where the σ bond is dative ($\text{O}:\rightarrow\text{Fe}$), rather than covalent ($\text{O}^{\cdot-} + \cdot\text{Fe}$).

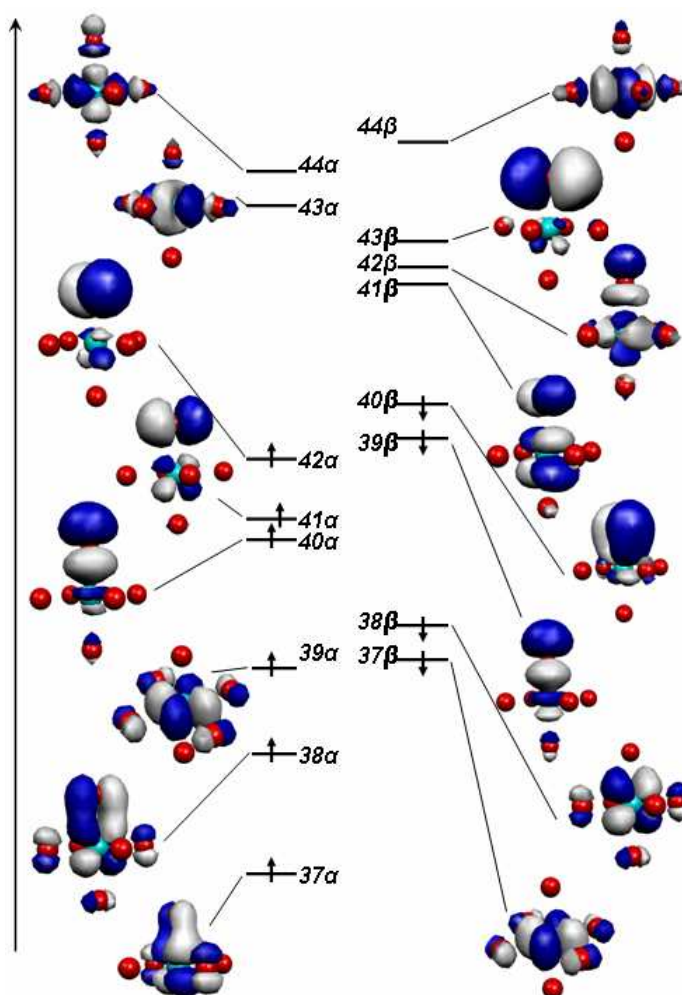


Scheme 1

Also consistent with expectations illustrated by Scheme 1, the two unpaired electrons in Scheme 2 are found to reside in the Fe-O π^* molecular orbitals. Orbital 43β (formally π^*) is empty, and is almost entirely localized onto the oxygen. The corresponding π orbital is accordingly localized on the iron. The other pair of π/π^* orbitals, 40β and 41β , feature the inverse situation: the bonding (occupied) orbital is mainly oxygen-localized, and the anti-bonding (empty) orbital has significant iron character. Thus, the system appears best described as featuring one unpaired electron on the oxygen, and one on the iron – implying a $\text{Fe}^{3+}\text{-O}^{\cdot-}$ description. Finally, notable as a general feature, is the significantly smaller covalence in the orbitals shown in Scheme 2, compared to orbitals obtained from DFT calculations (not shown).

The simplified model used here ignores covalence between iron and its other (“non-oxo”) ligands. Such covalence may lead to intricate orbital mixing, to the extent where the iron-oxygen interaction may appear entirely covalent. Furthermore,

non-covalent effects such as hydrogen bonding are known to affect the polarizability of the iron-oxygen interaction in $S=1$ $[\text{FeO}]^{2+}$ complexes.[9, 27] These effects may well be small, since, as shown in Supporting Information, the same " $\text{Fe}^{3+}+\text{O}$ " description in fact applies to a more realistic, solvated, $S=1$ Fe(IV)=O model, $[\text{Fe}(\text{NH}_3)_4(\text{CN})\text{O}]^{2+}$ (an adduct known to exist experimentally[1], albeit with aliphatic amine rather than ammonia equatorial ligands). Systems such as $S=1$ $[\text{FeO}]^{2+}$ are expected to have low-lying excited states, an issue not explicitly addressed by our computational approach. Thus, to conclude, our proposed " $\text{Fe}^{3+}+\text{O}$ " description is simply a limiting structure. To verify to which extent this limiting structure would be more realistic than the traditional Fe(IV)-oxo limiting structure, more sophisticated treatments of $S=1$ $[\text{FeO}]^{2+}$ complexes are underway.



Scheme 2

The key finding of our study appears to be that $S=1$ $[\text{FeO}]^{2+}$ complexes are far from being as covalent as previously assumed. This (together with the availability of low-lying excited states) differentiates $S=1$ $[\text{FeO}]^{2+}$ from $S=1$ O_2 (another diatomic featuring two singly-occupied π^* orbitals). Unlike molecular oxygen, $[\text{FeO}]^{2+}$ is known to be reactive as an oxygen transfer agent, performing oxygen *atom* insertion in aliphatic C-H bonds.[4] The latter reactivity is much more readily reconciled with our newly-proposed UMP2 description than with the classical “triplet dioxygen-like” description. Beyond this orbital argument, the reactivity of $S=1$ $[\text{FeO}]^{2+}$ (much like $S=1$ O_2) appears to also be governed by spin state conservation. Heme as well as non-heme mononuclear $S=1$ $[\text{FeO}]^{2+}$ complexes in fact exhibit significantly lower reactivity as oxygen transfer agents, compared to their one-electron oxidized counterparts. These latter complexes, known as Compound I in hemoproteins, feature a $S=1/2$ state when the axial ligand trans to the oxygen is a thiolate, and a $S=3/2$ state when the axial ligand is a histidine.[1, 2, 8] This difference in spin states is due to either ferromagnetic or antiferromagnetic coupling between $S=1$ $[\text{FeO}]^{2+}$ and the $S=1/2$ oxidized porphyrin in Compound I.[8] The reaction of Compound I with aliphatic hydrocarbons leads to a product-bound state which is $S=1/2$ Fe(III) with a thiolate ligand (i.e., ground state), but is $S=3/2$ Fe(III) with a histidine ligand (i.e., excited state). Consistently, thiolate-ligated hemoproteins are far more frequently involved in oxygen-transfer reactions than histidine-ligated hemoproteins.[2, 7] Similarly, di-iron non-heme $S=1$ $[\text{FeO}]^{2+}$ complexes are known to be more efficient oxygen atom-transfer reagents than their mononuclear counterparts,[1, 28, 29] with the second iron of the complex possibly playing the same role as the heme of Compound I in preserving spin state along the reaction coordinate. The extent of availability of excited states ($[\text{Fe(IV)-oxo}]$, $[\text{Fe(II)-oxygen atom}]$) for $[\text{FeO}]^{2+}$ complexes is also a likely “switch” whereby the other iron ligands (heme or non-heme) may control oxygen-transfer reactivity.

EXPERIMENTAL

The Gaussian98 suite of programs was used for all calculations. Further details are provided in text.

ACKNOWLEDGMENT. Dr. I. Silaghi-Dumitrescu (UBB) is thanked for helpful discussions.

REFERENCES

- [1] M. Costas, M. P. Mehn, M. P. Jensen, L. J. Que, 2004, DOI: 10.1021/cr020628n.
- [2] M. Sono, M. P. Roach, E. D. Coulter, J. H. Dawson, Chem. Rev. 1996, **96**, 2841-2887.
- [3] A. N. P. Hiner, E. L. Raven, R. N. F. Thorneley, G. Garcia-Canovas, J. N. Rodriguez-Lopez, J. Inorg. Biochem. 2002, **91**, 27-34.
- [4] S. Shaik, S. Cohen, S. P. de Visser, P. K. Sharma, D. Kumar, S. Kozuch, F. Ogliaro, D. Danovich, Eur. J. Inorg. Chem. 2004, 207-226.

- [5] R. Silaghi-Dumitrescu, D. M. Kurtz Jr., CHEMTRACTS-Inorg. Chem. 2003, **16**, 722-728.
- [6] J. C. Schoeneboom, H. Lin, N. Reuter, W. Thiel, S. Cohen, F. Ogliaro, S. Shaik, J. Am. Chem. Soc. 2002, **124**, 8142-8151.
- [7] F. Ogliaro, S. deVisser, S. Shaik, J. Inorg. Biochem. 2002, **91**, 554-567.
- [8] D. L. Harris, Curr. Opin. Chem. Biol. 2001, **5**, 724-735.
- [9] F. Ogliaro, S. Cohen, S. P. de Visser, S. Shaik, J. Am. Chem. Soc. 2000, **122**, 12892-12893.
- [10] H. Kuramochi, L. Noodleman, D. A. Case, J. Am. Chem. Soc. 1997, **119**, 11442-11451.
- [11] S. Yamamoto, J. Teraoka, H. Kashiwagi, J. Chem. Phys. 1988, **88**, 303-312.
- [12] G. H. Loew, Z. Herman, J. Am. Chem. Soc. 1980, **102**, 6173.
- [13] G. H. Loew, F. U. Axe, J. R. Collins, Inorg. Chem. 1991, **30**, 2291.
- [14] P. Du, F. U. Axe, G. H. Loew, S. Canuto, C. Zerner, J. Am. Chem. Soc. 1991, **113**, 8614.
- [15] S. F. Sontum, D. A. Case, J. Am. Chem. Soc. 1985, **107**, 4013.
- [16] A. Strich, A. Veillard, Theor. Chim. Acta 1983, **60**, 379.
- [17] T. H. Moss, A. Ehrenberg, A. J. Bearden, Biochemistry 1969, **8**, 4159.
- [18] T. Harami, Y. Maeda, Y. Morita, A. Trautwein, U. Gonser, J. Chem. Phys. 1977, **67**, 1164.
- [19] W. F. Simonneaux, W. F. Scholz, C. A. Reed, G. Lang, Biochim. Biophys. Acta 1982, **716**, 1.
- [20] B. Boso, G. Lang, T. J. McMurray, J. T. Groves, J. Chem. Phys. 1983, **79**, 1122.
- [21] M. Schappacher, R. Weiss, J. Am. Chem. Soc. 1985, **107**, 3736.
- [22] D. Mandon, R. Weiss, K. Jayaraj, A. Gold, J. Turner, E. Bill, A. Trautwein, Inorg. Chem. 1992, **31**, 4404.
- [23] C. E. Schulz, P. W. Devaney, H. Winkler, P. G. Debrunner, N. Doan, R. Chiang, R. Rutter, L. P. Hager, FEBS Lett. 1979, **103**, 102.
- [24] M. Li, D. Bonnet, E. Bill, F. Neese, T. Weyhermuller, N. Blum, D. Sellman, K. Wieghardt, Inorg. Chem. 2002, **41**, 3444-3456.
- [25] Gaussian 98 (Revision A.1), M. J. Frisch, G. W. Trucks, H. B. Schlegel, G. E. Scuseria, M. A. Robb, J. R. Cheeseman, V. G. Zakrzewski, J. A. Montgomery, R. E. Stratmann, J. C. Burant, S. Dapprich, J. M. Millam, A. D. Daniels, K. N. Kudin, M. C. Strain, O. Farkas, J. Tomasi, V. Barone, M. Cossi, R. Cammi, B. Mennucci, C. Pomelli, C. Adamo, S. Clifford, J. Ochterski, G. A. Petersson, P. Y. Ayala, Q. Cui, K. Morokuma, D. K. Malick, A. D. Rabuck, K. Raghavachari, J. B. Foresman, J. Cioslowski, J. V. Ortiz, B. B. Stefanov, G. Liu, A. Liashenko, P. Piskorz, I. Komaromi, R. Gomperts, R. L. Martin, D. J. Fox, T. Keith, M. A. Al-Laham, C. Y. Peng, A. Nanayakkara, C. Gonzalez, M. Challacombe, P. M. W. Gill, B. G. Johnson, W. Chen, M. W. Wong, J. L. Andres, M. Head-Gordon, E. S. Replogle and J. A. Pople, Gaussian, Inc., Pittsburgh PA, 1998.
- [26] . The model featured a Fe-O distance of 1.65 Å, with the remaining five "ligands" of the octahedral field being neon atoms, at Fe-Ne distances of 1.7 Å. Omitting the neon atoms did not alter the MO picture qualitatively, except that the s* orbital became singly-occupied.
- [27] R. Silaghi-Dumitrescu, unpublished results.
- [28] M. H. Baik, M. Newcomb, R. A. Friesner, S. J. Lippard, Chem. Rev. 2003, **103**, 2385-2420.
- [29] P. E. M. Siegbahn, J. Biol. Inorg. Chem. 2001, **6**, 27-45.

ATOMIC FORCE MICROSCOPY STUDIES OF LANGMUIR-BLODGETT FILMS. 4. THE INFLUENCE OF ALUMINUM SUBSTRATE ON DIPALMITOYL PHOSPHATIDYLCHOLINE NANOLAYERS

MARIA TOMOAI-A-COTIȘEL¹, VASILICA-DANIELA POP¹, GHEORGHE TOMOAI-A²,
AURORA MOCANU¹, CSABA RACZ¹, CRISTINA RAMONA ISPAS¹, OANA PASCU¹
and OLIMPIA CRISTINA BOROȘTEAN¹

¹"Babeș-Bolyai" University, Faculty of Chemistry and Chemical Engineering, Physical Chemistry Department, 400028 Cluj-Napoca, Romania

²"Iuliu Hațieganu" University of Medicine, Orthopedic Surgery, 400015 Cluj-Napoca, Romania

ABSTRACT. The dipalmitoyl phosphatidylcholine (DPPC) nanolayers in the absence and in the presence of procaine (P), in concentration of 10^{-3} mole dm^{-3} in the aqueous phase of pH 5.6, have been investigated using Langmuir-Blodgett (LB) technique and atomic force microscopy (AFM). The LB films were vertically transferred from DPPC Langmuir nanolayers to a substrate made of glass covered by aluminum thin layer, at two controlled surface pressures, namely at a low surface pressure (of about 8 mN/m) corresponding to the main two-dimensional phase transition from expanded liquid (EL) to condensed liquid (CL) for pure DPPC nanolayers, and at a high surface pressure (around 70 mN/m) corresponding to the over compressed (advanced collapse) state of DPPC nanolayers. The structure of pure DPPC films show regular rounded condensed domains with densely packed DPPC molecules with polar groups on the solid substrate and methyl ends of the chains sticking out from the surface. Depending on the surface pressure the condensed domains coexist with less ordered features (primarily expanded liquid domains) at the main phase transition or with three layered domains under over compression at advanced collapse. In the presence of P, the stability of DPPC films is highly increased. This effect is shown by the increased collapse pressure of mixed DPPC and P nanolayers at the air/water interface. The nano-structures visualized by AFM observations on LB mixed films of DPPC and P reveal some specific molecular interactions between these biologically relevant compounds through hydrogen bonds and electrostatic attractions. In addition a strong adhesion between LB films and aluminum substrate was found which might further stabilize the LB films.

INTRODUCTION

Various model membranes have been used in science including monolayers, also called nanolayers [1, 2], lipid vesicles or liposomes [3] and Langmuir-Blodgett (LB) films [4-8]. These models are of substantial importance in many industrial, environmental and biological processes, such as wastewater treatment, biocompatibility and molecular recognition as well as in the investigation of structure and properties of biological membranes [1, 9].

To obtain a better understanding of model membranes it is essential to find a suitable model system, such as phospholipid nanolayers. These nanolayers are very interesting in this respect and have attracted considerable interest during the past few decades [10-16] both for fundamental research and biological applications. In particular, dipalmitoyl phosphatidylcholine (DPPC) nanolayers were studied by different

techniques including Langmuir technique [10, 11], Langmuir-Blodgett technique coupled with fluorescence microscopy [12] and, recently, with atomic force microscopy [13, 14]. The obtained data lead to the molecular orientation of DPPC molecules within nanolayers at fluid interfaces.

In this study, we use AFM and LB technique to investigate the main two-dimensional phase transition and the collapse mechanism within DPPC nanolayers in the absence and in the presence of procaine (P). The substrate for LB films is a glass covered by a thin aluminum layer. The high resolution of AFM gives valuable information about the size of DPPC molecules and their lateral arrangement. These data allow for a detailed description of the influence of aluminum and of procaine on the surface behavior of DPPC nanolayers.

EXPERIMENTAL SECTION

Chemicals and materials

Dipalmitoyl phosphatidylcholine (DPPC) and procaine hydrochloride (P) were purchased from Sigma. The n-hexane was purchased from Merck. All chemicals were used without further purification. Our investigations have been performed on aqueous subphases of pH 5.6, where P molecules are positively charged [16-19]. All aqueous subphases were prepared with purified water of at least 18 Mohm cm obtained using an Elga system. Under these conditions DPPC forms a stable Langmuir nanolayer at the air/aqueous solution interface. The glass covered by aluminum thin layer, with size of 25x25 mm² and 0.1 mm thick, were used for the LB film fabrication.

LB sample preparation.

The Langmuir nanolayers of DPPC in the absence and in the presence of P at the air/water interface were studied by compression isotherms, which were experimentally obtained as described elsewhere [16-20]. In particular, DPPC was dissolved in n-hexane at a concentration of 1 mg/ml and spread on aqueous solutions of pH 5.6, at 20 °C, in a teflon trough. After waiting time for 5 to 10 minutes to allow the solvent to be fully evaporated, the DPPC nanolayer was manually compressed at a speed of 10 cm²/min to a chosen lateral surface pressure, e. g. corresponding to the main phase transition or for the advanced collapsed state.

The method of engineering LB films, known as Langmuir-Blodgett (LB) method, consists of vertically passing the hydrophilic solid substrate upwards to the air phase [8, 14, 21], at a controlled speed from aqueous phase through the Langmuir nanolayer, held at a constant chosen surface pressure.

In the present study we used the LB vertical deposition to engineer the LB samples of DPPC in the absence and the presence of P (0.001 mole dm⁻³ in aqueous phase) on glass covered with thin aluminum layer. At least three LB films were prepared for every independent sample, under controlled conditions.

During the vertical transfer of LB film, the area of the Langmuir nanolayer is decreased due to the transfer of DPPC amphiphilic molecules from air/water interface to the solid substrate. Usually, a transfer ratio is determined as the ratio of

the decreased Langmuir monolayer area divided by the total surface area of the substrate. The experimental transfer ratio was found comparable with that one for the transfer of DPPC on glass [14] and it was larger than 0.98. The transfer ratio indicates a good LB film deposition and consequently, a replica of Langmuir monolayer is obtained on the solid substrate. Then, AFM measurements were made in tapping mode for each LB sample.

Atomic force microscopy (AFM) tapping mode.

Investigation of the surface morphology and domain structure of the LB samples of DPPC in the absence and presence of P was conducted in tapping mode on a research AFM system with a 90 x 90 (x-y) μm scanner described elsewhere [14, 22] and on a scanning probe microscope (JSPM-4210) with a 10 x 10 (x-y) μm scanner, recently purchased by us from JEOL, Japan. The obtained AFM images were similar of high resolution. Standard cantilevers, non-contact conical shaped tips of silicon nitride coated with aluminum, were used. The tip was on a cantilever with a resonant frequency in the range of 200 - 300 kHz and with a spring constant of 17.5 N/m.

AFM observations were repeated on different areas from 30 x 30 μm^2 to 2 x 2 μm^2 of the same LB film. The images were obtained from at least five macroscopically separated areas on each LB sample. All images were processed using the standard procedures for AFM. Dimensions of the domains were measured directly from AFM topographic images and the thickness variations were estimated from vertical linear cross sections and height distributions on AFM images [23, 24]. Cross section analysis provides estimations of the size of nanolayer domains and various collapse phase structures. Therefore, a detailed morphological analysis of LB film can be reached.

AFM images consists of multiple scans displaced laterally from each other in y direction with 256 x 256 pixels [22]. Low pass filtering was performed to remove the statistical noise without to loose the features of the sample. All AFM experiments were carried out under ambient laboratory conditions (about 20 °C) as previously reported [14, 23, 24]. The dark regions in AFM topography indicate the substrate surface.

Through AFM image analysis, it was found that the interaction between LB film and aluminum surface was an important factor for the adhesion of LB film with the substrate and for the LB film stability.

RESULTS AND DISCUSSION

Phase behavior of Langmuir nanolayers.

The compression isotherm is obtained (Fig.1, curve 1) by compression of Langmuir nanolayers of pure DPPC, spread at the air/water interface, at 20 °C. The isotherm presents sharp breaks in curve slopes which illustrate phase transitions under known experimental conditions. Previously, we have already demonstrated that the DPPC film exhibits a variety of characteristic phases [10], like expanded liquid (EL) and condensed liquid (CL), and collapsed multilayer phases at advanced monolayer collapse under over compressed experimental conditions [14].

As a general behavior, one may observe that the isotherm (Fig.1, curve 1) contains a well defined two-dimensional phase transition from EL to CL at about 8 mN/m. This main phase transition was also identified by surface compressibility measurements [10] and shows that the two surface phases coexist in DPPC nanolayers.

The linear portion at high surface pressures corresponds to the CL state, followed by an intermediary liquid corresponding to intermediate surface pressures (between 8 and 20 mN/m) and by an EL under 8 mN/m.

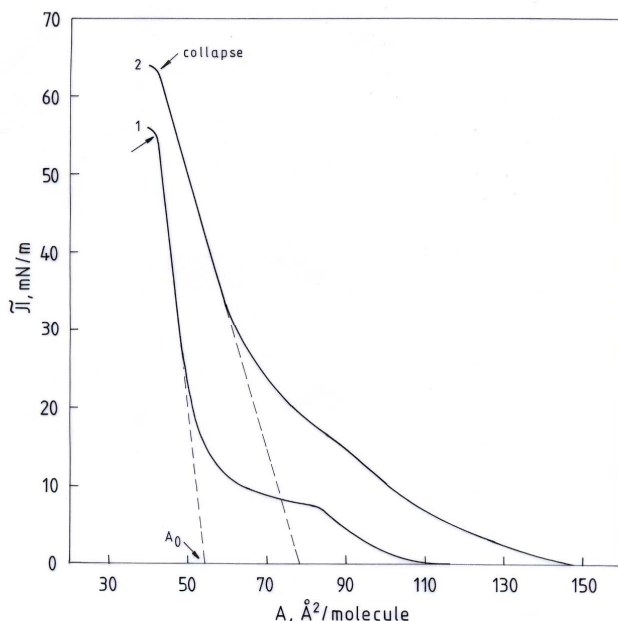


Fig. 1. Surface pressure versus mean molecular area of pure DPPC nanolayer (curve 1) at the air/water of pH 5.6 interface and for DPPC nanolayer in the presence of P (10^{-3} mole/dm³, curve 2), at 20 °C. Dashed lines indicate the limiting areas for DPPC molecule in CL state (A_0). Arrows at high surface pressures indicate the incipient collapse of DPPC nanolayers.

In the presence of procaine (10^{-3} mole dm⁻³; Fig. 1, curve 2) the compression isotherm is moved to larger molecular areas of DPPC showing the expansion of DPPC nanolayers. It appears that for this P concentration the main phase transition, existing in pure DPPC nanolayers, is almost vanished. From these compression isotherms, the surface characteristics of DPPC nanolayers were determined and they are given in Table 1.

The A_0 is the limiting molecular area for the CL state of DPPC monolayer in the absence or in the presence of procaine. These values are obtained by extrapolation to π equals zero of the linear portion of the isotherm recorded at high lateral surface pressures (Fig. 1).

The highest surface pressure to which a Langmuir monolayer can be compressed at the air/water interface [25-29], without the formation of a detectable bulk collapsed phase, represents the collapse pressure (π_c) and corresponds to the sudden slope change observed on the isotherms (indicated by arrows at high surface pressures, on Fig.1). The corresponding mean molecular areas are the collapse areas (A_c) and they are also given in Table 1.

Table 1.

Surface characteristics of DPPC nanolayers in the absence and in the presence of P (10^{-3} mole dm^{-3} in aqueous subphases of pH 5.6). The mean area values (A_0 , and A_c) are given in $\text{nm}^2/\text{molecule}$ of DPPC. The π_c values correspond to the monolayer collapse.

| Monolayer | A_0 (nm^2) | A_c (nm^2) | π_c (mN/m) | |
|------------|-------------------------|-------------------------|----------------|----------|
| | | | incipient | advanced |
| DPPC | 0.54 | 0.42 | 55 | (70) |
| DPPC and P | 0.78 | 0.42 | 63 | (70) |

In CL state the DPPC molecules are densely packed and A_c values are close to the packing area of hydrocarbon chains in crystalline lipids at 20 °C, e. g. 38 \AA^2 per pair of chains [30], and with the values found earlier for DPPC from geometric models [10].

It is important to emphasize the increased stability of DPPC nanolayers in presence of procaine as indicated by the enhanced collapse pressure of mixed DPPC and procaine nanolayers. The procaine effect on DPPC nanolayers reflects stronger specific interactions between these biocompounds, due to their ability to make stable self assembled supramolecular associations [31] primarily through hydrogen bonds.

To better understand the phase behavior of pure DPPC nanolayers and of mixed nanolayers of DPPC and P we have used AFM investigations on these nanolayers transferred on glass covered by aluminum thin layer using vertical LB deposition, under well controlled experimental conditions.

AFM images and analysis

LB FILMS OF DPPC

The morphology of LB films of pure DPPC at both the phase transition from EL to CL, for a lateral surface pressure of 8 mN/m (Fig. 2), and the advanced collapse state of 70 mN/m (Figs. 3 and 4), where another phase transition occurs from two-dimensional nanolayer to a collapsed bulk phase (Table 1), was examined by AFM tapping mode. The AFM allows simultaneous acquisition of both topographic data (topographic image) and material-properties data (phase image).

The topographic images show the morphology of LB samples which is obtained by monitoring the cantilever's oscillation amplitude changes in response to tip and sample spacing. Simultaneously, the phase image is obtained by monitoring of the phase lag between the signal that drives the cantilever to oscillate and the cantilever oscillation output signal. Changes in the phase lag reflect modifications in surface properties of LB sample, such as elasticity, friction and adhesion.

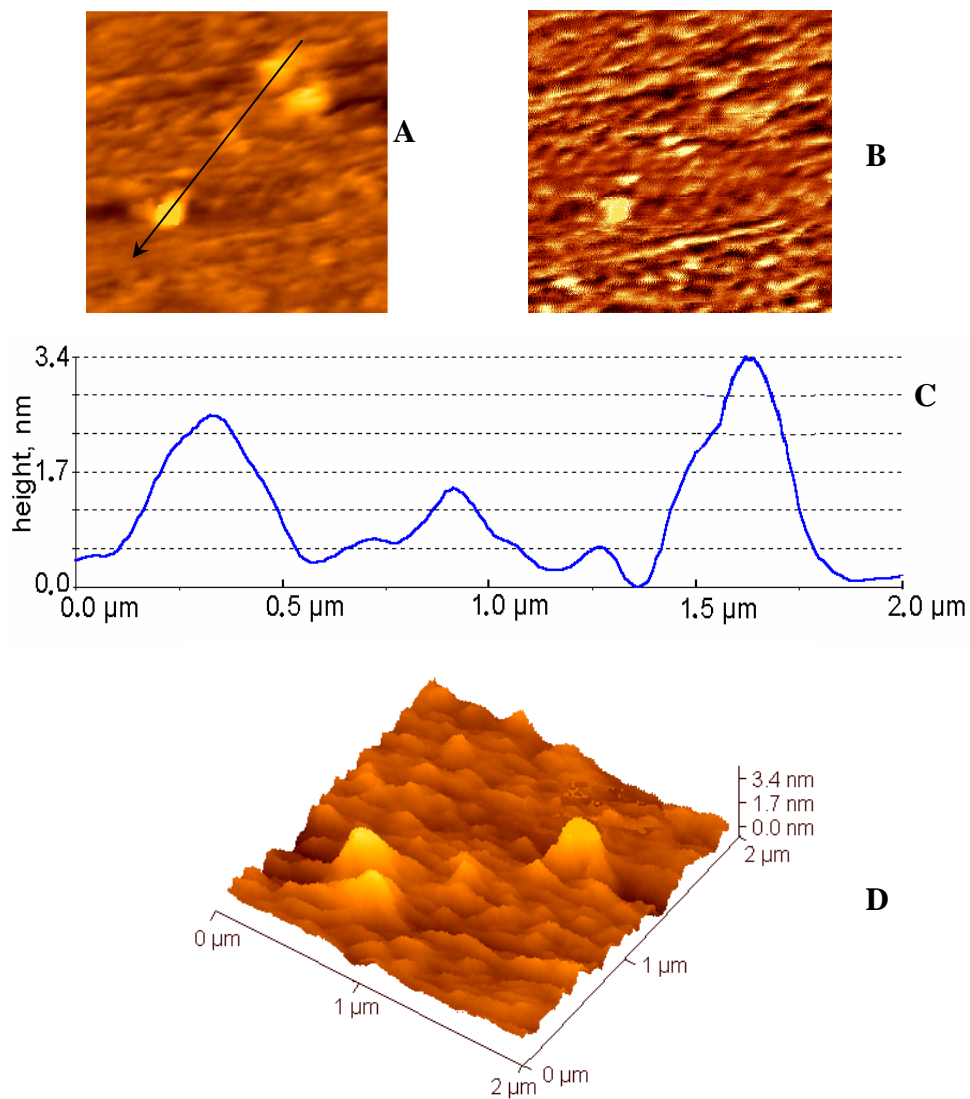


Fig. 2. Two-dimensional (2D) topographic (panel A) and phase (panel B) AFM images of LB films of pure DPPC transferred on aluminum substrate at main phase transition of 8 mN/m (Fig. 1, curve 1); scanned area $2 \times 2 \mu\text{m}^2$. Panel C represents the cross section profile along the arrow in Fig. 2A. The 3D view (panel D) of 2D topographic image (Fig. 2A).

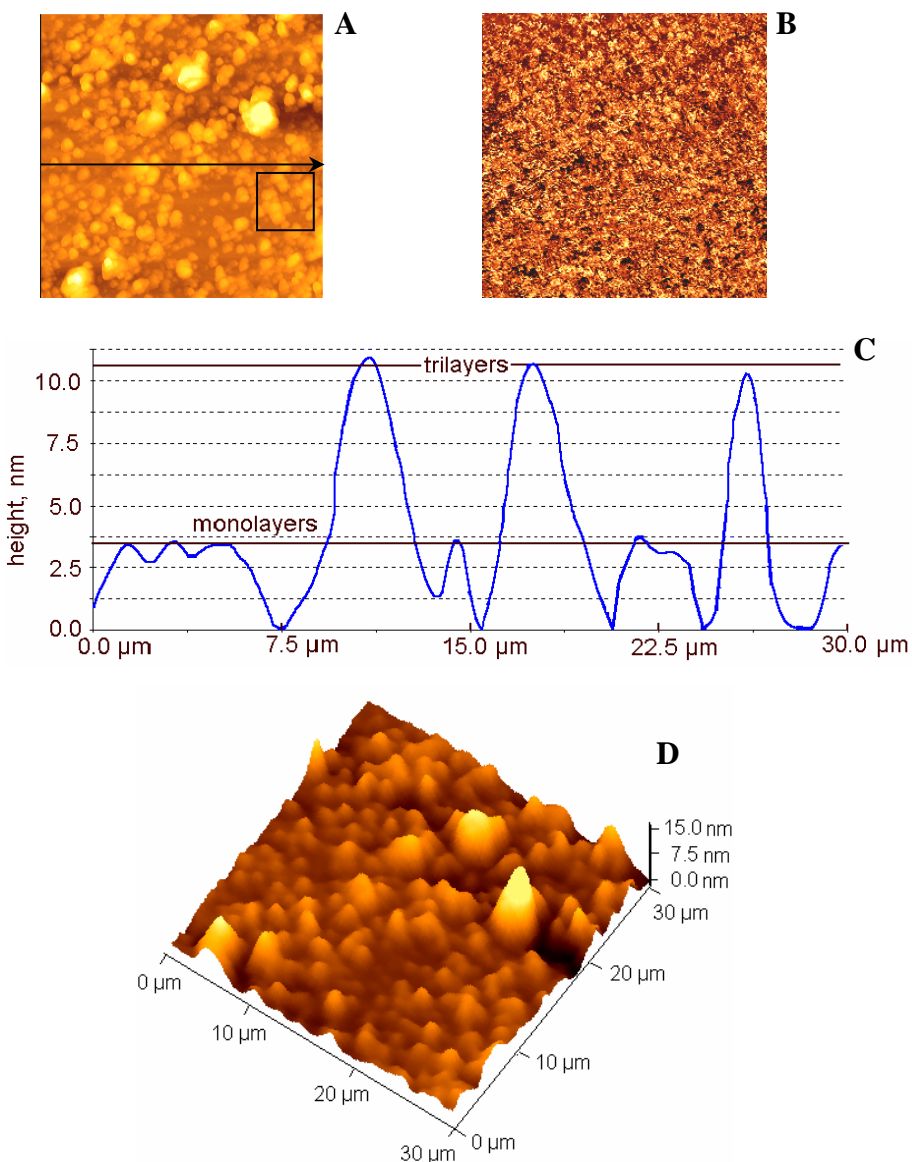


Fig. 3. 2D-topographic (panel A) and phase (panel B) AFM images of LB films of pure DPPC at advanced collapse state of 70 mN/m; scanned area 30 x 30 μm². Panel C represents the cross section profile along the arrow in Fig. 3A. The 3D view (panel D) of 2D topographic image (Fig. 3A); marked area indicates clusters of triple layer domains.

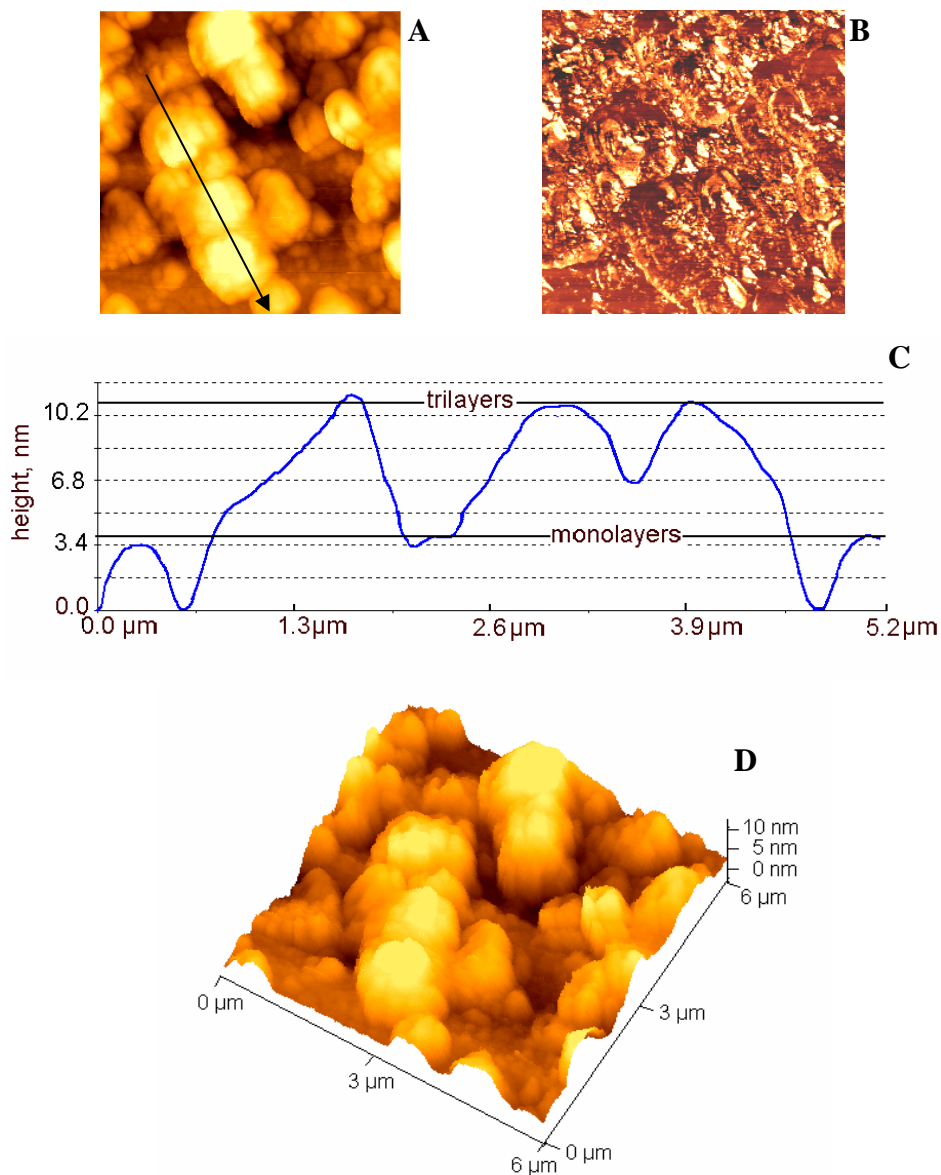


Fig. 4. 2D topographic (panel A) and phase (panel B) AFM images of LB films of pure DPPC; scanned area $6 \times 6 \mu\text{m}^2$; panel C represents the cross section profile along the arrow in Fig. 4A; 3D view (panel D) of 2D topographic image (Fig. 4A). Experimental conditions as for the marked area in Fig. 3A.

Fig. 2 shows the topographic image (panel A) and phase image (panel B) representing the morphology and surface properties, respectively, of LB film of DPPC at the main phase transition from EL to CL state. The topographic and phase images appear to be complementary to one another. They show clearly the coexistence of ordered CL and less ordered EL domains indicating that the pure DPPC film is not homogeneous at the main two phase transition as also evidenced by epifluorescent microscopy [12].

The topographical profile along the arrow, indicated in Fig. 2A, is shown in Fig. 2C. It can be seen that some condensed domains are found with the height up to about 3.4 nm, corresponding to a single molecular layer, when the DPPC molecules stand with hydrocarbon chains almost perpendicular and polar groups parallel to the aluminum substrate. This surface configuration corresponds to CL domains because the size of the DPPC molecule with the hydrocarbon chain extended is about 36 Å and it corresponds to calculated value using molecular geometric models [10]. In addition to these features the rest of the LB film is covered by nano-aggregates and their heights are less than 25 Å or equal to those of some islands comprised between 5 Å and 15 Å, corresponding to the EL domains. Molecules inside the EL aggregates may not orient straight on the aluminum surface in a single layer.

The images of the DPPC film at advanced collapse state (Fig. 3) correspond to a two-dimensional CL in equilibrium with collapsed fragments. At high resolution (Fig. 4) they show a film structure with a regular distribution of highly condensed domains mostly round in shape. These arrangements may include the interaction among DPPC molecules and between DPPC molecules and aluminum substrate. The collective effect of these interactions might lead to the formation of larger ordered structures, as seen in 2D-topographies (panels A), phase images (panels B), cross sections (panels C), and in 3D-topographies (panels D) of Figs. 3 and 4. The average size of CL domains varies from 0.5 µm up to 5 µm and for the triple layer structures from 2 µm up to 3 µm, as given in Figs. 3C and 4C, respectively.

The roughness of the LB film surface in the region of CL domains, defined as the root mean square (rms) of the height differences on the surface [5], is approximately 3 Å. This value is typical for lipid nanolayers and can be measured directly by atomic force microscopy. This is less than the roughness (7 Å) of glass covered by aluminum thin layer. Apparently, the LB film coating smoothens the aluminum surface. This effect might be probably explained by incorporation of water molecules between hydrophilic strongly hydrated DPPC head groups and the substrate surface. A decrease in surface corrugation caused by LB film transfer is consistent with other similar results reported using quartz [5] or glass [14] as substrates for LB samples.

At advanced collapse, the DPPC film structure consists of CL domains aggregated in rounded forms with bridges among them. The highest thickness of the DPPC film remains almost unchanged at 36 ± 2 Å as shown in cross section profile (Figs. 3C and 4C). This thickness corresponds to the height of DPPC molecule (36 Å) in extended conformation [10] of both hydrocarbon chains (19 Å) and the head phosphatidylcholine polar group in its all-trans conformation (17 Å) vertically oriented on the LB substrate. This value can be considered as an

important parameter relevant for the thickness of a DPPC nanolayer relatively well packed at collapse in condensed domains. Figs. 3A and 4A show also the presence of many three layered fragments (up to about 11 nm height, panel C, of Figs. 3 and 4) and some other colloidal particles (up to 15 nm height, Fig. 3D) around the condensed domains. By increasing the lateral surface pressure the width of CL domains increases from about 0.3 μm (Fig. 2C) to almost 5 μm (Fig. 3C) indicating an increased stability of CL domains at advanced collapsed state.

MIXED LB FILMS OF DPPC AND P

The surface structure and properties of mixed LB films of DPPC and P, vertically transferred from Langmuir nanolayers (Fig. 1, curve 2) on glass covered by aluminum thin layer, at the two surface lateral pressures as chosen in the case of pure DPPC films, are investigated using AFM observations. Accordingly, the AFM images are given for mixed LB films of DPPC and P at 8 mN/m (Fig. 5) and at advanced collapsed state of 70 mN/m (Fig. 6, Table 1).

Fig. 5 shows the topographic image (panel A) and phase image (panel B) representing the morphologies and surface properties of mixed LB films of DPPC and P at 8 mN/m. Topographic image corresponds to a mosaic mixture of CL with the height up to 34 Å and EL with the height between 10 and 22 Å, as shown in panel C of Fig. 5. The topographic image show a LB film structure with an irregular distribution of some highly condensed domains mostly rounded in shape (Fig. 5D).

Comparing the AFM observations for DPPC pure film (Fig. 2D) with those for mixed DPPC and P (Fig. 5D) it is to be noted that the presence of procaine facilitates the condensed domains formation at low surface pressure as 8 mN/m.

With the increasing lateral surface pressure to the advanced collapse state of mixed LB films of DPPC and P at 70 mN/m the number of condensed domains and of three layered fragments is increased (Fig. 6). These features are in equilibrium with several large domains of higher order, named multilayered colloidal particles with the height up to 20 nm (Fig. 6D).

The main feature observed in these images and in the cross section profile of Fig. 6C is that the DPPC molecules self-assemble in bright trilayers with the height up to 11 nm in equilibrium with condensed monolayer domains on aluminum surface and probably procaine penetrates within the DPPC domains and among the domains reducing the line tension, as demonstrated for DPPC and P in epifluorescent microscopy [12].

The analysis of phase images (Figs. 5B and 6B) reveals differences among the mixed LB films of DPPC and P as function of the lateral surface pressures. In all cases a good adhesion of LB film with the aluminum mirror is found. The width of CL domains in Figs. 5C and 6C, is up to 0.3 μm and corresponds to supramolecular aggregates, probably, made up from well oriented DPPC and P molecules through hydrogen bonds. The width of triple layers domains is between 0.2 and 0.3 μm (Fig. 6C).

The correlation between topographical and phase images of mixed DPPC and P, given in Figs. 5 and 6, and the corresponding Figs. 2, 3 and 4 for pure DPPC films suggests that the mixed aggregates of DPPC and P are smaller than those formed by pure DPPC in agreement with the P effect on stearic acid (SA) films [24].

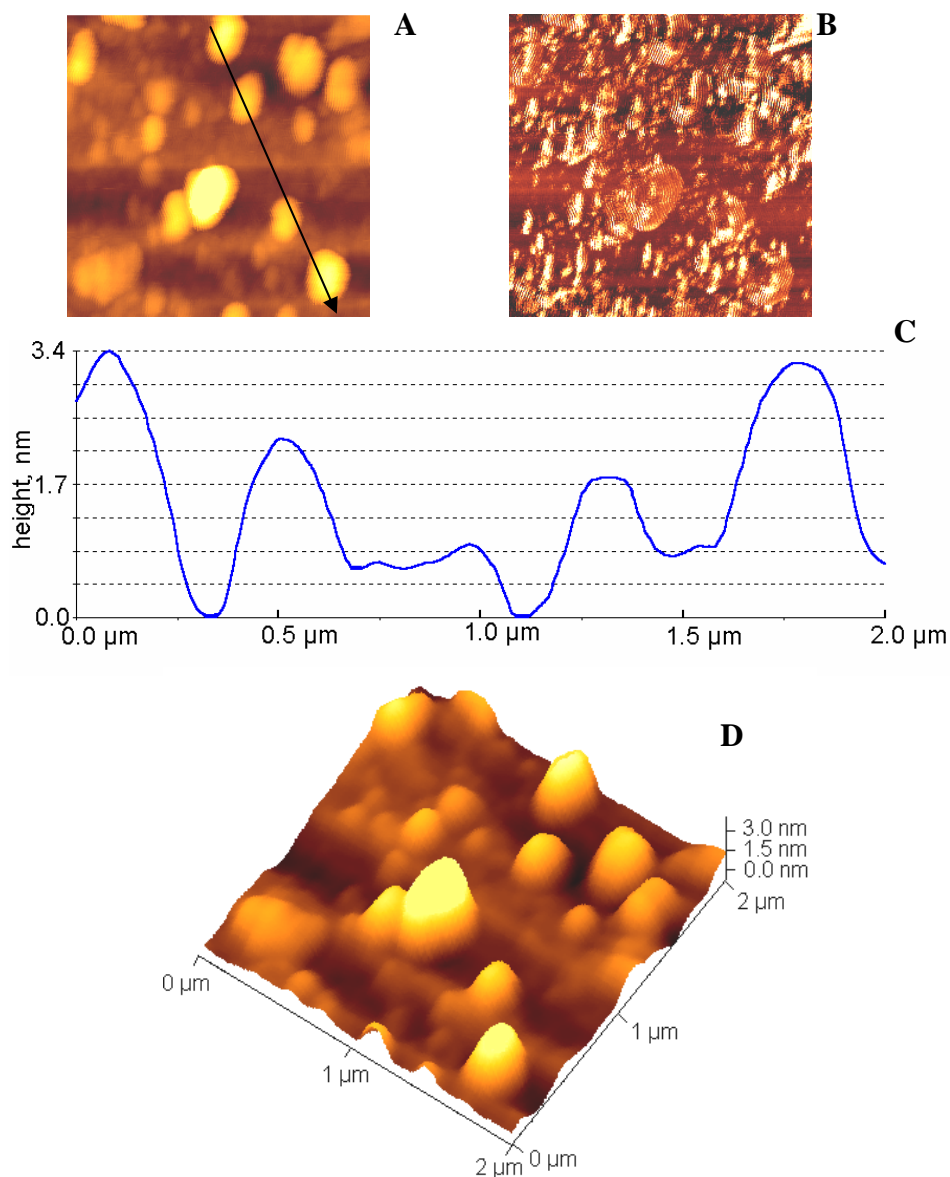


Fig. 5. 2D topographic (panel A) and phase image (panel B) AFM images of LB films of DPPC in presence of P (10^{-3} mole dm^{-3} in aqueous subphase of pH 5.6) transferred at 8 mN/m, see Fig. 1 (curve 2); scanned area $2 \times 2 \mu\text{m}^2$. Panel C represents the cross section profile along the arrow in Fig. 5A. The 3D view (panel D) of 2D topographic image (Fig. 5A).

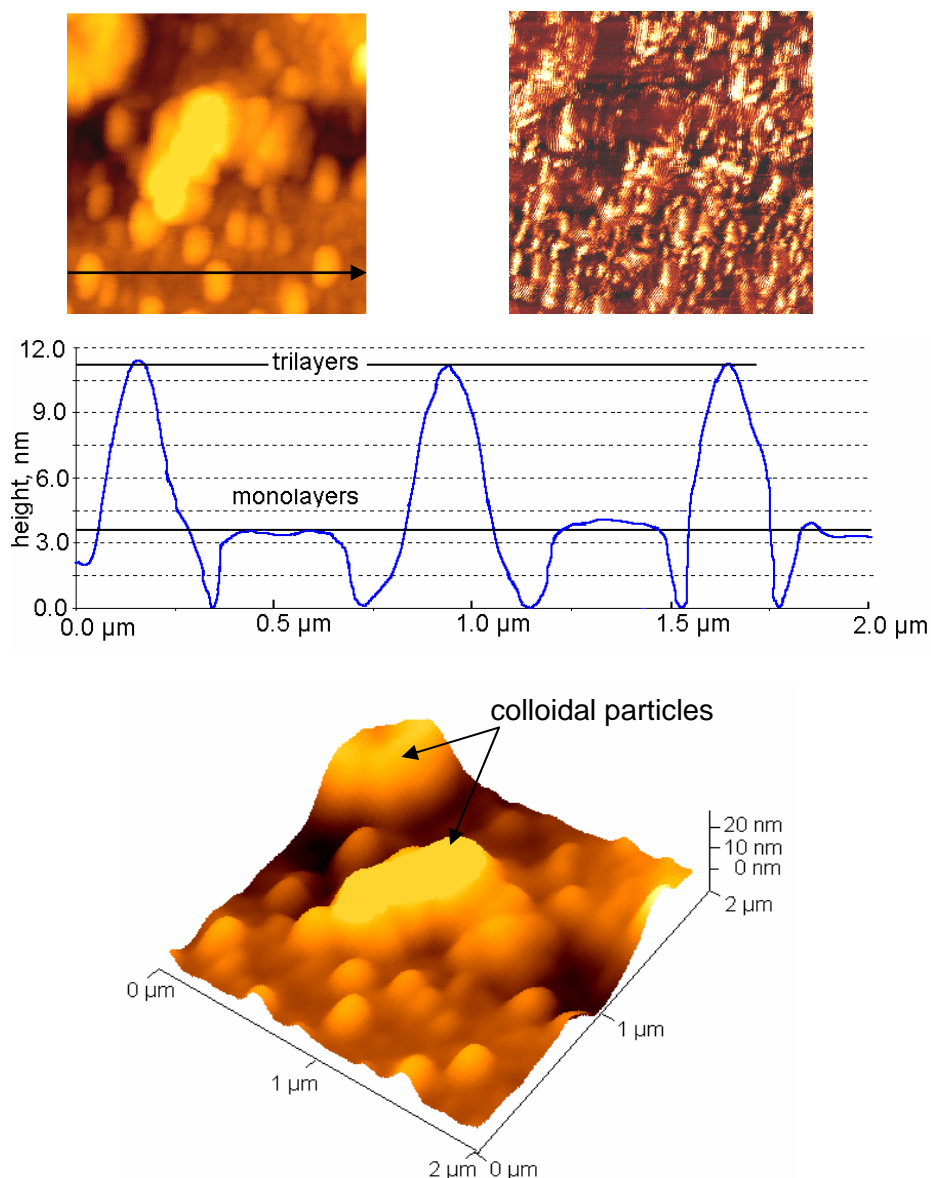


Fig. 6. 2D topographic (panel A) and phase (B) AFM images of mixed LB films of DPPC and P transferred at advanced collapse state (lateral surface pressure of 70 mN/m). Panel C indicates the cross section profile along the arrow in Fig. 6A. The 3D view (panel D) of 2D topographic image (panel A).

At advanced collapsed state, the total thickness of the CL domains remains almost unchanged at 36 ± 2 Å for the over compression at 70 mN/m for both LB films of pure DPPC (Figs. 3 and 4) and for the mixture of DPPC and P (Fig. 6). The measured thickness using AFM is again in good agreement with experimental and calculated value of 36 Å for the molecular length of DPPC [10].

The experimental collapsed structures of LB films visualized by AFM images (Figs 3, 4 and 6) and their section profiles can be explained quite suggestively by the collapse model of nucleation and subsequently growth of nuclei [26-29]. Several types of domains were observed, some are disk like and some are with rounded shape depending on the molecular interactions among molecules, their molecular shape and the interactions with the solid substrate. Sometimes, there are also irregularly shaped aggregates clustered lying beside or above the CL domains as observed in AFM images in the present study.

Further, the AFM images of DPPC and P revealed their association into less aggregated particles at advanced collapse (Fig. 6) on aluminum substrate. This effect of P on DPPC films is comparable with its effect on fatty acid monolayers transferred on glass substrate [24], but the stability of LB films is enhanced on aluminum substrate. Thus, we suggest that aluminum mirror is an effective substrate for DPPC to form stable LB films both in the absence and in the presence of P.

Usually, a high stability of LB films indicates also a high stability of their Langmuir nanolayers at air/water interface. Nevertheless, the high increased stability of DPPC nanolayer in the presence of P in the aqueous solution is strongly supported by its recorded high incipient collapse pressure (Table 1).

To describe the increased stability of Langmuir nanolayers we suggest that the electrostatic interaction between the zwitterions of polar head groups of DPPC and protonated amino terminal of P molecules [17] is an important factor in stabilizing the long-range structure in addition to the interaction between the hydrophobic tail groups of DPPC oriented in the air phase. Also P molecules oriented at the air/water interface can make surface complexes with DPPC molecules through hydrogen bonds facilitating the order in two dimensions. These complexes can have a physiologic role in vivo as well as in the molecular mechanism of anesthesia.

CONCLUSION

The present study demonstrates that AFM coupled with the LB technique gives valuable information on the film structure of the pure DPPC and its binary mixtures with P.

In Langmuir nanolayers of DPPC and P at the air/water interface, the stability of mixed films is highly increased as compared with pure DPPC nanolayers. The increased stability is strongly reflected in the high collapse pressure of DPPC nanolayer in the presence of P.

The Langmuir nanolayers of pure DPPC and of its binary mixtures with P were transferred from the air/water interface on aluminum substrate at two surface lateral pressures, namely, at 8 mN/m, which is characteristic for the main phase transition from EL to CL of pure DPPC nanolayers, and at 70 mN/m chosen for the advanced collapse state of Langmuir nanolayers. Then, the surface of their LB films was for the first time visualized using AFM observations on LB films.

The analysis of AFM images shows differences among the LB film surfaces of pure DPPC and mixed DPPC and P, suggesting that there is also a modification of the surface composition when single component and mixed films are compared.

The experimental collapsed structures of LB films visualized by AFM images and section profiles can be explained quite suggestively by the collapse model of nucleation and subsequently growth of nuclei. The AFM images of DPPC and P revealed their association into less aggregated particles at advanced collapse than in the case of pure DPPC film.

Our studies have also shown a long term stability of pure DPPC films and mixed DPPC and P films, transferred on aluminum substrate. This high stability may include the interaction among DPPC molecules and between DPPC and P molecules in addition to the interaction between the underlying aluminum substrate and the film forming molecules.

The LB films were measured several days after the transfer and several months up to one year after the transfer. The high stability of both LB films and Langmuir nanolayers would be useful in various applications for medicine, pharmacy and biology.

REFERENCES

1. R. Maget-Dana, *Biochim. Biophys. Acta*, **1999**, 1462, 109.
2. M. Tomoaia-Cotisel, P. J. Quinn, "Biophysical properties of carotenoids", *Subcellular Biochemistry*, Volume 30: Fat-Soluble Vitamins", Chapter 10, Edited by P.J. Quinn and V. E. Kagan, Plenum Press, New York, pp. 219-242 (**1998**).
3. M. Tomoaia-Cotisel, I. W. Levin, *J. Phys. Chem., B*, **1997**, 101, 8477.
4. K. S. Birdi, "Scanning Probe Microscopes. Applications in Science and Technology", CRC Press, New York, **2003**.
5. X. Zhai and J. M. Kleijn, *Thin Solid Films*, **1997**, 304, 327.
6. D. K. Schwartz, *Surface Science Reports*, **1997**, 27, 241.
7. J. A. DeRose and R. M. Leblanc, *Surface Science Reports*, **1995**, 22, 73.
8. A. Ulman, "An Introduction to Ultrathin Organic Films. From Langmuir-Blodgett to Self-assembly", Academic Press, New York, **1991**.
9. W. Knoll, M. Liley, D. Piscevic, J. Spinke and M.J. Tarlov, *Adv. Biophys.*, **1997**, 34, 231.
10. M. Tomoaia-Cotisel, J. Zsako and E. Chifu, *Ann. Chim.(Rome)*, **1981**, 71 (3-4), 186.
11. H. Mohwald, *Annu. Rev. Phys. Chem.*, **1990**, 41, 441.
12. B. Asgharian, D. A. Cadenhead and M. Tomoaia-Cotisel, *Langmuir*, **1993**, 9, 228
13. K. S. Birdi and D. T. Vu, *Langmuir*, **1994**, 10, 623.
14. M. Tomoaia-Cotisel, Gh. Tomoaia, V.D. Pop, A. Mocanu, N. Apetroaei and G. Popa, *Rev. Roum. Chim.*, **2005**, 50, 381.
15. Y. F. Dufrene and G. U. Lee, *Biochim. Biophys. Acta*, **2000**, 1509, 14.
16. M.I. Salajan, A. Mocanu and M. Tomoaia-Cotisel, "Advances in Thermodynamics, Hydrodynamics and Biophysics of Thin Layers", University Press, Cluj-Napoca, **2004**.
17. M. Tomoaia-Cotisel and D. A. Cadenhead, *Langmuir*, **1991**, 7, 964.
18. J. Zsako, M. Tomoaia-Cotisel, E. Chifu, A. Mocanu and P. T. Frangopol, *Biochim. Biophys. Acta*, **1990**, 1024, 227.

19. M. Tomoaia-Cotisel, *Progr. Colloid Polym. Sci.*, **1990**, 83, 155.
20. M. Tomoaia-Cotisel, J. Zsako, A. Mocanu, M. Lupea and E. Chifu, *J. Colloid Interface Sci.*, **1987**, 117, 464.
21. M. Tomoaia-Cotisel, E. Chifu, S. Jitian, I. Bratu, S. Bran, P. T. Frangopol and A. Mocanu, *Studia Univ. Babes-Bolyai, Chem.*, **1990**, 35 (2), 17.
22. N. Dumitrascu, G. Borgia, N. Apetroaei and Gh. Popa, *Plasma Sources Sci. Technol.*, **2002**, 11, 1.
23. M. Tomoaia-Cotisel, Gh. Tomoaia, A. Mocanu, V.D. Pop, N. Apetroaei and Gh. Popa, *Studia Univ. Babes-Bolyai, Chem.*, **2004**, 49, 1.
24. M. Tomoaia-Cotisel, Gh. Tomoaia, V.D. Pop, A. Mocanu, N. Apetroaei and Gh. Popa, *Rev. Roum. Chim.*, **2005**, 50, 473.
25. G. L. Gaines, Jr., "Insoluble Monolayers at Liquid-Gas Interfaces", Wiley Interscience, New York, 1966.
26. P. Baglioni, G. Gabrielli and G. G. T. Guarini, *J. Colloid Interface Sci.*, **1980**, 78, 347.
27. M. Tomoaia-Cotisel, J. Zsako, E. Chifu and P. J. Quinn, *Studia Univ. Babes-Bolyai, Chem.*, **1987**, 32 (1), 35.
28. M. Tomoaia-Cotisel, J. Zsako, A. Mocanu, I. Albu and E. Chifu, *Studia Univ. Babes-Bolyai, Chem.*, **1987**, 32 (1), 58.
29. M. Tomoaia-Cotisel, J. Zsako, E. Chifu, D. A. Cadenhead and H. E. Ries, Jr., "Collapse mechanism of some carotenoid monomolecular films - membrane model", in *Progress in Photosynthesis Research*, Edited by J. Biggins, Martinus Nijhoff Publishers, Vol. **2**, Chapter 4, pp 333-337, **1987**.
30. D. M. Small, "The Physical Chemistry of Lipids, Handbook of Lipid Research", Plenum, New York, **1986**.
31. J. M. Boggs, *Biochim. Biophys. Acta*, **1987**, 906, 353.

MOLECULAR STRUCTURE AND MONOLAYER PROPERTIES OF SOME CAROTENOIDS

MARIA TOMOAI-A-COTISEL^a, CSABA RACZ^a, GHEORGHE TOMOAI-A^b,
CALIN FLOARE^c, ROBERT TOTOS^d, LIVIU BOBOS^a,
OANA PASCU^a and ANCA DUMITRU^a

^a"Babes-Bolyai" University of Cluj-Napoca, Department of Physical Chemistry,
400028 Cluj-Napoca, Romania

^b"Iuliu Hatieganu" University of Medicine, Department of Orthopaedic Surgery,
400015 Cluj-Napoca, Romania

^cNational Institute for Research and Development of Isotopic and Molecular
Technologies, P.O. Box 700, Cluj-Napoca, Romania

^d"Raluca Ripan" Institute of Chemistry, 400294 Cluj-Napoca, Romania

ABSTRACT. Compression isotherms of some carotenoids: 4-oxo- β -carotene, 4,4'-dioxo- β -carotene and the di-apo-4, 4'-carotenodial, spread at the air / water interface, are reported. The high molecular area portions of the compression isotherms are described by means of van der Waals – type state equation and interaction parameters are derived. Simple HMO calculations are performed without and with induction parameters and dipole moments are calculated. Surface properties viz. collapse pressure and surface compressibility modulus and interaction parameters are discussed in terms of dipole-dipole interactions, as well as of conformational analysis of the carotenoid molecules in monolayers in good agreement with the experimental results.

Keywords: carotenoids, monolayer properties, molecular structure, dipole moment, state equation

INTRODUCTION

Carotenoids are important biological molecules that play vital roles in cellular differentiation, growth control, photooxidative protection, cell membrane stability, photosynthesis, vision process and nutrition [1]. Recently, more studies attempting to relate carotenoids to therapy of cancer, coronary heart disease, HIV infections or light-sensitive diseases are undertaken. These are exciting areas for the study of functions and actions of carotenoids in biological systems. Nevertheless, it is clear that the varied biological activities of carotenoids in living organisms are determined by the biophysical and chemical properties of these molecules. These properties and particularly the surface activity of carotenoids are determined by their molecular structure and geometry [2]. Further, carotenoids and their metabolites may influence or modulate the properties of cellular and subcellular structures [1].

In this paper we describe the monolayer behaviour of three carotenoid pigments, like 4-oxo- β -carotene (OC), 4,4'-dioxo- β -carotene (DOC) and the di-apo-4, 4'-carotenodial (DAC), in single-component monolayers. Then, we present the correlation between the monolayer properties and molecular structure of the three carotenoids spread at the air/water interface.

EXPERIMENTAL PART

The three carotenoids (OC, DOC and DAC) examined are all-trans isomers of high purity established by chromatography and spectral analysis. The spreading solvent for every carotenoid compound was benzene pro-analysis or a mixture of benzene and 2-4% absolute ethanol at the air/water interface. After 10 minutes allowed for solvent evaporation the spread monolayer of carotenoid compound was compressed at a chosen rate of compression and reproducible compression isotherms were recorded at $20 \pm 2^\circ\text{C}$ as described elsewhere [1].

RESULTS AND DISCUSSION

Compression isotherms, in terms of surface pressure (π , mN/m) versus mean molecular area (A , nm²) curves are recorded for three carotenoids, viz. 4-oxo- β -carotene (OC), 4, 4'-dioxo- β -carotene (DOC) and di-apo- 4, 4'-carotenodial (DAC), spread at the air/water interface.

The molecular structures and formulae of the studied carotenoids are given in Fig.1.

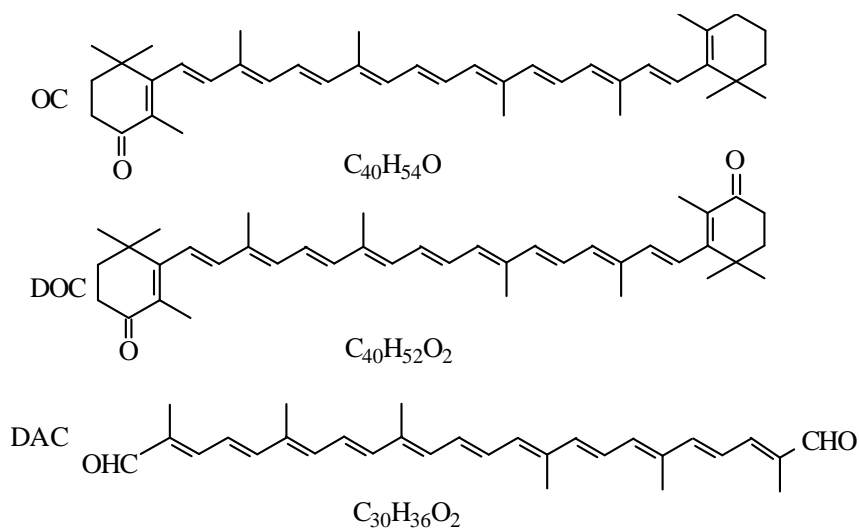


Fig. 1. Molecular structure of the three carotenoids: OC: 4-oxo- β -carotene, DOC: 4,4'-dioxo- β -carotene and DAC: di-apo- 4,4'-carotenodial.

The compression isotherms of the three carotenoids are presented in Fig. 2.

At high molecular area, the compression isotherms are described by means of the van der Waals type state equation:

$$(\pi + \alpha / A^{3/2}) (A - A_0') = kT \quad (1)$$

where α and A_0 are empirical parameters to be derived from the experimental curves, α being a measure of the intermolecular attraction and A_0 is coarea. These parameters have been derived from the experimental π -A pairs, obtained at low π values (up to about 15 mN/m). They are presented in Table 1, together with surface characteristics derived from the high π portion of the compression isotherms, viz. collapse pressure (π_c) and surface compressional modulus (C_s^{-1}), defined as :

$$C_s^{-1} = - A_0 (\partial \pi / \partial A)_T \quad (2)$$

where A_0 stands for the limiting molecular area (see Fig. 2) obtained by extrapolating to $\pi = 0$, the high pressure linear portion of the compression isotherm, having the slope $(\partial \pi / \partial A)_T$.

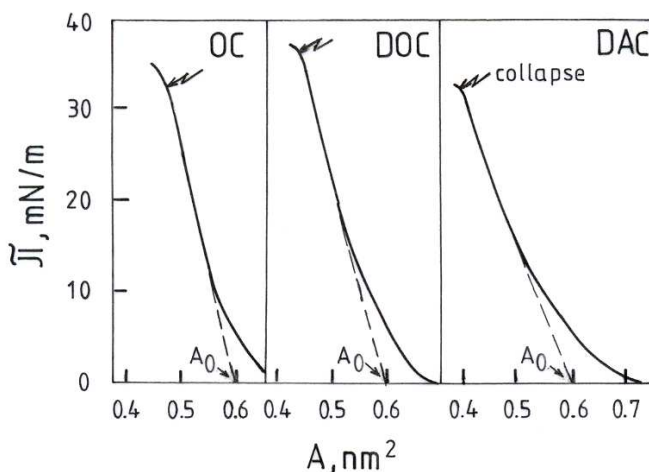


Fig. 2. Compression isotherms of the three carotenoids: 4-oxo- β -carotene (OC), 4,4'-dioxo- β -carotene (DOC) and di-apo-4,4'-carotenedial (DAC) spread as monolayers at the air/water interface.

From compression isotherms the surface characteristics are determined, namely π_c , C_s^{-1} , A_0 and α value, and given in Table 1.

Table 1.

Surface characteristics of the three carotenoids studied.

| Carotenoid | π_c (mN m ⁻¹) | C_s^{-1} (mN m ⁻¹) | $\alpha 10^{30}$ (N m ²) | A_0 (nm ²) |
|------------|----------------------------------|-------------------------------------|---|-----------------------------|
| OC | 32 | 151 | 9.02 | 0.438 |
| DOC | 36 | 145 | 8.74 | 0.432 |
| DAC | 32 | 95 | 6.71 | 0.392 |

In order to correlate π_c , α and C_s^{-1} values with the electronic structure of the molecules studied, HMO calculations have been performed in two approximation [3], by taking into account only the delocalized π -bond system, viz.:

- *approach 1* corresponds to the parametrization : $\alpha_C = 0$, $\alpha_O = 1$,
 $\beta_{CC} = \beta_{CO} = 1$;

- *approach 2* for the C - atoms carrying a CH_3 - group, an induction parameter of $\alpha_C = -0.5$ was used and for those linked to C - atoms of the ionone ring, not included into the conjugated system, $\alpha_C = -0.3$ was taken.

The π - electron density, q_r , and bond order, p_{rs} , values obtained from the HMO coefficients were used to calculate the dipole moment of each bond. For this purpose a semiempirical method was used, based upon the following hypotheses:

1. The dipole moment of CO in the sum of the dipole moment of the C-O σ -bond and of that of the C-O π -bond, both are directly proportional to the internuclear distance, the latter one being a linear function of the π -bond order, p_{rs} .
2. The dipole moment of the C-C σ -bond is equal to zero.
3. The dipole moment of the π -bonds, both of C-O and C-C ones, is directly proportional to the difference between the π -electron densities of the atoms linked to each other $\Delta q_{rs} = q_r - q_s$.

By using literature data concerning the length of C-O and C-C single and double bonds, dipole moments of ketones and ethers, as well as Δq_{rs} and p_{rs} values calculated in the HMO approximation for a C-O localized π -bond, the above hypotheses allowed us to derive the following semiempirical formulae:

$$\mu_{CO} = (0.5221 + 1.2614 \Delta q_{rs}) (6.3950 - p_{rs}) 10^{-30} \text{ C m} \quad (3)$$

$$\mu_{CC} = (8.6876 - 1.1283 p_{rs}) \Delta q_{rs} 10^{-30} \text{ C m}$$

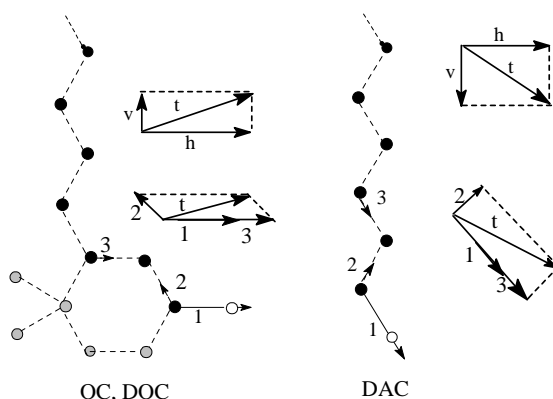


Fig. 3. Composition of the dipole moments of the first 3 bonds, and the decomposition of the total dipole moment in horizontal and vertical components.
 Symbols : \odot C - atom (sp^3); \bullet C - atom (sp^2); \circ O - atom (sp^2).

Table 2.
Dipole moments of the first n bonds (μ_t), their horizontal (μ_h) and vertical (μ_v) components, angles (β) formed with the air/water interface and correlations with surface characteristics (b)

| Surfactant | n | Approach 1 | | | | | | | Approach 2 | | | | | | |
|-------------------------|----|------------|---------|---------|---------|------------------------|--------------------------|-----------------------|------------|---------|---------|---------|------------------------|--------------------------|-----------------------|
| | | μ_t | μ_h | μ_v | β | $\frac{\alpha}{\mu_h}$ | $\frac{C_s^{-1}}{\mu_h}$ | $\frac{\pi_c}{\mu_h}$ | μ_t | μ_h | μ_v | β | $\frac{\alpha}{\mu_h}$ | $\frac{C_s^{-1}}{\mu_h}$ | $\frac{\pi_c}{\mu_h}$ |
| OC | 1 | 9.14 | 9.14 | 0.00 | 0.00 | - | - | - | 9.94 | 9.94 | 0.00 | 0.00 | - | - | - |
| | 3 | 9.82 | 9.53 | 2.36 | 13.90 | 0.95 | 1.59 | - | 9.79 | 9.63 | 1.73 | 10.18 | 0.94 | 1.57 | - |
| | 12 | 6.94 | 6.15 | 3.21 | 25.07 | - | - | 5.20 | 13.36 | 13.01 | 3.05 | 13.19 | - | - | 2.46 |
| DOC | 1 | 9.09 | 9.09 | 0.00 | 0.00 | - | - | - | 9.93 | 9.93 | 0.00 | 0.00 | - | - | - |
| | 3 | 9.69 | 9.41 | 2.31 | 13.81 | 0.93 | 1.54 | - | 9.58 | 9.43 | 1.68 | 11.12 | 0.93 | 1.54 | - |
| | 12 | 7.72 | 7.14 | 2.94 | 20.85 | - | - | 5.05 | 14.52 | 14.26 | 2.73 | 10.83 | - | - | 2.53 |
| DAC (DOC ⁺) | 1 | 9.09 | 4.55 | -7.87 | -60.0 | - | - | - | 9.93 | 4.96 | -8.60 | -60.00 | - | - | - |
| | 3 | 9.69 | 6.71 | -6.99 | -46.19 | 1.00 | 1.42 | - | 9.58 | 6.18 | -7.33 | -49.89 | - | - | - |
| | 12 | 11.01 | 8.98 | -6.37 | -35.33 | - | - | 3.56 | 6.72 | 1.35 | -6.59 | -78.39 | - | - | - |

Units: $\mu_t / 10^{-30} \text{ C m}$; $\mu_h / 10^{-30} \text{ C m}$; $\mu_v / 10^{-30} \text{ C m}$; $\beta / ^\circ$; $(\alpha / \mu_h) / \text{N m C}^{-1}$; $(C_s^{-1} / \mu_h) / 10^{28} \text{ N C}^{-1} \text{ m}^{-2}$; $(\pi_c / \mu_h) / 10^{27} \text{ N C}^{-1} \text{ m}^{-2}$

The dipole moment of the individual bonds have been composed vectorially, by taking into account the geometric configuration of the molecules [4-6] and by considering the latters to adopt a vertical orientation at compression of the monolayer [5]. The composition of the dipole moments of the first three bonds is visualized in Fig. 3.

The resulting total dipole moment, μ_t , characterizes the polarity of the head-group, anchored into the aqueous subphase. It was decomposed into a horizontal component, μ_h , parallel with the air / water interface, and a vertical one, μ_v , perpendicular to the interface. Also, the angle β , formed by μ_t with the interface has been computed.

Results are presented in Table 2, where n stands for the number of bonds taken into account at the calculation of μ , beginning from the C = O group. We mention that in Table 2 the values computed in approach 2 and given in the line of DAC (DOC') do not refer to DAC but to an isomer of DOC in which the ionone ring has the configuration given in Fig.4 and having for the conjugated system the same configuration as DAC.

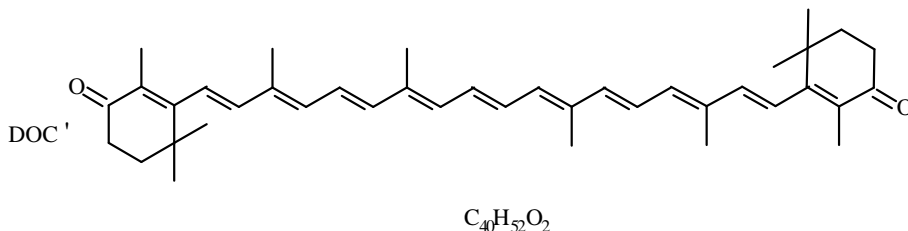


Fig. 4. Molecular structure of DOC'.

As seen from Table 2, the dipole moment of the head-group (μ_{h3}) decreases in the order OC > DOC > DAC and in the same order also varies α values, the dependence being almost linear, as seen from the constancy of the ratio α/μ_{h3} . The C_s^{-1} values vary in the same order and the ratio C_s^{-1}/μ_{h3} is also almost constant. This constancy is better in approach 2 than in approach 1, with respect to OC and DOC. This suggests the idea that both α and C_s^{-1} are determined mainly by the horizontal component of the head group dipole moment. The contribution of the hydrocarbon chain to μ_h is quite different with the substances studied and is reflected differently in approaches 1 and 2. In approach 1 one has $\mu_{h3} > \mu_{h12}$ with OC and DOC, but in approach 2 the reverse is observed. Since this overall dipole moment must play an important role near the collapse, the ratio π_c/μ_{h12} was calculated giving an almost constant value in the case of OC and DOC, the constancy being better in approach 2.

Calculations performed in approach 2 for the isomer DOC' reveal the correctness of the configuration of DOC given in Fig.1, which is consistent also with X-ray evidence [4]. According to our results the vertical component of the dipole moment of DAC differs fundamentally from those of OC and DOC, the negative pole being oriented downwards in the case of the former, and upwards with the latter ones. The correctness of this theoretical result would be worth to verify by means of surface potential measurements.

In future studies we will extend our theoretical and experimental investigations on various carotenoids to determine the correlation between the surface properties and actions of carotenoids in biological systems. Undoubtedly, it is clear that the varied biological activities of carotenoids in living organisms are determined by the structural and chemical properties of these molecules. The actual research on the relations between the dipole moments and surface potentials for different biosurfactants is in progress in our laboratories.

REFERENCES

- 1) M. Tomoaia-Cotișel and P.J. Quinn, Chapter 10: *"Biophysical Properties of Carotenoids"* in "Subcellular Biochemistry, Vol.30: Fat-Soluble Vitamins" Editors: P.J.Quinn and V. Kagan, Plenum Press, New York, pp. 219-242 (1998).
- 2) J. Zsako, M. Tomoaia-Cotișel and E. Chifu, *"Discussion of compression Isotherms of some carotenoid monolayers on the basis of HMO calculations"*, in *"Surfactants in Solution"*, Vol. 9, Edited by K.L. Mittal, Plenum Press, New York, pp 311-324 (1989).
- 3) A. Streitwieser, *"Molecular Orbital Theory for Organic Chemistry"*, John Wiley and Sons, New York (1961).
- 4) O. Isler, in *"Carotenoids"*, Birkhäuser Verlag, Basel, (1971).
- 5) J. Zsakó, E. Chifu and M. Tomoaia-Cotișel, "Rotating rigid-plate model of carotenoid molecules and the behavior of their monolayers at the air/water interface", *Gazz. Chim. Ital.*, **109** (11-12), 663-668 (1979).
- 6) M. Tomoaia-Cotișel, J. Zsakó, E. Chifu and P. J. Quinn, "Intermolecular interactions in lipid-carotenoid monolayers", *Biochem. J.*, **248**, 877-882 (1987).

LANGMUIR KINETICS AND ADSORPTION MECHANISM AT THE OIL/WATER INTERFACE

GHEORGHE TOMOAIA^a, MARIA TOMOAIA-COTISEL^b, CSABA RACZ^b
CRISTINA-RAMONA ISPAS^b and CALIN FLOARE^c

^a*Department of Orthopaedic Surgery, "Iuliu Hatieganu" University of Medicine,
400015 Cluj-Napoca, Romania*

^b*Department of Physical Chemistry, "Babes-Bolyai" University of Cluj-Napoca,
400028 Cluj-Napoca, Romania*

^c*National Institute for Research and Development of Isotopic and Molecular
Technologies, P.O. Box 700, Cluj-Napoca, Romania*

ABSTRACT. The adsorption mechanism of some biocompounds, e.g. two local anesthetics, like dibucaine and tetracaine, and of stearic acid, from bulk solutions to the oil/water interface was studied by using the pendant drop and ring methods. The biocompounds are approaching the oil/water interface from the opposite directions, namely anesthetics from water phase and stearic acid from oil phase. On the other hand, anesthetics are charged species and stearic acid is uncharged under working conditions. The kinetic analysis shows that Langmuir kinetic approach describes the dynamic interfacial pressures within the limits of the experimental errors over a wide range of time and for different surfactant concentrations in bulk solutions. It is also concluded that this approach allows the calculation of the ratio of the adsorption and desorption rate constants of these biocompounds at the oil/water interface. Obtained results are in substantial agreement with similar earlier reported data for the adsorption of different surfactants at various oil/water interfaces as well as with their molecular structure. The driving force for the adsorption of anesthetics (water soluble molecules) is the hydrophobic interactions among the penetrated hydrophobic chains and the oil phase, which are accompanied by the increase of the entropy of the system because of the destruction of the ordered structure of water molecules formed around the hydrophobic chains in aqueous phase. On the contrary, the driving force for the adsorption of stearic acid (practically water insoluble compound) is the change in the enthalpy of the system due to the hydration of hydrophilic polar head groups when they immerse in the water phase.

Key words: Dynamic interfacial pressures; dibucaine; tetracaine; stearic acid; oil/water interface; Langmuir adsorption kinetics; adsorption mechanism.

INTRODUCTION

The adsorption kinetics of various surfactants at the liquid interfaces has attracted a considerable attention in the last several decades [1-31] due to its industrial importance [6, 7, 28] and to its biological and medical significance [32-39]. These studies have involved various experimental techniques and different theoretical models describing the adsorption kinetics of surfactants at liquid interfaces.

Basically, the surfactant adsorption from a bulk solution to a liquid interface, like liquid/gas [6-18] or to a liquid/liquid interface [1-6, 19-27], occurs in two steps. Surfactant molecules are first transported from the bulk to the subsurface by diffusion; the subsurface is a liquid layer just below the interface, belonging still to the bulk. The second step consists of the transfer of surfactant molecules from the subsurface to the interface, implying sometimes a transfer through a potential barrier [25, 28-31]. The controlling rate may be either the diffusion or the transfer (i.e. the adsorption is barrier-controlled) and several theoretical models have been developed for both processes.

For instance, the adsorption kinetics of some aliphatic carboxylic acids and aliphatic alcohols [9-12], like 1, 9 nonane dicarboxylic acid and 1, 9 nonane diol [9], was studied at the air/water interface and described by Langmuir kinetics, considering the adsorption and desorption rate constants. Another example is related to the adsorption of some salts of fatty acids, like sodium laurate [13-16], sodium myristate [13-15], and sodium oleate [17], from aqueous solutions to the air/water interface, which was analyzed by means of diffusion controlled kinetics.

Recently, the very slow adsorption of two anesthetics from water phase to oil/water interface [4] and of stearic acid from oil phase to the oil/water interface [1] has received a considerable attention using the diffusion controlled kinetics. The calculated diffusion coefficient values are much lower values than the expected physical values. Usually, this decrease is interpreted as the effect of the energetic barrier to the adsorption according to the theoretical model proposed in [5, 29, 30].

The dynamic interfacial pressures of these biocompounds, namely two anesthetics and stearic acid, will be further studied and characterized at the oil/water interface by using the Langmuir kinetic approach. The strong adsorption of both types of compounds, anesthetics and fatty acids, is due to the considerable change in the free energy of the system due to the immersion of hydrophobic groups and of hydrophilic groups into the oil and into the water phase, respectively. Nevertheless, the mechanism of the change in adsorption free energy is different for anesthetics than that for a fatty acid.

The main goal of this study is to analyse the experimental data recorded in terms of the time dependent interfacial pressures for the adsorption of the two anesthetics, like dibucaine and tetracaine, and of stearic acid at the same benzene/water interface and to discuss the adsorption mechanism in Langmuir kinetic approach.

LANGMUIR ADSORPTION KINETICS AT LIQUID/LIQUID INTERFACES

Adsorption kinetics of a surfactant from the bulk solution to a clean (pure) interface, without convection currents in the liquid [40], is described by the Ward and Tordai's diffusion [1, 4, 8] equation.

Previously, we found for these systems that experimental data cannot be understood by a simple diffusion mechanism [1, 4] and we replaced it by the Langmuir kinetic approach [9-11, 41] of the following form:

$$\frac{d\Gamma(t)}{dt} = k_1 c_s \left(1 - \frac{\Gamma(t)}{\Gamma_\infty} \right) - k_2 \frac{\Gamma(t)}{\Gamma_\infty} \quad (1)$$

where k_1 and k_2 are the rate constants for the adsorption and for the desorption processes, respectively, and Γ_∞ represents the maximum adsorption for the saturation of the liquid interface with biocompound molecules.

Eq. (1) is valid also at equilibrium, when $\frac{d\Gamma(t)}{dt} = 0$, $\Gamma(t) = \Gamma_e$ and $c_s = c_0$.

With these conditions Eq. (1) yields:

$$k_1 c_0 = \frac{k_1 c_0 + k_2}{\Gamma_\infty} \Gamma_e = k \Gamma_e \quad (2)$$

For some cases, with biocompound concentrations high enough, a diffusion equilibrium can be thought to be established, involving $c_s = c_0$. In this case [9], a combination of Eqs. (1) and (2) entails:

$$\frac{d\Gamma}{dt} = -k(\Gamma - \Gamma_e) \quad (3)$$

where k is the rate constant.

Integration of the Eq. (3) yields:

$$\Delta\Gamma = \Delta\Gamma_0 e^{-kt} \quad (4)$$

with $\Delta\Gamma = \Gamma - \Gamma_e$, $\Delta\Gamma_0 = \Gamma_0 - \Gamma_e$, where Γ_0 stands for the adsorption at $t = 0$, i.e. $\Gamma_0 = 0$.

If the increase of adsorption is proportional to the decrease of interfacial tension, Eq. (4) may be written as:

$$\Delta\sigma = \Delta\sigma_0 e^{-kt} \quad (5)$$

or in a logarithmic form:

$$\ln \frac{\Delta\sigma_0}{\Delta\sigma} = \ln \frac{\sigma_0 - \sigma_e}{\sigma - \sigma_e} = kt \quad (6)$$

where σ , σ_e and σ_0 stand for the actual dynamic interfacial tension, for the equilibrium interfacial tension, and for the interfacial tension in the absence of the surfactant, respectively.

These equations derived for the Langmuir kinetic mechanism are considered in more detail in the followings. For the beginning Eq. (6) has been tested in the case of the two anesthetics, viz. dibucaine and tetracaine, and of stearic acid.

MATERIAL AND METHODS

Biocompounds used were two local anesthetics: dibucaine (2-butoxy-N-[2-(diethylamino) ethyl] - 4 -quinoline carboxamide hydrochloride) and tetracaine (4-butyl amino benzoic acid 2-(dimethyl amino) ethyl ester hydrochloride) and a fatty acid, namely stearic acid (octadecanoic acid); all synthetic commercial products of high purity (minimum 99%) were purchased from Sigma. The purity of biocompounds was checked by thin layer chromatography and they were used without an additional purification.

As oil phase, benzene pro-analysis was used and it was purchased from Merck. We measured the interfacial tension as a function of time for the pure benzene/aqueous solutions of pH 2 interface and a time independent value was recorded. Thus, benzene did not contain surface active contaminants and, consequently, it was used without additional purification. Twice-distilled water of pH 2 was used, containing 0.01 mole/dm^3 of hydrochloric acid. The water had a resistivity of at least 18 Mohm cm and a surface tension at the interface with air of 72 mN/m at 25°C.

In order to study the adsorption of the three biocompounds at the same liquid interface, the benzene/water of pH 2 systems were chosen. In the case of stearic acid, at pH 2, its adsorbed monolayer is an uncharged one, the molecules being completely unionized [32, 34], and insoluble in water phase [32]. On the other hand, dibucaine and tetracaine may exist in three forms [42] uncharged (free base) and charged ones, *i.e.*, monocation (mono-protonated) and dication (diprotonated) molecules. The calculations show at pH 2, that the dibucaine is almost in mono-protonated form, and the tetracaine is a mixture of monocation (45%, mono-protonated) and dication (55 %, di- protonated) molecular species [42]; all molecular species are completely insoluble in the bulk benzene phase.

Dynamic interfacial tensions in the time range from 1 minute up to 90 minutes were measured by pendant drop and by ring methods for the following systems: aqueous solutions (pH 2) of various anesthetic concentrations at the interface with pure benzene and benzene solutions of various stearic acid concentrations at the interface with water of pH 2. Therefore, due to the very low solubility of anesthetics in benzene and of stearic acid in water of pH 2, any transport across the benzene/water interface can be neglected.

The pendant drop technique was described by us elsewhere [26]. By using a computer program the dynamic interfacial tensions were determined. These values were finally transformed into the dynamic interfacial pressures by subtracting the actual interfacial tensions from the interfacial tension of the pure interface in the absence of surfactants.

Experimental data obtained by the pendant drop technique were compared with the data obtained by ring method, which was described by us previously [27, 35, 43]. The agreement between the two methods is good and the deviations do not exceed the error of the individual method. The accuracy of the interfacial tension or the interfacial pressure measurements was ± 0.1 mN/m, in agreement with literature data [23, 41]. All measurements were performed at constant temperature of 20 ± 0.1 °C.

RESULTS AND DISCUSSION

Dynamic interfacial tension $\sigma(t)$ values obtained experimentally allowed us to calculate the corresponding $\Pi(t) = \sigma_0 - \sigma(t)$ interfacial pressure values. The $\Pi(t)$ *versus* time (*t*) curves, characterizing the adsorption process of the three biocompounds investigated from bulk phase to the benzene/ water (pH 2) interface are presented in Figs. 1-3. As can be seen, the interfacial pressures vary with surfactant bulk concentrations and with time over a wide range of time, from 0 to 15 for local anesthetics and from 0 to 90 min for stearic acid.

Generally, the equilibrium interfacial pressures (Π_e in mN/m) are recorded at 30 min for anesthetics and at 120 min for stearic acid when the adsorption equilibrium is completely attained and it is demonstrated by the constant value of the interfacial pressures.

The validity of the Langmuir kinetic approach, given by Eq. (6), has been tested by calculating the left hand side of this equation, by using the $\sigma(t)$ and σ_e values (the latter ones being measured at 30 min for the two anesthetics and 120 min for stearic acid). The interfacial tension of the pure benzene/water interface in the absence of surfactant was taken $\sigma_0 = 34.7$ mN/m under the chosen experimental conditions.

SURFACTANT ADSORPTION AT THE OIL/WATER INTERFACE

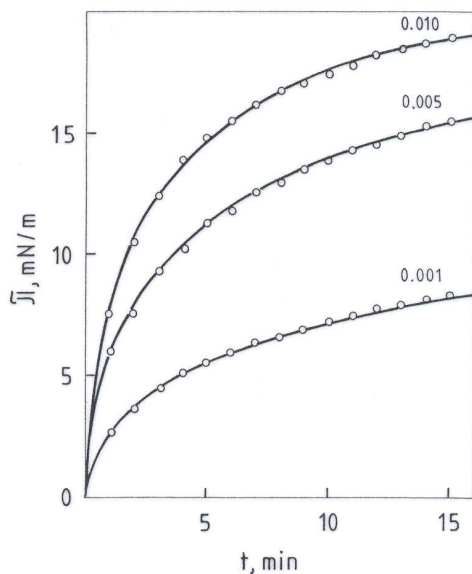


Fig. 1. Experimental dynamic interfacial pressure (Π in mN/m) of dibucaine aqueous solutions (pH 2) at the benzene/water interface, as a function of time (t , min). Figures indicate the dibucaine bulk concentration (c_0 in mole dm⁻³).

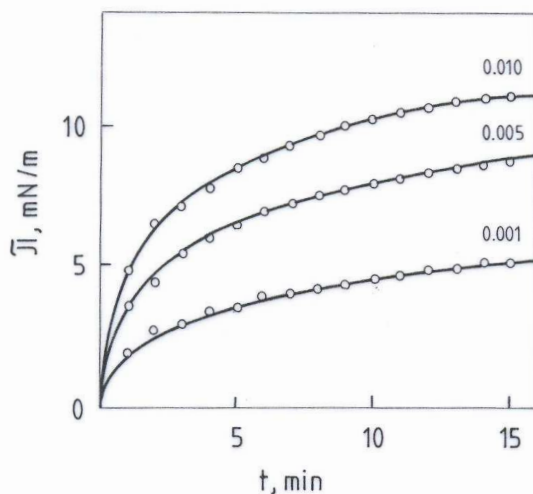


Fig. 2. Dynamic interfacial pressure (Π in mN/m) of tetracaine aqueous solutions (pH 2) at the benzene/water interface. Figures indicate the tetracaine bulk concentration c_0 in mole dm⁻³.

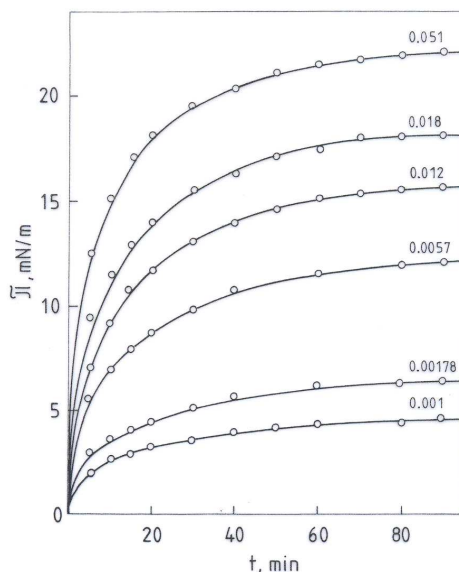


Fig. 3. Dynamic interfacial pressure (γ_{II} in mN/m) of stearic acid benzene solutions at the benzene/water (pH 2) interface. Figures indicate the stearic acid bulk concentration c_0 in mole dm^{-3} .

In order to explore Eq. (6), the logarithmic function *versus* t was investigated and it was found that it exhibits a quite good linearity as it is shown in a few examples given in Fig. 4 for the three biocompounds studied at the same bulk concentration of 10^{-3} mole dm^{-3} .

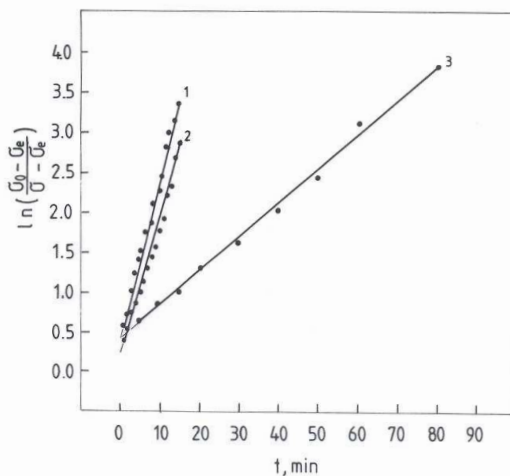


Fig. 4. The logarithmic function versus time, Eq. (6), for the adsorption of dibucaine (curve 1), tetracaine (2), and stearic acid (3) for the same biocompound bulk concentration c_0 of 10^{-3} mole dm^{-3} .

As it can be seen in Fig. 4, the straight lines do not pass through the origin of the coordinate system, and in reality Eq. (6) is of the following form:

$$y = \ln \frac{\sigma_0 - \sigma_e}{\sigma - \sigma_e} = a + kt \quad (7)$$

By performing a linear regression, the parameters a and k have been determined. Results are presented, together with the correlation coefficient (r), in Table 1. In the last column n indicates the number of experimental points used in the linear regression.

As shown in Table 1, the a values are different from zero, particularly for stearic acid. This means that the basic hypothesis used for deriving Eq. (6) is an approximation and it is not perfectly valid, presumably because the diffusion equilibrium is not completely established and the boundary condition $c_s = c_0$ is not yet fulfilled.

Table 1

The a and k parameters of Eq. (7).

| Biocompound | c_0 mole dm ⁻³ | a | k min ⁻¹ | r | n |
|--------------|--------------------------------|-------|--------------------------|--------|-----|
| Dibucaine | 0.001 | 0.152 | 0.169 | 0.9932 | 15 |
| | 0.005 | 0.202 | 0.190 | 0.9918 | 15 |
| | 0.01 | 0.284 | 0.234 | 0.9909 | 14 |
| Tetracaine | 0.001 | 0.342 | 0.154 | 0.9966 | 15 |
| | 0.005 | 0.340 | 0.176 | 0.9974 | 14 |
| | 0.01 | 0.330 | 0.199 | 0.9984 | 15 |
| Stearic acid | 0.001 | 0.430 | 0.0397 | 0.9991 | 9 |
| | 0.0018 | 0.374 | 0.0396 | 0.9977 | 7 |
| | 0.0057 | 0.395 | 0.0406 | 0.9990 | 8 |
| | 0.012 | 0.439 | 0.0415 | 0.9978 | 8 |
| | 0.018 | 0.568 | 0.0431 | 0.9994 | 9 |
| | 0.051 | 0.566 | 0.0501 | 0.9949 | 10 |

Nevertheless, from the k values reported in Table 1, some conclusions can be drawn. As seen, with increasing surfactant bulk concentrations c_0 the k values derived increase. This effect is expected on the basis of the Eq. (2) written in the following form:

$$k = \frac{k_1}{\Gamma_\infty} c_0 + \frac{k_2}{\Gamma_\infty} \quad (8)$$

and the k values *versus* c_0 exhibit indeed an acceptable linearity. To illustrate this situation, the relative k_1/Γ_∞ and k_2/Γ_∞ rate constant values and the corresponding correlation coefficients are presented in Table 2.

Table 2

Relative adsorption (k_1/Γ_∞) and desorption (k_2/Γ_∞) rate constants derived by Eq. (8) from k values given in Table 1.

| Biocompound | k_1/Γ_∞ mole ⁻¹ dm ³ min ⁻¹ | k_2/Γ_∞ min ⁻¹ | r | k_1/k_2 mole ⁻¹ dm ³ |
|--------------|---|--|--------|---|
| Dibucaine | 7.25 | 0.159 | 0.9914 | 45.6 |
| Tetracaine | 4.99 | 0.149 | 0.9988 | 33.5 |
| Stearic acid | 0.212 | 0.0392 | 0.9990 | 5.4 |

The analysis of data shown in Table 2 shows a quite good validity of Eq. (8). The relative rate constant values are rather reasonable and their ratios are in agreement with the published data for the adsorption of various surfactants at liquid interfaces [9-11].

ADSORPTION MECHANISM AT THE OIL/WATER INTERFACE

To give a better view on the adsorption mechanism, in Fig. 5, we have sketched the change of energy E versus distance Z to the interface and illustrated the energetic barriers for the adsorption and desorption process at the liquid-liquid interface.

The adsorption rate k_1 constant depends on the activation energy of adsorption, noted E_1 , by the following relation $k_1 \sim \exp(-E_1/k_B T)$, where k_B and T have their known meaning, and $E_1 > 0$. Similarly, the desorption rate k_2 constant depends on the activation energy of desorption, noted E_2 ($E_2 > 0$), by the relation $k_2 \sim \exp(-E_2/k_B T)$. Evidently, $E_a = E_1 - E_2$, where E_a is the adsorption energy. For $E_2 > E_1$, the adsorption energy is negative ($E_a < 0$) and the surfactant molecules spontaneously adsorb at the oil/water interfaces. The k_1/k_2 ratio gives the equilibrium adsorption constant (K) given by $K \sim \exp(-E_a/k_B T)$, which does not depend directly on the adsorption barrier.

In the case of anesthetics, the molecules adsorb from water to the oil/water interface by penetrating their hydrophobic chains into the oil phase. Their adsorption at the oil/water interface is controlled by the hydrophobic effect. According to this effect, the hydrocarbon chains in aqueous phase are surrounded with ordered water molecules [10]. In the activated state for adsorption, the water soluble anesthetic molecule is assumed devoid of the structured water [10] and the transition of hydrated molecule to its activated state is entropic. In fact, a change in entropy appears and it is due to the destruction of the ordered layers of water molecules around the alkyl chains. Even more, the activation E_1 energy of adsorption for the water soluble ionic compounds, like the two anesthetics, depends on the surface potential and of electrostatic interactions between ionized polar groups. Then, the activated state molecule gives the adsorbed anesthetic molecule (i.e. adsorbed state) at the oil/water interface with its polar head group hydrated and hydrocarbon tail immersed in the oil phase.

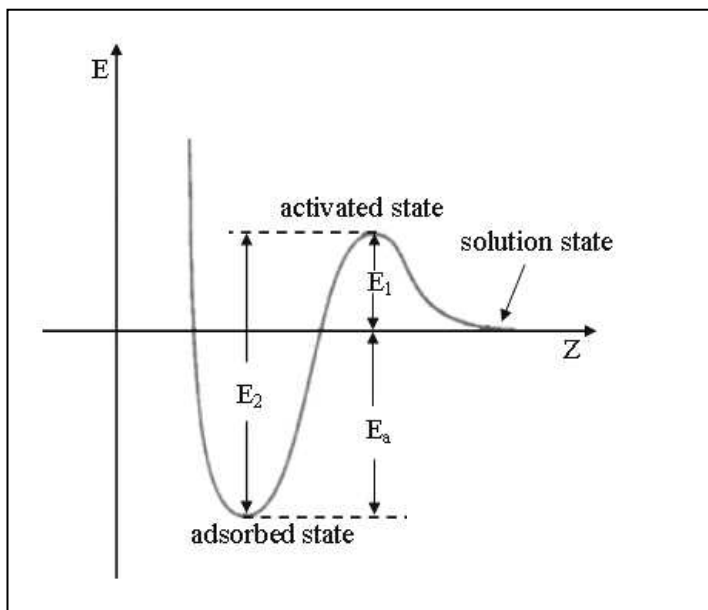


Fig. 5. Relation among the adsorption barrier E_1 (i.e. activation energy of adsorption), desorption barrier E_2 (i.e. activation energy of desorption) and the adsorption energy (E_a).

The adsorption k_1 rate constant is related to the transition energy (E_1) of a hydrated ionized anesthetic molecule in water (i.e. solution state) to its activated form (i.e. activated state). The driving force for adsorption, expressed by the adsorption rate constant, is at least in part entropic and might depend on the chain length and seems to be related to the hydrophobic effect. The activation E_1 energy of adsorption for the ionized anesthetics depends also on the surface potential and on the electrostatic interactions between ionized polar groups.

On the other hand, the desorption k_2 rate is related to the transition energy of the adsorbed anesthetic molecule at the oil/water interface to its activated complex described above, still in the water phase near the interface, devoid of its structured water particularly around its hydrocarbon chain. The desorption process apparently does not depend on the hydrocarbon chain length as we found in the case of anesthetics (see Table 2). This process is enthalpic and the activated molecule transforms into a surfactant molecule with the structured water around it in the aqueous phase. The desorption barrier E_2 is higher than E_1 and the adsorption E_a energy depends on the surface potential and on the adsorption energy of the hydrophobic tail.

In a first approximation, in the case of stearic acid, the adsorption energy and desorption barrier are assumed to be almost equal in magnitude mainly to the energy of transfer of the polar head group from the oil into the water phase. Because the hydrocarbon tail remains in the oil phase, the adsorption barrier is expected to be small and it might characterize the state of the adsorbed molecules due to the molecule reorientations in the oil/water interface [3]. Presumably, the

long saturated hydrocarbon chain must undergo a great number of conformational transitions to allow the polar headgroup of stearic acid to adopt a proper orientation and penetrate into the oil/water interface.

Stearic acid molecules adsorb from oil phase to the oil/water interface by immersing their unionized polar groups into the water phase. The driving force for the adsorption of stearic acid is the change in enthalpy due to the hydration of its adsorbed hydrophilic groups. Thus, stearic acid adsorbs strongly at the oil/water interface because the hydrophilic polar groups anchor and hydrate in water phase and may admit the possible conformational rearrangements in the adsorbed layer.

Returning to our data recorded in Table 2, one can observe that the relative adsorption k_1/Γ_∞ rate constant for dibucaine is higher than the k_1/Γ_∞ value for tetracaine, pleading for an adsorption barrier (i.e. an activation energy of adsorption) for dibucaine smaller than the corresponding one for tetracaine. This finding is also supported by the fact that the dibucaine is monocationic while tetracaine is a mixture of monocationic (45%) and dicationic (55%) forms, under the given working conditions. Therefore, it becomes clear that the electrostatic repulsion between the ionized polar groups represents at least a part of the barrier to the adsorption of the new arrival molecules.

Further, the relative desorption k_2/Γ_∞ rate constants are almost equal for both anesthetics and independent on the chain length, the chain being longer for dibucaine than for tetracaine. Thus, monolayers of anesthetics at the oil/water interface desorb at almost the same rate, also independent of the ionic molecular species existing within the monolayers.

It is interesting to compare the k_1/k_2 ratios, given also in Table 2. These ratios represent the equilibrium adsorption constants, given by $K \sim \exp(-E_a/k_B T)$, which are dependent on the adsorption energy and they are not dependent directly on the adsorption barriers. The equilibrium constants or the adsorption energies characterize the interfacial activity of these biocompounds at the oil/water interface. The value for dibucaine is higher than the corresponding value for tetracaine suggesting a higher interfacial activity of the dibucaine in excellent agreement with the interfacial pressure measurements.

It is to further observe an obvious similarity in the adsorption behaviour between these two types of biocompounds, i.e. anesthetics and stearic acid. They spontaneously adsorb at the oil/water interface leading to the decrease of the free energy of the system, but the mechanism of the adsorption is different as discussed above and consequently, the rate constants are determined by different factors.

Therefore, the adsorption of the two anesthetics and of stearic acid has completely different adsorption energy and adsorption barriers and different mechanism of desorption at the oil/water interface. However, the relative desorption rate k_2/Γ_∞ constants from monolayers of ionized anesthetics molecules are much higher than the corresponding value for monolayers of non-ionized stearic acid molecules at the same interface benzene/water of pH 2. This finding is plausible because the stability of the uncharged monolayers [32], like stearic acid on pH 2, is generally higher than that of the charged monolayers, namely mono-protonated dibucaine monolayers and the mixture of monocation and dication for tetracaine monolayers. At high interfacial pressures at the saturation of monolayers, the charged

molecules desorb faster being expelled from monolayers by the high lateral pressure and being loosed from monolayers of ionized anesthetics molecules due to the repulsive interaction forces.

Furthermore, considering the equilibrium adsorption of stearic acid $\Gamma_{\infty} = 2.1 \cdot 10^{-10}$ mole/cm² at the saturation [26] of monolayers at the benzene/water interface, the desorption rate constant k_2 in value of $8.26 \cdot 10^{10}$ molecules cm⁻² s⁻¹ was calculated. This value of the desorption rate constant k_2 of stearic acid from the oil/water interface appears as a plausible one, still higher than the desorption rate constant k_2 for the spread monolayers; e.g. hexadecanol monolayers [40] desorb at a rate of about $0.5 \cdot 10^{10}$ molecules cm⁻² s⁻¹ from the air/water interface.

Again, in spite of the different mechanism of desorption at the two different fluid interfaces, the difference between the two desorption rates might be explained due to the higher cohesive forces in the spread surfactant monolayers at the air/water interface than in the adsorbed monolayers at the oil/water interface. In adsorbed layers the oil molecules penetrate among the hydrocarbon chains of adsorbed stearic acid molecules diminishing the molecular interactions among the adsorbed biosurfactant molecules [27, 40, 43] and, consequently, the adsorbed molecules at the oil/water interface might desorb at a higher rate than the spread ones at the air/water interface.

CONCLUSION

The adsorption behavior of anesthetics (water soluble ionized dibucaine and tetracaine) and of stearic acid (oil soluble), which adsorb from the water phase and the oil phase, respectively, at the oil/water interface shows a certain type of similarity.

In the case of stearic acid, the molecules adsorb from oil phase to the oil/water interface by immersing their unionized polar groups into the water phase. Unlike the anesthetics, which are water ionisable soluble compounds, the driving force for the adsorption of stearic acid is the change in enthalpy due to the hydration of its adsorbed hydrophilic groups when they immerse in the water phase,

In the case of anesthetics, their adsorption at the oil/water interface is controlled by the hydrophobic effect, accompanied by the increase of the entropy due to the destruction of the ordered layers of water molecules structured around the alkyl chains, by the electrostatic interactions among the ionized polar groups oriented in the adsorbed layer and by the hydrophobic interactions among the hydrophobic chains and the oil phase.

The understanding of the adsorption kinetics and of adsorption mechanism of these biocompounds at fluid interfaces is important for the description of their dynamic surface properties. Nevertheless, the adsorption of these biocompounds at the oil/water interface might have an important role in vivo in various biological systems and in different pharmaceutical and biomedical processes.

REFERENCES

1. Tomoaia-Cotisel, M., Zsako, J., Tomoaia, Gh., Mocanu, A., Pop, V.-D., and Chifu, E., *Rev. Roumaine Chim.* **49**, 443 (2004).
2. Tomoaia-Cotisel, M., and Joos, P., *Rev. Roumaine Chim.*, **49**, 539 (2004).

3. Joos, P., Tomoaia-Cotisel, A., Sellers, A. J., and Tomoaia-Cotisel, M., *Colloids Surfaces. B. Biointerfaces* **37**, 83 (2004).
4. Tomoaia-Cotisel, M., Zsako, J., Mocanu, A., Salajan, M., Racz, Cs., Bran, S., and Chifu, E., *Stud. Univ. Babes-Bolyai, Chem.* **48**, 201 (2003).
5. Babak, V. G., and Boury, F., *Colloids Surfaces A: Physicochem. Eng. Aspects* **243**, 33 (2004).
6. Ravera, F., Ferrari, M., and Liggieri, L., *Adv. Colloid Interface Sci.* **88**, 129 (2000).
7. Eastoe, J., and Dalton, J. S., *Adv. Colloid Interface Sci.* **85**, 103 (2000).
8. Ward, A.F.H., and Tordai, L., *J. Chem. Phys.* **14**, 453 (1946).
9. Joos, P., Bleys, G., and Petre, G., *J. Chim. Phys.* **79**, 387 (1982).
10. Bleys, G., and Joos, P., *J. Phys. Chem.* **89**, 1027 (1985).
11. Joos, P., and Serrien, G., *J. Colloid Interface Sci.* **127**, 97 (1989).
12. Fainerman, V. B., Zholob, S. A., Miller, R., and Joos, P., *Colloids Surf. A* **143**, 243 (1998).
13. Van den Bogaert, R., and Joos, P., *J. Phys. Chem.* **83**, 2244 (1979).
14. Van den Bogaert, R., and Joos, P., *J. Phys. Chem.* **84**, 190 (1980).
15. Rillaerts, E., and Joos, P., *J. Colloid Interface Sci.* **88**, 1 (1982).
16. Coltharp, K. A., and Franses, E. I., *Colloids Surf. A* **108**, 225 (1996).
17. Theander, K., and Pugh, R. J., *J. Colloid Interface Sci.* **239**, 209 (2001).
18. Czichocki, G., Makievski, A.V., Fainerman, V. B., and Miller, R., *Colloids Surf. A* **122**, 189 (1997).
19. Vermeulen, M., and Joos, P., *Colloids Surf.* **33**, 337 (1988).
20. Liggieri, L., Ravera, F., and Passerone, A., *J. Colloid Interface Sci.* **169**, 226 (1995).
21. Liggieri, L., Ravera, F., and Passerone, A., *J. Colloid Interface Sci.* **169**, 238 (1995).
22. Li, J., Miller, R., and Mohwald, H., *Colloids Surf. A* **114**, 113 (1996).
23. Li, J., Fainerman, V. B., and Miller, R., *Langmuir* **12**, 5138 (1996).
24. Beverung, C. J., Radke, C. J., and Blanch, H. W., *Biophys. Chem.* **81**, 59 (1999).
25. Baret, J. F., *J. Chim. Phys.* **65**, 895 (1968).
26. Chifu, E., Salajan, M., Demeter-Vodnár, J., and Tomoaia-Cotisel, M., *Rev. Roum. Chim.* **32**, 683 (1987).
27. Chifu, E., Tomoaia-Cotisel, M., Andrei, Z., and Bonciu, E., *Gazz. Chim. Ital.*, **109**, 365 (1979).
28. Chatterjee, J., and Wasan, D. T., *Chem. Eng. Sci.* **53**, 2711 (1998).
29. Liggieri, L., Ravera, F., and Passerone, A., *Colloids Surf. A* **114**, 351 (1996).
30. Ravera F., Liggieri, L., and Steinchen, A., *J. Colloid Interface Sci.* **156**, 109 (1993).
31. Yousef, A., and McCoy, B. J., *J. Colloid Interface Sci.* **94**, 497 (1983).
32. Tomoaia-Cotisel, M., Zsako, J., Mocanu, A., Lupea, M., and Chifu, E., *J. Colloid Interface Sci.* **117**, 464 (1987).
33. Zsako, J., Tomoaia-Cotisel, M., Chifu, E., Mocanu, A., and Frangopol, P. T., *Biochim. Biophys. Acta* **1024**, 227 (1990).
34. Tomoaia-Cotisel, M., *Progr. Colloid Polym. Sci.* **83**, 155 (1990).
35. Tomoaia-Cotisel, M., and Cadenhead, D. A., *Langmuir* **7**, 964 (1991).
36. Asgharian, B., Cadenhead, A. D., and Tomoaia-Cotisel, M., *Langmuir* **9**, 228 (1993).
37. Zsako, J., Tomoaia-Cotisel, M., Chifu, E., Mocanu, A., and Frangopol, P. T., *Gazz. Chim. Ital.*, **124**, 5 (1994).
38. Hata, T., Matsuki, H. and Kaneshina S., *Biophys. Chem.*, **87**, 25 (2000).
39. Frangopol, P.T. and Mihailescu, D., *Colloids Surfaces. B. Biointerfaces*, **22**, 3 (2001).
40. Davies, J. T. and Rideal, E. K., *Interfacial Phenomena*, Second Edition, Academic Press, New York, 1963, Chapter 4, pp. 154-216.
41. Miller, R., Joos, P., and Fainerman, V. B., *Adv. Colloid Interface Sci.* **49**, 249 (1994).
42. Zsako, J., Tomoaia-Cotisel, M., Albu, I., Mocanu, A., Chifu, E. and Frangopol, P. T., *Rev. Roum. Biochim.*, **28**, 33 (1991).
43. Chifu, E., Tomoaia, M., and Ioanette, A., *Gazz. Chim. Ital.* **105**, 1225 (1975).

THERMODYNAMIC APPROACH ON SPECIFIC INTERACTIONS IN LIPID AND CAROTENOID NANOFILMS

AURORA MOCANU^a, GHEORGHE TOMOAIA^b, CALIN FLOARE^c,
ROBERT TOTOS^d, OLIMPIA-CRISTINA BOROSTEAN^a and
MARIA TOMOAIA-COTISEL^a

^a"Babes-Bolyai" University of Cluj-Napoca, Department of Physical Chemistry,
400028 Cluj-Napoca, Romania

^b"Iuliu Hatieganu" University of Medicine, Department of Orthopaedic Surgery,
400015 Cluj-Napoca, Romania

^cNational Institute for Research and Development of Isotopic and Molecular
Technologies, P.O. Box 700, Cluj-Napoca, Romania

^d"Raluca Ripan" Institute of Chemistry, 400294 Cluj-Napoca, Romania

ABSTRACT. The mixed lipid : carotenoid nanofilms spread at the air/water interface, namely (1) egg lecithin : β -cryptoxanthin; (2) egg lecithin : β -cryptoxanthin palmitate; (3) egg lecithin : zeaxanthin monopalmitate; (4) distearoyl lecithin : zeaxanthin; (5) distearoyl lecithin : astaxanthin; (6) distearoyl digalactosyl glycerol : astaxanthin have been investigated. The curves of surface collapse pressure versus nanofilm composition are discussed in terms of surface mixture thermodynamics. It has been found that the system (1) presents a perfect behaviour throughout the entire range of composition, while systems (2) and (3) can be satisfactorily described by the regular solution theory. For systems (4) - (6) a new approximation is proposed, considering the formation of supramolecular associations in nanofilms. The stability constants of the supramolecular complexes in nanofilms are calculated and correlated to the specific interactions that can occur in mixed nanofilms in substantial agreement with the molecular structures of the investigated biocompounds.

Keywords: *mixed lipid and carotenoid nanofilms, collapse surface pressures, thermodynamic approach, miscibility, phase rule.*

INTRODUCTION

Carotenoids are biologically important compounds and a vast research has been invested in studies of photochemistry, biochemistry and antioxidant properties. The physicochemical properties of carotenoids and their interactions with various lipids and proteins are also needed to clarify their effects and functions in biological membranes. The common chemical feature of carotenoids is the polyisoprenoid structure, a long conjugated chain of double bonds in the central portion of molecule. Within biomembranes, carotenoids are in the vicinity of lipids and proteins in organized supramolecular structures. Therefore, the carotenoid molecules must be able to fit into these complex systems with a correct molecular orientation [1-5]. Substantial differences in the activities of individual carotenoids are offered by certain polar groups attached to the terminal carbon rings and their structural details will define the precise position and molecular orientation in thin lipid nanofilms and in biological membranes.

The purpose of this study is to identify the carotenoid effects on the organization of the lipid nanofilms (monolayers or nanolayers). We have examined the monolayer characteristics of six individual carotenoids and three different lipids

in pure single-component nanolayers. We have also studied the miscibility of lipids and carotenoids, as well as the phase behavior and specific interactions in mixed lipid-carotenoid nanolayers by using the Langmuir monolayer technique and thermodynamic approach. The different behavior of mixed carotenoid-lipid nanolayers shows the differences among the surface properties of carotenoids with one polar group (such as β -cryptoxanthin), with two (e.g. zeaxanthin) or many polar groups (e.g. astaxanthin). Further, the incorporation of carotenoids into the lipid nanofilms revealed an increased stability of mixed lipid : carotenoid nanolayers at the air/water interface.

EXPERIMENTAL SECTION

The all-trans carotenoids, like β -cryptoxanthin, β -cryptoxanthin palmitate, zeaxanthin monopalmitate, zeaxanthin, and astaxanthin were provided by Hoffmann La Roche (Switzerland) in a chromatographically pure state. The investigated lipids, such as egg lecithin and distearoyl lecithin were products of Sigma. The distearoyl digalactosyl glycerol was kindly provided by P.J. Quinn (King's College, University of London). Details of the surface pressure measurements and on Langmuir nanolayer apparatus were published elsewhere [6-8]. The spread nanolayers at the air/water interface were compressed continuously and the compression isotherms and then collapse pressure values were recorded at about 22 °C. The precision of the surface pressure measurements was of 0.1 mN/m.

RESULTS AND DISCUSSION

The six systems of two-component nanofilms are presented consisting of lipid (A) and carotenoid (B) namely: system (1) made of egg lecithin (EL) : β -cryptoxanthin (3-hydroxy- β -carotene (C); (2) EL : β -cryptoxanthin palmitate (CP); (3) EL : zeaxanthin monopalmitate (ZP); (4) 1,2-distearoyl lecithin (DSL) : zeaxanthin (3,3'-dihydroxy- β -carotene : Z); (5) DSL : astaxanthin (3, 3'- dihydroxy, 4, 4'-dioxo- β -carotene : AX); (6) 1,2-distearoyl digalactosylglycerol (DGDG) : AX. These systems are investigated by collapse surface pressure measurements as a function of the system composition, given so called monolayer isotherms.

To illustrate the nanofilm surface behavior, the monolayer curves are given for some of these systems, namely for system (1) made of EL : C (Fig. 1), system (2) formed of EL : CP (Fig. 2), and system (4) realized by DSL : Z (Fig. 3).

As seen in Figs. 1-3, the collapse pressure is a unique function of the composition of the monolayers, the systems (1), (2) and (4) being monovariant. This situation is found with all the investigated systems (1) - (6). Accordingly to the surface phase rule [6-12], this means that the components A and B are totally miscible in both phases, in monolayer and in collapsed phase.

By presuming that a metastable equilibrium is established upon collapse between surface nanofilm phase (M) and collapsed phase (C), the equilibrium between the two phases can be characterized by the equality [6-8] of the chemical potentials, $\mu_i^M = \mu_i^C$, of each i molar species ($1 \leq i \leq m$) leading to the following relation:

$$\sum_{i=1}^m \frac{f_i^M}{f_i^C} x_i^M \exp \left[(\pi - \pi_i) \frac{A_i}{kT} \right] = 1 \quad (1)$$

where f_i^φ stands for the activity coefficient of the i component in the phase φ , x_i^φ is the molar fraction of the i component in phase φ , π is the collapse pressure of the mixed film, π_i and A_i represent the collapse pressure and the collapse area, respectively, in the single component monolayer formed of the pure i component. If there is no specific interaction between the carotenoid and lipid molecules, then, both M and C can be considered as perfect solutions, i. e. $f_i^C = f_i^M = 1$. The deviation of the experimental data from the calculated curve given by Eq. (1) with $f_i^\varphi = 1$ points out to the existence of some specific interactions in the investigated system.

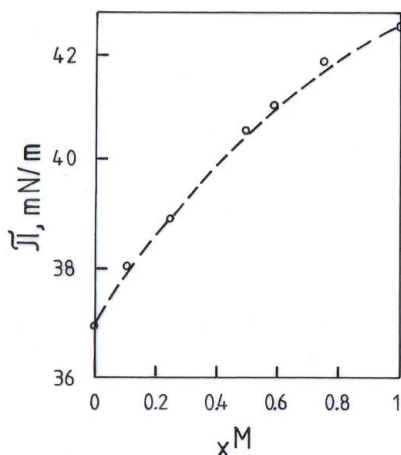


Fig. 1. Experimental collapse pressures and calculated monolayer curve at $T = 295$ K for system (1) made of EL : C; dashed line calculated by Eq. (1) with $f_i^\varphi = 1$.

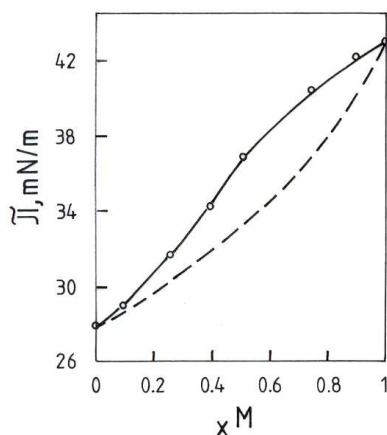


Fig. 2. Experimental collapse pressures and calculated monolayer curves for system (2) made of EL : CP; dashed line calculated by Eq. (1) with $f_i^\varphi = 1$; solid line, calculated with regular solution theory, with numerical values of ξ^φ given in Table 1.

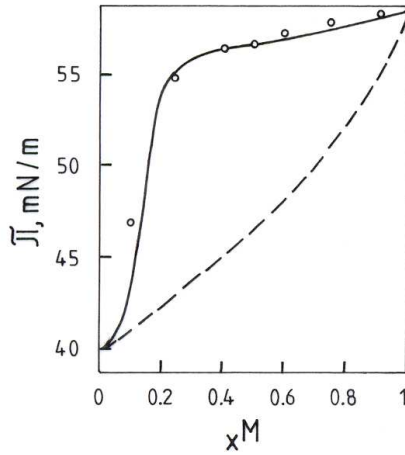


Fig. 3. Experimental collapse pressures and calculated monolayer curves for system (4) made of DSL : Z; dashed lines calculated by Eq. (1) with $f_i^\phi = 1$; solid line, calculated by Eq. (3) using $K = 3.9$ and $\Delta\pi = 2.5$ mN/m.

In the case of our systems containing the biosurfactants A and B, we use the notation $x_A^\phi = x^\phi$ and $x_B^\phi = 1 - x^\phi$, by considering in the monolayer the molar fraction of the subphase liquid to be at the collapse negligently small and on the other hand $\pi_A > \pi_B$. For the system (1), Eq. (1) with $f_i^\phi = 1$ describes very well the experimental curve (Fig. 1), while with all other systems positive deviations occur from the perfect system curve (Figs. 2 and 3).

An attempt to explain these deviations has been made by using the regular solution theory, giving the activity factors in both M and C as function of an interaction parameter (ξ^M and ξ^C) as shown previously [6-12], by using the following relations:

$$f_A^\phi = \exp[\xi^\phi(1 - x^\phi)^2] \quad \text{and} \quad f_B^\phi = \exp[\xi^\phi(x^\phi)^2] \quad (1a)$$

We have determined that this approximation can describe an experimental curve with positive deviations [6-8] from the perfect behavior when the maximum deviation occurs at $x^M \geq 0.5$, as in the situation of system (2) (Fig. 2) and system (3) (see, Table 1).

The interaction parameters have been obtained by double minimization of the standard deviation Δ of the experimental π data from the computed ones, by using the corresponding relations of regular solution theory [6-8]. The much greater values of interaction parameters obtained with system (3) as compared to system (2) point to the important role played by the OH-groups in the interaction between EL and carotenoids.

The maximum deviation from the perfect behavior being found at $x^M \leq 0.5$ with the systems (4) - (6), the regular solution theory is not applicable, and the shape of the experimental curves suggests the formation of molecular associations

or AB_n -type complexes, implying in the monolayer an equilibrium between $(n + 2)$ molecular species: A, B, AB, AB_2 , ... , AB_n , the equilibria being characterized by n stability constants. The equation of π versus x^M curves becomes:

$$\frac{f_A^M}{f_A^C} x_A^M \exp\left[(\pi - \pi_A) \frac{A_A}{kT}\right] + \frac{f_B^M}{f_B^C} x_B^M \exp\left[(\pi - \pi_B) \frac{A_B}{kT}\right] + \sum_{i=1}^n \frac{f_i^M}{f_i^C} x_i^M \exp\left[(\pi - \pi_i) \frac{A_i}{kT}\right] = 1 \quad (2)$$

in which the number of unknown parameters is 34. Their deriving from a single experimental curve is practically impossible. Therefore, we advance the following simplifications which lie at the basis of the approximation of the perfect solutions of regular associations: the molecular species i (A, B, AB_i ; $1 \leq i \leq n$) form perfect solutions in both M and C. The molecular areas are additive, i. e. $A_{AB_i} = A_A + iA_B$. The attachment of each molecule B to molecule A or to the complex AB_{i-1} ($AB_{i-1} + B \leftrightarrow AB_i$) brings about the same collapse pressure increment, $\Delta\pi$, of the pure monolayer consisting of A, i.e. $\pi_{AB_i} = \pi_A + i\Delta\pi$; upon formation of molecular associations the equilibrium constants have the same value for each complexing step:

$$K_i = \frac{x_{AB_i}^M}{x_{AB_{i-1}}^M \cdot x_B^M} = K.$$

Thus, for $n = 6$ Eq. (2) becomes:

$$x_A^M \exp\left[(\pi - \pi_A) \frac{A_A}{kT}\right] + x_B^M \exp\left[(\pi - \pi_B) \frac{A_B}{kT}\right] + \sum_{i=1}^6 x_{AB_i}^M \exp\left[(\pi - \pi_A - i\Delta\pi) \frac{A_A + iA_B}{kT}\right] = 1 \quad (3)$$

The molar fractions of all the molecular species AB_i are calculated by the following relation:

$$x_{AB_i}^M = \frac{(1 - x_B^M)(x_B^M \cdot K)^i}{1 + \sum_{i=1}^6 (x_B^M \cdot K)^i} \quad (4)$$

Table 1.

Interaction parameters (ξ^Φ), stability constants (K) and surface pressure increments ($\Delta\pi$) of the regular associations, and the minimum standard deviation.

| System | Component | | $\xi_{m,m}^M$ | ξ_m^C | K | $\Delta\pi$ (mN/m) | $\Delta_{m,m}$ (mN/m) |
|--------|-----------|----|---------------|-----------|------|-----------------------|--------------------------|
| | A | B | | | | | |
| (1) | EL | C | 0.00 | 0.00 | - | - | - |
| (2) | EL | CP | - 2.65 | - 1.73 | - | - | 0.169 |
| (3) | EL | ZP | - 9.48 | - 8.67 | - | - | 0.105 |
| (4) | DSL | Z | - | - | 3.90 | 2.50 | 0.340 |
| (5) | DSL | AX | - | - | 1.45 | 1.00 | 0.213 |
| (6) | DGDG | AX | - | - | 1.17 | 0.05 | 0.172 |

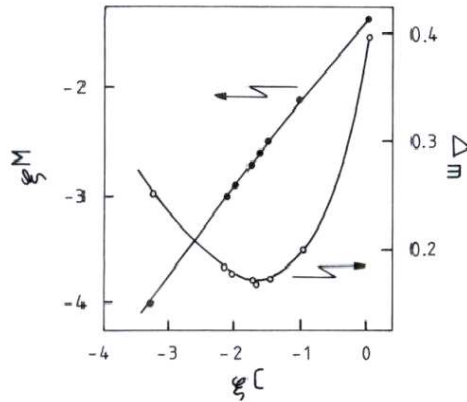


Fig. 4. Deriving the interaction parameters for the system (2) of EL : CP; for symbols see the text.

The x_B^M value is obtained as a solution of the seventh order of the following equation:

$$x_A^{oM}(1-x_B^M)\sum_{i=1}^6 i(x_B^M \cdot K)^i = (1-x_A^{oM}-x_B^M)\left[1+\sum_{i=1}^6 (x_B^M \cdot K)^i\right] \quad (5)$$

where x_A^{oM} stands for the apparent molar fraction of A component initially spread in the film. Thus, Eqs. (3) - (5) include only two unknown parameters namely K and $\Delta\pi$, which can be calculated from the experimental data (π versus x_A^{oM}) by also using a double minimization procedure for the standard deviation, this time however as a function of K and $\Delta\pi$. The procedure is illustrated by Fig. 5.

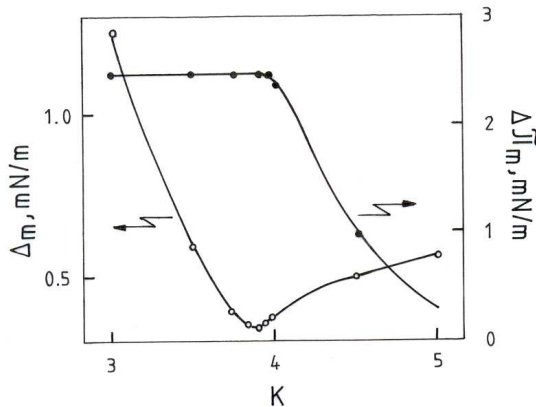


Fig. 5. Deriving of K and $\Delta\pi$ for regular associations within the system (4) of DSL : Z nanofilms.

Table 1 gives the K and $\Delta\pi$ values as well as the corresponding standard deviations $\Delta_{m,m}$. Once the value of K is known, the molar fractions of the molecular species versus the spread mixture composition can be computed by Eqs. (4) and (5). The x_i^M versus x_A^{oM} plots are given in Fig. 6 for the DSL : Z system.

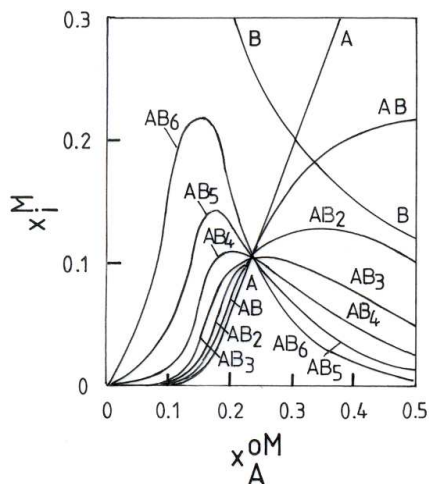


Fig. 6. Composition of the system (4) of DSL:Z nanofilms versus x_A^{oM} . The isotherms were computed by Eq. (4), using $K = 3.9$. The meaning of i is given near each curve.

It is to be noticed in Table 1 that for systems (4)-(6) the $\Delta_{m,m}$ values range below the mean experimental error of π , and the stability of the supramolecular associations is great in system (4) diminishing then in the order of DSL : Z > DSL : AX > DGDG : AX. This order points to the important role played by the carotenoid OH-group in the formation process of carotenoid and lipid supramolecular associations, while the carbonyl groups of AX seemingly disfavor such associations. The correlation of these thermodynamic results with the molecular structure of studied biomolecules in nanofilms is in progress in our laboratories.

It can generally be concluded that Eq. (3) provides good description of the experimental data of the systems (4) - (6), and the obtained K and $\Delta\pi$ values reveal specific interactions between the lipid and carotenoid molecules in nanofilms at the air/water interface.

REFERENCES

- 1) C. N. N'soukpoe-Kossi, J. Sielewiesiuk, R. M. Leblanc, R. A. Bone and J. T. Landrum, *Biochim. Biophys. Acta*, **940**, 255-265 (1988).
- 2) M. Tomoaia-Cotișel and P. J. Quinn, "Chapter 10: Biophysical properties of carotenoids" in *Subcellular Biochemistry, Vol. 30: Fat-Soluble Vitamins*, Editors: P. J. Quinn and V. E. Kagan, Plenum Press, New York, 1998, pp. 219-242.
- 3) A. Sujak, W. Okulski and W. I. Gruszecki, *Biochim. Biophys. Acta*, **1509**, 255-263 (2000).
- 4) A. Shibata, Y. Kiba, N. Akati, K. Fukuzawa and H. Terada, *Chem. Phys. Lipids*, **113**, 11-22 (2001).
- 5) M.-I. Salajan, A. Mocanu and M. Tomoaia-Cotișel "Advances in Thermodynamics, Hydrodynamics and Biophysics of Thin Layers", University Press, Cluj-Napoca, 2004.
- 6) M. Tomoaia-Cotișel, E. Chifu and J. Zsako, *Colloids and Surfaces*, **14**, 239 (1985).

- 7) J. Zsako, M. Tomoaia-Cotisel and E. Chifu, *J. Colloid Interface Sci.*, **102**, 186 (1984).
- 8) J. Zsako, M. Tomoaia-Cotisel and E. Chifu, *J. Colloid Interface Sci.*, **146**, 353-362 (1991).
- 9) M. Nakagaki, and N. Funasaki, *Bull. Chem. Soc. Japan*, **47**, 2482 (1974).
- 10) T. Handa and M. Nakagaki, *Colloid Polym. Sci.*, **257**, 374 (1979).
- 11) R. Defay, I. Prigogine, A. Bellemans and D. H. Everett, "*Surface Tension and Adsorption*", Longmans, Green, London, 1966.
- 12) P. Joos, *Bull. Soc. Chim. Belges*, **78**, 207 (1969).

BIOSENSOR FOR AMPEROMETRIC DETECTION OF CATECHOL BASED ON MUSHROOM TISSUE AND A METHYLENE GREEN-NAFION MODIFIED ELECTRODE

SONIA A. SPINEAN, GRAZIELLA L. TURDEAN*
and IONEL CATALIN POPESCU

*"Babes-Bolyai" University, Faculty of Chemistry and Chemical Engineering, Department of Physical Chemistry, Arany Janos St. 11, 400028 Cluj-Napoca, Romania;
E-mail:gturdean@chem.ubbcluj.ro*

ABSTRACT. An enzyme based biosensor for the amperometric detection of catechol is described. The bioelectrode architecture consists of a Nafion® film, as immobilization matrix, phenothiazine dye (Methylene Green, MG) as mediator and mushroom tissue as tyrosinase source. The electrochemical and electrocatalytical behavior of the bioelectrode was investigated by cyclic voltammetry and amperometry. The biosensor has a sensitivity of $2 \text{ mA} \cdot \text{M}^{-1}$, with a detection limit of $20 \text{ } \mu\text{M}$ catechol and reaches 95 % of the steady-state current within 50-100 s, when the applied potential was -0.05 V vs. Ag/AgCl , KCl_{sat} .

Keywords: Methylene Green, mushroom tissue, catechol, Nafion, amperometric biosensor.

INTRODUCTION

Most of the phenolic compounds are generated artificially and are present in wastewaters of chemical plants, exhaust gases of incinerators, sidestream smoke of cigarettes etc. [1]. They have toxic effects on animal and plants because of their skin and membrane penetration, determining a broad spectrum of genotoxic, mutagenic, carcinogenic and hepatotoxic effects, affecting also the biocatalysed reaction rates in respiration and photosynthesis [2]. The European Community directive (80/778/EEC) sets the maximum concentration permitted for all phenols in aquatic environments at $0.5 \text{ } \mu\text{g/l}$ and at $0.1 \text{ } \mu\text{g/l}$ for individual phenols [2].

The detection of mono- and polyphenols is usually performed by means of chromatography and/or spectrometry [2]. In particular, catechol could also be detected by inhibited chemiluminescence method [3]. Among the electrochemical methods, those using enzyme electrodes incorporating tyrosinase [4], lacasse [5] or peroxidase [1] are relative sensitive. For *in vivo* detection of catechol, the inhibitor effect of ascorbic acid could be eliminated using a Nafion film or a self-assembled monolayer [3]. There has been considerable interest in replacing isolated enzymes with tissue materials as the biocatalytic entity of electrochemical sensors. The major advantages resulting from the use of tissue materials are high stability and bioactivity (associated from the presence of the enzyme in large quantities in its natural environment), generally associated with low cost [6].

Tyrosinase (Ty) is a phenol oxidase present in microorganisms, animals and plants and is responsible for the browning of exposed surfaces on some fruits (i.e. banana) and tubers (i.e. potato) [7]. The two steps mechanism involving tyrosinase consists in the oxidation of monophenols or o-diphenols into their

corresponding o-quinones, with the expense of reducing oxygen to water [2]. The catalytic cycle of tyrosinase with catechol as substrate and subsequent electrochemical reduction of o-quinones occurring at the solution-electrode interface is presented in figure 1 [8].

Nafion is a linear copolymer derived from tetrafluoroethylene and perfluoro-sulphonic acid monomers. Over the last few years one important application of ion-exchange polymers was their use as immobilization matrices for different mediators or enzymes involved in the construction of amperometric biosensors [2].

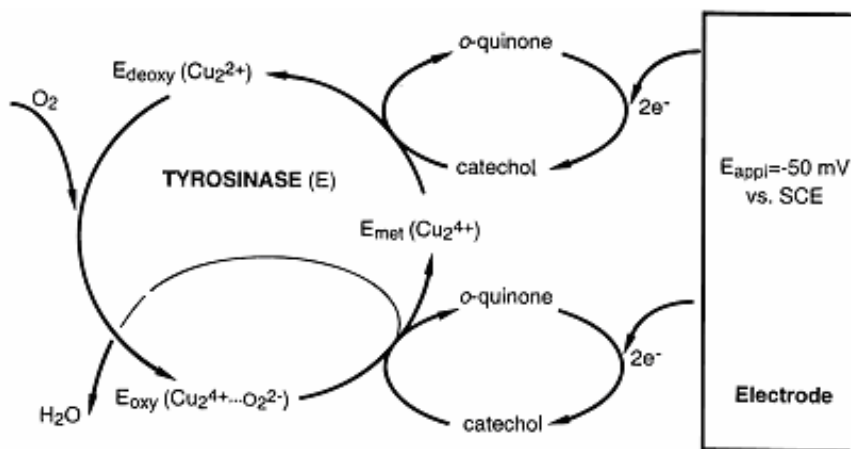


Figure 1. Catechol oxidation catalysed by tyrosinase at an enzyme-modified electrode [8].

Methylene Green, a water soluble phenothiazine derivative, has been used successfully as mediator either in solution, or immobilized on the electrode surface for H_2O_2 detection [9], NADH [10-11].

In the present work, a modified electrode was realized by incorporating Methylene Green into a Nafion thin layer on a graphite surface. The corresponding biosensor, based on tyrosinase was obtained by immobilizing on the tip of the modified electrode a thin layer of mushroom tissue using nylon net. The electrochemical behavior of the modified electrode and its operational stability have been studied and the kinetic aspects of the catechol detection process were also investigated. The analytical parameters of the biosensor were evaluated.

EXPERIMENTAL

Reagent and Materials

Methylene Green (MG) was purchased from *Janssen Chimica (Beerse, Belgium)*, Nafion® solution (5% in methanol with equivalent weight of about 1100) from *Fluka (Buchs, Switzerland)* and the phenol from "*Reactivul*" *Bucuresti*. A phosphate buffer solution (PBS, pH 7, ionic strength 0.1 M) was prepared from a 0.4 M NaH_2PO_4 and 0.4 M Na_2HPO_4 (*Sigma*) solutions and was always employed as supporting electrolyte. The mushrooms used throughout this study were purchased from a local grocery store and were stored at 5°C until use.

The 1 mM **MG** solution was prepared by dissolving its chloride salt in a 0.1 M phosphate buffer (pH 7). The Nafion 2.5 % solution was obtained by diluting in ethanol a 5% Nafion solution. The solution of 0.05 M PBS was prepared with distilled water. All chemicals were of analytical grade and were used without further purification. The buffer solutions were kept refrigerated to minimize bacterial growth.

Apparatus

Cyclic voltammetric investigations were carried out on a computer controlled Autolab voltammetric analyzer (*PGSTAT 10, EcoChemie, Netherlands*).

All measurements were done using a standard single-compartment three electrode cell equipped with a platinum counter electrode, an Ag/AgCl, KCl_{sat} reference electrode (*Radiometer, France*) and a spectral graphite (3 mm diameter) (*Ringsdorff-Werke, GmbH, Bonn-Bad Godesberg, Germany*) working electrode. All experiments were performed at room temperature.

Modified electrode preparation

Before modification, the graphite electrodes were polished with fine emery paper and then were rinsed thoroughly with distilled water. 5 μl of 2.5% Nafion solution was dropped onto the electrode surface. After solvent evaporation, the Nafion-coated graphite electrode was immersed into a 1 mM MG solution and the MG incorporation into Nafion film was electrochemically controlled by scanning the electrode potential in the range -0.7 to +0.7 V vs. Ag/AgCl, KCl_{sat} , for a specified number of cycles. The obtained modified electrodes were symbolized by G/Nafion-MG25, G/Nafion-MG50 and G/Nafion-MG100 where the associated number indicates the number of CV cycles used for MG incorporation.

The Ty modified electrode was obtained by immobilizing of a thin layer mushroom tissue on the tip of the graphite or of the MG modified electrode, using a Nylon membrane. The obtained bioelectrode was symbolized by G/Ty or G/Nafion-MG/Ty, respectively.

RESULTS AND DISCUSSION

Electrochemical behavior of G/Nafion-MG modified electrodes

The cyclic voltammograms recorded at G/Nafion electrode, in contact with a 1 mM MG/phosphate buffer, showed two couples of redox peaks at a formal standard potentials ($E^{\circ'}$; calculated as $(E_{\text{pa}} + E_{\text{pc}})/2$, where E_{pa} is the potential of the anodic peak and E_{pc} is the potential of the cathodic peak) of -0.325 V vs. Ag/AgCl, KCl_{sat} (peak A1/C1) and -0.105 V vs. Ag/AgCl, KCl_{sat} (peak A2/C2) (Figure 2.A). Both peaks pairs correspond to a single electron transfer, involved in the MG electrode reaction [10].

The increase of the peak currents for A1/C1 couple, with the increase of the number of cycles proves an increase of the MG concentration in the Nafion film. This immobilization/inclusion of MG within Nafion matrix is supposed to be facilitated by the electrostatic attraction between the negatively charged sulfonic acid groups of Nafion and the positively charge of the oxidized state of MG [9], as well as to the partial electropolymerization of MG. The second hypothesis may be advanced because after the first cycle, which shows two distinct pairs of peaks, in the following cycles the A2/C2 peaks progressively disappear and at the same time, the $W_{1/2}$ value of A1/C1 peaks increase [10].

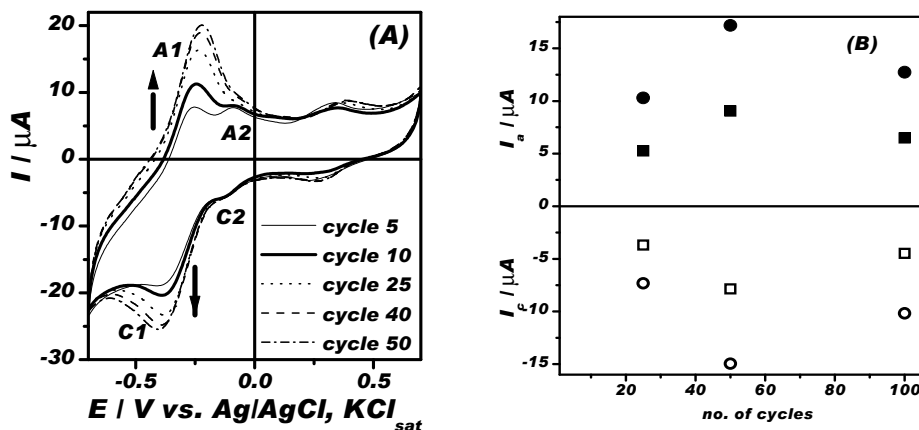


Figure 2. Cyclic voltammograms of G/Nafion electrode (A) and the dependence of the peak intensity for A1/C1 couple on the number of potential cycles (B). Experimental conditions: 1 mM MG in phosphate buffer 0.1 M (pH 7); starting potential, -0.5 V vs. Ag/AgCl/KCl_{sat}; potential scan rate, 50 mV*s⁻¹ (A) 25 mV*s⁻¹ (■, ●) or 50 mV*s⁻¹ (○, ○) (B).

After 50 cycles of potential scanning, the concentration of MG in the Nafion matrix reaches a maximum (figure 2.B).

The electrochemical behaviour of the G/Nafion-MG modified electrode was studied with respect to the potential scan rate (Figure 3A). In the investigated potential range, irrespective the modified-electrodes preparation, only one couple of peaks (A1/C1) appears at approximately the same formal standard potential: -0.110 V, -0.130 V and -0.125 V vs. Ag/AgCl, KCl_{sat} for G/Nafion-MG25, G/Nafion-MG50 and G/Nafion-MG100 respectively. Comparing the average formal standard potential with that reported for MG in aqueous solution (-0.070 V vs. SCE [11]), a negative potential shift was observed, indicating a stability increase of the MG incorporated in the Nafion matrix. In literature, this peak was attributed to the MGH/MG⁺ couple involved in the global reaction [9]:



As showed by the peak separation ($\Delta\epsilon_p = \epsilon_{pa} - \epsilon_{pc}$), which is significantly different from zero even at a low scan rate, the rate of the electron transfer between MG and the electrode is an important aspect to be considered in the investigated system [11]. For all type of investigated modified-electrodes, the peak potential separation is almost constant in the range of investigated potential scan rates (from 10 to 200 mV*s⁻¹) and does not exceed 100 mV [12], suggesting that the electron transfer process is not fully reversible.

This behaviour can be assigned to the presence of a small resistance at the electrode/solution interface [11], which could be due either to the difficulty of the supporting electrolyte species to diffuse through the Nafion matrix [11], or to a slower electron transfer rate between MG-incorporated into Nafion matrix than that of MG adsorbed on the glassy carbon electrode [9].

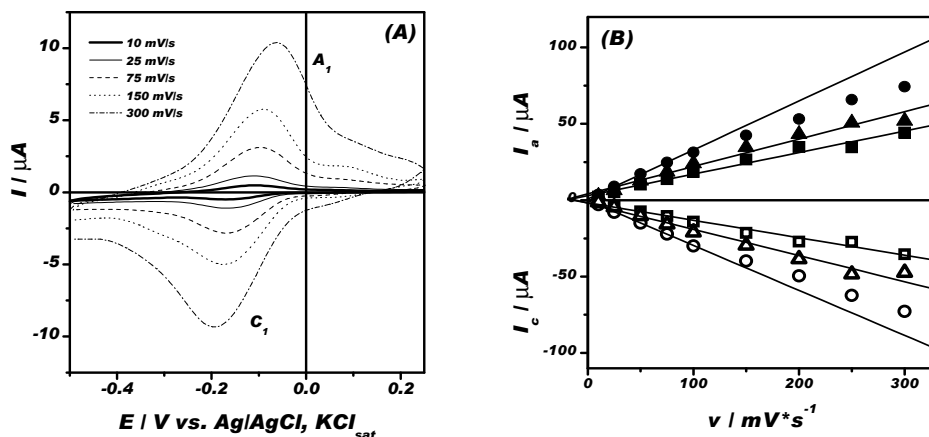


Figure 3. Influence of the scan rate on the cyclic voltammograms recorded at G/Nafion-MG50 electrodes (A) and the relationship between the peak current and the scan rate (B). Experimental conditions: phosphate buffer 0.1 M, pH 7; starting potential, -0.5 V vs. Ag/AgCl/KCl_{sat}; G/Nafion-MG25 (■, □), G/Nafion-MG50 (●, ○) and G/Nafion-MG100 (▲, Δ).

Another aspect that should be emphasised is the linear correlation observed between the peak currents and the potential scan rate (figure 3B and table 1). This behaviour suggests that MG is confined on the electrode surface and the redox process involving MG is not affected by the mediator diffusion [11].

Table 1.

The parameters of the linear regression for the $\log(I_p/\mu\text{A})$ vs. $\log(v/\text{mV}\cdot\text{s}^{-1})$ dependence.

| Electrode | slope | R/n |
|----------------|-----------------|-----------|
| G/Nafion-MG25 | 0.91 ± 0.01 | 0.9997/ 7 |
| G/Nafion-MG50 | 0.87 ± 0.01 | 0.9991/ 9 |
| G/Nafion-MG100 | 0.93 ± 0.01 | 0.9996/ 7 |

The stability of the G/Nafion-MG modified electrodes

The stability of the modified electrode was tested, simulating the operational conditions, by repetitive potential cycling in the potential range from -0.5 to 0.25 V. Using the surface coverage (Γ_0^+ /mol cm⁻³), estimated from the integrated anodic peak recorded at low scan rate (10 mV s⁻¹) [12], the activation constants for G/Nafion-MG25 ($4.82 \cdot 10^{-12}$ s⁻¹) and for G/Nafion-MG50 ($3.02 \cdot 10^{-11}$ s⁻¹), as well as the deactivation constant for G/Nafion-MG100 ($1.37 \cdot 10^{-11}$ s⁻¹) were evaluated. This estimation was done from the plots $\ln \Gamma_0^+$ vs. time, supposing a first order kinetic for both processes. The activation process could be due to the MG rearrangement into the Nafion matrix during the electrode potential scanning. Contrarily, the deactivation process could be assigned to the loss of MG excess, incorporated in the polymer matrix.

In conclusion, because the activation constant and the sensitivity of the MG inclusion in Nafion matrix are the highest for the G/Nafion-MG50 electrode, this type of electrode was used for further experiments.

Bioelectrocatalytic detection of catechol at G/Nafion-MG/Ty biosensor

The presence of MG mediator could modify the detection scheme of catechol (figure 4A) as is presented in figure 4B.

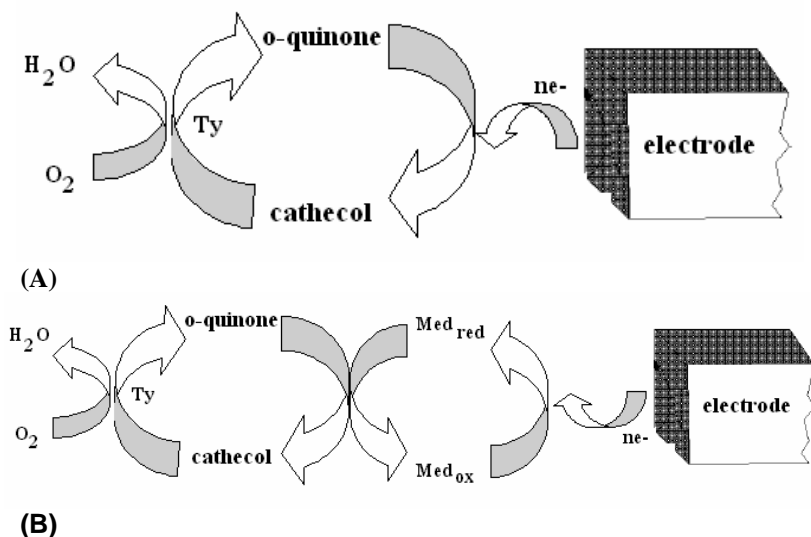


Figure 4. Catechol detection scheme in the absence (A) and in the presence of a mediator (B).

The cyclic voltammograms recorded at G/Nafion-MG50/Ty bioelectrode in the absence and in the presence of catechol are displayed in figure 5. It can be seen that, in the presence of Ty and of catechol, there is a great increase in the current intensity of peaks A1/C1, corresponding to the MGH/MG+ couple, comparatively to those observed in their absence. This current increase was supposed to be due to the restricted diffusion of MG towards solution side. The A3/C3 pair of peaks at a formal potential of -0.045 V vs. Ag/AgCl, KCl_{sat} was attributed to the catechol / quinone redox couple, existing in the mushroom tissue.

Also, in the presence of MG, a slight increase of the current intensity for C3 peak was noticed: from $-3.978 \cdot 10^{-6}$ A in the absence of catechol to $-4.964 \cdot 10^{-6}$ A in the presence of 0.56 mM catechol.

The amperometric response of the G/Nafion-MG50/Ty bioelectrode for different catechol concentration is described by a Michaelis-Menten type calibration curve. The steady-state current was measured at a fixed potential of -0.05 V vs. Ag/AgCl, KCl_{sat} . The analytical parameters calculated in the absence and in the presence of MG are presented in table 2.

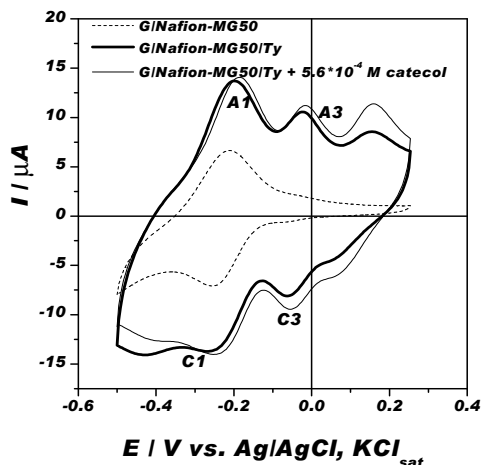


Figure 5. Cyclic voltammograms of the G/Nafion-MG/Ty bioelectrode in the absence (—) and in the presence of 0.56 mM catechol (—). Experimental conditions: phosphate buffer 0.1 M, pH 7; scan rate, 50 mV/s.

Table 2.

Analytical parameters for G/Ty and G/Nafion-MG50/Ty.

| Parameter | G/Ty | G/Nafion-MG50/Ty |
|--|----------|------------------|
| Sensitivity / mA·M⁻¹ | 22 | 2 |
| Linear range / μM | 5 – 50 | 100 – 300 |
| Detection limit* / μM | 2.5 | 20 |
| Response time (t_{95%}) / s | 50 - 100 | 50 - 100 |

* The detection limit was calculated considering the signal as three times the noise.

The biosensor response time could be influenced by one of the following rate limiting steps: (i) the diffusion and solubility of substrates (catechol and oxygen) into the vegetal tissue; (ii) the enzymatic reaction kinetics; (iii) the electrochemical reduction of the o-quinone at the electrode surface [2]. Generally, the biosensor response is kinetically controlled by the biochemical reaction rate. However, the presence of the polymer layer and the vegetal tissue on the surface of the working electrode acts as diffusion barrier for the substrates and/or the products, inducing an increase of the biosensor response time [2, 9].

If the solution stirring rate is sufficiently fast and the pore size of the vegetal tissue is relatively large, the diffusion through the vegetal tissue is not critical for the overall reaction rate. The presence of the polymer layer on the working electrode surface and/or the strong electrostatic forces existing between MG⁺ and SO₃⁻ groups [9] will hinder the diffusion of the substrates (oxygen and catechol) as well as the diffusion of the reaction products, resulting in increase of the biosensor response time [2].

The kinetic parameters values for the G/Ty bioelectrode without MG were estimated by fitting the experimental data with the Michaelis-Menten equation as well as by different linearizations. Almost identical values for the apparent Michaelis-Menten constant ($K_{M,app} \sim 0.17$ mM) and maximum current ($I_{max,app} \sim 3.7$ μ A) were obtained in all cases. The sensitivity (defined as the ratio $I_{max,app}/K_{M,app}$) was found of 21.8 mA/M. The values are in good agreement with those reported in literature for similarly architectures [2].

CONCLUSIONS

A biosensor using a simple immobilization method for enzyme and a low cost enzyme source from a vegetal tissue was developed. The obtained results suggest that the MG molecules were anchored into the Nafion polymer film either by electrostatic force between MG^+ and HSO_3^- [9], either by a partial electropolymerization of the MG monomer [10]. The high ionic conductivity, the high solubility of oxygen, the biocompatibility and the high stability of Nafion make it a particularly good matrix for MG immobilization [2]. Also, it was demonstrated that this type of positively charged mediator can be used to improve the electron transfer in the investigated system. The design of such architecture for the biosensor construction is promising for rapid low-cost toxicity testing.

ACKNOWLEDGEMENTS

The authors thank to the CNCSIS-Romania (Grants A-85-375-2005 and A-65-1716-2005) for financial support. SAS thanks to "Babes-Bolyai" University for the research fellowship.

REFERENCES

- [1] H. Notsu, T. Tatsuma, *J. Electroanal. Chem.*, **2004**, 566, 379.
- [2] C. Nistor, J. Emneus, L. Gorton, A. Ciucu, *Anal. Chim. Acta*, **1999**, 387, 309.
- [3] Z. Xu, X. Chen, X. Qu, S. Dong, *Electroanal.*, **2004**, 16(8), 689.
- [4] M.B. Moressi, A. Zon, H. Fernandez, G. Rivas, V. Solis, *Electrochem. Commun.*, **1999**, 1, 472.
- [5] J. Kulys, R. Vidziunaite, *Biosens. Bioelectron.*, **2003**, 18, 319.
- [6] J. Wang, S. A. Kane, J. Liu, M. R. Smyth, K. Rogers, *Food technol. biotechnol.*, **1996**, 34(1), 51.
- [7] E.S. Forzani, G. A. Rivas, V. M. Solis, *J. Electroanal. Chem.*, **1997**, 435, 77.
- [8] E. Burestedt, A. Narvaez, T. Ruzgas, L. Gorton, J. Emneus, E. Dominguez, G. Marko-Varga, *Anal. Chem.*, **1996**, 68, 1605.
- [9] B. Wang, S. Dong, *Talanta*, **2000**, 51, 565.
- [10] D-m. Zhou, H-Q Fang, H-y Chen, H-x. Ju, Y. Wang, *Anal. Chim. Acta*, **1996**, 329, 41.
- [11] A. R. de Lucca, A de S. Santos, A C. Pereira, L. T. Kubota, *J. Coll. Interface Sci.*, **2002**, 254, 113.
- [12] A. Ciszewski, G. Milczarek, *Anal. Chem.*, **2000**, 72, 3202.

THEORETISCHE BESCHREIBUNG DER KRISTALLISATION AUS ÜBERKRITISCHEN GASEN IN PORÖSER MATRIX

SIMION DRĂGAN¹, MIHAELA DRĂGAN²

¹Faculty of Chemistry and Chemical Engineering "Babes-Bolyai" University Cluj-Napoca

²Faculty of Economics, Department of Technology "Babes-Bolyai" University Cluj-Napoca

ZUSAMMENFASSUNG. In der vorliegenden Arbeit wird eine theoretische Beschreibung der Kristallisation aus überkritischem Fluid sowie die Partikelbildung in porösen Strukturen durchgeführt. Die Löslichkeit von Feststoffen im überkritischem Fluid hängt vom Druck und Temperatur ab. Schon kleine Druckdifferenzen führen zu großen Änderungen der Dichte und Löslichkeit, so dass sich die Prozesse gut steuern lassen.

EINFÜHRUNG

Die Kristallisation aus überkritischem Fluid sowie die Partikelbildung in porösen Strukturen wurden gut untersucht und sind in einer Vielzahl von Arbeiten beschrieben. Die Partikelbildung aus überkritischem CO₂ in porösen Strukturen, also die Kombination beider Gebiete, wurde bisher jedoch kaum untersucht.

In Vergleich zu der konventionellen Kristallisation zeigt die Kristallisation aus überkritischen Gasen folgende Vorteile: ermöglicht die Herstellung von Kristallen mit zugänglichen (nahen) Größen, ohne Unreinheiten [1], ermöglicht die Kontrolle bezüglich der Kristallgröße durch kleine Veränderungen der Prozessparameter [2], stellt eine effiziente Methode für die Trennung der festen Phase aus Mischungen dar [3], die Trennungsoperation flüssig-fest und die anschließende Trocknung der Kristalle ist nicht erforderlich.

Die Löslichkeit von Feststoffen im überkritischen Fluid hängt vom Druck und Temperatur ab. Schon kleine Druckdifferenzen führen zu großen Änderungen der Dichte und Löslichkeit, so dass sich die Prozesse gut steuern lassen. Ein häufig eingesetztes Lösungsmittel ist CO₂. Es ist wegen seiner moderaten kritischen Daten ($p_c=73,8$ bar, $T_c=304,18$ K, $\rho_c=10,6$ mol/l), vom Aufwand her gut zu beherrschen und problemlos im großen Mengen verfügbar. Da es nicht brennbar und nicht toxisch ist lässt es sich technisch einfach handhaben.

BESCHREIBUNG DER KRISTALLISATION AUS ÜBERKRITISCHEM FLUID

Der Kristallisationsprozess, gleichgültig unter welchen Bedingungen er durchgeführt wird, setzt folgende Etappen (Phasen) voraus:

1. die Erreichung der Übersättigung;
2. die Keimbildung (Nukleation);
3. Kristallwachstum

Die drei o.g. Etappen können in der selben Zeit stattfinden. Darum ist eine Kontrolle jeder Phase wünschenswert.

I. Erreichung der Übersättigung

Die Übersättigung wird laut Gleichungen (1) und (2) bestimmt:

$$\gamma_s = \frac{c}{c_e} \quad (1)$$

$$\gamma_r = \frac{c - c_e}{c_e} = \frac{\Delta c}{c_e} = \gamma_s - 1 \quad (2)$$

wo: c_e = Löslichkeit

c = Konzentration der Lösung

γ_s = absolute Übersättigung

γ_r = relative Übersättigung

Wenn $c > c_e$, dann $\gamma_s > 1$, bzw. $\gamma_r > 0$, ist die Lösung übersättigt.

Die Übersättigung wird durch Temperaturänderung, Druckabsenkung, hinzufügen eines Materials oder durch chemische Reaktion verwirklicht (realisiert).

II. Keimbildung kinetik

Es wird zwischen primärer Keimbildung (homogener und heterogener) und sekundärer Keimbildung unterschieden.

Im allgemeinen wird bei dieser Klassifikation der Keimbildung die Anwesenheit des festen Stoffes in Betracht gezogen.

Die primäre Keimbildung findet in Abwesenheit der festen Partikeln des zu kristallisierenden Stoffes statt, während die sekundäre Keimbildung, das Resultat der Anwesenheit von Kristallen in der Lösung (Impfkristalle) ist.

Die homogene Keimbildung findet in der Abwesenheit jeder festen Phase statt, im Unterschied zu der heterogenen Keimbildung, die von der Anwesenheit verschiedener Partikeln wie: Staub, kolloidale Partikeln, Wände des Kristallisators oder der porösen Träger/Wände der Poren) induziert wird. Die primäre Keimbildung findet nur nach der Erreichung eines bestimmten Übersättigungsgrades der Lösung statt, die sogenannte Grenze der Metastabilität.

Vor Erreichung dieser Grenze für die Bildung der primären homogenen Keime, liegt die Grenze für die Bildung der primären heterogenen Keime und der sekundären Keime.

Die Art der Keimbildung des Kristalls und die Erkenntnis der Metastabilitätszone sind die wesentlichen Bedingungen für die Kontrolle des Kristallisationsprozesses.

Außer der Übersättigung, ein anderer wichtiger Parameter für die Charakterisierung der metastabilen Zone ist die Induktions-Zeit τ_i welche die erforderliche Zeitspanne der Keime für die Erreichung der kritischen Größe darstellt über welche die Keime wachsen.

In der homogenen Keimbildung führt die Bildung der Keime zur Veränderung der freien Gibbs Enthalpie (ΔG) aufgrund von zwei Prozessen: die Verbindung der Moleküle in einen Keim und die Bildung der Oberfläche eines Partikels der neuen Phase:

$$\Delta G = A_N \cdot \sigma_{CL} - V_N \cdot \frac{\Delta \mu}{v_n} = 4\pi r^2 \cdot \sigma_{CL} - \frac{4\pi r^3}{3} \cdot \frac{\Delta \mu}{v_m} \quad (3)$$

wo: σ_{CL} = Oberflächenspannung Kristall-Flüssig;
 $\Delta\mu$ = Differenz des chemischen Potentials für die Bildung eines Keimes mit
 Radius r ;
 v_m = Molekülvolumen des kristallisierten festen Stoffes.

$$\left(v_m = \frac{M}{\rho \cdot N_A} = \frac{M_m}{\rho} \right)$$

M = Molmasse;
 N_A = Avogadrozahl;
 M_m = Masse eines Moleküls
 ρ = Dichte des festen Stoffes

Der kritische Radius des Keimes wird unter folgenden Bedingungen erlangt:

$$\frac{d(\Delta G)}{dr} = 0 \Big|_{r=r_c} \quad 8\pi r_c \cdot \sigma_{CL} - 4\pi r_c^2 \cdot \rho \cdot \frac{\Delta\mu}{M_m} = 0 \quad (4)$$

$$r_c = \frac{2 \cdot \sigma_{CL} \cdot M_m}{\rho \cdot \Delta\mu} \quad (5)$$

$$\Delta\mu = k \cdot T \cdot \ln\left(\frac{C}{C_e}\right) = k \cdot T \cdot \ln \gamma_s \quad (6)$$

Wenn man die Gleichung (6) und (5) ersetzt, erhält man für den kritischen Radius des Keimes:

$$r_c = \frac{2 \cdot \sigma_{CL} \cdot M_m}{\rho \cdot k \cdot T \ln \gamma_s} \quad (7)$$

wo: k = Boltzmannkonstante;
 T = Temperatur.

Wenn der Keim eine kleinere Dimension r im Vergleich zu dem kritischen Radius r_c aufweist, wird er aufgelöst und wenn der Wert des kritischen Radius erreicht wird, wird der Keim wachsen. Der Aggregat mit dem kritischen Radius r_c wird als Keim bezeichnet. Bildet man einen Keim, so muss das System die energetische Barriere laut Gleichung (3') überschreiten:

$$\Delta G_c = 4\pi \cdot r_c^2 \cdot \sigma_{CL} - \frac{4\pi}{3} \cdot r_c^3 \cdot \frac{\Delta\mu \cdot \rho}{3M_m} \quad (3')$$

Ersetzt man Gleichung (7) in (3'), gilt für die energetische Barriere entsprechend der Bildung des Keimes im System folgendes:

$$\Delta G_c = \frac{16\pi \cdot \sigma_{CL}^3 \cdot M_m^2}{3 \cdot \rho^2 \cdot k^2 \cdot T^2 (\ln \gamma_s)^2} \quad (8)$$

Die Partikelanzahl mit Radius r_c in der Volumeneinheit der Phase wird als Keimbildungsgeschwindigkeit bezeichnet:

$$v_N = \frac{dN_N}{V \cdot d\tau} = A \cdot \exp\left(-\frac{\Delta G_c}{k \cdot T}\right) \quad (9)$$

wo: v_N = Keimbildungsgeschwindigkeit;
 N_N =Partikelanzahl;
 V = Phasenvolumen, wo sich die Keime bilden;
 τ = Zeit;
 k =Boltzmannkonstante;
 A = Proportionalitätskoeffizient.

Die Induktionsspanne ist umgekehrt proportional mit der Keimbildungsrate v_N :

$$\tau_i = \frac{C}{v_N} = \frac{C}{A} \cdot \exp\left(\frac{\Delta G_c}{k \cdot T}\right) = C_1 \cdot \exp\left(\frac{\Delta G_c}{k \cdot T}\right) \quad (10)$$

oder in linearer Form:

$$\ln \tau_i = \ln C_1 + \left(\frac{\Delta G_c}{k \cdot T}\right) \quad (10')$$

wo: C_1 =Konstante bei Temperatur T .

Ersetzt man Gleichung (8) in (9), wird die Keimbildungsrate ausgedrückt:

$$v_N = A \cdot \exp\left[-\frac{16\pi \cdot \sigma_{CL}^3 \cdot M_m^2}{3\rho^2 \cdot k^3 \cdot T^3 (\ln \gamma_s)^2}\right] \quad (11)$$

Für die Induktionsperiode τ_i gilt:

$$\tau_i = C_1 \cdot \exp\left[\frac{16\pi \cdot \sigma_{CL}^3 \cdot M_m^2}{3\rho^2 \cdot k^3 \cdot T^3 (\ln \gamma_s)^2}\right] \quad (12)$$

Laut Gleichung (11) ist die Keimbildungsrate von folgenden Parametern beeinflusst:

- Übersättigung γ_s ;
- Temperatur T ;
- Eigenschaften des Systems (ρ, M_m, T_{CL}).

Es wird ein starker Einfluss der Temperatur beobachtet, bei deren Steigerung sich die erforderliche Induktionsperiode für die Erreichung der kritischen Dimension erniedrigt, weil die entsprechende Übersättigung für die Keimbildung sinkt.

Ebenfalls wird ein starker Einfluss der Übersättigung festgestellt.

Die Steigerung der Übersättigung bestimmt eine größere Keimbildungsrate, bzw. eine größere Anzahl von Keimen kleinerer Dimension. Die Keime, die den kritischen Radius überschritten haben, werden in Anwesenheit der Übersättigung

weiter wachsen. Die Geschwindigkeit des Keimwachstums kann man als ein lineares zeitabhängiges Wachstum des Radius annähern: $v_{cr} = \frac{dr}{d\tau}$.

Die Kristallisation aus superkritischen Gasen verläuft ähnlich der in der flüssigen Phase [4]. Derart findet die Kristallisation aufgrund der Übersättigung der überkritischen Lösung statt. Die Übersättigung ist von Druck, Temperatur der Lösung und Löslichkeit des festen Stoffes abhängig. Die Änderung eines der o.g. Parameter kann zur Bildung der Kristalle führen.

Im Falle der homogenen Keimbildung aus überkritischen Gasen hat die erforderliche Energie für die Bildung eines Keimes, bestehend aus n Molekülen von Solut in dem Volumen einer anderen Phase folgenden Ausdruck [5]:

$$E_{\min} = A_N \cdot \sigma_{CL} + n \cdot \Delta\mu \quad (13)$$

wo: σ_{CL} =Oberflächenspannung kritische Flüssigkeit;
 A_N =Oberfläche des Keimes;
 $\Delta\mu$ =Differenz des chemischen Potentials.

Für einen Keim, gebildet nur aus Solut-Molekülen, wird Gleichung (13):

$$E_{\min} = A_N \cdot \sigma_{CL} + n[\mu_1^s(T, P) - \mu_1(T, P, y_1)] \quad (14)$$

wo: E_{\min} = drückt die minimale erforderliche Energie für die Bildung eines Keimes aus n festen Partikeln im Volumen einer Lösung bei Druck P , Temperatur T und Molfraktion y_1 , aus.

$\mu_1^s(T, P)$ = chemisches Potential des reinen festen Soluts bei Temperatur T und Druck P ;

$\mu_1(T, P, y_1)$ = chemisches Potential des Soluts in der fluiden Phase.

Wenn $y_1^e(T, P)$ die Molfraktion im Gleichgewichtszustand des Solut in dem überkritischen Fluid ist, dann werden die beiden Potentiale gleich:

$$\mu_1^s(T, P) = \mu_1(T, P, y_1^e) \quad (15)$$

Ersetzt man Gleichung (15) in (14):

$$E_{\min} = A_N \cdot \sigma_{CL} + n[\mu_1(T, P, y_1^e) - \mu_1(T, P, y_1)] \quad (16)$$

Für das chemische Potential des Soluts gilt:

$$\mu_1 = k \cdot T \cdot \ln P \cdot y_1 \cdot \phi_1 + \lambda_1(T) \quad (17)$$

wo: ϕ_1 =der Fugazitätskoeffizient des Soluts

Für verdünnte Lösungen wird ϕ_1 mit folgender Gleichung berechnet:

$$\phi_1 = \phi_1^\infty \cdot \exp(-K \cdot y_1) \quad (18)$$

K - Konstante, abhängig von Temperatur und Druck

ϕ_1^∞ - Fugazitätskoeffizient des Solut in infinit verdünnten Lösungen

Anhand Gleichung (18) wird Gleichung (16) wie folgt geschrieben:

$$\mu_1(T, P, y_1^e) - \mu_1(T, P, y_1) = k \cdot T \ln P \cdot y_1^e \cdot \phi_1^\infty \exp(-K \cdot y_1^e) - k \cdot T \ln P \cdot y_1 \cdot \phi_1^\infty \cdot \exp(-k \cdot y_1) = \quad (19)$$

$$k \cdot T \cdot \ln \frac{y_1^e \exp(-K \cdot y_1^e)}{y_1 \cdot \exp(-K \cdot y_1)} = k \cdot T \left[\ln \frac{y_1^e}{y_1} - K \cdot y_1^e + K \cdot y_1 \right] = k \cdot T \left[\ln \frac{y_1^e}{y_1} - K \cdot y_1^e \left(1 - \frac{y_1}{y_1^e} \right) \right]$$

Ersetzt man Gleichung (19) in Gleichung (16) gilt:

$$\begin{aligned} E_{\min} &= A_N \cdot \sigma_{CL} + n \cdot k \cdot T \left[\ln \frac{y_1^e}{y_1} - K \cdot y_1^e \left(1 - \frac{y_1}{y_1^e} \right) \right] = \\ &= A_N \cdot \sigma_{CL} + n \cdot k \cdot T \left[K \cdot y_1^e \left(\frac{y_1}{y_1^e} - 1 \right) - \ln \frac{y_1}{y_1^e} \right] \end{aligned} \quad (20)$$

Wenn man die Übersättigung $\gamma_s = \frac{y_1}{y_1^e}$ in Gleichung (20) ersetzt:

$$E_{\min} = A_N \cdot \sigma_{CL} + n \cdot k \cdot T \left[K \cdot y_1^e (\gamma_s - 1) - \ln \gamma_s \right] \quad (21)$$

Wenn sich die fluide Phase wie ein ideales Gasmischungsverhält ($\phi_1 = 1$) oder wie eine ideale Lösung ($\phi_1 = \phi_1(T, P)$), dann bekommt Gleichung (21) die bekannte Form (22):

$$E_{\min} = A_N \cdot \sigma_{CL} - n \cdot k \cdot T \ln \gamma_s \quad (22)$$

Weil bei einem bestimmten T und P die Lösung entweder stabil ($y_1 < y_1^e$) oder metastabil ($y_1 > y_1^e$) aber nicht instabil ist, müssen wir

$$\left(\frac{\partial \mu_1}{\partial y_1} \right)_{T, P} > 0 \quad \text{also} \quad 1 + \left(\frac{\partial \ln \phi_1}{\partial \ln y_1} \right)_{T, P} > 0 \quad (23)$$

Diese Bedingung setzt noch voraus:

$$K \cdot y_1^e < 1, \text{ bzw. } \gamma_s < \frac{1}{K \cdot y_1^e} \quad (24)$$

Wenn die Keime kugelförmig sind, werden der kritische Radius (r_c) und die Anzahl der Solutmoleküle (n) mit folgenden Gleichungen berechnet:

$$r_c = \frac{2 \cdot \sigma_{CL} \cdot M_m}{\rho \cdot k \cdot T} \cdot \frac{1}{\left[\ln \gamma_s - K \cdot y_1^e (\gamma_s - 1) \right]} \quad (25)$$

$$n = \frac{32 \cdot \pi}{3} \cdot \frac{\sigma_{CL}^3 \cdot M_m^2}{\rho^2 \cdot k^3 \cdot T^3} \cdot \frac{1}{\left[\ln \gamma_s - K \cdot y_1^e (\gamma_s - 1) \right]^3} \quad (26)$$

Wenn die Übersättigung größer als 1 ist ($\gamma_s > 1$), ist die fluide Phase metastabil und die Keime instabil, bzw. werden die kleinen Keime aufgelöst und diejenigen mit größerem Radius als der kritisch, wachsen.

Im Falle der Kristallisation aus poröser Matrix, hängen die Charakteristiken der Keimbildung und des Kristallwachstums von der Struktur des Gels ab und die Übersättigung ist immer größer als die der Volumenlösung [6]. Die Keimbildung im Aerogel ist heterogen und ist immer kleiner im Vergleich zu der im Volumen der Phase; darum ist die Erreichung einer hohen Übersättigung erforderlich, so dass die Keimbildung in den Poren stattfindet [6]. Sherer [7] zeigt, dass die Wahrscheinlichkeit der homogenen Keimbildung im Gel klein ist, mit der Ausnahme, wenn hohe Übersättigungen vorhanden sind.

II.1 Die Kinetik der Keimbildung in den Poren

II.1.1. Die homogene Keimbildung

Für eine homogene Keimbildung in den Poren ist die Überschreitung der energetischen Schranke, verursacht durch die Oberflächenenergie des Keimes mit Radius r , erforderlich [7].

Die freie Enthalpie für einen kugelförmigen Keim mit Radius r , ist:

$$\Delta G(r) = \frac{4\pi r^3}{3} \cdot \Delta g_{fv} + 4\pi r^2 \sigma_{CL} \quad (27)$$

wo: Δg_{fv} = freie Kristallisationsenthalpie in der Volumeneinheit

$$\Delta g_{fv} = \int_{T_m}^T \Delta S_{fv} \cdot dT \quad (28)$$

σ_{CL} = Oberflächenspannung Kristall-Flüssigkeit;

T = Temperatur der Kristallisation im Por;

wo: $\Delta S_{fv} = (S_L - S_c) / v_c$ - ist die Entropie der Kristallisation per Volumeneinheit (>0).

Die homogene Keimbildung findet statt nur in dem Fall, wenn der Keim, den kritischen Radius (r_c^*) überschreitet:

$$4\pi r_c^{*2} \Delta g_{fv} + 8\pi r_c^{*2} \cdot \sigma_{CL} = 0$$

$$\left. \frac{\partial \Delta G}{\partial r} \right|_{r=r_c^*} = 0 \quad (29)$$

$$r_c^{*2} \cdot \Delta g_{fv} + 2\sigma_{CL} = 0$$

$$r_c^* = -\frac{2\sigma_{CL}}{\Delta g_{fv}} \quad (30)$$

wo: r_c^* - kritischer Radius des Keims in den Porenvolumen;

Derart hat die energetische Barriere nach dem Ersetzen der Gleichung (30) in (27) für die homogene Keimbildung folgenden Ausdruck:

$$\Delta G(r_c^*) = W^* = \frac{4\pi r_c^{*3}}{3} \cdot \Delta g_{fv} + 4\pi r_c^{*2} \cdot \sigma_{CL}$$

oder:

$$\Delta G(r_c^*) = W^* = \frac{16\pi \cdot \sigma_{CL}^3}{3 \cdot \Delta g_{fv}^2} \quad (31)$$

Die Geschwindigkeit der homogenen Keimbildung, Keime per Volumeneinheit der Lösung und Zeit, ist [7]:

$$I_v = \frac{n_v \cdot k \cdot T}{3\pi \lambda^3 \eta} \cdot \exp\left(-\frac{W^*}{k \cdot T}\right) \quad (32)$$

wo: n_v = Anzahl der moleküle per Volumeneinheit,

k = Boltzmann-Konstante

λ = molekulare Dimension

η = Viskosität der Lösung

$$I_v = \frac{\rho^2 \cdot k \cdot T}{3\pi \cdot M_m^2 \cdot \eta} \cdot \exp\left(-\frac{W^*}{k \cdot T}\right) \quad (32')$$

Unter der Voraussetzung, dass:

$$\Delta g_{fv} = \int_{T_m}^T \Delta S_{fv} \cdot dT = -\frac{2\sigma_{CL}}{r_p} \quad (33)$$

wo r_p = Porenradius, wird aus den Gleichungen (33) und (30) festgestellt, dass $r_c^* = r_p$ und Gleichung (31) wird:

$$W^* = \frac{16\pi \cdot \sigma_{CL}^3}{3 \cdot \Delta g_{fv}^2} = \frac{4\pi \cdot \sigma_{CL}^3}{3 \cdot \frac{\sigma_{CL}^2}{r_p^2}} = \frac{4\pi \cdot r_p^2 \cdot \sigma_{CL}}{3} \quad (34)$$

Die Keimbildungsgeschwindigkeit in einer kugelförmigen Pore mit Radius r_p ist:

$$I_p = \frac{4\pi}{3} \cdot r_p^3 \cdot I_v \quad (35)$$

II.1.2. Die heterogene Keimbildung in den Poren

Die energetische Barriere bei der Keimbildung in den Poren wird aufgrund der Porenwand eingeschränkt. Die Porenwand erfüllt die Rolle eines Katalysators mit einer kleineren Oberflächenspannung im Vergleich zu dem Kristall.

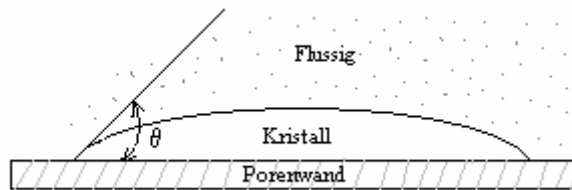


Abb. 1. Der Benetzungswinkel θ zwischen dem Kristall und einer flachen Oberfläche

$$W_{heterogen}^* = f_{(\theta)} \cdot W^* \quad (36)$$

wo θ = Benetzungswinkel zwischen Kristall und der festen Oberfläche [7]:

$$f_{(\theta)} = \frac{(\cos^3 \theta - 3 \cdot \cos \theta + 2)}{4} \quad (37)$$

Ist der Winkel $\theta = 180^\circ \Rightarrow f_{(\theta)} = 1$ und es liegt der Fall der homogenen Keimbildung vor.

Es wurde gezeigt, dass die Heterogenität einen starken Einfluss auf die Keimbildungsgeschwindigkeit hat, nur in dem Fall, wenn $\theta < 90^\circ$. Wenn die poröse Matrix selbst als Keimkatalysator wirkt, können die Kristalle in jeder Pore keimen, während die Keime nicht die vorausgesetzte Form wie bei der Ableitung der Gleichung (36) haben werden. Die optimale Form der Keime wird kugelförmig in den Knoten des Matrixnetzes sein.

II.2. Kristallwachstum in den Poren der Matrix

Die Krümmung zwischen dem Kristall und der Flüssigkeitsoberfläche ist mit folgender Gleichung ausgedrückt:

$$K_{CL} = \frac{1}{r_1} + \frac{1}{r_2} \quad (38)$$

wo: r_1 und r_2 sind die Hauptkrümmungsradien.

Der kapillare Druck im Inneren des Kristalls P_c , ist laut der Laplace Gleichung:

$$P_c = P_L + \sigma_{CL} \cdot K_{CL} \quad (39)$$

wo: P_L = Druck in der Flüssigkeit.

Wenn ein Kristall in eine Pore hineintritt, wird die Krümmung an der Oberfläche Kristall/Flüssigkeit wie folgt ausgedrückt:

$$K_{CL} = -\frac{2 \cos \theta}{r_p} \quad (40)$$

wo: r_p = Porenradius

θ = Benetzungswinkel zwischen Kristall und Porenwand

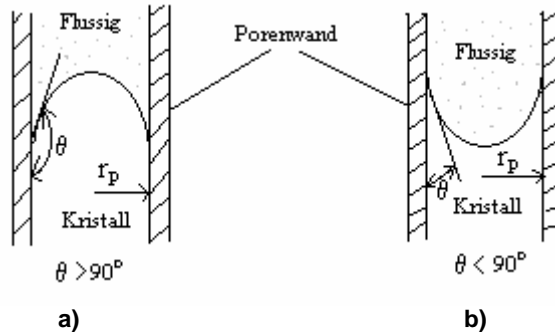


Abb. 2. Benetzungswinkel zwischen Kristall und Porenwand

Wenn $\theta > 90^\circ$ ist, $\cos \theta < 0$ und $K_{CL} > 0$. In diesem Fall wird Gleichung (39):

$$P_c = P_L + \frac{2\sigma_{CL} \cdot \cos \theta}{r_p} \quad (41)$$

Gleichung (41) zeigt vor, dass der Druck $p_c - p_L > 0$ ist und der Schmelzpunkt erniedrigt sich entsprechend der Gleichung:

$$T_m - T = \Delta T = \frac{\sigma_{CL} \cdot K_{CL}}{\Delta S_{fv}} \quad (42)$$

Gleichung (42) zeigt vor, dass die Gleichgewichtsschmelztemperatur eines Kristalls mit positiver Krümmung kleiner im Vergleich zu einem flachen Kristall ist ($\cos \theta = -1$). Der maximale Druck im Kristall entsteht bei $\theta = 180^\circ$, wenn der Kristall praktisch nicht mit der Porenwand benetzt ist. In diesem Fall kann Gleichung (41) anhand der Dicke des Lösungsfilms „ δ “ zwischen der Porenwand und Kristall verändert werden:

$$P_c = P_L + \frac{2\sigma_{CL}}{r_p - \delta} \quad (43)$$

Wenn $\theta > 90^\circ$, kann der Kristall bei der Schmelztemperatur T_m nicht in den Poren hineintreten; je kleiner die Pore ist, desto kleiner muss die Temperatur für den Eingang des Kristalls in die Poren sein.

Aus Gleichung (40) und (42) ergibt sich, dass der Kristall in die Pore hineintritt, bei:

$$\Delta T \cong - \frac{2\sigma_{CL} \cdot \cos \theta}{r_p \cdot \Delta S_{fv}} \quad (44)$$

Wenn $\theta < 90^\circ$, $\cos \theta > 0$ und der Schmelzpunkt verändert sich nicht. In diesem Fall tritt der Kristall bei der gewöhnlichen Schmelztemperatur in die Pore hinein.

Gleichung (44) zeigt vor, dass der Kristall über der Schmelztemperatur T_m stabil wird.

Generell ist $\theta > 90^\circ$ und die Kristalle propagieren sich in einer porösen Matrix, ohne Unterkühlung nicht. Trotzdem, wenn eine poröse Matrix existiert, so dass $\theta < 90^\circ$, dann werden sich die Kristalle in den Poren verbreiten ohne einen Widerstand der Schmelztemperatur T_m .

II.2.1 Spannungen an den Porenwänden

Die in den Poren gebildeten Kristalle üben auf dem umgebenden Netz eine Spannung aus [8].

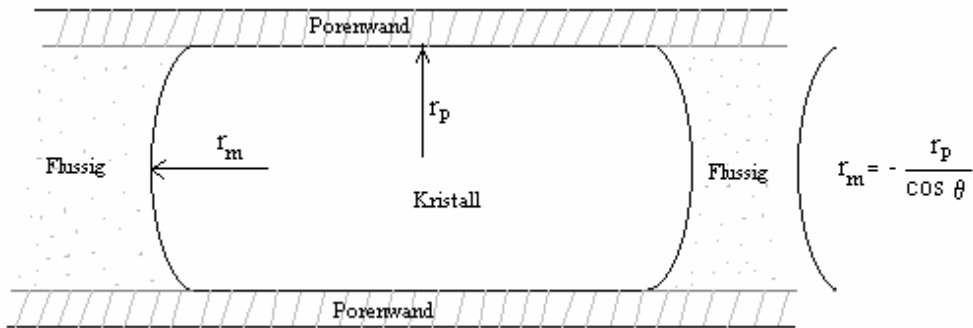


Abb. 3. Kristall in einer zylindrischen Pore mit unregelmäßiger Krümmung

In Abb.3 ist die Krümmung des Kristalls von Gleichung (40) beschrieben - zylindrische Seiten, deren Krümmung und kapillarer Druck, $1/r_p$ bzw. T_{CL}/r_p ist. Im Gleichgewichtszustand ist der Druck im Kristall gleichmäßig. Derart, für die Erreichung des Gleichgewichts eines Kristalls in der Pore, üben die Porenwände einen Druck aus, der die kapillare Druckdifferenz balanciert:

$$P_L - \frac{2\sigma_{CL} \cdot \cos \theta}{r_p} = \frac{\sigma_{cs}}{r_p} - \sigma_r \quad (45)$$

wo: σ_{CL} = Oberflächenenergie Kristall-Flüssigkeit;
 σ_{CS} = Oberflächenspannung Kristall-Fest;
 σ_r = Radiale Spannung auf die Porenwände;

$$\sigma_r = \frac{\sigma_{cs} + 2\sigma_{CL} \cdot \cos \theta}{r_p} - P_L \quad (46)$$

Es ist bekannt, dass:

$$\sigma_{SL} = \sigma_{cs} + \sigma_{CL} \cdot \cos \theta \quad (47)$$

und Gleichung (46) wird:

$$\sigma_r = \frac{\sigma_{CL} \cdot \cos \theta}{r_p} + \frac{\sigma_{SL}}{r_p} - P_L \quad (48)$$

Die letzten zwei Glieder der Gleichung (48) bestimmen die Größenordnung der radialen Spannung (σ_r). Folglich ist die Spannungsveränderung auf der Porenwand beim Eintritt des Kristalls in die Pore:

$$\Delta \sigma_r = \frac{\sigma_{CL} \cdot \cos \theta}{r_p} \quad (49)$$

Wenn $\theta = 90^\circ$ ist, $\cos \theta = 0$, ist der Kristall flach und laut Gleichung (49) ist $\Delta T_r = 0$, d.h. die radiale Spannung σ_r ändert sich nicht beim Eintritt des Kristalls in die Pore ($\sigma_{CS} = \sigma_{SL}$).

$$\sigma_r = \frac{\sigma_{CS}}{r_p} - P_L \quad (50)$$

Wenn $\theta > 90^\circ$, dann ist die Porenwand radial vom Kristall z zusammengepresst. Die größte Kompression findet bei dem Benetzungswinkel $\theta = 180^\circ$ statt, wenn die Lösungsschicht zwischen Kristall und Wand anwesend ist.

Der Druck im Kristall ist: $p_L + \frac{2\sigma_{CL}}{r_p - \delta}$ und in der zylindrischen Seite:

$p_L + \frac{\sigma_{CL}}{r_p - \delta}$; derart kann Gleichung (45) wie folgt geschrieben werden:

$$\left/ p_L + \frac{2\sigma_{CL}}{r_p - \delta} \right/ = p_L + \frac{\sigma_{CL}}{r_p - \delta} - \sigma_A \quad (51)$$

$$\sigma_A = \frac{\sigma_{CL}}{r_p - \delta} \quad \text{für } \theta = 180^\circ \quad (52)$$

σ_A = Ausgeübte Spannung der Wand auf der Kristallseite.

Die gesamte radiale Spannung ist:

$$\sigma_r = \frac{\sigma_{SL}}{r_p} - P_L + \sigma_A = \frac{\sigma_{SL}}{r_p} - \frac{\sigma_{CL}}{r_p - \delta} - P_L \quad \text{wo } \theta = 180^\circ \quad (53)$$

Die Spannungsveränderung in der Porenwand ist:

$$\Delta\sigma_r = -\frac{\sigma_{CL}}{r_p - \delta} \quad (54)$$

Neben σ_r muss man auch die kreisförmige Spannkraft σ_θ berücksichtigen.

Für eine zylinderförmige Pore mit dem inneren Radius r_p und dem externen Radius r_e gilt:

$$\sigma_\theta = -\sigma_r \cdot \left(\frac{r_e^2 + r_p^2}{r_e^2 - r_p^2} \right) \quad (55)$$

Die Porosität P , einer derartigen Struktur wird: $P = (r_p/r_e)^2$

Gleichung (55) wird in diesem Fall:

$$\sigma_\theta = -\sigma_r \cdot \left(\frac{1+p}{1-p} \right) \quad (56)$$

Bei kleinen Porositäten ergibt sich aus Gleichung (56) $\Rightarrow \sigma_\theta = -\sigma_r$.

Das Gelnetzwerk kann das Kristallwachstum über die Porendimensionen anhalten im Fall, wenn das Netz den Druck p_A ausübt:

$$p_A \cong P_L + \frac{\sigma_{CL}}{r_p} \quad (57)$$

Ansonst, wird das Gelnetz zerstört und der Kristall wächst über die Dimension der Poren. Es wurde festgestellt, dass die Zerstörung des Gels stattfindet, außer dem Fall, wenn die Übersättigung ausreichend groß ist für die Erzeugung von vielen und kleinen Kristallen in den Poren der Matrix.

Die Spannung zwischen Kristall und Wand kann durch die Erniedrigung des Benetzungswinkels θ , reduziert werden.

Wenn $\theta < 90^\circ$, werden keine Spannungen auf die Porenwände ausgeübt.

Die Erniedrigung des Winkels wird durch die Bedeckung mit einem Film, welcher die Oberflächenspannung ändert, ermöglicht.

SCHLUSSFOLGERUNGEN

1. Die Kristallisation aus überkritischen Gasen ermöglicht die Herstellung von Kristallen mit zugänglichen Größen und die Kontrolle der Kristallgröße durch kleine Veränderungen der Prozessparameter.
2. Die Partikelbildung aus überkritischem CO₂ in porösen Strukturen wurde bisher kaum untersucht. In der vorliegenden Arbeit wird eine mathematische Beschreibung der Kristallisation aus überkritischem Fluid in die poröse Matrix vorgeschlagen.
3. Es wurden die Spannungen an die Porenwände beschrieben. Die Zerstörung des Gels findet statt, außer dem Fall wenn die Übersättigung ausreichend groß ist für die Erzeugung von vielen und kleinen Kristallen in den Poren der Matrix.

LITERATURVERZEICHNIS

1. Paulaitis, M.E., Krukonis, V.J., Kurnik, R.T., and Reid, R.C., *Supercritical Fluid Extraction*, Rev.Chem.Eng., 1983, 1, p.179.
2. Mohamed, R.S., Debenedetti, P.G., and Prud'homme, *Effects of Process Conditions on Crystall obtained from Supercritical Mixtures*, AIChE Journal, 1989, 35, p.325.
3. Kelly, S.D., and Chimowitz, E.H., *Experimental Data for Crossover Process in a Model Supercritical System*, AIChE Journal, 1989, 35, p.981.
4. Tavana, A., and Randolph, A.D., *Manipulating Solids CSD in a Supercritical Fluid Crystallizer: CO₂- Benzoic Acid*, AIChE Journal, 1989, 35, p.1625.
5. Debenedetti, P.G., *Homogeneous Nucleation in Supercritical Fluids*, AIChE Journal, 1990, 36, p.1289.
6. Lefauchaux, F., and Robert, M.C., *Crystall Growth in Gels*, Hrsg.: Hurle DTJ; Handbook of Crystall Growth, Vol.2., Amsterdam, North-Holand, 1994, p.1271-1303.
7. Sherer, G.W., *Freezing gels*, J.of Non-Crystalline Solids, 1993, 155, p.1-25.
8. Sherer, G.W., *Crystallization in pores*, Cem. Concr. Res. 1999, 29, p.1437.

EXPERIMENTAL STUDY OF DRY DESULPHURIZATION PROCESS WITH CALCIUM OXIDE. CHARACTERIZATION OF CALCIUM OXIDE STRUCTURE

SIMION DRAGAN¹, MIHAELA DRAGAN²

¹ Faculty of Chemistry and Chemical Engineering "Babes-Bolyai" University Cluj-Napoca

² Faculty of Economics, Department of Technology "Babes-Bolyai" University Cluj-Napoca

ABSTRACT. Since the micro structure of the adsorbant has an important influence upon its reactivity, this paper presents the - in situ - generation of calcium oxide process from limestone. The calcium oxide obtained by calcination of limestone at temperatures of 973-1273 K and $p=0,3404$ bar was characterised by BET surface area, porosity and pore size distribution. The obtained surface areas are in the range between 18,9107 - 55,1966 m²/g and a porosity in the range of mesopores as a function of the particles size and the decomposition temperatures.

INTRODUCTION

Due to the important sulphur dioxide quantities emitted in the atmosphere, the flue gas desulfurization from the power plants, represents a strictly actual field of research.

Environmental pollution are consequences of the economic development and most of the industrial one. The energetic sector is one of the main pollutants of the atmosphere: SO₂ from the coal-burned power plant is one of the main sources. Coal contains a certain amount of sulfur, depending on its origin. During combustion, the sulfur reacts with the oxygen in the air and forms SO₂, which flows along with the flue gas into the atmosphere and contributes to the acid rains.

Romania registers pollutant emissions about 10-12% higher in comparison with some of the european countries, like: Holland, Belgium, Denmark or Germany. The energetic industry contributes to this situation, thus for producing of 1 kWh energy, the emissions are more higher in Romania as in Holland (about 40 – for sulphur oxide, 2 – for NO_x and 870 – for dust) [1].

Although the "international pollutant", character of sulphur oxide has been recognized at various international meetings and urgent and radical measures have been claimed, actually very little has been done so far.

Due to the important sulphur dioxide quantities emitted in the atmosphere, the flue gas desulphurization from the power plants, represents a strictly actual field of research [2 - 5].

From the great number of desulphurization methods (wet, semidry, dry) the practice confirms only the utilisation of alcaline, alcaline-earth, especially of limestone, and ammonia compounds. For the reactive dry adsorption of sulphur dioxide of flue gas, the most used adsorbants are: limestone, dolomite, lime and dolomitic lime.

Under identical experimental conditions, the reactivity of this adsorbants is significantly influenced of its chemical structure and composition [6].

If the limestone is utilised as adsorbant, its chemical composition may be a factor which contributes significantly to its reactivity.

In the case of dolomite, magnesium doesn't react in a significant manner but it has a favourable influence about the utilisation of calcium fraction. Silicium constitutes the most undesirable impurity because it reduces the reactivity of the particle in the interaction with sulphur dioxide.

The high content of iron in the adsorbant, through its catalitical oxidation action, seems to enhance the reactivity but sodium constitutes an impurity which determines diffusivity modifications in the reaction product layer (CaSO_4). However these hypotheses are not confirmed yet. Several researchers [5, 6] made estimations of the influence of particle size about the desulphurization degree and confirm a reverse correlation.

The optimal temperature of the dry injection of the adsorbant is a function of its origin, the particle size and reaction type, which always necessitates experimental determinations.

Since the micro structure of the adsorbant has an important influence about its reactivity, in this paper it would be presented the *- in situ -* generating of calcium oxide process from limestone. The generated calcium oxide was characterised by BET surface area, porosity and pore size distribution.

For this purpose, the calcination process were conducted in the temperature range 973-1273 K and the pressure in the system was $p=0,3404$ bar.

In the first stage it was established the evolution of the decarbonate degree in the heating and calcination period of the sample for the four used granulometric class.

EXPERIMENTAL

The experimental equipment used in our measurements was a CAHN TG-121 system presented in a previous paper [7].

It consisted of two sections: the main frame and the Data Acquisition and Control Station (DACS) which controls the system. The microbalance, the furnace, the cooling fan, the thermocouple, the gas and vacuum ports were the components of the main frame. The CAHN microbalance included in the TG-121 system is considered the finest apparatus available today for this application. Its sensitivity is of 0.1 g and the maximum capacity of 1.5 g. Each sample of limestone has been primarily calcinated for 40 minutes between 973 K- 1273 K, $P=0.3403$ bar and under a nitrogen stream. The probes belongs to one of the following average particle diameter: 25 μm , 90 μm , 450 μm and 900 μm . After the complete calcination, each sample has been characterised by BET surface area, porosity and pore size distribution. The operation parameters of the system are shown in Table 1.

Table 1.

Operate parameters of the system

| Crt. Nr. | Parameter | Value |
|----------|-------------------------|---|
| 1 | Calcination temperature | 973 K, 1023 K, 1123 K, 1173 K, 1273 K |
| 2 | Calcination time | 40 min |
| 3 | Pressure | 0,3403 bar |
| 4 | Particle size of CaO | 0-50; 80-100; 400-500; 800-1000 μm |

Materials

The adsorbant was obtained “in situ” through calcination of limestone with the following chemical composition: CaCO_3 (97 %), Fe_2O_3 (1,8 %), Al_2O_3 (0,88 %), SiO_2 (0,3 %).

The granulometric class of the particles were obtained through volumetric sizing of limestone with a Retsch set of sieves mesh between 0-1000 μm .

Each sample of calcium carbonate belonging to one granulometric class was subdue in a first stage to complete calcination. After the calcination each sample has been characterised by BET surface area, porosity and pore size distribution through the sorption method.

RESULTS AND DISCUSSION

The evolution of the decomposition of limestone for all granulocities was followed through the decomposition degree η_D . On the basis of the material balance, one can write:

$$\eta_D = \frac{m_s^0 - m_s}{m_s^0 \cdot \bar{x}_{PC}^0} = \frac{1}{\bar{x}_{PC}^0} \left(1 - \frac{m_s}{m_s^0} \right) \quad (1)$$

where: m_s^0, m_s – initial mass and at a moment of the sample [mg];

\bar{x}_{PC}^0 – mass fraction of the calcination losses (0,4397) determined as a arithmetical mean of four values obtained for four limestone samples submitted to calcination at 1323 K for two hours.

The obtained results are presented in figures 1, 2 and 3.

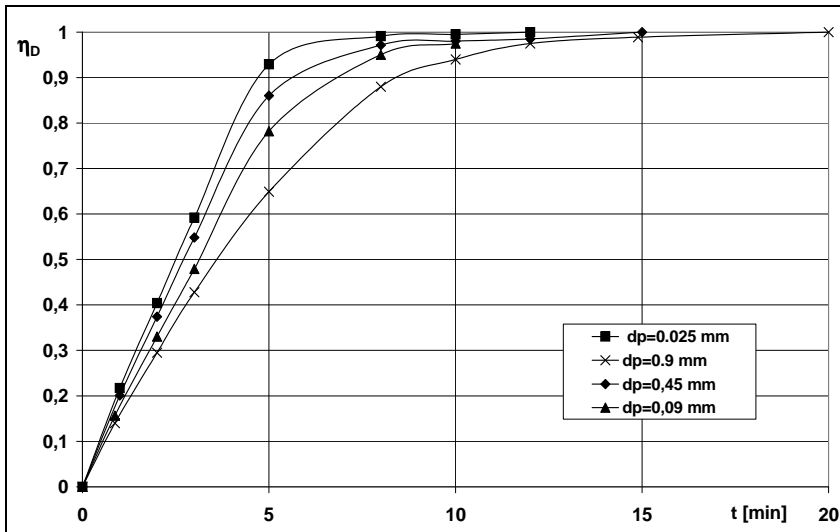


Fig. 1. Influence of particles sizes on the decomposition degree of CaCO_3 at $T_c=1173$ K

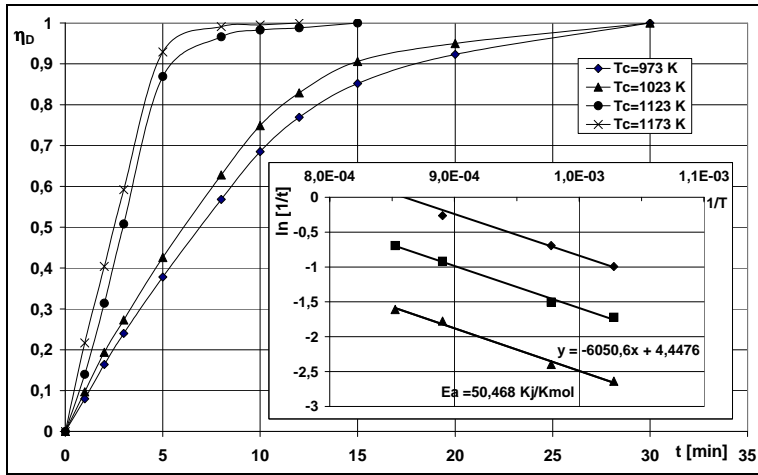


Fig. 2. Influence of temperature on the decomposition degree of CaCO_3 particles with $d_p=0,025\text{mm}$

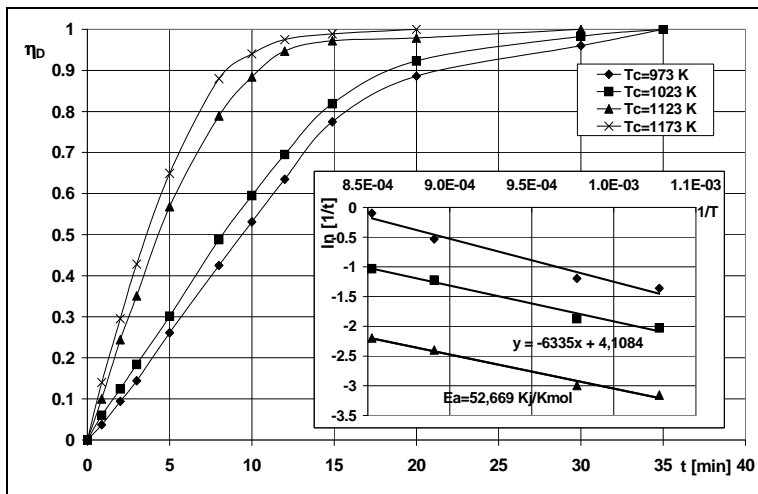


Fig. 3. Influence of temperature on the decomposition degree of CaCO_3 particles with $d_p=0,9\text{mm}$

The kinetic curves, show an insignificant influence of the particle size on the degree of decomposition. The difference that appears, is due to the different thermal conductivity of the particles layer from the examined samples. In all cases there would be reached the maximal decarbonation degree.

The calculated activation energy for both cases shown in figures 2 and 3 is about 50 – 53 KJ/mol and indicates that the calcination of limestone is generally kinetically controlled while the gas film resistance and pore diffusion limitation are negligible.

From the experimental data obtained in the sorption method the desorption isotherms shown in figure 4 are obtained.

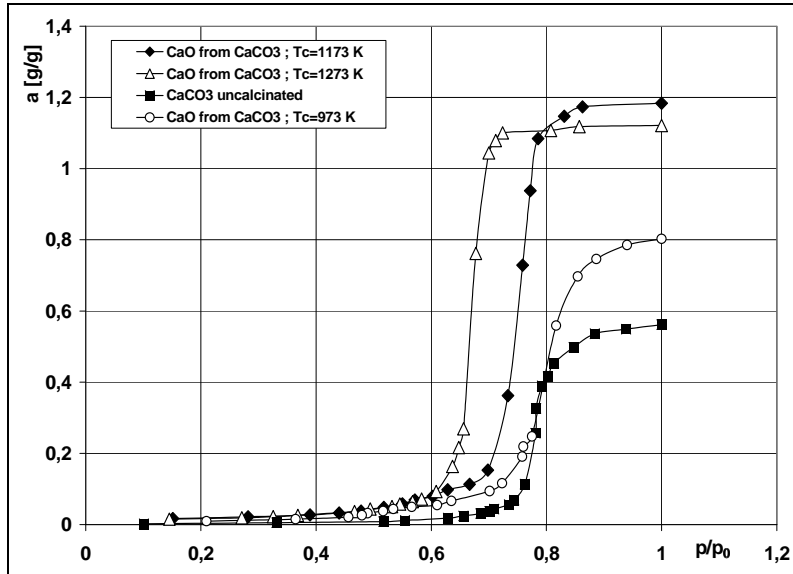


Fig. 4. Desorption isotherms for CaO particles with $d_p=0,025$ mm

In order to calculate the specific surface area there the Brunner, Emmet & Teller equation for the adsorption of benzen in polimolecular layers [8] was used:

$$\frac{x}{a(1-x)} = \frac{1}{a_m \cdot C} + \frac{C-1}{a_m \cdot C} \cdot x \quad (2)$$

Where: a – quantity of adsorbed benzen [g benzen/g CaO] at any value of the relative equilibrium pressure $x = p/p_0 = t_0/t$;

a_m - monomolecular load [g benzene /g CaO];

C – BET- parameter.

The BET – isotherm represented by equation (2) is a straight line given by:

$$y = m \cdot x + n \quad (3)$$

$$\text{Where: } y = \frac{x}{a(1-x)}; \quad m = \frac{(C-1)}{a_m \cdot C}; \quad n = \frac{1}{a_m \cdot C}$$

In the range of relative low pressures, the BET – equation is rigorous by linear and allows for the evaluation of a_m and C from the slope “ m ” and the ordinate intersection “ n ” of the line given by equation (3) (figure 5).

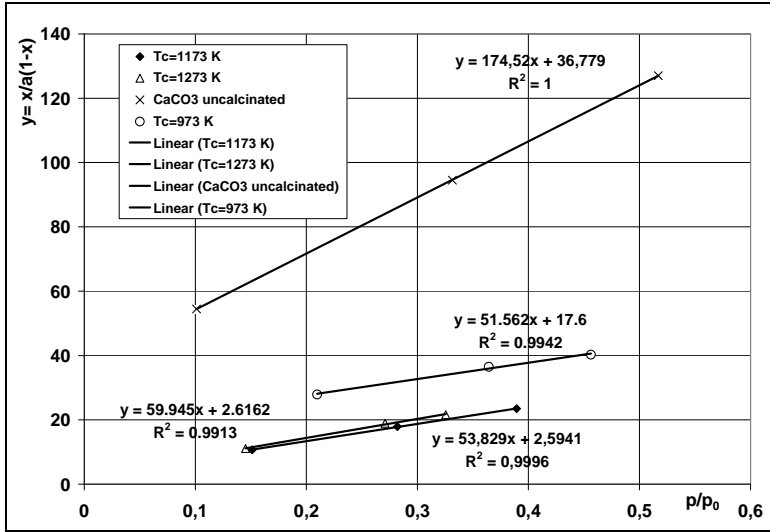


Fig. 5. BET-isotherms for CaO particles with $d_p=0,025$ mm

Considering that the covering is in monomolecular layer with compact and tangent arranged molecules and knowing the covering surface of one benzene molecule $s_0 = 40,3 \text{ \AA}^2$ at 293 K the specific surface can be calculated with following equation:

$$S_{sp} = \frac{a_m}{M_b} \cdot N_A \cdot s_0 \quad (4)$$

where: S_{sp} - BET specific surface area [m^2/g];

a_m - monomolecular load [g benzen/g CaO];

M_b - Molecular mass of the adsorbate (benzen) [g/mol];

N_A - Avogadro number [$6,023 \cdot 10^{23} \text{ mol}^{-1}$];

s_0 - covering surface of one benzene molecule [\AA^2].

The specific surfaces area calculated from the BET isotherms similar to those shown in figure 5 are presented in table 2.

Table 2.

Specific area of used adsorbant [m^2/g]

| $\bar{d}_p \downarrow$ [μm] | Uncalcinated | T [K] | | | | |
|---|--------------|---------|---------|---------|---------|---------|
| | | 973 | 1023 | 1123 | 1173 | 1273 |
| 25 | 14,7274 | 44,9941 | 47,4971 | 53,4127 | 55,1966 | 49,7292 |
| 90 | 11,3384 | 35,9535 | 38,0421 | 42,3875 | 44,0020 | 39,3590 |
| 450 | - | 29,8988 | 33,2475 | 40,1042 | 41,8644 | 36,8775 |
| 900 | 6,8443 | 18,9107 | 25,0107 | 36,6412 | 40,1346 | 35,0438 |

The values of the specific area increase with the temperature until 1173 K. At higher temperatures the surface area decreases due to the sinterisation effect. Using the desorption isotherms there was calculated the mean pores radius and the pores size distribution. The vertical portion of the desorption isotherms were attributed to the capillary condensation-vaporisation phenomenon. The relation between the relative pressure x and the pore radius when condensation-vaporisation occurs is given by the Kelvin equation [9]:

$$x = \frac{p}{p_0} = \frac{t_0}{t} = e^{-\frac{2 \cdot \sigma \cdot M}{r \cdot \rho \cdot R \cdot T}} \quad (5)$$

where: $x = p/p_0$ - relative equilibrium vapours pressure;

σ - superficial tension of the liquid adsorbate (benzen) at the isotherm temperature [dyn/cm];

ρ - adsorbate density (benzen) at the isotherm temperature [g/cm³];

r - pore radius, equal with the menisc radius curvature [m];

M - molar mass of the adsorbate (benzen) [g/mol];

R - general gases constant;

T - temperatura isotherm [K].

From the equality between the pore radius and menisc curvature radius the pore size can be evaluated [8-11]. The distribution function versus radius was calculated with following equation:

$$\frac{\Delta a}{\Delta r} = f(r_p) \quad (6)$$

which reproduced the variation of the evacuated adsorbant amount in successively stages Δa as a function of the pore radius Δr shown in the figure 6.

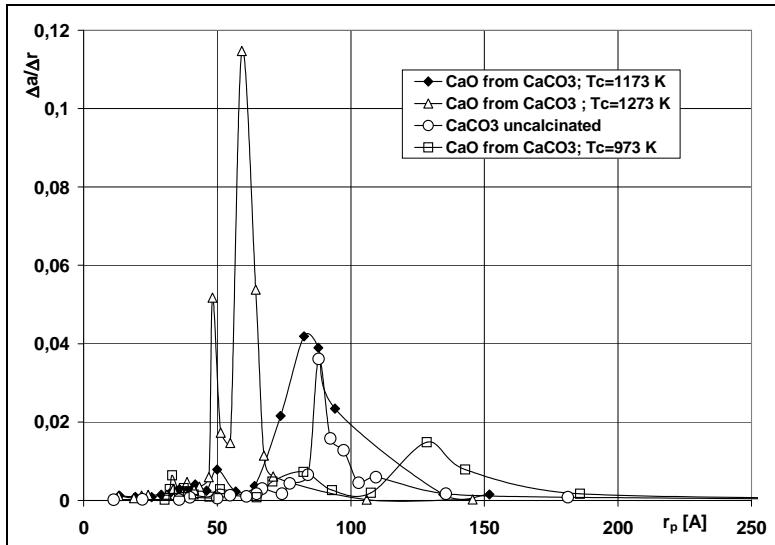


Fig. 6. Pore size distribution for CaO particles with $d_p=0,025$ mm

Figure 6 shows a modest proportion of micropores, predominant is the mesopores category.

CONCLUSIONS

1. The structure and the chemical composition of the adsorbant has a significant importance on the calcium oxide reactivity in the flue gas desulphurization processes;
2. The obtained surface areas for calcium oxide are in the range between 18,9107 - 55,1966 m²/g and a porosity in the range of mesopores as a function of the particles size and the decomposition temperatures;
3. The high specific surface area increased the degree of utilisation of calcium oxide because the sulfation reaction is initially a surface reaction.
4. The large range in which the surface area of calcium oxide is included showed the necessity of its correlation with the kinetic of the sulphatation process

REFERENCES

1. Felsvang, K., Spannbauer, H., Gedbjerg, P., "1990 SO₂ Control Symposium, Session 4C", (1990) May 8-11, New Orleans, Louisiana
2. Mersmann, A., Kutzer, St., "Absorptive Abgasreinigung" VDI-Berichte, (1993), Nr. 1034, VDI-Verlag, Dusseldorf, p.227-247
3. Sedman, C.B., Maxwell, M.A., Hall, B., "1991 SO₂ Control Symposium, Session 4B", (1991), December 3- 6, Washington D.C.
4. Nelson, S., "1991 SO₂ Control Symposium, Session 4B", (1991), December 3- 6, Washington D.C.
5. Ahman, S., Gottschalk, J., "Vortrag auf der VGB-Fachtagung: Industrie Heizkraftwerke und BHKW", (1996) , 5-6.Dezember, Münster, Deutschland.
6. G.B. Martin, J.H. Abbott, *Proceedings of the 1st Joint Symposium on Dry SO₂ and Simultaneous SO₂/NO_x Control Technologies*, San Diego, California, (1984) November 13-16.
7. S. Dragan, I. Siminiceanu, *Revista de Chimie*, (2004), Bucuresti, Nr.11, p.857-861.
8. J.M. Mc.Carthy, in *Proceedings: 1986 Joint EPRI/EPA Symposium on Dry SO₂ and Simultaneous SO₂/NO_x Control Technologies*, (1986), Volume 2, EPRI CS 4966, Dec.
9. S. Dragan, I. Siminiceanu – *Studia Univ."Babes-Bolyai" Cluj-Napoca*, 2001, Chem. vol.46 (1-2), p.309-315.
10. Hartman, J. Pata, R.W. Coughlin, *Ind.Eng.Chem., Process Des.Dev.*, (1978), 17, p. 411.
11. R.H. Borgwardt, R.D. Harvey, *Environ. Sci & Technol.*, (1972), 6, p. 350.

SEDIMENTATION. KOAGULATION. FLOCCULATION. II. ANWENDUNG POLYMERER FLOCKUNGSMITTEL

**ADINA GHIRIȘAN, ALEXANDRU POP, MARIANA MOCEANU
und VASILE MICLĂUȘ**

*Fakultät für Chemie und Chemieingenieurwesen, Universität "Babeș-Bolyai" Cluj-Napoca,
Arany Janos 11, 400028 Cluj-Napoca, Rumänien*

ZUSAMMENFASSUNG. Für die Verbesserung der Trennung einer Kaolin-Wasser-Suspension wurde die optimale Flockungsmittelmenge Praestol BC 611 durch Sedimentationsanalyse untersucht. Bei unterschiedlichen Feststoff-konzentrationen, über qualitative und quantitative Eigenschaften, wurde der Einfluss der Agglomeration auf die Feststoffabscheidung dargestellt.

EINLEITUNG

In der Industrie wie in der Abwasserwirtschaft ist die Zugabe von Flockungsmitteln ein weit vorbereiteter Lösungsansatz für den effektiveren Umgang mit den Suspensionen, die feine Partikel enthalten. Die Partikel, die in einer Flüssigkeit suspendiert vorliegen, besitzen eine sehr grosse spezifische Oberfläche. Um ihre freie Energie zu reduzieren neigen in der Regel die Teilchen dazu, Agglomerate zu bilden [1].

Die Agglomeration von suspendierten Partikeln zu Flocken hat in der Hauptsache zwei Ziele [2]:

- Die *Sedimentationseigenschaften* der Feststoffe sollen verbessert werden. Dies wirkt sich in folgender Hinsicht aus: a) Beschleunigung der Absetzgeschwindigkeit des Feststoffes; b) Abtrennung auch feinsten kolloidaler Inhaltsstoffe von Suspensionen; c) Beschleunigung von Eindickvorgängen; d) Reduzierung des COD (Chemical Oxygen Demand) und des BOD (Biological Oxygen Demand).

- Die *Kuchenbildungs- und Entwässerungseigenschaften*, von durch Filtration entstandenen Haufwerken, sollen durch günstige Beeinflussung der Porenstruktur, auch verbessert werden. Dies wirkt sich in folgender Hinsicht aus: a) Abtrennung eines von absetzbaren Feststoffen feinen Filtrates; b) Hohe Feststoffmassendurchsätze infolge der Verringerung des Kuchenwiderstandes; c) Verringerung des Restflüssigkeitsgehaltes im Filterkuchen; d) Schaffung der Voraussetzungen zum Einsatz bestimmter Entwässerungsapparate (Siebbandpressen).

Die Flocculation ist der Mechanismus der Entstabilisierung, der von einer Vernetzung der Einzelpartikel in einer Flocke durch hochmolekulare Flockungsmittel ausgeht [3].

Bei der Flocculation werden die Partikel mit Hilfe von synthetischen oder natürlichen Flockungsmitteln verbunden durch die Bildung permanenter Brücken aus makromolekularen Substanzen.

Es handelt sich bei diesen Flockungsmitteln in der Regel, um wasserlösliche Kohlenwasserstoffverbindungen mit unterschiedlichem Molekulargewicht und unterschiedlichen reaktiven Gruppen. Man unterscheidet zwischen natürlichen

organischen Flockungsmitteln, wie z.B. Stärke oder Glucose, und synthetischen hergestellten Polymeren. Synthetische Flockungsmittel haben in den letzten Jahren eine immer größer werdende Bedeutung erlangt. Es gibt inzwischen eine große Anzahl von speziell modifizierten synthetischen Flockungsmittel, die zum grössten Teil durch Polymerisation von Acrylsäureamiden hergestellt werden [3]. Man unterscheidet sie über ihren spezifischen Polymerisationsgrad, ihre reaktive Gruppe, ihr Molekulargewicht und ihre Ladung [4]. Die synthetischen Flockungsmittel sind auf dem Markt als Granulat in fester Form, als Emulsion oder als wässrige Lösung erhältlich. Bei der Verwendung werden verdünnte Lösungen eingesetzt, die der zu flockenden Suspension zugegeben werden. Die Flockungsmittel sollen im gesamten pH-Bereich von 1 bis 14 wirksam sein. Die Wirksamkeit der Flockungsmittel soll auch bei extremen Elektolytgehalten gegeben werden. Durch die Flocculation soll: a) eine Abtrennung von Feststoffen und nicht von gelösten Inhaltsstoffen einer Suspension entstehen; b) die Abtrennung aus wässrigen Medien und nicht aus organischen Lösungen oder Lösungsmitteln erfolgen; c) die Arbeit in einem Temperaturbereich von 0°C bis 100°C möglich machen.

Nach der Theorie von Healy und La Mer [5], die für die Flockenbildung im Wesentlichen von der beschriebenen Polymerbrückenbildung ausgeht, verläuft die Bildung der Flocken nach folgender Beziehung:

$$-\frac{dn}{dt} = k_1 \cdot n^2 \cdot \Theta(1 - \Theta) \quad (1)$$

mit: n - Anzahl der Teilchen; k - Geschwindigkeitskonstante; Θ - Bedeckungsgrad der Oberfläche mit Polymer ($\Theta = 0$ - keine Polymerbeladung; $\Theta = 1$ - volle Polymerbeladung).

Diese Funktion besitzt bei $\Theta = 0.5$ ein Maximum. Unter der Voraussetzung, dass bei $\Theta = 0.5$ nach dem Brückenbildungsmodell auch die maximale Stabilität der gebildeten Flocken erreicht ist, wobei bei $\Theta = 0$ als auch $\Theta = 1$ keine Agglomeration auftritt, ergibt sich für den Zerfall einer gebildeten Flocke die Gleichung:

$$\frac{dn}{dt} = k_2 R \frac{1}{\Theta(1 - \Theta)} \quad (2)$$

mit: k_2 – Zerfallgeschwindigkeitskonstante und R – Agglomeratradius.

Nach dieser Theorie sollte die Polymerkonzentration so gewählt werden, dass nach der Adsorption, 50% der Feststoffoberfläche mit Polymer bedeckt ist. Hierbei ist aber in der praktischen Anwendung zu berücksichtigen, dass die Polymeradsorption selbst einer Zeitfunktion unterliegt, die von dem Polymerkonzentrationsgefälle zwischen Feststoffoberfläche und Suspension abhängt. Ebenso, nicht berücksichtigt, sind auch andere Parameter wie Elektrolytkonzentration, pH-Wert, Turbulenzgrad usw.

Also, muss für jede Suspension das günstigste Flockungsmittel und dessen Zugabemenge durch Reihenuntersuchungen im Labor ermittelt werden.

VERSUCHSDURCHFÜHRUNG

Im Rahmen dieser Forschungsarbeit wurde durch Sedimentationsversuche der Kaolin-Wasser-Suspension (unterschiedlicher Konzentration), über die Absetzgeschwindigkeit des Trennspiegels, die optimale Konzentration (Menge) der Flockungsmittel beurteilt.

Für die Versuchsreihen stand als Feststoff Kaolin der Qualität **K 01** ($d_{\text{Kaolin}} < 63 \mu\text{m}$) zur Verfügung. Als Flockungsmittel kam das organisch-synthetische Praestol BC 611, der Firma Stockhausen GmbH, im Einsatz [6]. Dieses wirkt, durch einen geringen überwiegenden Anteil an positiv geladenen Gruppen, schwach kationisch. Praestol BC 611 ist ein langkettiges Copolymer auf Acrylamidbasis und quaternären Aminoester. Es besitzt ein hohes Molekulargewicht und dient der Vernetzung der, in der Suspension vorliegenden Feststoffpartikeln. Praestol BC 611 liegt als Ausgangsstoff in fester Form vor und wurde von uns unter Rühren in demineralisiertem Wasser gelöst.

Die Durchführung dieses Versuches ist die standardisierte Testmethode, die im ersten Teil dieser Forschung vorgestellt wurde [3], wobei die Sedimentation der geflockten Kaolinsuspensionen im Schüttelapparat (diskontinuierlicher Sedimentationsversuch) untersucht wurde.

Anfangs wurden Kaolin-Wasser-Suspensionen unterschiedlicher Konzentration, entsprechend 1 %, 3 % und 5 % (Masse %), vorbereitet. Dazu wurde der Standzylinder (Durchmesser $\phi = 50 \text{ mm}$ und Höhe $H = 300 \text{ mm}$) des Schüttelapparats mit 4 g, 12 g und 20 g Kaolin KO1 (die Dichte des trockenen Feststoffs $\rho_p = 2500 \text{ kg/m}^3$) und 400 ml demineralisiertes Wasser gefüllt. Der Zylinder wurde mit dem Stöpel verschlossen und im Schüttelapparat kräftig geschüttelt, so dass eine homogene Suspension/Trübe entstand.

Die Dosierung der Flockungsmittel wurde durch Herabsetzung der Flockungsmittellösungskonzentration variiert. Zuerst wurde das Flockungsmittel als Lösung 0,1% vorbereitet. Das Flockungsmittel wurde von 0,5 g nichtionisches Polyacrylamid und 500 ml Leitungswasser nach einer starken magnetischen Vermischung hergestellt.

Jede Kaolinsuspension wurde dann mit Praestol BC 611 (verschiedener Konzentration) vermischt. Also, wurden bei jedem neuen Versuch verschiedene Volumen des Flockungsmittels BC 611 zugegeben und so wurden flockulate Suspensionen unterschiedlicher Konzentration C_{FM} (ppm) erhalten und zwar: 250 ppm; 500 ppm; 750 ppm; 1000 ppm; 1250 ppm; 1500 ppm; 1750 ppm; 2000 ppm und 2500 ppm. Der Wert C_{FM} (ppm) ergibt sich als Quotient aus der Masse des Flockungsmittels (mg) und der Masse des Feststoffes (kg). Die pH-Werte liegen in dem Bereich 5,0 – 7,0 in jedem Fall.

Die Zylinder wurden danach im Apparat zehnmal geschüttelt. Weil der Flockungsvorgang mit der Art der Dosierung des Flockungsmittels und dessen Vermischung mit der Suspension beginnt, wurden alle Versuche in denselben Bedingungen mehrmals durchgeführt. Danach wurden die Mittelwerte vorgestellt.

Die Bewegung des Trennspiegels (die Grenze zwischen den sedimentierenden geflockten Suspensionen und der mehr oder weniger geklärten Flüssigkeit) entsprechend einer Höhe $h = 150 \text{ mm}$ wurde über die Zeit gemessen.

ERGEBNISSE UND DISKUSSION

In den hier beschriebenen Versuchen wurden Kaolin-Wasser-Suspensionen mit 1%, 3% und 5 % Feststoffkonzentration, die stabil sind und sehr schwach, unvollständig und langsam sedimentieren. Beim diskontinuierlichen Absetzversuch zeigen diese trübene Suspensionen, mit einem kolloidalen Aspekt, keine Grenzlinie zwischen den absetzenden Feststoffteilchen und dem Überstand. Die größeren Feststoffteilchen des Kaolins setzen sich mehr in Form einzelner Partikel ab.

Für eine Verbesserung der Fest-Flüssig-Trennung durch Sedimentation im Erdfeld wurde die Suspension mit dem Flockungsmittel vermischt. So können Kaolinteilchen der Suspension geflockt werden und nun besser als Flocken sedimentieren. Die Analyse des Sedimentationsverhaltens zeigt, dass die charakteristischen Eigenschaften der geflockten Suspensionen und die Trennspiegelgeschwindigkeit sich mit der Flockungsmittelkonzentration ändern.

In jedem Fall wird deutlich, dass die Steigung der Zugabemenge der Flockungsmittel zu einer schnellen Sedimentation der geflockten Teilchen führt, wie in der Abbildung 1 (bei einer Feststoffkonzentration $C = 3\%$) und Abbildung 2 (bei einer Feststoffkonzentration $C = 3\%$) gesehen ist. Bei einer Flockungsmittelkonzentration $C_{FM} = 250$ ppm war die Suspension noch eine Trübe, die sehr langsam sedimentiert, wie in der Abbildung 1 und in der Abbildung 2 gezeigt ist. Dann wurde mit zunehmender Flockungsmittelkonzentration eine deutliche Grenzlinie zwischen der Flüssigkeit und geflockten Suspension erschienen und eine Beschleunigung der Sedimentation bemerkt.

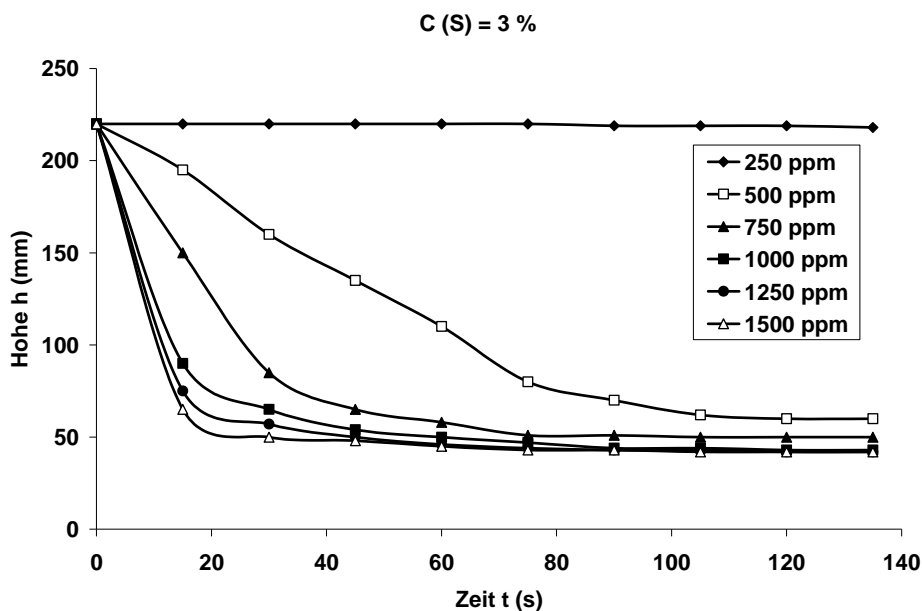


Abb. 1. Höhe des Trennspiegels Überstand/geflockte Suspension 3 % Feststoff in Abhängigkeit von der Zeit.

Für alle Versuche wurde die Absetzgeschwindigkeit (Trennspiegelgeschwindigkeit) nach der Gleichung (3) berechnet:

$$w_{\text{sed}} = \frac{h}{t} = \frac{150}{t} \quad (\text{mm/s}) \quad (3)$$

Die Absetzgeschwindigkeit des Trennspiegels sedimentierten Suspension/geklärten Wasser w (mm/s) wurde über den Flockungsmittelkonzentrationen C_{FM} (ppm) in dieser Forschungsarbeit verfolgt. Die Ergebnisse sind in Tabelle 1 vorgestellt.

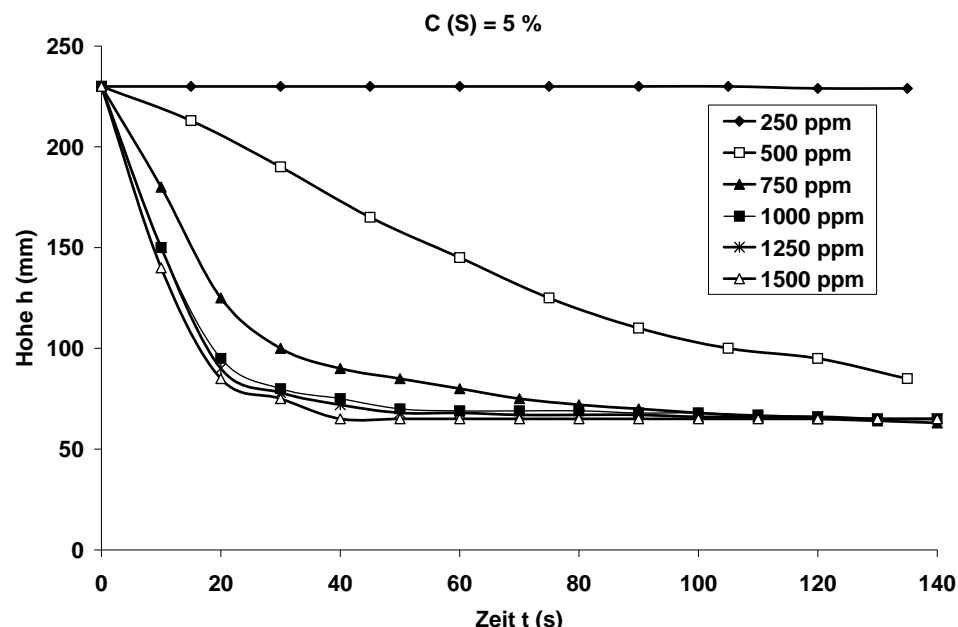


Abb. 2. Höhe des Trennspiegels Überstand/geflockte Suspension 5 % Feststoff in Abhängigkeit von der Zeit.

Tabelle 1.

Ergebnisse der Sedimentationsanalyse

| Kaolin-Wasser-Suspension unterschiedlicher Konzentration | | | | | | |
|--|---------------------|-------------|---------------------|-------------|---------------------|-------------|
| C _{FM} (ppm) | 1 % | | 3 % | | 5 % | |
| | V BC 611 (mL) | w (mm/s) | V BC 611 (mL) | w (mm/s) | V BC 611 (mL) | w (mm/s) |
| 500 | 2,00 | 3,28 | 6,00 | 2,95 | 10,00 | 1,74 |
| 750 | 3,00 | 4,89 | 9,00 | 4,30 | 15,00 | 3,63 |
| 1000 | 4,00 | 8,37 | 12,00 | 6,82 | 20,00 | 4,84 |
| 1250 | 5,00 | 10,71 | 15,00 | 8,50 | 25,00 | 6,52 |
| 1500 | 6,00 | 13,87 | 18,00 | 12,50 | 30,00 | 9,14 |
| 1750 | 7,00 | 12,50 | 21,00 | 11,54 | 35,00 | 9,00 |
| 2000 | 8,00 | 10,43 | 24,00 | 11,54 | 40,00 | 8,77 |

Während der Durchführung wurden mit zunehmender Menge der Flockungsmittel grössere Flocken und somit ein poröseres, weniger kompaktes Sediment, schnellere Sedimentation und bessere Aufklärung des Überstands beobachtet. Die Ergebnisse zeigen für die Suspension mit 1 % Kaolin eine deutliche Erhöhung der Sedimentationsgeschwindigkeit mit zunehmender Flockungsmittelkonzentration nur bis zu einer Konzentration der Flockungsmittel

$C_{FM} = 1500$ ppm BC 611. Bei den Versuchen in denen der C_{FM} kleiner als 250 ppm war, war keine Sedimentation zu sehen und bis 1000 ppm weist der Überstand noch eine hohe bis sehr hohe Trübung auf. Das bedeutet, dass in der Suspension nicht genug Flockungsmittel zur Makroflockenbildung vorgegeben war, um die Kaolinteilchen quantitativ zu fällen. Man weiss, dass sich durch die Agglomeration in einem ersten Flockungsschritt sogenannte Mikroflocken bilden. Diese Mikroflocken bestehen aus wenigen schwach miteinander verbundenen Feststoffteilchen. In weiteren Schritten können sich nun Mikroflocken zu grossen Makroflocken zusammenlagern, wobei auch weitere Einzelpartikeln miteingebunden werden können.

Die Absetzgeschwindigkeit nimmt nur bis zu einer bestimmten Konzentration der Flockungsmittel zu, die noch nicht einer Überdosierung entspricht. Bei einer Überdosierung von Flockungsmittel $C_{FM} > 1750$ ppm BC 611 führt die Sedimentation zum gegenteiligen Effekt, zu einer Stabilisierung der Flockungsmittel-Partikel (die Absetzgeschwindigkeit bleibt ungefähr konstant) und zu einer schwächeren Separation (Abb. 3).

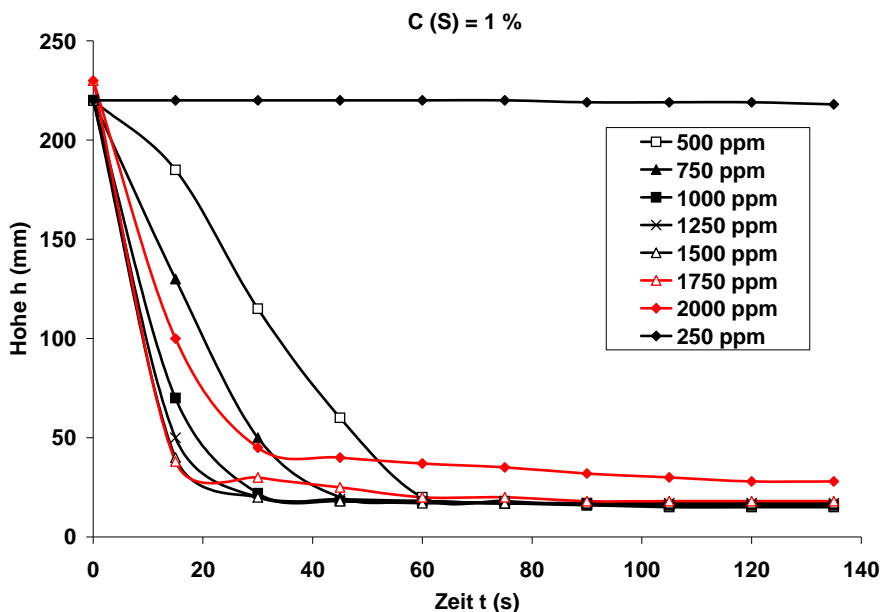


Abb. 3. Höhe des Trennspiegels Überstand/geflockte Suspension 1 % Feststoff in Abhängigkeit von der Zeit.

Trägt man die Trennspiegelgeschwindigkeit über die Flockungsmittelkonzentration als die Flockung einflussnehmenden Parameter in einer Suspension auf, ist nach Abbildung 4 ein Maximum der Flockunseffektivität zu bemerken.

Die Durchführung der Sedimentation einer Suspension 3 % Kaolin bestimmt das Optimum bei einer Flockungsmittelkonzentration $C_{FM} = 1500$ ppm, wenn alle feinen und feinsten Feststoffteilchen der Suspension in dem kompakten Netz gebunden sind und ein klarer Überstand erhalten wird. Das Flockungsergebnis war in diesem Fall sehr gut.

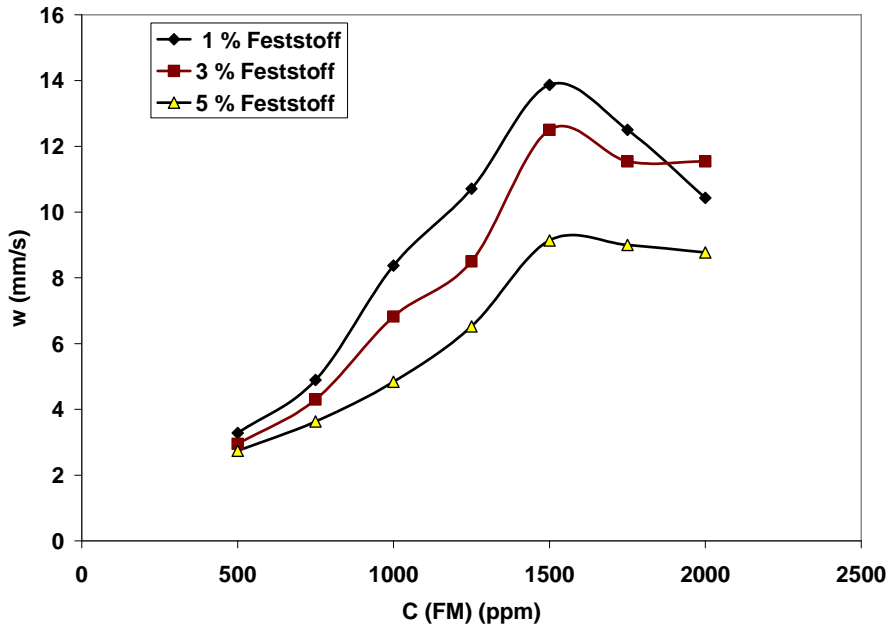


Abb. 4. Auftragung der Trennspiegelgeschwindigkeit w der unterschiedlichen Suspensionen über die Flockungsmittelkonzentration C_{FM} .

Eine höhere Flockungsmittelkonzentration lohnt sich nicht, weil das Flockungsmittel sehr teuer ist und die Trennspiegelgeschwindigkeit bleibt ungefähr gleich, wobei der Überstand nicht klarer wird.

Für die Suspensionen mit 5 % Kaolin sind die Ergebnisse ungefähr gleich, die maximale Absetzgeschwindigkeit wurde bei einer Konzentration der Flockungsmittel $C_{FM} = 1500$ ppm erreicht. Die Feststoffteilchen der Suspension wurden kompakt eingebunden und man erhält klares Wasser als Überstand, obwohl die Absetzgeschwindigkeiten geringer waren (Tabelle 1).

Die Ergebnisse dieser Forschungsarbeit zeigen, bei höherer Konzentration des Feststoffs und konstanter Flockungsmittelkonzentration in der Suspension, kleinere Absetzgeschwindigkeiten des Trennspiegels (wie z.B. für eine Flockungsmittelkonzentration $C_{FM} = 1000$ ppm ist die Absetzgeschwindigkeit $w = 8,37$ mm/s für 1%-ige Kaolinsuspension; $w = 6,82$ mm/s für 3%-ige Kaolinsuspension und $w = 4,84$ mm/s für 5%-ige Kaolinsuspension), weil der Einfluss der Agglomerate mit der Feststoffkonzentration steigt und so die Sedimentationsgeschwindigkeit reduziert werden kann.

In dem folgenden Schritt wurde der Einfluss der Flockung bei der Pressfiltration untersucht. In diesem Fall wurden Pressfiltrationsversuche der geflockten und ungeflockten Kaolin-Wasser-Suspensionen durchgeführt. Ungeflockte und geflockte Kaolinsuspensionen mit einer Feststoffkonzentration von 1 % und 3 % wurden bei einem Filtrationsvakuum von 50 mm Hg filtriert. Geflockte Suspensionen der Kaolin K 01 zeigen im Vergleich zu ungeflockten Suspensionen einen deutlich

verringerten spezifischen Kuchenwiderstand. Durch die Flockung konnte die lange Versuchsdauer aufgrund der großen Widerstandspotential der Kaolin Partikeln reduziert werden (Tabelle 2).

Es wurde gezeigt, dass, bei der Dosierung des Flockungsmittels vor der Versuchsdurchführung, nach kurzer Zeit eine bemerkbare Sedimentation der entstandenen Makroflocken eintritt. Es bildet sich ein Bodensatz aus geflockter Substanz mit hoher Porosität und kleinerem Kuchenwiderstand, so dass das Ausgangsvolumen des Filtratanfalls steigt.

Tabelle 2.

Ergebnisse der Filtrationsversuche

| Art der Kaolinsuspension | Kaolinkonzentration (Masse %) | Filtrationszeit bei einem Filtratanfall von 400 ml (Minute) |
|--|-----------------------------------|--|
| ungeflockte | 1 | 26,00 |
| geflockte ($C_{FM} = 1500\text{ppm}$) | 1 | 3,43 |
| ungeflockte | 3 | 38,00 |
| geflockte ($C_{FM} = 1500\text{ppm}$) | 3 | 1,56 |

SCHLUSSFOLGERUNGEN

Das Flockungsmittel dient in einer Suspension zur Agglomeration der Partikeln. Die geflockten Partikeln zeigen eine deutlich höhere Sedimentationsgeschwindigkeit bis zu einer Flockungsmittelkonzentration bei welcher eine Flockenzerstörung auftritt.

Die resultierenden Flockengrößen müssen so groß sein, dass die Größe diejenige der größten Teilchen deutlich übersteigt. Anderenfalls liegen die groben Teilchen nicht im Flockenverband vor, oder große Teilchen klassieren mit wenigen fest angebundenen kleineren Teilchen.

Durch die Flockung konnte die lange Versuchszeit der Pressfiltration aufgrund der hohen Porosität des Haufwerks reduziert werden.

LITERATURVERZEICHNIS

1. J.E. Roth, *Grenzflächeneffekte bei der Fest-Flüssig-Trennung*, Chem.Ind.Tech., 1991, 63(2), 104
2. J. Reuter, *Vortragunterlagen zum Kurs „Fest-Flüssig-Trennung“*, an der Universität Karlsruhe (TH), 1999, Deutschland
3. A. Ghirişan, V. Miclăuş, Al. Pop, *OSedimentation. Koagulation. Flocculation. I. Sedimentationsanalyse einer geflockten Kaolin-suspension*, STUDIA Univ. „Babeş–Bolyai“ Chemia, 2003, XLVI(1), 183-190
4. J.M. Reuter, *Aufbau und Reaktionsmechanismen von Polyelektrolyten und ihre Anwendung in Fest-Flüssig-Prozessen*, Aufbereitungstechnik, 1986, 27, 598
5. V.K. La Mer, *The rate of filtration in investigating the flocculation and redispersion of colloidal dispersions*, J. Phys. Chem., 1962, 66, 1833
6. Katalog der Chemischen Fabrik Stockhausen GmbH, 1995

BESCHREIBUNG DES HYDRODINAMISCHEN MODELLS DES DRUCKVERLUSTES DURCH EINE KATALYSATORSCHICHT

ALEXANDRU POP, ADINA GHIRIŞAN und SIMION DRAGAN

*Fakultät für Chemie und Chemieingenieurwesen, Universität "Babeş-Bolyai" Cluj-Napoca,
Arany Janos 11, 400028 Cluj-Napoca, Rumänien*

ABSTRACT. The pressure drops through a catalyst bed of $\text{Mn}_2\text{O}_3\text{-Fe}_2\text{O}_3$ were calculated with empirical equations and then compared with the obtained experimental pressure drops. The experimental results were correlated and a new equation for the calculation of the pressure drop with two coefficients specific to the analysed system was obtained.

EINLEITUNG. Wegen des starken Druckverlustes, der beim Fließen der Reaktionsmasse durch die Katalysatorschicht entsteht, sind die katalytischen Prozesse sehr stark energieverbrauchend.

Für die Beschreibung des Druckverlustes eines Fluids durch eine granuläre Schicht stehen verschiedene Modelle zur Verfügung [1, 2, 3]. Diese Modelle können als partikuläre Formen der Gleichung **Darcy-Weisbach** (1) betrachtet werden:

$$-\frac{dP}{dL} = \frac{\rho w^2}{2D} \quad (1)$$

Rose [4] hat, durch Ersetzung des Durchmessers des Durchflussquerschnittes D mit dem nominalen Durchmesser der Teilchen d und der linearen Geschwindigkeit w mit der fiktiven Geschwindigkeit w_0 , folgende Gleichung bestimmt:

$$-\frac{dP}{dL} = \lambda \frac{\rho w_0^2}{2d} \quad (2)$$

wobei: λ ist der Reibungsfaktor:

$$\lambda = 1000 \text{Re}^{-1} + 125 \text{Re}^{-1/2} + 14 \quad (3)$$

und das Reynolds-Kriterium ist definiert durch die Gleichung (4):

$$\text{Re} = \frac{\rho w_0 d}{\eta} \quad (4)$$

Die Gleichungen (2), (3) und (4) enthalten eine einzige Größe, die das System geometrisch charakterisiert, der nominale Durchmesser der Teilchen. Aus diesem Grund hat diese Gleichung ein begrenztes Anwendungsgebiet.

Brownell [5] charakterisiert die Gleichung (1) unter folgender Form:

$$-\frac{dP}{dL} = \lambda F_\lambda \frac{\rho w_0^2}{2d} \quad (5)$$

wobei, für turbulente Strömung:

$$\lambda = 0,014 + 1,056 \operatorname{Re}^{-0,42} \quad (6)$$

und

$$\operatorname{Re} = \frac{\rho w_0 d}{\eta} F_{\operatorname{Re}} \quad (7)$$

Die Faktoren F_λ und F_{Re} sind von den Diagrammen $F_\lambda = f(\psi, \varepsilon)$ und $F_{\operatorname{Re}} = f(\psi, \varepsilon)$ aus der Literatur [2] genommen. Wie zu sehen ist, enthält die Gleichung von Brownell noch zwei Eigenschaften neben dem nominalen Durchmesser d , die Porosität der Schicht ε und den Formfaktor der Teilchen ψ , die das System geometrisch charakterisiert.

Leva und Mitarbeiter [6] haben einige Bestimmungen aufgeführt. Sie haben dabei Schichten mit verschiedenen Porositäten ε , gebildet aus Teilchen von verschiedener Form ψ und Dimensionen d_v , untersucht:

$$-\frac{dP}{dL} = \lambda \frac{(1-\varepsilon)^{3-n}}{\varepsilon^3 \Psi^{3-n}} \frac{\rho w_0^2}{2d_v} \quad (8)$$

In diesem Fall ist das Reynolds-Kriterium nach der Gleichung (9) definiert:

$$\operatorname{Re} = \frac{\rho w_0 d_v}{\eta} \quad (9)$$

Die Gleichungen (8) und (9) sind von begrenzter Präzision, weil die Koeffizienten λ und Ψ graphisch in Abhängigkeit von Re bestimmt werden.

Ergun [7] hat eine viel angewendete Gleichung von folgender Form vorgeschlagen:

$$-\frac{dP}{dL} = \lambda \frac{(1-\varepsilon)}{\varepsilon^3} \frac{\rho w_0^2}{d_p} \quad (10)$$

wobei:

$$\lambda = 150 \operatorname{Re}^{-1} + 1,75 \quad (11)$$

und

$$\operatorname{Re} = \frac{\rho w_0 d_p}{\eta(1-\varepsilon)} \quad (12)$$

Mehta und Hawley [8] haben einen Faktor F_p in die Gleichung (10) eingeführt, damit man auch den Einfluss der Wand für die Verhältnisse $D/d < 50$ mit einbeziehen kann. Die Gleichung hat die Form:

$$-\frac{dP}{dL} = \lambda \frac{(1-\varepsilon)}{\varepsilon^3} \frac{\rho w_0^2}{d_p} F_p \quad (13)$$

Der Faktor F_p ist nach der Gleichung (14) definiert:

$$F_p = 1 + \frac{2d_p}{3D(1-\varepsilon)} \quad (14)$$

λ ist nach der Formel (15) definiert:

$$\lambda = 150F_p \text{Re}^{-1} + 1,75 \quad (15)$$

Wie die Gleichungen (2), (5), (8), (10) und (13) zeigen, ist der Druckverlust durch das granulare Festbett von den Eigenschaften des Fluids (Viskosität, Dichte), Eigenschaften eines Partikels (Größe, Formfaktor, Natur des Materials) und Eigenschaften der Schicht (spezifische Oberfläche, Leerefraktionen, Oberflächenzustand, äquivalenter Durchmesser der Lücken, Porosität der Schicht, Verhältnis zwischen dem Durchmesser der Schicht und Durchmesser der Teilchen) abhängig.

Die Gleichung von **Hyman** [9] gelangt zu folgender Form:

$$-\frac{dP}{dL} = 280,637\rho w_0^2 \quad (16)$$

Die Gleichung (16) enthält keine Eigenschaft der Schicht und auch nicht die Viskosität des Fluides. Deshalb ist sie von einer sehr begrenzten Genauigkeit.

VERSUCHSDURCHFÜHRUNG

Für die experimentellen Bestimmungen wurde ein Rohr mit Innendurchmesser $D = 0,021 \text{ m}$ verwendet. Das Rohr wurde mit dem industriellen Katalysator gefüllt und so eine Schicht mit identischer Geometrie wie die industrielle Schicht gebaut wurde. Der Katalysator besteht aus sphärischen Partikeln aus $\text{Mn}_2\text{O}_3\text{-Fe}_2\text{O}_3$, mit dem Durchmesser $d_p = 4 \text{ mm}$. Unter der Siebplatte, die den Katalysator hält, bleibt das Rohr etwas $0,1 \text{ m}$ leer. In diesem Abschnitt stabilisiert sich das Fluid bevor es in die Schicht eindringt. Der Durchsatz des Fluids wird vom Rotameter und der Druckverlust in der Schicht vom Wassermanometer gemessen. Die Porosität der Katalysatorschicht wurde auch experimentell ermittelt ($\varepsilon = 0,385$).

Es wurden die Durchsätze im Intervall $1 \dots 4 \text{ m}^3/\text{h}$ für 3 verschiedene Höhen der Schicht ($L_1 = 0,25 \text{ m}$, $L_2 = 0,50 \text{ m}$, $L_3 = 0,75 \text{ m}$) betrachtet. Für jede Höhe der Schicht wurden je vier Bestimmungen durchgeführt und der Mittelwert genommen.

ERGEBNISSE UND DISKUSSION

Korrelation der experimentellen Werten

Die experimentellen Werte des Verhältnisses $\Delta P/L$, die bei verschiedenen Höhen der Katalysatorschicht gemessen wurden, und die Mittelwerte sind in der Tabelle 1 eingetragen.

Tabelle 1.

Experimentelle Werte des Verhältnisses $\Delta P/L$ bei verschiedenen Höhen der Katalysatorschicht aus Partikeln mit dem Durchmesser $d_p = 4 \text{ mm}$.

| $Q_v \text{ (m}^3/\text{h)}$ | $\Delta P/L \text{ (N/m}^2 \cdot \text{m)}$ | | | Mittelwerte $\Delta P/L \text{ (N/m}^2 \cdot \text{m)}$ |
|------------------------------|---|----------------------|----------------------|--|
| | $L = 0,25 \text{ m}$ | $L = 0,50 \text{ m}$ | $L = 0,75 \text{ m}$ | |
| 1 | 1000,62 | 892,71 | 752,1 | 881,81 |
| 2 | 2668,32 | 2530,98 | 1844,133 | 2347,81 |
| 3 | 5120,82 | 4757,85 | 3459,66 | 4446,21 |
| 4 | 7573,32 | 8416,98 | 5768,28 | 7253,193 |

In der Tabelle 2 sind die Werte des Druckverlustes angegeben, die mit Hilfe der empirischen Gleichungen bestimmt wurden.

Tabelle 2.

Werte $\Delta P/L$ (N/m^2m) berechnet mit den verschiedenen empirischen Gleichungen

| Gleichung | Rose | Brownell | Leva | Ergun | Metha und Hawley | Hyman |
|-------------|----------|----------|----------|----------|------------------|--------|
| w_0 (m/s) | | | | | | |
| 0,802 | 2598,57 | 5212,92 | 2653,29 | 4477,95 | 5624,87 | 213,18 |
| 1,603 | 8525,26 | 17525,44 | 7418,64 | 16098,87 | 19874,10 | 851,65 |
| 2,405 | 17555,50 | 36118,56 | 12832,32 | 34894,05 | 42765,80 | 1917,1 |
| 3,207 | 29600,80 | 60580,20 | 15586,12 | 60835,93 | 74306,65 | 3408,7 |

Man kann bemerken, dass alle Gleichungen sehr unterschiedliche Werte von den experimentellen Werten ergeben haben. Die besten Werte entsprechen der Gleichung von Leva und Hyman.

Die experimentellen Werte wurden danach mit den Werten, die durch verschiedene empirische Gleichungen berechnet wurden, verglichen (Abb.1).

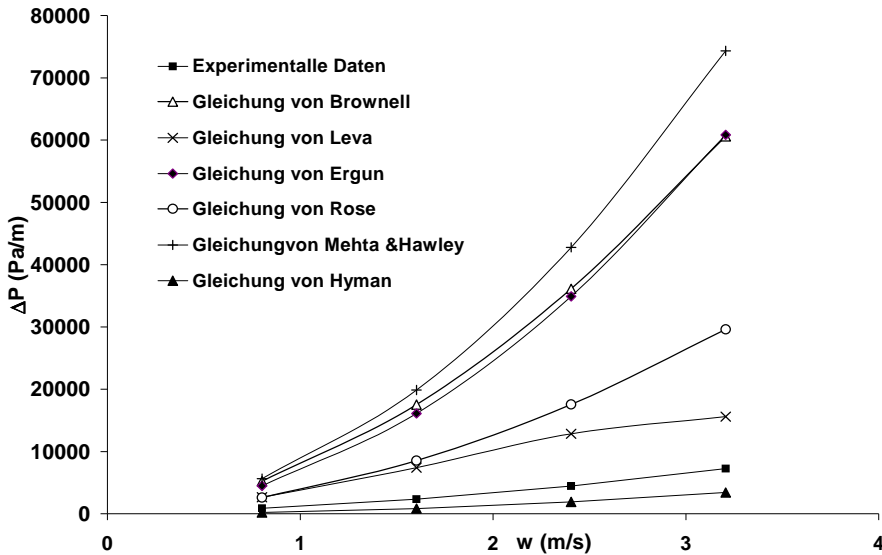


Abb.1. Experimentelle Daten und berechnete Daten für die Katalysatorschicht aus Partikeln mit dem Durchmesser $d_p = 4$ mm.

Wie zu sehen ist, gibt es keine von diesen Gleichungen, imstande, eine direkte Korrelation der experimentellen Werte zu geben werden zu können. Aus diesem Grund wird weiter eine neue Gleichung aufgebaut.

Zu diesem Zweck wird eine Impulsbilanz des Prozesses geschrieben:

$$-\frac{dP}{dL} = 32 \frac{\eta(w_0/\epsilon)}{d_e^2} + \frac{\rho(w_0/\epsilon)^2}{2d_e} \quad (17)$$

Das erste Glied der rechten Seite der Gleichung (17) stellt die Gleichung von Poiseuille für laminares Fliessen dar, das zweite ist der kinetische Ausdruck, der auf dem Fliessen in Kapillaren gegründet wurde.

Der hydraulische Durchmesser kann mit dem Durchmesser der Schicht D , der Porosität ε und der spezifischen Oberfläche der Füllung a_s korreliert werden:

$$n_c \frac{\pi d_e^2}{4} = \pi D^2 \frac{\varepsilon}{4} \quad (18)$$

$$a_s = \frac{4n_c d_e}{D^2(1-\varepsilon)} \quad (19)$$

wo n_c die Anzahl der Fliesskanäle pro Querschniteinheit der Schicht ist. Von Gleichung (18) und (19) erhält man den äquivalenten Durchmesser d_p :

$$d_e = \frac{4\varepsilon}{a_s(1-\varepsilon)} = \frac{2\varepsilon d_p}{3(1-\varepsilon)} \quad (20)$$

Wenn man Gleichung (20) in Gleichung (17) einsetzt und alle Konstanten mit den Koeffizienten K_1 und K_2 ersetzt, erhält man:

$$-\frac{dP}{dL} = K_1 \frac{\eta w_0 (1-\varepsilon)^2}{\varepsilon^3 d_p} + K_2 \frac{\rho w_0^2 (1-\varepsilon)}{\varepsilon^3 d_p^2} \quad (21)$$

Wenn man eine geänderte Re-Kennzahl definiert, erhält man die Gleichung:

$$-\frac{dP}{dL} \cdot \frac{\varepsilon^3 \rho d_p^3}{\eta^2 (1-\varepsilon)^3} = K_1 Re + K_2 Re^2 \quad (22)$$

Um die Konstanten K_1 und K_2 mit Hilfe der experimentellen Daten zu ermitteln, wird die Gleichung (22) geteilt mit der Re-Kennzahl. So erhält man die Gleichung (23), die in der Abb. 2. dargestellt ist:

$$-\frac{dP}{dL} \cdot \frac{\varepsilon^3 \rho d_p^3}{\eta^2 (1-\varepsilon)^3 Re} = K_1 + K_2 Re \quad (23)$$

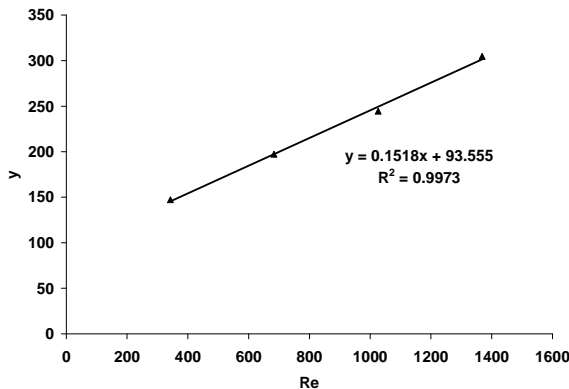


Abb. 2. Abhängigkeit des y -Re von den experimentellen Werten.

Von der linearen Kurve erhält man die Steigung $K_2 = 0,152$ und den Ordinatenabschnitt $K_1 = 93,56$.

Wenn man diese Werte in die Gleichung (22) einsetzt, erhält man:

$$-\frac{dP}{dL} \frac{\varepsilon^3 \rho d_p^3}{\eta^2 (1-\varepsilon)^3} = 93,56 Re + 0,152 Re^2 \quad (24)$$

Wenn man diese Gleichung so umändert, dass sie vergleichbar mit den empirischen Gleichungen der Literatur wird, erhält man:

$$-\frac{dP}{dL} = \frac{1-\varepsilon}{\varepsilon^3} \frac{\rho w_0^2}{d_p} \lambda \quad (25)$$

mit:

$$\lambda = 0,152 + 93,56 Re^{-1} \quad (26)$$

Man kann bemerken, dass die erhaltene Gleichung (25), die Form der Ergun-Gleichung hat, aber die Koeffizienten K_1 und K_2 in der Gleichung von λ (26) sehr unterschiedlich von den Koeffizienten der Ergun-Gleichung sind. Das bedeutet, dass die Koeffizienten der Ergun-Gleichung von der Geometrie der Schicht und der Art des Materials abhängig sind [10].

Die experimentellen Werte und die berechneten Werte nach der Gleichung (25) sind in der Abb. 3 aufgetragen.

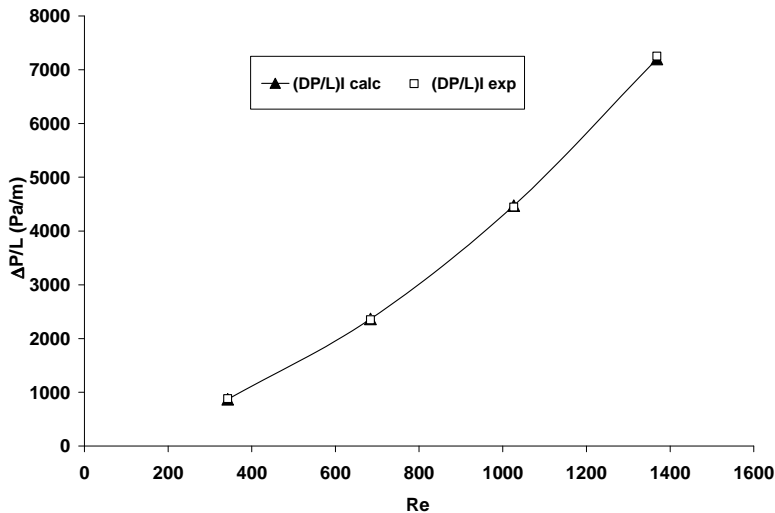


Abb. 3. Korrelation der experimentellen Werte und der berechneten Werte nach der erhaltenen Gleichung (25).

ZUSAMMENFASSUNG

Es wurden experimentelle Druckverluste durch eine granulare Katalysatorschicht bei turbulentem Fließen einer Gasphase bestimmt.

Die experimentellen Werte des Druckverlustes wurden mit den Werten, die mit den empirischen Gleichungen berechnet wurden, verglichen.

Aus der Impulsbilanz wurde eine neue Gleichung des Druckverlustes in einer Schicht aus sphärischen Partikeln mit dem Durchmesser $d_p = 4$ mm aus Mn_2O_3 - Fe_2O_3 bestimmt. Die Koeffizienten der neuen Gleichung sind von der Geometrie der Schicht abhängig.

LITERATURVERZEICHNIS

1. R. Z. Tudose und Mitarbeiter, *Procese, operații și utilaje în industria chimică*, Ed. Didactică și Pedagogică, București, 1977
2. E. P. Dutkai, *Coloane cu umplutură în tehnologia chimică*, Ed. Tehnică, București, 1977
3. G. Jinescu, *Procese hidrodinamice și utilaje specifice în industria chimică*, Ed. Didactică și Pedagogică, București, 1983
4. H. E. Rose, *Proc. Ind. Mech. Eng.* 1945, 153, 154
5. L. E. Brownell und D. L. Karz, *Chem. Eng. Progr.*, 1947, 43, 537
6. M. Leva, *Fluidization*, Mc. Graw-Hill, New-York, 1959, 42
7. S. Ergun, *Chem. Eng. Progr.*, 1952, 48, 89
8. H. Mehta und M. C. Hawley, *Ind. Eng. Sci.*, 1970, 26, 339
9. M. H. Hyman, *Hydrocarbon Processing*, 1968, 47, 131
10. I. Siminiceanu und Al. Pop, *Hydrodinamik des Reaktors für primäre Reformierung des Methans*, Bul. Ins. Politehnic Iasi, 1981, 51

SEDIMENTATION UND FLOCKUNG DER HEFESUSPENSION

ADINA GHIRIȘAN* und MEHRI AZAD**

**Fakultät für Chemie und Chemieingenieurwesen, Universität „Babeș-Bolyai“
Cluj-Napoca, Arany Janos 11, 400028 Cluj-Napoca, Rumänien*

***Institut für Mechanische Verfahrenstechnik und Mechanik, Universität Karlsruhe (TH),
Keiserstrasse 12, D-76128, Karlsruhe, Deutschland*

ABSTRACT. The paper presents the results of sedimentation and flocculation of the yeast suspension. The sedimentation behaviour and the optimal conditions of the flocculation with two different flocculants (PRAESTOL 611 BC and K 111 L) are determined in gravitational field using the batch method. The results show that the separation depends on the type and the dosage of flocculants. The best flocculant used in the separation of the yeast suspension is PRAESTOL K 111 L.

EINLEITUNG

Die mechanische Fest-Flüssig-Trennung feindisperser Partikeln, wie sie in realen Biosuspensionen vorliegen, spielt in vielen Industriebereichen eine wichtige Rolle (z.B. Chemische Industrie, Biotechnologie, Lebensmitteltechnologie, Behandlung industrieller und kommunaler Abwässer).

Sedimentation ist der Vorgang des Absetzens von Feststoffen, die schwerer als die umgebende Flüssigkeit sind. Die Trennung einer Suspension nach dem Prinzip der Sedimentation setzt eine größere Dichte des dispergierten Feststoffs gegenüber der Dichte der Flüssigkeit voraus. Aufgrund dieses Dichtenunterschiedes erfahren die Feststoffteilchen in einem Beschleunigungsfeld (Erdfeld oder Zentrifugalfeld) eine größere Kraft als die Flüssigkeitsteilchen, so dass es zu einem Absinken des sich absetzenden Feststoffes kommt.

Für die Fest-Flüssig-Trennung in Absetzbecken oder Dekantern sind die Sedimentationsgeschwindigkeit der Feststoffpartikeln in der Suspension und die Komprimierbarkeit des gebildenden Sediments wichtige trenntechnische Eigenschaften.

Zur Auslegung der für den Sedimentationsvorgang erforderlichen Trennapparate, stellt die Absinkgeschwindigkeit der Feststoffteilchen eine wichtige Größe dar. Diese ist in einem Fest-Flüssig-System von den folgenden Parametern abhängig:

- a) der Dichtendifferenz zwischen dem Feststoff und der Suspensionsflüssigkeit,
- b) der Partikelgröße bzw. Partikelgrößenverteilung sowie der Form der Einzelpartikeln des dispergierten Stoffes,
- c) der auf die Teilchen durch das Beschleunigungsfeld wirkenden Kraft,
- d) der Viskosität der Suspensionsflüssigkeit,
- e) der Feststoffkonzentration in der Suspension sowie
- f) dem Dispergierzustand

Bei den Partikeln, die so klein sind, dass sie im Erdfeld gar nicht oder nur langsam sedimentieren, um die Partikeln zu trennen und die Sedimentation zu verbessern, gibt man Flockungshilfsmittel zu. Damit bilden sich die Partikeln Agglomerate. Die Agglomerate bilden sich durch Entstabilisierung und Verknüpfung sehr vieler Feistpartikeln, die anschließend durch Sedimentation oder Filtration aus der Flüssigkeit entfernt werden [1].

VERSUCHSDURCHFÜHRUNG

Die Trennung einer Hefesuspension wurde durch Flockung in einer Schüttelapparatur (mit sechs Standzylindern; diskontinuierlicher Absetzversuch) durchgeführt. In diesem Fall wurden die Messzylinder (Durchmesser $\phi = 40$ mm und Höhe $H = 400$ mm) mit unterschiedlichen Konzentrationen der Hefesuspension gefüllt. So wurde jeder Zylinder mit 250 ml demineralisiertem Wasser, 0,073 g NaCl und folgende Menge Hefe: 3 g, 7,5 g, 15 g, 22,5 g, 30 g und 45g gefüllt. Die Hefekonzentration betrug: 1 %, 2,5 %, 5 %, 7,5 %, 10 % und 15 %. Die Zylinder wurden mit Stopfen verschlossen und kräftig geschüttelt, so dass eine homogene Hefesuspension entstand. Die pH-Werte lagen im Bereich von 4,25 - 4,29.

Dann wurde die Hefesuspension in jedem Zylinder mit 2 ml Eisensulfatlösung und gleicher Menge Flockungsmittel versetzt und 10 mal geschüttelt.

Anschließend wurde die Absinkgeschwindigkeit des Trennspiegels in jedem Zylinder beobachtet und die Höhe des Trennspiegels alle 15 Sekunden gemessen.

ERGEBNISSE UND DISKUSSION

Sedimentation mit Hilfe von Polyelektrolyten

Im Rahmen dieser Arbeit wurden zwei PRAESTOL-Marken der Chemische Fabrik Stockhausen (611 BC und K 111 L) untersucht. Die beide Flockungshilfsmittel sind schwach kationische Polyelektrolyte, die von der Firma für die Flockung von Biosuspensionen empfohlen sind. Die Praestol-Marken sind organische, synthetische, hochmolekulare, polymere Flockungsmittel auf der Basis von Polyacrylamid [2]. Die Praestol-Marken verfügen in wässriger Lösung über reaktive Gruppen, die eine starke Affinität zu den Oberflächen suspendierter Kolloide oder Feinstpartikel in wässrigen Systemen oder Trüben zeigen. Durch Entstabilisierung und Verknüpfung sehr vieler Einzelpartikel kommt es zur Bildung großvolumiger, leicht aus der Suspension abtrennbarer Flocken.

1. Flockung mit Praestol 611 BC

Praestol 611 BC ist ein langkettiges Copolymer auf Acrylamidbasis mit einem steigenden Anteil eines kationischen Comonomers. Praestol 611 BC ist eine Aggregationshilfe in Granulatform, so dass für den Einsatz mit fluiden Systemen eine Stammlösung hergestellt werden muss.

1.1. Hefesuspension im demineralisierten Wasser

Zur Herstellung der 5 % Hefesuspension wurde 10,0 g Hefe in 200 ml demineralisiertem Wasser suspendiert. Die verwendete Hefe wird als Bäckerhefe unter der Artikelbezeichnung "Frisch-Backhefe" von Dr. Moormanns Firma vertrieben. Die Dichte der Hefe beträgt ca. 1060 kg/m^3 . Ein Gramm des Hefeblocks enthält mehrere Milliarden lebender Hefezellen, wie auf dem Mikroskop zu sehen ist [3]. Hefezellen sind kugel- oder eiförmige Mikroorganismen, deren Größe zwischen $6 \mu\text{m}$ und $8 \mu\text{m}$ liegt. Ihre Zellwände sind von Schleimhüllen umgeben, die eine Vielzahl von Polymeren enthalten, so dass es zu einer natürlichen Flockung der Hefe kommen kann [4, 5].

Zum Bestimmen der Absetzrate wurde die Hand-Schüttelmethode verwendet, diese Methode eignet sich nur zu groben Voruntersuchungen.

Die Hefezellen sind negativ geladen und können mit kationischen Polymeren geflockt werden. Zur Flockung der Hefesuspension müsste zuerst ein geeignetes Flockungsmittel gefunden werden. Aus Erfahrung früherer Arbeiten [2], die sich mit der Flockung von Hefe befassen, haben die Ergebnisse gezeigt, dass schwach kationische Flockungsmittel in Verbindung mit dem dreiwertigen Eisensalz zu einer schnellen Sedimentation im Erdschwerefeld führt.

Für die Wirksamkeit der anionischen oder nichtionischen Polymere ist eine zusätzliche Anwesenheit mehrwertiger Ionen, insbesondere von Ca^{2+} , erforderlich.

Zur Hefesuspension wurde zunächst 1 ml 0,5 % Eisensulfat $\text{Fe}_2(\text{SO}_4)_3$ - Lösung als Koagulationsmittel (besonders wirkungsvoll) und anschließend 10 ml 0,05% Flockungsmittel (500 ppm) des schwach kationischen Flockungsmittels Praestol 611 BC zugegeben. Das Flockungsergebnis war nicht gut. Anschließend wurde die Flockungsmenge verdoppelt (1000 ppm), aber die Flockenqualität hat sich nicht wesentlich verbessert.

Um die Ionenstärke zu erhöhen wurde die Hefe in einer NaCl-Lösung (5 mM/L) suspendiert und der obengenannte Versuch noch einmal wiederholt. Die Flockenbildung hat sich nicht verbessert.

1.2. Hefesuspension in Leitungswasser

Bei der Herstellung der Hefesuspension wurde statt entionisiertes Wasser Leitungswasser verwendet und die Versuche mit Eisensulfat-Lösung und Praestol 611 BC wiederholt.

Das Flockungsergebnis war bei einer 500 ppm gut und bei einer Flockungsmittelkonzentration 1000 ppm sehr gut. Bei einer Flockungsmittelkonzentration 1000 ppm war der Überstand klar aber der Trennspiegel nicht eindeutig.

Ein weiterer Versuch wurde mit einer 1 % -igen Hefesuspension durchgeführt. Dieser Suspension wurde zunächst 1 ml 0,5-ige Eisensulfat-Lösung und anschließend 2 ml Praestol 611 BC (500 ppm) zugegeben, eine Flockung der Hefepartikel wurde nicht beobachtet. Nach der Zugabe von 8 ml Flockungsmittel kam eine relativ gute Flockung zustande. Das Flockungsergebnis wurde nach der Zugabe weiterer 10 ml Flockungsmittel schlechter (eventuelle Überdosierung) geworden.

1.3. Hefesuspension in NaCl-Lösung

Bei diesem Versuch wurde 10 g Hefe in 200 ml 5 mM/L NaCl-Lösung suspendiert und mit 1ml 0,5%-ige Eisensulfat-Lösung und 10 ml 0,05 %-ige Praestol 611 BC (500 ppm) versetzt. Eine Flockung wurde nicht beobachtet.

Durch weiterer Zugabe von 20 ml Flockungsmittel wurde ebenfalls keine Agglomeration beobachtet.

2. Flockung mit Praestol K 111 L

Praestol K111 L stellt ein weiteres organisches Polyelektrolyt dar, das ebenfalls schwach kationisch und zur Flockung der Hefesuspension sehr gut geeignet ist. Praestol K111 L stand als Emulsionspolymerisat zur Verfügung, der Gehalt an Polymermenge in der Emulsion beträgt 38 %. Somit waren zur Herstellung von 100 ml einer 0,1 % Gebrauchslösung 0,263 g der Emulsion Praestol K111 L nötig. Die Lösedauer beträgt ca. 15 Minuten.

Bei einem Zusatz von 1000 ppm des schwach kationischen Emulsionspolymers und ca. 0,17 mol/kg Feststoff der Eisensulfatlösung zu einer Hefesuspension ergaben sich die besten Flockungsergebnisse. Es bildeten sich sehr voluminöse Flockenverbände aus, die innerhalb kurzer Zeit im Erdschwerefeld sedimentierten.

Der Verlauf des absinkenden Trennsiegels in Abhängigkeit der Zeit ist in Abbildung 1 dargestellt. Das Diagramm (Abb. 1) zeigt, dass die Flockungsmittelkonzentration von 1000 ppm für kleine Feststoffkonzentrationen ausreichend und für höhere Konzentrationen (10%) nicht ausreichend ist. Der Überstand war bei allen Versuchen mit 1000 ppm trüb. Ein eindeutiger Trennspiegel wurde ebenfalls nicht beobachtet.

Im ersten Zylinder mit der Hefekonzentration von 2,5% haben sich Flocken mit unterschiedlichen Formen und Größen gebildet die auch mit verschiedenen Sinkgeschwindigkeiten sedimentierten. Nach 15 Minuten war die Sedimentation beendet. Die aus dem Diagramm berechneten Sinkgeschwindigkeiten für die verschiedenen Konzentrationen ergaben folgende Werte: 13 mm/min (2,5%), 11 mm/min (5%), 9,33 mm/min (7,5%) und 6,8 mm/min (10%).

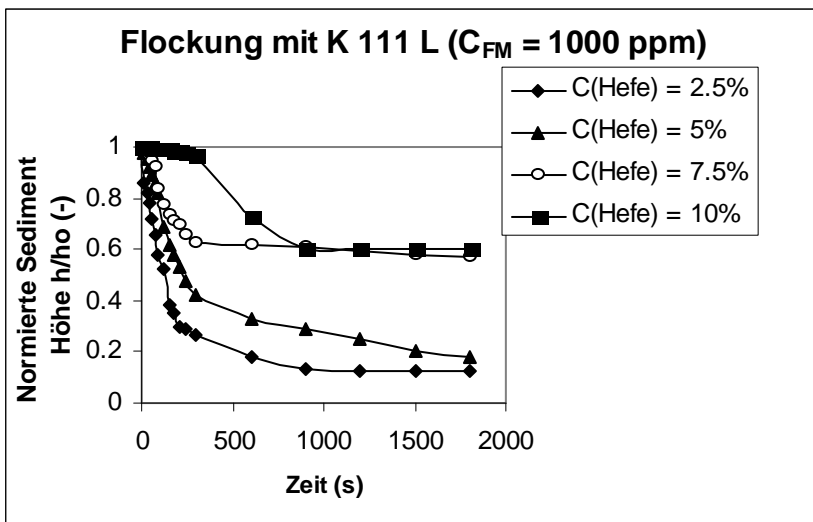


Abb. 1. Die normierte Sedimenthöhe im Verlauf der Zeit für verschiedene Hefekonzentrationen.

Die Erhöhung der Flockungsmittelkonzentration auf 1500 ppm lieferte bessere Ergebnisse (Abb. 2). Ein scharfer Trennspiegel hat sich gebildet, die Sinkgeschwindigkeiten wurden aus dem Diagramm berechnet: 13 mm/min (2,5%), 10,85 mm/min (5%), 9,4 mm/min (7,5), 6,7 mm/min (10%) und 1,33 mm/min (15%).

Der Verlauf der Trennspiegelhöhe einer 5% Hefesuspension über die Zeit ist im Diagramm 3 dargestellt. Das Diagramm zeigt, dass für die Sedimentation einer 5% Hefesuspension eine Flockungsmittelkonzentration von 1000 ppm ausreichend ist. Bei einer Erhöhung der Flockungsmittelkonzentration bleibt die Absetzgeschwindigkeit des Trennsiegels ungefähr konstant.

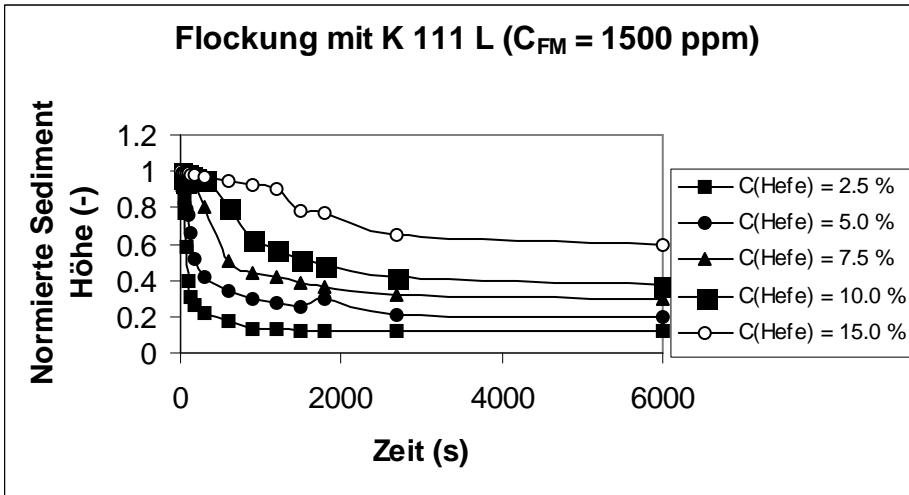


Abb. 2. Die normierte Sedimenthöhe im Verlauf der Zeit für verschiedene Hefekonzentrationen.

Bei einer Konzentration von 500 ppm waren die Flocken unterschiedlich groß und der Überstand war trüb.

Es war interessant zu beobachten, dass die Art der Flockungsmitteldosierung eine wichtige Rolle spielt und die Flockenbildung positiv beeinflussen kann. Die Abbildung 4 zeigt, dass die Sedimentation beschleunigt wird, wenn das Flockungsmittel in zwei Schritten (einmal 250 ppm, gemischt und dann noch einmal 250 ppm) zudosiert wird.

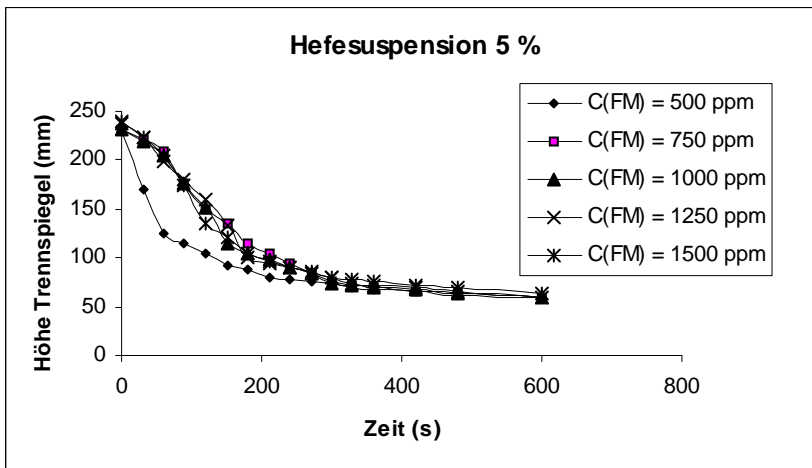


Abb.3. Die Trennspegelhöhe im Verlauf der Zeit für eine Hefesuspension 5% und verschiedene Praestol K 111 L Konzentrationen.

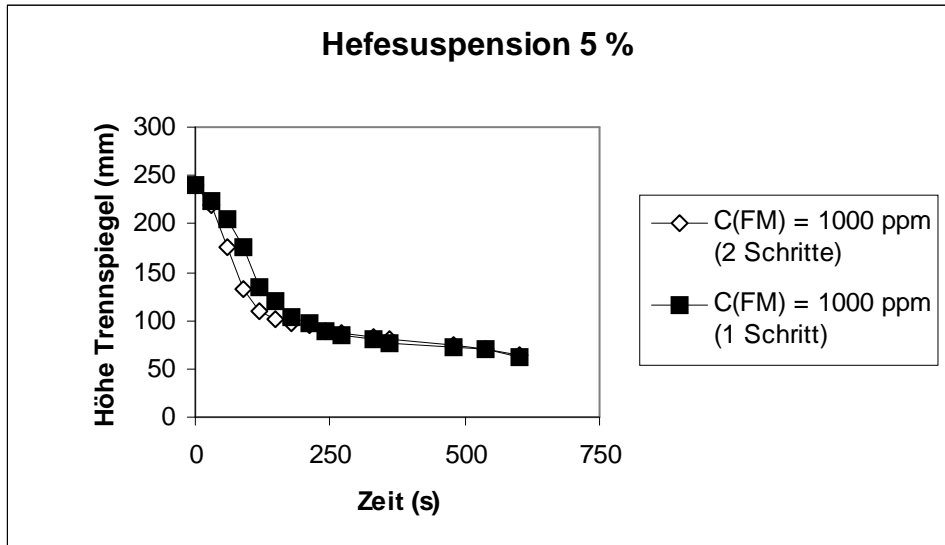


Abb. 4. Die Trennspegelhöhe im Verlauf der Zeit für eine 5 % Hefesuspension und 1000 ppm Praestol K 111 L.

Die gleichen Ergebnisse wurden ebenfalls bei einer 2,5% Hefesuspension beobachtet. Das Diagramm für unterschiedliche Flockungsmittelkonzentration ist in Abbildung (5) dargestellt.

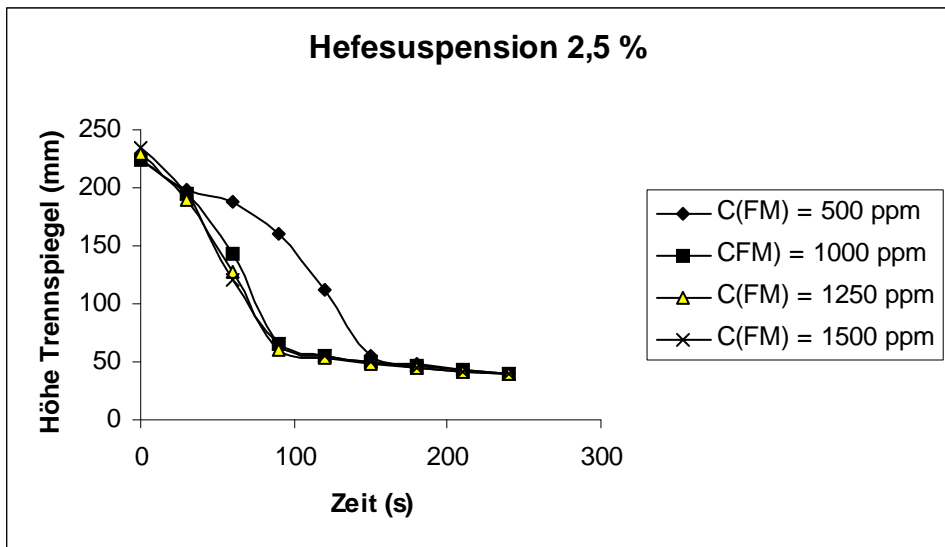


Abb.5. Die Trennspegelhöhe im Verlauf der Zeit für eine Hefesuspension 2,5 % und verschiedene Praestol K 111 L Konzentrationen.

Das Diagramm zeigt, dass eine Erhöhung der Praestolkonzentration oberhalb von 1000 ppm keinen Einfluss auf die Sedimentationsgeschwindigkeit hat. Es war auch hier zu beobachten, dass die Doppeldosierung die Absetzgeschwindigkeit erhöht (Abb.6).

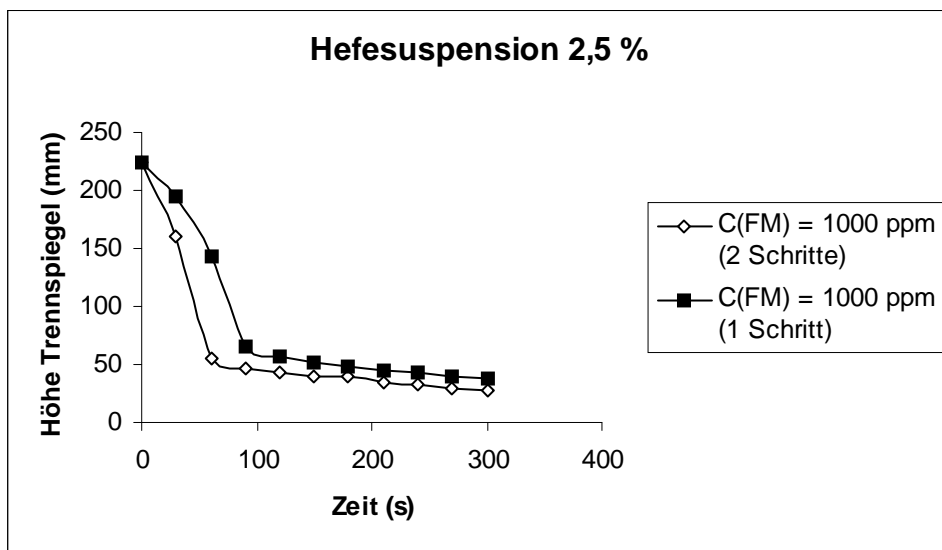


Abb. 6. Die Trennspegelhöhe im Verlauf der Zeit für eine 2,5 % Hefesuspension und 1000 ppm Praestol K 111 L.

ZUSAMMENFASSUNG

Ziel dieser Forschungsarbeit wurde die optimale Bedingungen für die Trennung der Hefesuspensionen durch Sedimentation im Erdschwerfeld mit Hilfe von Flockungsmittel (PRAESTOL 611 BC und K 111 L) zu finden.

Die Ergebnisse zeigen, dass die Art, die Dosierung der Flockungsmittel und die Bedingungen der Trennung die Flockenbildung positiv beeinflussen können.

Durch die Flockung mit PRAESTOL K111L wurden sehr gute Ergebnisse der Sedimentation einer Hefesuspension erhalten.

LITERATURVERZEICHNIS

1. Adina Ghirişan, Alexandru Pop und Vasile Miclăuş, *Sedimentation. Koagulation. Flocculation. 1. Sedimentationsanalyse einer geflockten Kaolinsuspension*, *Studia Universitatis Babes-Bolyai, Chemia*, XLVIII, 1, 2003, 183-190
2. Katalog „PRAESTOL-Marken“ der Chemischen Fabrik Stockhausen

3. B. Luda, „*Methoden zur Beeinflussung der Schlammkompression im Zentrifugalfeld*“, Diplomarbeit, MVM, Universität Karlsruhe (TH), 2002
4. B. Brohan, A. J. McLoughlin, *Appl. Microbiol. Biotechnol.* 1984, 20, 16-20
5. D. J. Bell, P. Dunnill, *Biotechnol. Bioeng.*, 1982, 24, 1271-1285

THE IDENTIFICATION BY MS AND GC/MS OF PHOTO-DEGRADATION PRODUCTS OF INDOMETHACIN OINTMENT

VASILE MICLĂUȘ¹, ILDIKÓ BROȘ², ZAHARIA MOLDOVAN²,
CLAUDIA CIMPOIU¹, EMANOIL SURDUCAN², NICOLAE PALIBRODA²

¹*Babeș-Bolyai University, Faculty of Chemistry*

²*National Institute R&D for Isotopic and Molecular Technologies*

ABSTRACT. This paper reports the photo degradation of indomethacin from a pharmaceutical cream formulation. For the determination of the degradation compounds a MS analysis was performed by direct introduction of the sample in high vacuum and a GC separation of the components. Mass spectra of electronic impact (EI) in GC-MS were also registered. Six compounds, which held the indomethacine moieties, were identified.

INTRODUCTION

Indomethacin ([1-(4-chlorobenzoyl)-5-methoxy-2-methyl-indol-3-yl] acetic acid) was introduced to the market in 1963, and since then it has been widely used in musculoskeletal and joint disorders such as rheumatoid arthritis, ankylosing spondylitis, osteoarthritis and gout. Its potency as an anti-inflammatory, analgesic, antipyretic agent is counterbalanced by accompanying adverse effects [1-4]. In the course of the 40-year history of indomethacin several papers have been published on its stability (including photostability) and the identification of its degradation products. Some of them are mentioned in the paper. With the exception of the Krzek-Starek paper (which takes into account the kinetics of the degradation of indomethacin in basic medium [4], all deal with photostability/photochemical degradation products of indomethacin [5-6]. So far little has been published on impurities and photo degradation products of the formulations.

This paper reports the photo degradation of an indomethacin ointment and determination of the products by a) mass spectrometry (MS) with direct insert of the sample in high vacuum and b) gas chromatography coupled with electronic impact mass spectrometry GC-MS(EI).

EXPERIMENTAL

1). Degradation of an indomethacin ointment

The degradation tests were performed on an indomethacin cream formulation. The ointment was subjected to irradiation by daylight for 60 days at room temperature. The degradation occurred simultaneously with the colour change.

The indomethacin and a part of the by-products contained in the photo-degraded ointment were transformed in soluble sodium salts with a diluted NaOH solution. For 35 g ointment were added 0,1565 g NaOH and 50 ml distilled water. For the obtained yellow emulsion, the pH was verified to be 7,5 - 9. This emulsion was washed with CH₃OH and filtered in vacuum. The filtrate, with a yellow colour was treated with diluted H₂SO₄ to a weak acidic medium (pH=6-6,5), and then

extracted with diethyl ether. After ether evaporation, a mixture of solid brownish crystals were obtained. GC/MS investigation revealed that in addition to indomethacin the extract contained fatty acid esters originating from the base cream .

2). Separation and determination of the degradation compounds

A separation of these compounds by thin layer chromatography (TLC) on Kieselgel 60 F₂₅₄ plates was performed. The solution was obtained by solving 1 mg extract in 1 ml methanol. The solution was applied with a micropipette as a spot on the plate. The plate was developed in an ascendant way using the mixtures of chloroform: methanol (3:1, V/V); chloroform: diethyl ether (1:1, V/V), n-butanol: water: glacial acetic acid (4:1:1, V/V/V) as mobile phase. After elution, the plates were dried in air and the spots were detected in UV light ($\lambda=254$ nm).

For the spectrometric mass analysis, a mass spectrometer MAT 311 was used, with direct introduction of the sample in high vacuum. The photodegraded indomethacin extract, in the solid phase, was introduced in a heated crucible into the high vacuum, with a programme of temperature ranging from 20 to 250 °C and a simultaneous registration of the mass spectra in repetitive scanning.

For chromatographic separation of photo degradation products a gas chromatograph Hewlett-Packard type 5840 A equipped with a capillary column of 30 m length of a DB5 stationary phase was used. The sample was injected as a methanol solution. The mass spectra were registered with a quadrupolar mass spectrometer HP 5985 with electronic ionisation (EI) for the mass range 35 - 400 dalton.

RESULTS AND DISCUSSION

The investigations by thin layer chromatography (TLC) could not offer conclusive identification of the separated spots. The TLC separation of degradation products emphasized the presence of some partially separated substances.

Figure 1 presents the fragmentogram of the degradation products of the extract, obtained by the direct introduction method in MS.

The sample components sublimed between 60–170 °C, the maximum of the total ions curve being recorded at 110 °C. Figure 1 put into evidence the sublimation of four components in vacuum.

The first component **a**, the most volatile, characterized by the ions with the mass $m/z = 139$ and 156 (M^+), represents p-chlorobenzoic acid (**A**). The mass spectrum of this compound is analogous to the mass spectrum known from the literature [6]. This compound derives from indomethacin either from the hydrolysis or from the fragmentation (**A**, Scheme 1).

The ions with the mass $m/z = 174$ and 219 describe the second degradation product (**b**), with the mass spectrum presented in Figure 2.

For this compound structure **B** from Scheme 1 was attributed. The main fragment, the ion $m/z = 174$ derives from the cleavage of the carboxyl function ($M^+ - 45$).

From the quantitative point of view, the compounds A and B represent the principal products of fragmentation.

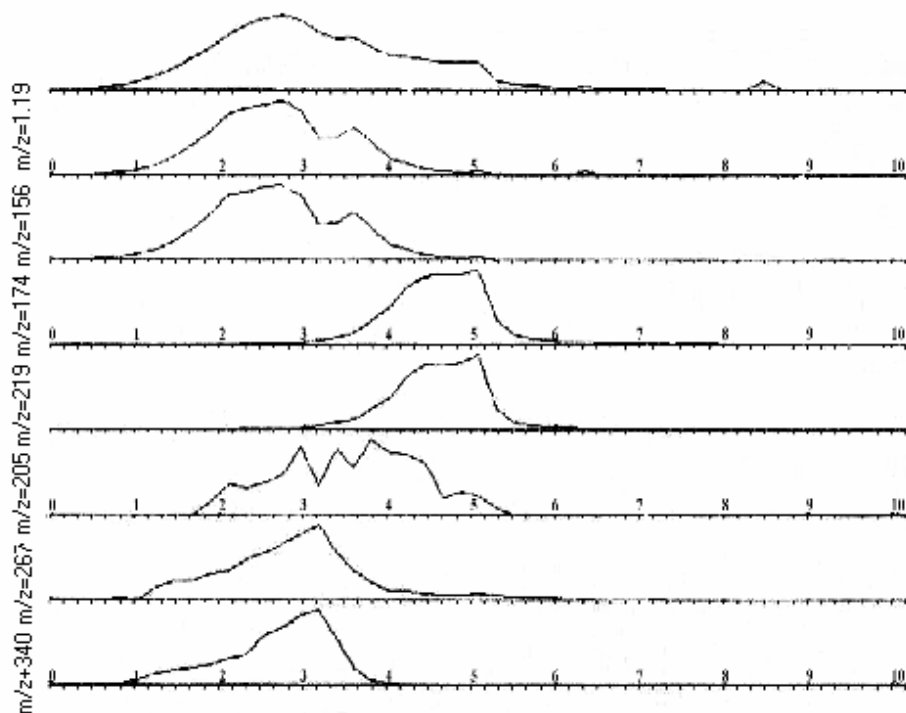
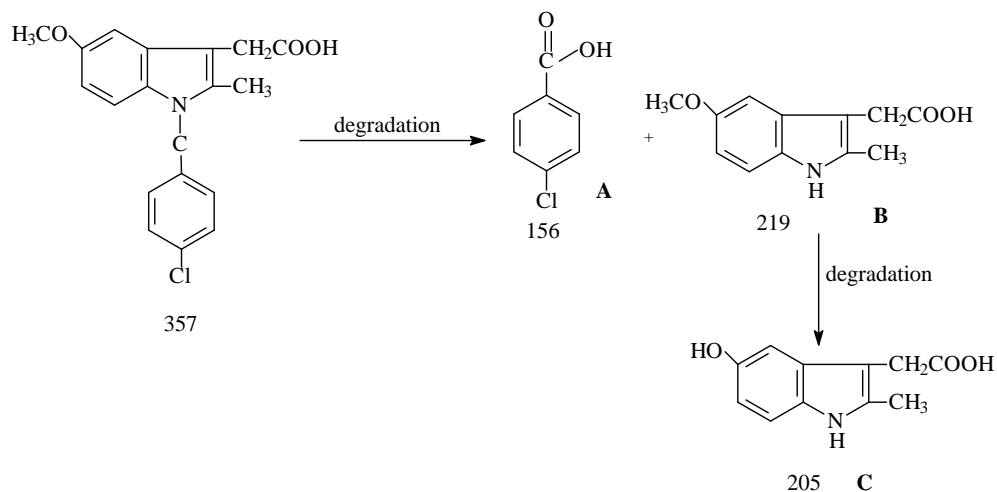


Fig. 1. The fragmentogram of the degradation products of indomethacin extract in direct MS



Scheme 1

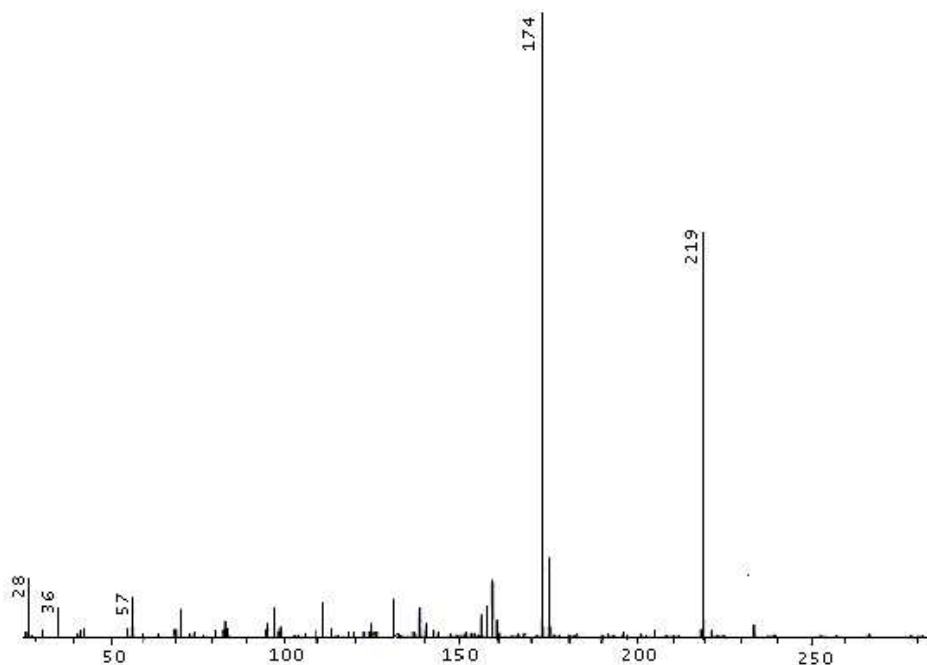


Figure 2. The Mass Spectra of compound **B**.

A third compound **c**, present in small amount, is represented in Figure 1 of the fragmentogram at the mass $m/z = 205$, with a maximum of sublimation in vacuum at 120 °C. A clean mass spectrum of this compound could not be obtained, due to the small intensity of the ions. A credible structure of the compound **c** could be the formula **C** from scheme 1 with $M^+ = 205$, obtained after demetilation of **B**.

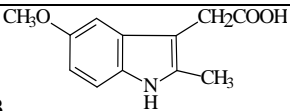
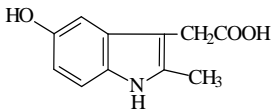
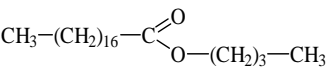
The last two fragmentogrames at the masses $m/z = 267$ and 340 represent the fragment ion $M^+ - 73$ and the molecular ion $M^+ = 340$ of butyl stearate which is found in creme composition.

The degradation products are summarized in Table 1.

Tabel 1

Some data of the determined structures (**a-d**) from direct MS

| Subst. | Abundance % | Molecular mass | Molecular Formula | Structural formula |
|----------|-------------|----------------|-------------------|--------------------|
| a | 55.755 | 156 | $C_7H_5O_2Cl$ | <p>A</p> |

| Subst. | Abundance % | Molecular mass | Molecular Formula | Structural formula |
|----------|-------------|----------------|--|--|
| b | 40.628 | 219 | C ₁₂ H ₁₃ O ₃ N |  B |
| c | 0.095 | 205 | C ₁₁ H ₁₁ O ₃ N |  C |
| d | 3.522 | 340 | C ₂₂ H ₄₄ O ₂ |  |

The gas chromatogram of the methanol solution of the degradation products of indomethacin, obtained with a flame ionisation detector, is presented in Figure 3.

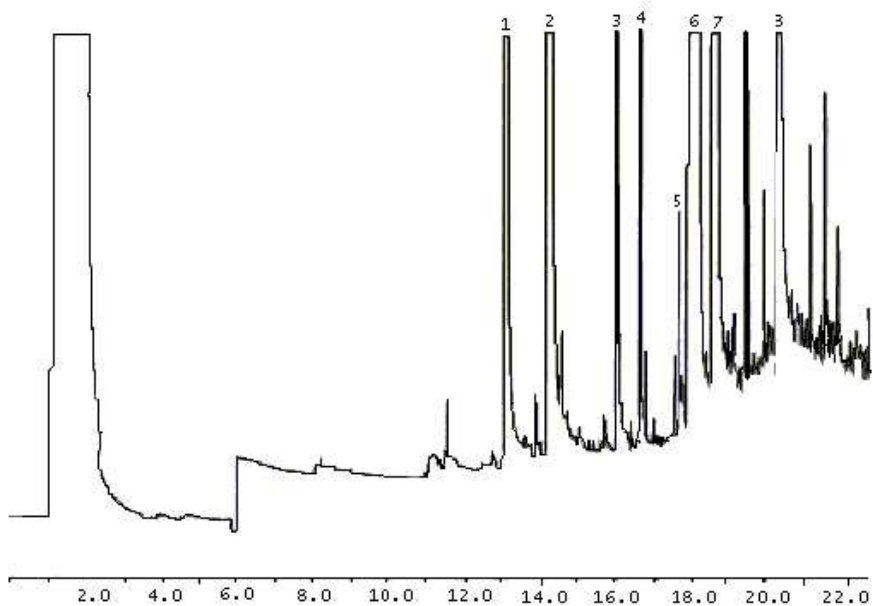


Figure 3. The gas chromatogram (GC) of the methanol solution of indomethacin degradation products

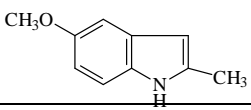
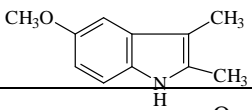
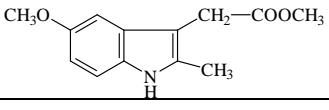
The mass spectra allowed the identification of five esters (3,4,5,7,8,) originating from the ointment, with the structures shown in Table 2.

The peaks numbered 1, 2 and 6 represent the indomethacin photo degradation compounds, with structures **D**, **E** and **F** respectively.

The compound **F** with $M^+=233$ is equivalent to the structure **B** (Scheme 1), but is methylated at the carboxyl function. Structure **B** could be methylated in the gas phase, either from the methanol solution or/and from the methyl fragments derived from temperature degradation of the substances along the column.

Table 2

The products identified through GC-MS(EI) from the sample

| Nr. peak | Retention time | Molecular mass | Molecular Formula | Structural formula |
|----------|----------------|----------------|--------------------|---|
| 1. | 13' | 161 | $C_{11}H_{11}NO$ | D  |
| 2. | 14'15" | 175 | $C_{11}H_{13}NO$ | E  |
| 3. | 16'10" | 270 | $C_{17}H_{34}O_2$ | $CH_3-(CH_2)_{14}-C(=O)OCH_3$ |
| 4. | 16'50" | 284 | $C_{18}H_{36}O_2$ | $CH_3-(CH_2)_{12}-C(=O)O-(CH_2)_3-CH_3$ |
| 5. | 17'45" | 298 | $C_{19}H_{38}O_2$ | $CH_3-(CH_2)_{16}-C(=O)OCH_3$ |
| 6. | 18'50" | 233 | $C_{13}H_{15}NO_3$ | F  |
| 7. | 19'30" | 312 | $C_{20}H_{40}O_2$ | $CH_3-(CH_2)_{14}-C(=O)O-(CH_2)_3-CH_3$ |
| 8. | 20'25" | 340 | $C_{22}H_{44}O_2$ | $CH_3-(CH_2)_{16}-C(=O)O-(CH_2)_3-CH_3$ |

CONCLUSIONS

For the determination of the photo degradation compounds of an indomethacin extract from the ointment, a MS analysis by direct introduction of the sample in high vacuum and a GC separation of the components was performed. Mass spectra in GC-MS (EI) were also registered.

These two methods are unable to reveal the presence of undegradated indomethacin in the extract. Out of six identified structures, five (**B**, **C**, **D**, **E**, **F**) retained the indol moieties.

Degradation products **A**, **B** and **E** are known degradants of indomethacin (products of hydrolytic splitting and decarboxylation). The structure **B** was the same as detected in the photooxidation of this drug, resulting from decarboxylation [7]. The revealed fragmentations for the other newly detected compounds (**C**, **D**, **E**, **F**), are partially analogues to the conversions of indomethacin in metabolic processes known in the literature [8].

There is no evidence that **C**, which appears as a minor component (0.1%>) in the course of the direct MS investigation and does not appear in the GC/MS scan, is a photodegradation product. **D** is an interesting, unusual structure but there is no clear evidence that the structure is really what is presented in Table 2: it could also be the isomeric 5-hydroxy-2,3-dimethyl or 5-methoxy-3-methyl derivative. In the same time we assume that **F** could be a GC/MS artefact.

BIBLIOGRAPHY

1. a) J.L. McGuire (ed), *Pharmaceuticals*, **2000**, 4, 1679, b) M. Nakajima, T. Inoue, N. Shimada, S. Tokudome, T. Yamamoto, Y. Kuroiwa, *Drug metabolism and disposition*, **1998**, 26 (3), 261-266.
2. a) A. Shawesh, A. Kaukonen, S. Kallioinen, O. Antikainen, J. Yliruusi, *Pharmazie*, **2003**, 58 (2), 130-135. b) B. A. Shawesh, S. Kallioinen, O. Antikainen, J. Yliruusi, *Pharmazie*, **2002**, 57 (10), 690-694. c) M.A. Hammad, B.W. Mueller, *Pharmazie*, **1998**, 53 (11), 790-794
3. C. Ju, J.P. Uetrecht, *Drug metabolism and disposition*, **1998**, 26 (7), 676-680.
4. J. Krzek, M. Starek, *J AOAC Int*, **2001**, 84 (6), 1703-1707.
5. a) J. Arcos, J. Lopez-Palacios, J.M. Leal, P. Sanchez-Batanero, F. Mata, *Bull. Soc. Chim. Fr.* **1991**, 3, 314-318, b) R. Dabestani et al.: *Photochem. Photobiol.*, 58, 367 (1993); c) N. Ekizgücer and J. Reisch: *Pharm. Acta Helv.*, 66, 66 (1991); d) A.C. Weedon and D.F. Wong: *J. Photochem. Photobiol. A, Chemistry*, 61, 27 (1991).
6. a) S. Hess, U. Teubert, J. Ortwein, K. Eger, *Eur. J. Pharm. Sci.*, **2001**, 14, 301-311
b) Y. Matsuki, T. Ito, M. Kojima, H. Katsumura, H. Ono, *Chem Pharm. Bull.* **1983**, 31(6), 2033-2038
7. D.E. Moore, K.A. Ghebremeskel, B.B.C. Chen, E.Y.L. Wong, *Photochim. Photobiol.*, **1998**, 68(5), 658-691
8. A.-B. Wu, H.-W. Cheng, C.-H. Hu, F.-A. Chen, T.-C. Chou, C.-Y. Chen, *Tetrahedron Lett.* **1997**, 38(4), 621-622

VOLTAMMETRIC INVESTIGATIONS OF SOME FOOD AND TEXTILE DYES

MARIAN STAN¹, MIHAELA LANG¹, A.SAVALL²,
KARINE-GROENEN SERANO², ELSA WEISS² and MARIA JITARU¹

¹ "Babes-Bolyai" University, Faculty of Chemistry and Chemical Engineering, Associated
Francophone Laboratory, 11, Arany Janos street, 400028 Cluj-Napoca, Romania,
Phone: 00 40 264 593833; FAX: 00 40 264 590818; mjitaru@chem.ubbcluj.ro

² Laboratoire de Génie Chimique UMR 5503, Université Paul Sabatier,
11 route de Narbonne, 31062 Toulouse cedex 4, France.

ABSTRACT. The removal of the color by oxidation or reduction can be carried out in an electrochemical cell directly without the addition of redox chemical reagents, working at room temperature [1,2].

The main purpose of this paper is the study of the electrochemical behavior of the azo linkage $-N=N-$ in oxidation and reduction for Methyl Orange (MO), Tartrazine (T) and Ponceau 4R (P) in order to establish the influence of the experimental conditions (pH, electrolytes, concentrations, nature of the electrode material) on the discoloration yield.

Preliminary electro-oxidation experiments for a model molecule (MO), on boron doped diamond electrodes (BDD) showed a decrease of the absorbance with 97-98%, a decrease of total organic carbon (TOC) with 88-90% and of the chemical oxygen demand (COD) with 86-90%.

Keywords: Electrochemical oxidation, azo dyes, boron doped diamond electrode.

INTRODUCTION

The effluents from textile dyeing are colored so these waters will have to be treated before being released back to environment [1]. On the other hand some of the synthetic dyes used in the food industry are toxic [2].

Azo compounds are among the most profoundly explored classes of organic compounds both from theoretical and practical viewpoints. The presence of an azo linkage in aromatic compounds makes them highly important in dye-stuff industry, pharmacy and dosimetry [3]. Various synthetic azo dyes have been shown to induce a variety of tumors in mice and rats and to exhibit inhibitory effects on the biosynthesis of proteins [4].

Electrochemical methods for color removal are new and environmental friendly techniques. Electrochemical reduction of azo compounds usually occurs in $2e^-$, $2H^+$ transfer to give hydrazo products. However in the presence of strong electron donating groups, reduction has been found to occur in $4e^-$, $4H^+$ reaction to give amino compounds as the final products. An excellent review on the electroreduction of azo compounds has also appeared in the literature [5].

The electrochemical oxidation of organics on different electrode material uses the hydroxyl anions produced on the anode, as electrogenerated oxidizing species [4, 5]. Studies of the oxidation of azo compounds in pure solvents, aqueous solutions or mixtures of aqueous buffers and organic solvents have appeared

occasionally in the literature and the number of studies concerning oxidations of azo compounds is by far less than those dealing with reductions. Electrochemical oxidation of azo compounds in aprotic solvents like acetonitrile has been performed in connections with studies involving light fading of azo dyes, synthesis and electrode mechanisms [9,10].

The oxidation of Solochrome Violet RS in connection with complexometric determinations of aluminum has been suggested to involve an oxidation to the azoxy compound [11,12]. Matrká et al. [13] reported that the hydroxyl derivatives 4'-hydroxy-4-N, N-dimethylazobenzene and 2'-hydroxy-4-N, N-dimethylazobenzene were initially oxidized to a quinoid structure, followed by demethylation. Ladanyi et al. [14] also studied the oxidation of 4-aminoazobenzene in 50% alcohol buffer and came to the conclusion that this oxidation was similar to the oxidation of substituted anilines [9,15] and the final product is N-[4-(p-phenylazo)-phenyl]-1,4-benzoquinone-monoimine [14]. Malik et al. [16] studied the bisazo dye Fast Sulfone Black-F both reductively and oxidatively in connection with an investigation of the electrochemical reduction mechanism of this dye. Fogg and Bhanot [17,18] used linear scan and cyclic voltammetry with glassy carbon and carbon paste electrodes for the determination of food colorants. Among the studied colorants were several common azo dyes, such as Tartrazine, Oxalazinesodium and related compounds [19], Amaranth, Sunset Yellow FCF and Black PN. Fogg and Bahnot also developed a flow injection system with amperometric detection for the determinations of these compounds, [18] but did not study the electrode process in detail.

EXPERIMENTAL

In order to obtain the voltamperometric data, fundamentals for the electrochemical color removal in waste water, cyclic voltammetry (BAS 100W and AUTOLAB PGSAT 12 computer aided electrochemical systems) have been used. The control of the electrochemical discoloration was achieved using UV-Vis spectrophotometer (UNICAM Helios β) and (TOC) and (COD) determination equipment (Shimadzu Corporation, Tokyo, Japan).

The textile and food azo dyes were obtained from Sigma Chemical Co. USA and were used as received. The stock solution of the dye (1.0 mM) was prepared in double distilled water. Voltammograms were recorded in different buffer solution of ionic strength 0.1. The pH of buffer solution was measured using the JENWAY 3330 pH meter, after standardization with potassium hydrogen phthalate and borax buffers. For recording voltammograms, equal volumes of dye solution and buffer solution of appropriate pH were mixed. Nitrogen gas was bubbled for 8–10 min. before recording the voltammograms. BDD electrodes for cyclic voltammetry (from CSEM, Neufchatel, Suisse) others working electrodes (GC, Au and Pb from BAS Co.) had an area of 0.2826 cm². All potentials refer to Ag/AgCl, KCl at an ambient temperature of 20 \pm 2 °C.

Controlled potential and current electrolysis of 0.1- 0.5 mM solution of the dye was carried out both in a conventional divided H-type cell and electrochemical undivided – BDD cell, at potential 50-70 mV more positive than the peak potential observed in the voltammograms. The working electrode for electrolysis was glassy carbon, PbO₂ and BDD plate (area 63,6 cm²), and counter electrode was cylindrical platinum gauze.

Voltamperometric behavior of Methyl Orange – influence of the electrode and electrolyte nature

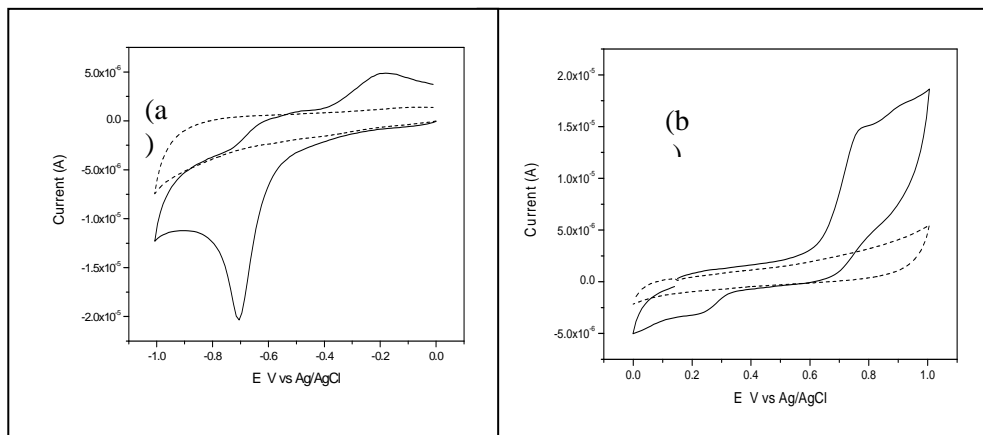
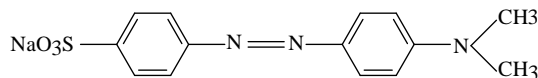


Figure 1. VOC of Methyl Orange 10^{-3} M in Na_2SO_4 0.1 M on glassy carbon electrode at 50mV/s; (a)- negative potential range, (b)-positive potential range.

The CVs on glassy carbon electrode confirm that in both reduction (Fig.1a) and oxidation (Fig.1b) direction the azo bond was affected, respectively at ≈ -700 mV and 750 mV. The electrochemical oxidation of (MO) on the investigated electrodes (glassy carbon, Au and BDD), has been demonstrated Fig. 2, the oxidation current on BDD is higher at the same concentration (10^{-3} M) and scan rate ($100 \text{ mV} \cdot \text{sec}^{-1}$). Figure 2 shows that the electro-oxidation process takes place in the same potential range (737-782 mV/Ag, AgCl, KCl) for all the investigated electrodes.

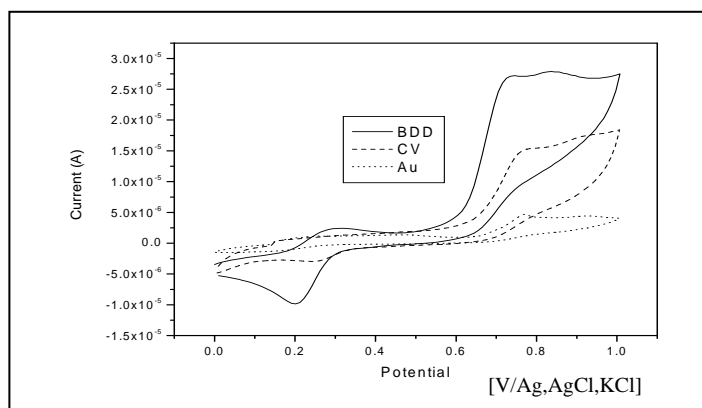


Figure 2. Voltammograms of 10^{-3} M (MO) at different scan rates on GC, Au and BDD electrode in Na_2SO_4 0,1M.

The dependence peak current-square root of the sweep rate is a straight line, a proof for a diffusion mechanism. As expected, the peak current increases with larger scan rates (Fig. 3).

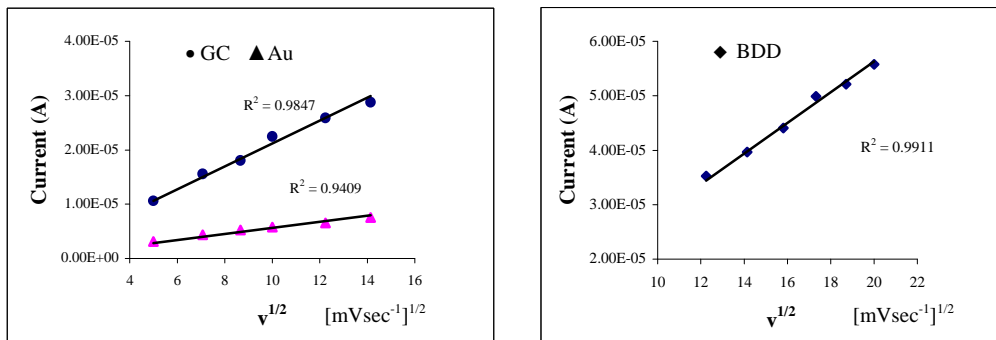


Figure 3. The plot of peak current versus the square root of sweep rate for oxidation of 10^{-3} M (MO) on different electrodes materials: glassy carbon (GC), gold (Au), boron doped diamond (BDD) in Na_2SO_4 0.1M.

The peak potential was dependent on pH and during the oxidation of (MO) shifted towards more positive values with pH increase. The plots of E_p vs. pH can be approximated as two segments of straight lines which intersect at pH 5.1 which correspond to the value of pK_a . The dependence of E_p on pH for the (MO) oxidation can be represented by the following equations:
for (MO)_{ox}: $\text{pK}_a = 5.1$

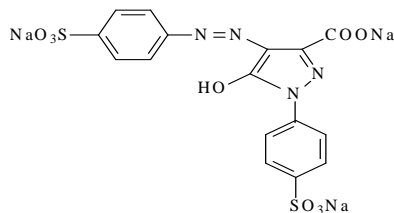
$$E_p (\text{pH } 2.0 - 5.1) = [716.4 + 21.4 \text{ pH}] \text{ mV vs. Ag/AgCl}$$

$$E_p (\text{pH } 5.1 - 11.0) = [909.59 - 17.9 \text{ pH}] \text{ mV vs. Ag/AgCl}$$

From the data presented in Table 1, the nature of the electrode seems to be not very important concerning the oxidation potential range, but we observe the electrocatalytic activity of BDD, proved by an important increase of the oxidation current, Fig.2. This behavior could be explained by the electrode surface modification of BDD during the polarization [20].

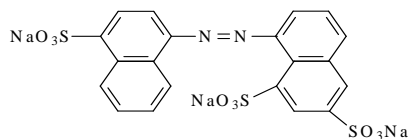
During the reduction of azo group in (MO), the peak potential shifted towards more negative potential with pH increase and the pK_a value could be estimated at 5.2-5.8 depending on the initial potential and scan rates.

Electrochemical reduction of food dyes (Tartrazine and Ponceau 4R)



TARTRAZINE (E₁₀₂)

trisodium 5-hidroxy-1-(4-sulphonatophenil)-4-(4-sulphonatophenilazo)-H-prazol-3-carboxylate



PONCEAU 4R (E₁₂₄)

trisodium 2- hidroxy-1-(4-sulphonato-1-naphtilazo) naphtalin-6,8-disulphonat

The CVs for the first scan, in negative potential range, exhibited two reduction peaks for (T), ($E_{1\text{red}} = -1.11\text{V}$; $E_{2\text{red}} = -1.51\text{V}$), Fig. 4 and only one ($E_{\text{red}} = -1.35\text{V}$) for (P) in the pH range 2.0–11.3.

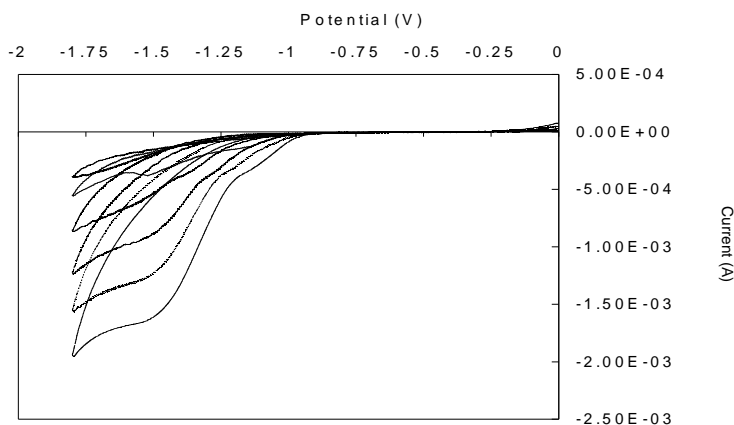


Figure 4. CV's for the reduction of Tartrazine on BDD in 0.1M Na_2SO_4 ; $\Delta C = 10^{-3}$ - 10^{-2}M

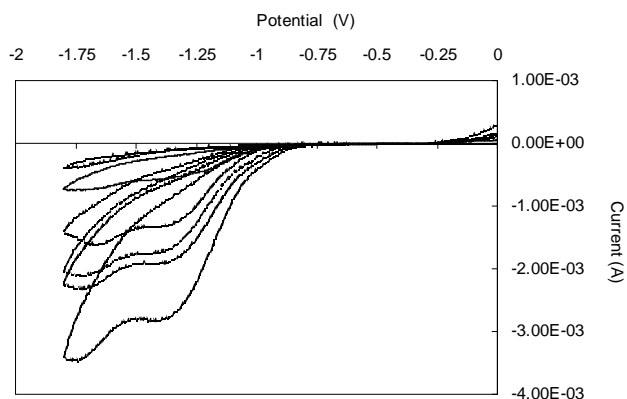


Figure 5. CVs for the reduction of Ponceau 4R on BDD electrode in 0.1M Na_2SO_4 ; pH=7.1; $v=50\text{mV}\cdot\text{sec}^{-1}$; $\Delta C = 10^{-3}$ - 10^{-2} .

The reduction of azo bond in Tartrazine and Ponceau 4R is a diffusion controlled processes for all the investigated electrodes (reduction: BDD, GC, Hg; oxidation: BDD, GC, Au), in KCl 0.1M and Na_2SO_4 0.1 M solutions, from 50-400 $\text{mV}\cdot\text{sec}^{-1}$. When the direction of sweep was reversed, one small anodic peak was observed in the entire pH range, for both (P) and (T). When the sweep direction was again changed, two new small reduction quasi-reversible peaks were noticed at $\text{pH} > 4.0$. The peak currents of the first peak was more or less constantly below pH 7.0 and showed a decrease at higher pH. It was concluded that supplementary peaks were due to reduction of the products generated in oxidation.

The reduction (T) and (P) on Hg takes place easier ($\epsilon_{\text{red}}=400\text{mV}$ for T) and ($\epsilon_{\text{red}}=254\text{mV}$ for P), due to the adsorptive interactions of azo dye with the mercury surface, but the use of Hg for the discoloration of the dyes aqueous solution could be a polluting alternative. For this reason our interest in the future will be the preparative reduction of (P) and (T) in boron doped diamond batch cell.

The cumulative data on the redox processes of azo linkage in (MO), (T) and (P), on different electrodes and at different pH, in Na_2SO_4 0.1M and Britton-Robinson buffers (BR) are presented in Table 1.

Table 1.

Peak potentials for the investigated compounds depending on pH and the electrode nature

| Potential (V/ vs. Ag/AgCl,KCl) | | | | | | | | | |
|--------------------------------|--------|------|-------|-------|------|-------|-------|------|-------|
| pH | ~2.51 | | | ~7.1 | | | ~12.7 | | |
| Dye | GC | Au | BDD | GC | Au | BDD | GC | Au | BDD |
| (T) _{red} | - 0.72 | - | -1.01 | -1.1 | - | -1.11 | - | - | -1.52 |
| (P) _{red} | -0.65 | - | -1.02 | -0.88 | - | -1.32 | -0.92 | - | -1.58 |
| (MO) _{ox} | 0.80 | 0.81 | 0.86 | 0.77 | 0.76 | 0.74 | 0.70 | 0.69 | 0.75 |

The data concerning the influence of pH over the electroreduction potential of the alimentary dye (P) and (T) has been achieved on Hg electrode.

The dependence of E_p on pH for (T) and (P) can be represented by the following equations:

for (T) $pK_a=6.8$:

$$E_p \text{ (pH } 2.0 - 6.8) = [79.96 + 97.38 \text{ pH}] \text{ mV vs. Ag/AgCl; } R^2=0.95$$

$$E_p \text{ (pH } 6.8 - 12.0) = [28.88 + 607.74 \text{ pH}] \text{ mV vs. Ag/AgCl; } R^2=0.99$$

for (P) $pK_a=5.9$:

$$E_p \text{ (pH } 2.0 - 5.9) = [174.1 \text{ pH} - 222.22] \text{ mV vs. Ag/AgCl; } R^2=0.95$$

$$E_p \text{ (pH } 5.9 - 12.0) = [579.83 + 34.16 \text{ pH}] \text{ mV vs. Ag/AgCl; } R^2=0.99$$

Discoloration of synthetic solution by electrochemical oxidation - preliminary results

The preliminary experiments on electrochemical oxidation of (MO) were carried out in a 1L reactor on BDD electrode, pH neuter ($0.1\text{M Na}_2\text{SO}_4$), at 0.5 A.

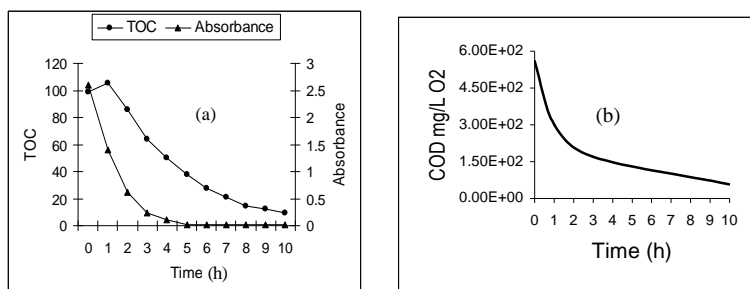


Figure 6. The variation of Absorbance, TOC and COD during the 10 hours electrolyses. pH=7.1 ($0.1\text{M Na}_2\text{SO}_4$); $I=0.5\text{ A}$; $D=168\text{ L/h}$

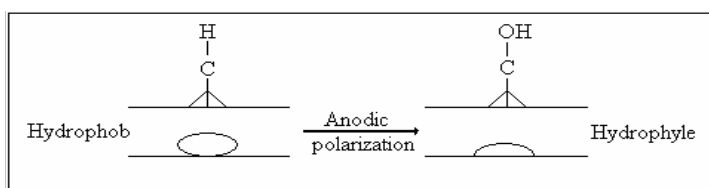
The electrode diameter was 10 cm with an area of 63.6 cm².

During the electrolyze samples were taken each hour and UV-VIS, TOC and COD determinations were made.

Figure 6 shows the evolution of absorbance, TOC (a) and COD (b).

CONCLUSIONS

Electrochemical oxidation of (MO), (T) and (P) on BDD electrodes can be used for treating and removal of azo dyes waste waters, in the accessible potential range, on BDD and GC electrodes. The good results obtained on BDD could be explained by the electrocatalytic activity of modified surface during the polarization.



The data on the dependence of peak potential on pH - $pK_a = 6.8$ for (T), $pK_a = 5.9$ for (P) and $pK_a = 5.9$ and $pK_a = 5.1$ for (MO), nature of electrode and electrolyte were reported.

During the electro-oxidation of (MO) on BDD electrode, after 10 hours the absorbance records a decreasing of 99.5%, the COT 90.3% and COD with 89.6%.

ACKNOWLEDGEMENTS

This work was financed by AUF-BECO, "Pôle d'excellence régional" ELCONDES 2700PL/309 and PNCDI-MATNANTECH 227(405)/2004.

REFERENCES

1. M.C. Gutierrez, M. Crespi, *A review of electrochemical treatments for color elimination*, JSDC, **115**, (1999) 342-345.
2. A. Fernandes, A. Morao, M. Magrinho, A. Lopez, *Electrochemical degradation of C.I. Acid Orange 7, Dyes and Pigments*, **61**, (2004), 247, www.sciencedirect.com;
3. Maria Jitaru, M. Stan, Mihaela Lang "Electrochemical behavior of Methyl Orange on different electrode materials. Fundaments for color removal in waste waters" Extended abstract at the Int. Symp. "Sustainability for Human&Environment", Timisoara, Romania, 24-24 febr.200, WAT050, p.153-157.
4. Z. F. Liu, K. Hashimoto, and A. Fujishima, *J. Electroanal. Chem.* **324** (1992) 259.
5. J. Barek, A. Berka, and J. Zima, *Collect. Czech. Chem. Commun.* **50** (1985) 1819.
6. U. Eisner and E. K. Eisner, *Encyclopedia of Electrochemistry of the Elements*, A. J. Bard (Ed.), Marcel Dekker, N. Y., 1979.

7. M. Stan, Elsa Weiss, Karine Groenen-Serrano, A. Savall, Maria Jitaru "Comportement électrochimique du méthyl orange. Utilisation d'une électrode de diamant dopé au bore" JE'05, 4-8th July 2005, Saint-Malo, France- *accepted*.
8. Mihaela Lang, Elsa Weiss, Karine Groenen-Serrano, André Savall and Maria Jitaru «Etude de la dégradation électrochimique de la Tartrazine (E_{102}) et du Ponceau 4R (E_{124}) en utilisant une électrode de diamant dopé au bore» JE'05, 4-8th July 2005, Saint-Malo, France - *accepted*.
9. S. Wawzonek, T. W. McIntyre, *J. Electrochem. Soc.*, **114**, (1967) 1025.
10. H. A. Abd El-Rahman, T. Ohsaka, F. Kitamura, K. Toduka, *J. Electroanal. Chem.* **315**, (1991) 161.
11. T. M. Florence, F. J. Miller, H. E. Zittel, *Anal. Chem.*, **33**, (1966) 1065.
12. M. Ma, K. E. Johnson, *J. Electroanal. Chem.*, **355**, (1993) 97.
13. M. Matrka, J. Marhold, Z. Sagner, *Coll. Czech. Chem. Comm.*, **34**, (1969) 1615-1619.
14. L. Ladanyi, M. Vajda, A. Magi, G. Vamos, *Acta Chim. Acad. Hung.*, **65**, (1970) 245.
15. J. Bacon, R. N. Adams, *J. Am. Chem. Soc.*, **90**, (1968) 6596-6599.
16. W. U. Malik, R. N. Goyal, N. C. Mathur, *J. Electroanal. Chem.*, **235**, (1987) 225.
17. A. G. Fogg, D. Bhanot, *Analyst*, **105**, (1980) 868.
18. A. G. Fogg, D. Bhanot, *Analyst*, **106**, (1981) 883.
19. A.Eriksson "Voltammetric Properties of Olsalazine Sodium and related Compounds" Comprehensive Summaries of Uppsala Disertation, Faculty of Science&Technology 638, Ed. Fytis-Tryck AB,Uppsala, Sweden (2001).
20. P.A. Michaud, *Comportement anodique du diamant synthétique dopée au bore*, Thèse EPFL, Lausanne, (2002).

ELECTROCHEMICAL BEHAVIOR OF PHENOLS IN AQUEOUS SOLUTION – FUNDAMENTS FOR THEIR ELECTROCHEMICAL DEGRADATION IN WASTE WATERS

MARIA JITARU, LUISA ROXANA MANDOC, CRISTINA MIHAI,
OANA TUDORAN

*"Babeș-Bolyai" University, Faculty of Chemistry and Chemical Engineering,
11, Arany Janos street, 400028 Cluj-Napoca, Phone: 00 40 264 59383, Romania
mjitaru@chem.ubbcluj.ro*

ABSTRACT. The main objective of this work is to bring information (influence of the nature of the electrode material, of pH, nature of the organic molecules) on the electrochemical parameters (peak potentials, current density) concerning the electrochemical behavior of some phenols, in different aqueous solution, having pH between 4 and 12 on different electrode materials (glassy carbon, Au, Hg, PbO₂). Both electrochemical processes on the level of hydroxyl and nitro group (in p-nitrophenol) have been studied.

Different phenols (phenol, p-nitrophenol, p-metoxypheol and 1-naphtol) derivatives have been of interest in this work, in order to establish their electrochemical behavior, useful for the electrochemical degradation.

In this work, cyclic voltammetry (using BAS 100W and AUTOLAB PGSAT computer aided electrochemical systems) and UV-Vis spectrophotometry (UNICAM Helios β) were used for the control of phenols concentration during the electro-oxidation. As compared to the electrochemical oxidation of naphthols, the electrochemical oxidation of phenols, having a strong aromatic character, takes place more difficult. The oxidation processes on the level of phenolic group strongly depends on the pH. On the other hand, the nitrophenols could be reduced on the level of nitro group and their oxidation is also possible.

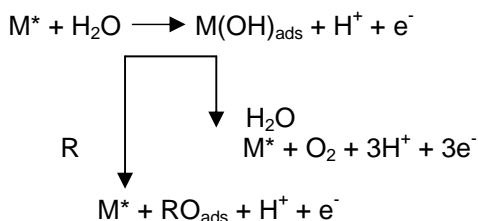
Keywords: Phenols, electrochemical oxidation, cyclic voltammetry, nitrophenols

INTRODUCTION

Removal or modification of the organic impurities in waste-waters is a major challenge for environmental science. Pollutants such phenols and their derivatives have been attracted special attention.

Phenol and related compounds are considered to be very toxic to humans through oral exposure. Ingestion of 1 g was reported to be lethal, with symptoms including muscle weakness and tremors, loss of coordination, paralysis, convulsions, coma, and respiratory arrest. Inhalation and dermal exposure to phenol is highly irritating to the skin, eyes, and mucous membranes in humans. The hydroquinone is probably carcinogen, toxic and severe skin irritant [4].

The destruction of the organic pollutants from the waste waters can be achieved either through chemical methods using different oxidant agents e.g. the ozone which is considered "a clean" reactive, or by unconventional alternatives with environmental favorable impact, like direct or indirect electrochemical oxidation. It has been proposed [5,6] that the mechanism involves the adsorption of OH species, produced from the oxidation of water molecules, or the oxides produced from electrochemical oxidation on the surface. Considering the participation of OH species, the reaction taking place on the electrode, may be written as:



where: M^* corresponds to an adsorption site and R is the organic compound.

In order to evaluate electrocatalytic activity of the electrode for the oxidation of R, contributions of both processes to the total current has to be determinate.

According to Bonfatti and co-workers [7] the electrochemical oxidation index (EOI) proposed by Comninellis [8] could be a measure towards the oxidative degradation of the organic substrates.

EXPERIMENTAL

In order to obtain the voltamperometric data, fundaments for the electrochemical phenols oxidation, cyclic voltammetry (BAS 100W and AUTOLAB PGSAT 12 computer aided electrochemical systems) have been used. The control of the electrochemical processes was achieved using UV-Vis spectrophotometer (UNICAM Helios β). Voltammograms were recorded in different buffer solution of ionic strength 0.1. The pH of buffer solution was measured using the JENWAY 3330 pH meter, after standardization with potassium hydrogen phthalate and borax buffers. Controlled potential and current electrolysis of 0.1- 0.5 mM solution of the dye was carried out both in a conventional divided H-type cell. The electrodes for cyclic voltammetry (from BAS Co.) had an area of 0.2826 cm^2 and PbO_2 for preparative scale oxidation of phenols had an area of 4.2 cm^2 ; it has been electrochemically preformed, according to our previous method [9]. All potentials refer to Ag/AgCl, KCl at an ambient temperature of $20 \pm 2 \text{ }^\circ\text{C}$.

Voltamperometric behavior of studied compounds on glassy carbon electrode – influence of the background and pH

Cyclic voltammograms on glassy carbon electrode, in alkaline media (NaOH 0.1M, pH = 13), reveal that the oxidation of 1-naphtol takes place easier (100-300mV) comparing to phenol oxidation (350–600 mV), due to different conjugation effects of the phenol comparing with 1-naphtol.

The oxidation potential slowly decrease at the same time with growing of phenols concentration, due to the increasing of the coverage degree, both for phenol (Fig. 1a) and p-nitrophenol (Fig. 1c) oxidation. Nitro group is more difficult to be adsorbed on glassy carbon, may be because of the expanded conjugation and of the stabilization of the molecule by resonance. The reduction of NO_2 group was performed on MDE (mercury drop electrode) with hanging drop (Fig. 1d).

The difference of the electrochemical reactivity of the investigated phenols cannot be explained by a simple steric hindrance of the π –electrons interaction of the benzene ring with the electrode.

The effect of the electrons withdrawal of nitro group in p-nitrophenol, correspond to the decrease of the pK_a value (7.14 for p-nitrophenols comparing to 9.95 for phenol, 10.0 for p-metoxypheol and 0.2-0.4 for 1-naphtol) [10]. The oxidation of the hydroxyl group in p-nitrophenols takes place more difficult (at about

960 mV most positive value) - Fig.2 and Table 1, comparing to phenol (525 mV) and p-metoxyphenol (540 mV). The weakest acid (1-naphtol) could be the easiest oxidized (247 mV).

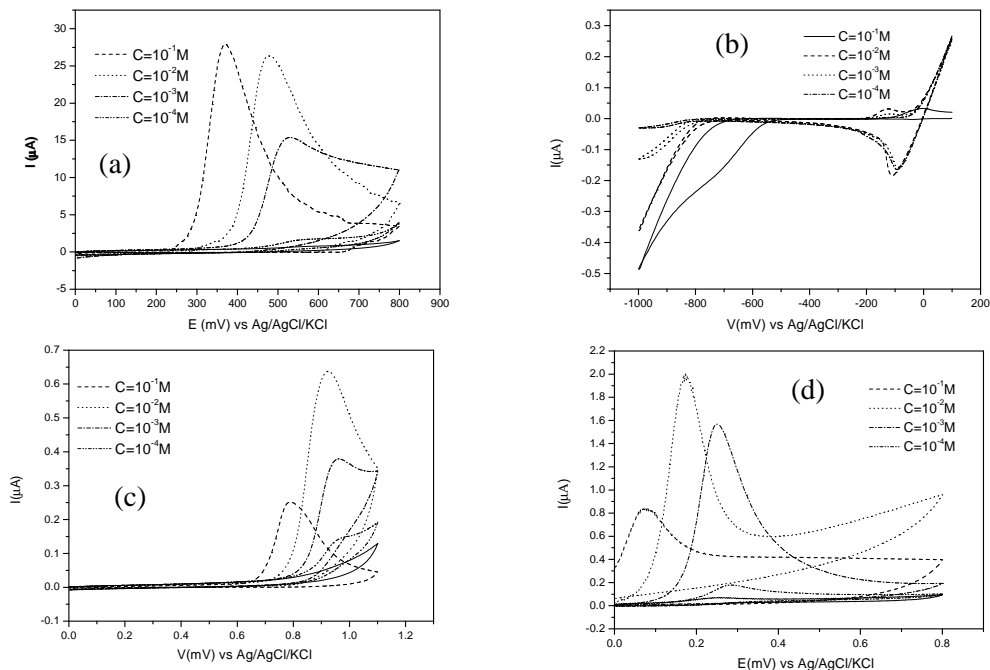


Figure 1. VOC in alkaline media, NaOH 0.1M, pH = 13 ± 0.2 of (a) phenol; (b) 1-naphtol; (c) p-nitrophenol; (d) reduction of p-nitrophenol; WE: GC; RE: Ag/AgCl,KCl; AE: Pt; v=50mV/s;

Phenoxide anion can be adsorbed on the electrode surface either due to the electrostatic interactions of the negatively charged oxygen and the anode surface or due to the π - electron interaction between the aromatic ring and the electrode. As a result of these two possibilities, phenoxide anions are oriented parallel or at a certain angle to the electrode surface, influenced by the electronic effects of the substitutes on the aromatic ring [10].

Because the stronger withdrawal exerted by the nitro group the negative charge of the oxygen atom diminishes and weakens electrostatic interaction between the phenoxide anion and the anode, maintaining the unfavorable flat orientation of the molecule at the electrode and the oxidation of hydroxyl group becomes more difficult.

In excited-state higher acidity of 1-naphtol ($pK_a = 0.2 - 0.4$) might be manifested in higher reactivity of 1-naphtol for electrochemical reaction, requiring excited-state naphtolate ions. A common explanation for the value of pK_a in 1-naphtol is intramolecular charge transfer (ICT) in the excited of acid, from the hydroxyl oxygen to the aromatic ring. It was subsequently realized that the ICT effect must be even larger in the conjugate anionic base [9]. According to this behavior, our results show that the oxidation of 1-naphtol takes place at lower positive potentials.

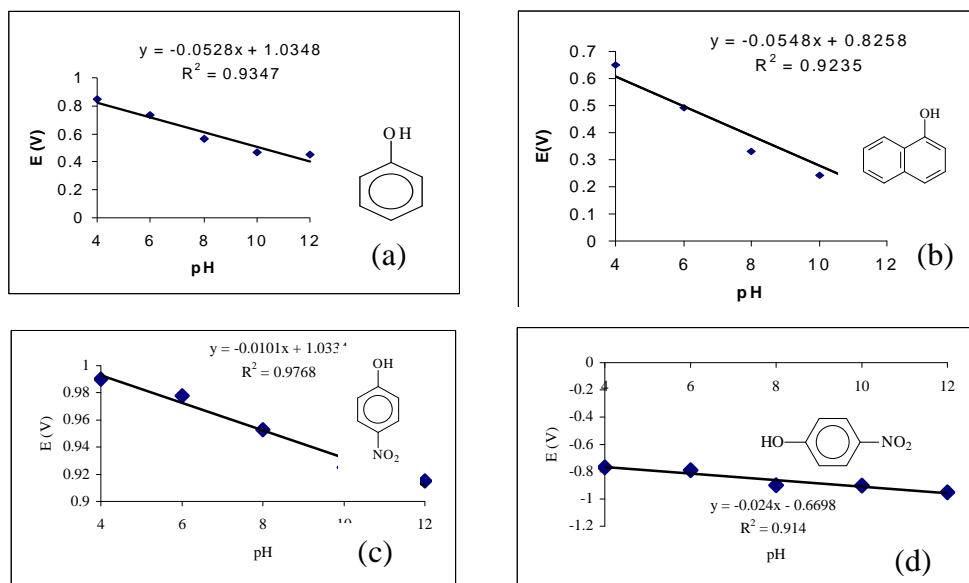


Figure 2. Potential – pH correlation for 10⁻³M (a) phenol ; (b) 1-naphtol; (c) p-nitrophenol oxidation and (d) p-nitrophenol reduction WE: GC; RE: Ag/AgCl,KCl; AE: Pt; v=50mV/s; electrolyte Na₂SO₄ 0.33 M with aliquots of H₂SO₄ or NaOH

| | ε_{ox} (V) |
|----------------|------------------------|
| Phenol | 0.525 |
| 1-naphtol | 0.247 |
| p-nitrophenol | 0.960 |
| p-metoxyphenol | 0.540 |

Table 1. Oxidation peaks potentials of the studied compounds in alkaline media (NaOH, 0.1 M) on GC electrode

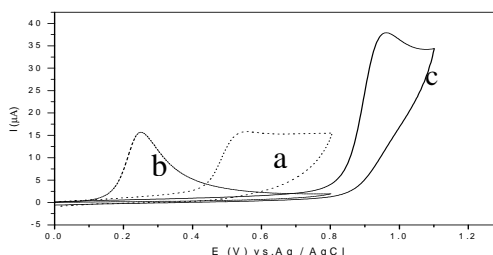


Figure 3. VOC on GC in alkaline media, NaOH 0.1M, pH = 13 ± 0,2 of (a) phenol; (b) 1-naphtol; (c) p-nitrophenol;

Determination of EOI for the oxidation of phenol and 1-naphtol

The electrochemical oxidation index (EOI), according to Bonfatti [7] and Comninellis [8] has been determinate, like a measure towards the oxidative degradation of phenol and 1-naphtol, using an experimental installation equipped with a divided cell described earlier [9]. The best results have been obtained on pre-formed PbO₂. Cyclic voltammetric determinations on PbO₂ are strongly affected by the oxidation.

For all the investigated phenols the high EOI have been obtained at lower pH values. The oxidation of the 1-naphtol seems to be more intensive, but the pH dependence is similar – Fig. 4.

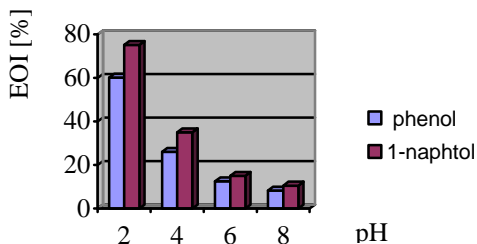


Figure 4. Dependence of the EOI as a function of pH. $T = 20 \pm 0.2$ °C; Na_2SO_4 0.33 M with aliquots of H_2SO_4 or NaOH , on PbO_2 electrode, $c_i = 1$ g/l and $i = 100 \text{ Am}^{-2}$.

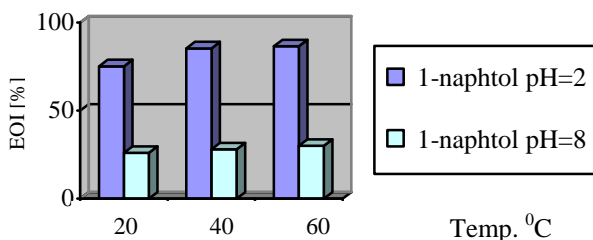


Figure 5. Dependence of the EOI on the temperature; electrolyte Na_2SO_4 0.33 M with aliquots of H_2SO_4 or NaOH on PbO_2 electrode, initial concentration 1 g/l; $i = 100 \text{ Am}^{-2}$.

On the other hand in the investigated temperature range, between 40-60 °C the EOI is practically constant, for different pH - Fig. 5.

CONCLUSIONS

The electrochemical behavior of different phenols, depending of their nature, pK_a , pH, etc. and the EOI on PbO_2 have been reported. The oxidative capacity of the investigated phenols strongly depends on pK_a :



Electrochemical decontamination of waste water containing phenols on PbO_2 becomes more efficient when the $\text{pH} \approx 2$, when the competitive oxygen formation diminishes. The electrochemical mineralization of the phenols on PbO_2 could be realized at accessible temperatures. These data are important for the electrochemical degradation of phenols in waste waters.

ACKNOWLEDGMENTS

We are grateful for the financial support from AUF-2700PL309& MATNANTECH-227(405) projects.

REFERENCES

1. M.Jitaru, A.Katona, N.Dulamita, M.Stanca and M.Birca, *Annales scientifiques de l'Université d'Etat de Moldova* (serie chimie-biologie), 282, 2001.
2. M.Stanca, M.Jitaru, N.Dulamita, *Annales scientifiques de l'Université d'Etat de Moldova* (serie chimie-biologie), 277, 2000.
3. M.Jitaru, M.Stanca and N. Dulamita, Series - SICHEM'2000, Ed. MATRIX ROM, 9-15 Oct., București, ISBN 973-685-163-X, p. 401, 2000.
4. U.S. Environmental Protection Agency. Drinking Water Health Advisory on Phenol. Office of Drinking Water, Washington, DC. 1990.
5. O.Simond, V.Schaller, Ch.Comninellis, *Electrochim. Acta*, 42, 2, 2009, 1997.
6. G.Foti, D.Gandini, Ch.Comninellis, *Current Topics in Electrochemistry*, 5, 71, 1997.
7. F.Bonfatti, S.Ferro, F.Lavezzo, M.Malacarne, G.Lodi and A.DeBattisti, *J. Electrochem.Soc.*, 146(6) 217, 1999.
8. Ch. Comninellis and C. Pulgarin *J.Appl.Electrochem.*, 21, 1403, 1991.
9. L. Oniciu, Maria Jitaru I. A. Silberg, F. Ciomos, D. A. Lowy, and O. H. Oprea, Rom. Pat. RO 91210, Mar 30, 1987; Chem. Abstr., 1987, 107, 245180q.
10. F. Lu, G.N. Salaita, L. Languren-Davidson, D.A. Stern, E. Wellner, D. G. Frank, N. Batina, D. C. Zapfen, A. T. Hubbard, *Langmuir* 4, 1988, 637.

AN ALTERNATIVE APPLICATION OF FLOW GRAPH THEORY IN CHEMISTRY, PHARMACOKINETICS AND CHEMICAL ENGINEERING PROCESSES

MARIUS SOCOL and IOAN BÂLDEA

Department of Physical Chemistry, Faculty of Chemistry and Chemical Engineering of "Babeș-Bolyai" University, 11 Arany Janos, 400028, Cluj-Napoca, Romania (e-mail:ibaldea@chem.ubbcluj.ro)

ABSTRACT. An alternative method for solving homogenous and non-homogenous differential equation systems used in physical chemistry has been developed. It was applied to some dynamic processes as radical polymerization, pharmacokinetics and the flow of fluids through a tank and tank series. For this, the flow graphs principles were used. The classical method for solving these systems with flow graphs requires the Laplace transforms before depicting a flow graph and the reverse transformation after using the Mason rules for calculus. The herein presented method is simpler and more direct, eliminating the Laplace transforms in describing these processes.

Keywords: flow graph, differential equation, and dynamic processes.

INTRODUCTION

A flow graph consists of a network in which nodes (or vertices) are connected by directed edges (or branches). Each node (vertex) represents a system variable, and each edge connecting two vertices acts as a signal multiplier. An arrow placed on the edge indicates the direction of the signal flow and the multiplication factor is indicated along the edge^{1,2}. This multiplication factor is named transmittance. It can be obtained from the coefficients of the equations. The signal flow graph depicts the flow of signals from one point of the system to another and gives the relationships between the signals. It represents the value of the determinant of the system³.

Some basic principles of flow graphs were presented previously⁴⁻⁶.

A flow graph example is presented in Figure 1.

Properties of flow graphs

A few important proprieties of flow graphs are as follows: A branch indicates the functional dependence of one signal on another.

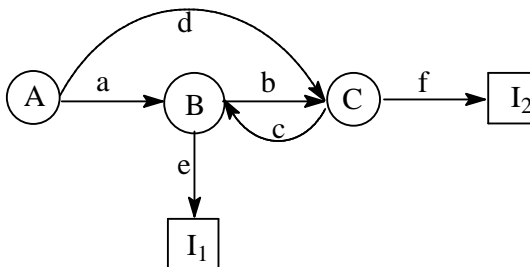


Fig. 1. An example of a flow graph. "A" is an input node (source); "I₁", "I₂" are output nodes (sinks); a, b, c, d, e and f are weights of the edges; "B", "C" are the internal nodes.

A signal passes through only in the direction specified by the arrow of the branch. A node adds the signals of all incoming branches and transmits their sum to all outgoing branches. An internal node, which has both incoming and outgoing branches, may be viewed as an output node by ignoring its outgoing branches. Note, however, that a mixed node never can be a source (input node) in this approach.

A flow graph is a diagram that represents a set of simultaneous linear algebraic situations (linear differential equations). It is used to represent an evolution of a physical system and to obtain the relationships between the system variables. By using the Cramer's method⁷ with determinants one could solve the system.

For a given system a flow graph is not unique. More than one flow graphs can be drawn for a given system by writing the system equations or the corresponding determinants in a different way^{3,8,9}.

Homogenous Linear Differential Equations Systems

Suppose we chose to solve the following system¹⁰⁻¹²:

$$\begin{cases} -\frac{dx}{dt} = a \cdot x - b \cdot y \\ -\frac{dy}{dt} = -c \cdot x + d \cdot y \end{cases} \quad \text{with initial conditions } x(0) = X_0 \text{ and } y(0) = 0; \quad (1)$$

The general solutions of the system are of the form^{11,12}:

$$x = A_1 e^{-\gamma_1 t} + A_2 e^{-\gamma_2 t} \quad \text{and} \quad y = B_1 e^{-\gamma_1 t} + B_2 e^{-\gamma_2 t} \quad (2)$$

The alternative flow graph theory:

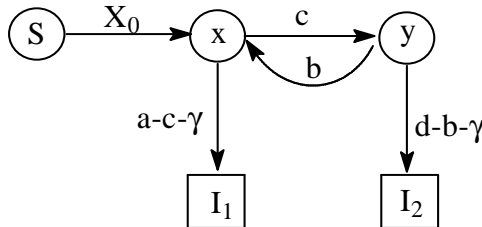


Fig. 2. The global flow graph

In this theory, the flow graphs are based on determinants³. The global flow graph is derived directly from the main determinant (the secular determinant), (3), by adding the initial conditions (the column of initial conditions are playing the role of source of unknowns x and y), as it was shown on the flow graphs algebra. For the classical flow graph method, the derivatives are also part of the mixed nodes and the formulas of calculus are different, as it can be seen in the numerical examples.

The consumption determinants (Δ_i), which are not unique now because they are function of γ_i , are derived from the main determinant (secular determinant), Δ :

$$\begin{matrix} x & y \\ \begin{matrix} x \\ y \end{matrix} & \begin{vmatrix} a-\gamma & -b \\ -c & d-\gamma \end{vmatrix} \end{matrix} = 0 \quad (3)$$

$$\Delta = [\gamma^2 - \gamma(a+d) + ad - bc] = (\gamma - \gamma_1)(\gamma - \gamma_2) = 0 \quad (4)$$

It means that the consumption determinants, which represent a Vandermonde determinant¹⁰, are:

$$\Delta_i = \prod_{\substack{j=1 \\ i \neq j}}^n (\gamma_j - \gamma_i) \neq 0 \quad (5)$$

In this case, $n = 2$. The corresponding flow graph (consumption flow graph) for the main determinant is:

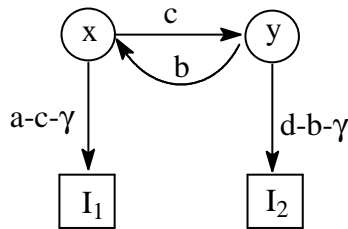


Fig. 3. The consumption flow graph

The formation determinants are obtained by replacing the columns of the secular determinant (3) by the column of free coefficients:

$$\Delta_A = \begin{matrix} S & y \\ \begin{matrix} x \\ y \end{matrix} & \begin{vmatrix} X_0 & -b \\ 0 & d-\gamma \end{vmatrix} \end{matrix} = X_0 (d - \gamma) \quad (6)$$

The formation flow graph for x is depicted in Figure 4:

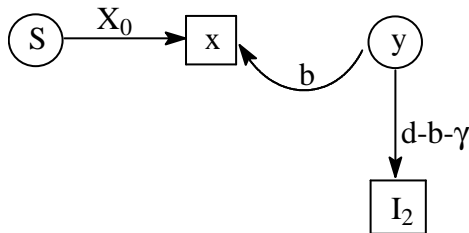


Fig. 4. The formation flow graph for x

Its gain, equivalent with the value of its determinant, is:

$$\Delta_A = X_0 b + X_0 (d - b - \gamma) = X_0 (d - \gamma) \quad (7)$$

The formation flow graph for y is depicted in Figure 5:

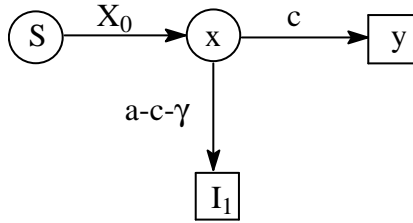


Fig. 5. The formation flow graph for y

The value of its determinant is presented below:

$$\Delta_B = X_0 c \quad (8)$$

The pre-exponential coefficients can be calculated as:

$$\begin{aligned} A_1 &= \frac{\Delta_{A_1}}{\Delta_1} = \frac{X_0 (d - \gamma_1)}{(\gamma_2 - \gamma_1)}; & A_2 &= \frac{\Delta_{A_2}}{\Delta_2} = \frac{X_0 (d - \gamma_2)}{(\gamma_1 - \gamma_2)}; \\ B_1 &= \frac{\Delta_{B_1}}{\Delta_1} = \frac{X_0 c}{(\gamma_2 - \gamma_1)}; & B_2 &= \frac{\Delta_{B_2}}{\Delta_2} = \frac{X_0 c}{(\gamma_1 - \gamma_2)}; \end{aligned} \quad (9)$$

Non-Homogenous Differential Equations Systems

A more complicated system in which a time dependent function, $f(t)$, acts like an input, is presented below¹³.

The following system has to be solved:

$$\begin{cases} -\frac{dx}{dt} = a \cdot x - b \cdot y + f(t) \\ -\frac{dy}{dt} = -c \cdot x + d \cdot y \end{cases} \quad (10)$$

with initial conditions

$$x(0) = 0 \text{ and } y(0) = 0; \quad (11)$$

The classical method of flow graphs^{3,8,9} consists the following sequence of steps: to apply the Laplace transforms¹⁴ in other variable (s), than Mason's rules and finally the finding of polynomial coefficients¹³ and the last step reverse transforms

in time variable. Our alternative method has the advantage of being simpler because it does not need the Laplace transforms. It needs only the integral of convolution¹³. The global flow graph for the system (10) is presented below:

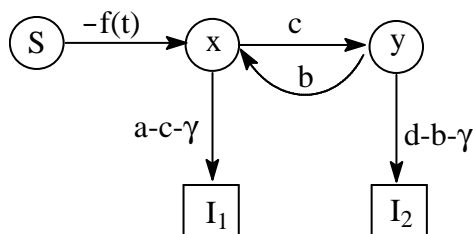


Fig. 6. The global flow graph

The role of the source is played by the input function $f(t)$. The coefficients have the same form, but instead of X_0 we have the input function $f(t)$.

$$\begin{aligned} A_1 &= \frac{\Delta_{A_1}}{\Delta_1} = \frac{-f(t)(d - \gamma_1)}{(\gamma_2 - \gamma_1)}; & A_2 &= \frac{\Delta_{A_2}}{\Delta_2} = \frac{-f(t)(d - \gamma_2)}{(\gamma_1 - \gamma_2)}; \\ B_1 &= \frac{\Delta_{B_1}}{\Delta_1} = \frac{-f(t) c}{(\gamma_2 - \gamma_1)}; & B_2 &= \frac{\Delta_{B_2}}{\Delta_2} = \frac{-f(t) c}{(\gamma_1 - \gamma_2)}; \end{aligned} \quad (12)$$

By applying the integral of convolution, which is the link between input and output¹³ it results:

$$x = \frac{-(d - \gamma_1)}{\gamma_2 - \gamma_1} \int_0^t f(t - \tau) e^{-\gamma_1 \tau} d\tau + \frac{-(d - \gamma_2)}{\gamma_1 - \gamma_2} \int_0^t f(t - \tau) e^{-\gamma_2 \tau} d\tau \quad (13)$$

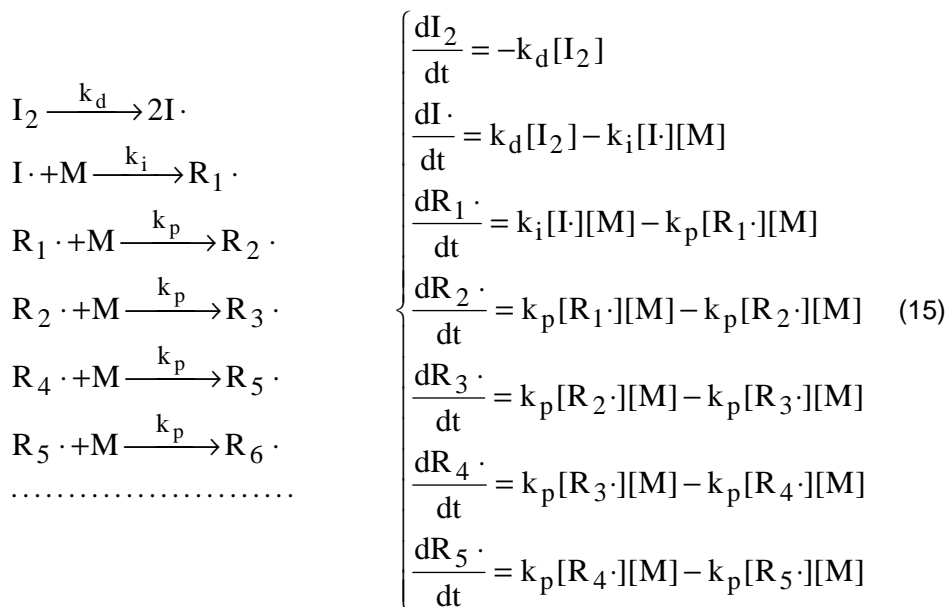
$$\text{and } y = \frac{-c}{\gamma_2 - \gamma_1} \int_0^t f(t - \tau) e^{-\gamma_1 \tau} d\tau + \frac{-c}{\gamma_1 - \gamma_2} \int_0^t f(t - \tau) e^{-\gamma_2 \tau} d\tau \quad (14)$$

where the above integrals are applied to the convolution product^{3,8,9,13}.

Examples:

We will apply the above theory to several examples that are of interest in Chemistry of polymers, pharmaco-kinetics and Chemical Engineering.

a). **The radical polymerisation** is treated by using the quasi steady-state approximation method (QSSA) and the long chain approximation¹⁵ in a batch reactor. To solve this problem it is necessary to implement a complex non-homogenous differential equation system as given below:



Here I_2 stands for the initiator, M for the monomer and various R_i for the increasing free radicals involved. This system has been solved using Mathematica 5.1¹⁶;

The notations are: $[I_2]_0 = 1\text{mmol/L}$; $k_d = k_i = u = 10^{-5} \text{ s}^{-1}$; $k_p[M]_0 = a$. The monomer concentration could be considered in large excess as compared to the concentration of the increasing free radicals. Therefore, each step can be considered as obeying first-order kinetics. On the other hand, the propagation rate constants can be considered equals, at least at smaller polymerisation degree.

The script file is presented as follows:

```

DSolve[{c'[x]==-u*c[x],d'[x]=2*u*c[x]-u*d[x],e'[x]=u*d[x]-a*e[x],f'[x]=a*e[x]-
a*f[x],g'[x]=a*f[x]-a*g[x],h'[x]=a*g[x]-a*h[x],i'[x]=a*h[x]-a*i[x],j'[x]=a*i[x]-
a*j[x],k'[x]=a*j[x]-a*k[x],l'[x]=a*k[x]
a*[x],c[0]=1,d[0]=0,e[0]=0,f[0]=0,g[0]=0,h[0]=0,i[0]=0,j[0]=0,k[0]=0,l[0]=0},{c,d,e,f,g,
h,i,j,k,l},x]

```

The solutions are:

$$\begin{aligned}
& \{c \rightarrow \text{Function}[\{x\}, e^{-u \cdot x}], \\
& d \rightarrow \text{Function}[\{x\}, 2e^{-u \cdot x} u x], e \rightarrow \text{Function}[\{x\}, \\
& \quad \frac{2e^{-a \cdot x} u^2 (1 - e^{(a-u) \cdot x} + a e^{(a-u) \cdot x} x - e^{(a-u) \cdot x} u x)}{(a-u)^2}], \\
& f \rightarrow \text{Function}[\{x\}, \frac{1}{(a-u)^3} (2 a e^{-a \cdot x - u \cdot x} u^2 \\
& \quad (-2 e^{a \cdot x} + 2 e^{u \cdot x} + a e^{a \cdot x} x + a e^{u \cdot x} x - e^{a \cdot x} u x - e^{u \cdot x} u x))], \\
& g \rightarrow \text{Function}[\{x\}, \frac{1}{(a-u)^4} \\
& \quad (a^2 e^{-a \cdot x} u^2 (6 - 6 e^{(a-u) \cdot x} + 4 a x + 2 a e^{(a-u) \cdot x} x - \\
& \quad 4 u x - 2 e^{(a-u) \cdot x} u x + a^2 x^2 - 2 a u x^2 + u^2 x^2))], \\
& h \rightarrow \text{Function}[\{x\}, \frac{1}{3(a-u)^5} (a^3 e^{-a \cdot x} u^2 (24 - 24 e^{(a-u) \cdot x} + \\
& \quad 18 a x + 6 a e^{(a-u) \cdot x} x - 18 u x - 6 e^{(a-u) \cdot x} u x + 6 a^2 x^2 - \\
& \quad 12 a u x^2 + 6 u^2 x^2 + a^3 x^3 - 3 a^2 u x^3 + 3 a u^2 x^3 - u^3 x^3))], \\
& i \rightarrow \text{Function}[\{x\}, \frac{1}{12(a-u)^6} (e^{-a \cdot x} (120 a^4 u^2 - 120 a^4 \\
& \quad e^{(a-u) \cdot x} u^2 + 96 a^5 u^2 x + 24 a^5 e^{(a-u) \cdot x} u^2 x - 96 a^4 u^3 x - \\
& \quad 24 a^4 e^{(a-u) \cdot x} u^3 x + 36 a^6 u^2 x^2 - 72 a^5 u^3 x^2 + 36 a^4 u^4 x^2 + \\
& \quad 8 a^7 u^2 x^3 - 24 a^6 u^3 x^3 + 24 a^5 u^4 x^3 - 8 a^4 u^5 x^3 + \\
& \quad a^8 u^2 x^4 - 4 a^7 u^3 x^4 + 6 a^6 u^4 x^4 - 4 a^5 u^5 x^4 + a^4 u^6 x^4))], \tag{16}
\end{aligned}$$

By taking into account that the following relation between rate constants holds $k_i \ll k_p$, then only the terms which contain exponential $e^{(a-u)x}$ should be to be considered. Therefore:

$$[R_i] = \frac{2 \cdot u^2 \cdot e^{-ut} \cdot t \cdot [I_2]_0}{a} = \frac{2 \cdot k_i^2 \cdot e^{-k_i t} \cdot t \cdot [I_2]_0}{k_p \cdot [M]} \tag{17}$$

for $i = 1$ to DP (degree of polymerisation).

This result is compared with that obtained by QSSA¹⁵:

$$R_i = \frac{2 \cdot k_i \cdot [I_2]_0}{k_p \cdot [M]} \tag{18}$$

which calculates the value of all radical concentrations for initial times and is the same in any moment of time, as long as the monomer exists in the system. This system (15) is valid for the youngest radicals (initial times) when still the interruption steps are negligible. When the amount of radicals grows and the quantities of

monomers decreases, the probability that interruptions occur is significant. Then the concentration of radicals obeys the QSSA rule¹⁵.

b) **The pharmacokinetics application.** Another example that is quite complex and cannot be solved literarly even by the Mathematica 5.1 program¹⁶ is given bellow:

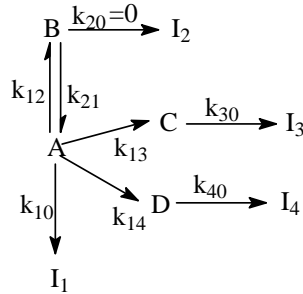


Fig. 7. The mechanism set of reactions

$$\left\{ \begin{array}{l} -\frac{dx}{dt} = (k_{10} + k_{12} + k_{13} + k_{14}) \cdot x - k_{21} \cdot y - k_0 \\ -\frac{dy}{dt} = -k_{12} \cdot x + k_{21} \cdot y \\ -\frac{dv}{dt} = -k_{13} \cdot x + k_{30} \cdot v \\ -\frac{dz}{dt} = -k_{14} \cdot x + k_{40} \cdot z \end{array} \right. \quad (19)$$

This example describes the time-evolution of a medicine in a human organism. After a perfusion, the drug enters the blood or other tissues and is eliminated either by kidneys or is metabolized¹⁷. The k values represent some first-order rate constants describing the various rate of transformation. The initial conditions are: $x(0) = y(0) = z(0) = v(0) = 0$.

The global flow graph based on the secular determinant and the column of input function $f(t) = k_0$, which is a constant, has the following form:

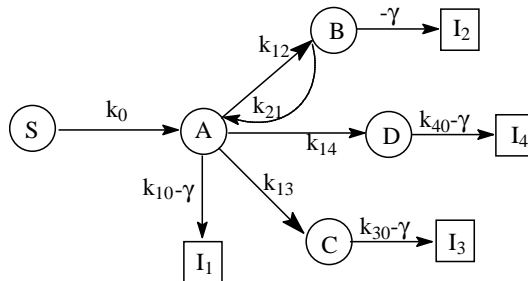


Fig. 8. The global flow graph

We symbolize $x = A$, $y = B$, $v = C$, $z = D$), representing the concentrations (quantities) of drug and its metabolites in blood or other tissues.

The consumption flow graph, which is based on secular determinant, is presented below:

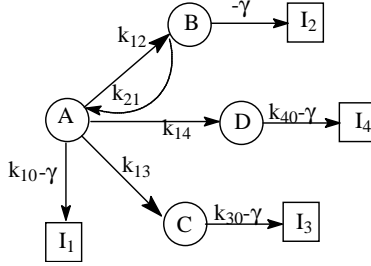


Fig. 9. The consumption flow graph

Its gain is equal with that of the secular determinant:

$$\Delta = (k_{30} - \gamma)(k_{40} - \gamma)[(-\gamma)(k_{12} + k_{13} + k_{14} + k_{10} - \gamma) + k_{21}(k_{13} + k_{14} + k_{10} - \gamma)] = 0 \quad (20)$$

$$\Delta = [\gamma^2 - \gamma(k_{12} + k_{13} + k_{14} + k_{10} + k_{21}) + k_{21}(k_{13} + k_{14} + k_{10})](k_{30} - \gamma)(k_{40} - \gamma) = 0$$

From the above equation the exponential factors, γ_1 , γ_2 (the solutions of the square equation), $\gamma_3 = k_{30}$ and $\gamma_4 = k_{40}$ can be found.

The formation graph for A is:

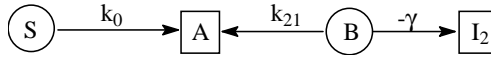


Fig. 10. The formation flow graph for A

$$\Delta_{A_i} = k_0(k_{21} - \gamma_i), \quad i = \overline{1,2} \quad (21)$$

$$A = \frac{k_0(k_{21} - \gamma_1) \int_0^t e^{-\gamma_1 \tau} d\tau}{(\gamma_2 - \gamma_1)} + \frac{k_0(k_{21} - \gamma_2) \int_0^t e^{-\gamma_2 \tau} d\tau}{(\gamma_1 - \gamma_2)} \quad (22)$$

$$A = \frac{k_0(k_{21} - \gamma_1)(e^{-\gamma_1 t} - 1)}{(\gamma_2 - \gamma_1)(-\gamma_1)} + \frac{k_0(k_{21} - \gamma_2)(e^{-\gamma_2 t} - 1)}{(\gamma_1 - \gamma_2)(-\gamma_2)}$$

The formation graph for B is:

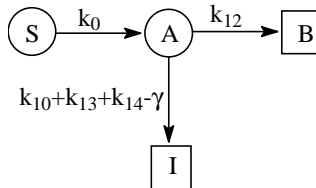


Fig. 11. The formation flow graph for B

Where I is the sum of all the outputs from node A.

$$\Delta_{B_i} = k_0 \cdot k_{12} \quad i = \overline{1,2} \quad (23)$$

$$B = \frac{k_0 k_{12} (e^{-\gamma_1 t} - 1)}{(\gamma_2 - \gamma_1)(-\gamma_1)} + \frac{k_0 k_{12} (e^{-\gamma_2 t} - 1)}{(\gamma_1 - \gamma_2)(-\gamma_2)} \quad (24)$$

The formation graph for C is:

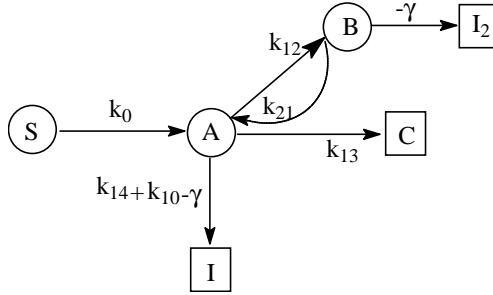


Fig. 12. The formation flow graph for C

$$\Delta_{C_i} = k_0 \cdot k_{13} \cdot (k_{21} - \gamma_i) \quad i = \overline{1,3} \quad (25)$$

$$C = \frac{k_0 k_{13} (k_{21} - \gamma_1) (e^{-\gamma_1 t} - 1)}{(\gamma_2 - \gamma_1)(\gamma_3 - \gamma_1)(-\gamma_1)} + \frac{k_0 k_{13} (k_{21} - \gamma_2) (e^{-\gamma_2 t} - 1)}{(\gamma_1 - \gamma_2)(\gamma_3 - \gamma_2)(-\gamma_2)} + \frac{k_0 k_{13} (k_{21} - \gamma_3) (e^{-\gamma_3 t} - 1)}{(\gamma_1 - \gamma_3)(\gamma_2 - \gamma_3)(-\gamma_3)} \quad (26)$$

The formation graph for D is:

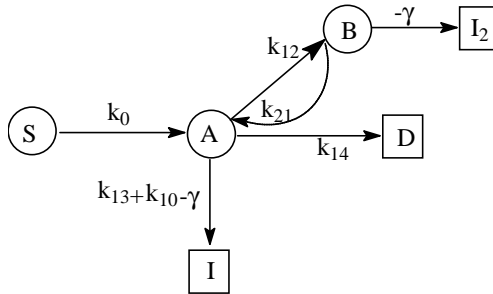


Fig. 13. The formation flow graph for D

$$\Delta_{D_i} = k_0 \cdot k_{14} \cdot (k_{21} - \gamma_i) \quad i = 1, 2, 4; \quad (27)$$

$$D = \frac{k_0 k_{14} (k_{21} - \gamma_1) (e^{-\gamma_1 t} - 1)}{(\gamma_2 - \gamma_1)(\gamma_4 - \gamma_1)(-\gamma_1)} + \frac{k_0 k_{14} (k_{21} - \gamma_2) (e^{-\gamma_2 t} - 1)}{(\gamma_1 - \gamma_2)(\gamma_4 - \gamma_2)(-\gamma_2)} + \frac{k_0 k_{14} (k_{21} - \gamma_4) (e^{-\gamma_4 t} - 1)}{(\gamma_1 - \gamma_4)(\gamma_2 - \gamma_4)(-\gamma_4)} \quad (28)$$

c). **The flow through of a vessel.** In order to exemplify how the differential relation in describing dynamic system behavior is used, we have chosen a system built by a tank that is fed with a liquid that is also evacuated continuously¹³. Input and output mass flows are $F_{mi} = u(t)$ and F_{me} , respectively. The initial level of the liquid is $y(0) = H_0$, hydraulic resistance is noted by R and the section area by A , as it can be observed in figure 7. If the value of H is symbolized by y , its behavior as a function of time is calculated by a differential equation as in equation (29)¹³:

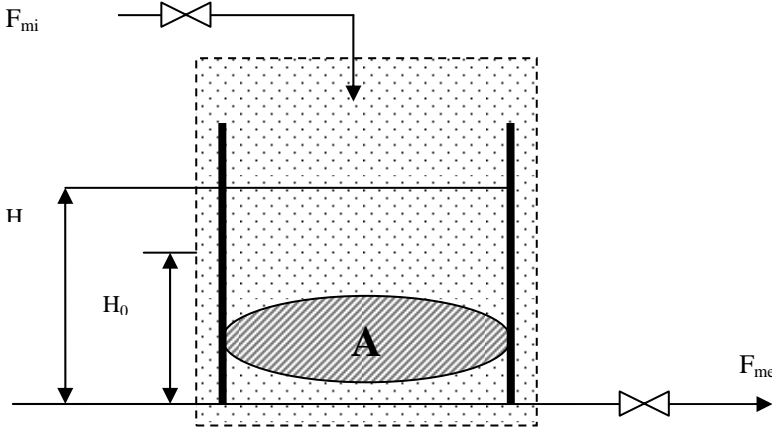


Fig. 14. Single liquid tank

$$-\frac{dy}{dt} = \frac{1}{A \cdot R} \cdot y - \frac{1}{A} \cdot u(t) \quad (29)$$

The secular determinant can be written as in equation (30):

$$\Delta = \left| \frac{1}{A \cdot R} - \gamma \right| = 0 \quad \gamma = \frac{1}{A \cdot R} \quad (30)$$

The formation flow graph for this simple system is⁴⁻⁶:

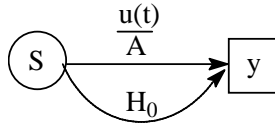


Fig. 15. The formation flow graph for y

It results that:

$$y = H(t) = H_0 \cdot e^{-t/A \cdot R} + \frac{1}{A} \cdot \int_0^t u(t - \tau) \cdot e^{-\tau/A \cdot R} d\tau \quad (31)$$

d). **The flow through a tank series.** A series of two tanks, as shown in Figure 16 is considered, where $F_{vi3} = 0$. The initial conditions are:

$$H_1(0)=0, H_2(0)=0; \quad (32)$$

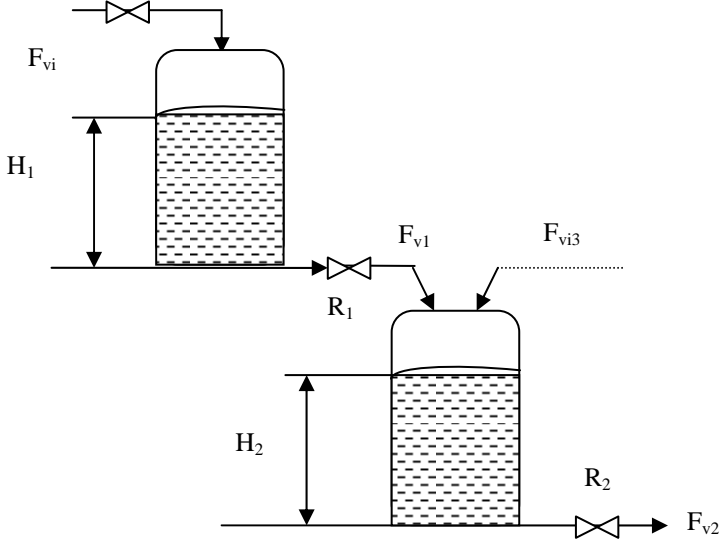


Fig. 16. Two tanks in series.

The system of differential equations describing the evolution of this series is given by:

$$\begin{cases} -\frac{dH_1}{dt} = \frac{H_1}{A_1 R_1} - \frac{1}{A_1} \cdot u(t) \\ -\frac{dH_2}{dt} = -\frac{H_1}{R_1 A_2} + \frac{H_2}{A_2 R_2} \end{cases} \quad (33)$$

$$\Delta = \begin{vmatrix} \frac{1}{A_1 \cdot R_1} - \gamma & 0 \\ -\frac{1}{R_1 A_2} & \frac{1}{A_2 R_2} - \gamma \end{vmatrix} = 0 \quad \gamma_1 = \frac{1}{A_1 \cdot R_1} \text{ and } \gamma_2 = \frac{1}{A_2 R_2} \quad (34)$$

The formation flow graph for H_2 is:

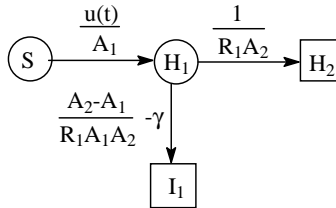


Fig. 17. The formation flow graph for H_2

The increase of the liquid height in the two tanks is¹³:

$$H_2 = \frac{1}{A_1 A_2 R_1} \cdot \frac{1}{\gamma_2 - \gamma_1} \int_0^t u(t - \tau) \cdot (e^{-\tau/A_1 R_1} - e^{-\tau/A_2 R_2}) d\tau \quad (35)$$

$$H_2 = \frac{R_2}{A_1 R_1 - A_2 R_2} \cdot \int_0^t u(t - \tau) \cdot (e^{-\tau/A_1 R_1} - e^{-\tau/A_2 R_2}) d\tau$$

d) **The flow through a tank series with an additional feed.** The fourth example considered is treated supposing that there is a new feed $F_{vi3} = u_2(t)$ (see figure 15) and $A_1 = A_2 = A$. The corresponding differential equations are¹³:

$$\begin{cases} -\frac{dH_1}{dt} = \frac{H_1}{AR_1} - \frac{1}{A} \cdot u_1(t) \\ -\frac{dH_2}{dt} = -\frac{H_1}{R_1 A} + \frac{H_2}{AR_2} + \frac{1}{A} \cdot u_2(t) \end{cases} \quad (36)$$

$$\Delta = \begin{vmatrix} \frac{1}{A \cdot R_1} - \gamma & 0 \\ -\frac{1}{R_1 A} & \frac{1}{AR_2} - \gamma \end{vmatrix} = 0 \quad \gamma_1 = \frac{1}{A \cdot R_1} \text{ and } \gamma_2 = \frac{1}{AR_2} \quad (37)$$

The formation flow graph for H_2 is:

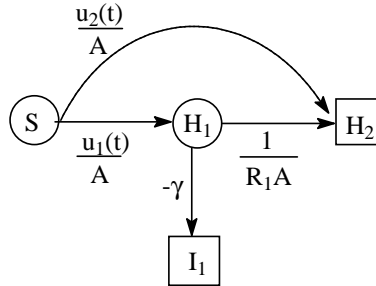


Fig. 18. The formation flow graph for H_2

It results that:

$$\Delta_{H_2} = \frac{u_1(t)}{A} \cdot \frac{1}{R_1 A} + \frac{u_2(t)}{A} \cdot \left(\frac{1}{R_1 A} - \gamma \right) \quad (38)$$

$$\begin{aligned} H_2 = & \frac{1}{A^2 R_1} \cdot \frac{1}{\gamma_2 - \gamma_1} \int_0^t u_1(t - \tau) \cdot e^{-\tau/AR_1} d\tau + \frac{1}{A} \cdot \left(\frac{1}{R_1 A} - \gamma_1 \right) \cdot \frac{1}{\gamma_2 - \gamma_1} \int_0^t u_2(t - \tau) \cdot e^{-\tau/AR_1} d\tau \\ & + \frac{1}{A^2 R_1} \cdot \frac{1}{\gamma_1 - \gamma_2} \int_0^t u_1(t - \tau) \cdot e^{-\tau/AR_2} d\tau + \frac{1}{A} \cdot \left(\frac{1}{R_1 A} - \gamma_2 \right) \cdot \frac{1}{\gamma_1 - \gamma_2} \int_0^t u_2(t - \tau) \cdot e^{-\tau/AR_2} d\tau \end{aligned} \quad (39)$$

CONCLUSIONS

This method seems to be very general. It applies equally well to complex chemical reactions, the description of drug time-evolution in a body or in chemical engineering. It solves systems of differential equations in a simple way. In chemistry, the image of the graph resembles with the reaction scheme or mechanism of the transformation.

REFERENCES

- [1]. M. V. Diudea, O. Ivanciuc, *Topologie Moleculara*, Ed. Complex, Cluj, 1995, p. 37.
- [2]. T. Ionescu, *Grafuri. Aplicatii. Vol 1*. Ed. Didactica si Pedagogica, Bucuresti, 1973, p. 198- 207.
- [3]. K. Ogata, *Modern Control Engineering*, Prentice Hall International, New Jersey, 1995.
- [4]. M. Socol, I. Baldea, *Stud. Univ. Babes-Bolyai, Chemia*, XLVIII, Cluj-Napoca, 1, 2003, p. 109-128.
- [5]. M. Socol, I. Baldea, *Stud. Univ. Babes-Bolyai, Chemia*, XLIX, Cluj-Napoca, 1, 2004, p. 101-110
- [6]. M. Socol, I. Baldea, *Stud. Univ. Babes-Bolyai, Chemia*, XLIX, Cluj-Napoca, 2, 2004, p. 93-107.
- [7]. A. C. Aitken, *Determinants and Matrices*, Oliver and Boyd, Edinburgh, 1939, Chap. 2.
- [8]. N. S. Nice, *Control System Engineering*, Addison-Westley Publishing Company, 1995, p. 240-260, 268-275.
- [9]. R. C. Dorf, R. H. Bishop, *Modern Control System*, Prentice Hall International, New Jersey, 2001, p. 66-80, 118-158.
- [10]. P. Juerge, *Reaktionskinetische Auswertung Spektroskopischer Hessdaten*, Braunschweig, 1995, p. 160-183.
- [11]. M. Roscule, *Analiza Matematica*, Ed. Didactica si Pedagogica, Bucuresti, **1984**, p. 618.
- [12]. C. Udriste, *Aplicatii de algebra, geometrie si ecuatii diferentiale*, Ed. Didactica si Pedagogica, Bucuresti, **1993**, p. 264.
- [13]. M. V. Cristea, S. P. Agachi, *Elemente de teoria sistemelor*, Ed. Risoprint, Cluj-Napoca, **2002**, p. 113-131.
- [14]. R. V. Churchill, *Operational matematics*, McGraw-Hill, New-York, **1958**, p. 323.
- [15]. I. Muresan, *Chimia Macromoleculelor*, Ed. Didactica si Pedagogica, Bucuresti, **1967**, p. 44.
- [16]. www.wolfram.com
- [17]. M. K. Ma, W. C. Zamboni, *Clinical Cancer Research*, 6, **2000**, p. 813-819.

KINETICS AND MECHANISM OF *p*-XYLENE OXIDATION BY Ce(IV) IN AQUEOUS ACID MEDIUM. LFER AS AN ARGUMENT TO THE OXIDATION MECHANISM

GABRIELA-CRISTINA BUCŞA and IOAN BÂLDEA

Department of Physical Chemistry, Faculty of Chemistry and Chemical Engineering of "Babeş-Bolyai" University, 11 Arany Janos, 400028, Cluj-Napoca, Romania (e-mail: ibalde@chem.ubbcluj.ro)

ABSTRACT. The oxidation of *p*-xylene in aqueous acidic media, (using perchloric acid), has been followed spectrophotometrically. The process proceeds in parallel with the water oxidation. This reaction follows a first-order kinetics and has been taken into consideration by subtracting its contribution to the consumption of Ce(IV). A first-order dependence on Ce(IV) concentration and a complex dependence on *p*-xylene and hydrogen ion concentrations have been established for the organic substrate oxidation. The effect of ionic strength on the reaction rate has been studied and activation parameters were calculated. The global reaction rate is consistent with a mechanism involving the rapid formation of a complex that suffers an intramolecular electron transfer. The linear free energy relationship of Hammett type has been obtained for the oxidation of various substituted toluenes with a negative and small reaction constant, which argues the suggested mechanism.

Keywords: cerium, *p*-xylene, toluene derivatives, kinetics, oxidation, LFER.

INTRODUCTION

Cerium (IV) is a strong one-equivalent oxidising agent for a large number of organic or inorganic substrates, due to the high standard oxidation-reduction potential of Ce(IV)/Ce(III) couple [1]. Various aromatic hydrocarbons have been oxidised [2-4]. A review of the literature shows that some of these electron-transfer reactions were approached from the kinetic point of view [1-28]. The rate laws and mechanisms for the oxidation of toluene and some substituted toluene in aqueous sulphuric acid media were reported [29-31], and in the case of *p*-xylene oxidation with Ce(IV), the activation energy has been determined [30]. Perchloric, nitric, sulphuric and acetic acids were used as hydrogen ion sources and involvement of hydroxo-, nitrate, sulphate or acetate cerium(IV) complexes were described.

We have undertaken kinetic studies on the oxidation of toluene [31] and *o*-xylene in sulphuric and perchloric media and gave some evidence of an adduct intermediate species between Ce(IV) and aromatic hydrocarbons [32]. On the other hand, at high perchloric acid concentration and temperatures higher than 35°C, Ce(IV) oxidises water along with the hydrocarbon reaction, a process that should be taken into consideration.

In order to get more details concerning the kinetic and the mechanism, we have investigated the electron-transfer reaction Ce(IV)- *p*-xylene by using perchloric acid as the hydrogen ion source, where no complex formation between Ce(IV) and ClO₄⁻ is to be expected.

EXPERIMENTAL

The chemicals used in this study were of reagent grade purity, purchased from commercial sources (Chimopar, Reanal, Merck, Aldrich and Fluka) and employed without further purification.

The various substrates were dissolved into boiled and cooled twice-distilled water under the solubility limits by using an ultrasonic bath. It ensured the elimination of dissolved air. The solutions were freshly prepared before each set of runs. Stock solutions of $\text{Ce}(\text{ClO}_4)_4$, HClO_4 and NaClO_4 were prepared and standardised spectrophotometrically and by acid - base titration, respectively. Aliquots of NaClO_4 solution were passed through an ion-exchange resin (Purolite C 110 H) and resulted HClO_4 was titrated against NaOH standard solution.

Kinetic measurements were performed by means of a Jasco V-530 spectrophotometer, provided with a temperature jacket surrounding the cell holder. The cuvette jacket was connected to a Lauda M-12 thermostat. Reaction mixtures were prepared directly in the quartz cell of the spectrophotometer having a 5 cm path length. A rapid adding of a measured amount of cerium perchlorate stock solution, kept in thermostat, over the reaction mixture containing HClO_4 , NaClO_4 , *p*-xylene or various substituted toluenes at desired concentration, started the reaction. The reaction progress was followed by monitoring the decrease of optical absorbance at 315 nm, where the UV/VIS spectrum of $\text{Ce}(\text{IV})$ exhibits an absorption band. Under each set of conditions, the water oxidation has been monitored in separate experiment. Each experiment has been carried out at least three times and the mean values of observed rate constants have been calculated.

RESULTS AND DISCUSSIONS

Preliminary investigations. *Check of Lambert-Beer law.* Lambert-Beer law's validity, over the concentration range used, was verified. A linear dependence of absorbance on $\text{Ce}(\text{IV})$ concentration in the absence and the presence of *p*-xylene has been obtained. A slight **decrease of molar** absorption coefficient occurs when the mixture contains *p*-xylene, but the linearity is maintained. Table 1 contains the values of the molar absorption coefficients under the given experimental conditions. This coefficient is about 7.5 % smaller in the presence of the aromatic hydrocarbon.

Table 1

Molar absorptivities in the absence and the presence of *p*-xylene

| Reaction mixture | $[\text{H}^+]=1 \text{ mole.L}^{-1}$; $[\text{ClO}_4]=1 \text{ mole.L}^{-1}$; $\mu=2.0$; $t=20^\circ\text{C}$ | | | |
|--|--|----------------|---|----------------|
| | Ce(IV) | | Ce(IV) - <i>o</i> -xylene $4 \cdot 10^{-4} \text{ mole.L}^{-1}$ | |
| λ , nm | 315 | 320 | 315 | 320 |
| $\epsilon \text{ L.mole}^{-1} \text{ cm}^{-1}$ | 4039 \pm 198 | 4047 \pm 207 | 3713 \pm 202 | 3690 \pm 206 |

Check for an intermediate species formation. By recording the spectra of the reaction mixture immediately after mixing at various increasing concentrations of organic hydrocarbon at 20°C , where both the oxidation of water and organic substrate are slow, a small but systematic decrease of the intensity of $\text{Ce}(\text{IV})$ absorption band and the occurrence of an isosbestic point located at 276 nm have been noticed. This is brought about by the presence of a new absorbing species besides $\text{Ce}(\text{IV})$. It may be a complex involving $\text{Ce}(\text{IV})$ and substrate.

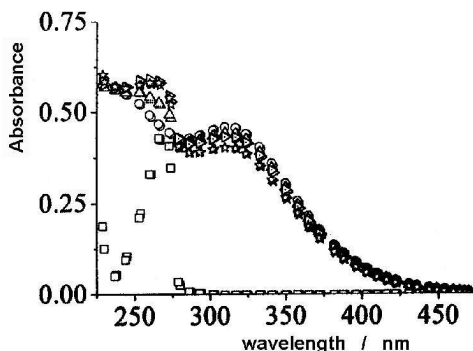
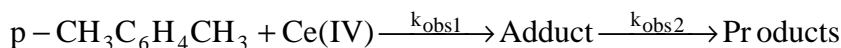


Fig. 1. Spectra recorded immediately after mixing of Ce(IV) 10^{-4} mole.L $^{-1}$, and *p*-xylene $2.8 \cdot 10^{-3}$ mole.L $^{-1}$ and mixtures of various concentration of substrate ($8.0 \cdot 10^{-5}$ to $2.8 \cdot 10^{-3}$ mole.L $^{-1}$)

Stoichiometry determination. The stoichiometry of the reaction has been determined by a spectrophotometrical titration [32]. Various mixtures having increasing ratios of [*p*-xylene]:[Ce(IV)] were allowed to react to completion at constant acidity. The absorbance values of the unreacted Ce(IV) were determined. Part of the Ce(IV) was consumed by the water molecule oxidation. Nevertheless, the mixture reacted the same period of time, and comparison has been done to the blank probe. The plot of the absorbance difference between blank probes and those with *p*-xylene shows two lines with an intersect and a turning point at the ratio 0.5, as in the case of toluene and *o*-xylene [32]. It predicts a ratio of 2 Ce(IV) ions to a molecule of *p*-xylene, indicating that the oxidation yields *p*-methylbenzylic alcohol as the main oxidation product.

Kinetics. An experiment consists in monitoring the optical absorbance against time. According to the shape of the absorbance- time curve, which looks like a bi-phasic plot, the oxidation of *p*-xylene by Ce(IV) consists of two consecutive stages of the type:



The first stage consists of a steep decline in absorbance at the beginning of the reaction. It could be attributed to the formation of an adduct between Ce(IV) and *p*-xylene. The second stage, perceptible at higher degrees of transformation, may be associated with the redox process consisting of an inner electron transfer within the complex, that finally yields the products of the reaction.

The reaction order with respect to Ce(IV) was determined from the dependence $\lg(r) = f(\lg[Ce(IV)])$. As it can be seen in figure 3, first-order with respect to cerium has been found for both stages of the reaction. The experimental curves, $A = f(t)$, were subjected to derivation, at the initial moment and at $t = 1000$ s, while the reaction rates (mole Ce(IV)/L.s) and the corresponding concentrations of cerium were calculated by taking $\epsilon = 4039 \text{ M}^{-1} \text{ cm}^{-1}$.

Once first-order dependence has been established, we preferred to determine the rate constants by a non-linear fitting of the experimental $A = f(t)$ curves, with the bi-exponential equation:

$$A - A_{\infty} = C_1 \exp(-k_{\text{obs1}}^0 \cdot t) + C_2 \exp(-k_{\text{obs2}}^0 \cdot t) \quad (1)$$

which describes the decay of the absorbance of the limiting component in a first-order series of reactions. A and A_{∞} stand for the absorbance at actual time and at the end of the reaction, respectively. The parameters C_1 and C_2 are constants including the molar absorptivities and Ce(IV) initial concentration; k_{obs1}^0 and k_{obs2}^0 are apparent rate constants of the two reaction steps for the overall reduction of Ce(IV). Good fit has been achieved. Table 2 contains these pseudo-first-order rate constants at various concentration of *p*-xylene. Replicate runs yielded close values of pseudo-first-order rate coefficients.

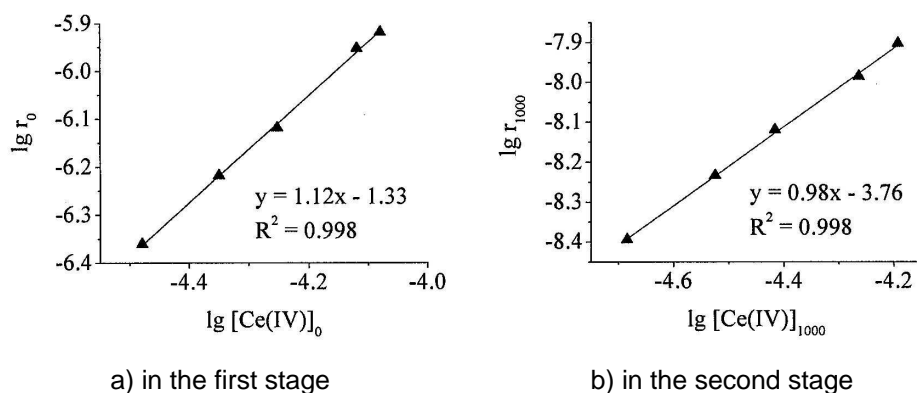


Fig. 2. Determination of reaction order with respect to cerium in the two stages of the above described reaction.

Table 2

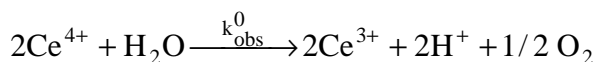
Apparent first-order rate coefficients of overall oxidation reaction as a function of *p*-xylene concentration: $[H^+] = 1.0 \text{ mole.L}^{-1}$, $[Ce(IV)] = 8.0 \cdot 10^{-5}$, $\mu = 2.0$ and 40°C

| $[p\text{-xylene}] \times 10^4$ mole.L^{-1} | $10^3 k_{\text{obs1}}^0 \text{ s}^{-1}$ | $10^3 k_{\text{obs1}}^0 \text{ s}^{-1}$ mean | $10^4 k_{\text{obs2}}^0 \text{ s}^{-1}$ | $10^4 k_{\text{obs2}}^0 \text{ s}^{-1}$ mean |
|---|---|---|---|---|
| 4.0 | 3.10 | 3.00 | 3.73 | 3.68 |
| | 2.92 | | 3.67 | |
| | 3.01 | | 3.57 | |
| 6.0 | 4.60 | 4.60 | 4.65 | 4.55 |
| | 4.50 | | 4.48 | |
| | 4.70 | | 4.52 | |
| 7.0 | 5.00 | 5.01 | 5.04 | 4.96 |
| | 5.11 | | 4.84 | |
| | 4.94 | | 5.01 | |
| 8.0 | 5.88 | 5.80 | 5.30 | 5.25 |
| | 5.74 | | 5.23 | |
| | 5.78 | | 5.22 | |

KINETICS OF *p*-XYLENE OXIDATION BY Ce (IV) IN AQUEOUS ACIDIC MEDIUM

| [<i>p</i> -xylene] $\times 10^4$ mole.L ⁻¹ | $10^3 k_{obs1}^0$ s ⁻¹ | $10^3 k_{obs1}^0$ s ⁻¹ mean | $10^4 k_{obs2}^0$ s ⁻¹ | $10^4 k_{obs2}^0$ s ⁻¹ mean |
|---|-----------------------------------|---|-----------------------------------|---|
| 9.0 | 6.76 | 6.70 | 5.60 | 5.59 |
| | 6.64 | | 5.58 | |
| | 6.70 | | 5.59 | |
| 10.0 | 7.53 | 7.50 | 5.90 | 5.88 |
| | 7.48 | | 5.88 | |
| | 7.49 | | 5.86 | |

Parallel to the oxidation of *p*-xylene, oxidation of water by Ce(IV) takes place, according to the stoichiometry:



The kinetics of this reaction obeys a first-order dependence on Ce(IV) for the whole duration of the reaction. It has been deduced by the same procedure as for the overall process that has been described before.

We have determined the influence of different parameters on the oxidation of water and both water and substrate. Because the literature [33] stipulates, and we have also found [34] that Ce(III) diminishes the rate of the water oxidation reaction, we introduced Ce(III) into the reaction mixture

Table 3

Several first-order rate constants at the oxidation of water [Ce(IV)] = 8.0×10^{-5}

| Temp °C | [Ce(III)] $\times 10^5$ mole.L ⁻¹ | [H ⁺] mole.L ⁻¹ | μ | $10^4 k_{obs}^0$ s ⁻¹ |
|---------|---|---|-------|-------------------------------------|
| 40.0 | 0.0 | 1.0 | 2 | 2.06 |
| | 0.4 | | | 1.54 |
| | 0.8 | | | 1.41 |
| | 1.0 | | | 1.28 |
| | 1.2 | | | 0.95 |
| | 1.6 | | | 0.77 |
| 40.0 | 0.8 | 0.5 | 3 | 0.92 |
| | | 1.0 | | 1.32 |
| | | 1.5 | | 1.96 |
| | | 2.0 | | 2.29 |
| | | 2.5 | | 2.60 |
| 35 | 0.8 | 1.5 | 3 | 1.20 |
| 40 | | | | 2.02 |
| 45 | | | | 3.65 |
| 50 | | | | 6.75 |
| 55 | | | | 9.00 |
| 60 | | | | 16.3 |

from the beginning in a ratio 1:1 ([Ce(IV)]:[Ce(III)]). The experimental curves for the water oxidation reaction were determined by a fitting method with the equation:

$$A - A_{\infty} = C_3 \exp(-k_{obs}^0 \cdot t) \quad (2)$$

Several rate constants are presented in table 3. The activation parameters were calculated.

Once we had all the first-order rate constants, we proceed by subtracting the rate constant of the oxidation of water from the rate constants of the overall reaction as follows:

$$k_{obs1} = k_{obs1}^0 - k_{obs}^0 \quad (3)$$

$$k_{obs2} = k_{obs2}^0 - k_{obs}^0 \quad (4)$$

where: k_{obs1} and k_{obs2} are the observed first-order rate constants of the xylene oxidation reaction for the first and the second step and k_{obs}^0 is the observed first-order rate constant for the water oxidation reaction under the same acidity or ionic strength conditions employed.

The effect of *p*-xylene concentration, always in a large excess, upon the apparent rate constant is presented in figure 3. Observed rate constants were obtained using equation (3) and (4).

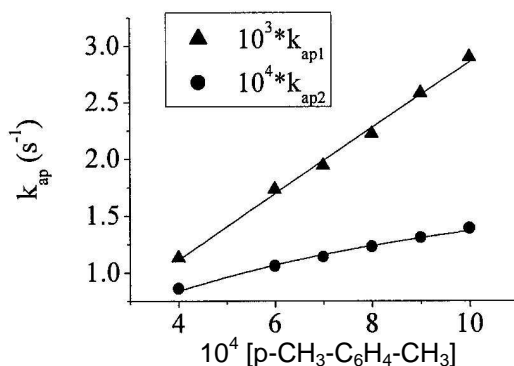


Fig. 3. The effect of *p*-xylene on the first and the second stage of the reaction: [Ce(IV)] = [Ce(III)] = $8 \cdot 10^{-5}$ mole.L⁻¹; [H⁺] = 1 mole.L⁻¹ μ = 2.0; $t = 40^\circ\text{C}$

The best fit has been obtained with the equations:

$$k_{obs1} = (-1.0 \cdot 10^{-5} \pm 7.2 \cdot 10^{-5}) + (7.3 \pm 0.2)[p\text{-xylene}]_0 \quad (5)$$

with $R^2 = 0.9910$, $\chi^2 = 2.0 \cdot 10^{-8}$ for $N = 18$, and respectively

$$k_{obs2} = \frac{(13.8 \pm 0.5)[p\text{-xylene}]_0}{1 + (139 \pm 90)[p\text{-xylene}]_0} \quad (6)$$

with $R^2 = 0.9800$, $\chi^2 = 7.50 \cdot 10^{-9}$ for $N = 18$. It is easy to recognise that the first stage of the reaction obeys also a first-order dependence on *p*-xylene, while the second stage follows a Michaelis – Menten pattern. A fractional sub-unitary order is obtained, suggesting also the involvement of an intermediate species.

Even under high acid concentration, the hydrolysis of Ce(IV) ion takes place and complicates the kinetics. It is revealed from the influence of hydrogen ion concentration on the rate constant that it is quite complex, investigated in the limits presented in the Table 4.

Table 4

Effect of hydrogen ion concentration on the apparent rate constant;
 $[\text{Ce(IV)}] = 8 \cdot 10^{-5} \text{ mole.L}^{-1}$; $[\text{Ce(III)}] = 8 \cdot 10^{-5} \text{ mole.L}^{-1}$; $[\text{p-xylene}] = 4.0 \cdot 10^{-4} \text{ mole.L}^{-1}$;
 $\mu = 3.0$ and temperature of 40°C

| $[\text{H}^+]$ (mole.L ⁻¹) | $10^3 \cdot k_{\text{obs1}}$ (s ⁻¹) | $10^4 \cdot k_{\text{obs2}}$ (s ⁻¹) |
|--|---|---|
| 0.5 | 11.9 | 2.58 |
| 1 | 6.60 | 3.16 |
| 1.5 | 5.38 | 4.07 |
| 2 | 4.43 | 5.08 |
| 2.5 | 3.39 | 5.98 |

A comparison with the oxidation of *o*-xylene under similar conditions reveals rate constants [32] larger than in that case, probable due to the absence of steric effects. As it can be seen from the table 3, the concentration of hydrogen ion has an opposite effect on the two stages of the reaction. It diminishes the rate constants of the first step, according to equation below, and reveals the loss of the proton:

$$k_{\text{obs1}} = \frac{(3.30 \cdot 10^{-2} \pm 4.5 \cdot 10^{-4})}{1 + (3.67 \pm 1.90)[\text{H}^+]} \quad (7)$$

with $R^2 = 0.9569$, $\chi^2 = 1.74 \cdot 10^{-6}$ for $N = 15$. It causes a linear increase of the rate constant of the second stage according to:

$$k_{\text{obs2}} = (1.6 \cdot 10^{-4} \pm 1.1 \cdot 10^{-5}) + (1.7 \cdot 10^{-4} \pm 7.6 \cdot 10^{-6})[\text{H}^+] \quad (8)$$

with $R^2 = 0.9750$, $\chi^2 = 4.4 \cdot 10^{-10}$, $N = 15$.

The influence of ionic strength on the reaction rate was also studied. As it can be seen from table 5, ionic strength has a positive effect on both the

Table 5

Influence of ionic strength on the rate constants for both processes
 $[\text{Ce(IV)}] = [\text{Ce(III)}] = 8.0 \times 10^{-5} \text{ mole.L}^{-1}$; $[\text{p-xylene}] = 4.0 \times 10^{-4} \text{ mole.L}^{-1}$; $t = 40^\circ\text{C}$

| μ | $10^3 k_{\text{obs1}}$ (s ⁻¹) | $10^4 k_{\text{obs2}}$ (s ⁻¹) |
|-------|---|---|
| 0.5 | 2.14 | 0.57 |
| 1 | 3.29 | 1.13 |
| 1.5 | 4.43 | 1.51 |
| 2 | 5.58 | 2.09 |
| 2.5 | 6.38 | 2.91 |
| 3 | 7.77 | 3.31 |

first and the second stage of the reaction. Although Debye – Hückel relation for activity coefficients could be applied only at lower ionic strengths ($\approx 10^{-2}$) we have plotted the equation of the form

$$\lg k_{\mu} = \lg k_{\mu=0} + \frac{\text{Const} \sqrt{\mu}}{1 + \sqrt{\mu}} \quad (9)$$

and have obtained a linear dependence for both stages of the oxidation process

$$\lg k_{\text{obs1}} = (-3.72 \pm 0.04) + (2.51 \pm 0.09) \frac{\sqrt{\mu}}{1 + \sqrt{\mu}} \quad (10)$$

with $R^2 = 0.9830$, $\chi^2 = 3.6 \cdot 10^{-3} \cdot 0.013$, $N = 18$ and

$$\lg k_{\text{obs2}} = (-5.89 \pm 0.06) + (3.43 \pm 0.13) \frac{\sqrt{\mu}}{1 + \sqrt{\mu}} \quad (11)$$

with $R^2 = 0.983$, $\chi^2 = 6.5 \cdot 10^{-3}$, $N = 18$., respectively. Even so, we can only say that the influence of ionic strength has a contribution of primary salt effect as well as secondary salt effect, and seems to involve ions of like charges (positive slopes).

Activation parameters were determined for both stages of the reaction from the Arrhenius and from the Eyring plots. The effect of the temperature is presented in table 6, and activation parameters in Table 7 along with those for the water oxidation.

The values of activation energy and enthalpy for the first stage are quite small. The negative activation entropy is in agreement with the involvement of the adduct formation pre-equilibrium. The reaction of electron-transfer claims a little bit higher activation energy. The entropy modification in this stage is also negative, suggesting a bimolecular process namely the proton assisted formation of Ce(III) and an uni-equivalent oxidised product.

Concerning the second step, by taking into consideration all the effects of concentrations, the rate law takes of the form:

$$r = k_2 \frac{a [\text{p-xylene}]_0 [\text{H}^+] [\text{Ce(IV)}]}{1 + b [\text{p-xylene}]_0} \quad (12)$$

A reaction mechanism can be suggested, based on recorded spectra, the stoichiometry, rate law of the two stages and the effect of ionic

Table 6

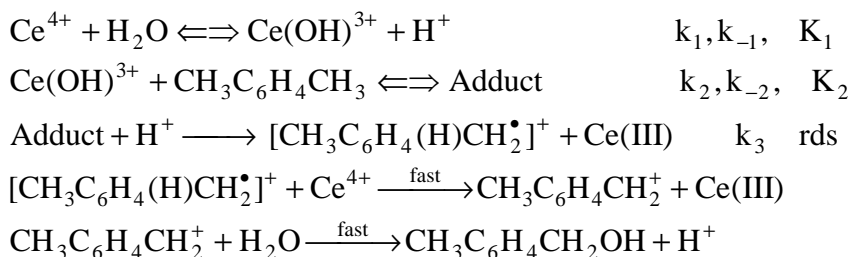
Temperature effect on the first-order rate constants. $[\text{H}^+] = 1.5 \text{ mole} \cdot \text{L}^{-1}$
 $\mu = 2.0$; $[\text{Ce(IV)}] = [\text{Ce(III)}] = 8.0 \times 10^{-5} \text{ mole} \cdot \text{L}^{-1}$; $[\text{p-xylene}] = 4.0 \times 10^{-4} \text{ mol} \cdot \text{L}^{-1}$

| Temp. (K) | 308 | 313 | 318 | 323 | 328 | 333 |
|--|------|------|-------|------|------|------|
| $10^{24} k_{\text{ap1}} (\text{s}^{-1})$ | 0.86 | 0.84 | 1.12. | 1.58 | 2.74 | 3.56 |
| $10^4 k_{\text{ap2}} (\text{s}^{-1})$ | 1.22 | 1.25 | 2.01 | 3.39 | 5.94 | 6.90 |

Table 7Activation parameters for the two stages of oxidation of *o*-xylene.

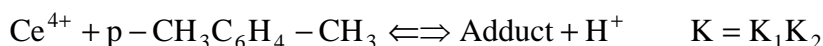
| Stage | E _a (kJ/mol) | ΔH [‡] (kJ/mol) | ΔS [‡] (J/K) |
|-----------------|-------------------------|--------------------------|-----------------------|
| 1 | 58.4±4.4 | 57.1±4.4 | -102.6±8.6 |
| 2 | 73.2±5.6 | 70.64±5.7 | -92.6±7.2 |
| Water oxidation | 88.6±3.4 | 86.0±3.5 | -40.9±2.6 |

strength. It involves the formation of an adduct between *p*-xylene and the hydroxo-complex of Ce(IV), followed by the oxidation of the adduct by an inner electron transfer. It is presented in the scheme below:



The species $[\text{CH}_3\text{C}_6\text{H}_4(\text{H})\text{CH}_2^\bullet]^+$ is a free radical cation. The rate-determining step involves a proton assisted electron transfer, to stabilise the formed free radical. It is difficult to assign the position of this hydrogen ion. It may be bound either to the nucleus (π electron system conjugated with the free electron on methylene group) or to the side group [36]. The subsequent steps - the oxidation to carbenium ion and its hydrolysis - are very rapid leading finally to the major oxidation product, which is *p*-methylbenzylic alcohol.

If the first two pre-equilibria are combined as follows:



than the rate equation determined from the mechanism suggested by us will have the form of equation (13)

$$r = k_3 K_1 K_2 \frac{[\text{Ce(IV)}][\text{H}^+][p\text{-xylene}]_0}{1 + K_1[\text{H}^+] + K_2[p\text{-xylene}]_0} \quad (13)$$

that is in agreement with the kinetic and extra-kinetic data we have obtained, provided that the second term in the denominator is not too important.

To get more arguments about the suggested mechanism, we have followed the oxidation reaction of substituted toluene, and tried to see if a Hammett correlation holds. Such LFER might be used to diagnose mechanism by determining the extent of bond formation or breakage in the transition state or by assessing the electronic and polar effects on the rate. As presented before, the apparent first-order rate constant for the second

Table 8

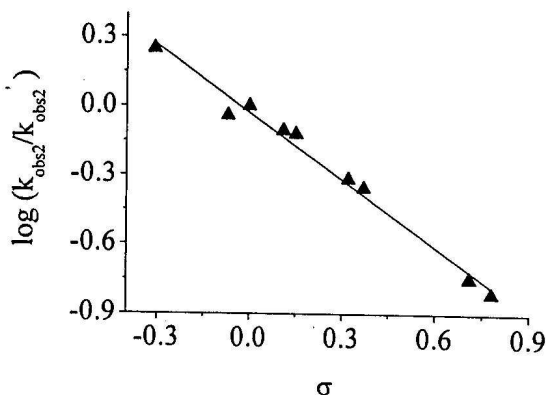
Observed first-order rate constants for the oxidation process ($k_{\text{obs}2}$) and substituent constants at $[\text{Ce(IV)}]_0 = [\text{Ce(III)}]_0 = 8 \cdot 10^{-5} \text{ mole.L}^{-1}$; $[\text{p-xylene}] = 1.0 \cdot 10^{-3} \text{ mole.L}^{-1}$; $\mu = 2.0$ and temperature of 40°C [37,38]

| Substrate | σ | $10^4 k_{\text{obs}2} (\text{s}^{-1})$ |
|---------------------------------|----------|--|
| <i>p</i> -Xylene | -0.31 | 7.80 |
| <i>m</i> -Xylene | -0.07 | 4.02 |
| Toluene | 0.0 | 3.92 |
| <i>p</i> -Chlorotoluene | 0.11 | 3.46 |
| <i>p</i> -Bromotoluene | 0.15 | 3.30 |
| <i>p</i> -Toluenesupphonic acid | 0.32 | 2.12 |
| <i>m</i> -Chlorotoluene | 0.37 | 1.95 |
| <i>m</i> -Nitrotoluene | 0.71 | 0.68 |
| <i>p</i> -Nitrotoluene | 0.78 | 0.45 |

stage (by allowing for the water oxidation) were calculated for nine compounds. Data are presented in table 8 and the line in figure 4. The Hammett equation in the form $\lg k_{\text{obs}2} = \lg k_0 + \rho\sigma$ by using the data in the table is:

$$\lg k_{\text{obs}2} = -(3.38 \pm 0.03) - (1.08 \pm 0.04)\sigma \quad (14)$$

with $R^2 = 0.951$, $\chi^2 = 2.1 \cdot 10^{-3}$, $N = 9$. It suggests a common mechanism. As the equation stipulates ($\rho < 0$) the electron-releasing substituents increase the oxidation rate, while the electron-withdrawing substituents have the

**Fig. 4.** Hammett plot of the second stage first-order rate constant

opposite effect. The reaction constant, negative and close to unity, suggests a free radical mechanism [39]. The $\rho = -1.08$ is in agreement with the one of the oxidation in acetic acid with perchloric acid addition of $\rho = -1.7$ [39]. Here, because of lower dielectric constant as compared to water, the field effects are more important and a higher reaction constant value should be expected.

ACKNOWLEDGEMENT. This work was supported by the National Research Council of the Ministry of Education and Research (CNCSIS) under Grant.33374/2004, no. 60 Code 164, for which the authors wish to acknowledge.

REFERENCES

1. Gopal Rao G., Madhava Rao B., *Anal. Chim. Acta*, **1972**, 59(3), 461
2. Trahanovsky, W. S., Young L. B., *J. Org. Chem.*, **1966**, 31, 2033
3. Syper L., *Tetrahedron Letters*, **1966**, 37, 4493
4. Baciocchi E., Rol C., Sebastiani G. V., *J. Chem. Research(Synopsis)*, **1983**, 9, 232
5. Das A. K., Das M., *J. Chem. Soc. Dalton Trans.*, **1994**, 589
6. Willard H. H., Young P., *J. Am. Chem. Soc.*, **1930**, 52, 132
7. Pondit A. K., Das A. K., Banerjee D., *Transitionmet. Chem.*, **1991**, 16, 324
8. Hintz H. L., Johnson D. C., *J.org.chem.*, **1967**, 32, 556
9. Duke F. R., Bremer R. F., *J. Am. Chem. Soc.*, **1951**, 73, 5179
10. Waters W. A., Jones J. R., Litter J. S., *J. Chem. Soc.*, **1961**, 240
11. Muhammad S. S., Rao K. V., *Bull. Chem. Soc. Jpn.*, **1963**, 36, 943
12. Ardon M., *J. Chem. Soc.*, **1957**, 1811
13. Hargreaves G., Sutcliffe L. H., *Trans. Faraday Soc.*, **1955**, 51, 1105
14. Sankhla P. S., Mehrotra R. N., *J. Inorg. Nucl. Chem.*, **1972**, 34, 3781
15. Rangaswamy M., Santappa M., *Acta Chim. Acad. Sci. Hung.*, **1968**, 56, 413
16. Grover V. K., Gupta Y. K., *J. Inorg. Nucl. Chem.*, **1969**, 31, 1403
17. Wells C. F., Husain M., *Trans. Faraday Soc.*, **1970**, 66, 679
18. Balasubramanian T. R., Venkata subramanian N., *Indian J. Chem.*, **1970**, 8, 305
19. Dayal R., Bakore G. V., *Indian J. Chem.*, **1972**, 10, 1165
20. Rao G. N., *Indian J. Chem.*, **1970**, 8, 328
21. Krishna B., Tewari K. C., *J. Chem. Soc.*, **1961**, 3077
22. Ignaczak M., Dziegiec J., Markiewicz M., *Pol. J. Chem.*, **1980**, 54, 1121
23. Sethuram B., Muhammad S. S., *Acta Chim. Acad. Sci. Hung.*, **1965**, 46, 115
24. Sethuram B., Muhammad S. S., *Acta Chim. Acad. Sci. Hung.*, **1965**, 46, 125
25. Trahanovsky W. S., Young L. B., Brown G. L., *J. Org. Chem.*, **1967**, 32, 3865
26. Paquette D., Zador M., *Can. J. Chem.*, **1968**, 46, 3507
27. Melicherik M., Treindl L., *Chem. Zvesti*, **1981**, 35, 153
28. Wiberg K. B., Ford P. C., *J. Am. Chem. Soc.*, **1969**, 91, 124
29. Ignaczak M., Deka M., *Pol. J. Chem.*, **1980**, 54, 259
30. Ramaswamy M. S., Venkatachalapathy M. S., Udupa H. V. K., *Bull. Chem. Soc. Jpn.*, **1962**, 35, 214
31. Claudia G. Muresanu, I. Baldea, Gabriela C. Bucsa *Rev. Roum. Chem.*, **2000**, 45, 111.
32. Gabriela C. Bucsa, Claudia G. Muresanu, I. Baldea, *Studia Univ. Babes-Bolyai, Chem.*, **2003**, 49(1), 125.
33. D. Kolp, H. C. Thomas., *J. Am. Chem. Soc.*, **1949**, 71, 3047
34. Gabriela C. Bucsa, Claudia G. Muresanu, I. Baldea, *Studia Univ. Babes-Bolyai, Chem.*, **2002**, 48(1-2), 67..
35. D. Kolp, H. C. Thomas., *J. Am. Chem. Soc.*, **1949**, 71, 3047

36. G. Calvaruso, F. P. Cavaşino, C. Sbriziolo, *Int. J. Chem. Kinet.*, **1981**, 13), 135
37. H. C. Brown, Y. Okamoto, *J. Am. Chem. Soc.*, 1958, 80, 4979.
38. H. Zollinger, *Helv. Chem. Acta.*, 1953, 36, 1730.
39. Radhakrishna P. S., Pati S. C., *Chem. Ind.*, **1967**, 17, 702

KINETIC STUDY ON OMEPRAZOLE ACID REACTION AT DIFFERENT PH VALUES BY USING HPLC

L. VLASE¹, I. BALDEA² S. LEUCUTA¹,
L. RUS³ and L. COPOLOVICI²

¹Department of Pharmaceutical Technology & Biopharmaceutics, University of Medicine and Pharmacy "Iuliu Hatieganu" Cluj, 13 Emil Isac St. Cluj 400023, Romania

²Department of Physical Chemistry, Faculty of Chemistry and Chemical Engineering of "Babeș-Bolyai" University, 11 Arany Janos, 400028, Cluj-Napoca, Romania

³Department of Drug Control, University of Medicine and Pharmacy "Iuliu Hatieganu" Cluj, 13 Emil Isac St. Cluj 400023, Romania

ABSTRACT. High performance liquid chromatography (HPLC) has been used to monitor the time evolution of omeprazole under various pH conditions. First-order rate constants for the transformation into sulphenamide, the active inhibitor of the gastric secretion, were determined at 25°C. They depend strongly on the acidity of the medium. From this dependence, the first pKa value of omeprazole was calculated, based on kinetic measurements. The acid-catalysed rate constant has been deduced.

Keywords: omeprazole, kinetics, pKa, acid catalysis.

INTRODUCTION

Omeprazole, 5-Methoxy-2-(4-methoxy-3,5-dimethyl-2-pyridinyl-methyl-sulfinyl)-1,4-benzimidazole (abbreviated as OPZ), with the chemical structure shown in figure 1 is a substituted benzimidazole that inhibits gastric secretion by altering the activity of H⁺/K⁺ATPase, which is the final common step of acid secretion in parietal cells [1-3]. OPZ itself is not an active inhibitor of this enzyme, but is transformed within the acid compartments of the parietal cells into the active inhibitor [4]. It has been used for more than two decades in the treatment of peptic ulcers [5], reflux esophagitis [6] and the Zollinger-Ellison syndrome [7]. The active inhibitor has been shown to be a cyclic sulphenamide (two isomers), which reacts with mercapto groups in the enzyme with the formation of a disulfide complex thus inactivating the H⁺ and K⁺-ATPase. These reactions lead to the blockade and have been studied both *in vivo* and *in vitro* [8]. Based on more than 200 million patient treatments it has been demonstrated that OPZ is a safe drug with no reported dose related side effects. OPZ is commercially available as enteric-coated granules encased in gelatine capsules, with a delayed-release of the medicine [9].

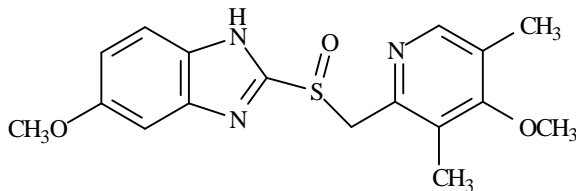


Fig. 1. Chemical structure of Omeprazole (OPZ)

The kinetics and the mechanism of the OPZ transformation have been studied by Arne Brändström and co-workers [10, 11] in the presence of 2-mercaptoethanol to simulate the formation of a disulfide bond with the enzyme.

In this study, we have followed the degradation of OPZ in buffered solutions of various pH and obtained the dependence of observed rate constant vs. hydrogen concentration. First acid dissociation constant has been determined on a kinetic base.

EXPERIMENTAL

Materials: Chemicals of analytical grade and ultra-pure water (de-ionised and tetra-distilled) were used throughout this study. A stock solution of 10 µg/mL of OPZ was prepared in methanol. The pH-buffer was prepared from K₂HPO₄ and citric acid. Working solution of OPZ (1 µg/mL) was prepared before each runs from 0.1 mL stock solution and 0.9 mL of previously prepared pH-buffer.

Apparatus: The HPLC system was an 1100 series model (Agilent Technologies, USA) consisted of a binary pump, an in line degasser, an auto sampler, a column thermostat and an UV detector. Data were achieved and computed by ChemStation software (ver. A.09.03). The detector wavelength was set as 303 nm. Chromatographic separation was performed in 3.5 minutes at 35 °C with a Zorbax SB-C18 100 x 3.0 mm I.D., 3.5 µm (Agilent Technologies, USA), protected by an on-line filter.

A Mettler-Toledo (Greifensee, Switzerland) model MP225 was used to adjust pH of sample solutions. The mobile phase consisted in an acetonitrile: sol K₂HPO₄ 20 mmol/L (27:73 v/v). Kinetic fitting was performed with WinNonlin Professional (Pharsight, USA).

Procedures: A series of pH-buffer solutions were prepared. The values of the pH for these solutions were 2.3, 3, 3.3, 4, 4.3, 5, 5.3, 6, 6.3 and 7. Each component solution was degassed for 10 minutes in an Elma Transsonic 700/H (Singen, Germany) ultrasonic bath. Using these solutions, every sample mixture was prepared from 0.1 mL stock solution of OPZ and 0.9 mL of pH buffer. Temperature has been maintained constant at 25.0±0.1 °C by means of a Lauda M-20 thermostat. Aliquots of the mixture were taken at different time periods and analysed by HPLC. The injection volume was 10 µL. The pump delivered the mobile phase at a flow of 1 mL/min.

RESULTS AND DISCUSSIONS

It is known that the OPZ concentration decreases with time in acidic solution. The samples were performed at pH values between 2.2 and 7. OPZ concentrations were determined by using high-performance liquid chromatographic (HPLC) methods used by Kobayashi *et. al.* [12] and Amantea and Narang [13]. The HPLC method can be used in stability studies because there is no interference between the drug and its decomposition products [14, 15].

Figure 2 shows chromatograms for OPZ at time 0 and after 4 minutes

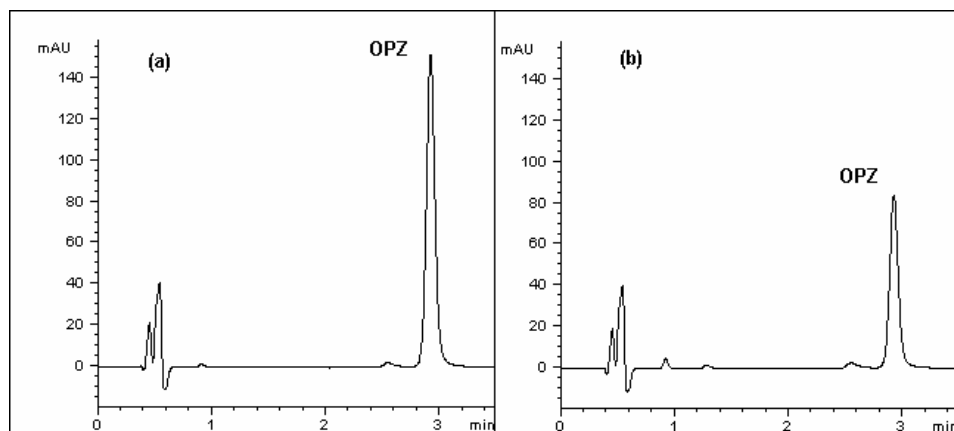


Fig. 2. Chromatograms of OPZ at $t = 0$ (a) and after 4 minutes (b)

Using chromatographic data it is possible to calculate the omeprazole concentrations at different time intervals elapsed after mixing. Figure 3 presents concentration dependence as a function of time for five pH values

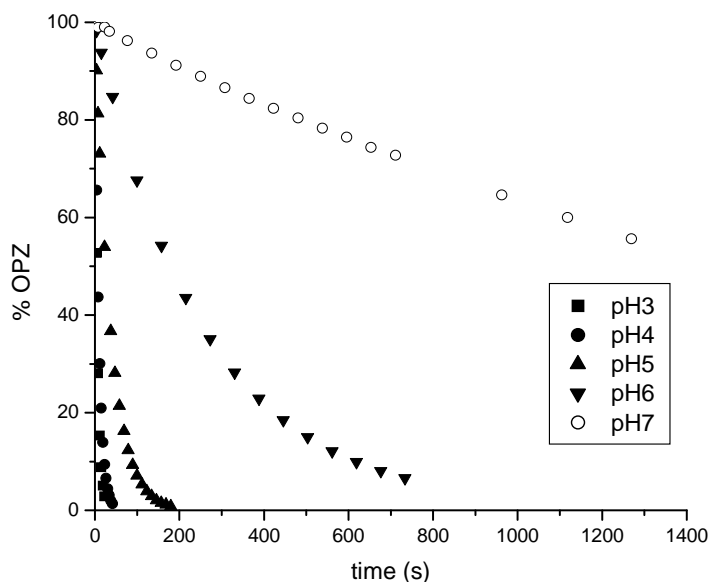


Fig. 3. The omeprazole concentration as a function of time

The concentration–time curves were well described by an exponential dependence:

$$[\text{OPZ}] = [\text{OPZ}]_0 \cdot e^{-k_{\text{obs}} \cdot t} \quad (1)$$

where k_{obs} stands for the apparent first-order rate constant, involving decomposition of OPZ. Indeed, good correlation coefficients were obtained (0.990 - 0.9990) by using a least-square method for linear first-order dependence. However, we took advantage of a non-linear WinNonlin Professional (Pharsight, USA) method to compute first-order rate coefficients k_{obs} at different pH values. Data are presented in Table 1 as means of two or three replicate runs.

The omeprazole degradation exhibits a complex dependence on the acidity. A plot of k_{obs} vs. pH is a curve with an inflexion point at pH=4.32. Observed first-order rate constant dependence on hydrogen ion concentration is well described by the following equation:

$$k_{\text{obs}} = \frac{a[\text{H}^+]}{b + [\text{H}^+]} = \frac{(0.189 \pm 0.007)[\text{H}^+]}{[\text{H}^+] + (8.1 \pm 1.2) \cdot 10^{-5}} \quad (2)$$

with $\chi^2 = 9.1 \cdot 10^{-5}$ and $r^2 = 0.9911$.

Table 1

Apparent first-order rate constant at various pH values.

| pH | $[\text{H}^+]$ (mmol/L) | k_{obs} (min^{-1}) |
|-----|-------------------------|--|
| 2.3 | 5.0119 | 0.2050 |
| 3 | 1.0000 | 0.1650 |
| 3.3 | 0.5012 | 0.1490 |
| 4 | 0.1000 | 0.1050 |
| 4.3 | 0.0501 | 0.0770 |
| 5 | 0.0100 | 0.0260 |
| 5.3 | 0.0050 | 0.0150 |
| 6 | 0.0010 | 0.0030 |
| 6.3 | 0.0005 | 0.0020 |
| 7 | 0.0001 | 0.0004 |

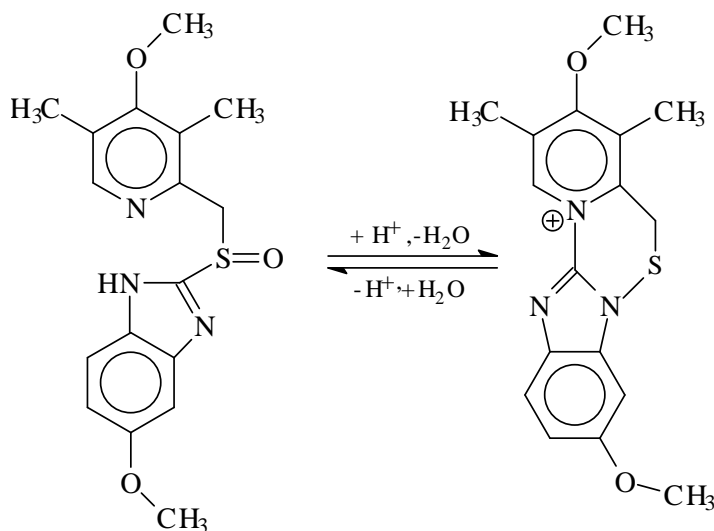
The form of experimental first-order rate constant in equation (2) also suggests the involvement of at least two consecutive reaction steps (two terms in the denominator). Kinetic data fit well with the following reaction scheme; the active species seems to be the protonated omeprazole:



The first stable product is sulfenamide, with the equilibrium shifted to the right.

OPZ can accept a proton on either the pyridine ring or the benzinidazole ring. The cationic species suffers a ring closure with the elimination of a water molecule to form cyclic sulfonamide, also as a cation. The first step in (3) is a rapid one. A plot of $1/k_{\text{obs}}$ as a function of $1/[\text{H}^+]$ should be linear as in equation (4):

$$\frac{1}{k_{\text{obs}}} = \frac{b}{a[\text{H}^+]} + \frac{1}{a} = \frac{2.18 \cdot 10^{-4}}{[\text{H}^+]} + 20.05 \quad (4)$$



If the only reactive species is OPZH^+ , then k_{obs} expressed by eq.2 has the form:

$$k_{\text{obs}} = \frac{k_2[\text{H}^+]}{[\text{H}^+] + k_{-1}/k_1} = \frac{k_2[\text{H}^+]}{[\text{H}^+] + K_a} \quad (5)$$

and the constants K_a and k_2 can be obtained using the above given equations or the Weighted Sum of Squares of Residuals program (WSSR). The calculated values are $K_a = 8.1 \cdot 10^{-5} \text{ mole} \cdot \text{L}^{-1}$ and $k_1 = 0.19 \text{ L} \cdot \text{mol}^{-1} \text{ min}^{-1}$. Therefore, $\text{p}K_a = 4.1$ for OPZH^+ is deduced from eqs (2) and (5). With the WSSR (WNL program) the best fit corresponds to $\text{p}K_a = 4.38$ and $k_2 = 0.16 \text{ L} \cdot \text{mol}^{-1} \text{ min}^{-1}$ respectively. The acidity constant is in agreement with the literature data [2,10, 11]. Maton, for example, has reported a value of $\text{p}K_a = 4.2$.

ACKNOWLEDGEMENT. Part of this work was supported by the National Research Council of the Ministry of Education and Research (CNCSIS) under Grant. 33374/2004, no. 60 Code 164, for which the authors wish to acknowledge.

REFERENCES

1. D. McTavish, M. T. Buckley, R.C. Heel, *Drugs*, 42, 1991, 138-170.
2. P. N. Maton, N. Engl, *J. Med.*, 324, 1991, 965-975.
3. B. Wallmark, P. Lorentzon, H. Larson, *Scand.J. Gastroenterol.* 20 Suppl., 108, 1985, 37-52.
4. B. Wallmark, A. Bradstrom, H. Larsen, *Biochem, Biophys. Acta.*, 260, 1985, 4591.

5. R. N. Brogden, A. A. Carmine, R. C. Heel, T. M. Spelght, G. S. Avery, *Drugs*, 24, 1982, 267-302; K. Lauritsen, S. J. Rune, P. Bytzer, H. Helback, K. G. Jansen, *N. Engl. J. Med.*, 312, 1985, 985-961.
6. J. G. Hatlebakk, A. Berstad, *Clin. Pharmacokinet.*, 31, 1996, 386-406.
7. K. Onberg, H. Lindstrom, *Lancet*, 1983, 66-67.
8. P. Lindberg, P. Nordberg, T. Almlinger, A. Brändström, *J. Med. Chem.*, 29, 1986, 1327-1336,
9. V. K. Sharma, *Am. J. Health-Syst. Pharm.*, 56(4), 1999, 518-521.
10. A. Brändström, P. Lindberg, N. Bergman, T. Almlinger, K. Ankner, U. Junngren, B. Lamm, P. Nordberg, M. Erickson, I. Grundevik, I. Hagin, K. Hoffmann, S. Johansson, S. Larsson, I. Loffberg, K. Ohlson, B. Persson, I. Skanberg, L. Tekenbergs-Hjelte, *Acta Chem. Scand.*, 43, 1989, 536-548.
11. A. Brändström, P. Lindberg, N. Bergman, T. Almlinger, K. Ankner, U. Junngren, B. Lamm, P. Nordberg, M. Erickson, I. Grundevik, I. Hagin, K. Hoffmann, S. Johansson, S. Larsson, I. Loffberg, K. Ohlson, B. Persson, I. Skanberg, L. Tekenbergs-Hjelte, *Acta Chem. Scand.*, 43, 1989, 549-568.
12. K. Kobayashi, K. Chiba, D. R. Sohn, *J. Chromatogr.*, 579, 1992, 299-305.
13. M. N. Amantea, P. K. Narang, *J. Chromatogr.*, 426, 1988, 216-222.
14. S. Mangalan, B. P. Ronanbhai, K. Balkriskna, *J. Planar. Chromatogr., Mod.*, 4, 1991, 492-493.
15. D. Castro, M. A. Moreno, S. Torrado, J. L. Lasters, *J. Pharm. Biomed. Anal.*, 21, 1999, 291-298.

COMPOSITE CARBON ELECTRODES WITH ENHANCED STABILITY BASED ON POLYANILINE INCORPORATING PRUSSIAN BLUE FOR AMPEROMETRIC DETECTION OF H₂O₂

LIANA M. MURESAN*, CRISTINA ISVORANU

*Faculty of Chemistry and Chemical Engineering, "Babes-Bolyai" University,
11 Arany Janos Str., RO-400028, Cluj-Napoca, Romania. *E-mail: limur@chem.ubbcluj.ro*

ABSTRACT. The obtaining of composite glassy carbon modified electrodes based on a conducting polymer (polyaniline, PANI) matrix entrapping a polynuclear inorganic compound (Prussian Blue, PB) with redox properties is reported. The electrocatalytic activity towards H₂O₂ reduction of PB+PANI modified glassy carbon electrodes and their electrochemical stability were studied and compared to those of PB modified electrodes prepared through simple electrodeposition of the inorganic compound onto glassy carbon (GC/PB). It was confirmed that the GC/PB+PANI modified electrodes present stable electrochemical behavior and showed good electrocatalytic efficiency for H₂O₂ reduction.

Keywords: composite electrodes, Prussian Blue, polyaniline, cyclic voltammetry, amperometric detection, hydrogen peroxide

INTRODUCTION

The development of amperometric sensors/biosensors on the basis of Prussian Blue (PB) modified electrodes aims to valorize the excellent catalytic efficiency of this inorganic mediator, comparable to that of biological catalysts, towards the reduction of both O₂ and H₂O₂ [1-3]. However, these modified electrodes still face some drawbacks with regarding the long-term stability and sensitivity to pH changes [4].

Among various techniques for increasing the electrodes stability, the mediator entrapment in an electrogenerated polymer film appears a simple and attractive method for fabricating PB modified electrodes [5]. Such one-step immobilization procedure allows the facile functionalization of electrode surfaces [6] as well as the electrochemical control of polymer film thickness [7].

Polyaniline (PANI) is one of the most studied and promising conducting polymers due to its chemical stability, easy polymerization, high electronic conductivity following partial oxidation, good protonic conductivity and a relatively long period of stability in acid media [8, 9]. The great interest in this polymer stems from its ability to be rapidly and reversibly cycled between the differently colored conductive (partially oxidized, emeraldine) and insulating (completely reduced and oxidized, leucoemeraldine and pernigraniline, respectively) states [10]. Additionally, in the case of PB, a hexacyanometallate, it is supposed to act the concept of electrostatic stabilization originating from the ability of the positively charged conducting polymer backbone (PANI) to attract the negatively charged cyanometallate [9].

In this context, in the present work, we propose to prepare composite glassy carbon (GC) modified electrodes based on a conducting polymer (PANI) matrix into which a polynuclear inorganic compound (PB) with redox properties is

introduced. The electrochemical stability of glassy carbon electrodes modified with PB and PANI (GC/PB+PANI) and their electrocatalytic activity towards H_2O_2 reduction were studied and compared to those of GC/PB modified electrodes prepared through simple electrodeposition of the inorganic compound on GC.

EXPERIMENTAL SECTION

Reagents

Hydrogen peroxide was purchased from Merck (Darmstadt, Germany). All other reagents were of analytical grade and used as received. The solutions were prepared using distilled water.

Preparation of modified electrodes

Prior to surface modification, the glassy carbon electrode of ~ 3 mm diameter, was mechanically wet polished with fine grade aqueous alumina slurry (grain size, 0.25 μm) on a polishing cloth.

The electrodeposition of Prussian Blue on glassy carbon was accomplished in a solution containing 2 mM FeCl_3 + 2 mM $\text{K}_3[\text{Fe}(\text{CN})_6]$ + 0.5 M KCl + 1M HCl as described in [9]. Typically, 20 full potential cycles were applied in the potential range from -0.10 to 1.0 V, at a scan rate of 50 mV/s. The GC/PB modified electrodes were then carefully washed with water and dried 1h at 100 °C.

Similarly, PANI was electrogenerated on the CV substrate from a solution containing 0.22 M aniline and 0.5 M KCl + 1 M HCl in the potential range from -0.10 to 1.0 V, at a scan rate of 50 mV/s.

The composite PB-PANI films were electrodeposited from a solution containing 2 mM FeCl_3 + 2 mM $\text{K}_3[\text{Fe}(\text{CN})_6]$ + 0.22 M aniline in 0.5 M KCl + 1M HCl through potential scanning in the same potential range as mentioned above.

Electrochemical measurements

Electrochemical measurements were performed using an electrochemical analyzer (Autolab-PGSTAT10, Eco Chemie, Utrecht, The Netherlands) connected to a PC for potential control and data acquisition. The electrochemical deposition of PB onto the GC electrode and the voltammetric investigation of the modified electrodes were carried out using a typical three-electrode electrochemical cell. The modified electrodes were used as working electrodes, a platinum ring as counter electrode and a saturated calomel electrode (SCE) as reference electrode.

For each electrode, the surface coverage (Γ , mol cm^{-2}) was estimated from the under peak areas, recorded during the cyclic voltammetry (CV) measurements at a low scan rate ($v < 10 \text{ mV s}^{-1}$), and considering the surface redox valence equal to unity [11]. All presented results are the average of at least 3 identically prepared electrodes, if not otherwise mentioned.

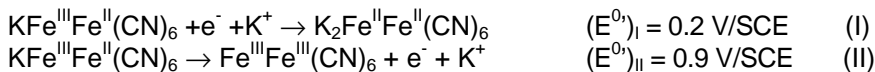
Amperometric batch measurements were carried out with the modified electrodes at an applied potential of - 50 mV vs. SCE and under constant magnetic stirring, in the presence of various concentrations of H_2O_2 .

Stability measurements were carried out for GC/PB and GC/PB+PANI modified electrodes under potentiodynamic conditions. The electrode potential was cycled continuously at 50 mV/s, within the potential range covering the mediator redox activity ($\pm 120 \text{ mV}$ relative to its standard formal potential), during 80 cycles, in a 0.5 M KCl + 1M HCl solution.

RESULTS AND DISCUSSION

Preparation of modified electrodes

The cyclic voltammograms recorded during GC modification with PB in a solution containing 2 mM FeCl_3 + 2 mM $\text{K}_3[\text{Fe}(\text{CN})_6]$ in 0.5 M KCl + 1 M HCl (figure 1a) exhibited two peak pairs corresponding to the following redox processes [13]:



The formal standard potentials were estimated as the average of the cathodic and anodic peak potentials [12]. All following results will refer to the first peak pair, due to its redox formal potential, well placed in the optimal potential domain for amperometric detection [14]. The electrochemical parameters of this voltammetric wave ($\Delta E_{\text{peak, I}} = 60 \text{ mV}$; $\Gamma = 3 \text{ nmol cm}^{-2}$) point to a monoelectronic, quasi-reversible couple. The increase of peak currents with the number of cycles confirms the increase of film thickness during electrodeposition.

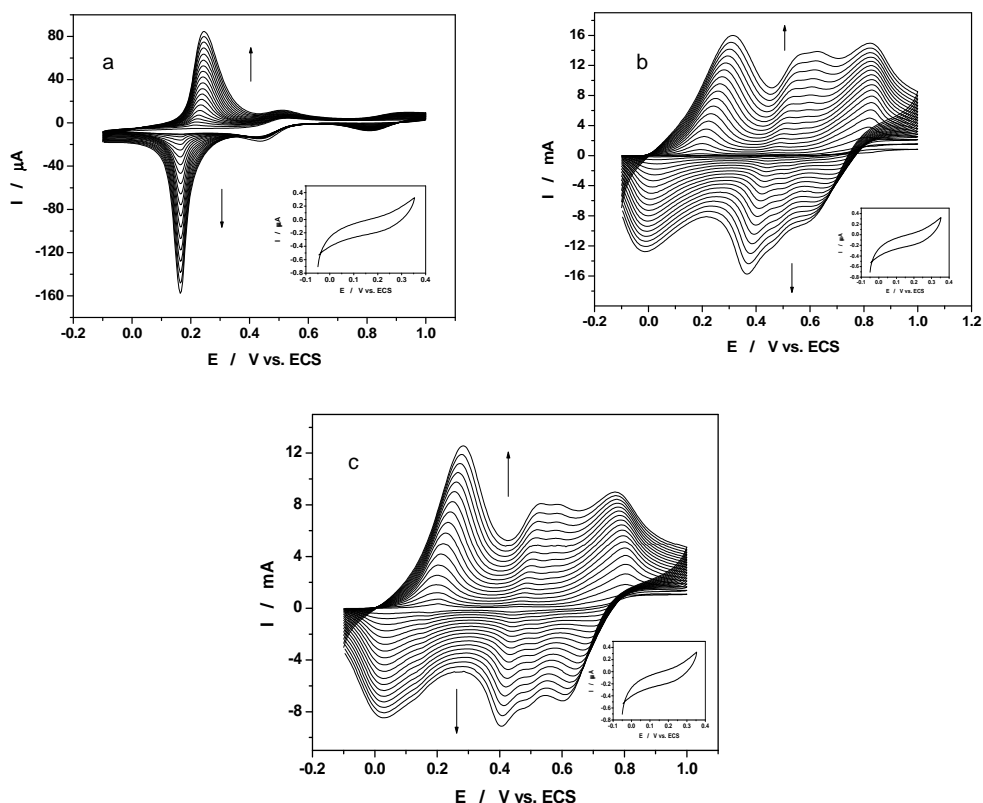
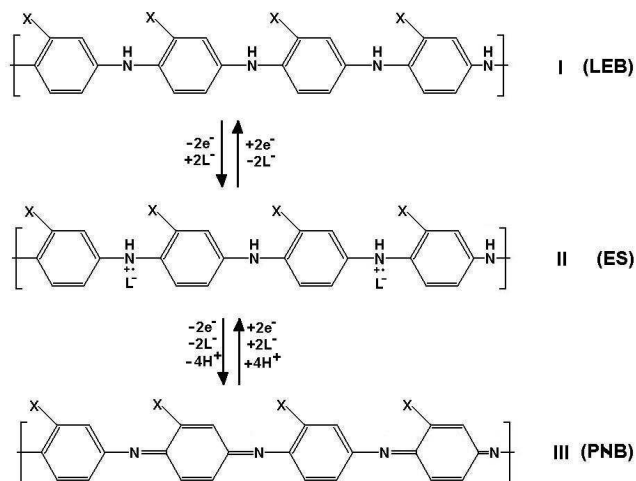


Figure 1. The CVs corresponding to (a) PB; (b) PANI and (c) PB+PANI film formation on a GC surface. Scan rate: 50 mV / s. *Insets:* The CV for GC in 0.5 M KCl + 1 M HCl.

The growth of PANI on the GC surface during electro-polymerization is slow at the beginning of the polymerization, but increases considerably after the first cycles. In the corresponding cyclic voltammogram, (figure 1b), the first redox couple with $E^0 = 153$ mV vs. SCE is attributed to the Leucoemeraldine (LEB)-Emeraldine salt (ES) transition from Scheme 1 [10]. The second redox couple with $E^0 = 464$ mV vs. SCE is usually associated with a degradation product of PANI. The third redox couple at $E^0 > 600$ mV vs. SCE corresponds to the ES- Pernigraniline (PNB) transition [9].



Scheme 1. The redox behavior of PANI

The only electrically conducting form is, the emeraldine salt form (ES), which is the protonated form of LEB. The protonation process is reversible and represents the basis for the pH sensitivity of PANI [10].

The voltammograms corresponding to the composite PB-PANI films electro-deposition from a solution containing 2 mM FeCl_3 + 2 mM $\text{K}_3[\text{Fe}(\text{CN})_6]$ + 0.22M aniline in 0.5 M KCl + 1M HCl are presented in Figure 1c. As expected, the peak currents systematically increase in the course of voltammetric potential cycling. The result is consistent with the view that, as usual, organic polymer (PANI) layers are generated on the electrode surface during positive potential scans, whereas polynuclear PB microstructures are electrodeposited during negative potential scans [9].

It should be noticed that the anodic peak potentials characteristic of PANI behavior in composite film are slightly shifted towards more negative values when compared to their position in PANI (PB-free) film investigated in the same electrolyte. The most likely explanation of this observation lies on the existence of electrostatic attraction forces between the negatively charged PB and the positively charged PANI fragments. Another argument in this sense is the decrease of width at half height of the voltammetric peaks (results not shown), pointing to the existence of

lateral interactions between the species inside the film [15]. Consequently, regardless of the nature of interactions between PB and PANI, the composite PB/PANI system cannot be considered as a simple mixture of single components, PB and PANI.

Electrocatalytic activity for H_2O_2 electro-reduction

In order to check the electrocatalytic activity of the above-mentioned modified electrodes towards H_2O_2 reduction, their amperometric responses were recorded in the absence and in the presence of different concentration of H_2O_2 in an electrolyte containing 0.5 M KCl + 1M HCl (pH 0), at $E = -0.05$ V vs. SCE.

Contrarily to GC/PB and GC/PB+ PANI modified electrodes, GC/PANI modified electrode exhibited no activity towards H_2O_2 reduction. The analytical parameters for H_2O_2 detection extracted from the amperometric calibration curves for GC/PB and of GC/PB+PANI modified electrodes, in the presence of different concentrations of H_2O_2 (figure 3) are presented in Table 1.

Table 1.

The analytical parameters of amperometric calibration curves for GC/PB and GC/PB+PANI modified electrodes in the presence of H_2O_2 at different pH values. Electrolyte: 0.5 M KCl + 1M HCl; $E = -0.05$ V vs. SCE.

| Electrode | pH | Sensitivity ($\mu A/mM$) | Detection limit (mM) | R / No. points |
|--------------|----|----------------------------|----------------------|----------------|
| GC/PB | 0 | 4.75 ± 0.66 | 0.417 | 0.9967 / 6 |
| GC/PB + PANI | 0 | 28.38 ± 2.78 | 0.294 | 0.9994 / 9 |
| | 3 | 15.43 ± 1.84 | 0.359 | 0.9982 / 8 |

As it can be observed, the slope of the amperometric curves (equal to the electrode sensitivity) is higher in the case of composite GC/PB+PANI electrodes than in the case of GC/PB electrodes. As expected, taking into account the pH sensitivity of polyaniline, based on the protonation-deprotonation equilibrium and the decrease of PB activity at higher pH values, the GC/PB+PANI electrode sensitivity decreases at increasing pH. For the same reasons, the detection limit is improved at more acid pH values and in presence of the polymer.

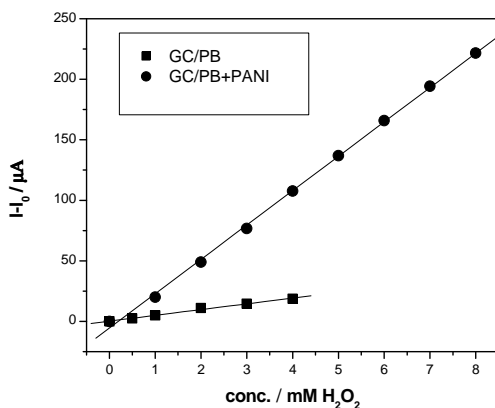


Figure 3. Amperometric calibration curves for GC/PB and GC/PB+PANI modified electrodes. $E = -0.05$ V vs. SCE; Supporting electrolyte: 0.5 M KCl + 1M HCl (pH 0).

Electrochemical stability measurements

Stability tests were carried out for all modified electrodes under potentiodynamic conditions. The electrode potential was cycled continuously at 50 mV/s, within the potential range covering the mediator redox activity (± 120 mV relative to its standard formal potential), during 80 cycles, in 0.5 M KCl + 1M HCl solution. Monitoring the surface coverage, a progressive decrease was observed (results not shown). The electrode deactivation process obeys first-order kinetics as confirmed by the $\ln I_a$ vs. t dependence analysis (figure 4).

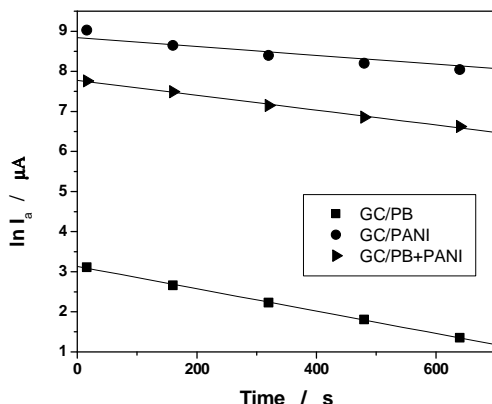


Figure 4. Experimental dependence of $\ln I_a$ vs. time for GC/PB, GC/PANI and GC/PB+PANI modified electrodes cycled in 0.5 M KCl + 1M HCl.

The relatively low values of the deactivation rate constants (Table 2), expressed as the slope of $\ln I_a$ vs. t dependence, proved a good stability of GC/PB + PANI modified electrodes in the investigated potential range, as well as an enhancement of stability in comparison with GC/PB electrodes.

Table 2.

The parameters of $\ln I_a$ vs. t dependence for GC/PB, GC/PANI and GC/PB+PANI modified electrodes

| Electrode | Deactivation constant (s^{-1}) | R / No. of points |
|--------------|------------------------------------|-------------------|
| GC/PB | 0.0028 ± 0.0224 | 0.9996 / 5 |
| GC/PANI | 0.0011 ± 0.1446 | 0.9673 / 5 |
| GC/PB + PANI | 0.0018 ± 0.0381 | 0.9979 / 5 |

CONCLUSIONS

In the present study, the stabilization of Prussian Blue modified electrodes for electroanalytical purposes was achieved by mediator entrapment in an electroconductive polymer (PANI). The attractiveness of this composite system concerns the fact that the formal potential of the Prussian Blue redox process lies in the potential range where PANI is conductive.

The investigated modified electrodes showed good electrocatalytic efficiency and a high electrochemical stability.

ACKNOWLEDGEMENTS

The authors thank to CNCSIS (Grant A 34/349-2004 and A 51/349-2005) for financial support.

REFERENCES

- [1] R. Koncki, *Anal. Chem.*, **2002**, 32, 79;
- [2] A.A. Karyakin, E.E. Karyakina, L. Gorton, *Electrochem. Commun.* **1999**, 1, 78;
- [3] A.A. Karyakin, *Electroanalysis* 2001, 13 (10), 813;
- [4] L. I. Matos, L. Gorton, T. Laurell, A. Malinauskas, A.A. Karyakin, *Talanta*, **2000**, 52, 791;
- [5] P.N. Bartlett, J.M. Cooper, *J. Electroanal. Chem.* **1993**, 362, 1;
- [6] W. Schuhmann, C. Krantz, J. Huber, H. Wohlschläger, *Synth. Met.* **1993**, 61, 31;
- [7] M. Umana, J. Waller, *Anal. Chem.* **1986**, 58, 2979;
- [8] S. Pruneanu, E. Csahok, V. Kertesz, G. Inzelt, *Electrochim. Acta* **1998**, 43, 2305;
- [9] P.J. Kulesza, K. Miecznikowski, M.A. Malik, M. Galkowski, M. Chojak, K. Caban, A. Wieckowski, *Electrochim. Acta* **2001** 46, 4065;
- [10] T. Lindfors, A. Ivaska, *J. Electroanal. Chem.* **2002**, 531, 43;
- [11] H. Huck, *Phys. Chem. Chem. Phys.*, **1999**, 1, 855
- [12] R.W. Murray, *Electroanalytical Chemistry*; Bard, A. J., Ed.; Marcel Dekker: New York, vol. 13, **1984**
- [13] D. Ellis, M. Eckhoff, V.D. Neff, *J. Phys. Chem.*, **1981**, 85, 1225;
- [14] L. Gorton, *Electroanalysis* **1995**, 7(1) 23
- [15] M.J. Honeychurch, G.A. Rechnitz, *Electroanalysis*, **1998**, 5, 285

COMPARATIVE STUDY OF DIGESTION PROCEDURES OF SOILS AND WATER SEDIMENTS USING DIFFERENT HCl/HNO₃ RATIOS FOR MULTIELEMENTAL DETERMINATION

TIBERIU FRENTIU*, MICHAELA PONTA*, EUGEN DARVASI*,
MONICA URSU**, MARIN SENILA**, EMIL CORDOS*

*Babes-Bolyai University, Department of Analytical Chemistry,
Str. Arany Janos 11, 400028 Cluj-Napoca, Romania
**Research Institute for Analytical Instrumentation,
Str. Donath 67, 400293 Cluj-Napoca, Romania

ABSTRACT. The suitability of three digestion procedures using aqua regia (a), Lunge mixture with (b) and without evaporation to dryness (c) was investigated to determine Al, As, Cd, Cr, Cu, Fe, Mn, Ni, Pb, Ti, V and Zn in soils and water sediments. The results for metals determined by ICP-AES in four certified materials digested using the three procedures were compared with the certified values. The dissolution effects for different HCl/HNO₃ ratios are explained and the most adequate digestion methods for the determination of these 12 heavy metals are recommended based on the recovery degree. Cadmium, Cr, Cu, Mn, Ni, Pb and Zn could be determined subsequent any of the three digestion procedures. Aluminium and Fe were quantitatively extracted only in aqua regia, while V and Ti either in aqua regia or Lunge mixture with evaporation to dryness. In the case of As, a volatile element, only the extraction in aqua regia with the collection of gases gave a good recovery degree, while the Lunge procedure without evaporation resulted in an unsatisfactory result.

INTRODUCTION

For most of the determination methods it is necessary to digest the solid samples. The heavy metals like Cd, Cr, Cu, Ni, Pb and Zn in sediments and soils are determined after different digestion procedures including various mixtures of concentrated acids such as HF, HCl, HNO₃, HClO₄ and H₂SO₄ [1,2]. Different digestion equipment can be used: open beakers heated on hot plates, block digestors and digestion bombs placed in conventional and microwave ovens [1,2]. The main advantage of the dissolution of sediment and soil in concentrated inorganic acids are low cost and low salt matrix in final solution resulting in a decreased matrix effect on heavy metals determination [3].

The suitability of four digestion procedures for river sediments in aqua regia, pressure digestion using HNO₃/HF, HNO₃/HF + HCl and HNO₃/HF + HCl in microwave oven were investigated by Krause et al. [4]. The analytical results have showed that only the digestion using HNO₃/HF with subsequent evaporation to dryness and dissolution in HCl have led to appropriate results for more than 50 elements. The procedure involving bombs and microwave oven offers the best digestion compared to the total contents of elements determined directly in the solid phase by total reflection X-ray spectrometry (TXRF) and instrumental neutron activation analysis (INAA). Hseu et al. [6] investigated digestion methods for Cd, Cr, Cu, Ni, Pb and Zn in freshwater sediments and soils with aqua regia and different combinations of concentrated acids (HClO₄, HNO₃, H₂SO₄, HF), similarly

to Burau [1] who used $\text{HNO}_3\text{-HClO}_4$ or Reisenauer [2], Backer and Amaker [5] who employed $\text{HF-HNO}_3\text{-HClO}_4\text{-H}_2\text{SO}_4$. The Baker and Amaker procedure is flexible and adequate for the total determination of Cd, Cr, Cu, Ni and Zn in freshwater sediment and soil samples but not recommended for Pb because of its precipitation as sulfate and the greater dispersion of the recovery degree in standard reference materials. The Burau method had proved to be the most appropriate procedure for the dissolution of Pb in both sediment and soil samples. The Reisenauer method is suitable for Cr, while aqua regia can destroy the organic matter, metal oxides and other parts of mineral phases as silicate minerals with higher recovery degree for Cu, Ni and Zn. The most frequently used techniques for the determination of metals in soils and sediments are flame atomic absorption spectrometry (FAAS) [6,7], inductively coupled plasma atomic emission spectrometry or mass spectrometry (ICP-AES/MS) [4], TXRF and INAA [4]. The methods used to collect and digest soil and sediment have been reviewed by Beck and Sneddon [7]. However, it is interesting and necessary to complete the comparison of different digestion ways for the total determination of heavy metals in this kind of samples.

The aim of this study was to investigate the suitability of some digestion procedures based on different HCl/HNO_3 mixtures to determine the contents of Al, As, Cd, Cr, Cu, Fe, Mn, Ni, Pb, Ti, V and Zn in soils and sediments. Two certified soils and two certified water sediments were digested using aqua regia and Lunge mixture with and without evaporation to dryness. The analytical results for metals determined in solutions by ICP-AES were compared with the certified values. The best digestion procedure in respect with each element was chosen based on the recovery degree.

INSTRUMENTATION

The determinations were carried out using the ICP scanning spectrometer SPECTROFLAME and the ICP multichannel spectrometer SPECTRO CIROS^{CCD} (Spectro Analytical Instruments Kleve, Germany). All relevant ICP spectrometer operating parameters such as r.f. power level, gas flows, sample uptake rate and positioning of the torch in the front of the optical plasma interface are controlled by the software. Thus, optimum operating conditions can be easily selected. Details about instrumentation and operating conditions are given in Table 1.

Stock solutions and certified reference materials (CRMs)

All reagents used in this study (65 % HNO_3 , 32 % HCl) were puriss p.a. quality (Flucka). Stock solution of $1000\text{ }\mu\text{g mL}^{-1}$ As and Cd, $2000\text{ }\mu\text{g mL}^{-1}$ Cr, Ni, V, Ti and $4000\text{ }\mu\text{g mL}^{-1}$ Cu, Zn, Pb, Fe, Mn and Al were prepared starting from oxide (As) or metallic powder. A multielement standard solution of ($\mu\text{g mL}^{-1}$) 50 As, 20 Cd, 100 Cr, Ni, V and Ti, 160 Pb, 200 Cu, Zn, Al and 400 Fe, Mn was prepared using the single elemental solutions. This solution was used for line selection and to analyze the samples by the multielemental standard addition method. All dilutions were made with 2 % (v/v) HNO_3 .

Two certified soils (CRM 025-050, RTC-Laramie New York, USA; LGC 6135 Soil Hackney Brick Works, LGC-Middlessex, UK), a certified river sediment (NSC DC 78301 River sediment, China National Analysis Center for Iron and Steel, Beijing, China) and a freshwater sediment (BCR 701, Institute for Reference Materials and Measurements, Geel, Belgium) were used to evaluate the accuracy of extraction procedures. All CRMs were purchased from LGC Promochem GmbH, Germany.

Table 1

Instrumentation and operating conditions for the ICP atomic emission spectrometers

| Equipment | SPECTROFLAME | SPECTRO CIROS ^{CCD} |
|----------------------------|---|---|
| Generator: | Free – running 27.12 MHz, operated at 1200 W | Free – running 27.12 MHz operated at 1400 W. |
| Plasma torch | Inductively coupled plasma, radial viewing, observation height: 15 mm Argon flow rates: Outer gas 12 L min ⁻¹ . Intermediate gas 0.6 L min ⁻¹ . Nebulizer gas 1 L min ⁻¹ . | Inductively coupled plasma, axial viewing; torch position (mm): X= -3.9; Y=+3.6 ; Z=+2.6. Argon flow rates: Outer gas 12 L min ⁻¹ . Intermediate gas 0.6 L min ⁻¹ . Nebulizer gas 1 L min ⁻¹ . |
| Sample introduction system | 2 channel peristaltic pump, glass concentric nebulizer Meinhardt type K (TR-30-K3), double pass Scott type spray chamber sample uptake rate: 2 mL min ⁻¹ flushing time: 40 s delay time: 20 s | 4 channel peristaltic pump, K2 cross-flow nebulizer, double pass Scott type spray chamber sample uptake rate: 2 mL min ⁻¹ flushing time: 40 s delay time: 20 s |
| Optics | 160-800 nm double scanning monochromator chamber filled with N ₂ | 160 – 800 nm double-grating Paschen-Runge multichannel spectrometer chamber filled with Ar |
| Detector | 9781 R photomultiplier tube supplied at 1000 V (Thorn EMI, Ruislip, Middlesex, UK). | 22 CCD detectors |
| Data processing | Smart Analyzer Software Background correction: linear two points model, integration time 10 s and 3 successive measurements for each parallel sample | Smart Analyzer Software Background correction: linear and square two points models, best SNR strategy, integration time 45 s and 3 successive measurements for each parallel sample |

Digestion procedures of the CRMs

Three different wet digestion procedures were investigated to optimize the requirements for the quantitative determination of 12 elements: (i) aqua regia (HCl/HNO₃ 3:1); (ii) Lunge mixture (HCl/HNO₃ 1:3) without evaporation; (iii) Lunge mixture (HCl/HNO₃ 1:3) with evaporation to near dryness. For each procedure 3 parallel digestions were performed. All solutions were analyzed by ICP-AES and the average content and uncertainty as standard deviation has been given.

Method 1. Aqua regia digestion

A volume of 1 mL water was used to turn 2.5000 g sample into a slurry in a reaction flask, then 21 mL of 32 % (v/v) HCl followed by 7 mL of 65 % HNO₃ were added drop by drop to reduce foaming. A volume of 15 mL 0.5 M HNO₃ was

introduced into the absorption vessel connected to the reflux condenser of the reaction flask. The sample was allowed to stand for 16 h at room temperature for low oxidation of the organic matter of soil or sediment. Then the temperature of the reaction mixture was slowly risen until reflux conditions and maintained for 2 h. The content of the absorption vessel was added into the reaction vessel through the reflux condenser and both rinsed with 10 mL of 0.5 M HNO_3 . After cooling at room temperature, the sample was transferred in a 100 mL graduated flask with 2 % (v/v) HNO_3 . The slurry was filtered through a cellulose based membrane filter with medium pores and the filtrate was used to determine the metals.

Method 2. Lunge mixture without evaporation

The procedure was similar to that using aqua regia but employing in this case 28 mL of Lunge reagent.

Method 3. Lunge mixture with evaporation to near dryness

A volume of 25 mL 1+1 HCl was added to 2.5000 g certified reference material in a 150 mL vessel, then heated on a hot plate to near dryness. After cooling, 25 mL Lunge mixture were added and again the solution was evaporated to near dryness. The residue was dissolved in 25 mL 1+4 HCl and heated for approximately 15 min. The sample was transferred into a volumetric flask and diluted to 100 mL with 2 % (v/v) HNO_3 . The contents of metals were determined in the clear solution resulted after filtration.

RESULTS AND DISCUSSION

The comparison of the found analytical results following the three digestion ways with the certified values are illustrated in Tab. 2-5.

Table 2

Comparison of the found content of metals (n=3 parallel samples) with the certified concentrations in CRM 025-050 Soil using ICP-AES.

| Element | Certified ($\mu\text{g g}^{-1}$) | | Found ($\mu\text{g g}^{-1}$) | | |
|---------|---------------------------------------|--------------|--------------------------------|--------------------------------|-----------------------------|
| | | | Aqua regia | Lunge mixture without evap. | Lunge mixture with evap. |
| Al | 7637±1602 | Ciros CCD | 8594±1115 | 8305±1130 | 8662± 1250 |
| | | Spectroflame | 8547±870 | 7842±920 | 9600±1100 |
| As | 339±51.1 | Ciros CCD | 339±59.4 | 263±26.2 | - |
| | | Spectroflame | 329±40.0 | 263±32.5 | - |
| Cd | 369±46.3 | Ciros CCD | 311±51.0 | 302±56.4 | 314±34.8 |
| | | Spectroflame | 340±45.0 | 332±42.5 | 292±41.3 |
| Cr | 441±50.1 | Ciros CCD | 448±41.0 | 388± 40.4 | 452±42.9 |
| | | Spectroflame | 453±39.5 | 387±51.3 | 446±50.7 |
| Cu | 7.76±1.68 | Ciros CCD | 8.35±1.68 | 8.11± 1.27 | 8.00±1.73 |
| | | Spectroflame | 8.25±1.25 | 8.65±1.34 | 8.65±1.34 |
| Fe | 9439±1229 | Ciros CCD | 10000±1590 | 10290±1130 | 8335±1170 |
| | | Spectroflame | 10027±1450 | 9240±1520 | 7577±1168 |
| Mn | 173±15.0 | Ciros CCD | 187± 8.4 | 178± 7.0 | 224± 17.0 |
| | | Spectroflame | 176±11.5 | 184±7.5 | 220±18.5 |

| Element | Certified ($\mu\text{g g}^{-1}$) | | Found ($\mu\text{g g}^{-1}$) | | |
|---------|---------------------------------------|--------------|--------------------------------|--------------------------------|-----------------------------|
| | | | Aqua regia | Lunge mixture without evap. | Lunge mixture with evap. |
| Ni | 12.2 \pm 3.54 | Ciros CCD | 12.0 \pm 3.25 | 19.0 \pm 4.28 | 11.3 \pm 3.89 |
| | | Spectroflame | 16.0 \pm 4.45 | 15.2 \pm 2.63 | 10.2 \pm 3.29 |
| Pb | 1447 \pm 203 | Ciros CCD | 1448 \pm 108 | 1352 \pm 237 | 1458 \pm 226 |
| | | Spectroflame | 1482 \pm 227 | 1370 \pm 226 | 1408 \pm 189 |
| Ti | - | Ciros CCD | 1004 \pm 82 | 268 \pm 12 | 954 \pm 98 |
| | | Spectroflame | 955 \pm 70 | 287 \pm 45 | 1000 \pm 80 |
| V | 19.3 \pm 4.48 | Ciros CCD | 14.8 \pm 2.47 | 14.3 \pm 3.42 | 14.2 \pm 4.29 |
| | | Spectroflame | 19.8 \pm 3.56 | 19.0 \pm 4.13 | 17.2 \pm 3.89 |
| Zn | 51.8 \pm 8.29 | Ciros CCD | 44.4 \pm 7.76 | 48.6 \pm 3.88 | 46.0 \pm 5.68 |
| | | Spectroflame | 55.0 \pm 8.14 | 52.1 \pm 4.11 | 56.0 \pm 7.34 |

* uncertified value

Table 3

Comparison of the found content of metals (n=3 parallel samples) with the certified concentrations in LGC 6135 Soil Hackney Brick Works using ICP-AES.

| Element | Certified ($\mu\text{g g}^{-1}$) | | Found ($\mu\text{g g}^{-1}$) | | |
|---------|---------------------------------------|--------------|--------------------------------|--------------------------------|-----------------------------|
| | | | Aqua regia | Lunge mixture without evap. | Lunge mixture with evap. |
| Al | 22700 \pm 4600 | Ciros CCD | 21000 \pm 1800 | 2520 \pm 2600 | 6200 \pm 800 |
| | | Spectroflame | 19800 \pm 2300 | 2400 \pm 1900 | 6300 \pm 900 |
| As | 66 \pm 12 | Ciros CCD | 67 \pm 2 | 57 \pm 4 | - |
| | | Spectroflame | 64 \pm 7 | 62 \pm 6 | - |
| Cr | 336 \pm 28 | Ciros CCD | 349 \pm 12 | 382 \pm 14 | 340 \pm 24 |
| | | Spectroflame | 315 \pm 26 | 390 \pm 22 | 320 \pm 18 |
| Cu | 105 \pm 5 | Ciros CCD | 100 \pm 5 | 104 \pm 5 | 118 \pm 10 |
| | | Spectroflame | 108 \pm 4 | 103 \pm 8 | 103 \pm 8 |
| Fe | 40900 \pm 2700 | Ciros CCD | 39200 \pm 2000 | 7000 \pm 800 | 11625 \pm 2300 |
| | | Spectroflame | 37100 \pm 2300 | 6900 \pm 1100 | 10250 \pm 920 |
| Mn | 348 \pm 18 | Ciros CCD | 338 \pm 21 | 280 \pm 12 | 338 \pm 25 |
| | | Spectroflame | 348 \pm 16 | 287 \pm 22 | 370 \pm 16 |
| Ni | 277 \pm 13 | Ciros CCD | 260 \pm 30 | 199 \pm 33 | 310 \pm 21 |
| | | Spectroflame | 240 \pm 16 | 206 \pm 24 | 291 \pm 6 |
| Pb | 391 \pm 16 | Ciros CCD | 411 \pm 31 | 355 \pm 32 | 355 \pm 32 |
| | | Spectroflame | 400 \pm 21 | 373 \pm 32 | 350 \pm 36 |
| Ti | 200 | Ciros CCD | 190 \pm 20 | 50 \pm 4 | 245 \pm 18 |
| | | Spectroflame | 235 \pm 28 | 58 \pm 8 | 203 \pm 24 |
| V | 78 \pm 11 | Ciros CCD | 70 \pm 10 | 64 \pm 6 | 84 \pm 8 |
| | | Spectroflame | 77 \pm 6 | 58 \pm 9 | 83 \pm 6 |
| Zn | 316 \pm 41 | Ciros CCD | 316 \pm 18 | 321 \pm 27 | 321 \pm 27 |
| | | Spectroflame | 318 \pm 22 | 318 \pm 18 | 339 \pm 23 |

** indicative value

Table 4

Comparison of the found content of metals (n=3 parallel samples) with the indicative values of the supplier in BCR 701 Freshwater sediment using ICP-AES.

| Element | Indicative values ($\mu\text{g g}^{-1}$) | | Found ($\mu\text{g g}^{-1}$) | | |
|---------|--|--------------|--------------------------------|-----------------------------|--------------------------|
| | | | Aqua regia | Lunge mixture without evap. | Lunge mixture with evap. |
| As | - | Ciros CCD | 41 \pm 4 | 40 \pm 3 | - |
| | | Spectroflame | 56 \pm 6 | 65 \pm 7 | - |
| Cd | 11.7 \pm 1.0 | Ciros CCD | 12.5 \pm 1.0 | 11.8 \pm 0.6 | 12.3 \pm 1.0 |
| | | Spectroflame | 10.3 \pm 1.5 | 10.9 \pm 0.8 | 10.5 \pm 0.9 |
| Cr | 272 \pm 20 | Ciros CCD | 275 \pm 17 | 265 \pm 18 | 295 \pm 26 |
| | | Spectroflame | 280 \pm 12 | 271 \pm 22 | 301 \pm 20 |
| Cu | 275 \pm 13 | Ciros CCD | 280 \pm 18 | 279 \pm 19 | 279 \pm 19 |
| | | Spectroflame | 276 \pm 15 | 273 \pm 10 | 267 \pm 10 |
| Mn | - | Ciros CCD | 604 \pm 35 | 502 \pm 18 | 656 \pm 22 |
| | | Spectroflame | 675 \pm 45 | 560 \pm 23 | 645 \pm 20 |
| Ni | 103 \pm 4 | Ciros CCD | 100 \pm 10 | 100 \pm 6 | 100 \pm 9 |
| | | Spectroflame | 100 \pm 8 | 98 \pm 7 | 105 \pm 4 |
| Pb | 143 \pm 6 | Ciros CCD | 144 \pm 8 | 140 \pm 10 | 133 \pm 14 |
| | | Spectroflame | 140 \pm 6 | 148 \pm 10 | 149 \pm 9 |
| Ti | - | Ciros CCD | 1529 \pm 91 | 891 \pm 42 | 1530 \pm 75 |
| | | Spectroflame | 1550 \pm 80 | 1093 \pm 110 | 1345 \pm 86 |
| Zn | 454 \pm 19 | Ciros CCD | 457 \pm 20 | 458 \pm 18 | 458 \pm 18 |
| | | Spectroflame | 458 \pm 14 | 445 \pm 12 | 484 \pm 12 |

* uncertified value

Table 5

Comparison of the found content of metals (n=3 parallel samples) with the certified concentrations in NCS DC 78301 River sediment using ICP-AES.

| Element | Certified ($\mu\text{g g}^{-1}$) | | Found ($\mu\text{g g}^{-1}$) | | |
|---------|------------------------------------|--------------|--------------------------------|-----------------------------|--------------------------|
| | | | Aqua regia | Lunge mixture without evap. | Lunge mixture with evap. |
| As | 56 \pm 5 | Ciros CCD | 53 \pm 2 | 51 \pm 4 | - |
| | | Spectroflame | 59 \pm 5 | 55 \pm 6 | - |
| Cd | 2.45 \pm 0.2 | Ciros CCD | 2.50 \pm 0.5 | 2.40 \pm 0.5 | 2.45 \pm 0.3 |
| | | Spectroflame | 2.35 \pm 0.3 | 2.50 \pm 0.3 | 2.31 \pm 0.4 |
| Cr | 90 \pm 4 | Ciros CCD | 84 \pm 6 | 83 \pm 5 | 93 \pm 9 |
| | | Spectroflame | 88 \pm 5 | 85 \pm 7 | 96 \pm 5 |
| Cu | 53 \pm 3 | Ciros CCD | 54 \pm 5 | 54 \pm 4 | 51 \pm 3 |
| | | Spectroflame | 52 \pm 3 | 51 \pm 3 | 50 \pm 4 |
| Mn | 975 \pm 17 | Ciros CCD | 858 \pm 50 | 864 \pm 26 | 821 \pm 30 |
| | | Spectroflame | 920 \pm 40 | 865 \pm 30 | 977 \pm 28 |

| Element | Certified ($\mu\text{g g}^{-1}$) | | Found ($\mu\text{g g}^{-1}$) | | |
|------------------|---------------------------------------|--------------|--------------------------------|--------------------------------|-----------------------------|
| | | | Aqua regia | Lunge mixture without evap. | Lunge mixture with evap. |
| Ni ^{**} | 32 | Ciros CCD | 34±6 | 42±7 | 41±8 |
| | | Spectroflame | 30±8 | 30±6 | 33±6 |
| Pb | 79±6 | Ciros CCD | 78±5 | 78±4 | 78±4 |
| | | Spectroflame | 83±8 | 81±5 | 81±6 |
| Ti [*] | - | Ciros CCD | 423±30 | 199±8 | 370±15 |
| | | Spectroflame | 392±28 | 184±20 | 400±30 |
| Zn ^{**} | 251 | Ciros CCD | 248±38 | 252±14 | 285±14 |
| | | Spectroflame | 245±25 | 255±12 | 265±18 |

* uncertified value

** indicative value

The average recovery degrees considering the found values for the reference materials are presented in Tab.6.

Table 6
Average recovery degrees based on the results for the reference materials

| Element | Recovery degree / (%) | | |
|-----------------|-----------------------|--------------------------------|-----------------------------|
| | Aqua regia | Lunge mixture without evap. | Lunge mixture with evap. |
| Al ¹ | 101±16 | 56±70 | 73±65 |
| As ² | 99±1 | 88±9 | - |
| Cd ³ | 95±6 | 94±7 | 92±9 |
| Cr ⁴ | 100±3 | 99±12 | 104±5 |
| Cu ⁴ | 102±4 | 103±4 | 102±6 |
| Fe ¹ | 100±9 | 60±61 | 55±41 |
| Mn ² | 98±7 | 92±12 | 108±18 |
| Ni ⁴ | 101±10 | 99±19 | 103±12 |
| Pb ⁴ | 102±2 | 97±4 | 97±5 |
| Ti ⁵ | 106±17 | 27±4 | 112±15 |
| V ¹ | 95±7 | 82±6 | 94±18 |
| Zn ⁴ | 99±2 | 100±2 | 104±5 |

¹ CRM 025-050, LGC 6135

² CRM 025-050, LGC 6135, NCS DC 78301

³ CRM 025-050, BCR 701, NCS DC 78301

⁴ CRM 025-050, LGC 6135, BCR 701, NCS DC 78301

The digestion in aqua regia resulted in very good recovery degrees for As, Cr, Cu, Fe, Mn, Pb and Zn. Recoveries (%) were also good for Al, Ni and Ti but the dispersion were large: 101±16, 101±10 and 106±17, respectively. Relatively good results were found for Cd (95±6) and V (95±7).

For the Lunge mixture used as digesting reagent without evaporation, best recovery degrees were achieved for Cu (103 ± 4) and Zn (100 ± 2) and relatively good for Cd (94 ± 7) and Pb (97 ± 4). With regard to Cr, Mn and Ni the digestion method proved to be correct but resulted in a greater dispersion of the results: 99 ± 12 ; 92 ± 12 and 99 ± 19 , respectively. The poor recoveries for As (88 ± 9) and V (82 ± 6) indicated negative systematic errors. For Ti also a very low recovery degree was encountered (27 ± 4). The digestion method was equally unsatisfactory for Al and Fe with recoveries of 56 ± 70 and 60 ± 61 . With regard to these two elements in a mineral type of soil, which is the case of CRM 025-050, the digestion using Lunge mixture without evaporation is satisfactory as suggest the found results compared to the certified values in Tab. 2. The procedure was not suitable for clay soil with higher silicate content as LGC 6135 Hackney Brick Works (Tab. 3).

The digestion procedure using Lunge mixture with dryness evaporation led to best recoveries for Cr (104 ± 5), Cu (102 ± 6) and Zn (104 ± 5) and relatively good results for Cd (92 ± 9) and Pb (97 ± 5). Larger dispersions were encountered for Mn (108 ± 18), Ni (103 ± 12), Ti (112 ± 15) and V (94 ± 18). For Al and Fe the results were similar to those found using Lunge mixture without evaporation. The procedure with dryness evaporation proved to be not suitable for volatile elements such as As because of loss during evaporation to dryness.

For the materials with uncertified content of Ti, the ratio of amounts extracted in aqua regia: Lunge mixture with evaporation: Lunge mixture without evaporation were: 1:1:0.28 in CRM 025-050; 1:0.94:0.47 in NCS DC 78301 and 1:0.93:0.64 in BCR 701. It can be stated that the extraction degree is generally better in aqua regia followed by the Lunge mixture with evaporation to dryness.

CONCLUSIONS

The digestion procedures using aqua regia, Lunge mixture with and without evaporation were suitable for Cd, Cr, Cu, Mn, Ni, Pb and Zn in soil and sediment. Aluminium and Fe were quantitatively extracted only in aqua regia, while V and Ti either in aqua regia or Lunge mixture with evaporation to dryness. In the case of As, a volatile element, only the extraction in aqua regia with the collection of gases gave a good recovery degree.

Aqua regia or Lunge mixture without evaporation are more suitable for the routine determination of the acid-extractable fraction of the elements from soil and sediment, while the digestion with Lunge mixture with evaporation to dryness is more laborious and time consuming. Only a quantitative digestion with an oxidant mixture of acids resulting in clear solutions guarantees the determination of at least 12 elements. In hot plate digestion procedures, the presence of HNO_3 helps to destroy easily organic species and to convert some elements into the higher, less volatile valence states. A gently pre-digestion with HCl or HNO_3 is also beneficial to avoid overheating through exothermic sample decomposition reactions.

The investigated digesting procedures can be used to determine the acid-extractable fraction of heavy metals in different types of soil from forest regions, industrial parks, residential and commercial areas.

REFERENCES

1. R.E. Burau, "Lead" A.L. Page et al. (eds), Methods of Soil Analysis, Part 2, Chemical and Microbiological Properties, 2nd ed., Agron. Monogr. Vol. 9, ASA and SSSA, Madison, WI, USA, 1982.
2. H.M. Reisenauer, "Chromium" A.L. Page et al. (eds), Methods of Soil Analysis, Part 2, Chemical and Microbiological Properties, 2nd ed., Agron. Monogr. Vol. 9, ASA and SSSA, Madison, WI, USA, 1982.
3. L.R. Hossner, "Dissolution for Total Elemental Analysis", D.L. Sparks et. al. (eds), Methods of Soil Analysis, Part 3, Chemical Methods, SSSA Book Series No. 5, ASA and SSSA, Madison, WI, USA, 1996.
4. P. Krause, B. Erbslöh, R. Niedergesäß, R. Pepelnik, A. Prange, *Fresenius J. Anal Chem*, **1995**, 353, 3-11.
5. D.E. Baker, M.C. Amacher, "Nickel, Copper, Zinc and Cadmium", A.L. Page et al. (eds), Methods of Soil Analysis, Part 2, Chemical and Microbiological Properties", 2nd ed., Agron. Monogr. Vol. 9, ASA and SSSA, Madison, WI, USA, 1982.
6. Z.Y. Hseu, Z.S. Chen, C.C. Tsai, C.C. T, S.F. Cheng, C.L. Liu, H.T. Lin, *Water, Air and Soil Pollution*, **2002**, 141, 189-205.
7. J.N. Beck, J. Sneddon, *Microchem J.*, **2000**, 66, 73-113.

ENVIRONMENTAL AND OCCUPATIONAL EXPOSURE TO Cr, Cu, Pb AND Zn OF POPULATION IN BAIJA-MARE USING AS INDEX THE ABSORPTION OF CONTAMINANTS IN HAIR

MICHAELA PONTA, TIBERIU FRENTIU, EUGEN DARVASI,
AUGUSTA BONDA, EMIL CORDOS

*Babes-Bolyai University, Department of Analytical Chemistry,
Str. Arany Janos 11, 400028 Cluj-Napoca, Romania*

ABSTRACT. The extent of environmental and professional exposure to Cr, Cu, Pb and Zn as a result of the industrial activity in the Baia-Mare area was investigated. The environmental exposure was estimated through the metal content in hair samples from five children aged between 7 and 13 years, while the occupational exposure was assessed on 5 adults between 40-70 years. The alert and intervention levels of Cu, Pb and Zn and sometimes Cr in soil were many fold exceeded but in hair only Pb was suited to evaluate the risk to exposure as it was much over the normal value. It has been found an accumulation of Pb in hair with age, but children are a more useful tool for epidemiological assessment of environmental exposure to toxic elements. In high polluted area such as Baia-Mare, the Pb level in hair is less influenced by the distance of the residential zone from polluter and more dependent on people's age. Results underline the relevance of health care preventive measures for children, who are the most sensitive groups to pollution.

INTRODUCTION

Monitoring trace elements in human body is of great concern as their changes can be used as an index of the excess or deficiency of specific nutrients in the diet or as an index of the absorption of contaminants from environment. The levels of trace elements in the human body are often evaluated in blood, urine, hair and tissues [1, 2]. Although blood and urine analysis are the most traditional approaches to evaluate trace element levels in the human body, hair can provide a more permanent record of these elements associated with normal and abnormal metabolism as well as trace elements assimilated from the environment. In addition, hair is easily collected and stored and can be easily digested [3,4]. Various factors influence the level of elements in hair, such as residence place [5], sex and hair color [6], age [7], occupational exposure [8] and hair dyeing. Many authors [9,10] believe that examining hair is a good non-invasive method, which should be used in screening studies of children living in heavily polluted areas. Thus, Jenkins [11] and Chlopicka et al. [12] consider that hair is a material ideally suited to the biological monitoring of As, Cd, Cr, Pb and Hg.

The aim of the study was to investigate the extent of Cr, Cu, Pb and Zn exposure via environmental pollution and occupational exposure as a result of the industrial activity in the Baia-Mare area. To evaluate the exposure to environmental pollution, we determined the metal content in hair samples from children, while the occupational exposure was assessed on adults working or having worked in the processing of non-ferrous ores. The subjects were selected to have different residential locations in Baia-Mare in order to study the relationship between exposure and distance from the polluter in a high-polluted environment. For correlation, heavy metals were also determined in interstitial water and soil samples collected from different locations.

The town of Baia-Mare is situated in a depression in north-west Romania, bordered on the east by a mountain chain and with a wind direction from east to west. At the beginning of the 14th century several foundries were established in the neighborhood to process non-ferrous ores extracted from the mountains in the region. These foundries were unified in 1884 in new plant in the northeastern side of the town, known after 1990 as the Romplumb Company. Nowadays, the main activity of the plant is production of free-copper lead and copper matte by roasting non-ferrous ores. After 1907 another plant under the name of Phoenix Company situated in the south-east of the town was established to produce sulfuric acid, electrolytic copper, lead sheet and tubes, lead oxides, silver and gold ingots. Residual sulphurous gases resulted from the processing of non-ferrous ores are evacuated in the atmosphere through high chimneys. Although the sulphurous gases containing SO₂, SO₃, fog of sulfuric acid are purified during the chemical process, they still contain both traces of heavy metals, especially Cu, Pb, Zn and Cd. Thus, airborne particulate matters deposit and consequently generate pollution with inorganic heavy metal compounds non only in the proximity of the industrial site but also in the town and its surroundings [13]. Previous studies [14, 15] showed a significant pollution with Pb, Zn, Cu, Cd as oxides, carbonates, sulfates, sulfides and silicates of soil collected in Baia-Mare. The sulfides are accumulated in soil and their content in the surface layer in the proximity of the polluting sources is comparable to that of some ores. Generally, for all species, the content decreases with the distance from the polluting source. Thus, these two industrial units became the main polluters of the town for almost a century, with a peak between 50's and early 90's. To these two polluters it should be added the Central Flotation Station situated in the south east of the town and the tailings deposited around it.

Besides industrial pollution by smelting activity there is a continual environmental exposure especially to lead generated by the car traffic. Human exposure occurs mainly through oral (drinking water, food), inhalative and dermal pathways. Lead from environmental pollution is not carcinogenic but even low dose exposure has been shown to have detrimental and long-lasting effects on the renal homeopoetic and nervous system.

EXPERIMENTAL

Apparatus

A scanning inductively coupled plasma atomic emission spectrometer (ICP-AES) SPECTROFLAME type (Spectro Analytical Instruments, Kleve, Germany) was employed (Table 1).

Table 1.

Operating conditions for the SPECTROFLAME ICP -AES

| Equipment | Characteristics |
|--------------|--|
| Generator | Free – running 27.12 MHz, manually controlled power level between 750 – 1400 W, 1200 W in this experiment. |
| Plasma torch | Water-cooled copper induction coil inductively coupled plasma, radial viewing through an optical fiber for the VIS range and 8 optical fibers for the UV range (10 µm wide), observation height 15 mm. |

| Equipment | Characteristics |
|----------------------------|--|
| | Ar flow rates: <ul style="list-style-type: none"> - Outer gas 12 L min⁻¹. - Intermediate gas 0.6 L min⁻¹. - Nebulizer gas 1 L min⁻¹. |
| Torch cooler system | Cooling water without automated control of the temperature. |
| Sample introduction system | 2 channel peristaltic pump, 2 mL min ⁻¹ solution up-take rate, concentric nebulizer Meinhardt type K (TR-30-K3), double pass Scott type spray chamber mounted in a thermostated room controlled by the computer. |
| Optics | Double scanning monochromator. UV range 160 – 336 nm chamber filled with high purity nitrogen, grating with 3600 lines mm ⁻¹ , focal length 750 mm, thermostated at 15 ± 0.5 °C, entrance slit width 15 µm, resolution 15 pm. Vis range 335 – 800 nm, grating with 2400 lines mm ⁻¹ , focal length 750 mm, thermostated at 15 ± 0.5 °C, resolution 15 pm. Optical detector: 9781 R photomultiplier tube supplied at 1000 V (Thorn EMI, Ruislip, Middlesex, UK). |
| Data processing | Soft: Smart Analyzer, Pentium III CPU 450 MHz, background correction two points linear model, integration time 10 s, 3 successive measurements for each sample. |

Reagents and standard solutions

The stock solutions (1000 µg mL⁻¹) of the elements determined in this study (Cr, Cu, Zn, Pb) were prepared from high purity metals. Amounts of 1.0000 g powder were dissolved in 1+1 HNO₃ (Cu, Pb and Zn) or in 1+1 HCl (Cr) and filled up to 1 L with 2 % (v/v) HNO₃. All solutions were prepared using analytical-grade reagents (Fluka-Germany) and double distilled water.

Preparation of calibration standards

Dilution of the most concentrated multielement standard solution in order to prepare the lower concentration solutions is not permitted because of unknown error propagation. The analytes concentrations ought to be distributed randomly in such a way that the overall analyte concentration is approximately constant in all solutions. Ideally, the analyte concentrations should lie between a half and two-fold the concentration of real samples. In order to correct drifts and fluctuations of the spectral device during calibration and sample measurement the external standardization (recalibration) was used after the analysis of each sample. The external standard used for this purpose had a concentration corresponding to the medium calibration standards for each analyte. To each standard solution the acid amounts used for hair samples digestion (25 mL 65% HNO₃ and 5 mL 80% HClO₄) were added for a final volume of 50 mL. The dilution was made with 2% HNO₃ (v/v). The same solution without analytes was used as blank. A list of Cr-Cu-Zn-Pb calibration solutions used in this investigation is given in Table 2.

Table 2.

Calibration standards for Cr-Cu-Zn-Pb

| | Blank [*] | STD 1 | STD 2 | STD 3 | STD 4 | STD 5 |
|---------|---------------------------------------|-------|-------|-------|-------|-------|
| Element | Concentration / $\mu\text{g mL}^{-1}$ | | | | | |
| Cr | 0 | 0.020 | 0.005 | 0.030 | 0.010 | 0.040 |
| Cu | 0 | 0.6 | 0.2 | 0.5 | 0.4 | 0.1 |
| Zn | 0 | 0.5 | 2 | 4 | 6 | 8 |
| Pb | 0 | 2.0 | 1.2 | 0.8 | 0.4 | 0.2 |

^{*} 25 mL 65 % HNO_3 , 5 mL 80% HClO_4 diluted to 50 mL with 2% HNO_3 (v/v)

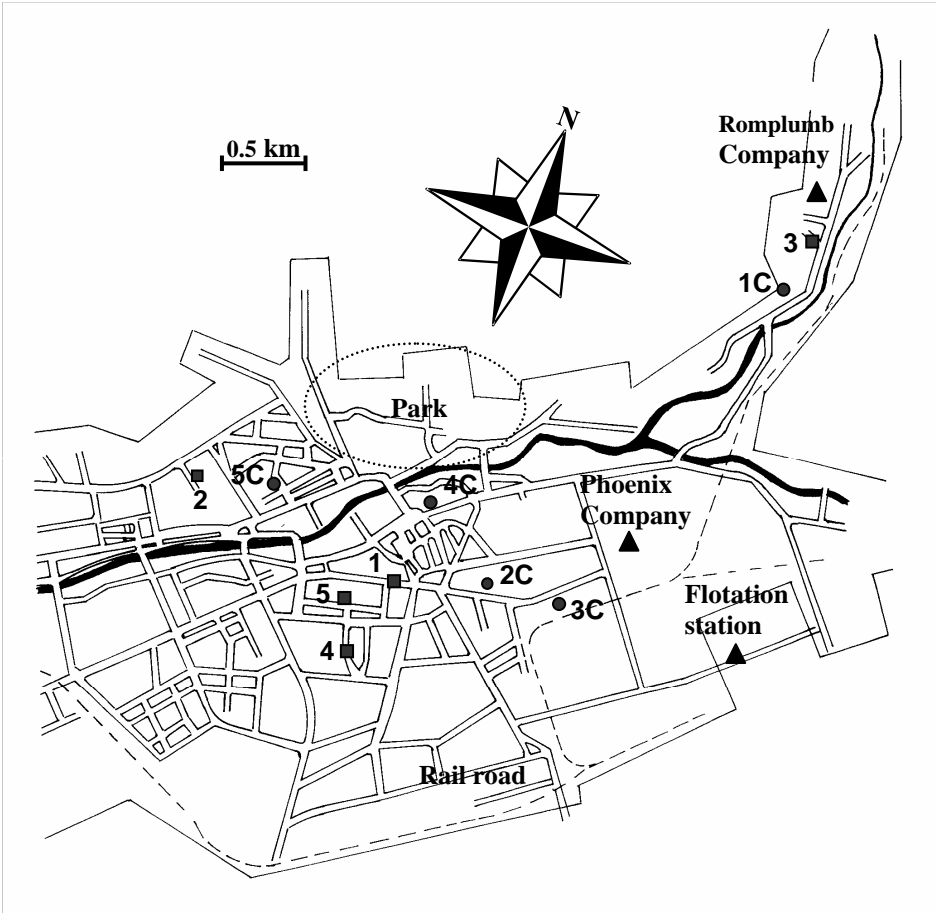


Fig. 1. Residence of subjects in the Baia-Mare town

- children
- adults

Hair samples collection and digestion procedure

The subjects involved in this study live in Baia-Mare near Romplumb and Phoenix Companies as well as in the center of the town and next to the park (Fig. 1). Human hair samples were collected in hairdressing establishments from 10 persons, 5 children aged between 7-13 years and 5 men aged between 40-70 years. The adult subjects have been living at their residence for at least 30 years, while children from birth. Adults admitted to be or to have been subjects of an occupational exposure to heavy metals. Hair samples were taken from various parts of the scalp, 1 – 1.5 cm measured from the root and cut to 2 – 5 cm long using a stainless-steel scissors. The collected samples were stored in bags in a cool and dry place until analysis. The adult donors were asked to fill out a detailed questionnaire concerning age, address, occupation, smoking habits.

Hair samples were washed threefold with acetone, then with double distilled water and dried at a temperature between 40 - 60°C. After drying, an amount of 1.0000 g of each hair sample was placed in a 150 mL Pyrex glass with cover and soaked with 25 mL 65% HNO₃ overnight at room temperature. Afterwards, the sample was heated at 120°C and kept at this temperature for about 5 – 6 h until fading of solution. After cooling, 5 mL of 80 % HClO₄ were added and the solution was heated again at 120°C for 2 h. The residue was transferred in a 50 mL volumetric flask and the volume was adjusted with 2 % HNO₃ (v/v), then filtrated. The blank solution was subjected to the same procedure.

Limits of detection for Cr, Cu, Zn and Pb in hair by ICP-AES

Table 3 presents the limits of detection (LODs) for Cr, Cu, Zn and Pb (3 σ) by ICP-AES in human hair samples. The LODs were calculated in $\mu\text{g g}^{-1}$ dry mass taking into account the amount of hair sample and the dilution factor.

Table 3

Limits of detection for Cr, Cu, Zn and Pb by ICP-AES in human hair

| | Cr | Cu | Pb | Zn |
|-------------------------------|---------|---------|---------|---------|
| λ (nm) | 283.563 | 324.754 | 283.307 | 213.586 |
| LOD (ng mL ⁻¹) | 0.2 | 2 | 30 | 4 |
| LOD ($\mu\text{g g}^{-1}$)* | 0.01 | 0.1 | 1.5 | 0.2 |

* expressed in dry mass taking into account the amount of sample and the dilution factor

The method allows the quantitation of at least ($\mu\text{g g}^{-1}$): 0.05 Cr, 0.5 Cu, 7.5 Pb and 1.0 Zn.

Evaluation of soil and water pollution in the Baia-Mare area

Table 4 presents the total content of Cr, Cu, Zn and Pb in soil from different sites at 20 cm depth extracted in *aqua regia* and the leachable content in water, while Table 5 indicates the contents of these elements in the interstitial water in soil at the same depth.

Table 4

Mean results $\pm s$ of heavy metals in soil at 20 cm depth determined by ICP-AES
(n= 3 successive measurements)

| Area | Cr | Cu | Zn | Pb |
|---|--------------|-----------------|------------------|------------------|
| <i>Aqua regia</i> extractable contents (mg Kg ⁻¹) | | | | |
| Around Romplumb | 294 \pm 20 | 8320 \pm 330 | 21400 \pm 360 | 41242 \pm 829 |
| | 457 \pm 32 | 4154 \pm 130 | 5760 \pm 130 | 17090 \pm 230 |
| | 84 \pm 13 | 21647 \pm 420 | 14720 \pm 330 | 26112 \pm 860 |
| Around Phoenix | 300 \pm 5 | 31200 \pm 540 | 11586 \pm 310 | 12800 \pm 300 |
| | 595 \pm 26 | 9503 \pm 1400 | 54000 \pm 3100 | 10509 \pm 2400 |
| | 349 \pm 18 | 22490 \pm 520 | 9805 \pm 300 | 14195 \pm 300 |
| Park | 75 \pm 10 | 257 \pm 32 | 418 \pm 28 | 320 \pm 193 |
| | 19 \pm 5 | 314 \pm 33 | 444 \pm 29 | 366 \pm 19 |
| Town Center | 388 \pm 14 | 607 \pm 43 | 1333 \pm 47 | 1503 \pm 70 |
| | 434 \pm 26 | 593 \pm 40 | 514 \pm 36 | 2560 \pm 44 |
| | 130 \pm 15 | 609 \pm 40 | 1086 \pm 80 | 920 \pm 50 |
| Water leachable contents (mg Kg ⁻¹) | | | | |
| Town Center | < 0.02 | 45 \pm 5 | 433 \pm 36 | 526 \pm 44 |
| Alert/Intervention limits for sensitive soils | 100/300 | 100/200 | 300/600 | 50/100 |

Table 5

Content of heavy metals in interstitial water (mg L⁻¹) at 20 cm depth determined by
ICP-AES (n= 3 successive measurements)

| | Cr | Cu | Zn | Pb |
|--|----------|------|------|------|
| mg L ⁻¹ | | | | |
| Interstitial water | < 0.0002 | 0.10 | 0.10 | 0.16 |
| Maximum admitted level (STAS 4706/88) | 0.05 | 0.05 | 0.03 | 0.05 |

According to data in Table 4, soil is highly polluted with Cu, Zn and Pb especially around the Romplumb and Phoenix Companies, where the alert and intervention limits are much exceeded. Although the amounts of these metals are lower in soils collected from the town and the park, here also the limits are many fold surpassed. In the case of Cr, both the alert and intervention limits are exceeded around Phoenix and Romplumb (2 samples), while in the town the amounts are higher than the alert limits. In the park area the Cr level in soil is not over the alert value. For all elements the lower contents were found in the park area.

The average level of water leachable metals in soils collected from the center of the town were (mg Kg⁻¹): 45 Cu, 433 Zn, 526 Pb and below 0.02 Cr. Thus, the levels of Cr and Cu were not over the alert limit, while that of Zn

exceeded it 1.5 times and that of Pb was more than 5 times the intervention value. Copper, Zn and Pb exceeded approximately 2; 3 and 3 times respectively, the admitted level in surface water (Table 5).

The high level of heavy metals in soil and relatively high level of Cu, Zn and Pb in water represent a high pollution of all environment compartments and a risk to long-time exposure of population in Baia-Mare via oral, dermal and inhalative pathways.

Levels of Cr, Cu, Zn and Pb in human hair of individuals in Baia-Mare area

The mean results and standard deviations ($n = 3$ successive measurements) for hair samples collected from 10 subjects are shown in Table 6.

Table 6

Mean results $\pm s$ ($\mu\text{g g}^{-1}$) in human hair analyzed by ICP-AES
($n = 3$ successive measurements)

| Sample | Age/ years | Smoking habits | Occup. exposure | Cr | Cu | Zn | Pb |
|---|---------------|-------------------|--------------------|-------------------|-------------------|-------------------|-------------------|
| 5 C _{**} | 7 | - | - | 0.96 \pm 0.26 | 10.53 \pm 0.42 | 114.5 \pm 3.5 | 27.92 \pm 5.96 |
| 3 C _{**} | 7 | - | - | 0.52 \pm 0.29 | 10.83 \pm 0.33 | 188.6 \pm 7.4 | 23.14 \pm 5.85 |
| 2 C _{**} | 8 | - | - | < 0.03 | 12.56 \pm 0.24 | 235.9 \pm 9.3 | 25.72 \pm 6.35 |
| 4 C _* | 10 | - | - | 1.14 \pm 0.34 | 12.81 \pm 0.51 | 169.7 \pm 8.3 | 30.82 \pm 7.23 |
| 1 C _* | 13 | - | - | < 0.03 | 11.05 \pm 0.25 | 129.6 \pm 5.2 | 27.15 \pm 7.12 |
| 1 | 40 | yes | yes | < 0.03 | 12.28 \pm 0.42 | 133.1 \pm 5.3 | 28.50 \pm 4.25 |
| 4 | 44 | yes | yes | 0.65 \pm 0.23 | 15.65 \pm 0.27 | 79.6 \pm 2.6 | 33.37 \pm 5.24 |
| 5 | 54 | no | yes | 1.12 \pm 0.31 | 11.52 \pm 0.43 | 141.2 \pm 9.5 | 28.47 \pm 6.93 |
| 2 _* | 55 | yes | yes | < 0.03 | 10.12 \pm 0.36 | 130.2 \pm 1.4 | 34.12 \pm 4.48 |
| 3 _* | 70 | no | yes | 1.05 \pm 0.25 | 10.16 \pm 0.24 | 129.4 \pm 1.2 | 43.07 \pm 2.38 |
| Normal values in human hair (group of 21 persons) [16] | | | | 0.814 \pm 0.401 | 11.54 \pm 1.237 | 171.1 \pm 41.16 | 4.476 \pm 7.295 |

* residence next to Romplumb; ** residence next to Phoenix; the others in the center and next to the park

According to data in Table 6, only the contents of Pb, a toxic element, are much over the normal values, while Zn, Cu and Cr are close to normal values in human hair. Thus, the average content of Zn was 145.2 \pm 6.2 $\mu\text{g g}^{-1}$, with higher values for children as compared to adults. Hair Zn concentrations were lower in anorexic patients (adult 44 years, 79.6 \pm 2.6 $\mu\text{g g}^{-1}$; one of the two children of 7 years, 114.5 \pm 3.5 $\mu\text{g g}^{-1}$). The average content of Cu was 11.75 \pm 0.36 $\mu\text{g g}^{-1}$, while that of Cr was 0.91 \pm 0.29 $\mu\text{g g}^{-1}$ and there was no significant difference between the concentration levels for adults and children. The results were in good agreement with those reported in literature [17,18].

Although there is an advanced pollution with Cu and Zn in the Baia-Mare area, the levels of these metals in hair do not reflect it and consequently they can not be employed as an index of the exposure assessment. Copper, Zn and Cr are considered to be essential elements for organism and their levels are influenced by diet and health status. The level of Cr in hair could be a good indicator for occupational exposure to chromate but it was not the case of our subjects.

The average level of Pb was $30.23 \pm 5.76 \mu\text{g g}^{-1}$ with an almost systematic increase with age revealed by the difference between children and adults values attributed to the supplementary occupational exposure of adults besides the indirect exposure of children to environmental pollution. In the case of children, the average Pb level was $26.95 \pm 6.53 \mu\text{g g}^{-1}$, six fold higher than the normal value. For adults, 30-45 years after childhood age, Pb accumulation in hair was only up to 1 fold the normal value. Our results exhibited also a more accentuated Pb accumulation for individuals over 60 years compared to those of medium age, similarly with As accumulation [19]. Thus, in the case of the 70 years old subject, the accumulation index was 2.7 fold the normal value (4.476) in the last 15 years of life. Therefore, in this study the Pb content in children's hair was found to be a useful tool in the environmental study of pollution and epidemiological purposes. However, the permanent stay of people in the highly polluted areas causes an accumulation of Pb in hair that represents a risk factor of morphofunctional abnormalities and chronic diseases. From this point of view, hair analysis seems to be a useful tool for epidemiological assessment of environmental exposure to toxic elements (Pb) and occupational exposure. In high polluted area such as Baia-Mare, the Pb level in hair is less influenced by the location of residential zone relative to polluter and more dependent on the age. These results underline the relevance of health care preventive measures for children, who are the most sensitive groups to pollution.

REFERENCES

1. K. Bencze, *Fresenius' J Anal Chem*, **1990**, 337, 867-876.
2. K. Bencze, *Fresenius' J Anal Chem*, **1990**, 338, 58-61.
3. P. Bermejo-Barrera, A. Moreda-Pineiro, T. Romero-Barbeito, J. Moreda-Pineiro, A. Bermejo-Barrera, *Talanta*, **1996**, 43, 1099-1107.
4. J.E. Tahan, V.A. Granadillo, R.A. Romero, *Anal. Chim. Acta*, **1994**, 295, 187-197.
5. Y. Takagi, S. Matsuda, S. Imai, Y. Ohmuri, T. Masuda, J.A. Vinson, M.C. Mehra, B.K. Puri, A. Kaniewski, *Bull. Environ. Contam. Toxicol.*, **1986**, 36, 793-800.
6. V. Valkovic, "Trace Elements in Hair", CRC Press, Boca Raton, FL, 1988.
7. D.C. Paschal, E.S. DiPietro, D.L. Phillips, E.W. Gunter, *Environ. Res.*, **1989**, 48, 17-28.
8. I.A. Randall, R.S. Gibson, *Br. J. Ind. Med.*, **1989**, 46, 171-175.
9. A.A.E. Wibowo, R.F.M. Herber, H.A. Das, N. Roeleveld, R.L. Ziehuus, *Environ. Res.*, **1986**, 40, 346-356.
10. N. Limic, V. Valkovic, *Bull. Environ. Contam. Toxicol.*, **1986**, 37, 925-930.
11. D.W. Jenkins, "Toxic Trace Metals in Mammalian Hair and Nails", EPA Report No. 600/4-79-049, 1979.
12. J. Chlopicka, P. Zagrodzki, Z. Zachwieja, M. Krosniak, M. Folta, *Analyst*, **1995**, 120, 943-945.
13. E. Cordos, R. Rautiu, C. Roman, M. Ponta, T. Frentiu, A. Sarkany, L. Fodorpatiki, K. Macalik, C. McCormick, D. Weiss, *Eur. J. Mineral. Proc. Environ. Prot.* **2003**, 3, 324-335.
14. T. Frentiu, M. Ponta, A.M. Rusu, S.D. Anghel, A. Simon, E.A. Cordos, *Anal. Lett.*, **2000**, 33, 323-335.
15. E.A. Cordos, T. Frentiu, A.M. Rusu, G. Vatca, *Analyst*, **1995**, 120, 725-731.
16. Y. Ren, Z. Zhang, Y. Ren, W. Li, M. Wang, G. Xu, *Talanta*, **1997**, 44, 1823-1831.
17. X. Dong, Y. Nakaguchi, K. Hiraki, *Analytical Sciences*, **1998**, 14, 785-789.
18. F. Watt, J. P. Landsberg, J. J. Powell, R. J. Ede, R. P. H. Thompson, J. A. Cargnello, *Analyst*, **1995**, 120, 789-791.
19. G. Bozsai, *Microchem. J.*, **1992**, 46, 159-166.

FIRST REPORT ON 3,7-DIOXA-*r*-1-AZABICYCLO[3.3.0]OCT-*c*-5-YLMETHOXY SYSTEM SUBSTITUTING *s*-TRIAZINE

CAMELIA BERGHIAN,^{a,b} NELLY PLÉ,^b ALAIN TURCK^b
and MIRCEA DARABANTU^{a,b*}

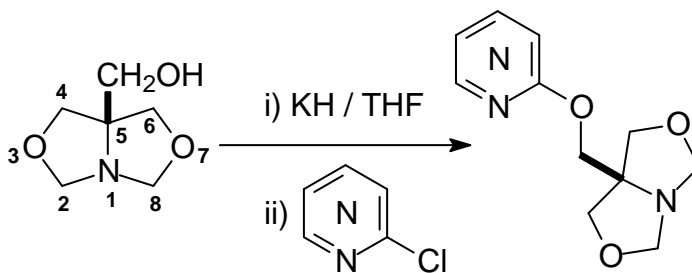
^aDepartment of Organic Chemistry, "Babes-Bolyai" University,
11 Arany János Str., 400028 Cluj-Napoca, Romania

^bInstitut de Recherche en Chimie Organique Fine (I.R.C.O.F.),
Université de Rouen, BP 08, F-76131 Mont Saint-Aignan Cedex, France

ABSTRACT. The nucleophilicity of two representative *c*-5-hydroxymethyl-3,7-dioxa-*r*-1-azabicyclo[3.3.0]octanes against cyanuryl chloride was investigated. Surprisingly, the C-2, -8 substitutions on the bicyclic system was found to decide the type of reactive species involved in the nucleophilic displacement of chlorine.

1. INTRODUCTION

We have recently reported the O-functionalisation of *c*-5-hydroxymethyl-3,7-dioxa-*r*-1-azabicyclo[3.3.0]octane *via* alkoxide form upon treatment with chlorodiazines (**Scheme 1**).^{1,2}



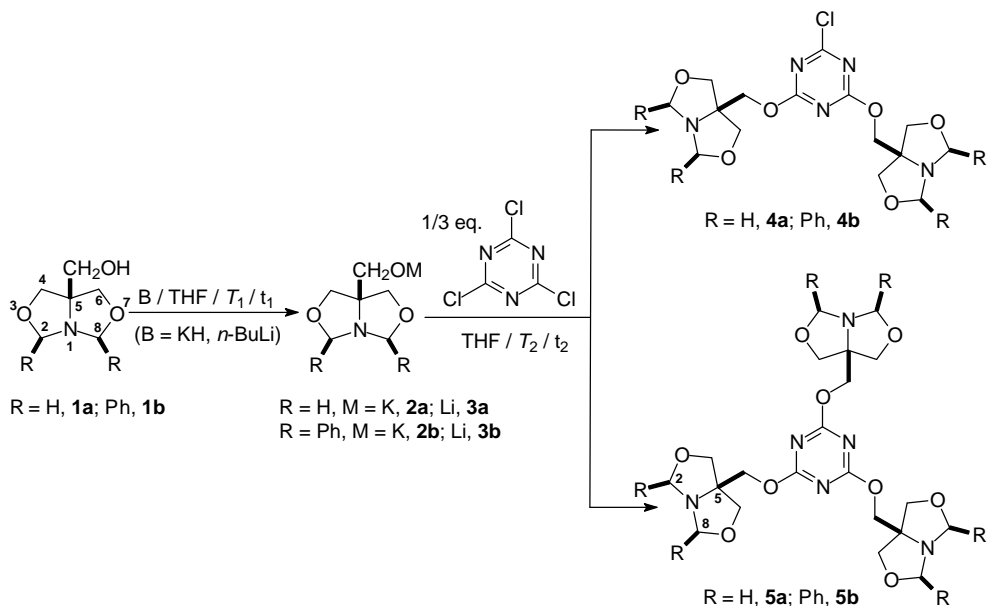
Scheme 1

By developing the Broadbent pioneering work,³ our methodology extrapolated the clean and selective access to a large variety of π -deficient systems (pyrazines and pyrimidines) bearing 1-3 3,7-dioxa-*r*-1-azabicyclo[3.3.0]oct-*c*-5-ylmethoxy groups linked at the α -positions to the (di)azine nitrogen atoms.

Following the above up to date promising results, the present work focused on the reactivity of certain *c*-5-hydroxymethyl-3,7-dioxa-*r*-1-azabicyclo[3.3.0]octanes against cyanuryl chloride. Thus, if the nucleophilic displacement of its chlorine atoms by simple alcohols in neutral or basic conditions is already "classic",⁴⁻⁶ the same reaction in our dedicated class of compounds is inexistent so far.

2. RESULTS AND DISCUSSIONS

The selected *c*-5-hydroxymethyl-3,7-dioxa-*r*-1-azabicyclo[3.3.0]octanes were **1a**, **b** (Scheme 2) because of their previously very well documented synthesis, stereochemistry and applications.² The strategy we used is resumed below and the results are collected in Table 1.



Scheme 2

The target compounds were the *s*-triazines **5a**, **b**.

Preliminary attempts already demonstrated unexpected great differences (reactivity, chemoselectivity, analytical control, NMR behaviour etc.) with respect to the previously described by us chlorodiazines: pyrimidine and pyrazine.^{1,2}

As shown by the data collected in Table 1, starting from **1a**, a strong dependence of the nucleophilicity with respect to the *O*-metallated form (as **2a** or **3a**) was observed.* Thus, **2a** allowed only the disubstitution of chlorine to yield the *s*-triazine **4a** (entry 1) with poor yield. In fact, one may assume, as main process, rather the decomposition of cyanuric chloride since, besides the unreacted **1a** and **4a**, no intermediate originating from the monosubstitution of chlorine we detected. By varying the temperature, as milder conditions (entries 3-5), it appeared to us that the ring opening of *s*-triazine occurred to provide exclusively resins structures with complex NMR spectra of the crude reaction mixtures.

In contrast, the use of **3a**, seen as soft nucleophile, permitted rapidly the optimisation of the synthesis towards **5a** (entry 6→7) in mild and reproducible conditions.

* the sodium hydride was *a priori* ruled out since it promotes only partial deprotonation of **1a**, **b**, as we earlier pointed out.^{1,2}

Table 1

Results of the synthesis of the compounds **4a**, **b**, **5a**, **b**

| Starting material | Entry | B | T_1 (°C) | t_1 (hrs.) | T_2 (°C) | t_2 (hrs.) | Results | |
|-------------------|-------|----------------|---------------|-----------------|------------------------|-----------------|--|-----------------|
| | | | | | | | Compd. | Yield (%) |
| 1a | 1 | KH | 45 | 2 | 65 | 36 | 4a | 34 |
| | 2 | | | | -78→r.t. 40 | 19 24 | 1a | 44 |
| | 3 | | | | -78→r.t. 65 | 18 72 | dec. | - |
| | 4 | | | | -78→r.t. r.t. 45 | 19 24 24 | dec. | - |
| | 5 | | | | 40 65 | 1 48 | dec. | - |
| | 6 | <i>n</i> -BuLi | -78 | 0.3 | -78→r.t. r.t. 65 | 19 24 24 | 5a (70) ^a 1a (30) | 39 ^b |
| | 7 | | | | -78→r.t. | 20 | 5a | 82 |
| | 8 | | | | 0 65 | 1 40 | 5b (51) 4b (10) 1b (39) | 37 |
| | 9 | <i>n</i> -BuLi | -60 | 0.3 | r.t. | 68 | 5b (24) 4b (4) ^c 1b (65) | 15 |
| | 10 | | | | | | -60→r.t. r.t. 65 | 20 48 4 |

^aas molar percentages issued from the ¹H NMR spectra of the crude reaction mixture; ^bthe recovered amounts of the starting materials **1a**, **b** were not taken into account; ^c7% assigned comparatively as non isolable product of monosubstitution *s*-triazine; ^d17 % assigned comparatively as non isolable product of monosubstitution.

Analytical discrimination between the *s*-triazines **4a** and **5a** was less simple than would expect. In the ¹³C-NMR spectrum of **4a**, the triazine carbons were found accidentally isochronous at 171.0 in CDCl₃ and 170.6 ppm in DMSO-*d*₆ (75 MHz) meanwhile in **5a** the most deshielded resonance was 173.3 ppm. The ¹H singlet assigned to 5-CH₂O group in **4a** was located 0.52 ppm downfield than in the starting **1a** whereas in **5a** the same deshielding was 0.87 ppm. That is, only the mass spectra of **4a**, **5a** (ESI and FAB⁺ respectively) fully validated the envisaged structures.

The TLC monitoring of the reaction was very cumbersome because of the very weak absorption in UV (254 nm) of the compounds and almost absent during flash column chromatography. Moreover, the routine as typical visualisation of the starting **1a** in I₂-bath was quite difficult in the case of **4a** and **5a**.

These serious complications arose presumably from the retention of the products on silica gel: indeed, this behaviour is already known to be useful methodology to access silica gel HPLC chiral *s*-triazines selectors for enantiomeric separation.⁸⁻¹¹

They were also encountered in the synthesis of the compound **5b**. The starting **1b** was used as pure *all cis*-2,5,8 diastereomer (*meso* form, **Scheme 1**).^{2,12} The potassium alkoxide derivative **2b** of **1b**, afforded this time the highest content of **5b** in the crude reaction mixture (entry 8): the depicted yield in **Table 1** refers to isolated amounts after flash column chromatography (eluent ligroin : acetone 3.5:1 v/v) as follows: the unreacted **1b** was recovered as a first fraction then pure **5b**. Complete elution of the column with pure acetone yielded supplementary amounts of **5b** as a non separable mixture with the **4b** in about 2:1 molar ratio. Discrimination between **4b** and **5b** was solved by MS-(FAB⁺) only: the spectrum clearly displayed both the peaks 967.9 [M⁺+1] (100 % abundance of **5b**) and 704 [M⁺-1] (20 % abundance of **4b**). In the ¹H NMR spectra (CDCl₃), the most influenced signals were again those belonging to 5-CH₂O group: the corresponding singlet was located at 3.45 ppm in **1b**, 4.24 ppm in **5b** and 4.31 ppm in **4b**. Similarly, the triazine carbons were accidentally isochronous in **4b** (171.8 vs. 172.9 ppm in **5b**).

Finally we note that, according to data in **Table 1** issued from the ¹H NMR spectra of the crude reaction mixtures, the major components in all successful cases were the desired trisubstituted compounds **5a** (or **5b**) together with the corresponding starting materials **1a** (or **1b**). This supports our hypothesis about the partial uncontrollable decomposition of the cyanuryl chloride, as ring cleavage, in the depicted protocols. Thus, agreement was found with its related behaviour against dimethylformamide and active methylene compounds.¹³

3. CONCLUSION

The nucleophilic displacement of chlorine in cyanuryl chloride by the *c*-5-hydroxymethyl-3,7-dioxo-*r*-1-azabicyclo[3.3.0]octanes as *O*-potassium- or *O*-lithio-derivatives can be successfully achieved in mild conditions, to promote the di- or trisubstitution. The feasibility of the syntheses depends on the C-2, -8 functionality of the bicycle and the base (KH or *n*-BuLi) used to deprotonate the hydroxymethyl group.

4. EXPERIMENTAL

Melting points are not corrected; they were determined on an ELECTROTHERMAL[®] instrument.

NMR spectra were recorded on Brucker[®] AM 300 instrument operating at 300 and 75 MHz for ¹H and ¹³C nuclei respectively. No SiMe₄ was added; chemical shifts were measured against the solvent peak. All NMR spectra were measured in anhydrous commercially available deuterated solvents. All chemical shifts (δ values) were given throughout in ppm; all coupling patterns (*J* values) were given throughout in Hz. In the stereochemical assignment based on ¹H NMR spectra of the compounds **4a**, **b**, **5a**, **b**, the lone pair of the bridged N-1 was designed as fiducial substituent (reference); the bicyclic protons are labelled as H-*c* (*cis*) or H-*t* (*trans*) with respect to the fiducial substituent.

IR spectra were performed on a Perkin-Elmer[®] 16 PC FT-IR spectrometer. Only relevant absorptions were listed [throughout in cm⁻¹: weak (w), medium (m) or (s) strong].

Mass spectra (MS) were recorded on an ATI-Unicam Automass[®] apparatus, fitted (or not) with a GC-mass coupling (high-resolution J&W column, 30 m, 0.25 mm ID, flow rate: 1.2 mL min⁻¹).

All syntheses were performed under dry nitrogen atmosphere. THF was freshly distilled from Na/benzophenone prior to use. All solvents and starting materials were of commercial quality. The synthesis of the starting materials **1a** and **1b** were reported elsewhere.^{2,12}

Preparation of the compound 4a

A solution of *c*-5-hydroxymethyl-3,7-dioxa-*r*-1-azabicyclo[3.3.0]octane **1a** (1.450 g, 10.0 mmol) in THF (50 mL) was added to potassium hydride isolated by repeated washing with dry ligroin of 1.337 g as 30 % KH in mineral oil suspension (0.401 g 100 %, 10.0 mmol). The resulted suspension was stirred at 45 °C for 2 hrs. until no more hydrogen was formed. Cyanuryl chloride (0.571 g, 3.1 mmol) was added as THF (20 mL) solution. The reaction mixture was heated at 65 °C for 36 hrs. with vigorous stirring, until the starting **1a** was reasonably absent, as shown by the TLC monitoring (eluent ligroin : acetone 2:1 v/v). The reaction was quenched with isopropanol (1 mL) with stirring for additional 30 min. The mineral compounds were filtered off and washed with excess of THF. The combined THF solution was evaporated under vacuum to dryness to provide the crude product as yellow oil. Purification by flash column chromatography (eluent ligroin : acetone 2:1 v/v visualisation in I₂-bath) afforded the desired **4a** as a yellowish crystalline powder: 0.420 g (34 % yield).

2-Chloro-4,6-bis[(3,7-dioxa-*r*-1-azabicyclo[3.3.0]oct-*c*-5-yl)methoxy]s-triazine **4a** (34 %) yellowish crystalline powder, m.p. 91.8-93.4 °C; (flash column chromatography, eluent ligroin : acetone 2:1 v/v); *R*_f 0.75 (66 % ligroin/acetone); [Found: C, 44.91; H, 5.19; N, 17.63. C₁₅H₂₀N₅O₆Cl requires: C, 44.84; H, 5.02; N, 17.43 %]; *v*_{max} (KBr) 2971 (m), 2868 (s), 1731 (s), 1390 (m), 1252 (s), 1138 (m), 1038 (s), 926 (s), 885 (w), 792 (m), 673 (s), 610 (s), 505 (w) cm⁻¹; *δ*_H (300 MHz CDCl₃) 4.39 (4 H, s, H-2, -8-*c*), 4.37 (4 H, s, H-2, -8-*t*), 4.06 (4 H, s, 5-OCH₂), 3.73 (4 H, d, *J*=9.0 Hz, H-4, -6-*c*), 3.68 (4 H, d, *J*=9.0 Hz, H-4, -6-*t*); *δ*_C (75 MHz CDCl₃) 171.0 (3 C, C-2, -4, -6 triazine), 88.6 (4 C, C-2, -8), 74.2 (4 C, C-4, -6), 71.5 (2 C, C-5), 66.9 (2 C, 5-OCH₂); *δ*_H (300 MHz DMSO-*d*₆) 4.47 (4 H, d, *J*=5.7 Hz, H-2, -8-*c*), 4.33 (4 H, d, *J*=5.7 Hz, H-2, -8-*t*), 4.10 (4 H, s, 5-OCH₂), 3.80 (4 H, d, *J*=8.7 Hz, H-4, -6-*c*), 3.67 (4 H, d, *J*=8.7 Hz, H-4, -6-*t*); *δ*_C (75 MHz DMSO-*d*₆) 170.6 (3 C, C-2, -4, -6 triazine), 87.8 (4 C, C-2, -8), 73.5 (4 C, C-4, -6), 71.0 (2 C, C-5), 66.2 (2 C, 5-OCH₂); MS (EI), *m/z* (rel. int. %) 402 (< 1) [*M*⁺+1], 324 (38), 256 (57), 145 (58), 127 (100).

Preparation of the compound 5a

A solution of *c*-5-hydroxymethyl-3,7-dioxa-*r*-1-azabicyclo[3.3.0]octane **1a** (0.740 g, 5.10 mmol) in THF (25 mL) was cooled at -78 °C with stirring, then *n*-BuLi (1.6 M in hexane, 3.35 mL, 5.35 mmol) was injected to provide a clear white fine suspension. After 20 min., cyanuryl chloride (0.320 g, 1.70 mmol) was injected as THF (15 mL) solution. The reaction mixture was let very gently to reach the room temperature (20 hrs.) with vigorous stirring. The reaction was quenched with water (5 mL). The reaction mixture was evaporated to dryness then water (50 mL) and dichloromethane (50 mL) were added with stirring. After separation, the dichloromethane solution was washed with water to neutrality and then dried over MgSO₄. After

filtering and washing with dichloromethane, the organic solution was concentrated in vacuum to provide the crude product which was taken with Et₂O to yield the compound **5a** as white crystalline powder: 0.720 g (82 % yield).

2,4,6-Tris[(3,7-dioxa-*r*-1-azabicyclo[3.3.0]oct-*c*-5-yl)methoxy]s-triazine **5a** (82 %) white crystalline powder, m.p. 238.9-239.5 °C; (direct crystallization from Et₂O); *R*_f 0.30 (50 % ligroin/acetone); [Found: C, 49.44; H, 5.98; N, 16.44. C₂₁H₃₀N₆O₉ requires: C, 49.41; H, 5.92; N, 16.46 %]; *v*_{max} (KBr) 3444 (m), 2969 (w), 2858 (s), 1589 (s), 1414 (s), 1334 (s), 1189 (m), 1141 (m), 1096 (s), 1044 (s), 1028 (s), 943 (m), 807 (s), 750 (m), 718 (w), 676 (m), 572 (m) cm⁻¹; δ_{H} (300 MHz CDCl₃) 4.49 (6 H, d, *J*=5.6 Hz, H-2, -8-*c*), 4.42 (6 H, d, *J*=5.6 Hz, H-2, -8-*t*), 4.41 (6 H, s, 5-OCH₂), 3.85 (12 H, s, H-4, -6-*c*, -*t*); δ_{C} (75 MHz CDCl₃) 173.3 (3 C, C-2, -4, -6 triazine), 88.5 (6 C, C-2, -8), 74.3 (6 C, C-4, -6), 71.5 (3 C, 5-OCH₂) 71.3 (3 C, C-5); δ_{H} (300 MHz D₂O) 4.56 (6 H, d, *J*=6.0 Hz, H-2, -8-*c*), 4.51 (6 H, s, 5-OCH₂) 4.48 (6 H, d, *J*=6.8 Hz, H-2, -8-*t*), 3.99 (6 H, d, *J*=9.2 Hz, H-4, -6-*c*), 3.91 (6 H, d, *J*=9.2 Hz, H-4, -6-*t*); MS (ESI), *m/z* (rel. int. %) 532 [M⁺-1+Na⁺] (100), 511 (40) [M⁺], 384(10).

Preparation of the compounds **4b** and **5b**

A solution of *c*-5-hydroxymethyl-*c*-2,*c*-8-diphenyl-3,7-dioxa-*r*-1-azabicyclo[3.3.0]octane **1b** (1.48 g, 5.00 mmol) in THF (50 mL) was added to potassium hydride isolated by repeated washing with dry ligroin of 0.668 g as 30 % KH in mineral oil suspension (0.200 g 100 %, 5.00 mmol). The resulted yellow-greenish suspension was stirred at 45 °C for 2 hrs. until no more hydrogen was formed, then cooled at 0 °C. Cyanuryl chloride (0.302 g, 1.64 mmol) was rapidly added as THF (30 mL) solution. The reaction mixture was gently heated at 65 °C for 40 hrs. with vigorous stirring, until the starting **1a** was reasonably absent, as shown by the TLC monitoring (eluent ligroin : acetone 3.5:1 v/v, visualisation in UV-254 nm). The reaction was quenched with water (50 mL) and dichloromethane (125 mL) with stirring for additional 30 min. After separation, the aqueous layer was extracted with dichloromethane (3 × 25 mL) and the combined dichloromethane solution was washed with water to neutrality. After drying on MgSO₄, the organic solution was evaporated in under vacuum to yield 1.10 g of the crude reaction mixture. Purification by flash column chromatography (eluent ligroin : acetone 3.5:1 v/v visualisation in UV-254 nm) afforded the following fractions: 0.137 g recovered **1b**; 0.370 g desired **5b** as a white crystalline powder. The column was then completely eluted with pure acetone to afford 0.310 g mixture **5b** (66 %) + **4b** (34 %), according to the ¹H NMR spectrum.

2,4,6-Tris[(*c*-2,*c*-8-diphenyl-3,7-dioxa-*r*-1-azabicyclo[3.3.0]oct-*c*-5-yl)methoxy]s-triazine **5b** (37 %) white crystalline powder, m.p. 162.5-164.2 °C; (flash column chromatography, eluent ligroin : acetone 3.5:1 v/v); *R*_f 0.40 (78 % ligroin/acetone); [Found: C, 70.61; H, 5.70; N, 8.44. C₅₇H₅₄N₆O₉ requires: C, 70.80; H, 5.63; N, 8.69 %]; *v*_{max} (KBr) 3063 (w), 2871 (m), 1571 (s), 1417 (s), 1334 (s), 1210 (m), 1131 (s), 1088 (m), 1068 (m), 922 (m), 820 (w), 762 (m), 735 (s), 698 (s) cm⁻¹; δ_{H} (300 MHz CDCl₃) 7.51 (12 H, m, phenyl), 7.32-7.26 (18 H, m, phenyl), 5.59 (6 H, s, H-2, -8-*t*), 4.24 (6 H, s, 5-OCH₂), 4.06 (6 H, d, *J*=9.2 Hz, H-4, -6-*c*), 3.98 (6 H, d, *J*=9.2 Hz, H-4, -6-*t*); δ_{C} (75

MHz CDCl₃) 172.9 (3 C, C-2, -4, -6 triazine), 139.5 (6 C, Cq., phenyl), 129.1 (6 C, CH, phenyl), 128.8 (12 C, CH, phenyl), 127.5 (12 C, CH, phenyl), 97.6 (6 C, C-2, -8), 73.6 (6 C, C-4, -6), 72.8 (3 C, 5-OCH₂), 72.2 (3 C, C-5); MS (FAB⁺), *m/z* (rel. int. %) 968 (100) [M⁺+1].

2-Chloro-4,6-bis[(*c*-2,*c*-8-diphenyl-3,7-dioxa-*r*-1-azabicyclo[3.3.0]oct-*c*-5-yl)methoxy]-*s*-triazine 4b (8 %) white crystalline powder (flash column chromatography, eluent ligroin : acetone 3.5:1 v/v; δ_H (300 MHz CDCl₃) as detected from the mixture with **5b**: 5.59 (4 H, s, H-2, -8-*t*), 4.31 (4 H, s, 5-OCH₂), 4.06 (4 H, d, *J*=9.2 Hz, H-4, -6-*c*), 3.98 (4 H, d, *J*=9.2 Hz, H-4, -6-*t*); δ_C (75 MHz CDCl₃), 171.8 (3 C, C-2, -4, -6 triazine), 139.3 (4 C, Cq., phenyl), 127.5 (8 C, CH, phenyl); MS (FAB⁺), *m/z* (rel. int. %) 704 (20) [M⁺-1].

REFERENCES

- Berghian, C.; Maieranu, C.; Plé, N.; Plé, G.; Darabantu, M. *Studia Univ. Babes-Bolyai, Serie Chimia*, XLVII **2003**, 2, 113
- Darabantu M.; Maieranu, C.; Silaghi-Dumitrescu, I.; Toupet, L.; Condamine, E.; Ramondenc, Y.; Berghian, C.; Plé, G.; Plé, N. *Eur. J. Org. Chem.* **2004**, 12, 2644 and the patents cited therein.
- Broadbent, H. S.; Burnham, W. S.; Sheely, R. M.; Olsen, R. K. *J. Heterocyclic Chem.* **1976**, 13, 337
- Dudley, J. R.; Thuyston, J. T.; Schaefer, F. C.; Holm-Hansen, D.; Hull, C.J.; Adams, P. J. *Am. Chem. Soc.* **1951**, 73, 2986
- Weber, A. J. M.; Huysmans, W. G. B.; Mijs, W. J.; Bovee, W. M. M. J.; Smidt, J.; Vriend, J. *Recl. Trav. Chim. Pays-Bas* **1978**, 97, 107
- Menicagli, R.; Malanga, C.; Peluso, P. *Synth. Commun.* **1994**, 24, 2153
- Cronin, J. S.; Ginah, F. O.; Murray, R. A.; Copp, D. J. *Synth. Commun.* **1996**, 26, 3491
- Oi, N.; Nagase, M.; Sawada, Y. *J. Chromatogr. A* **1984**, 292, 427
- Iuliano, A.; Pieroni, E.; Salvadori, P. *J. Chromatogr. A* **1997**, 786, 355
- Lin, C. E.; Li, K. K.; Lin, C. H. *J. Chromatogr. A* **1996**, 722, 189
- Lin, C. E.; Li, K. K.; Lin, C. H. *J. Chromatogr. A* **1996**, 722, 211
- Darabantu, M.; Plé, G.; Maieranu, C.; Silaghi-Dumitrescu, I.; Ramondenc, Y.; Mager, S. *Tetrahedron* **2000**, 56, 3799-3816
- Katritzky, A.; Pozharskii, A. F. *Handbook of Heterocyclic Chemistry*, 2nd Edition, Pergamon **2000**, pp. 205, 215

FIRST SYNTHESIS, ROTAMERISM AND HERBICIDAL EVALUATION OF SUBSTITUTED *s*-TRIAZINES WITH SERINOLIC FRAGMENTS (I): OPEN-CHAIN STRUCTURES

MONICA PINTEA,^a MIRCEA DARABANTU,^{a,b*} MARIJANA FAZEKAS,^a
PEDRO LAMEIRAS,^b CAMELIA BERGHIAN,^{a,b} ISABELLE DELHOM,^{a,b}
CONSTANTIN BELE^c and NELLY PLÉ^b

^a"Babes-Bolyai" University, Department of Organic Chemistry, 11 Aranyi János str.,
RO-400028 Cluj-Napoca, Romania

^bUniversité de Rouen, Institut de Recherche en Chimie Organique Fine (I. R. C. O. F.),
BP-08, F-76131 Mont Saint-Aignan Cedex France

^cUniversity of Agricultural Sciences and Veterinary Medicine, 3-5 Manastur str.,
RO-400375 Cluj-Napoca, Romania

ABSTRACT. First series of melamines and precursors, starting from commercially *C*-substituted-2-amino-1,3-propanediols (pharmaceutical chemistry nomenclature as *serinols*) in reaction with cyanuryl chloride is reported. The diastereomerism generated by the more or less restricted rotation about the C^{sp2}(*s*-triazine)-N<(serinol) bond in this series is for the first time discussed along with a preliminary herbicidal evaluation of some representative terms.

INTRODUCTION

The chemistry of highly elaborated *N*-substituted triamino-*s*-triazines (*melamines*) is, nowadays, a part of supramolecular chemistry as dendrimers, tectons and macrocycles¹. In the last decade, the knowledge focused on their use as antiangiogenic, anticancer or antimicrobial agents^{2a-d}. They also led to new generation of herbicides and highly specific enzyme inhibitors^{2e}.

Among the suitable amines to provide interesting architectures, almost no attention was paid to *C*-substituted-2-amino-1,3-propanediols (the so called *serinols*): to our knowledge there are only two papers dealing with their reactivity against cyanuryl chloride^{3,4}. On the other hand, according to Katritzky and Ghiviriga recent findings, in *N*-substituted melamines as well as in their precursors, more or less hindered rotamerism phenomena are encountered with respect to the C^{sp2}(*s*-triazine)-N<(exocyclic) bond⁵⁻⁷. Extension of this concept rapidly disseminated the chemistry of melamine based anticancer drugs and dyes⁸⁻¹¹.

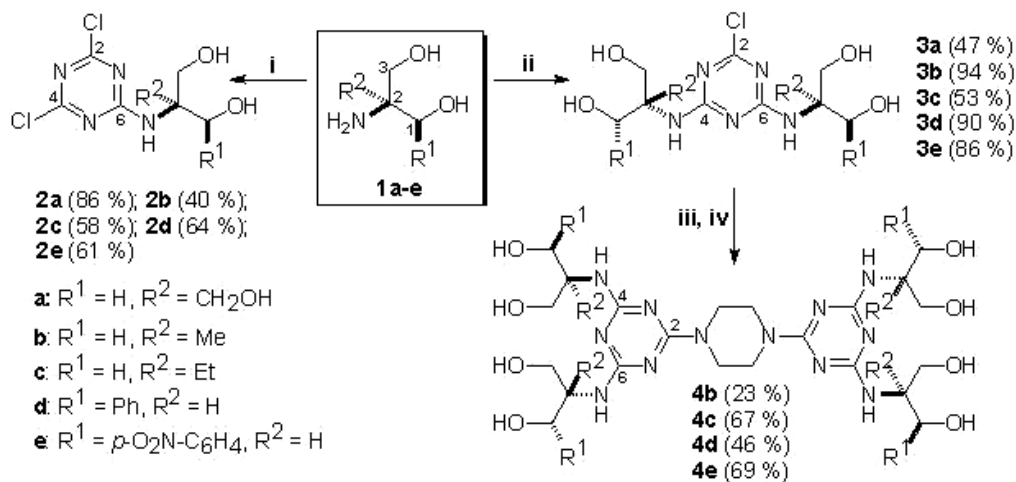
Starting from our previous expertise in the domain of *C*-substituted serinols chemistry^{12,13}, we got some insight on testing their versatile nucleophilicity against cyanuryl chloride. Thus, the aim of this preliminary communication is to report the synthesis and some properties of the first series of substituted *s*-triazines, including melamines, bearing serinolic fragments.

RESULTS AND DISCUSSION

1. Synthesis

The compounds under study were prepared following the synthetic pathway depicted in **Scheme 1**. It started from the commercially available serinols **1a-e**; the chiral serinols **1d, e** were used as pure 1*S*,2*S* enantiomers. Since the "dimeric" melamines **4b-e** were the target series, a convergent synthetic strategy was straightforward.

* darab@chem.ubbcluj.ro; darabantu@cluj.astral.ro; Fax: 00 40 264 59 08 18; Tel.: 00 40 264 59 38 33



Scheme 1

i) The first nucleophilic replacement of chlorine in cyanuryl chloride yielded the series **2a-e**. The preliminary results indicated this synthesis to be not quite of routine. Except the TRIS® (α,α,α -trimethylolaminomethane) derivative **2a**, all other compounds required isolation by flash column chromatography since, in the crude reaction mixture, the TLC monitoring revealed, besides unreacted starting materials, some traces of the disubstituted products **3a-e** together with traces of other side products. These by products originated presumably from the competitive statistic replacement of chlorine by the hydroxyl groups¹⁴. Serious complications also arose from the retention of the products on silica gel. However, our work up (e.g. *s*-triazines **2d**, **2e**) is only apparently a “drawback”: indeed, this behavior is already very well documented as useful methodology to access silica gel HPLC chiral *s*-triazines selectors for enantiomeric separation¹⁵. Accordingly, our yields were calculated as isolated amounts after flash column chromatography.

ii) Hence, the second nucleophilic substitution of chlorine was performed starting directly from **1a-e** in a one pot process. This option appeared correct, as shown by the yields obtained in the cases of compounds **3b**, **3d** or **3e** which were isolated by simple crystallization. Under identical conditions, pure **3a** was obtained only as a gummy solid despite repeated crystallizations.

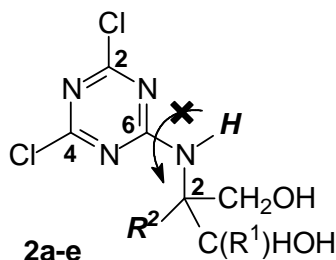
iii, iv) The last *s*-triazine chlorine was replaced by using piperazine as nucleophile to give the compounds **4b-e**. At this stage, we readily concluded that the hygroscopic piperazine should be preliminarily converted into its anhydrous hydrochloride. Next, upon treatment with the triazines **3** in refluxing 1,4-dioxane, the corresponding free base was *in situ* re-generated by the excess of proton scavenger:

the anhydrous potassium carbonate. Only this protocol was successful in order to avoid the formation of monosubstituted piperazines as side-products. However, in the case of the *s*-triazine **3a**, the TLC monitoring of the reaction indicated unpredictable decomposition; in contrast, starting from **3b-e**, the coupling was clean enough to afford the expected **4b-e** with satisfactory yields. These yields refer again to isolated products after flash column chromatography when the previously mentioned retentions on silica gel were observed.

2. Stereochemistry and rotameric behavior

At room temperature, all the series **2-4** exhibited peculiar stereochemistry consistent throughout with the hindered rotation about the C^{sp2}(*s*-triazine)-N<(exocyclic) bond. The supporting NMR study, in all cases, was carried out in DMSO-*d*₆ only.

2.1. 6-Amino-2,4-dichloro-*s*-triazines bearing one serinolic fragment: compounds **2a-e** (Scheme 1, Scheme 2)



Scheme 2

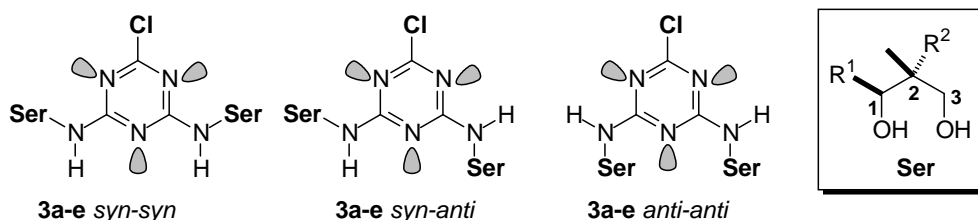
In the case of compounds **2a-e**, the ¹H NMR spectra performed at room temperature located the NH protons as the most deshielded and "rigid": 8.05 ppm (**2a**), 8.39 ppm (**2b**), 8.26 ppm (**2c**), 9.14 ppm (**2d**), 9.02 ppm (**2e**); yet, the 2D-¹H, ¹H-COSY Experiment of the phenylserinols derivatives **2d** and **2e** (R¹ = Ph, *p*-O₂N-C₆H₄, R² = H) evidenced a significant coupling pattern between the proton NH (as clear doublets, ³J=9.1-9.4 Hz) and H-2 from the aliphatic motif. In the ¹³C NMR spectra, the triazinic carbons C-2, -4 were found diastereotopic (two different signals around 161 ppm) in agreement with a hindered rotation about C-6-N(serinol) bond. The ¹³C diastereotopicity between positions 2, 4 (Δδ values, ppm) was independent on the type of serinol: 0.5-0.7 ppm.

By increasing the temperature (up to 80 °C in DMSO-*d*₆), the ¹³C NMR spectra reached no coalescence of the discussed signals, but some decomposition of the investigated compounds was observed.

2.2. 4,6-Diamino-2-chloro-*s*-triazines bearing two serinolic fragment: compounds **3a-e** (Scheme 1, Scheme 3)

For the present communication, discussion is constrained to the results obtained by ¹H NMR analysis at room temperature.

Thus, the same hindered rotation was twice found in the series **3a-e** to proof the combined effect of the two amino groups (+M) with the (-M) effect of the remaining chlorine atom. If so, the rotation barrier ΔG^\ddagger in series **3a-e** should be higher than those previously discussed in the literature in the case of 2-chloro-4,6-bis(dialkylamino)-s-triazines, 50.6-75.4 kJ/mol⁸⁻¹⁰. Symmetry considerations establish the compounds **3a-e** to exist as three diastereomers (blocked rotamers), discriminated by the stereochemical descriptors previously proposed by Ghiviriga⁷: *syn* (*s*) and *anti* (*a*) (the Serinol group and the C-2 chlorine atom as references, **Scheme 3**)



Scheme 3

At room temperature, the analysis of the ^1H NMR spectra disclosed, in each case, the presence of all three stereoisomers (**Table 1**).

The assignments were based on the well separated peaks displayed by the NH protons: sharp singlets in **3a-c** and typical doublets ($^3J=9.1\text{-}9.4$ Hz) in the cases of **3d** and **3e**. The stereochemistry as (*s-s*), (*s-a* \equiv *a-s*) and (*a-a*) was established starting from the rotamers of type **3(a-s)** since, besides twice statistically favored, they revealed unambiguously two different with equal intensity environments for the two serinolic groups, including the NH and OH protons. Therefore, in connection to this observed stereochemistry, we considered as pertinent the following two factors:

Table 1

Relevant ^1H NMR data and contribution of the blocked rotamers in the series **3a-e** (DMSO- d_6 , 293 K)

| Compound | Rotamers (averaged %) according to NH and OH signals | | | δ_{NH} (ppm) | | |
|-----------|--|----------------|----------------|----------------------------|----------------|----------------|
| | (<i>s-s</i>) | (<i>s-a</i>) | (<i>a-a</i>) | (<i>s-s</i>) | (<i>s-a</i>) | (<i>a-a</i>) |
| 3a | 24 ^a | 70 | 6 | 6.50 | 6.50 6.58 | 6.29 |
| | 29 ^b | 64 | 7 | | | |
| | 32 ^c | 62 | 6 | | | |
| 3b | 49 ^a | 48 | 3 | 6.78 | 6.75 6.66 | 6.41 |
| | 50 ^b | 45 | 5 | | | |
| 3c | 61 | 35 | 4 | 6.70 | 6.70 6.59 | 6.34 |
| 3d | 44 | 45 | 11 | 7.03 | 6.99 6.80 | 6.69 |
| 3e | 51 | 39 | 10 | 7.07 | 7.10 6.88 | 6.82 |

^astandard sample; ^bdilution as 1/3; ^cdilution as 1/9

a) The steric hindrance between the serinolic groups related to their C-1 (or C-2) substitution (**Scheme 3**, **Table 1**).

b) The solvation interactions required by the chelating DMSO- d_6 .

Calculations in **Table 1** were made by means of the signals of the protons *NH* and *OH*. It must be observed that in rotamers of type **3(a-a)** the resonance of the protons *NH* was found throughout upfield, in agreement with the weakest character of double bond of the linkage $C^{sp^2}(s\text{-triazine})-N<(\text{exocyclic})$. This assignment should be plausible since the steric hindrance conflicts with the coplanarity mandatory to the **Ser-NH-C(N)=N-** sequence (**Scheme 3**).

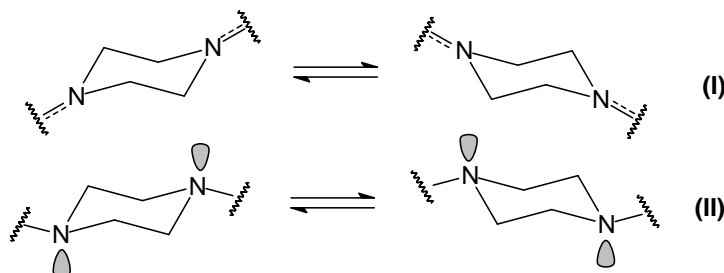
In the case of **3a**, possessing six hydroxyl groups, the strongest solvation interactions were expected. Thus, successive dilution showed a decreasing proportion of the rotamer **3a(s-a)** whilst the proportion of the less hindered rotamer **3a(s-s)** increased; probably because, in this latter case, the exposure of the hydroxyl groups to chelation was more favored.

By replacing one hydroxymethyl group with methyl (**3b**) or ethyl (**3c**), the resulted *s*-triazines were nearly an equimolar mixture of (*s-s*) + (*s-a*) rotamers (**3b**) or slightly dominant (*s-s*) rotamers (**3c**). No effect on stereochemistry was found following dilution, but the importance of the substitution at C-2 (methyl vs. ethyl) was evidenced.

The *s*-triazines **3d**, **3e** were also mainly (*s-s*) + (*s-a*) rotamers; however, the presence of a bulky substituent on the serinolic chain (to interact with the triazine skeleton) promoted the noteworthy occurrence of rotamers of type **3(a-a)**.

2.3. "Dimeric" melamines: compounds **4b-e** (**Scheme 1**, **Scheme 4**, **Scheme 5**)

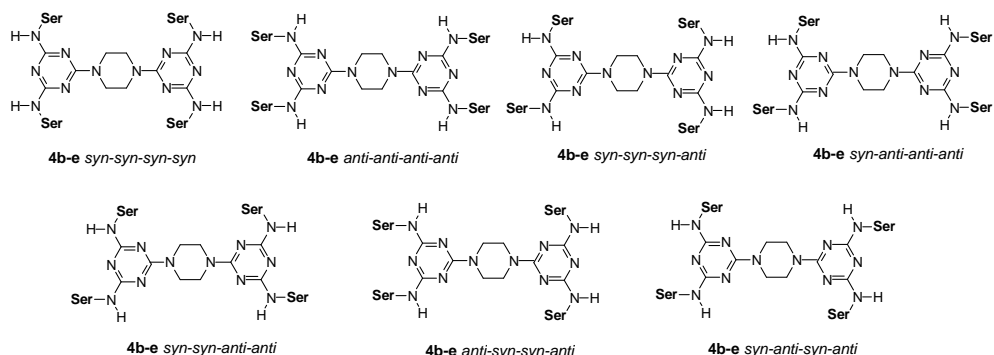
Based on literature data^{8,9}, we expected that the "dimeric" melamines **4b-e** possessing three donating (+M) ligands be free rotating structures ($\Delta G^\ddagger=59.3\pm 1$ kJ/mol in the range 315-325 K) with a mobile piperazine ring (chair-chair ring **I** and / or double pyramidal inversion **II**, **Scheme 4**).



Scheme 4

The same stereochemical analysis as in the series **3a-e** provided this time seven rotamers (**Scheme 5**, the serinol and piperazine groups as references; *syn* and *anti* descriptors are cited clockwise).

Obviously, it was not viable to assign a preferred arrangement by mean of NMR methods. Indeed, the NMR spectra carried out at room temperature had a very complex appearance and by far ambiguous (**Figure 1**, 293 K, compound **4e** considered as an illustrative example): it was hazardous to ascertain whether the signals belong to a blocked multicomponent mixture of rotamers (overlapped peaks ?)



Scheme 5

or a slow exchange between anisochronous sites occurring at room temperature. Moreover, on the 75 MHz ^{13}C NMR time scale, we only detected a single set of signals.

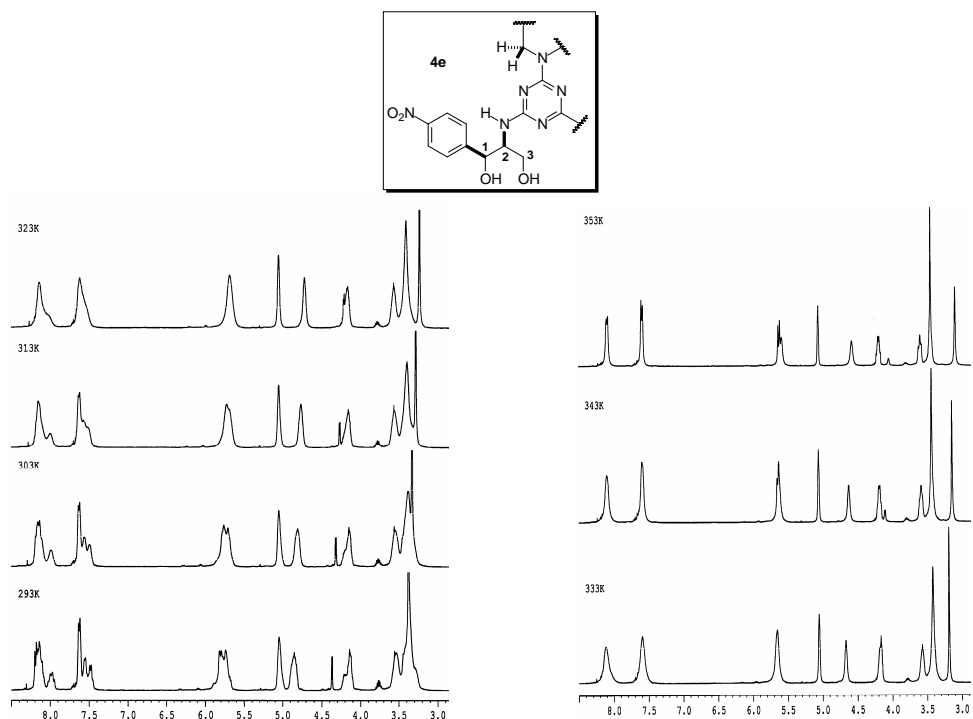


Figure 1: ^1H DNMR of the compound **4e** (400 MHz, $\text{DMSO}-d_6$); at 353 K from left to right, δ (ppm): 8.09 (2 H, d, H-Ar); 7.60 (2 H, d, H-Ar); 5.62 (1 H, d, NH); 5.58 (1 H, bs, OH-sec.); 5.06 (1 H, s, H-1); 4.57 (1 H, bs, OH-prim.); 4.18 (1 H, ddd, H-2); 3.59 (1 H, m, H-3); 3.44 (3 H, s, H-3 + 2 H-piperazine).

In contrast, the ^1H NMR spectra run by progressive increasing the temperature (**Figure 1**) permitted to observe the general coalescence at about 333 K and a single mediated structure at 353 K. The overlapped multiplet of *NH* protons was shifted upfield, from 5.80 ppm (293 K) to a clear unique doublet ($^3J=9.2$ Hz) at 5.62 ppm (353 K). That is, even at 80 °C, we avoided to consider the *NH* resonance as a typical “amine mobile proton”. In addition, the 2D- ^1H , ^1H -COSY Experiment at 353 K located all the other expected coupling patterns including the piperazine protons. They exhibited just a sharp singlet: no diastereotopicity due to the vicinity of (1*S*,2*S*)-serinolic chains was detected (**Figure 1**, 353 K).

3. Herbicidal evaluation

Following literature methodology¹⁶, the herbicidal activity of the series **3a-e** was evaluated by using seeds of *Cucumis sativus* and *Raphanus sativus*. Upon treatment with the compounds **3a-e**, the mean (\pm SD) values on the inhibition of root length were determined. They are collected in **Table 2**.

Table 2

Percent inhibitions of root length of *Cucumis sativus* and *Raphanus sativus* in response to different concentrations of the compounds **3a-e** compared to that of control

| Tested species Conc. | Root length | | | | |
|-------------------------|---------------|---------------|---------------|--------------|--------------|
| | 3a | 3b | 3c | 3d | 3e |
| <i>Cucumis</i> 0.50 mM | 66 \pm 5.4 | 70 \pm 6.4 | 68 \pm 5.8 | 56 \pm 3.7 | 54 \pm 4.3 |
| <i>sativus</i> 0.75 mM | 89 \pm 4.2 | 93 \pm 4.5 | 90 \pm 3.3 | 77 \pm 3.2 | 76 \pm 2.5 |
| 1.00 mM | 100 \pm 0.0 | 100 \pm 0.0 | 100 \pm 0.0 | 92 \pm 1.3 | 90 \pm 1.7 |
| <i>Raphanus</i> 0.50 mM | 67 \pm 3.5 | 72 \pm 4.6 | 69 \pm 3.8 | 61 \pm 6.5 | 59 \pm 7.4 |
| <i>Sativus</i> 0.75 mM | 90 \pm 2.1 | 94 \pm 1.8 | 92 \pm 2.4 | 79 \pm 5.7 | 76 \pm 2.6 |
| 1.00 mM | 100 \pm 0.0 | 100 \pm 0.0 | 100 \pm 0.0 | 93 \pm 1.9 | 91 \pm 2.3 |

As indicated by the preliminary data, compounds **3a-c** exhibited higher inhibition (including complete) effect in comparison with **3d**, **3e**. Although no reference compound was used along with the synthesized compounds, they already appeared active at 5×10^{-4} M as compared, in similar conditions, with Atrazine® ($> 10^{-4}$ M)^{16a}.

CONCLUSIONS

As shown by our preliminary results, the *C*-substituted-2-amino-1,3-propanediols react with cyanuryl chloride to afford amino-*s*-triazines in medium to good yields. Selectivity of the first and second chlorine replacement is complete, with respect to the polyfunctionality of the starting serinol. At room temperature, all *C*-substituted chloro-*s*-triazines with a serinolic *NH* group and serinols based melamines are blocked rotamers due to the partial double bond character of the $\text{C}^{\text{sp}^2}\text{-N}$ (serinol) site. The herbicidal activity in this class of *s*-triazines was tested. The full report of our findings is under consideration for the near future.

EXPERIMENTAL

General

Melting points were uncorrected; they were carried out on Electrothermal[®] instrument. Current NMR spectra were recorded on Brucker[®] AM 300 instrument operating at 300 and 75 MHz for ¹H and ¹³C nuclei respectively. The ¹H DNMR spectra were run on Brucker[®] AM 400 instrument operating at 400 MHz for ¹H nuclei with each step 10 K increasing the temperature. No SiMe₄ was added; chemical shifts were measured against the solvent peak. All chemical shifts (δ values) are given throughout in ppm; all coupling patterns (ⁿJ_{H,H} values) are given throughout in Hz. TLC was performed by using aluminium sheets with silica gel 60 F₂₅₄ (Merck[®]); flash column chromatography was conducted on Silica gel Si 60 (40–63 μ m, Merck[®]). IR spectra were performed on a Perkin-Elmer[®] 16 PC FT-IR spectrometer. Only relevant absorptions are listed [throughout in cm⁻¹: weak (w), medium (m) or (s) strong]. Mass spectrum (MS) was recorded on an ATI-Unicam Automass[®] apparatus, fitted (or not) with a GC-mass coupling (high-resolution J&W column, 30 m, 0.25 mm ID, flow rate: 1.2 mL min⁻¹).

For the present preliminary communication, only the synthetic pathway **2b** → **3b** → **4b** is listed below:

2,4-Dichloro-6-(1,3-dihydroxy-2-methylprop-2-yl)-amino-s-triazine (2b): (40 %) white crystalline powder; m.p.=141.0-142.5 °C (flash column chromatography, eluent toluene : *i*-Pr-OH 4:1 v/v); [Found: C, 33.11; H, 4.25; N, 21.89. C₇H₁₀N₄Cl₂O₂ requires C, 33.22; H, 3.98; N, 22.13 %]; IR (ν_{\max} , KBr) 3351 (s), 3220 (s), 2894 (s), 1702 (m), 1604 (s), 1563 (s), 1517 (s), 1333 (s), 1161 (s), 1066 (m), 1019 (s), 950 (w), 856 (m), 795 (w) cm⁻¹; ¹H NMR (300 MHz, DMSO-*d*₆, 293 K): 8.39 (1 H, s, NH), 4.84 (2 H, bs, OH), 3.62 (2 H, d, ²J=10.9 Hz, CH₂), 3.55 (2 H, d, ²J=10.9 Hz, CH₂), 1.26 (3 H, s, CH₃); ¹³C NMR (75 MHz, DMSO-*d*₆, 293 K): 168.8 (1 C, C-Cl), 168.3 (1 C, C-Cl), 165.2 (1 C, C-N), 62.5 (2 C, C-OH), 60.4 (1 C, C-q), 18.4 (1 C, CH₃); MS (CI, 200 eV); m/z (rel. int. %): 253 (100) [M⁺], 219 (20), 117 (15), 99 (10).

2-Chloro-4,6-bis(1,3-dihydroxy-2-methylprop-2-yl)-amino-s-triazine (3b): (94 %) white crystalline powder; m.p.=169.0-170.3 °C (Et₂O); [Found: C, 40.96; H, 6.55; N, 21.69. C₁₁H₂₀N₅ClO₄ requires C, 41.07; H, 6.27; N, 21.77 %]; IR (ν_{\max} , KBr) 3269 (s), 3103 (s), 2983 (s), 1625 (m), 1555 (s), 1391 (s), 1205 (s), 1161 (s), 1075 (s), 1041 (s), 959 (w), 802 (m), 737 (w) cm⁻¹; ¹H NMR (300 MHz, DMSO-*d*₆, 293 K): 6.78 (2 H, s, NH_{s-s}), 6.75 (1 H, s, NH_{s-a}), 6.66 (1 H, s, NH_{s-a}), 6.41 (2 H, s, NH_{a-a}), 5.20 (4 H, bs, OH_{a-a}), 4.82 (2 H, bs, OH_{s-a}), 4.65 (6 H, bs, 2 × OH_{s-a}, 4 × OH_{s-s}), 3.55 (24 H, m, CH_{2s-s, s-a, a-a}), 1.24 and 1.22 (18 H, s, CH_{3s-s, s-a, a-a}); ¹³C NMR (75 MHz, DMSO-*d*₆, 293 K): 167.2 (3 C, C-Cl), 165.3, 165.0 and 164.6 (6 C, C-N), 63.8, 63.4 and 63.1 (12 C, C-OH), 58.7 and 58.5 (6 C, C-q), 18.7 (6 C, CH₃); MS (CI, 200 eV); m/z (rel. int. %): 322 (100) [M⁺], 288 (10), 88 (5).

1,4-Bis[4,6-bis(1,3-dihydroxy-2-methylprop-2-yl)-amino-s-triazin-2-yl]-pipe-razine (4b): (23 %) white crystalline powder; m.p.=245-246 °C (flash column chromatography, eluent CHCl₃ : MeOH 2.5:1.0 v/v); [Found: C, 47.88; H, 6.99; N, 25.50. C₂₆H₄₈N₁₂O₈

requires C, 47.55; H, 7.37; N, 25.59 %]. IR (ν_{\max} , KBr) 3404 (s), 3329 (s), 2935 (s), 2854 (s), 1586 (m), 1543 (s), 1390 (m), 1354 (m), 1262 (m), 1185 (w), 1049 (s), 1016 (m), 983 (w), 806 (m) cm^{-1} ; ^1H NMR (300 MHz, DMSO- d_6 , 293 K): 5.66 (4 H, bs, NH), 4.87 (8 H, bs, OH), 3.64-3.47 (24 H, m, CH_2), 1.25 (12 H, s, CH_3); ^{13}C NMR (75 MHz, DMSO- d_6 , 293 K): 165.5 (2 C, C-N), 165.3, 164.3 (4 C, C-N), 63.4, (8 C, C-OH), 52.0 (4 C, C-q), 19.2 (4 C, CH_3); ^1H NMR (400 MHz, DMSO- d_6 , 353 K): 5.53 (4 H, s, NH), 4.68 (8 H, bs, OH), 3.67 (8 H, s, CH_2 piperazine), 3.62 (8 H, d, $^2J=10.8$ Hz, CH_2), 3.52 (8 H, d, $^2J=10.4$ Hz, CH_2), 1.28 (12 H, s, CH_3); MS (FAB $^+$); m/z (rel. int. %): 657 [M^+] (22), 442 (100), 286 (80), 223 (60).

REFERENCES

1. **a)** Whitesides, M. G.; Simanek, E. E.; Mathias, P. J.; Seto, C. T.; Chin, N. D.; Mammen, M.; Gordon, M. D. *Acc. Chem. Res.* **1995**, *28*, 37-44; **b)** Zhang, W.; Simanek, E. E. *Org. Lett.* **2000**, *2*(6), 843-845; **c)** de Hoog, P.; Gumez, P.; Driessen, W. L.; Reedijk, J. *Tetrahedron Lett.* **2002**, *43*, 6783-6785; **c)** Sauriat-Dorizon, H.; Maris, T.; Wuest, D. J. *J. Org. Chem.* **2003**, *68*, 240-246; **d)** Sandford, G. *Chem. Eur. J.* **2003**, *9*(7), 1465-1469; **e)** Anelli, P. L.; Lunazzi, F.; Montanari, F.; Quici, S. *J. Org. Chem.* **1984**, *49*, 4197-4203; **f)** Lowik, D. W. P. M.; Lowe, C. R. *Tetrahedron Lett.* **2000**, *41*, 1837-1840; **g)** Lowik, D. W. P. M.; Lowe, C. R. *Eur. J. Org. Chem.* **2001**, 2825-2839; **h)** Schara, S.; Germeroth, L.; Schneider-Mergener, J.; Wenschuh, H. *J. Org. Chem.* **2001**, *66*, 507-513; **i)** Bork, J. T.; Lee, W. J.; Khersonsky, S. M.; Moon, H.-S.; Chang, Y.-T. *Org. Lett.* **2002**, *5*(2), 117-120
2. **a)** Ono, M.; Kawahara, N.; Goto, D.; Wakabayashi, Y.; Ushiro, S.; Yoshida, S.; Izumi, H.; Kuwano, M.; Sato, Y. *Cancer Res.* **1996**, *56*, 1512-1516; **b)** Draber, W.; Tietjen, K.; Kluth, J. F.; Trebst, A. *Angew. Chem. Int., Ed. Engl.* **1991**, *30*, 1621-1633; **c)** Hajduk, P. J.; Dinges, J.; Schkeryantz, J. M.; Janowick, D.; Kaminski, M.; Tufano, M.; Augeri, D. J.; Petros, A.; Nienaber, V.; Zhong, P.; Hammond, R.; Coen, M.; Beutel, B.; Katz, L.; Fesik, S. W. *J. Med. Chem.* **1999**, *42*, 3852-3859; **d)** Maeda, M.; Iogo, M.; Tsuda, H.; Fujita, H.; Yonemura, Y.; Nakagawa, K.; Endo, Y.; Sasaki, T. *Anti-Cancer Drugs Des.* **2000**, *15*, 217-223; **e)** Silen, J. L.; Lu, A. T.; Solas, D. W.; Gore, M. A.; MacLean, D.; Shah, N. H.; Coffin, L. M.; Bhinderwala, N. S.; Wang, Y.; Tsutsui, K. T.; Look, G. C.; Campbell, D. A.; Hale, R. L.; Navre, M.; Deluca-Flaherty, C. R. *Antimicrob. Agents Chemoter.* **1998**, *42*, 1447-1453
3. Kraiz, B. O.; Remizov, A. L. *Zh. Org. Khim.* **1979**, *15*(16), 1282-1283
4. Baxi, G.; Pandya, A.; Pakikh, A. R. *J. Inst. Chem. (India)* **1996**, *68*(2), 44-45
5. Katritzky, A. R.; Ghiviriga, I.; Oniciu, D. C.; Barkock, A. *J. Chem. Soc. Perkin Trans. 2* **1995**, 785-792
6. Katritzky, A. R.; Ghiviriga, I.; Steel, P. G.; Oniciu, D. C. *J. Chem. Soc. Perkin Trans. 2* **1996**, 443-447
7. Ghiviriga, I.; Oniciu, D. *Chem. Commun.* **2002**, *22*, 2718-2719
8. Amm, M.; Platzer, N.; Guilhem, J.; Bouchet, J. P.; Volland, J. P. *Magn. Reson. Chem.* **1998**, *36*, 587-596
9. Amm, M.; Platzer, N.; Bouchet, J. P.; Volland, J. P. *Magn. Reson. Chem.* **2001**, *39*, 77-84
10. Birkett, H. E.; Harris, R. K.; Hodgkinson, P.; Carr, K.; Charlton, M. H.; Cherryman, J. C.; Chippendale, A. M.; Glover, R. P. *Magn. Reson. Chem.* **2000**, *38*, 504-511

11. Birkett, H. E.; Cherryman, J. C.; Chippendale, A. M.; Evans, J. O. S.; Harris, R. K.; James, M.; King, I. J.; Mc. Pherson, G. *Magn. Reson. Chem.* **2003**, *41*, 324-336
12. Maieranu, C.; Darabantu, M.; Plé, G.; Berghian, C.; Condamine, E.; Ramondenc, Y.; Silaghi-Dumitrescu, I.; Mager, S. *Tetrahedron* **2002**, *58*, 2681-2693
13. Darabantu, M.; Maieranu, C.; Silaghi-Dumitrescu, I.; Toupet, L.; Condamine, E.; Ramondenc, Y.; Berghian, C.; Plé, G.; Plé, N. *Eur. J. Org. Chem.* **2004**, *12*, 2644-2661
14. Cronin, S. J.; Ginah, F. O.; Murray, A. R.; Copp, J. D. *Synth. Commun.* **1996**, *26*(18), 3491-3493
15. **a)** Oi, N.; Nagase, M.; Sawada, Y. *J. Chromatogr. A* **1984**, *292*, 427; **b)** Iuliano, A.; Pieroni, E.; Salvadori, P. *J. Chromatogr. A* **1997**, *786*, 355; **c)** Lin, C. E.; Li, K. K.; Lin, C. H. *J. Chromatogr. A* **1996**, *722*, 189; **d)** Lin, C. E.; Li, K. K.; Lin, C. H. *J. Chromatogr. A* **1996**, *722*, 211
16. **a)** Grossmann, K.; Tresch, S.; Plath, Z. *Naturforsch* **2001**, *56c*, 559-569; **b)** Omokawa, H.; Konnai, M. *Pestic. Sci.* **1992**, *35*, 83-86; **c)** Omokawa, H.; Ichizen, N.; Takematsu, T. *Agric. Biol. Chem.* **1987**, *51*, 2563-2568

FIRST SYNTHESIS, ROTAMERISM AND HERBICIDAL EVALUATION OF SUBSTITUTED *s*-TRIAZINES WITH SERINOLIC FRAGMENTS (II): AMINO-1,3-DIOXANES OF (1*S*,2*S*)-*p*-NITROPHENYLSERINOLS

MARIJANA FAZEKAS,^a MIRCEA DARABANTU,^{a,b*} MONICA PINTEA,^a
PEDRO LAMEIRAS,^b CONSTANTIN BELE,^c CAMELIA BERGHIAN^{a,b}
and NELLY PLÉ^b

^a"Babes-Bolyai" University, Department of Organic Chemistry, 11 Aranyi
János str., RO-400028 Cluj-Napoca, Romania

^bUniversité de Rouen, Institut de Recherche en Chimie Organique Fine (I.
R. C. O. F.), BP-08, F- 76131 Mont Saint-Aignan Cedex France

^cUniversity of Agricultural Sciences and Veterinary Medicine, 3-5
Manastur str., RO-400375 Cluj-Napoca, Romania

ABSTRACT. Pure enantiomeric amino-1,3-dioxanes, obtained by total diastereospecific ring closure of (1*S*,2*S*)-2-(substituted)amino-1-(4-nitrophenyl)-propane-1,3-diols ("*nitrophenylserinols*") reacted with cyanuryl chloride to afford *N*-substituted triamino-*s*-triazines (*melamines*) and precursors. Their rotameric behaviour around the C^{sp2}(triazine)-N(1,3-dioxane) bond is discussed in terms of NMR, as steric and electronic influence of the substituents. The herbicidal evaluation of two of the new compounds is also pointed out.

INTRODUCTION

We have previously reported our methodology to prepare pure enantiomeric 5-amino-1,3-dioxanes¹⁻⁵ by direct diastereospecific ring closure of (1*S*,2*S*)-2-amino-1-(4-nitrophenyl)-propane-1,3-diol (the so called "*nitrophenylserinol*") and its *N,N*-dimethyl analogue upon treatment with certain aldehydes in strong acidic media (98 % H₂SO₄, 0 °C). These aminodioxanes exhibited useful reactivity upon treatment with typical electrophiles: aryl(di)aldehydes and acid (poly)chlorides¹⁻³.

For the present preliminary communication, our outstanding attention is dedicated to the reaction between two representative compounds in this class and cyanuryl chloride with a concise stereochemical approach of the products. To the best of our knowledge, amino-1,3-dioxanes were never considered as nucleophiles against cyanuryl chloride though some *N*-substituted-amino-*s*-triazines bearing an acetal motif are mentioned in the literature to be potential anticancer agents⁶.

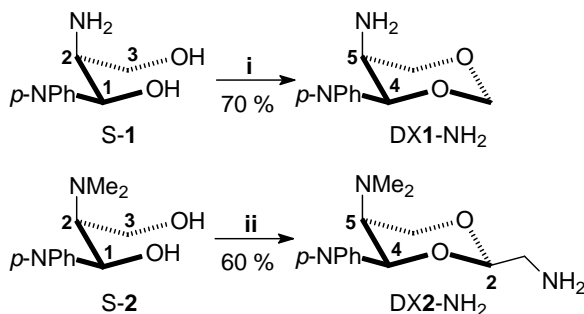
RESULTS AND DISCUSSION

1. Synthesis

The starting amino-1,3-DioXanes (DX-NH₂) were prepared from the enantiomerically pure (1*S*,2*S*) serinols **S-1** and **S-2** (**Scheme 1**, *p*-Nitro-Phenyl: *p*-NPh). The synthesis and stereochemistry of DX1-NH₂ we reported elsewhere^{1,4}; the same protocol gave DX2-NH₂ in satisfactory optimized yield and total diastereoselectivity

* darab@chem.ubbcluj.ro; darabantu@cluj.astral.ro; Fax: 00 40 264 59 08 18; Tel.: 00 40 264 59 38 33

(*R*) with respect to the absolute configuration at C-2. Both compounds are stable solid crystalline and anachomeric structures, possessing the aromatic group in equatorial position. It is already useful to observe that in DX1-NH₂ the amino group is placed in axial position flanked by the preferred bisectonal orientation of the aromatic ring (*cis* relationship) whereas in DX2-NH₂ the methyleneamino sequence is equatorial.

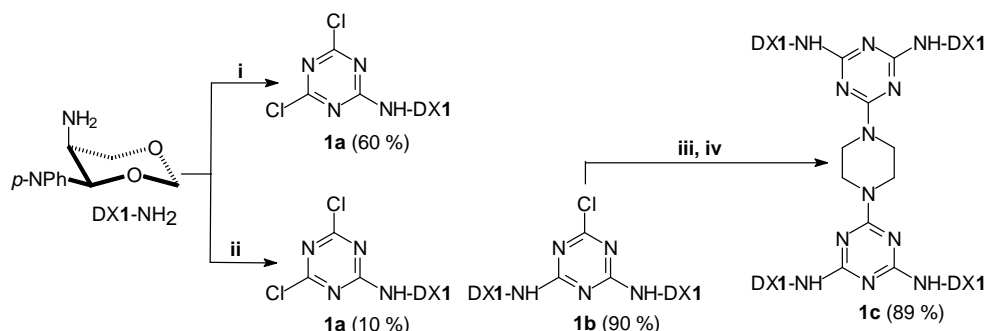


i: 1 eq. CH₂O / 10 eq. H₂SO₄ 98 % / 24 hrs. from 0 °C to r.t.; ii: 1 eq. H₂N-CH₂-CH(OR)₂ (R = Me, Et) / 10 eq. H₂SO₄ 98 % / 24 hrs. from 0 °C to r.t.

Scheme 1

The nucleophilicity of DX1-NH₂ against chloro-*s*-triazines was first tested (**Scheme 2**, partial conversions of cyanuryl chloride is presented in round brackets).

In a first effort (route i) we obtained the expected **1a** with a satisfactory yield; TLC monitoring of the reaction evidenced also the noticeable presence of the unreacted starting materials. Attempting at a melamine based on DX1-NH₂ (route ii) failed: the successive replacement of chlorine in cyanuryl chloride stopped after the second substitution. Instead, the chloro-diamino-*s*-triazine **1b** was isolated with excellent yield, together with **1a** as side product. They were separated by flash column chromatography. Matching results we reached when the proton scavenger was the "proton sponge" (1,8-bis-dimethylaminonaphthalene). However, if reducing

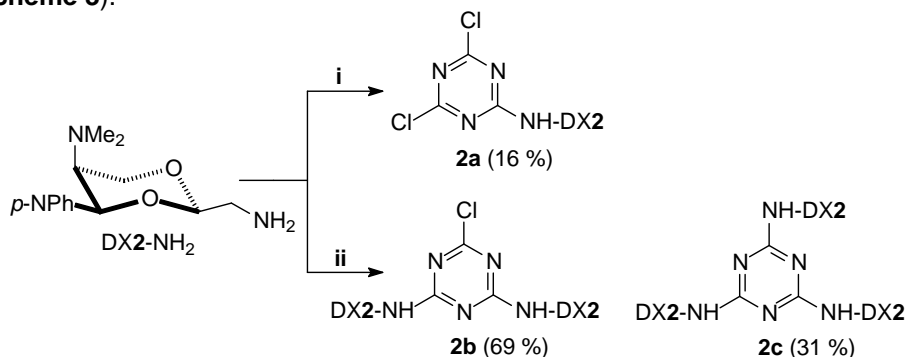


i: 1.05 eq. C₃N₃Cl₃ / 1.00 eq. anh. K₂CO₃ / THF / 24 hrs. from 0 °C to r.t.; ii: 0.33 eq. C₃N₃Cl₃ / 1.00 eq. anh. K₂CO₃ / toluene / 24 hrs. at reflux; iii: 0.49 eq. piperazine hexahydrate, 1.15 eq. HCl / *i*-PrOH; iv: 0.49 eq. piperazine hydrochloride / 2.00 eq. anh. K₂CO₃ / toluene / 12 hrs. at reflux.

Scheme 2

the amount of cyanuril chloride (0.47 eq., 1.0 eq. K_2CO_3), the partial conversions changed as 47 % (**1a**) and 53 % (**1b**). That is, it was impossible to link three DX1-NH units to the triazine ring, presumably because the intimate stereochemistry of the DX1-NH₂ which influenced the nucleophilicity of the 5-amino group. Consequently, in order to access melamines based on aminodioxane DX1-NH₂, our option focused on a stronger nucleophile, piperazine (**Scheme 2**, routes **iii**, **iv**). Its hygroscopicity was avoided by preliminary conversion into hydrochloride. The “dimeric” melamine **1c** was prepared in good yield in a very clean reaction.

The same chemistry starting from DX2-NH₂ provided different results (**Scheme 3**).



i: 1.05 eq. $C_3N_3Cl_3$ / 1.05 eq. anh. K_2CO_3 / THF / 24 hrs. from 0 °C to r.t.; **ii**: 0.30 eq. $C_3N_3Cl_3$ / 1.00 eq. anh. K_2CO_3 / toluene / 24 hrs. at r.t. / 24 hrs. at 70 °C / 24 hrs. at reflux

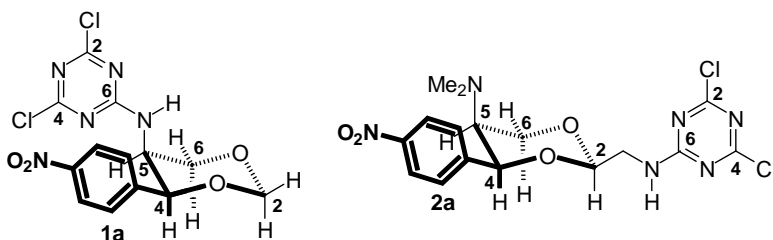
Scheme 3

As depicted in **Scheme 3**, dissimilarity was clearly evidenced. Thus, in route **i**, despite the very slow contact between reagents, the compound **2a** was isolated by flash column chromatography in poor yield. The side product, with complex NMR spectra, appeared to be an oligomeric structure, most probably issued from the competitive replacement of chlorine by both the nucleophilic sites in DX2-NH₂. In cyanuril chloride chemistry (seen as electrophile) this *N*-dealkyl-*N*-acylation of tertiary amines is already very well documented⁷. In route **ii**, we overcame this behaviour by involving, from the beginning, a large excess (300 %) of the aminodioxane. This method allowed obtaining the melamines **2b** and **2c**. No traces of **2a** were found in the crude reaction mixture.

2. Stereochemistry and rotameric behaviour

2.1. *N*-Substituted-2,4-dichloro-6-amino-*s*-triazines with 1,3-dioxane fragments: compounds **1a**, **2a** (**Scheme 4**)

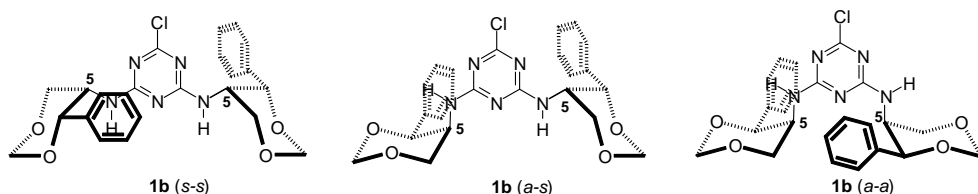
Both the compounds are anachomeric structures with a double bond character of the linkage C-6(*s*-triazine)-N(1,3-dioxane), hence a restricted rotation in this sequence: in the ¹³C NMR spectra, the triazine positions 2 and 4 were found diastereotopic (e.g. $\Delta\delta=0.5$ ppm, **1a**). The protons NH displayed a typical ³J splitting (e.g. ³J=9.2-9.4 Hz, **1a**) to support a fixed location. In the case of **1a**, one can also anticipate some hindered rotation about the axial C-5-N bond, due to the proximity of the ligands H-6-eq. and *p*-NPh, predicting an *out* orientation of the triazine moiety.



Scheme 4

2.2. *N*-Substituted-2-chloro-4,6-diamino-*s*-triazines with 1,3-dioxane fragments: compounds **1b**, **2b**

For the present communication, discussion is limited to assignments at room temperature. The NMR spectra of the compounds **1b**, **2b** revealed the diastereomerism issued from the restricted rotation about the C^{sp²}(triazine)-N(dioxane) bond as mixtures of three blocked rotamers^{8,9}: *syn-syn* (*s-s*), *syn-anti* (*s-a*) and *anti-anti* (*a-a*). The dioxane fragments and the triazine chlorine are references for these descriptors (**Scheme 5**, **Table 1**, **Figure 1** and **2**; in **Scheme 5** the *p*-nitro group was omitted for reason of simplicity).



Scheme 5

Table 1

Relevant ¹H NMR data and contributions of the blocked rotamers for the compounds **1b**, **2b**

| | Solvent | Rotamers (%) according to NH signals | | | δ_{NH} (³ J, Hz) | | |
|-----------|-------------------------------|--------------------------------------|----------------|----------------|--|---------------------------|----------------|
| | | (<i>s-s</i>) | (<i>s-a</i>) | (<i>a-a</i>) | (<i>s-s</i>) | (<i>s-a</i>) | (<i>a-a</i>) |
| 1b | DMSO- <i>d</i> ₆ | 34 | 53 | 13 | 7.55 (8.8) ^a | 7.55 (8.8), 7.13 (9.6) | 7.10 (11.6) |
| | C ₆ D ₆ | 53 | 24 | 23 | 6.48 (8.3) | 5.57 (9.1), 5.78 (9.8) | 5.85 (9.8) |
| | CDCl ₃ | 26 | 54 | 20 | 6.09 (9.4) | 5.88 (9.4), 5.71 (9.8) | 6.00 (9.8) |
| 2b | DMSO- <i>d</i> ₆ | 43 | 47 | 10 | 8.15 (8.4) ^b | 8.06 (8.0), 8.01 (6.0) | 7.79 (6.0) |
| | C ₆ D ₆ | 43 | 46 | 11 | 7.45 ^c | 7.55, 5.49 | 6.63 |
| | CDCl ₃ | 50 | 41 | 9 | 6.36 | 6.20, 5.62 | 6.03 |

^adoublets; ^btriplets (overlapped doublets of doublets); ^coverlapped doublets of doublets as coalescent triplets

As expected, the “reference” protons were *NH* and used for the calculations (**Table 1**): isochronous in environments (*s-s*) and (*a-a*) but anisochronous in (*s-a*). The rotamerism appeared strongly dependent on the stereochemistry of the linkage dioxane-triazine, axial or equatorial (**Figure 1** and **2**).

Thus, the contributions of the rotamers of **2b** showed the minor occurrence of the most hindered one (*a-a*), quite similar with the corresponding open-chain derivatives⁸. The protons *NH* were splitted as overlapped doublets of doublets [(coalescent) triplets] with mediated 3J values (6-8 Hz) with the diastereotopic adjacent methylene group, to prove the free rotation around the $>CH_2-N<$ bond (**Figure 2**). The A.S.I.S. (**Aromatic Solvent Induced Shifts**) phenomena¹⁰ had no influence on the content of rotamers.

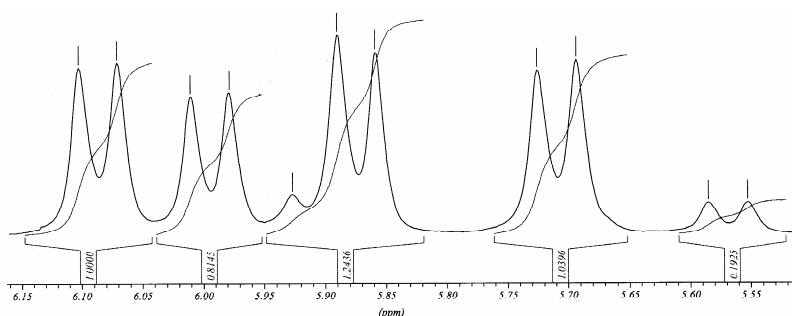


Figure 1: 1H -NMR spectrum of the compound **1b** (300 MHz, $CDCl_3$, 293 K), detail in the region of the protons *NH*.

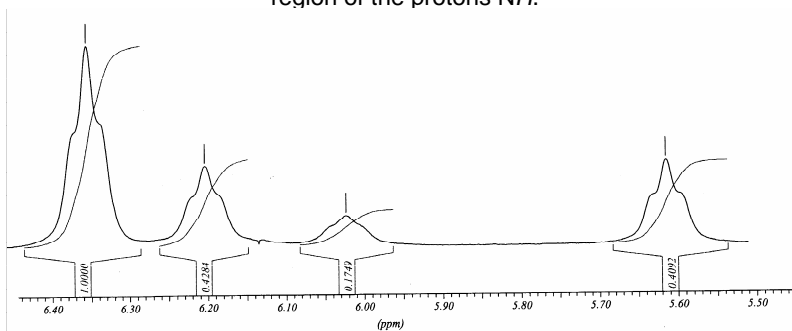


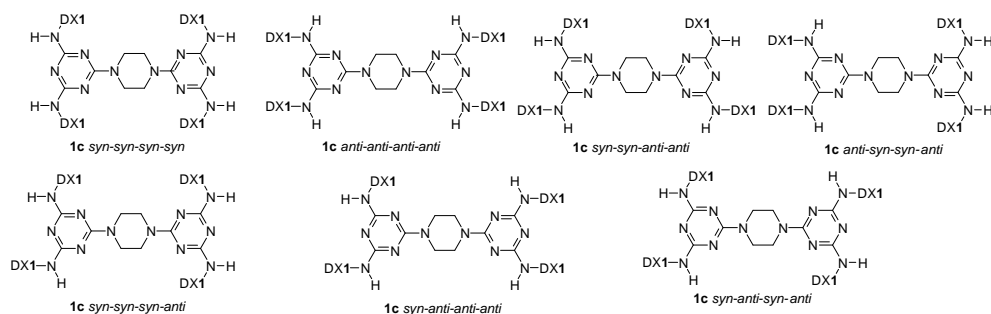
Figure 2: 1H -NMR spectrum of the compound **2b** (300 MHz, $CDCl_3$, 293 K), detail in the region of the protons *NH*.

Surprisingly, the NMR spectra of **1b** clearly indicated that this molecule, arising from a bulky nucleophile, can adopt all possible spatial arrangements (*s-s*, *s-a*, *a-a*) suggested by the manipulation of the Drieding models (**Scheme 5**, **Figure 1**). Moreover, as shown in **Figure 1**, in $CDCl_3$, another pair of doublets was revealed to indicate a fourth minor rotamer which was not assigned. It must be observed that, in all stereoisomers, the coupling pattern as 3J between protons *NH* and H-5-*eq.* were more significant, in agreement with some hindrance to rotation about the axial C-5-*NH* bond (**Table 1**). A major dependence on the solvent was determined

related to the content of rotamers of **1b**: the statistically favoured (*s-a*) rotamer was dominant in polar and chelating solvent (DMSO- d_6) or only polar (CDCl₃). In contrast, the A.S.I.S. interactions required the rotamer (*s-s*) as prevailing.

2.3. *N*-substituted melamines with dioxane fragments: compounds **1c**, **2c**

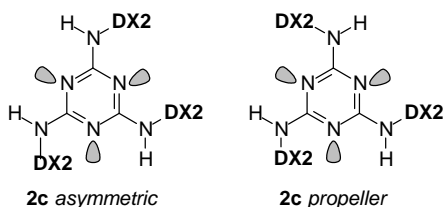
The “dimeric” melamine **1c** can exist as seven distinct rotamers (**Scheme 6**, the 1,3-dioxane and piperazine rings as references; the *syn* and *anti* descriptors are cited clockwise)⁸. At room temperature, the ¹H NMR 300 MHz spectra (CDCl₃ and DMSO- d_6) were complex and allowed only to identify the type of compound as the envisaged one. The ¹H DNMR (400 MHz, DMSO- d_6) recorded by increasing the temperature ($\Delta T=10$ K) provided at 80 °C a single mediated structure with however some residual coalescence in the aromatic and C-6 methylene regions.



Scheme 6

The melamine **2c** can exist as two distinct rotamers: *asymmetric* and *propeller*⁹ (**Scheme 7**) the first being statistically three times favoured.

Indeed, at room temperature, the ¹H NMR spectra (300 MHz, DMSO- d_6 and C₆D₆) were consistent with the statistics displaying four equal broad singlets of the best separated protons NH: 75 % *asymmetric* and 25 % *propeller*. All other signals were overlapped; however, they permitted, as in the case of **1c**, to confirm the type of structure as the desired one. It is noteworthy that the NMR spectra of compound **2c** performed at room temperature in CDCl₃ indicated a single mediated structure on both ¹H (300 MHz) and ¹³C (75 MHz) NMR spectra with some residual coalescence involving the NH-CH₂ sequence. The ¹H DNMR (400 MHz, DMSO- d_6) experiment of **2c** exhibited progressive coalescence of the signals between 323–353 K and a single mediated rotamer at 353 K (**Figure 3**, labelling of the dioxane position as depicted in **Scheme 4**).



Scheme 7

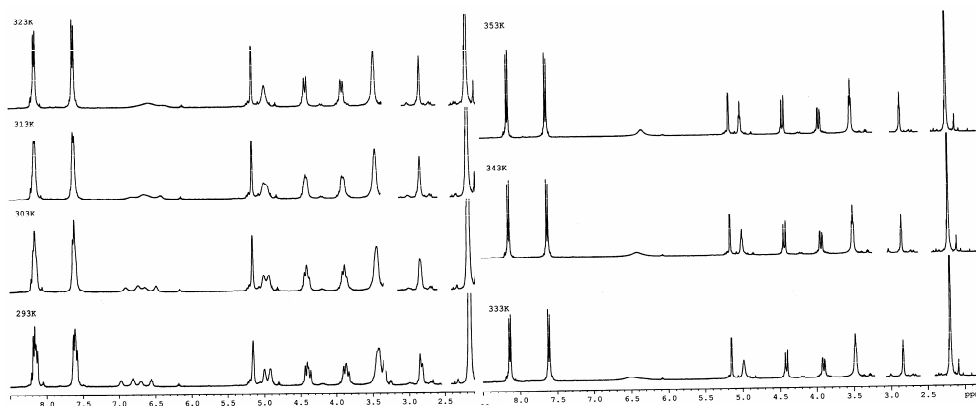


Figure 3: ^1H DNMR of the compound **2c** [400 MHz, $\text{DMSO}-d_6$, 353 K, from left to right, δ (ppm), nJ (Hz)]: 8.13 (6 H, d, $^3J=8.8$ Hz, H-Ar); 7.62 (6 H, d, $^3J=8.8$ Hz, H-Ar); 6.32 (3 H, bs, NH); 5.15 (3 H, d, $^3J=3.6$ Hz, H-4-ax.); 5.00 (3 H, dd as t, $^3J=4.6$ Hz, H-2-ax.); 4.42 (3 H, d, $^2J=12.4$ Hz, H-6-eq.); 3.92 (3 H, dd, $^2J=12.4$ Hz, $^3J=3.2$ Hz, H-6-ax.); 3.50 (6 H, dd as t, $^3J=5.2$ Hz, $\text{CH}_2\text{-NH}$); 2.83 (3 H, dd as t, $^3J=2.6$ Hz, H-5-eq.); 2.23 (18 H, s, CH_3).

3. Herbicidal evaluation

Compounds **1b** and **2b** were in addition tested as potential herbicides on seeds of *Cucumis sativus* and *Raphanus sativus*. Literature methods were straightforward¹¹. The results, as mean (\pm SD) percentage values of germination inhibition and root length are collected in **Table 2**.

Table 2

Percent inhibitions of seeds germination and root length of *Cucumis sativus* and *Raphanus sativus* in response to different concentrations of the compounds **1b** and **2b** compared to control

| Tested species | Conc. | Germination | | Root Length | |
|-------------------------|---------|---------------|---------------|--------------|--------------|
| | | 1b | 2b | 1b | 2b |
| <i>Cucumis sativus</i> | 0.50 mM | 59 \pm 4.8 | 60 \pm 3.9 | 65 \pm 5.4 | 67 \pm 6.5 |
| | 0.75 mM | 87 \pm 2.3 | 89 \pm 2.5 | 88 \pm 3.2 | 92 \pm 3.8 |
| | 1.00 mM | 100 \pm 0.0 | 100 \pm 0.0 | - | - |
| <i>Raphanus sativus</i> | 0.50 mM | 64 \pm 7.3 | 66 \pm 5.3 | 70 \pm 4.6 | 73 \pm 6.7 |
| | 0.75 mM | 88 \pm 3.5 | 90 \pm 2.7 | 91 \pm 3.9 | 93 \pm 5.6 |
| | 1.00 mM | 100 \pm 0.0 | 100 \pm 0.0 | - | - |

Our introductory data evidenced an important inhibition in germination seeds of the tested species, even complete (c. 1mM). The root length was also significantly reduced. Although no reference compound was used along with the synthesised **1b**, **2b**, they already appeared active at 5×10^{-4} M in comparison with Atrazine[®] ($>> 10^{-4}$ M), in the same conditions^{11a}.

CONCLUSIONS

As demonstrated by our preliminary findings, the amino-1,3-dioxanes built on some *p*-nitrophenylserinol skeleton react with cyanuryl chloride to yield amino-*s*-triazines in medium to good yields. The substitution of the second and third chlorine depends on the orientation of the amino group (C-5-axial or C-2-equatorial). At room temperature, all *N*-substituted-amino-*s*-triazines with a 1,3-dioxane group are distinct type of rotamers due to the partial double bond character of the C^{sp2}-N(serinol) site. The content of rotameric species is dependent on the orientation of this bond with respect to the 1,3-dioxane ring: axial or equatorial and the solvent. The herbicidal activity in this class of *s*-triazines was tested. The full report of our complete results is under consideration for the near future.

EXPERIMENTAL

General

Melting points were uncorrected; they were carried out on Electrothermal[®] instrument. Current NMR spectra were recorded on Bruker[®] AM 300 instrument operating at 300 and 75 MHz for ¹H and ¹³C nuclei respectively. The ¹H DNMR spectra were run on Bruker[®] AM 400 instrument operating at 400 MHz for ¹H nuclei with each step 10 K increasing the temperature. No SiMe₄ was added; chemical shifts were measured against the solvent peak. All chemical shifts (δ values) are given throughout in ppm; all coupling patterns (ⁿJ_{H,H} values) are given throughout in Hz. TLC was performed by using aluminium sheets with silica gel 60 F₂₅₄ (Merck[®]); flash column chromatography was conducted on Silica gel Si 60 (40–63 μ m, Merck[®]). IR spectra were performed on a Perkin- Elmer[®] 16 PC FT-IR spectrometer. Only relevant absorptions are listed in cm⁻¹ [weak (w), medium (m) or (s) strong]. Mass spectrum (MS) was recorded on an ATI-Unicam Automass[®] apparatus, fitted (or not) with a GC-mass coupling (high-resolution J&W column, 30 m, 0.25 mm ID, flow rate: 1.2 mL min⁻¹).

For the present preliminary communication, only the synthetic pathway **1a** → **1b**→**1c** is listed below:

2,4-Dichloro-6-[(4*S*,5*S*)-4-(4-nitrophenyl)-1,3-dioxan-5-yl]-amino-*s*-triazine (1a**):** (60 %) yellowish crystalline powder; m.p.=194-195 °C (Et₂O); [Found: C, 42.11; H, 2.77; N, 19.09. C₁₃H₁₁N₅Cl₂O₄ requires C, 41.96; H, 2.98; N, 18.82 %]; IR (ν_{\max} , KBr) 3305 (s), 2875 (m), 1585 (s), 1556 (s), 1510 (s), 1410 (s), 1346 (s), 1325 (s), 1240 (m), 1183 (s), 1167 (s), 1103 (s), 1043 (m), 1028 (m), 964 (m), 842 (m), 798 (m), 713 (m) cm⁻¹; ¹H NMR (300 MHz, CDCl₃, 293 K): 8.18 (2 H, d, ³J=8.7 Hz, H-Ar), 7.51 (2 H, d, ³J=8.7 Hz, H-Ar), 6.65 (1 H, d, ³J=9.4 Hz, NH), 5.35 (1 H, d, ²J=6.4 Hz, H-2eq.), 5.11 (1 H, s, H-4-ax.), 5.02 (1 H, d, ²J=6.4 Hz, H-2-ax.), 4.56 (1 H, d, ³J=9.8 Hz, H-5-eq.), 4.24 (1 H, d, ²J=12.1 Hz, H-6-eq.), 4.14 (1 H, d, ²J=11.3 Hz, H-6-ax.); ¹³C NMR (75 MHz, CDCl₃, 293 K): 171.1 (1 C, C-Cl), 170.6 (1 C, C-Cl), 165.8 (1 C, C-N), 148.0 (1 C, Cq.-Ar), 144.4 (1 C, Cq.-Ar), 126.8 (2 C, CH-Ar), 124.0 (2 C, CH-Ar), 94.9 (1 C, C-2), 78.9 (1 C, C-4), 70.6 (1 C, C-6), 50.2 (1 C, C-5); MS (EI, 70 eV); m/z (rel. int. %): 371 (40) [M⁺-1], 341 (25), 311 (100), 277 (18), 218 (39), 190 (25), 164 (27).

2-Chloro-4,6-bis[(4S,5S)-4-(4-nitrophenyl)-1,3-dioxan-5-yl]-amino-s-triazine (1b): (90 %) yellow crystalline powder; m.p.=154-155 °C (flash column chromatography, eluent ligroine : acetone 1.5:1 v/v); [Found: C, 48.97; H, 4.14; N, 17.99. $C_{23}H_{22}N_7ClO_8$ requires C, 49.34; H, 3.96; N, 17.51 %]; IR (ν_{\max} , KBr) 3404 (m), 3314 (m), 2859 (s), 1573 (s), 1518 (s), 1510 (s), 1346 (s), 1240 (m), 1174 (s), 1167 (s), 1094 (s), 1026 (s), 1028 (s), 987 (s), 851 (m), 805 (m), 711 (m) cm^{-1} ; 1H NMR (300 MHz, $CDCl_3$, 293 K): 8.12-8.05 (12 H, m, H-Ar), 7.45-7.39 (12 H, m, H-Ar), 6.09 (2 H, d, $^3J=9.4$ Hz, NH_{s-s}), 6.00 (2 H, d, $^3J=9.8$ Hz, NH_{s-a}), 5.88 (1 H, d, $^3J=9.4$ Hz, NH_{s-a}), 5.71 (1 H, d, $^3J=9.8$ Hz, NH_{s-a}), 5.35-5.30 (3 H, m, H-2eq.), 5.25-5.20 (3 H, m, H-2eq.), 4.99-4.91 (12 H, m, H-2-ax., H-4-ax.), 4.41-3.88 (18 H, m, H-5-eq., H-6-eq., H-6-ax.); ^{13}C NMR (75 MHz, $CDCl_3$, 293 K): 169.5 (3 C, C-Cl), 165.8, 165.4, 165.3, 165.2 (6 C, C-N), 147.9, 147.7 (6 C, C-q.-Ar), 145.2, 145.0 (6 C, Cq.-Ar), 126.9, 126.73, 126.66 (12 C, CH-Ar), 123.80, 123.77, 123.73 (12 C, CH-Ar), 94.9, 94.8 (6 C, C-2), 79.33, 79.27, 79.21, 79.1 (6 C, C-4), 71.1, 70.8, 70.7, 70.5 (6 C, C-6), 49.6, 49.5, 49.3, 49.2 (6 C, C-5); MS (ESI, 35 eV); m/z (rel. int. %): 559 (100) $[M^+]$, 541 (27), 529 (22), 511 (10).

1,4-Bis{4,6-bis[(4S,5S)-4-(4-nitrophenyl)-1,3-dioxan-5-yl]-amino-s-triazine-2-yl}-piperazine (1c): (89 %) yellow crystalline powder; m.p.=224-225 °C (flash column chromatography, eluent ligroine : acetone 1.25:1 v/v); [Found: C, 53.37; H, 5.02; N, 19.69. $C_{50}H_{52}N_{16}O_{16}$ requires C, 53.00; H, 4.63; N, 19.78 %]; IR (ν_{\max} , KBr) 3414 (m), 2855 (m), 1576 (s), 1548 (s), 1520 (s), 1442 (s), 1346 (s), 1244 (w), 1173 (s), 1095 (m), 1027 (m), 985 (m), 852 (w), 810 (m), 742 (w), 711 (w) cm^{-1} ; 1H NMR (400 MHz, $DMSO-d_6$, 353 K): 8.06 (8 H, bs, H-Ar), 7.59 (8 H, d, $^3J=7.6$ Hz, H-Ar), 5.58 (4 H, d, $^3J=7.6$ Hz, NH), 5.22 (4 H, d, $^2J=6.0$ Hz, H-2eq.), 5.20 (4 H, s, H-4-ax.), 4.99 (4 H, d, $^2J=6.0$ Hz, H-2-ax.), 4.37 (4 H, d, $^3J=7.6$ Hz, H-5-eq.), 4.10 (4 H, d, $^2J=10.4$ Hz, H-6-eq.), 3.94 (4 H, bs, H-6-ax.), 3.36 (8 H, s, CH_2 piperazine); ^{13}C NMR (75 MHz, $CDCl_3$, 293 K): 165.7 (4 C, C-N), 165.5 (2 C, C-N), 147.6 (4 C, Cq.-Ar), 146.0 (4 C, Cq.-Ar), 127.0 (8 C, CH-Ar), 123.4 (8 C, CH-Ar), 94.7 (4 C, C-2), 79.8 (4 C, C-4), 71.4 (4 C, C-6), 49.0 (4 C, C-5), 42.8 (4 C, CH_2 -piperazine); MS (FAB $^+$); m/z (rel. int. %): 1132 (95) $[M^+-1]$, 952 (20), 663 (33), 551 (33), 459 (100).

REFERENCES

1. Darabantu, M.; Mager, S.; Puscas, C.; Bogdan, M.; Cotoră, E.; Plé, G.; Bratu, I. *Rev. Rom. Chim.* **1994**, 39, 955-965
2. Darabantu, M.; Mager, S.; Puscas, C.; Bogdan, M.; Plé, G.; Cotoră, E.; Kovacs, D. *Rev. Rom. Chim.* **1995**, 40, 453-461
3. Darabantu, M.; Mager, S.; Puscas, C.; Plé, G.; Bogdan, M.; Cotoră, E. *Rev. Rom. Chim.* **1995**, 40, 907-916
4. Darabantu, M.; Maierăanu, C.; Plé, G.; Berghian, C.; Condamine, E.; Ramondenc, Y. *Heterocyclic Commun.* **2001**, 7(6), 593-596
5. Darabantu, M.; Plé, G.; Mager, S.; Puscas, C.; Cotoră, E. *Tetrahedron* **1997**, 53, 1909-1922
6. Kraiz, B. O.; Remizov, A. L. *Zh. Org. Khim.* **1979**, 15(16), 1282-1283

7. recent data, for example: Boncic-Caricic, G.; Tadic, Z. D.; Muskatirovic, M. *J. Serb. Chem. Soc.* **1994**, 59(12), 929-933; Reddy, N. D.; Elias, A.; Vic, A. *J. Chem. Res., Synop.* **1998**, 9, 504-505
8. see Part I of our communication.
9. **a)** Katritzky, A. R.; Ghiviriga, I.; Oniciu, D. C.; Barkock, A. *J. Chem. Soc. Perkin Trans. 2* **1995**, 785-792; **b)** Katritzky, A. R.; Ghiviriga, I.; Steel, P. G.; Oniciu, D. C. *J. Chem. Soc. Perkin Trans. 2* **1996**, 443-447; **c)** Ghiviriga, I.; Oniciu, D. *Chem. Comm.* **2002**, 22, 2718-2719
10. **a)** Laszlo, P. *Bull. Soc. Chim. Fr.* **1964**, 10, 2658-2661; **b)** Nikki, K. *Magn. Res. Chem.* **1990**, 28, 385-388
11. **a)** Grossmann, K.; Tresch, S.; Plath. *Z. Naturforsch* **2001**, 56c, 559-569; **b)** Omokawa, H.; Konnai, M. *Pestic. Sci.* **1992**, 35, 83-86; **c)** Omokawa, H.; Ichizen, N.; Takematsu, T. *Agric. Biol. Chem.* **1987**, 51, 2563-2568

MASS TRANSFER RATES DURING THREE PHASE CATALYTIC REDUCTIVE AMINATION OVER SUPPORTED NOBLE METALS

J. BÓDIS¹, L. BÓDIS² and J. A. LERCHER³

¹ "Babes-Bolyai" University, Department of Organic Chemistry, str. Arany Janos nr. 11, 400028 Cluj, Romania. E-mail: jbodis@chem.ubbcluj.ro. Fax: 40-264-190818

² Swiss Federal Institute of Technology Zürich, ETH Hönggerberg, HCI E 312, CH-8093 Zürich, Switzerland

³ Institut für Technische Chemie, Technische Universität München, Lichtenbergstrasse 4, D-85747, Garching bei München, Germany

ABSTRACT. Reductive amination of butanal and methyl ethyl ketone (MEK) with ammonia (at ammonia/MEK molar ratios of ~ 14.5) and hydrogen has been performed at 50 bar and 323-353 K over graphite and charcoal supported noble metal catalysts. Rhodium and platinum based catalysts showed the highest activity in reductive amination of butanal and MEK. The rhodium catalysts had high selectivity towards primary amines while the platinum catalysts towards secondary amines. Tertiary amines were detected only in the reaction products resulted from butanal. The BET area and metal dispersion were found to have a pronounced influence on activity and selectivity. By varying the speed of stirring it was found that the mass transfer of hydrogen from the gas phase into the liquid did not limit the rate of reactions. Model calculations showed that mass transfer limitations of hydrogen diffusion from the liquid to the solid did not also influence the measured reaction rates.

Keywords: Reductive amination, Butanal, Methyl ethyl ketone, Noble metal catalysts, Mass transfer

INTRODUCTION

The reductive amination of aldehydes and ketones is an important synthetic route to amines. The reaction proceeds through an intermediately formed imine, hydrogenated with the help of a reducing agent or with molecular hydrogen in the presence of a catalyst. [1-3]. The resulting amines or imines are of great importance for the chemical and pharmaceutical industry. While the new amines are potential drug candidates, the pharmaceutical companies have a serious deficit concerning their amine libraries [4].

Butanal and methyl ethyl ketone were chosen as test molecules because of lack of literature information concerning the three phase catalytic reductive amination of these substrates with ammonia and hydrogen over supported noble metal catalysts [1-3]. In order to verify whether mass transfer limitations occur or not, experiments and mass transfer calculations were done [5].

EXPERIMENTAL

CATALYSTS: The catalysts tested in the reductive amination of butanal and methyl ethyl ketone (MEK) are presented in Table 1 together with some physicochemical characterization data as well. The charcoal supported catalysts contained 55-60% moisture. The quantitative values used for these samples refer to dry material.

Table 1

Catalysts characterization data (metal dispersions were calculated by using n_s values estimated according to literature [6]).

| Type of catalyst | S_{sp} (m^2/g) | S_M (m^2/g) | Metal location | Dispersion (%) | BET area (m^2/g) |
|-------------------|-------------------------|----------------------|----------------|-------------------|-------------------------|
| 5%Rh/charcoal | 950 | 11.1 | Intermediate | 50.43 | 817.8 |
| 5%Rh/HSAgraphite | 130 | 9.5 | Surface | 43.17 | 94.6 |
| 5%Ru/HSAgraphite. | 130 | 8.0 | Surface | 43.78 | 41.6 |
| 5%Pd/HSAgraphite | 130 | 11.4 | Surface | 51.10 | 87.6 |
| 5%Pt/HSAgraphite | 130 | 5.0 | Surface | 40.48 | 80.1 |
| 5%Pt/LSAgraphite | n.a. | 3.5 | Surface | 28.0 | 56.7 |

S_{sp} specific surface area of the support

S_M metal surface area determined by hydrogen chemisorption

HSA high surface area

LSA low surface area

CATALYSTS TESTING: The reactions were carried out in batch reactors with a volume of about 65 ml. Magnetic stirring at a speed of 1100 rpm was used. The temperature inside the autoclave was measured by a thermocouple mounted on the lid of the autoclave. Weighed amount of catalysts were introduced into the autoclave. In order to assure a well-defined starting time for every reaction, the following experimental procedure was applied:

After addition of carbonyl compound (MEK or butanal) and of the solvent (ethanol), the autoclave was flushed with nitrogen to remove the atmospheric oxygen. Ammonia was then added from the liquid ammonia cylinder at room temperature. Then the autoclave was placed in a thermostat bath preset to the reaction temperature. The addition of hydrogen and the rapid completion to the working pressure occurred only after the preformed imine solution reached the desired reaction temperature ($t = 0$ is set for the time when the final pressure was established).

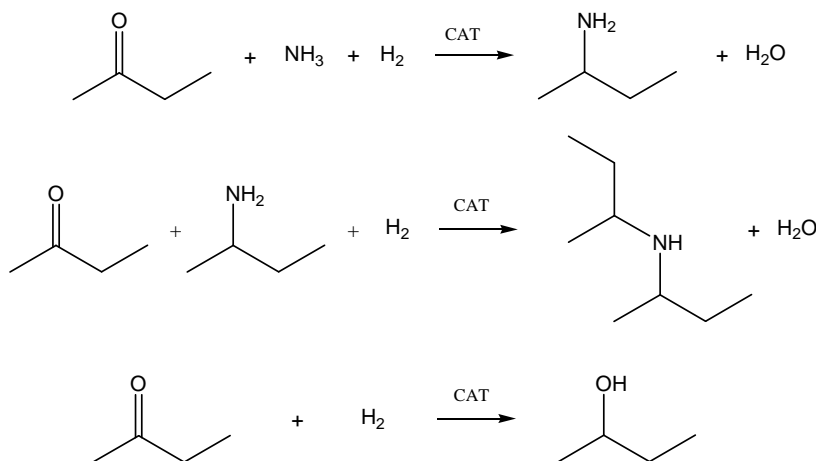
The progress of reaction in time was evaluated from the hydrogen consumption by measuring the hydrogen flow with a flow meter (BROOKS) having the pressure inside the autoclave controlled by a pressure regulator (BROOKS). Liquid sampling was used for monitoring the evolution of products in time.

Reductive amination of MEK (>99%, Merck) and butanal (>99%, Merck) were conducted mostly at 50 bar and 80 °C. The products were analyzed by using a Hewlett Packard 5890A gas chromatograph equipped with a DB Wax 1701 column and FID detector. Pure amines (butylamine, di-butylamine, tri-butylamine, sec-butylamine and di-sec-butylamine) were used for the identification of the main products in the reaction mixtures. GC/MS analyses were performed in order to identify reaction intermediates. The metal leaching was followed by XRF analysis of the filtered reaction mixtures.

Experiments and calculations were done in order to find whether mass transfer rate limitations occurred or not for the highly active catalysts. According to the results obtained, mass transfer limitations of hydrogen diffusion from liquid to solid had no influence on the measured reaction rates.

RESULTS AND DISCUSSION

In the product mixtures resulted from the reductive amination of MEK with ammonia and hydrogen over supported noble metal catalysts were identified sec-butylamine, di-sec-butylamine and 2-butanol. Tri-sec-butylamine was never obtained. According to the analysis results, the reactions occurring in the reactor under the working conditions used ($V_{\text{EtOH}} = 8 \text{ cm}^3$, $n_{\text{MEK}} = 0.0222 \text{ mol}$, $n_{\text{NH}_3} = 0.3235 \text{ mol}$, $n_{\text{NH}_3}/n_{\text{MEK}} = 14.57$, $V_{\text{EtOH}}/V_{\text{MEK}} = 4$, $p = 50 \text{ bar}$, $T = 353 \text{ K}$) are given in Scheme 1.



Scheme 1. Chemical reactions during the reductive amination of MEK.

In order to probe for mass transfer limitations, reductive amination experiments of MEK at different stirring speeds (1100 and 600 rpm), and at different catalysts concentrations were carried out. The experimental conditions and the results obtained for the reductive amination of methyl ethyl ketone on Rh/charcoal and Rh/HSA graphite catalysts are presented in Table 2.

The results on conversions, yields and rates of formation at different stirring speeds presented in Table 2 indicate that under the working conditions used, mass transfer limitations are unimportant in case of reductive amination of MEK over 5% Rh/HSA graphite and 5%Rh/charcoal.

Fig.1 illustrates the hydrogen consumption as a function of time for the tested catalysts.

Fig. 1 shows that Rh/charcoal is the most active catalyst, followed by Pt/HSA graphite, Rh/HSA graphite, Ru/HSA graphite while Pd/HSA graphite being the less active catalyst. The maximum rate of hydrogen consumption calculated from these curves for Rh/charcoal is: $\sim 5 \cdot 10^{-8} \text{ mol/cm}^3 \cdot \text{s}$ and $\sim 5 \cdot 10^{-9} \text{ mol/cm}^3 \cdot \text{s}$ for Rh/HSA graphite catalyst.

Table 2

Experimental conditions and results for the reductive amination of MEK on charcoal and graphite supported rhodium catalysts at different stirring speeds. n_M : moles of metal, $n_M = 1.11 \cdot 10^{-4}$ mol, Solvent: EtOH, $V_{EtOH} = 8 \text{ cm}^3$, $n_{MEK} = 0.0222 \text{ mol}$ (2 cm^3), $n_{MEK}/n_M = 200$, $n_{NH_3} = 0.3235 \text{ mol}$, $n_{NH_3}/n_{MEK} = 14.57$, $p = 50 \text{ bar}$, $T = 353 \text{ K}$.

| Catalyst | t_{react} (min) | X (%) | Y_{pr} (%) | Y_{sec} (%) | $Y_{2\text{-ol}}$ (%) | r_{pr} (mol/mol·h) | r_{sec} (mol/mol·h) | $r_{2\text{-ol}}$ (mol/mol·h) |
|-------------|-----------------------------|----------|------------------------|-------------------------|--------------------------|--------------------------------|---------------------------------|----------------------------------|
| Rh/HSAGraph | | | | | | | | |
| 1100 rpm | 60 | 98 | 86 | 0.4 | 12 | 175 | 0.7 | 23.9 |
| 600 rpm | 65 | 98 | 85 | 0.7 | 10 | 170 | 1.3 | 19.8 |
| 600 rpm* | 200 | 83 | 54 | 0.0 | 1 | 163 | 0.0 | 3.0 |
| Rh/charcoal | | | | | | | | |
| 1100 rpm | 8 | 99 | 98 | 0.4 | 0.6 | 1371 | 5.9 | 13.6 |
| 1100 rpm* | 40 | 97 | 92 | 0.9 | 2.7 | 1384 | 40.8 | 12.7 |
| 600 rpm* | 45 | 98 | 95 | 0.9 | 2.8 | 1262 | 36.8 | 11.3 |

X conversion (molar percentage of MEK converted to different products).
Y yield (molar percentage of MEK converted to the corresponding amine).
r rate of product formation
* $n_{Rh} = 2.22 \cdot 10^{-5} \text{ mol}$, $n_{MEK}/n_M = 1000$.

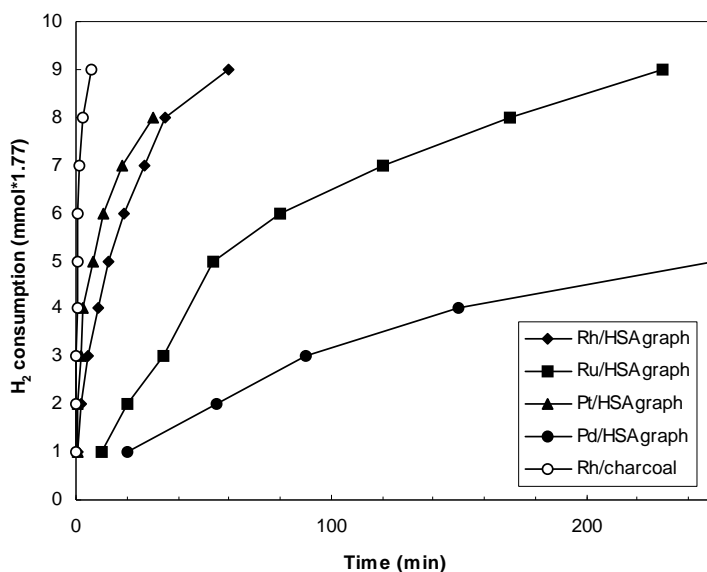
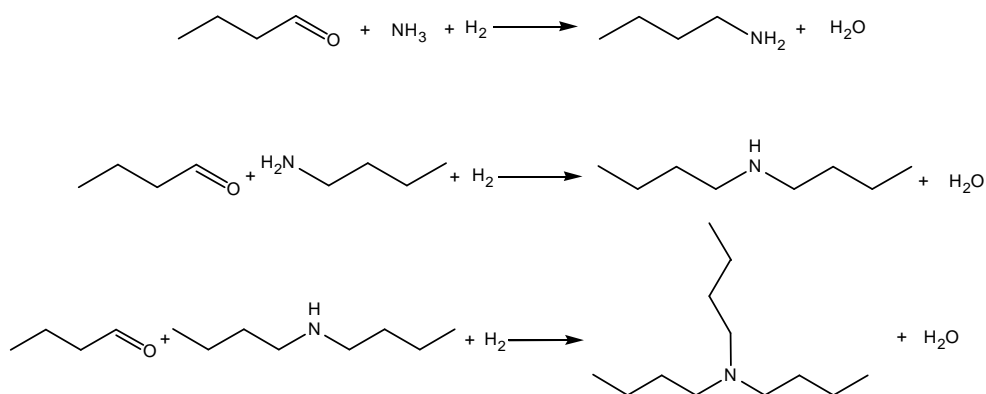


Fig. 1. Hydrogen consumption versus reaction time during the reductive amination of MEK on graphite and charcoal supported noble metal catalysts. n_M : moles of metal, $n_M = 1.11 \cdot 10^{-4}$, Solvent: EtOH, $V_{EtOH} = 8 \text{ cm}^3$, $n_{MEK} = 0.0222 \text{ mol}$, $n_{MEK}/n_M = 200$, $n_{NH_3} = 0.3235 \text{ mol}$, $n_{NH_3}/n_{MEK} = 14.57$, $p = 50 \text{ bar}$, $T = 353 \text{ K}$.

In the product mixture resulted during the reductive amination of butanal with ammonia and hydrogen over supported noble metal catalysts butylamine, dibutylamine and tributylamine were identified. According to the obtained analysis results, the reactions occurring in the reactor under the working conditions used ($V_{\text{EtOH}} = 8 \text{ cm}^3$, $n_{\text{Butanal}} = 0.0222 \text{ mol}$ (2 cm^3), $n_{\text{NH}_3} = 0.3235 \text{ mol}$, $n_{\text{NH}_3}/n_{\text{Butanal}} = 14.57$, $V_{\text{EtOH}}/V_{\text{Butanal}} = 4$, $p = 50 \text{ bar}$, $T = 323\text{-}353 \text{ K}$) are given in Scheme 2.



Scheme 2. Chemical reactions during the reductive amination of butanal.

The hydrogen consumption (normalized to moles of metal in the catalysts) indicates that Pt and Rh are the most active metals (Fig.2).

The very high activity of 5%Rh/charcoal relative to 5%Rh/HSA graphite (HSA = high surface area) can be attributed to the high surface area of the charcoal support, which resulted in a higher metal dispersion. The increased activity of 5%Pt/HSA graphite versus 5%Pt/LSA graphite can be attributed to the higher metal dispersion of the 5%Pt/HSA graphite catalyst.

The maximum reaction rate calculated from the hydrogen uptake for the 5%Rh/charcoal catalyst is $r_{\text{max}} = 2.2 \cdot 10^{-7} \text{ mol/cm}^3 \cdot \text{s}$ and for the 5%Rh/HSA graphite catalyst is $r_{\text{max}} = 3.6 \cdot 10^{-8} \text{ mol/cm}^3 \cdot \text{s}$.

For the calculation of mass transfer rates of hydrogen from liquid phase to solid catalyst (considered as being the rate determinant step of mass transfer processes) the following equations were used [7]:

$$R_A = k_s a_p (A_l - A_s)$$

$$a_p = 6w/\rho_p d_p$$

where:

| | |
|----------|--|
| R_A | rate of hydrogen mass transfer from liquid-to-catalyst, $\text{mol/cm}^3 \cdot \text{s}$ |
| k_s | liquid-to-catalyst mass transfer coefficient, cm/s |
| a_p | external area of particles per unit volume of reactor, cm^2/cm^3 |
| A_l | concentration of A in the bulk liquid, mol/cm^3 |
| A_s | concentration of A at the catalyst surface, mol/cm^3 |
| w | catalyst mass per unit volume of the reactor, g/cm^3 |
| ρ_p | density of the catalyst particle, g/cm^3 |
| d_p | average diameter of the catalyst particles, cm |

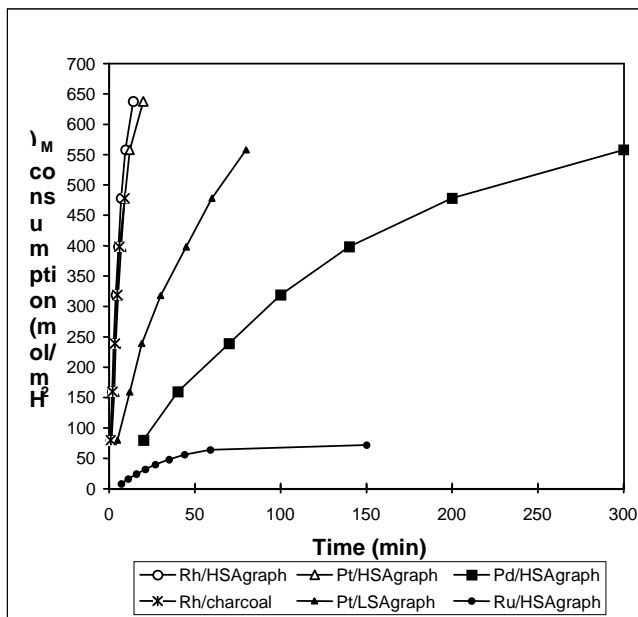


Fig. 2. Hydrogen consumption normalized to moles of metal as a function of reaction time for the reductive amination of butanal over carbon supported noble metal catalysts (n_M : moles of metal, $n_M = 2.22 \cdot 10^{-5}$ mol, $n_{Ru} = 2.22 \cdot 10^{-4}$ mol, $n_{Butanal} = 0.0222$ mol, $n_{NH_3} = 0.3235$ mol, $n_{NH_3}/n_{Butanal} = 14.57$, $p = 50$ bar, $T = 353$ K).

The correlation for k_s in agitated vessels proposed by Boon-Long *et al.* [7] can be given as below:

$$k_s = 0.046(D/d_p)(2\pi^2 d_p \rho_L d_T N / \mu_L)^{0.283} (\rho_L^2 g d_p^3 / \mu_L^2)^{0.173} \cdot (wV_L / \rho_L d_p^3)^{-0.011} (d_T / d_p)^{0.019} (\mu_L / \rho_L D)^{0.461}$$

where:

- $d_p = 2.7 \cdot 10^{-3}$ cm for charcoal and $1.85 \cdot 10^{-3}$ cm for the graphite (diameter of the particle)
- $D = 1.27 \cdot 10^{-4}$ cm²/s, diffusion coefficient of A (hydrogen) in the liquid phase, cm²/s.
- $\rho_p = 0.4$ g/cm³ for charcoal and 2.26 g/cm³ for the graphite (apparent density)
- $\rho_L = 0.6$ g/cm³ (the density of the liquid)
- $d_T = 4$ cm (the diameter of the tank)
- $w = 0.00114$ g/cm³ for the Rh/charcoal, and 0.00228 g/cm³ for the Rh/HSA graphite (w = catalyst loading)
- $N = 18.33$ s⁻¹ (speed of agitation employed, s⁻¹)
- $g = 980$ cm/s²
- $\mu_L = 0.00504$ g/cm·s (viscosity of the liquid, g/cm·s)
- $A_l = A_{H_2} = (0.0864/22400 + 2/22400)$ mol/cm³ (solubility of H₂ in EtOH) [8].
- $A_s = 0.0$ mol/cm³, solubility of H₂ in the solid catalyst
- $V_L = 12$ cm³, the volume of the liquid

Introducing these values in the equation of R_A , the rate of hydrogen mass transfer from the liquid to the surface of the 5%Rh/charcoal catalyst is:

$$R_A = 3.9 \cdot 10^{-5} \text{ mol/cm}^3 \cdot \text{s}$$

about 100 times higher than the measured maximum reaction rate, $r_{\max} = 2.2 \cdot 10^{-7} \text{ mol/cm}^3 \cdot \text{s}$ calculated from the hydrogen uptake for the reductive amination of butanal and around 1000 times higher than we got for MEK ($5 \cdot 10^{-8} \text{ mol/cm}^3 \cdot \text{s}$). Even, at the minimum hydrogen solubility:

$$R_A = 1.6 \cdot 10^{-6} \text{ mol/cm}^3 \cdot \text{s}$$

The mass transfer rate of hydrogen from liquid to catalyst obtained for the 5%Rh/HSA graphite catalyst is:

$$R_A = 1.1 \cdot 10^{-5} \text{ mol/cm}^3 \cdot \text{s}$$

much higher compared to the measured maximum reaction rates for butanal on this catalyst ($r_{\max} = 3.6 \cdot 10^{-8} \text{ mol/cm}^3 \cdot \text{s}$) and for MEK ($5 \cdot 10^{-9} \text{ mol/cm}^3 \cdot \text{s}$), calculated from the hydrogen uptake. For the lowest solubility value of hydrogen:

$$R_A = 8.7 \cdot 10^{-7} \text{ mol/cm}^3 \cdot \text{s}$$

According to calculations, mass transfer limitations are not influencing the kinetic measurements. However, to be sure about it, experiments with 1% Rh loading catalysts were also performed. The maximum reaction rates (normalized per mol metal) obtained on 1% Rh/HSA graphite were lower or almost identical to those measured on 5%Rh/HSA graphite catalyst.

CONCLUSIONS

Among the studied catalysts the Rh and Pt based ones show the highest activity in reductive amination of butanal and methyl ethyl ketone. This underlines the major role of metal in determining the activity and selectivity of the supported catalysts.

Charcoal appears to be a good catalyst support providing high activity and selectivity for the supported Rh catalyst (having high BET area and high metal dispersion) being significantly more active compared to Rh/graphite, emphasizing the important role of the support materials. The BET area and especially the metal dispersion have a strong influence on the catalyst activity for the reductive amination of butanal.

According to experimental and calculation results, mass transfer limitations have no influence on the kinetic measurements during three phase catalytic reductive amination of butanal and methyl ethyl ketone over carbon supported noble metals.

ACKNOWLEDGEMENT

Financial support from the DSM company is greatly appreciated.

REFERENCES

1. S. Yada, Y. Takagi and M. Hiyamizu, *Nippon Kagaku Kaishi*, 1995, (2), 107.
2. J. Bódis and J.A. Lercher, *Studia-Chemia*, *Studia-Chem.*, 2002, **47**, 169.
3. J. Bódis and J.A. Lercher, *Studia-Chemia*, *Studia-Chem.*, 2004, **49**, 53.
4. W. Bender, From Synthons to Bioactive Molecules: Efficient Strategies in Modern Lead structure Research, lecture at ICS-UNIDO Workshop on Trends and Applications of Combinatorial Chemistry and Combinatorial Technologies, Budapest, Hungary, October 15-18, 2001, pp. 20-46.
5. J. Bódis and J.A. Lercher, Confidential Reports to DSM Company, 1997-1998.
6. J.J.F. Scholten, A.P. Pijpers and A.M.L. Hustings, *Catal. Rev.-Sci. Eng.*, 1985, **27**, (1), 151.
7. P.A. Ramachandran and R.V. Chaudhari, Three Phase Catalytic Reactors, in *Topics in Chemical Engineering*, volume 2, A series edited by R. Hughes, Gordon & Breach Science Publishers, New York-London-Paris, 1983.
8. W.F. Linke, *Solubilities, Inorganic and Metal-Organic Compounds*, volume I., Fourth Edition, D. Van Nostrand Company, Inc., Princeton, New Jersey, Toronto, London, New York, 1958.

SYNTHESIS AND STRUCTURE ASSIGNMENT OF SOME NEW ALKYL-(10H-PHENOTHIAZIN-3-YL)-CARBONATES

RADU GROPEANU,^a TEODORA PANEA,^b IOAN PANEA^a

a: Organic Chemistry Department, Faculty of Chemistry and Chemical Engineering, Babes-Bolyai University, 11th Arany Janos st., 400028 Cluj-Napoca, Romania

b: Research and Production Centre "BIOS", Academy of Agricultural and Forest Sciences, OP1 CP2, Cluj-Napoca, Romania

ABSTRACT. By acylation with alkyl chloroformate **1** of six N(10)-unsubstituted- (**2a-c,e,g,h**) and two N(10)-methyl substituted- (**5a,b**) 3-hydroxy-10H-phenothiazine derivatives eight new alkyl-(10H-Phenothiazin-3-yl)-carbonates (**4a-c,e,g,h,7a,b**) were synthesized. Two carbonates **7e,f** were obtained by 5,5-dioxidation with peroxybenzoic acid. The structural assignments were made on the basis of chemical and spectral methods, and by a study of the derivatization effects (acylation, methylation and 5,5-dioxidation effect) on the chemical shifts of the phenothiazine protons.

Keywords: 3-hydroxy-10H-phenothiazines, Selective O-alkoxycarbonylation; Derivatization effect on ¹H-NMR chemical shifts.

INTRODUCTION

Some carbamates, derivatives of phenothiazine, are drugs¹ or exhibit other biological actions, respectively are intermediates for such compounds.²⁻⁷ It is claimed^{3,5b} that several of these have been synthesized by N-acylation with alkyl chloroformates of the corresponding 10-unsubstituted 10H-phenothiazines, including derivatives of 3-hydroxy-10H-phenothiazine. At the same time it was shown^{5b} that some 3-hydroxy-10H phenothiazines and theirs 5,5-dioxides, as well as different acylation products of these, exhibit therapeutic actions. All these have prompted us to investigate the monoacylation with alkyl chloroformates **1** of some 3-hydroxy-10H-phenothiazines (**2a-h**). As it is known⁸ the alkyl chloroformates are acylation agents that act as acyl chlorides, introducing thus the alkoxycarbonyl group (COOR) into a substrate.

The 3-hydroxy-10H-phenothiazines **2a-h** have two acylable groups, namely a phenolic type –OH group (in position 3) and a secondary aromatic amine (the bridging NH, position 10). Consequently, the monoacylation of **2a-h** with **1** may take place, like to the few other previously^{1b,5b,9} acylated 3-hydroxy-10H-phenothiazines, either at N(10)H or at 3-OH, leading to carbamates **3** or/and to alkyl (10H-phenothiazin-3-yl) carbonates **4**.

Therefore we have attempted a selective monoacylation of **2a-h** by two procedures ("a" or "b", see Experimental) that would should lead one ("a") to N-acyl derivatives **3a-h** and the other ("b") to O-acyl derivatives **4a-h**. Indeed, previously it was claimed that the "a" procedure leads to N-acylation.⁵ Otherwise, owing to the *p*-amino-phenol nature¹⁰ of the 3-hydroxy-10H-phenothiazines **2a-h** it was expected that theirs monoacylation to occur at aromatic type N(10)H group, since in amino phenols the amino group reacts with acyl chlorides prior to the phenolic group.^{8,11} The

"b" procedure correspond to the Schotten-Baumann conditions when the acylation should take place at the phenolate anion (3-O⁻) that is more reactive as nucleophile⁸ comparative to the secondary aromatic amine type NH^{12,13} from phenothiazine heterocycle. Otherwise, for such acylations of the 3-hydroxy-phenothiazines carried out previously⁹ it is claimed the obtainment of O-acyl derivatives. Consequently, the goal of this work is the selective obtainment of monoacylation products from some 3-hydroxy-10H-phenothiazine derivatives **2a-h** and alkylchloroformates **1**, as well as the determination of N- (**3**) or O- (**4**) acyl derivatives nature of these. With the aim to make this determination reliable it was attempted also the monoacylation of some 3-hydroxy-10H-phenothiazines protected by N- (**5a,b**) or O- (**6c,d**) methylation. The possible structure corresponding to the studied transformations are presented in Scheme 1.

EXPERIMENTAL

The starting materials (**2a-h**), were prepared as previously described.¹⁴⁻¹⁷ The melting points were determined on a Kleinfeld Apotek apparatus and are uncorrected. Elemental analyses for the acylation products isolated by us were carried out at the Chemistry and Pharmaceutical Research Institute Cluj-Napoca, and the obtained data correspond satisfactorily to the assigned monoacylation products structures.

The IR spectra were recorded with a JASCO 615 FT-IR spectrometer in KBr pellets, as dispersion in Nujol or as film. Mass spectra were performed using a Matt 3.11 spectrometer using electron impact technique. The NMR spectra were recorded using a Varian Gemini 300 (300 MHz) spectrometer and hexadeuterated dimethylsulfoxide (DMSO-d₆) or deuteriochloroform (CDCl₃) as solvent, at room temperature. The chemical shifts are related to tetramethylsilane and the signal of the solvent was the internal standard. The NMR data were obtained directly from the spectra. A combination of the chemical shifts, multiplicities and integration data obtained in the case of each spectrum has allowed us the assignment of the present signals to the individual types of protons characteristic to the corresponding 10H-phenothiazine derivative (Table 1, 2). This assignment has been facilitated by a) the existence of very good analyses on the ¹H-NMR spectra of the 10H-phenothiazine itself and of some derivatives of this;^{1c, 17-22} b) the fact that the two benzene rings of the phenothiazine system can be considered^{1c,20} independent of each other, being possible the analysis of the spectra as sum of the quasi-first order subspectra of the two marginal benzene rings; c) the simplification of the spectra brought by the substitution in the phenothiazine system; d) the known effects of the substituents (OH, OCH₃, Cl, Br)²³ and the derivatization (O-acylation, N- or O- methylation)^{1c,23} on the chemical shift of the protons from the system in which has been introduced the substituent, respectively is present the derivatized group.

General procedures for the preparation of alkyl (10-H-phenothiazin-3-yl) carbonates **4a-h**:

Procedure "a"

The 3-hydroxy-10H-phenothiazine derivative (**2a-h**) was refluxed with alkylchloroformate (**3**) in THF for 20 hours, in the conditions described in some patents.⁵ By column chromatography (silica gel, petroleum ether : ethyl acetate = 5:1), we could isolate each time only the alkoxycarbonylation product at the 3-hydroxy-

group (**4a-h**), but only in very low yields. The most of the starting 3-hydroxy-10H-phenothiazine derivative has been recovered unchanged.

Procedure "b"

To 10^{-3} Mol 3-hydroxy-10H-phenothiazine derivative (**2a-h**) dissolved in 50 mL isopropanol were added 70 mg ($1.2 \cdot 10^{-3}$ Mol) KOH and the mixture was refluxed for 5 minutes; after cooling down to room temperature, 1 mL ($9 \cdot 10^{-3}$ Mol) ethyl- or methyl-chloroformate (**3**) was added. The precipitate which appeared in 5-10 minutes was filtered off, washed with isopropanol and crystallized from benzene or toluene.

Some characteristics of the carbonates **4a-h** are presented in Tables 1 and 2. The reported yields (Table 1) are referring to the *Procedure "b"*.

General procedure for the methylation of 3-hydroxy-10H-phenothiazines (2a-d)

A mixture of 0.01 Mol 3-hydroxy-10H-phenothiazine derivative, 1 g potassium carbonate, 2 mL methyl iodide and 50 mL DMF was stirred at room temperature. After 2 hours potassium carbonate (1 gram) and methyl iodide (2 mL) were added, followed by two other such additions at two hours intervals. The stirring of the mixture is continued over the night. Next day the reaction mixture was poured into 100 mL water and was extracted with 3×25 mL ethyl acetate. The organic layer was washed twice with water, dried over anhydrous sodium sulfate and the solvent removed in vacuum. The residue was purified by column chromatography (silica gel, petroleum ether:ethyl acetate=5:1). This procedure is similar to that indicated⁵ for the O- methylation of the 3-hydroxy-10H-phenothiazine derivatives.

As we shown (see results and discussion) the methylation by this procedure of the 3-hydroxy-10H-phenothiazines (**2a-d**) has furnished the O-methylated derivatives (**6c,d**) only for **2c,d** while in the case of **2a,b** the corresponding N(10)-methyl derivatives (**5a,b**) were isolated. Some ¹H-NMR data for **6c,d** and **5a,b** are presented in Table 2.

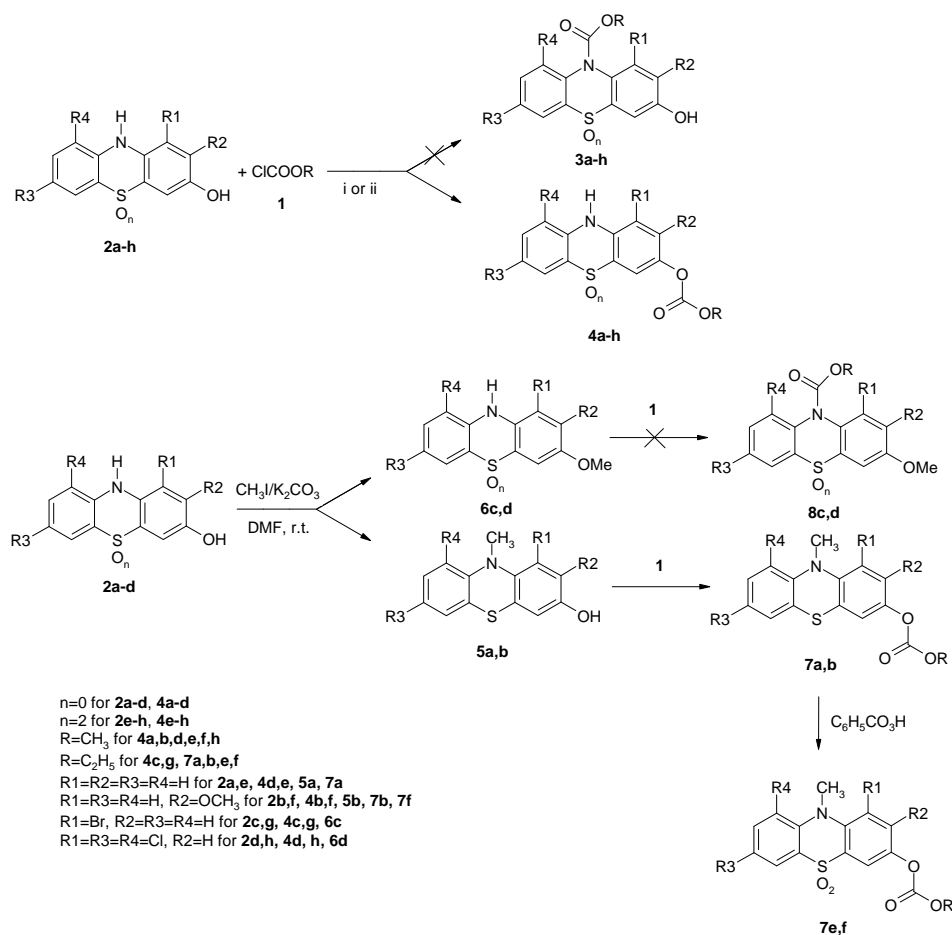
Procedure for the preparation of ethyl [N(10- methyl-10H-phenothiazin-3-yl)] carbonates **7a,b**^{9c}

To a solution of 10^{-3} Mol N(10)-methyl-3-hydroxy-10H-phenothiazine derivative (**5a,b**) in 20 mL pyridine was added dropwise and under vigorous stirring 1 mL ($9 \cdot 10^{-3}$ Mol) ethylchloroformate and the solution was stirred at 20-50°C for 1 hour. After cooling down, the solution was poured over 100 mL water and ice and was extracted with 3×25 mL ethyl acetate; the organic layer was dried over anhydrous sodium sulfate, the solvent was removed in vacuum and the residue was purified by column chromatography on silica gel and eluting with petroleum ether: ethyl acetate (5:1). Some characteristics of **7a,b** are presented in Tables 1,2.

Procedure for the S,S-dioxidation¹⁸ of ethyl [N(10)-methyl-10H-phenothiazin-3-yl] carbonates **7a,b**

To a solution of 10^{-3} Mol **7a,b** in 20 mL 1,4-dioxane was added dropwise 2 mL 7% chloroform solution of peroxybenzoic acid and stirred over night; next day the solution was poured onto 100 mL 2% aqueous NaHCO₃ solution and extracted

with 3×25 mL ethyl acetate. The organic layer was dried over anhydrous sodium sulfate and the solvent removed in vacuum. The residue was crystallized from petroleum ether: methylene chloride (5:1). Some characteristics of the obtained dioxides **7e,f** are presented in Tables 1 and 2.



Scheme 1. Conditions: i: THF, reflux; ii: KOH, 2-propanol.

RESULTS AND DISCUSSION

The isolated acylation products, their yields and some characteristic properties of these are presented in Table 1. As is shown in Experimental part, the expectations for the obtainment of two different monoacylation products from each 3-hydroxy-10H-phenothiazine derivatives **2a-h** namely of the N- (**3**, by “a” procedure) and of the O- (**4**, by “b” procedure) monoacyl derivative, respectively, have not been confirmed. The acylation product isolated by us from the resulted mixture in the reaction of each 3-hydroxy-10H-phenothiazine **2a-h** with a certain chloroformate,

in both experienced procedures ("a" or "b") has been the same. Anyway, the acylation in the examined conditions has been selective. In addition the mass and NMR spectra (Tables 1,2) have proved that each acylation product isolated by us is a monoacyl derivative. Thus, e.g., in ^1H -NMR spectrum in DMSO-d_6 of the acylation product **4a** (prepared from **2a** and methyl chloroformate) appears (Table 1) one singlet due to three protons that was absent in the spectrum of the starting **2a**. The chemical shift of this singlet (3.79 ppm) is characteristic^{19,24,25} for the methoxycarbonyl group. On the other hand, in the same ^1H -NMR spectrum of the **4a** appears only one singlet due to a sole exchangeable hydrogen atom (NH or OH) at 8.68 ppm, whilst in spectrum of **2a** were two such singlets (8.27 and 9.05 ppm). These data are compatible only with a monoacyl derivative nature of **4a**. This is also confirmed by the ^{13}C -NMR spectrum of **4a** that presents 14 signals corresponding to 14 unequivalent carbon atoms, exactly the number of the carbon atoms in **4a**. Among these signals, only one corresponds to a sp^3 hybridized carbon (55.37 ppm) with a chemical shift characteristic to the methoxy group C-atom from methoxycarbonyl group.²⁴

Table 1.

Some physical-chemical data of the synthesized
alkyl-(10H-phenothiazin-3-yl)-carbonates

| Com pd. | m.p. (°C) | yield (%) | ^1H -NMR data* for substituents | | | | $\nu_{\text{C=O}}$ (cm^{-1}) | MS |
|------------|--------------|--------------|--|-----------------------------|--------------------|-------------------|--|-------------|
| | | | 3-OCOO-alkyl | $\text{N}^{10}\text{-CH}_3$ | 2-OCH ₃ | Solvent | | |
| 4a | 188-9 | 73 | CH_3 : 3.79; s; 3H | - | - | DMSO-d_6 | 1769 | 273; 60 |
| 4b | 128-30 | 64 | CH_3 : 3.78; s; 3H | - | 3.72 | DMSO-d_6 | 1768 | 303; 100 |
| 4c | 80-2 | 81 | $\text{CH}_3\text{-CH}_2$: 1.38; t; 3H; $J=7.08$; 4.31; q; 2H | - | - | CDCl_3 | 1759 | - |
| 4e | 216-8 | 71 | CH_3 : 3.85; s; 3H | - | - | DMSO-d_6 | 1759 | 305; 5 |
| 4g | 143-5 | 68 | $\text{CH}_3\text{-CH}_2$: 1.42; t; 3H; $J=7.14$; 4.36; q; 2H | - | - | CDCl_3 | 1761 | - |
| 4h | 181-2 | 74 | CH_3 : 3.87; s; 3H | - | - | DMSO-d_6 | 1769 | 407; 03 |
| 7a | 72-3 | 73 | $\text{CH}_3\text{-CH}_2$: 1.29; t; 3H; $J=7.08$; 4.26; q; 2H | 3.28; s; 3H | - | DMSO-d_6 | 1761 | - |
| 7b | 134-5 | 64 | $\text{CH}_3\text{-CH}_2$: 1.26; t; 3H; $J=7.0$; 4.20; q; 2H | 3.35; s; 3H | 3.82 | DMSO-d_6 | 1760 | - |
| 7e | 149-50 | 67 | $\text{CH}_3\text{-CH}_2$: 1.29; t; 3H; $J=7.08$; 4.26; q; 2H | 3.73; s; 3H | - | DMSO-d_6 | 1760 | - |
| 7f | 181-2 | 61 | $\text{CH}_3\text{-CH}_2$: 1.29; t; 3H; $J=7.08$; 4.25; q; 2H | 3.77; s; 3H | 4.00 | DMSO-d_6 | 1757 | - |

* There are presented the chemical shift (δ , ppm), the multiplicity (s=singlet, d=doublet, t=triplet, q=quartet) and the coupling constant (J , Hz)

The O-acyl derivative nature of our acylation products **4a-h** was established especially on the basis of the comparative analysis of the ^1H -NMR data for each pair starting 3-hydroxy-10H-phenothiazine derivative and its acylated product. Thus the effects caused by the introduction of the alkoxycarbonyl group on the chemical shifts of the protons from phenothiazine core in each 3-hydroxy-10H-phenothiazine derivative **2a-h** have been assigned. The use of these effects for the determination

of N- or O- derivative nature of the acylation products takes into account the known fact that the N-acylation (at position 10) causes ^{2d,21} a significant and relative constant (~ 0.5 ppm) deshielding of each proton (H^1 - H^9) from both benzene rings of each 10-acylated 10H-phenothiazine, as compared with the correspondent proton in the starting compound. For the same goal it was taken into account also the fact that the O-acylation at the 3-OH group of some 3-hydroxy-10H-phenothiazines determines¹⁸ a significant deshielding (0.17-0.37 ppm) only of the protons (H^1 , H^2 , H^4) from the benzene ring that contains the 3-O-acylated group. The deshielding for the protons (H^6 - H^9) of the other benzene ring is much lower (0.06-0.1 ppm). Consequently the manifestation manner (alike or differently) and the size (significant or insignificant) of the deshielding of the protons from two benzene ring of each previously N(10)-^{2d,21} or O-¹⁸ acylated phenothiazine derivative is a function of the N- or O- acyl derivative nature of this. The mentioned deshielding of the protons express the difference ($\Delta\delta_i$) between chemical shifts of two protons located in the same position (i), one in the acylated derivative ($\delta_{i,a}$) and the other in the starting 3-hydroxy-10H-phenothiazine ($\delta_{i,u}$). Such a deshielding effect ($\Delta\delta_i$) is called often "acylation shift".^{23,26} Just the evaluation of the acylation shift of the aromatic protons in the acylated products isolated by us proves the O-acyl derivative nature of the products **4a-h**. Indeed, the evaluated acylation shifts ($\Delta\delta_i$, Table 2) have a significant size (0.11-0.77 ppm) only for the protons (H^1 , H^2 , H^4) of the OH-substituted benzene ring. The acylation shifts of the protons H^6 - H^9 from the other benzene is much lower (0.00-0.10 ppm). These results are compatible only with a 3-O-acyl derivative nature of the acylation products.

Table 2.

The ^1H -NMR chemical shifts (δ_i)^a in the different type of 10H-phenothiazine derivatives and the effect of the derivatization on the ^1H chemical shifts ($\Delta\delta_i$)^b

| Compounds / The significance of the $\Delta\delta_i$ | The ^1H -chemical shifts (δ_i) and the $\Delta\delta_i$ values, for the 10-H-phenothiazine hydrogens in the following positions: | | | | | | | | Other hydrogens/ Type of derivatization |
|--|--|------|------|------|------|------|------|------|---|
| | 1 | 2 | 4 | 6 | 7 | 8 | 9 | 10 | |
| 2a | 6.54 | 6.43 | 6.89 | 6.92 | 6.70 | 6.96 | 8.65 | 8.27 | 3-OH : 9.05 |
| 4a | 6.68 | 6.85 | 6.87 | 6.92 | 6.77 | 7.00 | 6.68 | 8.68 | 3-OCOOCH ₃ : 3.79 |
| $\Delta\delta_i = \delta_{i,4a} - \delta_{i,2a}$ | 0.14 | 0.42 | 0.49 | 0.03 | 0.07 | 0.04 | 0.03 | 0.41 | 3-O-acylation |
| 2b | 6.39 | - | 6.39 | 6.90 | 6.70 | 6.96 | 6.64 | 8.26 | 2-OCH ₃ : 3.69 3-OH : 8.60 |
| 4b | 6.50 | - | 6.85 | 6.93 | 6.78 | 7.01 | 6.69 | 8.70 | 2-OCH ₃ : 3.72 3-OCOOCH ₃ : 3.78 |
| $\Delta\delta_i = \delta_{i,4b} - \delta_{i,2b}$ | 0.11 | - | 0.46 | 0.03 | 0.08 | 0.05 | 0.05 | 0.44 | 3-O-acylation |
| 2c | - | 6.79 | 6.53 | 7.00 | 6.86 | 7.04 | 6.66 | 6.31 | 3-OH: 4.52 |
| 6c | - | 6.83 | 6.59 | 7.01 | 6.86 | 7.04 | 6.66 | 6.32 | 3-OCH ₃ : 3.73 |
| $\Delta\delta_i = \delta_{i,6c} - \delta_{i,2c}$ | - | 0.04 | 0.06 | 0.01 | 0.00 | 0.00 | 0.00 | 0.01 | 3-O-methylation |
| 2h | - | 7.37 | 7.37 | 8.20 | - | 8.07 | - | 8.59 | 3-OH: 10.34 |
| 4h | - | 8.14 | 8.05 | 8.30 | - | 8.14 | - | 8.93 | 3-OCOOCH ₃ : 3.87 |
| $\Delta\delta_i = \delta_{i,4h} - \delta_{i,2h}$ | - | 0.77 | 0.68 | 0.10 | - | 0.07 | - | 0.34 | 3-O-acylation |
| 5a | 6.78 | 6.63 | 6.60 | 7.12 | 6.91 | 7.19 | 6.90 | - | N(10)-CH ₃ : 3.23 3-OH: 9.26 |
| $\Delta\delta_i = \delta_{i,5a} - \delta_{i,2a}$ | 0.24 | 0.20 | 0.22 | 0.23 | 0.21 | 0.23 | 0.25 | - | N(10)-methylation |

| Compounds / The significance of the $\Delta\delta_i$ | The ^1H -chemical shifts (δ_i) and the $\Delta\delta_i$ values, for the 10-H-phenothiazine hydrogens in the following positions: | | | | | | | | Other hydrogens/ Type of derivatization |
|---|--|------|------|------|------|------|------|----|---|
| | 1 | 2 | 4 | 6 | 7 | 8 | 9 | 10 | |
| 7a^c | 6.94 | 7.06 | 7.09 | 7.15 | 6.96 | 7.22 | 6.93 | - | N(10)-CH ₃ : 3.28 |
| $\Delta\delta_i = \delta_{i7a} - \delta_{i5a}$ | 0.16 | 0.43 | 0.49 | 0.03 | 0.05 | 0.03 | 0.03 | - | O-acylation |
| 7e^c | 7.61 | 7.66 | 7.89 | 7.99 | 7.37 | 7.77 | 7.64 | - | N(10)-CH ₃ : 3.73 |
| $\Delta\delta_i = \delta_{i7e} - \delta_{i7a}$ | 0.67 | 0.60 | 0.80 | 0.84 | 0.41 | 0.55 | 0.71 | - | 5,5-dioxidation |
| 7b^c | 6.69 | - | 7.05 | 7.16 | 6.97 | 7.23 | 6.98 | - | N(10)-CH ₃ : 3.73 2-OCH ₃ : 3.83 |
| 7f^c | 7.13 | - | 7.82 | 7.96 | 7.37 | 7.76 | 7.62 | - | N(10)-CH ₃ : 3.77 2-OCH ₃ : 4.00 |
| $\Delta\delta_i = \delta_{i7f} - \delta_{i7b}$ | 0.44 | - | 0.77 | 0.80 | 0.40 | 0.53 | 0.64 | - | 5,5-dioxidation |

- a) The ^1H -NMR spectra of the compounds **2a**, **2b**, **2h**, **4a**, **4b**, **4e**, **4h**, **5a**, **7a**, **7e**, **7f** were recorded in DMSO- d_6 and those of **2c** and **6c** in CDCl_3 .
- b) ($\Delta\delta_i$) represent the derivatization effect through functionalization on the chemical shift of the protons of the phenothiazine heterocycle. It express the difference between the chemical shifts (δ_i) of the corresponding protons (i) in the derivatized (δ_{id}) and the starting (δ_{is}) 3-hydroxy-10H-phenothiazine derivative.
- c) See Table 1 for the ^1H -NMR data of the ethoxycarbonyloxy group in the corresponding compound.

Such a determination of the N- or O-acyl derivative nature should be more precise in the case of the acylation products obtained from 3-hydroxy-10H-phenothiazines protected by N- (**5a,b**) or O- (**6c,d**) methylation. Therefore, we have methylated some 3-hydroxy-10H-phenothiazine derivatives in conditions that are claimed ⁵ to lead to O-methylation. The ^1H -NMR spectra of the isolated methylation products have shown that only the products obtained from **2c,d** are 3-O-methyl derivatives (**6c,d**), while those from **2a,b** are N(10)-methyl derivatives. The N(10)-methyl derivative nature of **5a,b** is proved by the chemical shifts of the methyl group protons that have practically the same values (3.25 ppm in DMSO- d_6 , respectively 3.36 ppm in CDCl_3) with those of the methyl group in other 10-methyl-10H-phenothiazines^{1c,e,19,27} and correspond to the chemical shifts range of the N-CH₃ protons (3-3.5 ppm).²⁸ The 10-methyl derivative structure of **5a,b** is confirmed by a significant and relative constant deshielding of all of the aromatic protons (~ 0.25 ppm, Table 2) comparative to the correspondent protons in the starting **2a,b**, since it is known^{1f} that N-methylation of 10H-phenothiazines determines such a deshielding. Similarly, the 3-methoxy-10H-phenothiazine derivative nature of **6c,d** is proved by the chemical shift values of their methyl group protons (3.73 ppm, in CDCl_3 , Table 2). This value corresponds to the chemical shift range of the OCH₃ group protons (3.5-4 ppm)^{23a,24,28} and was found^{1c,f,22} in other 3-methoxy-10H-phenothiazines. The insignificant values of the deshielding effect for the aromatic protons in this case confirm the 3-methoxy derivative structure of **6c,d** since it is known^{23a} that the derivatization of the phenolic 3-OH to 3-OCH₃ has a very low effect on the chemical shift of the protons in the afferent benzene ring.

The acylation of **5a,b** with ethyl chloroformate may lead only to the O-acylated products **7a,b**. In accordance with this, the ^1H -NMR spectra of **7a,b** show the presence of the N-CH_3 group by a singlet at 3.30 ppm and the corresponding acylation shifts ($\Delta\delta_i$) are significant (up to 0.5 ppm) only for the protons of 3-OH substituted benzene ring (Table 1,2). So is undoubtedly confirmed that the acylation at the group situated unsymmetrical with respect to the two benzene rings of a 10H-phenothiazine derivative (3-OH, in our case) determines significant acylation shifts only for the protons of the benzene ring in which is located the acylated group.

The carbonate structures of the products **7a,b** is confirmed by their ^{13}C -NMR spectra. Thus, in both spectra of these compounds appears a signal (35.3 ppm) corresponding to a N-CH_3 group^{28b,29} inclusively in 10-methyl phenothiazine.¹⁹ In addition, in each ^{13}C -NMR spectrum of **7a,b** appear another two signals (65 and 14 ppm) corresponding to the ethoxycarbonyl group introduced by acylation of **5a,b**.

These carbonates (**7a,b**) were converted by oxidation with peroxybenzoic acid into the corresponding 5,5-dioxides **7e,f**. The sulfone structure of the oxidation products was confirmed by the NMR spectra, in which all the aromatic protons are strong deshielded relative to the protons of the starting compounds **7a,b** (Table 2). Such strong deshielding effects were found previously^{1c,h,17,18} even by derivatization through 5,5-diooxidation.

The O-acylderivative structure of all acylation products described in this paper has been confirmed also by their IR spectra, in which appear an absorption band in the range $1757\text{-}1769\text{ cm}^{-1}$ (Table 1) characteristic³⁰ for the C=O of organic carbonates.

The carbamates **3a,h** and **8c,d** could not have been isolated in the acylation conditions examined by us, even using as starting compounds the 3-methoxy derivatives **6c,d**.

CONCLUSIONS

By selective alkoxy-carbonylation of some 3-hydroxy-10H-phenothiazine derivatives **2a-c,e,g,h**, **5a,b** were synthesized eight new mixed alkyl (10H-phenothiazin-3-yl) carbonates **4a-c,e,g,h**, **7a,b**. Two of these were transformed into the corresponding sulfones (**7a,b**) by oxidation. The structure of the synthesized compounds was established chemically and by spectral analysis. The presented data proved the utility for structure elucidation of the derivatization effects on the proton chemical shift by the N- (or O-) methylation, O-acylation or 5,5-diooxidation of 3-hydroxy-10H-phenothiazine derivatives.

REFERENCES

1. R.R. Gupta and M. Kumar, in "Phenothiazines and 1,4-Benzothianes", Ed. Gupta, R.R., Elsevier (Amsterdam), 1988. a) p. 4,6; b) p. 101-103; c) Martin, A.R., ibidem, p. 357-439; d) p. 388, 389; e) p. 367-370; f) p. 373-375; g) p. 439-442; h) p. 389-394.
2. W. Weston, R. W. de Net and R. J. Michaels, *J. Amer. Chem. Soc.*, **1953**, 75, 4006.

3. R. Dahlbom, *Acta Chem. Scand.*, **1953**, 7, 879; *Chem Abstr.* **1955**, 49, 4659d;
4. J. Schmitt, J. Boitard, P. Comoy, A. Hallot and M. Suquet, *Bull. Soc. Chem. Fr.*, **1957**, 938.
5. Y. Guindon, Y. Girard, C. K. Lau, R. Fortin, J. Rokach and, C. Yoakim, 1986, **U.S. Pat.** 4.611.056A; b) R. Fortin, Y. Guindon, C. K. Lau, J. Rockach and Ch. Yoakim, 1985, **Eur. Pat.** 138.481 A2, *Chem. Abstr.* **1986**, 104, P.15081s; 1987, **U.S. Pat.** 4.666.907 A, 1989; **US Pat.** 4.845.083A; c) R. Fortin, Y. Girard, Y. Guindon, C.K. Lau, J. Rochach and C. Yoakim, 1985, **Eur. Pat.** 136.893 A2; *Chem Abstr.* **1985**, 103, P.11.474.
6. A. Andreani, M. Rambaldi, A. Locatelli, A. Fraccari, R. Boss and I. Galatulas *Pharm. Acta Helv.* **1992**, 67, 234; *Chem. Abstr.* **1992**, 117, 212240.
7. D. Bebbington, J.D. Charrier, D. Kay, R. Knegetel, J. Golec, M. Mortimore and J. Studley **WO0172707A₂** **2001**, *Chem. Abstr.* **2001**, 135, 273216.
8. H. Matzner, R.P. Kurkijy and R.J. Cutter, *Chem. Rev.*, **1964**, 64, 645.
9. a) R. Pummerer and S. Gassner, *Chem. Ber.* **1913**, 46, 2310 b) C. Bodea and V. Fărcășan, *Studii și Cercetări de Chim., Acad. RPR, Fil Cluj*, **1960**, 11, 121; c) E.A. Nadif, T.W. Hofmann and H.L. Shasma, *J. Heterocyclic Chem.*, **1971**, 8, 493
10. J.P. Billon, *Ann. Chim. (France)*, **1962**, 7, 183
11. J.E.C. Hutchins and T.H. Fife *J. Am. Chem. Soc.* **1973**, 95, 2282; A.F. Hegarty, L.N. Frost and D. Cremin *J. Chem. Soc., Perkin Trans. 2* **1974**, 1249.
12. A. Albert, *Heterocyclic Chem.*, Athlone Press, Univ. London **1959**, p 74.
13. M. Mikulla and R. Muhlhaupt, *Chem. Ber.* **1994**, 127, 1723
14. Bodea and M. Răileanu, *Studii și Cercetări de Chim., Acad RPR, Fil. Cluj*, **1960**, 11, 325.
15. T. Panea and M. Moldovan, *Rev. Roum. Chim.*, **1980**, 25, 691.
16. C. Bodea and M. Raileanu, *Liebigs Ann. Chem.* **1958**, 614, 171; b) T. Panea and C. Bodea, **Rom. Pat.**, 1970, 53.099; Fr. Pat. 1970, 2.105.307, *Chem. Abstr.* **1972**, 77, 164765u.
17. V. Girard, P. Hamel, M. Therien, J.P. Springer and J. Hirschfield, *J Org. Chem.*, **1987**, 52, 4000.
18. R. Gropeanu, I. Panea and T. Panea *South Braz. J. Chem.*, **2000**, 8(9), 13.
19. D. Clarke, B.C. Gilbert, P. Hanson and C.M Kirk, *J Chem. Soc. Perkin Trans. 2*, **1978**, 1103.
20. J. Cymerman Craig, D. E Green, S. K. Roy, L. H. Pitte and K.O. Loeffler, *J. Med. Chem.*, **1965**, 8, 392.
21. E. Gipstein, W. A. Hewett and O. U. Need *J. Polym. Sci. part A-1* **1970**, 8, 3285.
22. R. L. Mital and R.C. Chaudhary *J. of Chem. and Eng. Data* **1975**, 20, 204.
23. a) L.M. Jackman and S. Sternhell, Applications of Nuclear Magnetic Resonance Spectroscopy in Organic Chemistry, 2nd Edition, Pergamon Press, London, 1969, p. 176, 179, 180, 201- 204. b) H. Friebolin, Basic One – and two – Dimensional NMR Spectroscopy, 2. ed. VCH, 1993, Weinheim, p. 144, 146.
24. M. Ferrero, S. Fernadez and V. Gotor *J. Org. Chem.* **1997**, 62, 4358.
25. I. Panea, L. Bodochi, T. Panea, D. Zinveliu and V. Pașcalău *South. Braz. J. Chem.* **1999**, 7(8), 25.
26. I. Panea and M. Ionescu *Studia Univ. "Babeș- Bolyai". Ser. Chem.* **1973** 18(1), 11; S. Kitanaka and M. Takido, *Chem. Pharm. Bull.*, **1984**, 32(3), 860.
27. M.H. Litt, J. W. Summers and T. M. Shimko, *J. Org. Chem.*, **1972**, 37, 1045.
28. E. Breitmaier, Structure elucidation by NMR in Organic Chemsitry, J. Willey, Chichester, **1995**, a) pp. 13, b) pp. 15

29. H.O. Kalinowski, S. Berger and S. Braun, Carbon -13 NMR Spectroscopy, J. Willey, New York, **1991**, pp.112, - 115, 175, 222, 315, 396.
30. L.J. Bellamy "The Infrared Spectra of Complex Molecules" 2nd ed. Methuen, London, **1964**, pp. 125 –127.

SYNTHESIS AND STEREOCHEMISTRY OF A NEW SERIES OF 2,2'-DISUBSTITUTED-5,5-BIS(BROMOMETHYL)-1,3-DIOXANES

RADU GROPEANU, ADRIAN WOICZECOWSKI-POP, MIHAELA TINTAS,
RALUCA TURDEAN, ION GROSU

*Organic Chemistry Department, Faculty of Chemistry and Chemical Engineering,
Babes-Bolyai University, 11th Arany Janos st., 400028-Cluj-Napoca, Romania*

ABSTRACT. The synthesis of a new series of 2,2'-disubstituted-5,5-bis(bromomethyl)-1,3-dioxanes is reported. The stereochemistry of the products was studied using NMR spectra. These compounds present flexible, semi-flexible and anancomeric structures in solution at room temperature.

INTRODUCTION

Cyclic disulfides have become interesting motifs in nanotechnologies, being used especially as adsorbents on gold surfaces,¹ or on colloidal gold.² Our strategy for obtaining a new series of cyclic disulfides is based on the synthesis of bis(bromomethyl) derivatives as intermediates. Some interesting features revealed by NMR spectroscopy have prompted us to extend the number and the type of bis(bromomethyl)-1,3-dioxane derivatives.

RESULTS AND DISCUSSION

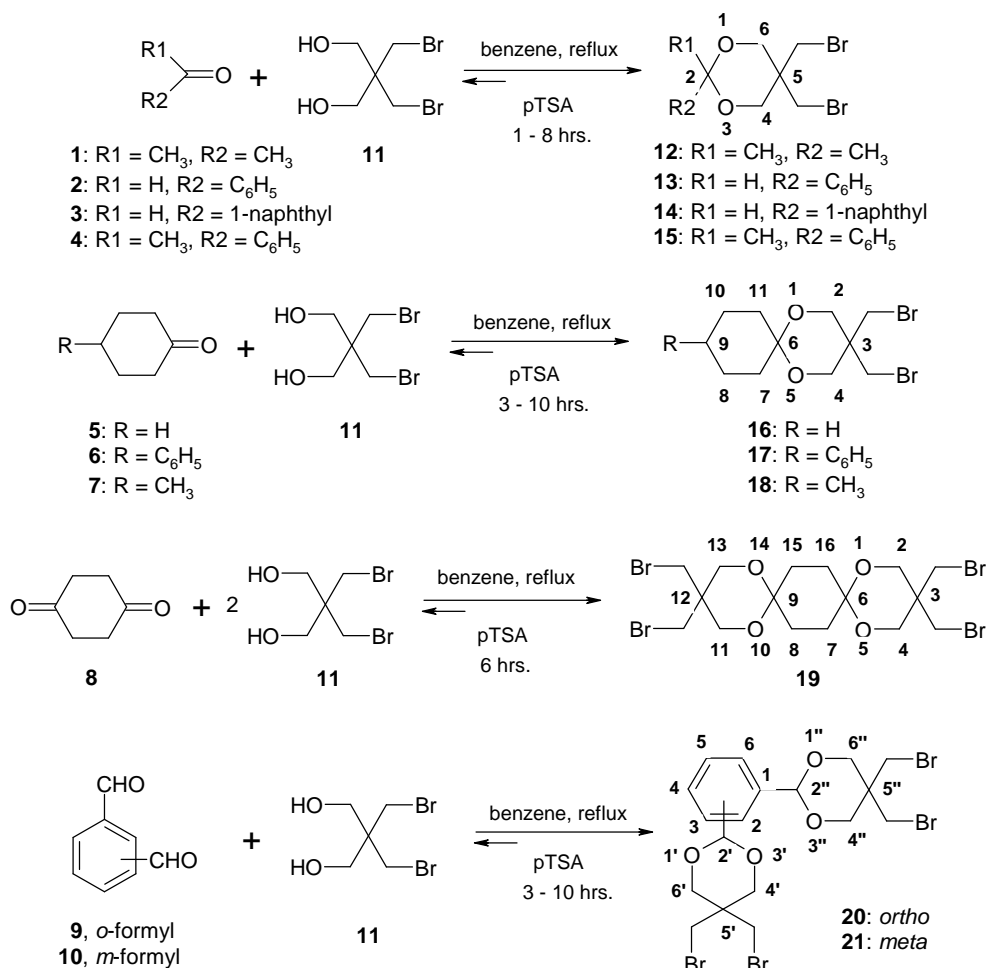
The Synthesis

The title compounds were obtained by acid catalyzed (a)cetalization³ of the starting carbonyl compounds **1-10** with 2,2-bis(bromomethyl)-1,3-propanediol in good and very good yields. The reaction equilibrium was shifted to products by azeotropic distillation of the resulted water with solvent (benzene or toluene, Scheme 1).

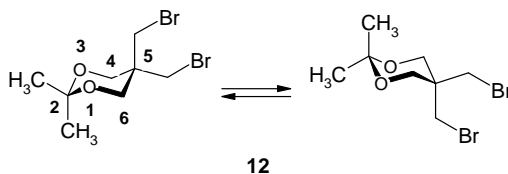
The assigned structures were confirmed by NMR spectra. As a general observation, the (a)cetalization had as effect a general shifting to upfield higher fields of the signals corresponding to the starting carbonyls, especially of the acetalic proton or of the α -methyl or methylene group in the case of ketones (**1, 4-8**).

The Stereochemistry of the Products

The structure of **12, 16** and **19** is flexible due to the symmetrically substitution pattern of the 1,3-dioxane and of the carbocycle rings. The conformational equilibrium between the two chair conformers of the 1,3-dioxane ring (Scheme 2) causes in the ¹H-NMR spectrum of **12** the appearance of singlet signals for the protons of 1,3-dioxane and of its substituents at mediated values ($\delta_{2-\text{Me}}=1.41$, $\delta_{5-\text{MeBr}}=3.58$ and $\delta_{4,6}=3.80$ ppm).



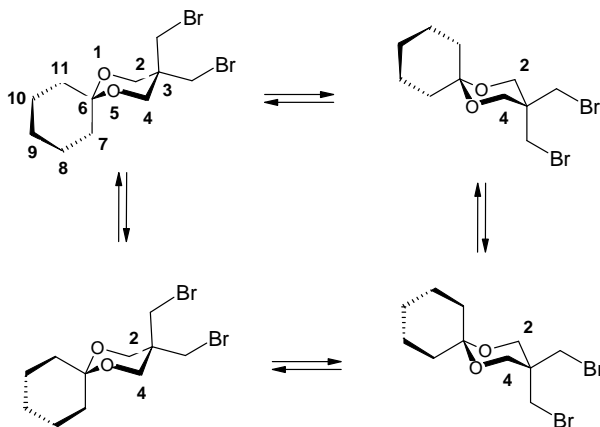
Scheme 1



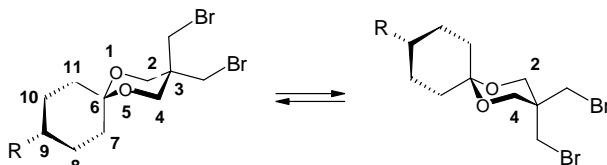
Scheme 2

Compound **16** presents four isomers of configuration due to the chirality of the monospiranes with six-membered rings.^{4,5} The flipping of the 1,3-dioxane and cyclohexane rings at r.t. determines the conformational equilibrium of all possible isomers (Scheme 3). The ¹H-NMR spectrum of **16** presents two singlets for the 1,3-dioxane ring and for the bromomethyl substituents ($\delta_{3\text{-MeBr}}=3.58$ and $\delta_{4,6}=3.81$

ppm). The ^1H -NMR spectrum of **19** shows the same flipping behavior of the 1,3-dioxane and cyclohexane rings, having singlets for cyclohexane ($\delta_{7,8,15,16}=1.90$ ppm) and 1,3-dioxane ($\delta_{2,4,11,13}=3.82$ ppm) rings protons and bromomethyl substituents ($\delta_{3,12-\text{MeBr}}=3.60$ ppm), respectively.

**16****Scheme 3**

The monospiranes **17** and **18** present, like **16**, four isomers of configuration due to the chirality of the monospiranes with six-membered rings, with the difference that the carbocycle adopts an anancomeric structure due to the presence of a substituent which prefers the equatorial orientation.⁶⁻⁸ The 1,3-dioxane rings of **17** and **18** are flexible (Scheme 4), proved by the singlet signals of the bromomethyl substituents [$\delta_{3-\text{MeBr}}=3.62$ ppm (**17**) and 3.59 ppm (**18**)]. The signals of the 1,3-dioxane unit methylenes are also singlet, but, due to the anancomeric structure of the cyclohexane ring, the positions 2 and 4 are diastereotopic (*procis* and *protrans*, respectively, referred to the substituent at position 9) and present different chemical shifts [$\Delta\delta=0.03$ ppm (**17**) and 0.05 ppm (**18**)].



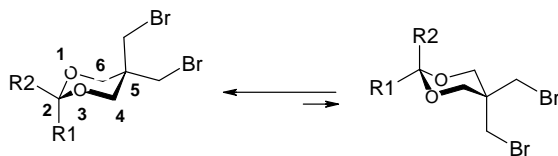
17: R = $-\text{C}_6\text{H}_5$

18: R = $-\text{CH}_3$

Scheme 4

In the case of **13-15**, **20**, **21** the conformational equilibrium is shifted at r.t. to the isomer in which the more bulky substituent at position 2 lies in the equatorial orientation (Scheme 5). This causes the freezing of the conformational equilibrium

and, consequently, the diastereotopicity of the axial and equatorial protons from positions 4 and 6. The signals of these protons appear in $^1\text{H-NMR}$ spectra as an AB system (e.g., $\delta_{4,6\text{-ax.}}=3.85$ ppm, $\delta_{4,6\text{-eq.}}=4.26$ ppm for **13**). Also, the two methylene residues from bromomethyl substituents give in the spectrum two different singlets (e.g., $\delta_{5\text{-MeBr eq.}}=3.31$ ppm, $\delta_{5\text{-MeBr ax.}}=4.00$ ppm for **13**).



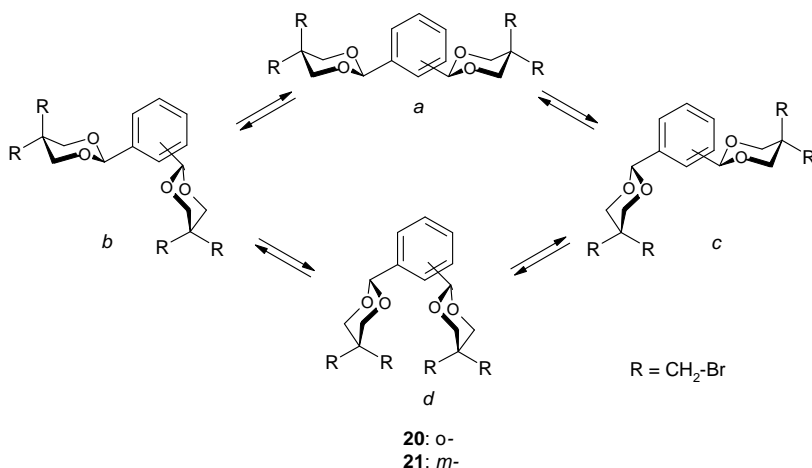
13: R1 = H, R2 = $-\text{C}_6\text{H}_5$

14: R1 = H, R2 = 1-naphthyl

15: R1 = $-\text{C}_6\text{H}_5$, R2 = $-\text{CH}_3$

Scheme 5

In **13**, **14**, **20**, **21** the phenyl substituent of the 1,3-dioxane ring adopts, as we have expected, the equatorial conformation. In the case of **20** and **21** there are four conformers due to the free rotation of the 1,3-dioxane rings around the σ bond phenylene-(1,3-dioxane-2-yl) (Scheme 6).



Scheme 6

While for **21** all four conformers *a-d* are possible, in the case of **20** the *d* conformer is less probable due to the steric repulsions between the bromomethyl substituents and the unshared pair of electrons of the oxygen atoms, respectively, of the both 1,3-dioxane units. This fact has as result a shift of the acetalic protons signal to lower fields ($\Delta\delta_{\text{H}_2}=0.22$ ppm).

Conclusions

The synthesis of a series of 5,5-bis(bromomethyl) 1,3-dioxane derivatives (**12-15**, **20**, **21**) and 1,3-dioxane-based (poly)spiranes (**16-19**) was achieved by (a)cetalization of the corresponding carbonyl derivatives with 2,2-bis(bromomethyl)-1,3-propanediol (**11**). Their stereochemistry was discussed using NMR spectra. The study revealed that, depending of the type of substituents on the position 2 of the 1,3-dioxane unit, these compounds have three main conformational behavior: flexible (**12**, **16**, **19**), semi-flexible (**17**, **18**), and anancomeric (**13-15**, **20**, **21**).

Experimental

The solvents were purified according to standard procedures⁹ and were distilled prior to use. Column chromatography: silica gel 60 (Merck, Darmstadt), mesh 70–230 nm. Thin layer chromatography (TLC): silica gel layered aluminum foil (60 F₂₅₄ Merck, Darmstadt). Melting points (uncorrected) were taken using a Kleinfold APOTEK apparatus. 2,2-bis(bromomethyl)-1,3-propanediol (Aldrich), acetophenone (**4**), 4-phenyl-cyclohexane-one (**6**), 4-methyl-cyclohexane-one (**7**), 1,4-cyclohexanedione (**8**), ftaldialdehyde (**9**), *iso*-ftaldialdehyde (**10**) were purchased and used without further purification. ¹H and ¹³C NMR spectra were recorded with Varian Gemini 300 and Bruker ARX 300 (300 MHz for ¹H and 75 MHz for ¹³C) or Bruker ARX 200 (200 MHz for ¹H and 50 MHz for ¹³C) using CDCl₃ as solvent.

General procedure for the synthesis of compounds 12-21

A solution of 10 mmol of 2,2-bis(bromomethyl)-1,3-propanediol (**11**), 10 mmol of the corresponding carbonyl compound (**1-10**) and 0.1 g *p*-toluene sulfonic acid in 100 ml benzene was refluxed for two hours. The water was removed using a Dean-Stark trap. After cooling down, the catalyst was neutralized with excess of sodium acetate and the suspension was washed twice with 50 ml water. The organic layer was separated, dried with anhydrous sodium sulfate and the solvent was removed in vacuum. The resulted residue was deposited on silica gel and was purified using column chromatography.

5,5-bis(bromomethyl)-2,2-dimethyl-1,3-dioxane (12)

White solid, m.p. 89-91°C, yield 89%. ¹H-RMN (δ , ppm) 1.41 (6H, s), 3.58 (4H, s), 3.80 (4H, s).

5,5-bis(bromomethyl)-2-phenyl-1,3-dioxane (13)

White solid, m.p. 101°C, yield 91%. ¹H-RMN (δ , ppm) 3.31 (2H, s), 3.85 (2H, d, ²J=12 Hz), 4.00 (2H, s), 4.26 (2H, d, ²J=12 Hz), 5.41 ppm (1H, s), 7.40-7.44 (2H, m), 7.48-7.51 (2H, m). ¹³C-RMN (δ , ppm) 34.41 (CH₂), 35.97 (CH₂), 37.30 (C_{quat}), 71.83 (CH₂), 102.21 (CH), 125.98 (CH), 128.30 (CH), 129.20 (CH), 137.22 (C_{quat}).

5,5-bis(bromomethyl)-2-(1'-naphthyl)-1,3-dioxane (14)

White solid, m.p. 128-9°C, yield 3%. ¹H-RMN (δ , ppm) 3.36 (2H, s), 4.00 (2H, d, ²J=12 Hz), 4.06 (2H, s), 4.36 (2H, d, ²J=12 Hz), 6.03 (1H, s), 7.56-8.00 (7H, m).

5,5-bis(bromomethyl)-2-methyl-2-phenyl-1,3-dioxane (15)

White solid, m.p. 115°C, yield 90%. ¹H-RMN (δ , ppm) 1.56 (3H, s), 3.10 (2H, s), 3.61 (2H, d, ²J=11,74 Hz), 3.88 (2H, d, ²J=11,74 Hz), 4.00 (2H, s), 7.35-7.43 (5H, m). ¹³C-RMN (δ , ppm) 31.53, 34.67, 36.06, 37.46, 66.07, 76.57, 76.99, 77.42, 101.37, 126.48, 128.12, 128.91, 139.39.

3,3-bis(bromomethyl)-1,5-dioxaspiro[5.5]undecan (16) White solid, m.p. 79-80°C, yield 85%. ¹H-RMN (δ , ppm) 1.38-1.76 ppm (10H, m), 3.58 ppm (4H, s), 3.81 ppm (4H, s); ¹³C-RMN (δ , ppm) 22.53 (CH₂), 25.60 (CH₂), 32.25 (CH₂), 36.21 (CH₂), 37.31 (C_{quat}), 64.04 (CH₂), 98.90 (C_{quat}).

3,3-bis(bromomethyl)-9-phenyl-1,5-dioxaspiro[5.5]undecan (17)

White solid, m.p. 125-7°C, yield 80%. ¹H-RMN (δ , ppm) 1.46-1.73 (6H, m), 2.31-2.62 (3H, m) 3.62 (4H, s), 3.85 (2H, s), 3.88 (2H, s); 7.18-7.33 ppm (5H, m). ¹³C-RMN (δ , ppm) 30.12 (CH₂), 32.34 (CH₂), 36.18 (CH₂), 37.99 (C_{quat}), 43.80 (CH), 64.31 (CH₂), 64.45 (CH₂), 98.59 (C_{quat}), 126.9 (CH), 128.43 (CH), 146.38 (C_{quat}).

3,3-bis(bromomethyl)-9-methyl-1,5-dioxaspiro[5.5]undecan (18)

White solid, m.p. 98-9°C, yield 92%. ¹H-RMN (δ , ppm) 0.90 (3H, d, ³J=6.30 Hz), 1.07-1.62 (7H, m), 2.12-2.18 (2H, m), 3.59 (4H, s), 3.78 (2H, s), 3.83 (4H, S); ¹³C-RMN (δ , ppm) 21.67 (CH₃), 30.74 ppm, (CH₂), 31.87 ppm (CH₂), 31.86 (CH), 36.10 (CH₂), 37.90 (C_{quat}), 64.16 (CH₂), 64.29 (CH₂), 99.01 (C_{quat}).

3,3,12,12-tetrakis(bromomethyl)-1,5,10,14-tetraoxaspiro[5.2.5.2]hexadecan (19)

White solid, m.p. 159-60°C, yield 75%. ¹H-RMN (δ , ppm) 1.90 (8H, s), 3.60 (8H, s), 3.82 (8H, s).

1,2-bis[5',5'-bis(bromomethyl)-1',3'-dioxane-2'-yl]-benzene (20)

White solid, m.p.= 135-6, yield 70%. ¹H-RMN (δ , ppm) 3.32 (2H, s), 3.86 (2H, d, ²J=11.7 Hz), 4.00 (2H, s), 4.29 (2H, d, ²J=11.7 Hz), 5.65 ppm (2H, s), 7.40-7.43 (2H, m), 7.65-7.68 (2H, m). 34.33 (CH₂), 36.00 (CH₂), 72.18 (CH₂), 100.50 (CH), 115.90 (CH), 119.2 (CH).

1,3-bis[5',5'-bis(bromomethyl)-1',3'-dioxane-2'-yl]-benzene (21)

White solid, m.p.= 142-4°C, yield 76%. ¹H-RMN (δ , ppm) 3.33 (2H, s), 3.86 (2H, d, ²J=11.6 Hz), 3.98 (2H, s), 4.27 (2H, d, ²J=11.6 Hz), 5.43 ppm (2H, s), 7.40-7.43 (2H, m), 7.65-7.68 (2H, m). ¹³C-RMN (δ , ppm) 34.33 (CH₂), 36.00 (CH₂), 72.18 (CH₂), 100.50 (CH), 115.90 (CH), 119.2 (CH).

REFERENCES

1. see for example: a) Nuzzo, R.G.; Allara, D.L. *J. Am. Chem. Soc.* **1983**, *105*, 4481; b) Herranz, M.A.; Yu, L.; Martin, N.; Echegoyen, L. *J. Org. Chem.* **2003**, *68*, 8379.
2. See for example: Daniel, Astuc *Chem. Rev.* **2004**, *104*(1), 290.
3. Anteunis, M.J.O.; Tavernier, D.; Borremans, F. *Heterocycles* **1976**, *4*, 293.
4. Grosu, I.; Mager, S.; Ple, G.; Horn, M. *J. Chem. Soc., Chem. Commun.* **1995**, 167.
5. Grosu, I.; Mager, S.; Ple, G. *J Chem Soc Perkin Trans 2* **1995**, 1351.
6. Terec, A.; Grosu, I.; Condamine, E.; Breau, L.; Ple, G.; Ramondenc, Y.; Rochon, F.D.; Peulon-Agasse, V.; Opris, D. *Tetrahedron* **2004**, *60*, 3173.
7. Mager, S.; Grosu, I. *Stud. Univ. "Babes-Bolyai", Chemia* **1988**, *33*, 47.
8. Grosu, I.; Plé, G.; Mager, S.; Mesaros, E.; Dulau, A.; Gego, C. *Tetrahedron* **1998**, *54*, 2905.
9. Various authors, *Organikum*, Wiley VCH Verlag GmbH, Weinheim, 2001, p. 741.

IS IT POSSIBLE TO APPLY UNITARY MATHEMATICAL TREATMENT TO FLUID FLOW?

MISCA B.R.H.¹

¹ *Departement of Chemical Engineering, Faculty of Chemistry and Chemical Engineering,
"Babes-Bolyai" University, Cluj-Napoc, Romania, miscal@chem.ubbcluj.ro*

ABSTRACT. In the paper are presented the fundamental ideas of modified general dimensional analysis and its application for the fluid flow in contact with solids having different geometries. A mathematical study is performed and a correlation between the working parameters is proposed resulting equation deduced by application of the modified general dimensional analysis. Comparison between the obtained and classical relationship is also presented.

Keywords: dimensional analysis, fluid flow, dimensionless relations

Cases in which fluids, liquids and gases are contacted by solids through chemical reactions, the transfer phenomenon intensification, or due to the necessity of physical presence of parting walls of conducting pipes are often encountered in the chemical practice. This phenomenon is interesting from the point of view for transfer phenomena intensification as well for the materials transport through pipes. Due to the large number of possible situations: fluid flow in a pipe, contacting into packed columns, the presence of other interfaces, the passage through different pipe details: elbows, tees, valves, derivations, entrances and exists from storage tanks, etc... even though there are specific parameters precisely determined for each particular situation, the question arises: is it possible to apply a unitary treatment to this phenomenon, irrespective of obstacle's geometrical form.

In this work we propose a way to present the unitary treatment of hydrodynamic process of fluid flow by means of the general dimensional analysis method. Thus, we try to give an answer to the question in the title of this article. In this sense, in conformity with the General Dimensional Analysis Theory, (GDAT), presented by Staicu, [1], there are three fundamental stages that must be followed to find the solution:

1. – establish the list of variables that influence the process directly or in reverse sense;
2. – establish the monomial type relationship describing the treated phenomenon;
- 3 – determine the numerical coefficient describing the process.

I propose to introduce another working stage in the methodology [10]. This new stage should be placed between the two first stages and is expected to lead to a certain hierarchy upon the importance of variables describing the process. Thus, the real mathematical basis may be revealed by neglecting certain variables that are empirically considered to be less important, a situation often encountered in the practical and experimental studies. Moreover, after establishing the monomial type

relation, we may operate mathematically upon it to obtain some criteria relations describing the process. Criteria expressions show the influence that different types of forces exert on the system, presenting details about this process phenomenology that would not be relevant otherwise, being dissimulated by several aspects.

The model below describes pure fluid flow through spaces with any geometry and develops the working algorithm to find the general relation to calculate fluid flow and all explanations that derive from here in the light of the question in the title.

In the 1st stage, the matrix line of the variables describing the fluid flow process and their directly or reverse influence is formed. The list of all possible variables and the way of their distribution is presented below:

$$// \Delta p, d_{ech}, ; w, H, \rho, \eta, \sigma, g //$$
 (1).

The following may appear on the list of variables: pressure drop, Δp , the equivalent diameter, d_{ech} , flow length or the height of packed bed, H , the flow speed, w , the dynamic viscosity, η , interfacial strength, σ and earth acceleration, g . Into the matrix line, variables are distributed according to the influence they have upon the process as follows:

- equivalent diameter of flow, d_{ech} operates reversely upon the pressure loss, which represents the studied parameter;
- length or height of flow and speed, density, dynamic viscosity of fluids and earth acceleration have a direct effect upon the increase of the pressure drop.

The grouping of certain physical particularities of the solid can also be noticed. These are as follows: specific surface, S_p , and void fraction, ε , in a single one, $d_{ech} = 4\varepsilon/S_p$, which is in fact the specific dimension of fluid flow, or considering the fluid speed as the real one, w , either the fluid fictive one w_i in the packed bed or on the geometrical area causing fluid flow deformation. Other measures describing the flow can also be taken into account as mass or volumetric flow rate. These parameters are considered to be composed of simpler ones:

$$Q_M = Q_V \cdot \rho = w \cdot A \cdot \rho, \text{ so the result of calculus is the same.}$$

The additional proposed stage development is, that of evaluation of the importance of functional parameters and we may start form the minimum list of variables describing the process. This can be determined from the solving condition of the system of undetermined diophantian equations imposed by GDAT: minimum, integer, positive and non-null solution. The only combination of variables which complies with the imposed condition is the one below:

$$// \Delta p, d_{ech}, ; w, H, \rho //$$
 (2),

and the dimensional matrix and the system of non-determined equations attached to the matrix are presented hereinafter:

| | Δp^a | d_{ech}^b | w^c | H^e | ρ^f |
|---|--------------|-------------|-------|-------|----------|
| L | -1 | 1 | 1 | 1 | -3 |
| M | 1 | 0 | 0 | 0 | 1 |
| T | -2 | 0 | -1 | 0 | 0 |

$$\begin{cases} -a + b = c + e - 3f \\ a = f \\ -2a = -c \end{cases}$$

The system of undetermined equations can be solved by the method of progressive homogenization of diophantian relations:

The solution is as follows: $a = 1, f = 1; \quad c = 2; \quad b = 1, e = 1;$ and the monomial type relation generated by it, according to GDAT is:

$$\Delta p = k_1 \frac{w^2 H \rho}{d_{ech}}, \quad (3).$$

The relation is dimensionally homogenous and after the mathematical operations have been performed upon it, the result is an expression also accepted by the classical method of dimensional analysis, Buckingham:

$$\frac{\Delta p}{w^2 \rho} = k_1 \cdot \frac{H}{d_{ech}}; \quad (4), \quad \text{or} \quad Eu = k_1 \frac{H}{d_{ech}}, \quad (5).$$

We may notice that the fluid flow over a solid is, in the most general case, caused by the following fundamental parameters: pressure drop, speed, density and geometrical configuration of the flow space. Moreover, under constant conditions, the pressure drop Δp is constant. As these are basic parameters, they will be also present in all the other relations, and therefore they, as such, would present their most "rude" influence on fluid flow.

If we add to the minimum list of variables some other additional variables, one by one extracted from the general list, we can obtain the following lists of variables:

$$// \Delta p, d_{ech}, ; w, H, \rho, \eta //, \quad (6),$$

$$// \Delta p, d_{ech}, ; w, H, \rho, \sigma //, \quad (7),$$

$$// \Delta p, d_{ech}, ; w, H, \rho, g // \quad (8).$$

For each list there's a specific relation:

$$\Delta p^2 = k_2 \frac{w^3 H \rho \eta}{d_{ech}^2}, \quad (9), \quad \frac{\Delta p^2}{w^4 \rho^2} = k_2 \frac{\eta}{w d_{ech} \rho} \cdot \frac{H}{d_{ech}}, \quad (10),$$

$$Eu^2 = k_2 Re^{-1} \frac{H}{d_{ech}}, \quad (11);$$

$$\Delta p^2 = k_3 \frac{w^2 H \rho \sigma}{d_{ech}^2}, \quad (12), \quad \frac{\Delta p^2}{w^4 \rho^2} = k_3 \frac{\sigma}{w^2 d_{ech} \rho} \cdot \frac{H}{d_{ech}}, \quad (13),$$

$$Eu^2 = k_3 We^{-1} \frac{H}{d_{ech}}, \quad (14).$$

In the case of the third list, (8), NO solution is accepted by GDAT, which means that the variable introduced additionally does not influence the process directly and fundamentally. This proves that earth acceleration is a secondary parameter for the flow process. In fact, the pressure drop is the key element for the fluid movement. From the practical and phenomenological point of view, we may ascertain that fluid movement is only sometimes influenced by gravitation or either acceleration forms, which is proved by particular calculation relations.

After the introduction in the matrix line of the variables that were not studied, we obtain the following result:

$$// \Delta p, d_{ech}, ; w, H, \rho, \eta, \sigma //, \quad (15),$$

$$// \Delta p, d_{ech}, ; w, H, \rho, \eta, g // \quad (16).$$

The result of the general dimensional analysis is:

$$\Delta p^3 = k_4 \frac{w^3 H \rho \eta \sigma}{d_{ech}^3}, \quad (17),$$

$$\frac{\Delta p^3}{w^6 \rho^3} = k_4 \frac{\eta}{w d_{ech} \rho} \cdot \frac{\sigma}{w^2 d_{ech} \rho} \cdot \frac{H}{d_{ech}}, \quad (18),$$

$$\text{or } Eu^3 = k_4 Re^{-1} We^{-1} \frac{H}{d_{ech}}, \quad (19).$$

$$\Delta p^2 = k_5 \frac{w H \rho g}{d_{ech}} ; (20), \frac{\Delta p^2}{w^4 \rho^2} = k_2 \frac{\eta}{w d_{ech} \rho} \cdot \frac{H g}{w^2 d_{ech}} \quad (21),$$

$$\text{or } Eu^2 = k_5 Re^{-1} Fr^{-1}, \quad (22).$$

The fact that earth acceleration can complete fluid flow relation only in the presence of other parameters is now relevant.

For the complete list of variables:

$$// \Delta p, d_{ech}, ; w, H, \rho, \eta, \sigma, g //, \quad (23).$$

the following are obtained:

$$\Delta p^3 = k_6 \frac{w H \rho \eta \sigma g}{d_{ech}^2}, \quad (24),$$

$$\frac{\Delta p^3}{w^6 \rho^3} = k_6 \frac{\eta}{w d_{ech} \rho} \cdot \frac{\sigma}{w^2 d_{ech} \rho} \cdot \frac{H g}{w^2}, \quad (25),$$

$$Eu^3 = k_6 Re^{-1} We^{-1} Fr^{-1}, \quad (26).$$

The relation generated by all considered parameters is in agreement with the bases of the dimensional analysis, the π theorem of Buckingham, which means that a physical phenomenon is described by a product of dimensionless groups at a certain index. Moreover, as compared to the initial theorem, the general dimensional analysis may indicate the form of function, except the numerical factor for the analyzed case:

$$Eu^3 \cdot Re \cdot We \cdot Fr = \text{constant}, \quad (27).$$

The literature [2,3,4] shows in the case of fluid flow over solids, dimensionless relations in the following form:

$$Eu = f(Re), \quad (28), \quad Eu = f(Re, d_{ech}/e), \quad (29), \quad Eu = f(Re, We, Fr), \quad (30), \quad \text{etc...}$$

similarly to those inferred by general modified dimensional analysis, but defining the form of functions f only after the experimental determination of all numerical factors.

In the case of bi or multiphase fluids flow, the problem is very much the same, only the point of view has shifted to determine the drop or ascension speed of particle, this being the main parameter of the process. In fact, we are dealing again with liquid displacement, this time as compared to a mobile point of reference, the particle. In this particular case, the list of variables also include, besides the principal parameter, w , the diameter of the particle, d_{ech} the density difference between phases $\Delta\rho$, fluid viscosity, η , and acceleration, g .

The matrix line of distributed variables can be written as follows:

$$// w, \eta ; d_{ech}, \Delta\rho, g //, \quad (31).$$

We can now notice that the place of some variables was reversed, due to the different phenomenology of processes. The lack of interfacial strength in the line matrix is due to absence of experimental data to quantify the model.

The dimensional matrix and the system of undetermined equations are shown below:

| | w^m | η^n | d_{ech}^p | $\Delta\rho^q$ | g^r |
|---|-------|----------|-------------|----------------|-------|
| L | 1 | -1 | 1 | -3 | 1 |
| M | 0 | 1 | 0 | 1 | 0 |
| T | -1 | -1 | 0 | 0 | -2 |

The system attached to the matrix line becomes as follows:

$$\begin{cases} m - n = p - 3q + r \\ n = q \\ -m - n = -2r \end{cases}$$

and has the solution accepted by GDAT: $n = 1, q = 1; \quad r = 1, m = 1; \quad p = 2;$
with monomial-type relation:

$$w = k_7 \frac{d_{ech}^2 \Delta\rho g}{\eta}, \quad (32).$$

The mathematical transformation of monomial type relation leads to the dimensionless relation:

$$\frac{w d_{ech} \rho}{\eta} = k_7 \frac{d_{ech}^3 \Delta\rho \rho g}{\eta^2}, \quad (33), \quad \text{or} \quad Re = k_7 Ar, \quad (34),$$

Thus, a correlation between Reynolds and Archimedes's criterion is shown as a final relation. The well-known expressions in literature are particularized as follows:

$$1. \text{Re} = \frac{Ar}{18} \quad Ar \leq 36, \quad \text{Stockes's relation, [2,3],}$$

$$2. \text{Re} = \left(\frac{Ar}{13,9} \right)^{5/7} \quad 36 \leq Ar \leq 84\,000, \quad \text{Allen's relation, [3,4],}$$

$$3. \text{Re} = 1,73 \sqrt{Ar} \quad Ar \geq 84\,000, \quad \text{Newton's relation, [3,4],}$$

$$4. \text{Re}_{cr} = \frac{Ar}{1400 + 5,29 \sqrt{Ar}}, \quad \text{Thodes's relation for determination of minimum fluidization speed, [5,6],}$$

$$5. \text{Re}_{pl}^2 = \frac{4 Ar}{3 C_f} \quad \text{Relation for floating speed of some monodispersed particles, [8],}$$

$$6. \text{Re}_{pl} = f(Ar, D/d_{ech}, \beta, \varphi,) \quad \text{Relation for floating speed of some polydispersed irregular particles, [7],}$$

$$7. \text{Re}_{antr} = \frac{Ar}{18 + 0,61 \sqrt{Ar}} \quad \text{Relation for minimum transport speed from exhaust particles of fluidized bed, [6],}$$

$$8. w_{\min} = 8 \cdot 10^{-4} \frac{d_{ech}^2 \Delta \rho g}{\eta}, \quad \text{Rowe's relation for minimum fluidization speed, [7,8],}$$

$$9. w_{\min} = 9,35 \cdot 10^{-3} \frac{d_{ech}^{1,88}}{v_{fluid}^{0,88}} \cdot \left(\frac{\Delta \rho}{\rho_{fluid}} \right)^{0,94}, \quad \text{Leva's relation for minimum fluidization speed of some polydispersed non spherical particles, [7],}$$

$$10. w_{\min} = \frac{1}{200} \cdot \frac{\varepsilon}{\varepsilon - 1} \cdot \frac{d_p^2 \rho_p g}{\eta}; \quad \text{Lewis's relation for minimum fluidization speed of some monodispersed non spherical particles, [7],}$$

$$11. \text{Re} = 0,049 Ar (1 - \varepsilon)^{0,8} \left(\frac{d_M}{d_m} \right)^{0,48} \left(\frac{\rho_f}{\rho_p} \right)^{0,2}, \quad \text{Carpov's relation for fluidization speed of some polydispersed non spherical particles, [8],}$$

$$12. \text{Re}_m = \frac{Ar_M}{150 \cdot \frac{1 - \varepsilon}{\varepsilon} \cdot \left[1 + \sum_{i=1}^{n-1} m_i (d_i - 1) \right]^2 + \sqrt{\frac{1,75}{\varepsilon_0^3}} \left[1 + \sum_{i=1}^{n-1} m_i (d_i - 1) \right] \cdot Ar}, \quad \text{Petrov's relation for fluidization speed of some screening non spherical particles, [8],}$$

13. $Re = 5,1 \cdot 10^{-2} Ar^{0,59} (d/D)^{0,1} (H/D)^{0,25}$, Nicolaev's and Golubev's relation for spouted bed speed of mono-dispersed particles, [8].

We can thus notice a similitude between the relation obtained through application of modified general dimensional analysis and those particularized formulas generated by means of specific experiments. The differences consist in the value of numerical constants. This fact proves the existence of identical phenomenology, differentiated only by strict particularities of the systems which provided us with the experimental data.

To conclude, we can now assert that the method of general dimensional analysis, modified by the introduction of some differentiating criteria between variables, can be used for a global approach of some phenomena which have a common basis phenomenology.

NOTATIONS

L, M, T = the symbols for measurement units for length, mass and time;

a, b, c, d, e, f, h, i, j, m, n, p, q, r = exponents for measurement units;

$$Eu = \frac{\Delta p}{w^2 \rho} \quad \text{Euler number;} \quad Re = \frac{wd\rho}{\eta} \quad \text{Reynolds number;}$$

$$Fr = \frac{w^2}{d_{ech} g} \quad \text{Froude number;} \quad We = \frac{d_{ech} w^2 \rho}{\sigma} \quad \text{Weber number;}$$

$$Ar = \frac{d_{ech}^3 g \rho \Delta \rho}{\eta^2} \quad \text{Archimede number.}$$

REFERENCES

1. C.I. Staicu, *Analiza dimensionala generala*, Ed. Tehnica, Bucuresti, **1975**.
2. L. Literat, *Fenomene de transfer si utilaje in industria chimica*, Ed. UBB, Cluj-Napoca, **1985**, p. 73 - 92.
3. E.A. Bratu, *Operatii unitare in ingineria chimica*, vol I., Ed. Tehnica, Bucuresti, **1985**, p. 31 - 51.
4. R.Z. Tudose, M. Vasiliu, Gh. Cristian, I. Ibanescu, A. Stancu, Lungu M., *Procese, operatii utilaje in industria chimica*, Ed. Did. si Ped., Bucuresti, **1977**, p. 10 - 24.
5. O. Floarea, O. Smigelschi, *Calcul de operatii si utilaje in industria chimica*, Ed. Tehnica, Bucuresti, **1966**, p. 65 - 77.
6. C.F. Pavlov, P.G. Romankov, A.A. Noskov, *Procese si aparate in ingineria chimica*, Ed. Tehnica, Bucuresti, **1981**.
7. Gh. Ivanus, I. Todea, Al. Pop, S. Nicola, Gh. Damian, *Ingineria fluidizarii*, Ed. Tehnica, Bucuresti, **1996**, p. 26 - 31.
8. C. Mihaila, *Procese termodinamice in sisteme gaz-solid si aplicatiile lor in industrie*, Ed. Tehnica, Bucuresti, **1982**, p. 80 - 108.
9. R.Z. Tudose, *Ingineria proceselor fizice din industria chimica*, Ed. Academiei Romane, **2000**, p. 45 - 63.
10. B.R.H. Misca, *Aspecte ale transferului de impuls, caldura si masa la extractia cu fluide*, Teza de doctorat, UBB Cluj-Napoca, **1998**.

ELECTROCHEMICAL BEHAVIOUR OF OLT – 35 LOW CARBON STEEL IN ALKALINE (1M KOH) AQUEOUS SOLUTION

ELEONORA MARIA RUS*, GEORGETA ȚARĂLUNGĂ**, DELIA MARIA CONSTANTIN*

**"Babes-Bolyai" University, Faculty of Chemistry and Chemical Engineering, 11, Arany Janos str., 3400, Cluj-Napoca, Romania*

***University of Agricultural Sciences and Veterinary Medicine, 3-5 Mănăștur Street, 3400 Cluj-Napoca, Romania*

ABSTRACT. Cyclic voltammetry, under rigorously controlled conditions (scan rates, positive and negative reversal potentials, polarizations at definite potentials and times) has been used to obtain details on the electrochemical behaviour of OLT – 35 low carbon steel in 1M KOH (pH 14) open aqueous solution. The formation of anodic layers and their reduction on the steel surface in various experimental conditions were investigated.

INTRODUCTION

Many works using a variety of different analytical techniques and voltammetry measurements have been reported in literature on the chemical and electrochemical properties of iron and iron oxides in various aqueous environments. [1 -6].

The study of electrochemical behavior of an alloy, such as low carbon steel OLT – 35, may give scattered results to those obtained on iron pure metal or monocrystals. Such studies provide relevant information about the corrosion of buried steel pipes or storage tanks in various soils and serve as a rational basis for evaluation of coating performance and determination of controlling parameters [7 -10].

In urban areas, residual wasters, slightly alkaline, containing carbonate, chloride and possibly sulfate ions, may be in contact with underground pipelines, made from mild steel coated with an electrically insulating paint system and cathodically protected. Each ionic species has a different effect on the electrochemical behaviour of mild low carbon steel depending on the ion concentration, potential, pH and temperature.

The corrosion of steel in soil is due to electrochemical oxidation of metal at the anodic sites coupled to the reduction of oxygen at cathodic sites. Despite these processes occur in presence of dissolved oxygen, the most of electrochemical studies of steel pipelines corrosion are done in anaerobic conditions [11 -13].

It was established that when the pipeline steel is under cathodic polarization, electrochemical reactions, such as oxygen or oxide reduction, occurring at a cathodic potential can greatly affect the integrity of the protective coating film at pipeline surface [14]. Disbanding of the protective coatings leads to corrosion of steel pipe.

The cathodic protection level is recommended to be lower (more negative) than $-0.85\text{ V vs Cu/CuSO}_4$, equivalent to -0.78 V vs SCE .

Depending of the soils properties, pipeline coating, anode placement and their geometry, the actual potential of cathodically protected pipeline can vary in a wide range and can easily reach to -1.5 V vs SCE or even lower values. According to Song *et al.* in such conditions the pH in the vicinity of the pipeline may

increase, to a value higher than 13, either or both by oxygen reduction and/or by water reduction [15]. Because the volume of electrolyte in the crevice between disbonded coating and pipeline is obviously small, obtaining such a high pH environment is conceivable.

In such strong alkaline environments the fluctuation of the cathodic protection can make the solid passive iron oxide unstable, and the solid species will dissolve into the ground water as soluble species.

The objective of this research was to investigate the electrochemical behaviour of low carbon steel OLT – 35 in open aqueous alkaline solution (pH = 14) in the range of anodic active potential of iron. The voltammetric characteristics of surface films formed on OLT – 35 were studied.

EXPERIMENTAL

Cyclic voltammetry was used to investigate the electroformation and the electroreduction of various iron compounds on low carbon OLT – 35 steel whose composition is (wt%): C 0.17, Si <0.35, Mn <0.4, P <0.05, S <0.05, Fe 98.98.

The working electrode was a disk of OLT – 35 steel with a surface area of 0.154 cm². The disk was press-fitted into a Teflon holder in order to ensure a reproducible and well-defined surface area. Before each experiment the OLT-35 steel electrode surface was mechanically polished with abrasive paper, thoroughly rinsed with distilled water and cathodically polarized (for 5 minutes i.e.) in the range of hydrogen evolution potential, to provide a reproducible electroreduced steel surface.

The experiments were carried out using a three-compartment glass cell, at room temperature and quiescent solutions. The volume of the used experimental cell was large (~ 0.35 l) so that the concentration of eventually dissolved iron compound in the bulk of the solution could be neglected.

Potentials were measured and referred to in the text with respect to a saturated calomel electrode (SCE) as reference. This was connected to the main compartment of the cell by a salt bridge and a Luggin capillary.

The counter electrode, separated from the main compartment of the cell by a Nafion membrane, was a platinum sheet of 5 cm² in area.

Aqueous solution of 1M KOH (pH 14) was used as electrolyte. The electrolyte solution was prepared from analytical grade reagents using high distilled water.

The cyclic voltammograms were obtained by sweeping the potential linearly in a positive direction from a certain starting negative potential to a maximum, at different sweeping rates and then the direction was reversed.

The measurements were performed with an Autolab PGSTAT 10 system.

RESULTS AND DISCUSSION

First informations about the corrosion system created at OLT – 35 low carbon steel/aqueous 1M KOH solution interface were obtained by measurements of open circuit potential (o.c.p.). In this experiment the freshly polished electrode was submerged in electrolyte and kept until the value of o.c.p. was constant, Fig.1.

In such experiment the system is not disturbed by any external voltage or current source, so that no additional corrosion effects are induced and the measured potential value must be considered as corrosion potential, E_{corr} .

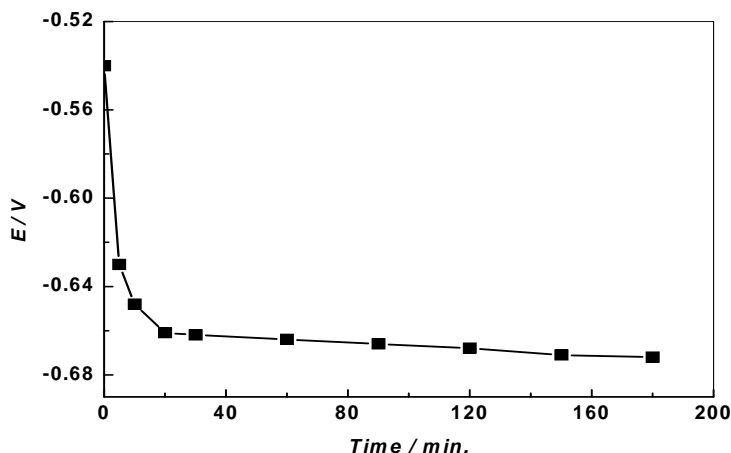


Fig. 1. Open circuit potential against time for OLT – 35 electrode in 1 M KOH solution (pH = 14).

At the beginning, the o.c.p. of the system was -0.542 V but the potential decreased continuously (shifted in negative direction) with the exposure time before to reach, after around 180 minutes, a constant value at about -0.672 V. This negativation of potential in time denotes a relative high corrosion tendency of OLT – 35 steel in our experimental conditions.

Fig. 2 (solid line curve) shows a typical cyclic voltammogram for OLT – 35 steel in 1M KOH open aqueous solutions. Such voltammograms in steady-state could be obtained after a few cycles over the whole potential range. The range of the potential was varied from hydrogen evolution (-1.3 V) to prepasive potential of iron (0.2 V) so that no any oxygen evolution from electrolyte can occur.

The freshly polished electrode was submerged in electrolyte and kept until the change in the o.c.p. was less than $1\text{ mV} / \text{min}$. Starting at o.c.p., the potential of electrode was scanned, at $30\text{ mV} / \text{s}$, to the negative direction until -1.3 V when it was held for 10 min. in order to bring the electrode surface to the reduced metallic state.

The electrode was then cycled between -1.3 V (the hydrogen evolution potential) and 0.1 V (the prepasive potential for our experimental conditions) for 15 times. The 2nd and the 15th cycle were recorded.

The recorded voltammograms (Fig.2.) show that, in our experimental conditions, the first 10 cycles have great influence on the shape or height of the oxidation and reduction peaks.

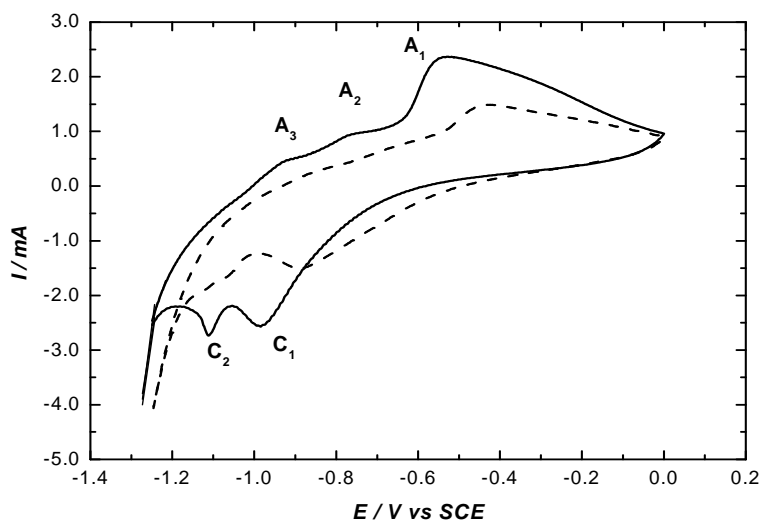


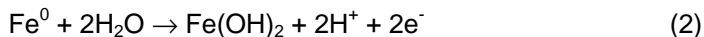
Fig. 2. Cyclic voltammograms of OLT – 35 steel electrode in aqueous 1M KOH (pH 14) open aqueous solution. Scan rate: $v = 30$ mV/s. Key: (----) 2nd cycle and (—) the 15th cycle.

The features of the 15th voltammogram in Fig.2. are similar to those reported by Gervasio *et al.* for a mild steel electrode in aqueous anaerobic 1M KOH solution [14].

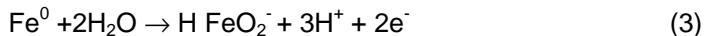
The scan in the positive direction shows only one proeminent peak A_1 at around -0.56 V, which is attributed to the oxidation of $\text{Fe}(\text{OH})_2$ to FeOOH according to the following reaction [16, 17]:



Some oxidation (positive current) waves are visible at approximately -0.76V (A_2) and -0.92 V (A_3). Shallow peaks A_2 and A_3 corresponds to the formation of $\text{Fe}(\text{OH})_2$ from Fe metal (A_2):



and (A_3) to the formation of a ferrous soluble compound (e.g. dihypoferrite):



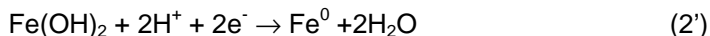
The formation of this dihypoferrite is in agreement with the iron potential – pH diagram (Pourbaix) which predicts that there are several regions where iron exists as soluble species [18]. One of the regions is in strong alkaline solution (pH 14) and near -1.0V potential.

At potentials more positive than 0.1 V the steel surface appeared to be passivated. Other voltammograms (not included in this paper) indicate that although the positive potential was reversed at more high values (0.2 V or 0.3 V) no additional oxidation current would have been see before water is oxidized to molecular oxygen [19].

In the negative direction scan, there are two peaks before hydrogen evolution at -1.3 V. The first cathodic peak C_1 at -0.98 V is due principally to the reduction of FeOOH to $\text{Fe}(\text{OH})_2$ [16, 17]:



The second cathodic peak C_2 , at -1.13V corresponds to the reduction of $\text{Fe}(\text{OH})_2$ to Fe metal:



At the end of the scan in negative direction a large current can be seen at -1.3V. This is associated to water reduction to molecular hydrogen:



We have seen that the oxidation peak A_1 and the reduction peaks C_1 and C_2 , corresponding to the electroformation and to the electroreduction of insoluble iron species, becomes larger with the increase of scans number, but the peaks A_2 and A_3 stayed the same in magnitude.

It seems that in our experimental conditions at pH 14 the dissolved ferrous state (H FeO_2^-) is more stable than solid state ($\text{Fe}(\text{OH})_2$ or Fe) when the electrode potential passes -1.0 V during cycling.

This suggests that one possible route to the disbanding of insulating coating from steel pipelines may due to the dissolution of solid species ($\text{Fe}(\text{OH})_2$, FeOOH or Fe) at the coating/oxide compounds/steel interface during cycling.

The effect of the polarization time (t_{pol}), in the cathodic range potential characteristic for hydrogen evolution, $E_{\text{pol}} = -1.3\text{V}$, just prior to the electrode potential sweep in the anodic direction, was investigated. The recorded voltammograms (Fig.3.) shows that the heights of the oxidation current peak A_1 and the reduction current peaks C_1 and C_2 increases with the polarization time, from $t_{\text{pol}} = 15$ min. to $t_{\text{pol}} = 35$ min., but the current peaks A_2 and A_3 heights are more less dependent of t_{pol} .

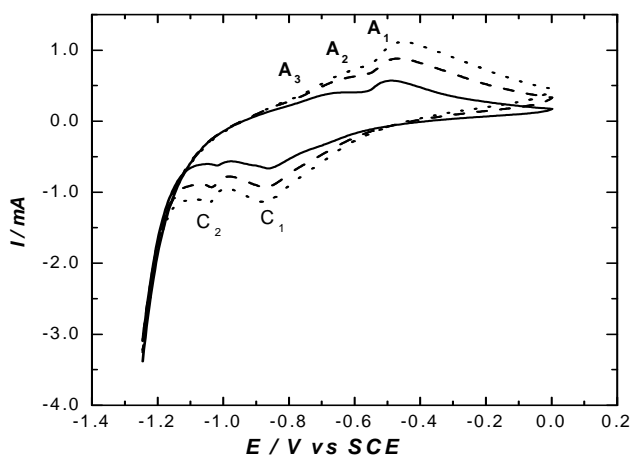


Fig. 3. Effect of polarization time, t_{pol} , at $E_{\text{pol}} = -1.3\text{ V}$ on the voltammograms of OLT – 35 steel electrode in aqueous 1M KOH solution. Scan rate: $v = 30\text{ mV/s}$.

Key: (—) $t_{\text{pol}} = 15\text{ min.}$, (----) $t_{\text{pol}} = 25\text{ min.}$, (...) $t_{\text{pol}} = 35\text{ min.}$

According to Simard *et.al.* this behaviour is more likely related to the adsorption and/or absorption of hydrogen on the electrode surface [20].

Consequently, in the following experiments, prior to each potential scan in the anodic direction, the working electrode was held 35 minutes at -1.3V in order to minimize the influence of hydrogen evolution on oxidation processes. Using this procedure the recorded voltammograms, for the same experimental conditions, were reproducible. Such results indicate that the OLT-35 surface films characteristics are strong function of the cathodic applied potential and polarization time.

Establishment of the sweep-rate dependence of an electrochemical process is of primary importance in determination of reaction mechanism, since it permits the identification of diffusion-controlled processes.

Figure 4 shows the effect of increasing the scan rate, from 10mV/s to 30mV/s , on the voltammograms recorded on OLT-35 low carbon steel/ aqueous 1M KOH solution electrodes. Each voltammogram was taken after the electrode was cycled 15 times and held at -1.3V for 35 min.

For various sweeping rates the form of voltammograms changes slightly. The peaks current height increases with the increase of sweep rates and the peak potentials slightly shift towards more positive values (peak A_1) and towards more negative values, (peaks C_1 and C_2).

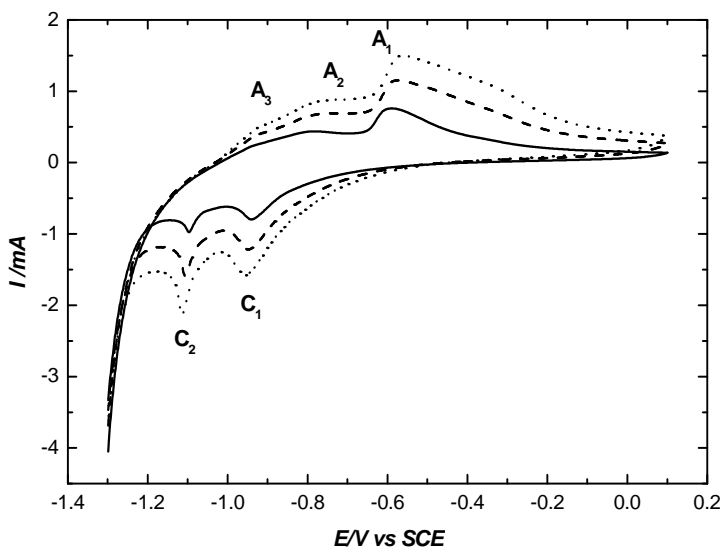


Fig. 4. Effect of scan rates on the voltammograms obtained for OLT – 35 steel electrodes in aqueous 1M KOH ($\text{pH} = 14$) solution. Key: (—) 10 mV/s , (---) 20 mV/s , (...) and 30 mV/s .

This would be consistent with a kinetically limited electrochemical process such as transfer of a species through a passive layer.

In the present experiments, all observed peaks exhibited a linear relationship between the peak current and the square root of the scan rate (Fig.5.).

This suggests that the processes are diffusion rather than activation limited.

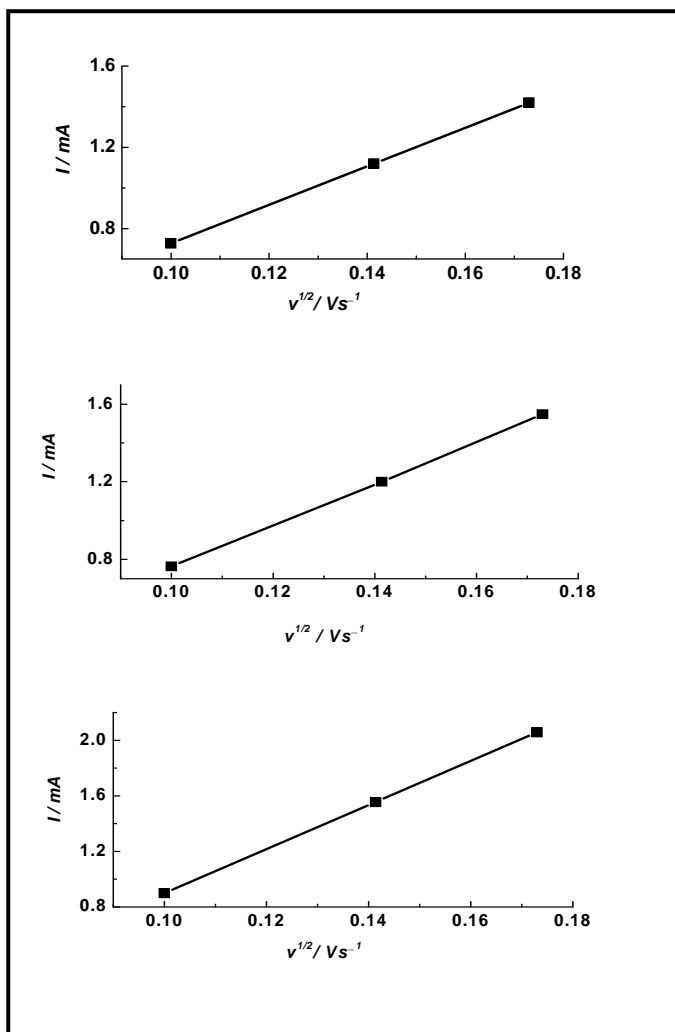


Fig. 5. The peak current vs. (scan rate)^{1/2} relations for: a) the anodic peak A_1 ; b) the cathodic peak C_1 and c) the cathodic peak C_2 .

Correspondence between successive anodic and cathodic processes in a voltammogram can usually be demonstrated by slowly increasing the reversal potential along the anodic sweep.

Voltammograms with an increase in the anodic potential sweep limit ($E_{l,a}$) greater than -0.4V , for the OLT-35 steel electrode in 1M KOH aqueous solutions, are presented in Fig.6.

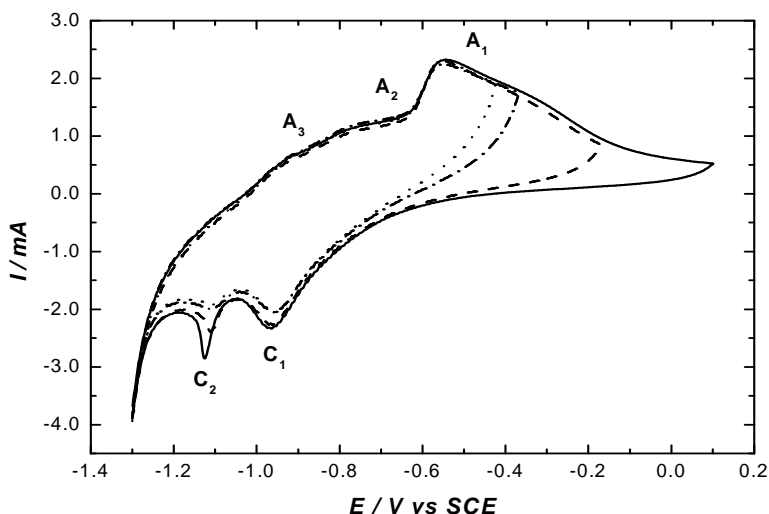


Fig. 6. Cyclic voltammograms of OLT – 35 steel electrode in aqueous 1M KOH (pH = 14) solution recorded for different anodic potential limits, $E_{l,a}$.
Key: (—) 0 V, (---) - 0.16 V, (-.-) - 0.36 V, (...) - 0.42 V; $v = 30$ mV/s.

The potential and the current peak height for oxidation peak A_1 remained unchanged when the anodic potential sweep limit was increased.

The more anodic potential sweep limit, the higher the reduction current peaks C_1 and C_2 .

It seems that this is due to longer time needed to reduce the greater amount of oxides, hydroxides or oxihydroxides formed at electrode surface when the upper anodic potential limit is higher. At higher than 0.2V potential the formation of $\gamma\text{-Fe}_2\text{O}_3$ has been proposed and at lower potentials, the presence of Fe_3O_4 is suggested [19-21].

Simultaneously increase of the cathodic current peaks C_1 and C_2 indicate that the product reduced at C_1 (more positive potential) is at higher oxidation state.

The fact that the changes in both C_1 and C_2 peaks, with increasing of the reversal anodic potential limit, are similar (Fig.6) and the fact that their peak current follows the same trend with regard to scan rate (Fig.5.), suggests that than two peaks represent successive steps which lead to complete reduction of oxide layer formed in above positive going scan.

The potential of both, C_1 and C_2 , reduction peaks shifted in positive direction indicating that the anodic product changed with the increase of anodic potential scan limit.

Our voltammetry results make it clear that the C_1 and C_2 current peaks recorded in all experimental conditions are related to the presence, the amount and the properties of passive formed layer.

CONCLUSIONS

The voltammetry of OLT – 35 low carbon steel in open 1M KOH aqueous solution seems to be similar to that of iron in same conditions. Cyclic voltammetry provide a means for identifying various types of oxidated species formed on the OLT – 35 steel surface and monitoring their stability. The results indicated that the characteristics of OLT – 35 steel surface layers are strong function of the applied potential.

It seems that the rate – determining step, in active dissolution of OLT – 35 steel, in open alkaline aqueous solutions is a diffusion process.

The formation of soluble Fe^{2+} species (HFeO_2^-) during cycling at cathodic potential lower than -1.0V , where this dihypoferrite is stable with respect to iron and insoluble iron species ($\text{Fe}(\text{OH})_2$) was confirmed.

We can say that our results are in agreement to that reported by Song *et al.* [15] according to which in strong alkaline environment in the presence of cathodic protection, temporal fluctuation of the pipelines potential, may cause chemical and possibly structural changes in the surface passive oxide layers. Such changes can lead to an instability of the the coating/steel interface. Voltammetric results suggest that one possible route to disbanding of coating layer from low carbon steel pipelines may be due to the dissolution of solid species at the steel/coating interface.

Thus, an excessive cathodic protection may produce an electrochemical environment in which the coating layer on steel pipelines may disbond.

Although the cyclic voltammetry enables us to accurately identify the changes in the electrode reactions, the method itself does not lead to an intimate study of these processes.

Further experimental works (maybe spectroscopic studies) are required to identification of the surface oxides layers formed under the experimental conditions of the present study.

REFERENCES

1. Y. M. Liou, S. Y. Chiu and C. L. Lee, *J. Appl. Electrochem.*, **1999**, 29, 1977 - 1981.
2. J. A. Bardwell, J. W. Fraser, B. MacDougall and M. J. Graham, *J. Electrochem. Soc.*, **1992**, 139, 366 - 375.
3. R. D. Armstrong, L. Peggs and A. Walsh, *J. Appl. Electrochem.*, **1994**, 24, 1244 - 1253.
4. G. Vatankhah, M. Drogowska, H. Menard and L. Brossard, *J. Appl. Electrochem.*, **1998**, 28, 173 - 183.
5. J. H. Pottgieter, *J. Appl. Electrochem.*, **1996**, 26, 1103 - 1110.
6. R. D. Grimm, A. C. West and D. Landolt, *J. Electrochem. Soc.*, **1992**, 139, 1622 – 1631.
7. I. Song, M. R. Antonio and J. H. Payer, *J. Electrochem. Soc.*, **1992**, 142, 2219 – 2237.
8. M. Drogowska, H. Menard and L. Brossard, *J. Appl. Electrochem.*, **1996**, 26, 217 - 225.
9. M. Drogowska, L. Brossard and H. Menard, *J. Appl. Electrochem.*, **1998**, 28, 491 - 501.
10. M. K. Ravikumar, T. S. Balasubramanian and A. K. Shukla, *J. Appl. Electrochem.*, **1996**, 26, 1111 - 1115.
11. S. Simard, H. Menard and L. Brossard, *J. Appl. Electrochem.*, **1998**, 28, 151- 160.
12. J. A. Bardwell, B. MacDougall and M. J. Graham, *J. Electrochem. Soc.*, **1988**, 135, 413 - 421.
13. J. A. Bardwell, B. MacDougall and G. I. Sproul, *J. Electrochem. Soc.*, **1988**, 136, 1331 - 1342.

14. D. Gervasio, I. Song and J. H. Payer, *J. Appl. Electrochem.*, **1998**, 28, 979 - 992.
15. D. Gervasio, I. Song and J. H. Payer, *J. Appl. Electrochem.*, **1998**, 26, 1045 - 1052.
16. W. Tschinkel, H. Neugebauer and Neckel, *J. Electrochem. Soc.*, **1995**, 142, 2219 - 2231.
17. L. J. Simpson and C. A. Melendres, *J. Electrochem. Soc.*, **1996**, 143, 2146 - 2153.
18. M. Pourbaix, *"Atlas of Electrochemical Equilibria in Aqueous Solution"*, National Association of Corrosion Engineers, Cebelcolor, Brussels, **1974**, 307 – 321.
19. C. Calin, Eleonora Maria Rus, I. Baldea, *Analele Universitatii Oradea, Fascicola Chimie*, **2001**, VIII, 5 – 10.
20. S. Simard, M. Drogowska, H. Menard and L. Brossard, *J. Appl Electrochem.*, **1997**, 27, 317 - 324.
21. Y. T. Chin and B.D. Cahan, *J. Electrochem. Soc.*, **1996**, 139, 2432 - 2443.

ELECTROCHEMICAL POWER SOURCES WITH RbAg_4I_5

GEORGETA ȚARĂLUNGĂ*, CS. BOLLA**, ELEONORA MARIA RUS**,
DELIA MARIA CONSTANTIN**

**University of Agricultural Sciences and Veterinary Medicine,
3-5 Mănăștur Street, 400372 Cluj-Napoca, Romania*

*** "Babes-Bolyai" University, Faculty of Chemistry and Chemical Engineering,
11 Arany Janos Street, 400028 Cluj-Napoca, Romania*

ABSTRACT. A variety of battery power implantable devices are routinely implanted into patients to treat ailments ranging from irregular heartbeat to pain and epilepsy. Solid state batteries are used for the safety of patients, which have a number of very desirable features. The batteries with RbAg_4I_5 solid electrolyte are part of these galvanic cells. The solid electrolyte RbAg_4I_5 belongs to the compounds-group with general formula MAg_4I_5 (where $\text{M}^+ = \text{Rb}^+, \text{K}^+, \text{NH}_4^+$) having an exceptionally high ionic conductivity (about 10^{-1} S/cm) at room temperature.

In this paper we present our method for obtaining of RbAg_4I_5 solid electrolyte and the main characteristics of $\text{Ag}/\text{RbAg}_4\text{I}_5/\text{AgI}_3$ cell. The electrochemical behavior of the batteries with RbAg_4I_5 solid electrolyte was studied through performance curves in two discharge regimes.

INTRODUCTION

The advances in battery technology, electronics and medical knowledge have produced a wide variety of sophisticated implantable devices to treat ailments ranging from irregular heartbeat to pain and epilepsy. Also a great diversity of battery powered external devices are used to administer drugs, treat ailments and monitor bodily functions. Solid state batteries are used for the safety of patients, which have a number of very desirable features such as absence of any possible liquid leakage or gassing and the possibility of operation over a wide temperature range. The batteries with RbAg_4I_5 solid electrolyte are part of these galvanic cells.

The solid electrolyte RbAg_4I_5 belongs to the compounds-group with the general formula MAg_4I_5 (where $\text{M}^+ = \text{Rb}^+, \text{K}^+, \text{NH}_4^+$) having an exceptionally high ionic conductivity (about 10^{-1} S/cm) at room temperature. The structures of these solid electrolytes are not close-packed, but contain two- or three networks of passageways intercalated in crystalline structures.

According to the literature data [1 – 4], the crystallographic structure of RbAg_4I_5 was determined by X-ray diffraction. There are three crystalline modifications of RbAg_4I_5 , labeled as the α , β and γ phases in the decreasing order of their transformation temperature. The α form has a cubic crystal lattice of $\text{P4}_1 32 (\text{O}^7)$ or $\text{P4}_3 32 (\text{O}^6)$ symmetry, β form has a rhombohedral crystal lattice of $\text{R } 32 (\text{D}_3^7)$ symmetry and γ modification has a hexagonal structure of lower $\text{P } 321 (\text{D}_3^2)$ symmetry. The high conductivity is due to a combination of a high concentration of mobile ions and a low activation energy for ionic motions from site to site. For these materials the silver ion is the mobile specie and its transport into the lattice takes place by a defect mechanism.

EXPERIMENTAL DATA

The solid electrolyte RbAg_4I_5 was prepared through an original method. RbAg_4I_5 samples were obtained by isothermal crystallization (at 55°C) from an acetone solution containing a mixture of RbI and AgI in the molar ratio 1:2. RbAg_4I_5 was obtained but impurified with Rb_2AgI_3 which favours the decomposition of the desired substance. To prevent that, AgI was added to the acetone solution in small portions until saturation. Through gravimetric and chemical analyses, it was established that the prepared powder is RbAg_4I_5 having a 98.894% purity. The structural characterization of the prepared RbAg_4I_5 was performed by X-ray diffraction X-ray diffractograms were obtained with a DRON 3 powder diffractometer, with a Cu-cathode, using k_α radiation ($\lambda = 1.57051\text{\AA}$).

Two types (I- and II-type) of $\text{Ag}/\text{RbAg}_4\text{I}_5/\text{RbI}_3$ button cells with 8 mm diameter were realized with the prepared RbAg_4I_5 solid electrolyte. The cathodes for both types of batteries were performed from a mixture of RbI_3 (87.30%), graphite (6.75%) and RbAg_4I_5 (5.95%), which was pressed. The anode for the I-type cell was an amalgamated silver disk of 0.02 mm thickness and for II-type cell a mixture of Ag powder (88.00%), graphite (8.00%) and RbAg_4I_5 (12.00%), which was pressed. The cells were assembled by pressing their components (anode, solid electrolyte and cathode) at 1700 kgf/cm^2 for 20 minutes [5-8].

RESULTS AND DISCUSSION

X-ray diffraction pattern of the obtained powder shows that only specific diffraction lines of α - RbAg_4I_5 solid electrolyte are present (Fig.1).

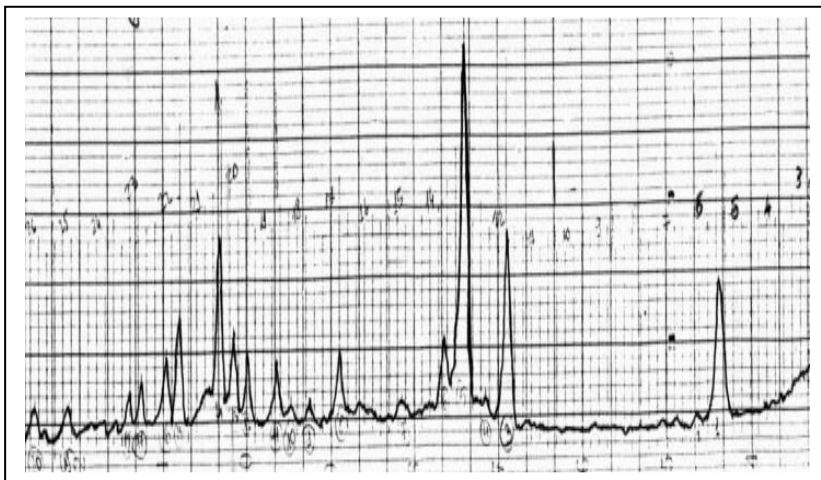


Fig.1. X-ray diffraction pattern of α - RbAg_4I_5

The values of e.m.f. for I-type cells were situated in the range 590-600 mV and for II-type were 650-660 mV. The electrochemical behavior of RbAg_4I_5 solid state cells was investigated through performance curves under constant load and galvanostatic regime.

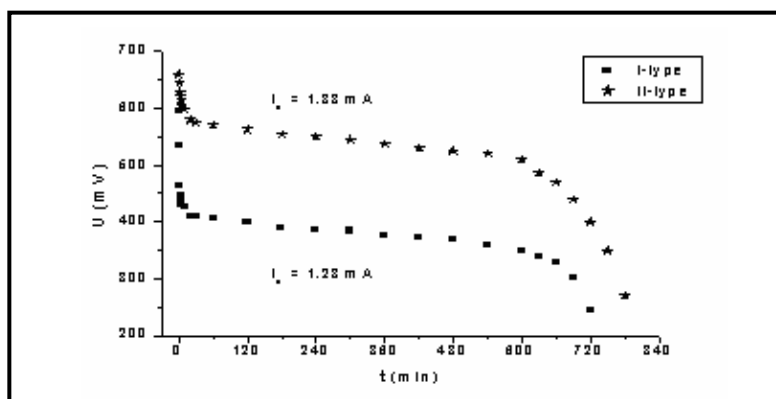


Fig.2. Discharge curves of I-type and II-type cells under $R=100\Omega$

From Fig.2, where the discharge curves of I-type and II-type cells under constant resistance ($R=100\Omega$) are shown, it can be seen that the II-type cell has higher characteristics than the I-type battery. Thus the discharge plateau of II-type was situated in the domain 525-575 mV, whereas for I-type in range 350-400 mV. The average discharge intensity was of 1.33mA for II-type and 1.28mA for I-type cell.

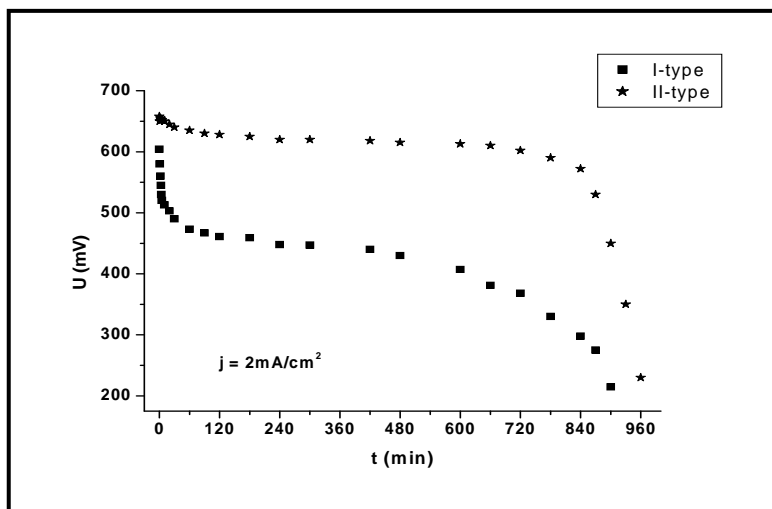


Fig.3. Discharge curves of cells at $i=2\text{mA/cm}^2$

The batteries were discharged at two current densities: $i=2\text{mA/cm}^2$ (Fig.3) and $i=0.2\text{mA/cm}^2$ (Fig.4) in galvanostatic regime. From the discharge curves it can be ascertained that, at lower current density (0.2mA/cm^2), the discharge plateaus have higher values for I-type cell, close to those of II-type cell. At the current density of 0.2mA/cm^2 , the total yielded energy was of 10.20mWh for I-type cell and 11.89mWh for II-type cell.

The electrochemical characteristics of $\text{Ag/RbAg}_4\text{I}_5/\text{RbI}_3$ cells are presented in Table 1. The mass capacities (C_g), the energy densities (W_g), and the utilization coefficients (u) of active material (silver) were calculated from the experimental data.

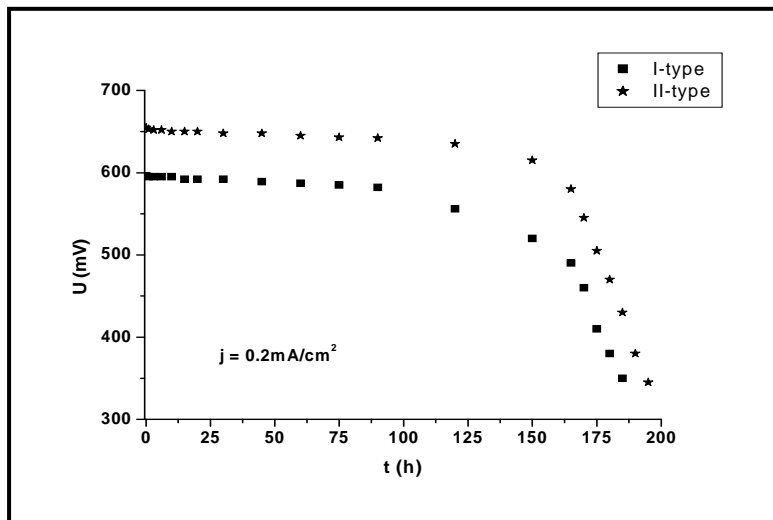


Fig.4. Discharge curves of cells at $i = 0.2 \text{ mA/cm}^2$

Table 1.

The electrochemical characteristics of batteries with RbAg_4I_5 solid electrolyte

| Type cell | Mass [g] | Discharge regime | i [mA/cm^2] | C_g [Ah/kg] | W_g [Wh/kg] | u [%] |
|-----------|----------|------------------------|--------------------------|--------------------------|--------------------------|---------|
| I | 1.096 | Load $R=100 \Omega$ | 2.52 | 13.80 | 5.92 | 55.2 |
| II | 1.037 | | 2.63 | 16.49 | 9.79 | 66.0 |
| I | 0.995 | galvanostatic | 2 | 15.07 | 6.22 | 62.8 |
| II | 1.053 | | | 15.20 | 9.00 | 63.3 |
| I | 0.915 | galvanostatic | 0.2 | 20.22 | 11.15 | 84.3 |
| II | 0.954 | | | 20.44 | 12.46 | 85.2 |

As it can be seen from Table 1, all calculated parameters are better for II-type cells than for I-type cells. The mass capacities and energy densities depend on the discharge regime. They are higher under galvanostatic regime at lower current densities (0.2 mA/cm^2).

CONCLUSIONS

On the basis of the experimental data it can be conclude that the method proposed by authors is simple and allows the obtaining of RbAg_4I_5 solid electrolyte in a pure state. The $\alpha\text{-RbAg}_4\text{I}_5$ form is the most stable crystallographic modification and presents a high ionic conductivity.

From the obtained results it can be establish that Ag/RbAg₄I₅/RbI₃ batteries present good electrochemical characteristics for usage in medical devices such as cardiac pacemaker.

REFERENCES

1. J.N. Bradley, P.D. Greene, *Trans. Faraday Soc.*, **1967**, 63, 424-429.
2. K. Funke, *Ber. Bunsenges. Phys. Chem.* **1989**, 93, 1197-1201.
3. C.F. Holmes, *The Electrochemical Society-Interface*, **1999**, 8, 32-34.
4. C.A. Vincent, F. Bonino, M. Lazzari, B. Scrosati, "Modern Batteries", Chap.7, edited by Edward Arnold (Publishers) Ltd., London, 1984.
5. Cs.C. Bolla, Georgeta Tarălungă, A.Borbely-Keri, L.D. Bobos, Silvia Avram, L.Oniciu, „Batteries for Portable and Electric Vehicle Applications”, A. Landgrebe Ed., The Electrochemical Society Inc. Pennington, N.J. USA, 1997, 518-523.
6. Cs. Bolla, Ildiko Szekely, A. Borbely-Keri, L. Oniciu, Georgeta Tarălungă, *Producerea, Transportul si Utilizarea Energiei*, vol. XIV, **1995**, 101-105.
7. Cs. C Bolla, Ph. D. Thesis *Electroliti solizi și aprotici pentru pile galvanice neconvenționale*, "Babeș-Bolyai" University, Cluj-Napoca, 2001.
8. Georgeta Taralunga, Eleonora Maria Rus, *Romanian J. Biophys.*, **2002**, 12, (3-4), 97-101.

MODELING AND SIMULATION OF THE CARBONATION PROCESS OF AMMONIACAL BRINE USING CHEMCAD

CALIN CORMOS, ANA-MARIA CORMOS, SERBAN AGACHI

*Babes – Bolyai University, Faculty of Chemistry and Chemical Engineering,
11 Arany Janos Street, RO-400028, Cluj – Napoca, Romania, Tel: +40264593833,
Fax: +40264590818, E-mail: cormos@chem.ubbcluj.ro, cani@chem.ubbcluj.ro,
sagachi@chem.ubbcluj.ro*

ABSTRACT. In this paper the model and the simulation results for carbonation process of ammoniacal brine solution have been presented. Carbonation process of ammoniacal sodium chloride solution (brine) is used to obtain sodium bicarbonate and sodium carbonate in soda ash plants (according to Solvay process).

The carbonation process of ammoniacal sodium chloride solution is done using tray absorption columns, typically in a three columns sequence. The first absorption column is used to saturate the ammoniacal brine with carbon dioxide. The second column is a scrubbing unit used to recover residual carbon dioxide from the gaseous effluent coming from first and third columns. In the third column, the final saturation of the liquid phase with carbon dioxide and the precipitation of sodium bicarbonate take place.

The carbonation process of ammoniacal sodium chloride solution is a complex process because of chemical reactions that involve the species present in the liquid phase. Modeling and simulation of the carbonation process of ammoniacal sodium chloride solution and precipitation of sodium bicarbonate were done using ChemCAD software package.

The evolutions of the process parameters were studied during the carbonation process. The model and the simulation results proved to be a reliable tool for analyzing the carbonation and precipitation processes and can be used to improve the real plant operation.

1. INTRODUCTION

Sodium carbonate is a common inorganic industrial chemical, also known as soda ash (Na_2CO_3). It is widely used in the manufacture of glass, chemicals, such as sodium silicates and sodium phosphates, the pulp and paper industries, the manufacture of detergents and for the treatment of water.

The synthesis process of soda ash (sodium carbonate) using Solvay process is done starting from sodium chloride, limestone, coke and ammonia as raw materials [1, 2, 3].

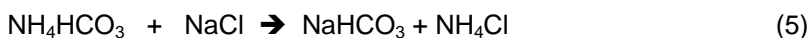
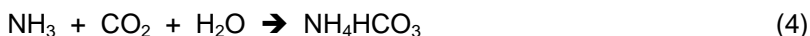
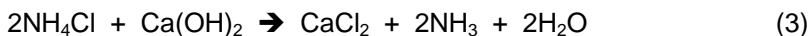
The natural sodium chloride solution (brine) is extracted from soil and purified (removal of solid impurities by filtration and removal of calcium and magnesium ions by precipitation).

Into the purified sodium chloride solution, ammonia is absorbed. After ammonia absorption, the solution is carbonated with gaseous carbon dioxide coming from two main sources: thermal decomposition of the limestone and sodium bicarbonate calcination process.

After carbonation of ammoniacal brine, a suspension of sodium bicarbonate is obtained. Sodium bicarbonate is filtered and the residual liquid phase is treated with calcium hydroxide solution (slaked lime) in order to recover the ammonia from ammonium salts (ammonium chloride, carbonate, bicarbonate etc.). The recovered ammonia is recycled into the process at absorption stage into the sodium chloride solution (brine).

Sodium bicarbonate resulted after filtration is washed, dried and calcined in order to obtain sodium carbonate (soda ash).

The main chemical reactions involved in sodium carbonate (soda ash) synthesis are presented below [2]:



The carbonation process is done using tray absorption columns, typically in a three columns sequence. The first absorption column is used to saturate the ammoniacal brine with carbon dioxide coming from limestone decomposition process (35 – 40 % CO_2 mole fractions).

The second column is a scrubbing unit used to recover residual carbon dioxide from the gaseous effluent coming from the first and the third columns (5 – 10 % CO_2 mole fractions).

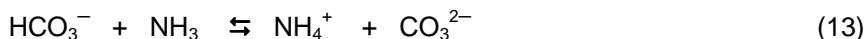
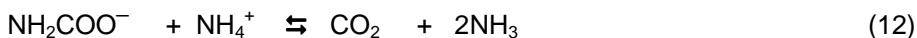
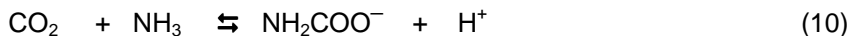
The third absorption column has two gaseous inlets: one situated at the bottom of the column and one situated at the middle of the column. The bottom inlet gas is coming from sodium bicarbonate calcination process (60 – 70 % CO_2 mole fractions). The middle inlet gas is coming from the limestone decomposition process (35 – 40 % CO_2 mole fractions). In the third column the final saturation of the liquid phase with carbon dioxide and the precipitation of sodium bicarbonate take place.

2. MODELING AND SIMULATION OF THE PROCESS

The carbonation process of ammoniacal sodium chloride solution is a complex process because of the following factors: presence of a three phase system (gas – liquid – solid), chemical species present in the liquid phase, chemical reactions that take place, the carbonation process is exothermic, precipitation of sodium bicarbonate that affects the heat transfer coefficients etc.

Most of the authors agreed with the following description of the chemical reactions that take place during the carbonation process of ammoniacal brine and the precipitation process of sodium bicarbonate [1, 5, 6]:





The parameters used for modeling and simulation of the carbonation process of ammoniacal sodium chloride solution (brine) are presented in the tables 1, 2 and 3.

Table 1.

The properties of the inlet gaseous streams

| Parameter | Unit | First column - bottom - | Third column - bottom - | Third column - middle - |
|------------------|----------|----------------------------|----------------------------|----------------------------|
| Temperature | [°C] | 30 | 30 | 30 |
| Pressure | [bar] | 2.6 | 2.8 | 1.5 |
| CO ₂ | [mole %] | 37.3 | 68 | 40 |
| CO | [mole %] | 0.6 | 0.2 | 0.5 |
| O ₂ | [mole %] | 2 | 0.2 | 0.5 |
| N ₂ | [mole %] | 58.6 | 30.5 | 58 |
| H ₂ O | [mole %] | 1.5 | 1 | 0.5 |
| NH ₃ | [mole %] | 0 | 0.1 | 0.5 |
| Flow | [kg/h] | 1033 | 1420 | 760 |

Table 2.

The properties of the inlet liquid stream (ammoniacal brine)

| Parameter | Unit | First column |
|------------------|----------|--------------|
| Temperature | [°C] | 30 |
| Pressure | [bar] | 1 |
| NaCl | [mass %] | 22.7 |
| NH ₃ | [mass %] | 7.5 |
| H ₂ O | [mass %] | 69.8 |
| Flow | [kg/h] | 11460 |

Table 3.

The parameters of the absorption columns

| Parameter | Column 1 | Column 2 | Column 3 |
|-----------------------------|-------------------------|----------|---------------------------|
| No. of stage | 35 | 10 | 35 |
| Top pressure | 1 bar | 1 bar | 1 bar |
| Feed tray for liquid stream | 1 | 1 | 1 |
| Feed tray for gas stream | 35 | 10 | 25 35 |
| Cooling duty | 2 * 10 ⁷ J/h | 0 | 1.9 * 10 ⁹ J/h |

The modeling and simulation of the carbonation process of ammoniacal brine, precipitation and filtration of sodium bicarbonate were done using ChemCAD (version 5.1.3) software package. As thermodynamic option used for simulation of the carbonation process, the electrolyte package was used [6, 7].

The main window of the application is presented in the figure 1.

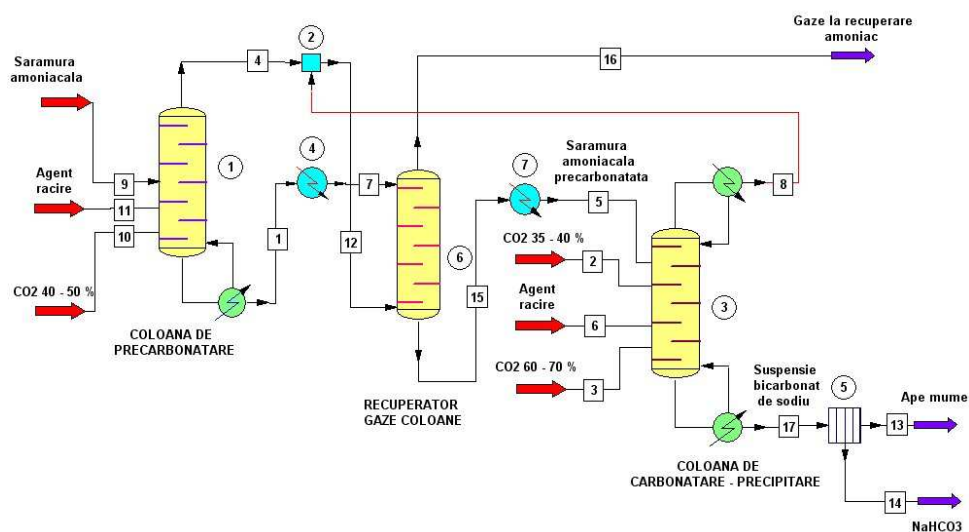


Figure 1. Simulation of the carbonation process using ChemCAD

3. RESULTS AND DISCUSSIONS

In the first column, the ammoniacal brine is saturated with carbon dioxide coming from thermal limestone decomposition process.

The variation of total vapor flow, total liquid flow and temperature for the first absorption column are presented in the figures 2, 3 and 4.

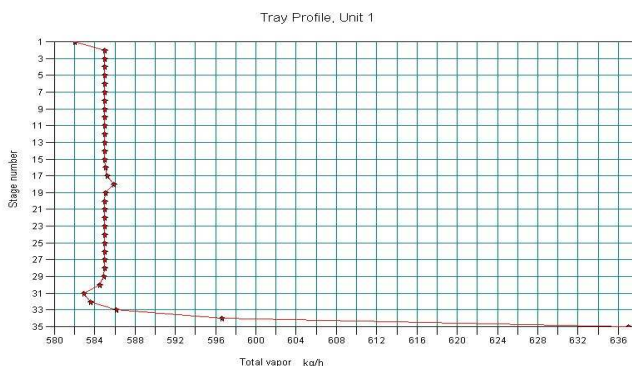


Figure 2. Variation of the total vapor flow for the first column

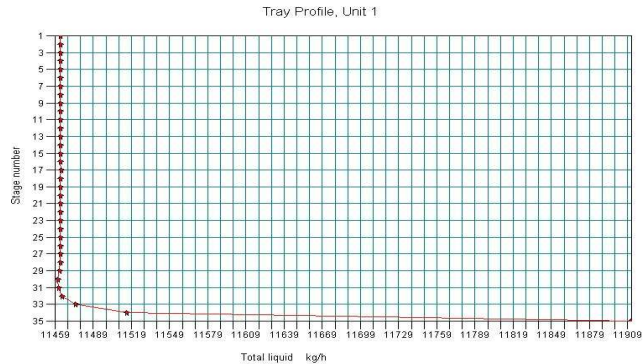


Figure 3. Variation of the total liquid flow for the first column

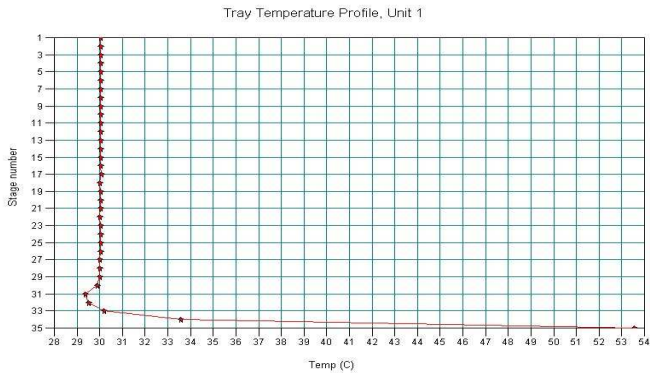


Figure 4. Variation of the temperature for the first column

The variation of total vapor flow, total liquid flow and temperature for the second column (scrubbing unit) are presented in the figures 5, 6 and 7.

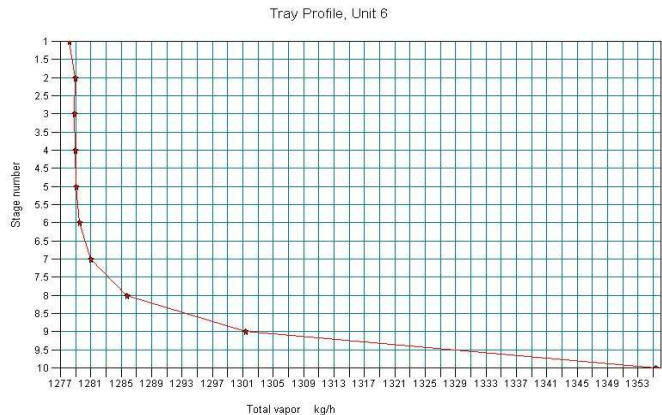


Figure 5. Variation of the total vapor flow for the second column (scrubber)

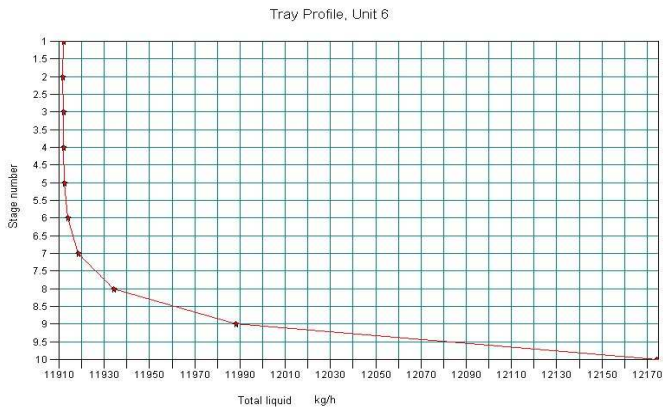


Figure 6. Variation of the total liquid flow for the second column (scrubber)

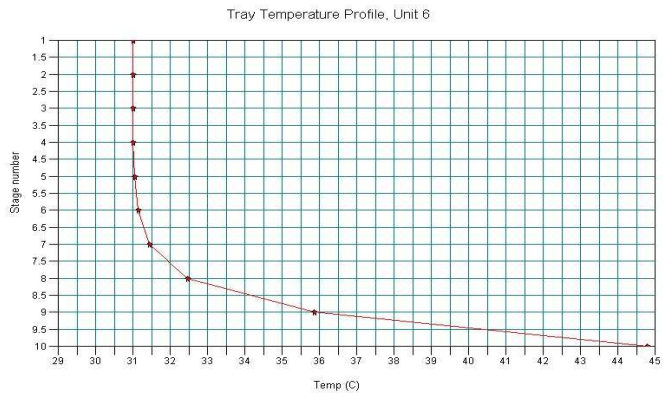


Figure 7. Variation of the temperature for the second column (scrubber)

The variation of total vapor flow, total liquid flow and temperature for the third column are presented in the figures 8, 9 and 10.

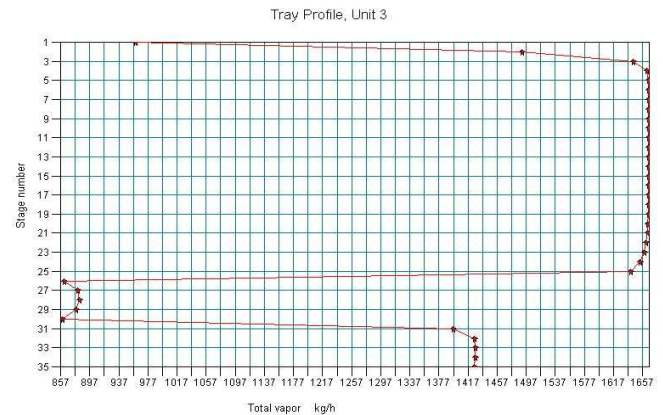


Figure 8. Variation of the total vapor flow for the third column

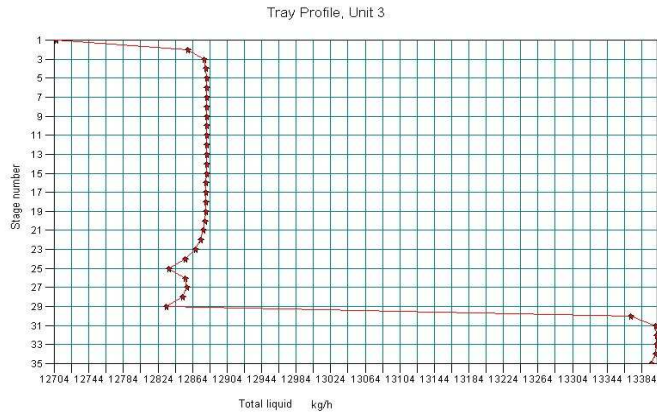


Figure 9. Variation of the total liquid flow for the third column

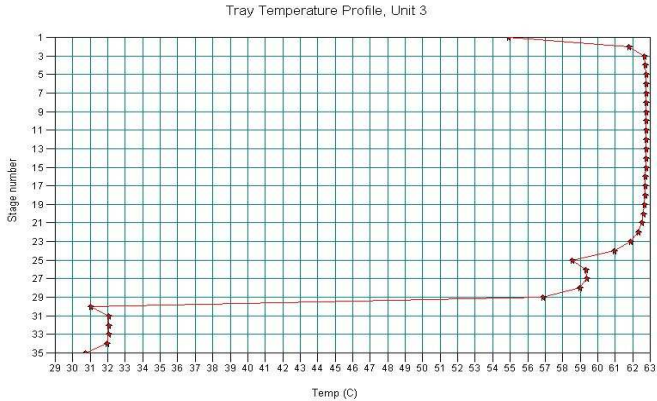


Figure 10. Variation of the temperature for the third column

The calculated properties of the output liquid streams resulted from the simulation of the carbonation columns are presented in the table 4.

Table 4.

The properties of the column liquid streams (simulation results)

| Parameter | Unit | First column | Second column | Third column |
|------------------------------|----------|--------------|---------------|--------------|
| Temperature | [°C] | 53.5 | 44.8 | 30.7 |
| Pressure | [bar] | 1 | 1 | 1 |
| H ₂ O | [mass %] | 63.8 | 63 | 53.86 |
| NH ₃ | [mass %] | 1.4 | 1.07 | 0.06 |
| NH ₄ OH | [mass %] | 5.29 | 4.5 | 0.22 |
| NaHCO ₃ | [mass %] | 0 | 0 | 15.66 |
| Na ⁺ | [mass %] | 8.6 | 8.4 | 3.34 |
| NH ₄ ⁺ | [mass %] | 2 | 2.56 | 6.1 |
| Cl ⁻ | [mass %] | 13.25 | 12.95 | 11.77 |

| Parameter | Unit | First column | Second column | Third column |
|----------------------------------|----------|----------------------|----------------------|-----------------------|
| OH ⁻ | [mass %] | 0.00025 | 0.00012 | 0.0000023 |
| H ⁺ | [mass %] | $2.3 \cdot 10^{-12}$ | $2.2 \cdot 10^{-12}$ | $5.49 \cdot 10^{-11}$ |
| HCO ₃ ⁻ | [mass %] | 1.15 | 1.56 | 8.19 |
| CO ₃ ²⁻ | [mass %] | 1.01 | 1.18 | 0.16 |
| NH ₂ COO ⁻ | [mass %] | 3.5 | 4.78 | 0.71 |
| Flow | [kg/h] | 11911 | 12175 | 13395 |

The calculated properties of output gaseous streams resulted from the simulation of the carbonation columns are presented in the table 5.

Table 5.

The properties of the column gaseous streams (simulation results)

| Parameter | Unit | First column | Second column | Third column |
|------------------|----------|--------------|---------------|--------------|
| Temperature | [°C] | 30 | 31 | 55 |
| Pressure | [bar] | 1 | 1 | 1 |
| CO ₂ | [mole %] | 2.15 | 0.09 | 10.95 |
| CO | [mole %] | 0.8 | 0.77 | 0.53 |
| O ₂ | [mole %] | 2.83 | 1.72 | 0.55 |
| N ₂ | [mole %] | 81.04 | 89.09 | 69.93 |
| H ₂ O | [mole %] | 2.88 | 3.22 | 11.55 |
| NH ₃ | [mole %] | 10.43 | 5.11 | 6.49 |
| Flow | [kg/h] | 582 | 1278 | 960 |

The suspension of sodium bicarbonate resulted at the bottom of the third column is filtrated on a rotary drum filter and 2918 kg/h wet product is obtained. The wet product obtained after filtration contains 2100 kg/h sodium bicarbonate.

The overall yield of the carbonation process of ammoniacal sodium chloride solution (transformation of sodium chloride into sodium bicarbonate) is 72 %.

The simulation results presented above were compared with data collected from real plant operation [1, 3, 4]. Regarding the liquid streams compositions, data collected from a real plant operation are presented in the table 6.

Table 6.

The properties of the column liquid streams (real plant operation)

| Parameter | Unit | First column | Second column | Third column |
|---|----------|--------------|---------------|--------------|
| Temperature | [°C] | 40 – 55 | 35 – 45 | 30 – 40 |
| Pressure | [bar] | 1 | 1 | 1 |
| H ₂ O | [mass %] | 60 – 65 | 60 – 65 | 50 – 55 |
| NH ₄ OH | [mass %] | 4 – 7 | 3 – 6 | 0 – 0.5 |
| NH ₄ HCO ₃ | [mass %] | 0 | 0 | 6 – 7 |
| NaHCO ₃ | [mass %] | 0 | 0 | 15 – 22 |
| NaCl | [mass %] | 15 – 22 | 15 – 22 | 3 – 5 |
| NH ₄ Cl | [mass %] | 0 | 0 | 12 – 15 |
| Na ₂ CO ₃ | [mass %] | 0 – 0.5 | 0 – 0.5 | 0 |
| (NH ₄) ₂ CO ₃ | [mass %] | 10 – 15 | 10 – 15 | 0 |

Regarding the gaseous streams compositions, data collected from a real plant operation are presented in the table 7.

Table 7.

The properties of the column gaseous streams (real plant operation)

| Parameter | Unit | First column | Second column | Third column |
|------------------|----------|--------------|---------------|--------------|
| Temperature | [°C] | 30 – 40 | 30 – 40 | 45 – 55 |
| Pressure | [bar] | 1 – 1.2 | 1 – 1.1 | 1 – 1.2 |
| CO ₂ | [mole %] | 2 – 5 | 1 – 3 | 8 – 12 |
| N ₂ | [mole %] | 79 – 85 | 80 – 90 | 65 – 72 |
| H ₂ O | [mole %] | 2 – 5 | 2 – 5 | 10 – 15 |
| NH ₃ | [mole %] | 5 – 10 | 5 – 12 | 5 – 10 |

In a real plant, the overall carbonation yield of ammoniacal brine (transformation of sodium chloride into sodium bicarbonate) is 72 – 75 %.

From the comparison, one can observe a close similarity between simulation results and data collected from a real plant. This fact validates the application developed for simulation of the process and proves the utility of the model in analyzing and optimization of the real plant operation.

4. CONCLUSIONS

Modeling and simulation of the carbonation process of ammoniacal sodium chloride solution (brine) was done using ChemCAD software package (version 5.1.3).

The carbonation process of ammoniacal brine and precipitation of sodium bicarbonate were done in three absorption columns. The first absorption column is a precarbonation column and is used to saturate the liquid phase with carbon dioxide, the second column is a scrubbing unit used to recover the remaining carbon dioxide from the other two columns and the third column is used to complete the carbonation process and to precipitate sodium bicarbonate from the liquid phase.

The evolutions of the process parameters (liquid and gaseous flows, composition of the streams, temperatures) were studied during the carbonation process of ammoniacal brine. The simulation results were compared with real plant operation data in order to validate the application developed for the carbonation process.

The mathematical model and the simulation results proved to be a reliable tool for analyzing and optimizing the real plant operation of the carbonation process of ammoniacal sodium chloride solution used in soda ash manufacture according to Solvay technology.

REFERENCES

- 1 Filipescu L., Tehnologia produselor sodice si clorosodice, vol. 1, Editura Tehnica, Bucuresti, 1983, page 88 – 120
- 2 Calistru C., Leonte C., Tehnologia substantelor anorganice, Editura Didactica si Pedagogica, Bucuresti, 1972
- 3 Petcu I., Procesul de carbonatare in fabricatia sodei, Revista de Chimie, nr. 9, 1971, page 541 – 549

- 4 Ritter S., Optimizarea bilanturilor de masa in vederea urmaririi operative a productiei, Simpozionul de Informatica si Conducere, Cluj – Napoca, 1975
- 5 Ritter S., Analiza comparativa a doua metode de elaborare a bilanturilor de masa pentru procesul global de carbonatare din tehnologia sodei, Revista de Chimie, nr. 4, 1977, page 348 – 352
- 6 Ritter S., Calistru C., Analiza procesului de carbonatare a saramurii amoniacale prin simularea acestuia cu ajutorul calculatorului electronic digital, Revista de Chimie, nr. 3, 1978, page 240 – 267
- 7 Cormos C., Modelarea matematica si simularea sintezei pantotenatului de calciu racemic, Teza de doctorat, Cluj – Napoca, 2004

MODELING AND SIMULATION OF THE SCRUBBING UNIT WASTE INCINERATION PLANT

ANA-MARIA CORMOS¹, CALIN CORMOS¹, ANTON FRIEDL²,
SERBAN AGACHI¹

¹ Babes – Bolyai University, Faculty of Chemistry and Chemical Engineering, 11 Arany Janos Street,
RO-400028, Cluj-Napoca, Romania, Tel: +40264593833, Fax: +40264590818,
E-mail: cani@chem.ubbcluj.ro, cormos@chem.ubbcluj.ro, sagachi@chem.ubbcluj.ro

² Vienna University of Technology, Institute of Chemical Engineering, Fuel Technology and
Environmental Technology, Getreidemarkt 9/159, 1060 Vienna, Austria, Tel: +43158801/15920,
Fax: +43158801/15999, E-mail: afriedl@mail.zserv.tuwine.ac.at

ABSTRACT. In many incineration processes, especially in waste incineration plants, the resulting flue gas contains acid components such as sulfur dioxide (SO₂) and hydrogen chloride (HCl) that have to be removed to meet environmental standards.

A scrubbing with alkaline solution (sodium hydroxide or calcium hydroxide) is used as absorption liquor to reduce the content of HCl and SO₂ of the flue gas coming from waste incineration plants.

The absorption process is done in two absorption columns. In the first column the hydrochloric acid (HCl) content of flue gas is reduced at pH value of 1. Second absorption column uses a pH of 8 to reduce sulfur dioxide (SO₂). Simulation of the Scrubbing Unit Waste Incineration Plant was done using ChemCAD software package.

The evolutions of the process parameters were studied during the scrubbing process. The model and the simulation results proved to be a reliable tool for analyzing the process of removing HCl and SO₂ from gaseous emissions coming from waste incineration plants.

1. INTRODUCTION

Because of the passage of the Clean Air Act Amendments in 1990, many industrial processes must reduce acid gases emissions. In many incineration processes, especially in waste incineration, the resulting flue gas contains acid components such as sulfur dioxide (SO₂), hydrogen chloride (HCl), hydrogen fluoride (HF), sulfur trioxide (SO₃) and nitrous oxides (NO_x) that have to be removed to meet environmental standards.

In order to meet legal limits, it is necessary to reduce the content of acid components (especially HCl and SO₂) of the flue gas coming from waste incineration plants.

The removal of the toxic acid gases is performed through reactions with alkaline sorbents (sodium hydroxide or calcium hydroxide) in wet, semi-dry, and dry processes [1, 2].

Flue gas cleaning is normally done in several steps. Dust and particulates are removed first in cyclones, filters or electrostatic precipitators. Gaseous pollutants such as hydrochloric acid (HCl) or sulfur dioxide (SO₂) are removed in spray towers, scrubbers, where the gas is sprayed counter-current with a liquid.

A typical effect in scrubbing processes is the variations of scrubber liquid pH when the control system fails to respond in an appropriate way, variations that affect the absorption of pollutants from the flue gas. Scrubber liquid pH is thus an important aspect in flue gas cleaning.

2. MODELING AND SIMULATION OF THE SCRUBBING PROCESS

A scrubbing process with alkaline solution (calcium hydroxide) is used as absorption liquor to reduce the content of hydrochloric acid (HCl), hydrofluoric acid (HF) and sulfur dioxide (SO₂) from gaseous emissions coming from waste incineration plants. The absorption process of acid gases is done in two columns.

In the first scrubbing unit, the saturated flue gas is contacted with calcium hydroxide solution at sour conditions (pH~1). In this column, the neutralization processes of hydrochloric acid and hydrofluoric acid take place. Hydrochloric acid (HCl) and hydrofluoric acid (HF) are removed in the shape of its ions, respectively the corresponding calcium salts.

In the second scrubbing unit at pH~8, sulfur dioxide (SO₂) from waste gases is removed. In this absorption column, sulfur dioxide is neutralized forming calcium sulfite and calcium bisulfite.

Both scrubbers are supplied with pump-around (in order to use efficiently the absorption liquor). The flow ratio waste water 1: recycled is 0.9:0.1 for the first scrubber and flow ratio waste water 2: recycled is 0.9:0.1 for the second scrubber (see figure 1).

The acid gas components from waste gaseous emissions coming from incineration plant are absorbed in the alkaline calcium hydroxide solution to form salts according to the following chemical reactions:



The temperature, pressure, composition and mass flow of flue gas coming from waste incineration plants are presented in the table 1 [3].

Table 1.
The composition of flue gas

| | | |
|------------------|--------|----------|
| Temperature | [°C] | 52 |
| Pressure | [atm] | 1 |
| CO ₂ | [wt%] | 14.4894 |
| CO | [wt%] | 0.0033 |
| O ₂ | [wt%] | 8.7586 |
| N ₂ | [wt%] | 70.0324 |
| H ₂ O | [wt%] | 6.7484 |
| SO ₂ | [wt%] | 0.1247 |
| SO ₃ | [wt%] | 0.0002 |
| NO ₂ | [wt%] | 0.0416 |
| HCl | [wt%] | 0.0696 |
| HF | [wt%] | 0.0017 |
| Flow | [kg/h] | 120816.3 |

The modeling and simulation of the scrubbing unit waste incineration plant were done using ChemCAD (version 5.1.3) software package. As thermodynamic option used for simulation of the plant, the electrolyte package was used [4].

The main window of the application for wet flue gas purification using calcium hydroxide as absorption liquor is presented in the figure 1.

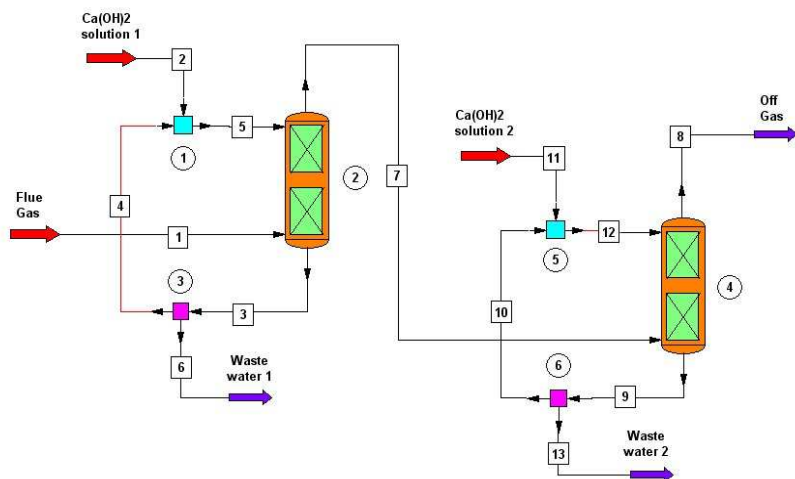


Figure 1. Simulation of wet flue gas purification using ChemCAD

For simulation the scrubbing unit waste incineration plant, the parameters presented in the table 2 were used [2, 3].

Table 2.

| Parameters of the model | | |
|-------------------------|----------------------------|------------------------|
| Column | 1 | 2 |
| Component removed | HCl | SO ₂ |
| Scrubbing - Liquor | 10 wt% Ca(OH) ₂ | |
| pH | 1 | 8 |
| No. of stage | 2 | 4 |
| Top pressure | 1 atm | 1 atm |
| Legal Limits | 15 mg/Nm ³ | 100 mg/Nm ³ |

*) calculated as Cl⁻

3. RESULTS AND DISCUSSIONS

The scrubbing unit waste incineration plant was modeled and simulated using process data presented above. In the both columns, the total vapor flow decrease because of the absorption of acid gas components (hydrochloric acid, hydrofluoric acid and sulfur dioxide) in the alkaline solution (calcium hydroxide).

In the first absorption column, the hydrochloric acid and hydrofluoric acid content of flue gas is reduced at pH value of 1, and in the second absorption column the sulfur dioxide is reduced at pH value of 8.

The variation of total vapor flow, total liquid flow and hydrogen chloride flow for the first column are presented in the figures 2, 3 and 4.

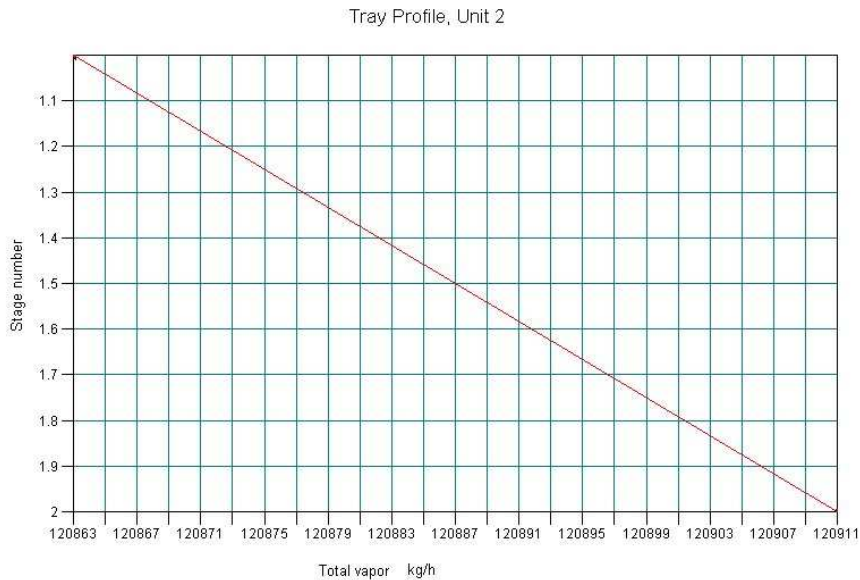


Figure 2. Variation of the total vapor flow for the first absorption column

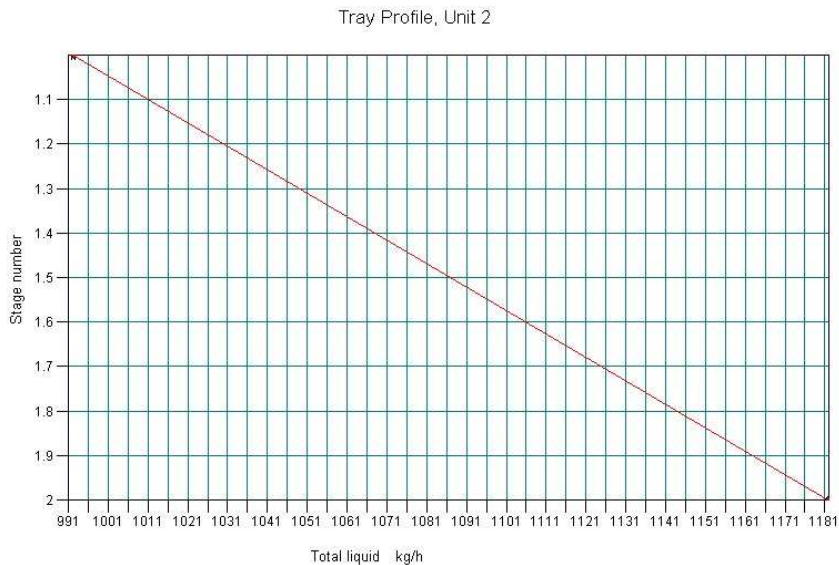


Figure 3. Variation of the total liquid flow for the first absorption column

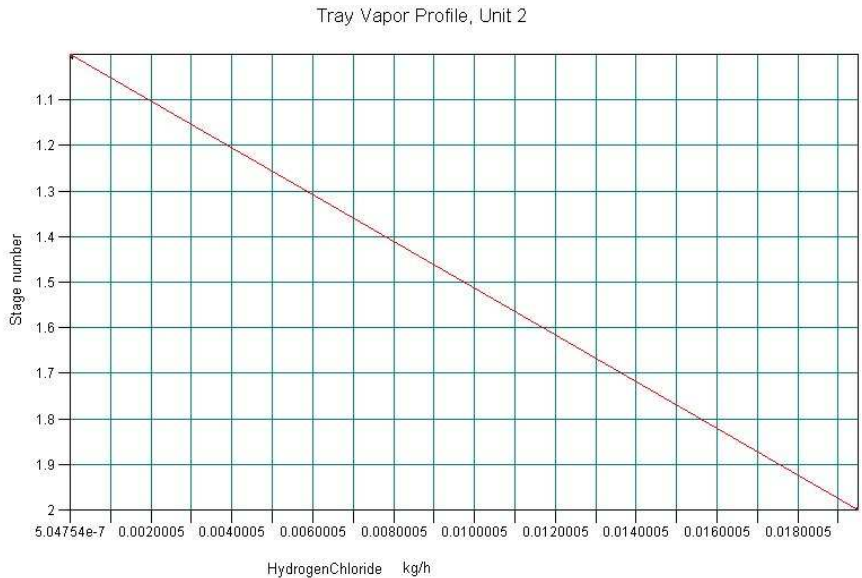


Figure 4. Variation of the hydrogen chloride flow for the first absorption column

The variation of total vapor flow, total liquid flow and sulfur dioxide flow for the second column are presented in the figures 5, 6 and 7.

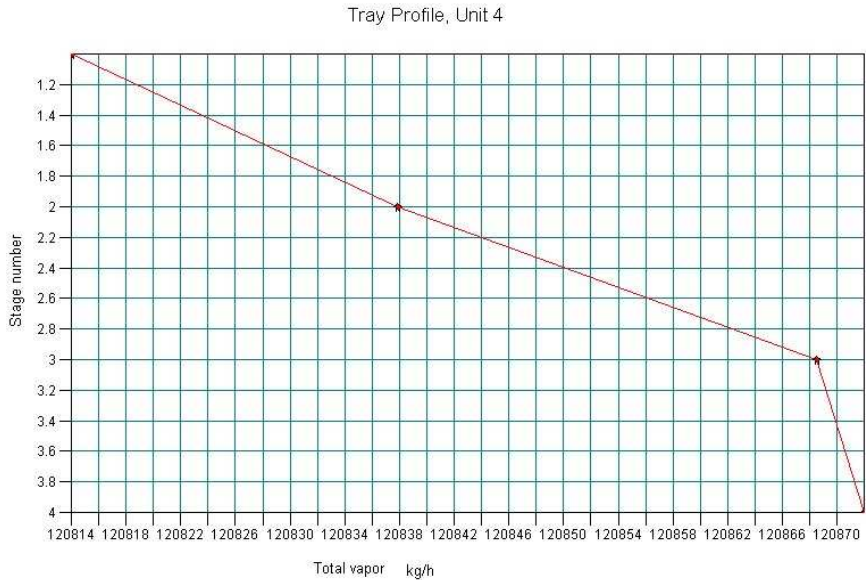


Figure 5. Variation of the total vapor flow for the second absorption column

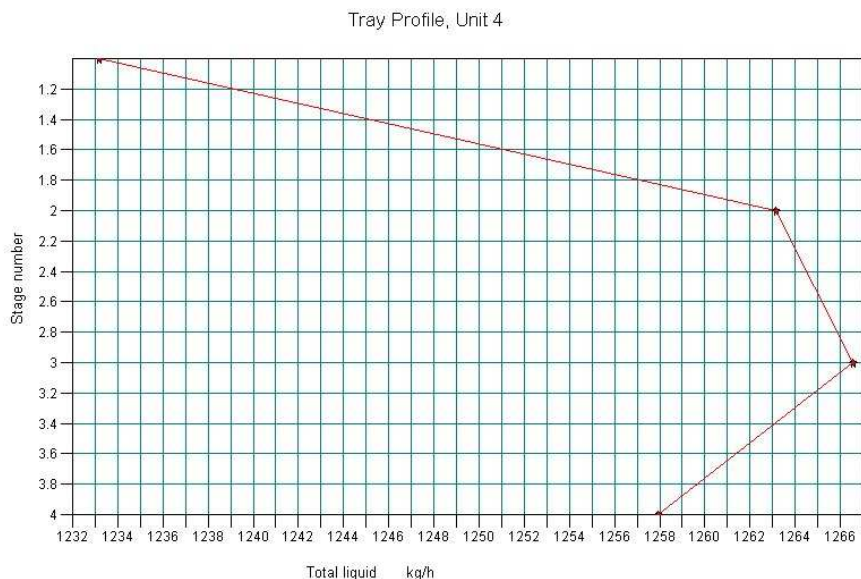


Figure 6. Variation of the total liquid flow for the second absorption column

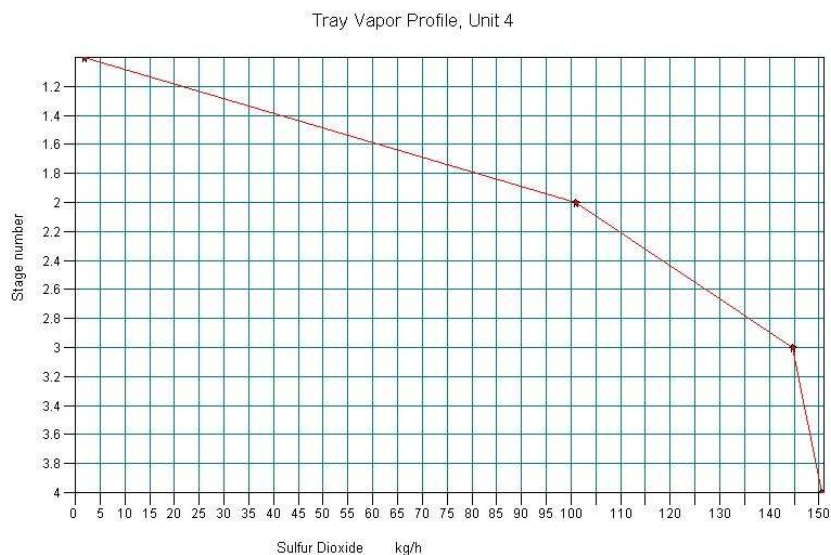


Figure 7. Variation of the sulfur dioxide flow for the second absorption column

The results obtained from simulation using ChemCAD show that the hydrochloric acid and sulfur dioxide content of the flue gas coming from waste incineration plants was reduced in order to meet the legal limits.

The hydrogen chloride and sulfur dioxide content of the off gas is 1.8243×10^{-10} [wt%] and respective 0.0016 [wt%]. The calcium hydroxide solution consumption is 825 kg/h for the first absorption column and 1100 kg/h for the second absorption column.

The simulation results and real plant operation data [3] for output gas flows from the first and second columns are presented in the table 3.

Table 3.

The composition of output gas flow from first and second scrubbing unit

| Parameter | Unit | Output first column (flow 7) | Output second column (flow 8) | Real plant data (plant emissions) |
|------------------|--------|---------------------------------|----------------------------------|--------------------------------------|
| CO ₂ | [wt%] | 14.4685 | 14.4733 | 14.5 |
| CO | [wt%] | 0.0033 | 0.0033 | 0.0032 |
| O ₂ | [wt%] | 8.9868 | 8.9863 | 8.4 |
| N ₂ | [wt%] | 69.9314 | 69.9552 | 70.58 |
| H ₂ O | [wt%] | 6.453 | 6.5453 | 6.5 |
| SO ₂ | [wt%] | 0.1242 | 0.0016 | 0.002 |
| SO ₃ | [wt%] | 0.0001 | 0.0001 | 0.0001 |
| NO ₂ | [wt%] | 0.0355 | 0.0344 | 0.0066 |
| HCl | [wt%] | 1.8257×10^{-10} | 1.8243×10^{-10} | 0.000375 |
| HF | [wt%] | 0.0002 | 0.4025×10^{-8} | 0.000016 |
| Flow | [kg/h] | 120863.2 | 120227.5 | 120000 |

The output liquid flows coming from the first and the second absorption columns (flows 3 and 9 from the figure 1) have the following pH values: 1.02 for the first column and 8.76 for the second column (in a real plant pH values are 1 and 8). The calcium hydroxide consumption resulted by simulation is 192 kg/h, compared with 190 kg/h in a real plant [3].

Modeling and simulation of the scrubbing unit waste incineration plant using ChemCAD, certifies a good pollutants removal at low calcium hydroxide consumption.

4. CONCLUSIONS

Modeling and simulation of the scrubbing unit waste incineration plant was done using ChemCAD software package (version 5.1.3).

The absorption process of acid components (HCl, SO₂, HF) coming from incineration plant was done using calcium hydroxide solution (10 % mass percent) in two absorption columns. The first absorption column is used to reduce hydrochloric acid (HCl) and hydrofluoric acid (HF) from flue gas at pH value of 1. The second absorption column is used to reduce sulfur dioxide (SO₂) from flue at pH value of 8.

The evolutions of the process parameters (liquid and gaseous flows, composition of the flue gas) were studied during the process. The simulation results were compared with real plant operation data in order to validate the application developed for the absorption process.

The mathematical model and the simulation results, using ChemCAD proved to be a reliable tool for analyzing the process of removing hydrochloric acid (HCl) and sulfur dioxide (SO₂) from gaseous emissions coming from waste incineration plants.

REFERENCES

- 1 Schuster G., Weigl K., Friedl A., Implementation of flue gas cleaning systems into an object-oriented process simulator for practical use, European Symposium on Computer Aided Process Engineering, ESCAPE 10, 7 – 10 May 2000, Florence, Italy
- 2 Kaiser S., Weigl K., Spiess-Knafl K., Aicherling C., Friedl A., Modeling a dry scrubbing flue gas cleaning process, Chemical Engineering and Processing 39, 2000, page 425 - 432
- 3 Schausberger P., Weigl K., Friedl A., Process Simulation: Enhancement of waste incineration plant simulation by covering flue gas cleaning balances, Pres'01 Proceedings, 20 – 23 May 2001, Florence, Italy
- 4 Cormos C., Mathematical modeling and simulation of racemic calcium pantothenate synthesis, Ph.D. Thesis, 2004, Cluj – Napoca, Romania

STRUCTURAL, ENERGETIC AND ELECTRONIC PROPERTIES OF PURE/DOPED BN NANOTUBES

SIMONA RADA¹, IOAN SILAGHI DUMITRESCU¹

¹Department of Chemistry, "Babeș-Bolyai" University, Cluj-Napoca, Ro-400084, Romania

ABSTRACT. The effects of chirality, length of tube, the influence of possible defects of atoms (due to deviations from the 1:1 stoichiometry or by the presence of other elements like aluminum or carbon) inside of single walled boron-nitride nanotubes on structural, energetic and electronic properties has been considered in this paper. The doping leads to thermodynamic instability of the armchair tubes. The chiral BN nanotubes can behave as a semiconductor or as an insulator depending on their chirality, diameter or length of tube whereas their analogues with armchair and zigzag geometry exhibit a constant band gap of 5-6eV.

1. Introduction

Experimental data and theoretical calculations have shown that carbon nanotubes¹ can behave either as a semiconductor or as a metal depending on their radius and chirality²⁻⁶, which is not desired in applications on nanodevices. The BN nanotubes may be good for possible applications in nanodevices because they have a constant band gap around 5,5eV independent of their diameter and chirality⁷⁻¹⁵.

Solids are characterized by a band structure in which the highest occupied band is called the valence band (*HOMO* orbital) and the lowest unoccupied band is called the conduction band (*LUMO* orbital). The energy difference between the bottom of the conduction band and the top of the valence band in a semiconductor or an insulator is called the band gap energy, E_g . The bandwidth of the band gap provides a distinction between a semiconductor and an insulator. When the band gap is not very large, usually ranging from 0,5 to 3,0eV, the material is a semiconductor, while an insulator has an $E_g > 3\text{eV}$,^{16, 17}.

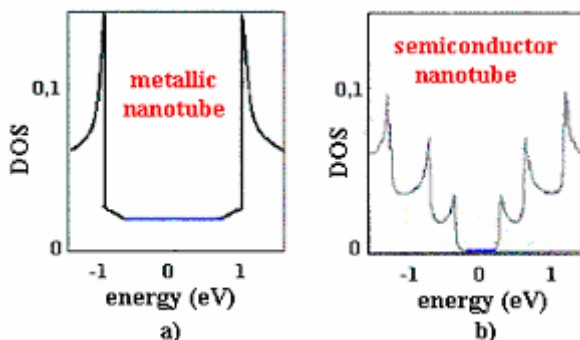


Figure 1. The density of states plots for metallic and semiconductor carbon nanotube^{18, 19, 20}.

Electrons in metals, semiconductors and insulators are described by the Bloch wave function. This function is a plane wave $e^{ik \cdot R}$ in the 3D space modulated by a function $\Phi_k(x, y, z)$ having the periodicity of the crystal lattice in which the electrons move. According to Pauli exclusion principle no more than two electrons can found in the same Bloch wave function. The number of Bloch wave function states in the range of energies from E to $E + dE$ is called the density of states (DOS).

The shapes of the DOS plot for metallic and semiconductor nanotubes are shown in figure 1. The density of states at the Fermi energy is finite for a metallic tube and zero for a semiconductor tube.

The sharp peaks in density of states represent Van Hove singularities. They are typical for one-dimensional systems and dominate the density of states²⁰.

The aim of this study was to determinate the structural, energetic and electronic properties of the pure/doped boron nitride nanotubes. In order to examine these properties we explored theoretical models. The effects of chirality, length of tube, the influence of possible defects of atoms have been investigated. The electronic properties analysis has been carried out by density of states plots.

2. Methods of calculation

In this paper, various open ended single-walled BN nanotubes of the zigzag, armchair and chiral types, have been submitted to molecular-mechanics²¹ and semiempirical molecular orbital calculations²² (at AM1 and PM3 levels²³) using the HyperChem 4.5 and Spartan'02 software^{24, 25}.

To obtain the densities of state (DOS) of BN nanotubes, Hückel tight-binding calculations by BICON-CEDIT package²⁶ have been performed.

3. Results and discussion

A) Structural and energetic properties of BN nanotubes

The structures of the BN nanotubes with armchair, zigzag and chiral geometry^{27,28} were taken from reference²⁹. For the optimized structures at PM3 level, we found that the boron-nitrogen distances vary between 1,40 and 1,45Å, the B-N-B angles ranging from 112 and 120° and the N-B-N angles between 109 and 120°.

In the present work we have calculated the enthalpies of formation (ΔH) for a series of single-walled boron nitride nanotubes with zigzag ($n=5,6,7,\dots,14$), armchair ($n=m=5,6,7$) and chiral ($n=7, m=1,2,3,\dots,6$) geometry of various chirality and compared with those for carbon nanotubes.

Figure 2 giving the variation of the enthalpies of formation/atom of the carbon and boron nitrogen nanotubes, shows that thermodynamic stabilization depends on the chiral vector, n . It is noteworthy to mention that the boron nitride nanotubes are thermodynamically stabilized with the increasing of the chiral vector, n . We got similar conclusions for tubes with armchair and chiral geometry, figures 3 and 4. These studies suggest that all BN nanotubes are thermodynamically more stable than their carbon analogues.

In order to check the validity of these trends, ab initio RHF/3-21G calculations have been carried out on the AM1 optimized geometries of (5,5), (10,0), (7,3)BN nanotubes. The results confirm that the (5,5)BN tube is more stable than the (7,3)BN (with 258.41kcal/mol) and (10,0)BN nanotube (with 501.95kcal/mol), respectively.

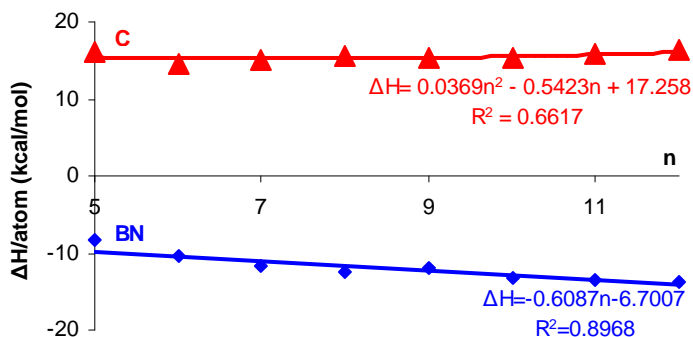


Figure 2. Enthalpy of formation (per atom) as a function of the chiral vector n for $(n,0)$ C/BN nanotubes with $n=5, 6, \dots, 14$.

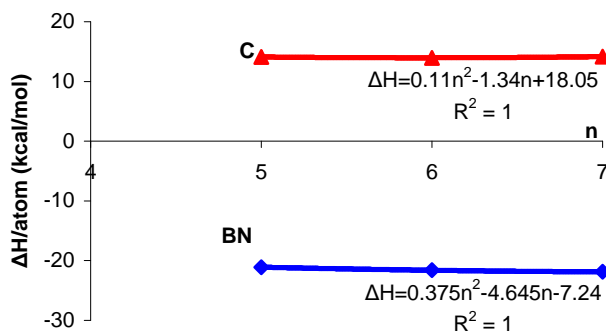


Figure 3. Enthalpy of formation (per atom) as a function of the chiral vector n for (n,n) C/BN nanotubes with $n=5, 6, 7$.

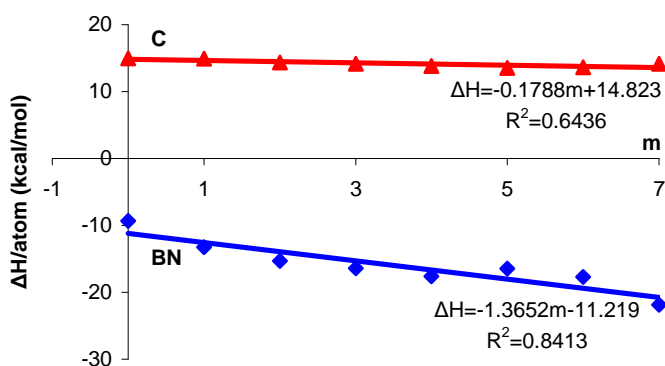


Figure 4. Enthalpy of formation (per atom) as a function of the chiral vector m for $(7,m)$ C/BN nanotubes with $m=0, \dots, 7$.

The above-mentioned reasons, motivated us to study the possible defects of the BN nanotubes that might stabilize the zigzag and chiral geometry.

B)The influence of possible defects of the BN nanotubes

In the synthesis of BN nanotubes, different kinds of defects due to the deviation from the 1:1 stoichiometry or to the presence of other elements like carbon or aluminum may appear in their structure. We analyzed these influences on energetic and electronic properties of the tubes. For this, we substituted two atoms of nitrogen located at the tip edges of the tubules with boron, carbon or aluminum, figure 5.

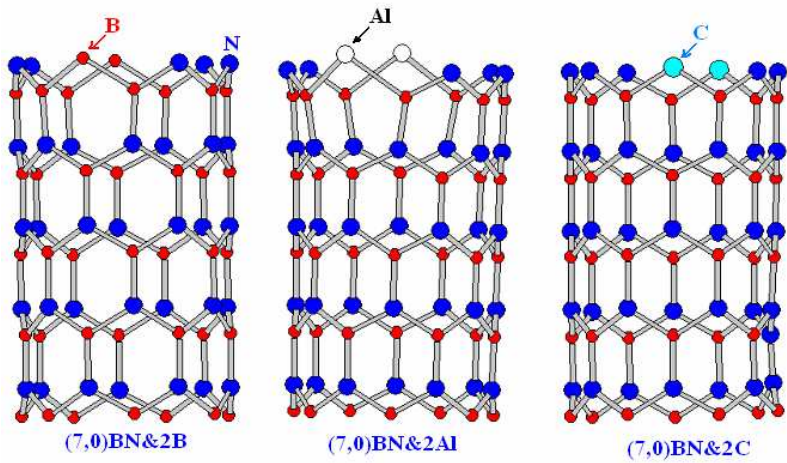


Figure 5. Structural models of doped boron nitride nanotube (L=4).

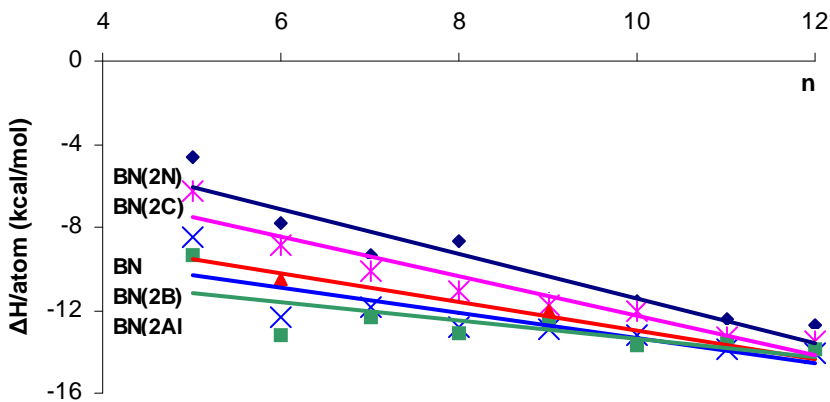


Figure 6. Enthalpy of formation (per atom) as a function of the chiral vector n for the doped $(n,0)$ BN nanotubes with $n=5,6,\dots,14$. Display equations and R-square values on chart:

$$\begin{aligned}
 \text{BN(2N): } \Delta H &= -1.0671n - 0.7518; & R^2 &= 0.8845 \\
 \text{BN(2C): } \Delta H &= -0.9481n - 2.8187; & R^2 &= 0.915 \\
 \text{BN: } \Delta H &= -0.6835n - 6.1419; & R^2 &= 0.8659 \\
 \text{BN(2B): } \Delta H &= -0.6079n - 7.2857; & R^2 &= 0.7101 \\
 \text{BN(2Al): } \Delta H &= -0.4486n - 8.9121; & R^2 &= 0.5618.
 \end{aligned}$$

Graph 6 shows comparatively the stability of the BN tubes for different doping atoms. Boron and aluminium doping stabilises the zigzag BN nanotubes while carbon or an excess of nitrogen leads to instability of the tubes. Chiral BN nanotubes are stabilized only by aluminium, figure 7. In contrary to these, the presence of any dopant conducts to instability of the armchair tubes, figure 8.

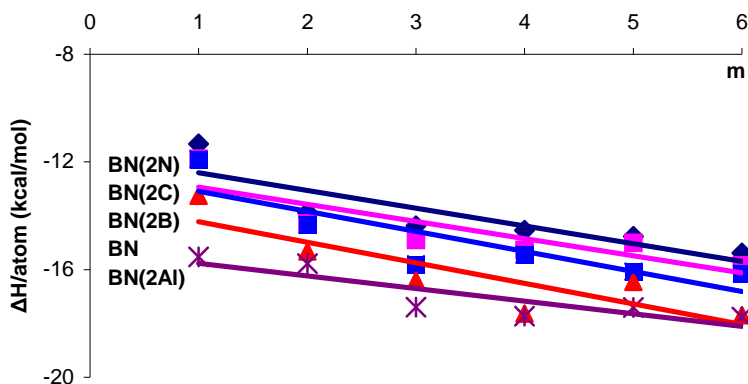


Figure 7. Enthalpy of formation (per atom) as a function of the chiral vector m for the doped $(7, m)$ BN nanotubes with $m=1, \dots, 6$. Display equations and R-square values on chart:

$$\begin{aligned}
 \text{BN(2N): } \Delta H &= -0.6597m - 11.736; & R^2 &= 0.7573 \\
 \text{BN(2C): } \Delta H &= -0.638m - 12.295; & R^2 &= 0.7339 \\
 \text{BN(2B): } \Delta H &= -0.7449m - 12.348; & R^2 &= 0.7299 \\
 \text{BN: } \Delta H &= -0.7646m - 13.454; & R^2 &= 0.7441 \\
 \text{BN(2Al): } \Delta H &= -0.4691m - 15.295; & R^2 &= 0.7583.
 \end{aligned}$$

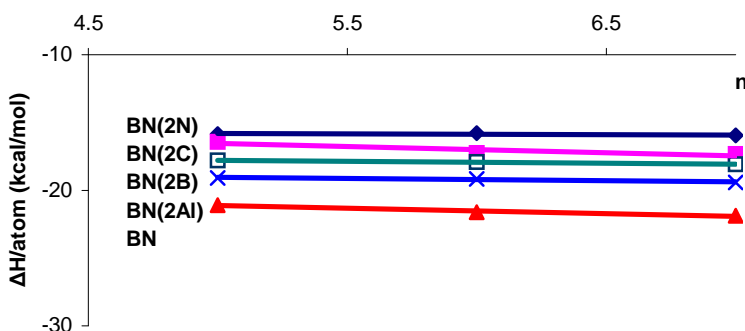


Figure 8. Enthalpy of formation (per atom) as a function of the chiral vector n for the doped (n, n) BN nanotubes with $n=5, 6, 7$. Display equations and R-square values on chart:

$$\begin{aligned}
 \text{BN(2N): } \Delta H &= -0.05n - 15.57; & R^2 &= 0.3425 \\
 \text{BN(2C): } \Delta H &= -0.45n - 14.3; & R^2 &= 0.8242 \\
 \text{BN(2B): } \Delta H &= -0.145n - 17.057; & R^2 &= 0.9902 \\
 \text{BN(2Al): } \Delta H &= -0.165n - 18.227; & R^2 &= 0.9187 \\
 \text{BN: } \Delta H &= -0.395n - 19.157; & R^2 &= 0.9677.
 \end{aligned}$$

Table 1.

Calculations of the $E_{\text{HOMO}}-E_{\text{LUMO}}$ for doped BN nanotubes.

| tube | $E_{\text{HOMO}}-E_{\text{LUMO}}$ (eV) | | | | |
|---------|--|---------|--------|--------|------|
| | BN(2C) | BN(2Al) | BN(2B) | BN(2N) | BN |
| (5, 0) | 4.49 | 4.28 | 4.68 | 4.69 | 5.57 |
| (6, 0) | 4.5 | 4.45 | 4.7 | 5.09 | 5.37 |
| (7, 0) | 4.79 | 4.74 | 5.04 | 5.25 | 5.66 |
| (8, 0) | 4.67 | 5.03 | 4.97 | 5.28 | 5.59 |
| (9, 0) | 4.57 | 5.18 | 5.1 | 5.97 | 5.59 |
| (10, 0) | 4.32 | 5.33 | 5.58 | 5.3 | 5.57 |
| (11, 0) | 4.4 | 4.9 | 5.02 | 5.4 | 5.5 |
| (12, 0) | 4.5 | 5.2 | 5.45 | 5.52 | 5.61 |
| (13, 0) | 4.6 | 5.3 | 5.3 | 5.5 | 5.7 |
| (14, 0) | 4.7 | 5.1 | 5.4 | 5.6 | 5.4 |
| (5, 5) | 2.68 | 6.51 | 8.09 | 8.27 | 8.67 |
| (6, 6) | 1.92 | 6.5 | 8.16 | 8.24 | 8.66 |
| (7, 7) | 4.73 | 6.59 | 5.52 | 8.49 | 8.66 |
| (7, 1) | 4.64 | 5.4 | 4.3 | 4.96 | 4.01 |
| (7, 2) | 4.72 | 4.44 | 5.14 | 4.86 | 5.58 |
| (7, 3) | 1.81 | 4 | 4.64 | 4.15 | 4.28 |
| (7, 4) | 3 | 4.1 | 4.5 | 4.7 | 4.92 |
| (7, 5) | 2.7 | 4 | 4.25 | 4.5 | 4.7 |
| (7, 6) | 3.84 | 3.9 | 4 | 4.35 | 4.5 |

The possible defects of the BN nanotubes lead to small values of their energies gap ($E_{\text{HOMO}}-E_{\text{LUMO}}$), table 1, so the kinetic stability is lower compared to the corresponding pure analogues.

C) Electronic properties of the pure/doped BN nanotubes

The effect of chirality and length of the tube

The fact that the electronic properties of the carbon nanotubes depend upon their chirality and diameter makes them unsuitable for use in some electronic devices.

One of the current research topics in this area is the influence of different chiralities and lengths of the BN tubes on electronic properties for possible applications on nanodevices (actuators³⁰, nanoscale diodes^{31, 32}). We calculated the electronic properties of zigzag ($n=5, \dots, 9$), armchair ($n=5, 6, 7$) and chiral ($n=5, m=1, 2, 3$) BN nanotubes.

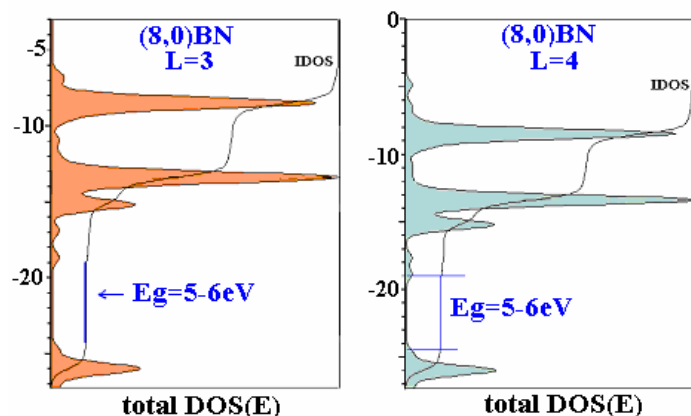


Figure 9. The total DOS(E) and IDOS plots of the zigzag BN nanotubes.

The results obtained for (8,0)BN nanotubes with $L=3$ and 4 are revealed in figure 9. From the DOS(E) plots it is obvious that the lowest bands (valence band) are composed of N(2s) derived states and the conduction bands consist of N(2p) and B(2s, 2p) derived states.

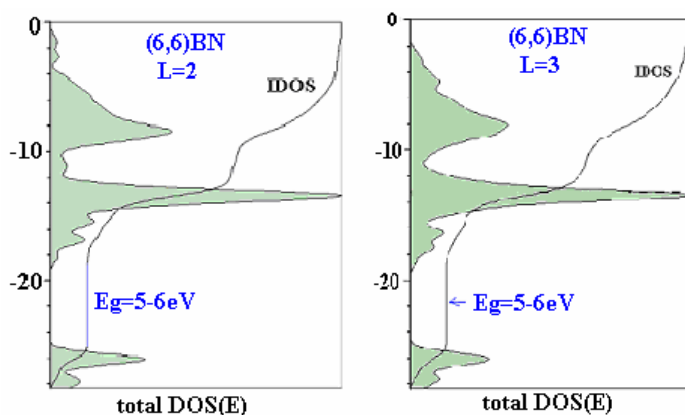


Figure 10. The total DOS(E) and IDOS plots of the armchair BN nanotubes.

An important aspect of this section is that all zigzag tubes can exhibit an insulating behavior (figure 9). Similar conclusions are derived from figure 10 for armchair nanotubes, in agreement with the predictions of Blasé¹⁹.

The total DOS for (5,3)BN nanotube with $L=3$ and 4 is shown in figure 11. From the DOS(E) plots it is clear that the long tube ($L=4$) is a semiconductor while the short tube ($L=3$) have an insulator character. It is also important to notice that the chiral tubes can behave either as a semiconductor or as an insulator dependent on chirality, diameter or length of the tube.

Consequently, these simple studies provide evidence for possible applications of the armchair and zigzag BN nanotubes on nanodevices.

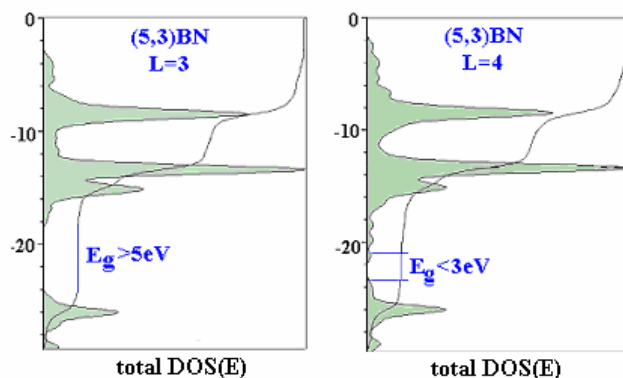


Figure 11. The total DOS(E) and IDOS diagrams of the chiral BN nanotubes.

The influence of possible defects of the BN nanotubes

In case of doping with boron, nitrogen and aluminum, the electronic states near the forbidden bands displays gap energies of 5-6eV independent on the geometry of the tube. Thus, the lowest bands are composed of N (2s) derived states and the highest band of N(2p), B(2s, 2p) and Al(3s, 3p) contributions, figure 12. The valence bands are slightly affected by metal intercalation.

The Fermi level is located in the middle of Van Hove singularities corresponding to N p-orbital derived states. This is considered an indication [33] that there is overlap with boron and aluminium s, p-orbital. The gap energy of 5eV implies insulator properties.

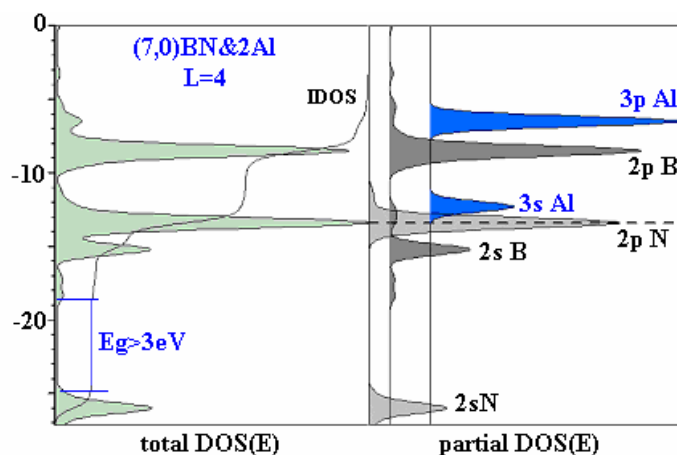


Figure 12. The partial, total DOS(E) and IDOS plots for (7,0)BN&2Al nanotube.

Doping the BN tube with carbon changes the electronic properties of the zigzag and chiral tube by new bands (Figure 13a,b). This bands correspond to an acceptor level in semiconductors with very low dopant concentration, so that both gap energies are smaller than 3eV and the tube became semiconductors.

Defects brought by deviations from the 1:1 stoichiometry or by the presence of aluminium lead to slight tube-impurities interactions and insignificant modification of the electronic properties. By contrast, doping with carbon decreases the energy gap until a semiconductor behavior.

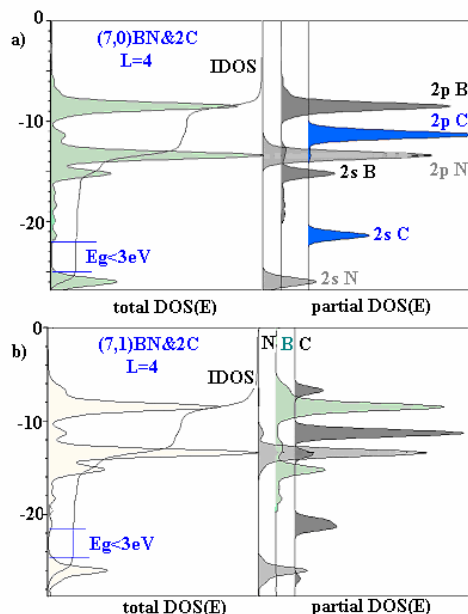


Figure 13. The total DOS and IDOS plots of the (7,0) and (7,1)BN&2C nanotube. The N(2s, 2p), B(2s, 2p) and C(2s, 2p) contributions to the DOS are projected.

Interestingly, the chiral BN nanotubes can behave either as a semiconductor or as an insulator and only changing their structure (chirality, length) controls their band gap.

The armchair and zigzag BN nanotubes may also be suitable for electronic devices because they have a constant band gap around 5-6 eV independent of their radius, chirality, length and different kinds of defects due to the deviation from the 1:1 stoichiometry or the presence other elements like aluminum.

Conclusion

All BN nanotubes are thermodynamically more stable relative to their carbon analogues. The armchair BN tubes are more stable than the chiral and zigzag nanotubes, respectively. The thermodynamic stability of the zigzag BN nanotubes can be enhanced by adding aluminium or boron while the chiral tubes can be stabilized by adding only aluminium.

The zigzag and armchair BN nanotubes possess a band gap of 5-6 eV independent of the chirality, length of tube and defects types. In contrast, the energy gaps of the chiral BN tubes can be controlled only by changing their structure. Note also that boron, nitrogen and aluminum doping modifies insignificantly the electronic properties of the BN nanotubes whereas carbon atoms diminish the energy gap until a semiconductor behavior.

Acknowledgements. We thank Prof. G. Calzaferri for the access to the BICON-CEDIT packages of programs.

REFERENCES

1. S. Iijima, *Nature*, **1991**, 354, 56.
2. N. Hamada, S. Sawada, A. Oshiyama, *Phys. Rev. Lett.*, **1992**, 68, 1579.
3. A. Hassanien, M. Tokumoto, Y. Hamazawa, H. Kataura, Y. Maniwa, S. Suzuki, Y. Achiba, *Appl. Phys. Lett.*, **1998**, 73, 3839.
4. A. Hassanien, M. Tokumoto, S. Ohshima, Y. Kuriki, F. Ikazaki, K. Uchida, M. Yumura, *Appl. Phys. Lett.*, **1999**, 75, 2755.
5. R. Saito, M. Fujita, G. Dresselhaus, M. S. Dresselhaus, *Appl. Phys. Lett.*, **1992**, 60, 2204.
6. N. Hamada, S. Sawada, A. Oshiyama, *Phys. Rev. Lett.*, **1992**, 68, 1579.
7. X. Blasé, A. Rubio, S. G. Louie, M. L. Cohen, *Europhys. Lett.*, **1994**, 28, 335.
8. X. Blasé, J. C. Charlier, A. De Vita, R. Car, *Appl. Phys. Lett.*, **1997**, 70, 197.
9. D. L. Carroll, P. Redlich, X. Blasé, J. C. Charlier, S. Curran, P. M. Ajayan, S. Roth, M. Ruthle, *Phys. Rev. Lett.*, **1998**, 81, 2332.
10. R. Czerw, M. Terrones, J. C. Charlier, X. Blasé, B. Foley, R. Kamalakaran, N. Grobert, H. Terrones, D. Tekleab, P. M. Ajayan, W. Blau, M. Rühle, D. L. Carroll, *Nano Lett.*, **2001**, 1, 457.
11. J. C. Charlier, M. Terrones, M. Baxendale, V. Meunier, T. Zacharia, N. L. Rupasinghe, W. K. Hsu, N. Grobert, H. Terrones, G. A. J. Amaratunga, *Nano Lett.*, **2002**, 2, 1191.
12. G. Calzaferri, R. Rytz, *J. Phys. Chem.*, **1995**, 99, 12141.
13. J. O. Lu, *Phys. Rev. Lett.*, **1995**, 74, 1123.
14. A. Rubio, Y. Miyamoto, X. Blasé, M. L. Cohen, S. G. Louie, *Phys. Rev.*, **1996**, 53B, 4023.
15. J. Zhao, J. Han, J. P. Lu, *Phys. Rev.*, **2002**, 65B, 193401.
16. N. C. Greenham, R. H. Friend, *Solid State Physics, Advances in Research and Application*, edited by H. Ehrenreich and F. Spaepen, **1995**, 49, 1, Academic Press, New York.
17. C. Dekker, *Physics Today*, **1999**, may, 22.
18. J. Kongsted, A. Osted, L. Jensen, P. O. Astrand, K. V. Mikkelsen, *J. Phys. Chem.*, **2001**, 105 B, 10243.
19. X. Blasé, J. C. Charlier, A. De Vita, R. Car, *Appl. Phys. (Materials-Science-Processing)*, **1999**, 68 A, 293.
20. K. Gofron, H. Ding, C. Gu, R. Liu, B. Dabrowski, B. Veal, W. Cramer, G. Jennings, *J. Phys. Chem. Solids*, **1993**, 54, 1193.
21. N. L. Allinger, *J. Am. Chem. Soc.*, **1977**, 99, 8127.
22. J. J. P. Stewart, *QCPE Bulletin*, **1989**, 9, 80.
23. M. J. S. Dewar, E. G. Zebisch, E. F. Healy, J. J. P. Stewart, *J. Am. Chem. Soc.*, **1985**, 107, 3902.
24. *HyperChem*, release 4.5 for SGI, 1991-1995, HyperCube, Inc.
25. *Spartan'02*, Wavefunction, Inc., Irvine, C.A.
26. M. Brandle, R. Rytz, G. Calzaferri, *BICON-CEDIT – manual*, Bern, **1997**.
27. N. Hamada, S. Sawada, a. Oshiyama, *Phys. Rev. Lett.*, **1992**, 68, 1579.
28. Ş. Erkoc and S. Ozkaymak, *Eur. Phys. J.*, **1998**, 4D, 331.
29. S. Weber, <http://www.jcystal.com/steffenweber/JAVA/jnano/jnano.html>, 2000.
30. K. H. Baughman, C. Cui, A. A. Zakhidov, Z. Iqbal, J.N. Baricci, G. M. Spinks, G. G. Wallace, A. Mazzoldi, D. De Rosi, A. G. Rinzier, O. Jaschinski, S. Roth, M. Kertesz, *Science*, **1999**, 284, 1340.
31. S. F. Bent, *Conference 2003: Novel Electronic Materials*, Stanford.
32. P.E. Lammert, V. H. Crespi, A. Rubio, *Phys. Rev. Lett.*, **1999**, 299, 368.
33. E. Cappelluti, L. Pietronero, *Europhys. Chem.*, **1996**, 36, 619.

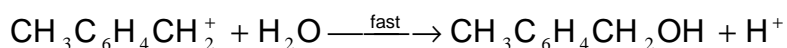
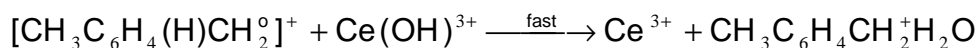
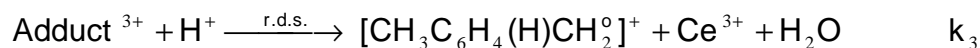
ERRATUM

KINETICS AND MECHANISM OF *P*-XYLENE OXIDATION BY CE(IV) IN AQUEOUS ACID MEDIUM. LFER AS AN ARGUMENT TO THE OXIDATION MECHANISM

GABRIELA-CRISTINA BUCȘA AND IOAN BÂLDEA

(Article appeared in *Studia Univ. Babeș-Bolyai. Chem. L (1)*, 2005, 157-168)

Some errors were discovered in the article mentioned concerning the mechanism of the title reaction (p.165) and the rate law from the mechanism (eqn. 13). The correct mechanism and rate law are as follows:



$$r = \frac{d[\text{Ce}(\text{IV})]_t}{dt} = \frac{k_3 K_2 [\text{p-xylene}][\text{H}^+]}{1 + K_h^{-1}[\text{H}^+] + K_2[\text{p-xylene}]} [\text{Ce}(\text{IV})]_t \quad (13)$$

The rate law has the same form as the published one and the conclusions remain the same.